1st Euro-Mediterranean Conference on Structural Dynamics and Vibroacoustics

PROCEEDINGS

23-25 April 2013 Marrakech (Morocco)

Organizing associations

ADYVA: A French association for Structural Dynamics and Vibroacoustics created in 2011
SFA-GVB: The Vibroacoustic group of the French Society of Acoustics
AMVA: The Moroccan Association for Acoustic and Vibration
ATAVI: The Tunisian association for Acoustic and Vibration
IOA: The Institute of Acoustic of the Chinese Academy of Sciences

Organizing Board

Manuel Collet (FEMTO-ST – CNRS, France) - General Chair
Mohamed Ichchou (LTDS – ECL, France) - General Co-Chair
Charles Pézerat (LAUM – Univ du Maine, France) - Technical Program Co-Chair
Rhali Benamar (EMI - Um5a, Morocco) - Regional Program Co-Chair – Morocco
Mohamed Haddar (ENIS, Tunisia) - Regional Program Co-Chair – Tunisia
Fusheng Sui (IOA-CAS, China) - Regional Program Co-Chair – Asia
Emmanuel Foltête (FEMTO-ST – ENSMM, France) - Organizing Committee Co-Chair – Treasurer

Honorary Chairs

Daniel Juvé (Professor Ecole Centrale de Lyon)
Anders Nilsson (Royal Institute of Technology, Stockholm)
Roger Ohayon (Emeritus Professor CNAM, Paris)
Jing Tian (President of Acoustical Society of China)

Scientific Committee

Makrem Arfaoui (ENIT, TN)
Pierre Argoul (ENPC, FR)
J. Roberto Arruda (Unicamp, BR)
Noureddine Atalla (GAUS, CAN)
Mohamed Belhaq (FSAC, MA)
Mabrouk Ben Tahar (UTC, FR)
Noureddine Bouhaddi (FEMTO, FR)
Claude Boutin (ENTPE, FR)
Scott Cogan (FEMTO-ST, FR)
Kenneth A. Cunefare (GT, US)
Sergio Da Rosa (UNINA, IT)
Arnaud Deraemaeker (ULB, BE)
Wim Desmet (KUL, BE)
Jean-François Deü (CNAM, FR)
Régis Dufour (INSA, FR)
Tahar Fakhakh (TN)
François Gautier (LAUM, FR)
Bilal Harras (FST Fes, MA)
Jean-Claude Golinval (ULG, BE)
Mohamed-Ali Hamdi (UTC, FR)
Lotfi Hammami (ENIS, TN)
Jan Holnicki (IPPT, POL)
Eric Jacquelin (UCBL, FR)
Chafik Karra (TN)
Alexandre Kawano (U Sao Paolo, BR)
Gaetan Kerschen (ULG, BE)
Robin Langley (Cambridge, UK)
Alain Le Bot (ECL, FR)
Lin Li (SPJ, CN)
Hervé Lissek (EPFL, CH)
Brian Mace (U. Southampton, UK)
Jarir Mahfoud (INSA, FR)
Morvan Ouisse (FEMTO-ST, FR)
Joel Perret-Liaudet (ECL, FR)
Stephan Rinderknecht (TUD, DE)
Rubens Sampaio (PUC, BRA)
Fabrizio Scarpa (U. Bristol, UK)
Jun Yang (IOA, CN)
Abdelmalek Zine (ECL, FR)

Organizing Committee

B. Harras (Univ. Fez, MA), M. Belhaq (Univ. Casablanca, MA) - Accommodations, Registrations
M. Ouisse (FEMTO-ST – ENSMM, FR), Y. Li (IOA-CAS, CN) - Program
V. Guicheret-Retel (FEMTO-ST – ENSMM, FR), O. Bareille (ECL, FR) - Web site
M. Ouisse (FEMTO-ST – ENSMM, France), J.F. Deü (CNAM, FR) - Proceedings Edition
M.S. Abbes (ENIS, TU), X. Cheng (IOA-CAS, CN) - Logistics

Conference information

Registration

The registration desk will be open from 8.00 to 17.30 on Tuesday 23rd, from 8.30 to 17.00 on Wednesday 24th July and from 8.15 to 13.00 on Thursday 25th April. Each registered person will receive a conference badge, conference program and bag at the conference registration and check-in area. Please wear your badge at all times. In your bag you will find a USB drive with the proceedings of the conference. There will be no printed book of abstracts.

Venues

The opening and closing ceremonies and plenary lectures will take place in the Yves Rocard amphitheater. Special sessions and contributed talks will take place in parallel sessions in the Yves Rocard amphitheater and in the lecture rooms (Daa-You Maa, Al-Khawarizmi and Philip Ellis Doak).

Internet access

You can access the Internet via Palm Plaza hotel's Wi-Fi network using your own devices. The access code is palmplaza1

Important note to speakers

A PC computer with projector will be provided in each room on which all authors should load their presentations. Authors should bring computer presentations on a CD or USB drive to load onto the provided computer and should arrive at the rooms at least 20 minutes before the start of their sessions. Assistance in loading presentations onto the computers will be provided. Note that only PC format will be supported so authors using Macs must save their presentations for projection in PC format (ppt, pptx, pdf).

Best student paper award

The Medyna 2013 Best Student Paper Award will be delivered to encourage young researchers which will lead the next generation. The selection will be based upon the quality of the written paper and the presentation. The eligible authors must be enrolled as students at the time of the conference; must be the first author of the paper; must present the paper at the conference. Nominations must be made by the time of opening ceremony of the conference. The nominations will be evaluated by the Medyna 2013 Awards Committee. The winner of the 2013 Best Student Paper Award will receive a certificate and a money prize donated by the ADYVA association. The Award will be delivered during the Medyna 2013 closing ceremony.

Invited speakers

Adnan Akay (Bilkent University, Ankara, Turkey & Carnegie Mellon University, USA)

Dr. Akay started his tenure at Carnegie Mellon as a professor and head of the Mechanical Engineering Department in 1992. In 1997, he was awarded the endowed Lord Chair in Engineering. Between 2005 and 2008, Dr. Akay served as the Director of Civil, Mechanical and Manufacturing Innovation Division at the National Science Foundation. Currently he is on leave of absence at Bilkent University in Ankara, Turkey serving as Vice President and Professor, and founding head of the Mechanical Engineering Department. Professor Akay has held visiting appointments at the MIT Aeronautics and Astronautics Department, the University of Rome "La Sapienza," and INSA Lyon in France and other institutions. Dr. Akay continues to serve as a member of industry boards and regularly consults with international industries as a technical advisor and serves on advisory boards of several universities and government agencies including the US NSF - Taiwan NSC Summer Institute on Bio-inspired Sensing & Bio-inspired Actuation Technology. Professor Akay is an active member of the engineering professional community, and has been recognized for his contributions to research, education and professional service. Professor Akay is the recipient of the ASME Per Brüel Gold Medal (2005) and Humboldt Research Award (2011). He is a fellow of the American Society of Mechanical Engineers, a fellow of the Acoustical Society of America, and a member of several honor societies. Professor Akay's research lies in applied mechanics with emphasis on vibrations, acoustics, tribology, and dissipation theories. His earlier research that addressed impact and transient noise mathematically described conversion of energy associated with the acoustic mass to sound during transient motion. His work on fluid-layer damping later led to a discovery and visualization of streaming that develops within a thin fluid layer. Much of his current research focuses on friction-induced sounds and on contact damping. A current collaborative research project with the University of Rome applies the concept of thermalization of vibrations, inspired by the dynamics of atoms in a solid, to reduce vibrations in complex structures. This work is now extended to model dissipation in thermal baths that surround nano-scale devices. His current research with colleagues at INSA-Lyon focuses on measurement and modeling of parameters that can describe tactile sensation and wave generation between sliding surfaces.

Sound and Vibration From Friction Between Soft Materials Under Light Loads

Understanding the properties and consequences of friction under light normal loads is fundamental to further advancing areas such as tactile sensing, haptic systems used in robotic gripping of sensitive objects, and characterization of products that range from the softness of fabrics to effects of surfactants, such as lotions, on skin. In tactile sensing, as a finger is lightly rubbed over a surface, the mechanoreceptors in the dermis become excited and send signals to the brain for processing. Their excitation results from the asperities, adhesion, and other geometric and chemical surface properties that come into contact with the skin. These same sources also give rise to vibration and sound as two surfaces are in sliding contact even under light load, such as a finger pad over a silk fabric. Whereas the mechanoreceptors respond around 200 - 300 Hertz, spectrum of the actual sounds and vibrations that are generated can go beyond these values, thus presenting additional opportunities for surface characterization through acoustic response. A modest body of literature exists on the acoustic response of soft surfaces under friction. However, only a limited number of those address friction sounds and vibrations under light loads. Much of the previous work in this area relates to perception and tactile sensing with limited attention to the generation mechanisms of sound and vibration between soft surfaces. This paper describes a new apparatus to measure friction simultaneously with dynamic quantities such as accelerations, forces, and sound pressures resulting from a light contact over a soft material, much like a friction finger lightly rubbing over a soft material.

Hachmi Ben Dhia (Ecole Centrale Paris, FR)

Headmaster of MSSMat laboratory (Laboratoire Mécanique des Sols, Structures et Matériaux, Ecole Centrale Paris). Head of « structure-structure interaction » research team. Professor Ben Dhia main research concerns the modeling of interaction between structural components. Precisely, among Professor Ben Dhia developments are: the friction contact numerical modeling through three dimensional mixted formulation, extension of friction contact modeling to vibrating structures under impacts, extension of the Arlequin strategy and its analysis for multiscale mechanical problems.

Title of presentation: **Coupling of models and scales in the Arlequin framework**

Jérôme Buffe (Thales Alenia Space, FR)

Head of the mechanical department of THALES Alenia Space, Satellites and telecommunication Branch (CANNES). General Coordinator of mechanical activities across THALES Alenia Space. Senior Member of the 3AF (Aeronautics Astronautics French Association) into the "Stuctures" Commission. Active member in the development and implementation of European standardizations in the space sector (ECSS) and especially for the mechanical aspects.

New considerations on the validation and on the optimization of designs in the space domain

If there is one domain where optimizations on the designs are mandatory with regard to the mass constraints, where the reliability on the performances has to be well handled and where dynamic and static environments are of first importance, there are, for sure, the space activities and more specially the satellites.

The aim of this proposed presentation for Medyna 2013 conference is to talk about the different ways of dealing with the question of this complex situation and the compromise which has to be found. The current way is commonly called a deterministic process by using standard rules whatever the designs and by minimizing the safety margins. Another way is to use a probabilistic approach allowing the decider to design at an optimized technico economic level with regard to the performances and their criticality. Finally, another way could be to use a robustness approach when a lack of knowledge on the characteristics is there.

This new consideration on the validation of the designs is more and more up to date since the variability on the characteristics of the components and on the elementary pieces is increasing. The industrial world, even in space field, is faced to some evolutions dealing with eventual different characteristics to those already seen in the past and, so, impacting the current rules for validation and, by consequence, the optimizations.

Otherwise, due to the so very few numbers of specimens involved in the satellites production and with a so scattered growing distribution of the performances, the philosophy for an adequate qualification by test is also impacted with an appropriate choice on models and/or with a validation by an analytical process to be done in parallel.

As a conclusion, the presentation will be focused on the sensitization of this new situation which could be relatively critical for satellites and on the interest of some new methods to put into place in order to handle as much as possible the designs and to get the most appropriate solution for the optimization and robustness purposes.

In that context, a pertinent view has to be provided on the designs and their robustness. The risk analysis on the final objective to be reached for the satellite performance has to be done by using the growing complexity of the situations to be met. More than previously, the decision for the research of the best design through a probabilistic approach or a robustness approach in its choice has to be taken for the most efficient final product with the technico economic goals.

Peter Eberhard (University of Stuttgart, DE)

Peter Eberhard is Full Professor of Mechanics and Director of the Institute of Engineering and Computational Mechanics at the University of Stuttgart in Germany. He studied Mechanical Engineering with focus on Dynamics and Control and did his doctoral degree on optimization of mechanical systems and his habilitation about contact problems. After a professorship at the University Erlangen-Nuremberg he joined the University of Stuttgart. He and his coworkers research interests include Multibody Systems, Contact Mechanics (especially particles), Optimization, Mechatronics and Control, Biomechanics, and Uncertainties. He received the Richard-von-Mises-Award and he holds a Honorary Professorship from the Nanjing University of Science and Technology in China. He is author and coauthor of several books and about 275 scientific papers.

Modern Model Reduction in Dynamics - much more than just a Mathematical Toy

In this talk some introduction to the model reduction of elastic structures is given so that these huge models can be used in a dynamic multibody simulation. During the last decade there was a lot of research activity going on and the focus shifted from modal methods to approaches using moment-matching or balanced truncation. These methods are not just mathematically beautiful but are also very useful for engineering applications. Examples will be shown including also comparisons with different methods. A special focus will be on the model reduction of coupled elastic structures.

Daniel Juvé (Ecole Centrale de Lyon, FR)

Professor at Ecole Centrale de Lyon, head of the Centre Acoustique and head of the excellency laboratory on Acoustics (CeLyA) . Research interests concern: generation of sound by turbulent flows; subsonic and supersonic jets; grazing flows over cavities; wall-pressure fluctuations and Propagation of acoustic waves in non-homogeneous and random moving media; micrometeorological effects in atmospheric sound propagation. Prof D. Juvé was awarded Chavasse Prize of the French Acoustical Society (1990) Great Prize Alexandre Joannidès of the French Academy of Sciences (2001, together with Christophe Bailly), fellow of the Acoustical Society of America (1998), associate fellow in the American Institute of Aeronautics and Astronautics (AIAA, 2009), member of the French Acoustical Society (SFA), of the French Association for Aeronautics and Space (AAAF), of the French Society of Mechanics (AFM). He is editor of the Journal of Sound and Vibration (Acoustics) and the International Journal of Aeroacoustics. He is member of the Aeroacoustics Specialists Committee of the Council of European Aerospace Societies (CEAS- ASC), Evaluation and Orientation Committee of Department DSNA of Onera, Management Committee of the French Network on Aeroacoustics IROQUA and Scientific Committee of the French Research Foundation for Aeronautics and Space (FRAE).

Turbulent wall-pressure fluctuations: models and relation with fluid dynamics computations

Modeling wall-pressure fluctuations beneath a turbulent boundary layer is an important issue for the prediction of flow-induced structural vibrations and subsequent noise emission.

In this talk we will first give a short review of current models of point-spectra, spatial correlations and cross-spectra of turbulent pressure fluctuations. The possibility of using fluid dynamics computations (averaged “RANS” computations or time-resolved “LES”) to identify the various flow parameters used in these models will be discussed. Finally recent results obtained in measuring or computing the “acoustic” component (associated with supersonic wavenumbers) of wall-pressure fluctuations will be presented together with a new experimental set-up designed to study the effect of favorable or adverse mean-pressure gradients.

Anders Nilsson (Royal Institute of Technology, Stockholm, SE)

Anders Nilsson holds MSc in Engineering Physics from University of Lund, Sweden and Dr.Tech. in Sound and Vibration from Chalmers University. Anders Nilsson has worked on problems relating to the propagation of sonic booms at Boeing Co., Seattle , USA. At Det Norske Veritas he became head of the Acoustics Department at the Research Division. At Veritas Anders Nilsson worked on the propagation of structure borne sound in large built up structures like ships and on the excitation of plates from flow and cavitation. Anders Nilsson was head of the Danish Acoustical Institute for four years. His main activity in Denmark was building acoustics. In 1987 Anders Nilsson was appointed professor of Applied Acoustics at KTH in Stockholm, Sweden. He was also the head of the Department of Vehicle Engineering and the founder and head, until 2002, of the Marcus Wallenberg Laboratory of Sound and Vibration Research (MWL). Anders Nilsson has been a guest professor at James Cook University, Australia, INSA-Lyon, France and the Institute of Acoustics, Chinese Academy of Sciences in Beijing. He is the author of the book Vibro-Acoustics, the first volume published in 2012 and the second in early 2013. Anders Nilsson is since 2008 professor emeritus at MWL, KTH. His main interests are problems relating to composite structures as well as vehicle acoustics.

Acoustic properties of sandwich and honeycomb panels

For many vehicle applications the use of lightweight structures is of great importance. To meet a growing demand, a variety of different types of sandwich panels has been developed during the last few decades. The term “sandwich panel” here refers to a structure with a fairly thick lightweight core with thin laminates bonded to each side of either a foam or honeycomb core. This type of plate can combine low weight with high strength. However, for certain types of sandwich plates, the acoustic properties can be very poor. The absence of acoustic qualities can severely restrict the use of sandwich elements. It is therefore essential to optimize through prediction the acoustic properties of sandwich structures. Some of the basic parameters of a sandwich structure can be determined by means of some simple tests using a beam element of the structure. Alternatively, the material parameters can be determined from simple point mobility measurements on a plate element. The apparent bending stiffness of a sandwich construction strongly depends on frequency. Once the material properties are determined the sound transmission loss and sound radiation ratio can be predicted using some simple algorithms. The model can also be used for parameter studies of the influence on the sound transmission loss and radiation ratios due to changes of dimensions of laminates, core etc.

Goran Pavic (INSA Lyon, FR)

Goran Pavić holds BSc in Mechanical Engineering and PhD in Acoustics and Vibration. After having spent 24 years in research in shipbuilding, electrotechnical and mechanical industries, he was elected to professorship at the National Institute of Applied Sciences in Lyon, France. His duties involve research and teaching in vibration, acoustics and signal processing.

The present research activities of G. Pavić are in the areas of vibroacoustics of mechanical systems, virtual noise synthesis and energy related techniques of sound and vibration analysis. G. Pavić has participated in 9 international projects concerning noise and vibration, out of which in 4 as the coordinator, in several tens of industry funded projects as well as in the European Doctorate in Sound and Vibration programme. He is former associate editor of Acta Acustica and current associate editor of Technical Acoustics; former director of International Institute of Acoustics and Vibration and member of 2 ISO standardisation committees. He has published a number of journal articles and has presented a number of papers on various topics in the field of sound and vibration.

Virtual Noise Synthesis

The synthesis of noise of an industrial product can be done by sub-structuring it into its basic components. A particular sub-structuring method predicts the trends in the overall noise by combining data from the real source(s) with a simplified modelling of the main frame. The coupling between the source(s) and the frame is ensured by impedance coupling rules. The critical components are the noise sources which have to be characterised by measurements. The characterisation techniques are not simple, but reveal a lot of useful information to the designer apart from providing the input data to synthesis method itself. The simplified frame model has the advantage of being robust and easy to implement. The output of the synthesis is the noise level and the noise waveform for audible reproduction. The paper outlines the basics of the source characterisation techniques and of the noise synthesis approach accompanied by several examples.

Pedro Ribeiro (Faculty of Engineering, University of Porto, PT)

Pedro Ribeiro earned a Doctor of Philosophy degree at the Institute of Sound and Vibration Research (ISVR), University of Southampton, in 1998. He currently is an Assistant Professor at the Department of Mechanical Engineering, Faculty of Engineering of the University of Porto, where he lectures subjects in the area of Applied Mechanics.

His research field is nonlinear dynamics of structures, mainly with geometrical nonlinearity, but with some incursions into plasticity. He has been and is involved in research projects related with nonlinear dynamics of structures. Currently he supervises two PhD theses in non-linear oscillations of composite laminates.

Pedro Ribeiro is author or co-author of over forty international journal papers. He present several communications in conferences and other international meetings, presented seminars in diverse universities and lectured in CISM advanced school "Exploiting Nonlinear Behaviour in Structural Dynamics" in 2010. He was chairman of EUROMECH Colloquium 483, "Geometrically non-linear vibrations of structures" in 2007, has been involved in the organization of a few symposia and acted as co-editor of journal special issues related with nonlinear dynamics.

Non-linear modes of vibration of structural elements

When structures experience large amplitude vibrations, some characteristics present in modes of vibration of linear systems are not preserved. It is intended in this presentation to explore the extension of the mode of vibration notion to vibrations in the geometrically non-linear regime. After a short review on work and concepts presented by different authors, the presentation proceeds to the analysis of periodic, conservative, free vibrations of structural elements, specifically beams, plates and shells. For that purpose, the displacement components are expanded as sums of products of functions of time and functions of space. Writing the time functions as truncated Fourier series, sets of algebraic equations in the frequency domain are derived and, by solving these equations, one can investigate the variation of frequency and shape of vibration with the vibration amplitude. With the procedures presented, it is also possible to analyse internal resonances, that is, couplings between modes that are induced by the non-linearity and that lead to interesting oscillations.

Massimo Ruzzene (Georgia Institue of Technology, Atlanta, US)

Massimo Ruzzene is a Professor in the Schools of Aerospace and Mechanical Engineering at Georgia Institute of Technology. He received a Ph.D in Mechanical Engineering from the Politecnico di Torino (Italy) in 1999. He is author of approximately 105 journal papers and about 130 conference papers, and has participated as a PI or co-PI in various research projects funded by the Air Force Office of Scientific Research (AFOSR), the Army Research Office (ARO), the Office of Naval Research (ONR), NASA, the US Army, TRW Corporation, DARPA and the National Science Foundation (NSF). Most of his current and past research work has dealt with structural health monitoring, wave propagation analysis, high frequency vibration modeling, and vibration and noise control techniques. M. Ruzzene is a Fellow of ASME, and member of AIAA, AHS, and ASA.

Nonlinearities and multifield interactions for adaptive metamaterials

Metamaterials consist of engineered microstructural assemblies that exhibit superior properties in comparison to less-composed or naturally-occurring materials. Their unusual wave properties include band-gap behavior, response directionality, left-handedness, and negative acoustic refraction, among others. These features, and their application for the design of acoustic filters, waveguides, logic ports, and ultrasonic transducer arrays, motivate the investigation of elastic wave propagation in micro-structured media.

The seminar presents in particular the directional properties of periodic media, as defined by their ability to direct waves in preferential direction. Such properties are first illustrated on simple spring-mass systems, and subsequently demonstrated in complex structural lattices operating in linear and nonlinear deformation regimes. In addition, periodic arrays of electromechanical resonators, and lattices that undergo topological changes resulting from structural instabilities are discussed as examples of adaptive metamaterials. Tunable local resonating systems, and local instabilities are investigated as effective means to provide the considered periodic assemblies with adaptive bandgaps and wave steering characteristics.

Jing Tian (President of Acoustical Society of China, CN)

Professor TIAN Jing, president of Chinese Society of Acoustics; Honorary fellow of International Institute of Acoustics and Vibration (IIAV); Executive Editor in Chief for Acta Acustica, Director member of Technical Committee of National Acoustical Standardization.

Graduated from the Department of Physics of Nanjing University majored in acoustics on February 1982, then he got his Master's degree in 1984 and his Ph.D. from Institute of Acoustics, Chinese Academy of Sciences (IACAS) on December 1991. As a researcher on electro-acoustic and noise control for more than 30 years, Prof. Tian has been the principal investigator for 40 research projects supported by various funding bodies including National Ministry of S&T, National Natural Science Foundation, Chinese Academy of Sciences (CAS), and other organizations. The research covers several areas of acoustics: active noise and vibration control, electronic anti-noise communication devices, audio characteristic signal control, acoustical MEMS, transmission and evaluation of traffic noise and applications of finite amplitude sound wave.

Bernard Troclet (Senior Expert in Structural Mechanics, professor at ENS Cachan, FR)

Bernard TROCLET is R&D project manager (Structural Engineering) in EADS ASTRIUM ST and professor at ENS CACHAN. He is engineer from ISAE-ENSMA (Ecole Nationale Supérieure de Mécanique et d'Aéronautique de Poitiers) and obtained is Habilitation of Research in Mechanics & Energetics from Paris VI. His domains of expertise are Dynamics computation, Acoustic, deterministic and random Vibration, Mid & High Frequency Analysis and Pyrotechnic shocks.

Synthesis of Ariane 4 & Ariane 5 vibroacoustic studies and perspectives

The objective of this conference is to present the vibroacoustic approach on Ariane launchers. Early in the design development of the Ariane 5 launcher, it was anticipated that the acoustic environment would be a severe case load. Consequently, very soon, noise reduction means have been investigated.

This conference will address:

- The acoustic environment experienced by the launchers lift-off and during flight ascent and the work undertaken to reduce noise surrounding the ARIANE 5 launch vehicle and the noise inside the Fairing on the one hand. The reduced scale test to characterize the lift-off noise and to investigate potential noise reduction means, the Fairing full scale acoustic test are presented,
- And the methods used to estimate the vibroacoustic response of launch vehicles on the other hand.

Finally, perspectives, particularly in the field of mid frequency response will be presented.

Eberhard Haug (ESI, DE)

Eberhard Haug is one of the founding members of ESI Group, the well-known virtual prototyping company, where he held the position of Scientific Director. He is now retired and acts as a consultant. Eberhard Haug graduated from the University Stuttgart (W.G.) in Civil Engineering and he earned his Ph.D. degree in Structural Engineering at the University of California, Berkeley, where he wrote a program for the large displacement finite element analysis of lightweight cable and membrane structures. He was a Research Associate at the University of Stuttgart with Professors Frei Otto and J.H. Argyris. At ESI Group, he was the driving force behind the development of various non-linear FE analyses programs and material model developments and he is the principal inceptor of the world's premier crash, occupant safety and stamping simulation codes. His recent computational developments focused on biomechanics. He has published many papers on the theory and industrial application of modern numerical simulation techniques. His recent consulting activities include the wind simulation of lightweight structures.

Numerical Design and Analysis of Flexible Structures

This article extends the application of ESI Group Products into the spectacular field of Special and Lightweight structures, a domain situated in the field of high-rise building construction, in recent SL Rasch GmbH and ESI France joint projects.

ESI Group is a global compagny working on Virtual prototyping and Testing and is a pioneer in Realistic FE Simulation, in particular for pre-certification of structural integrity with respect of accidental and extreme operating conditions. SL-Rasch GmbH, an internationally operating architectural and engineering office, located in Stuttgart, Germany, is specialized in the architectural and structural design of Special and Lightweight structures, often made of pre-stressed flexible cables and membrane fabrics. The industrial application of this principle was pioneered in the 1950-s by the German architect Professor Frei Otto. Flexible buildings made with fiber reinforced technical membranes are particularly sensitive to wind loads. ESI France has developed, calibrated and validated an analysis and design methodology to investigate wind load effects, ranging from constant wind velocity profiles to input of wind fields with natural turbulence (gusts) (Ph.D. thesis A. Michalski). While for most conventional high-rise buildings the structural response to wind load can be evaluated via computational fluid.

MEDYNA 2013 - 1st Euro-Mediterranean Conference on Structural Dynamics and Vibroacoustics

Tuesday, April 23, 2013

8:00 - 8:30	Registration										
8:30 - 8:40	Opening Ceremony - *Manuel Collet (FEMTO-ST, FR)*										Yves Rocard
8:40 - 9:20	Plenary I - Acoustic properties of sandwich and honeycomb panels *Anders Nilsson (Royal Institute of Technology, SE)*										Yves Rocard
9:20 - 10:00	Plenary II - Turbulent wall-pressure fluctuations: models and relation with fluid dynamics computations *Daniel Juvé (École Centrale de Lyon, FR)*										Yves Rocard
10:00 - 10:30	Coffee break										
10:30 - 12:30	Nonlinear System Dynamics *Mohamed Belhaq (FSAC, MA)*	Yves Rocard	Reduced Order Models in Structural Dynamics and Vibroacoustics *Jean-François Deü (CNAM, FR)*	Daa-You Maa	Smart Materials, Smart Structures and Metacomposites *Manuel Collet (FEMTO-ST, FR), Hervé Lissek (EPFL, CH)*	Al-Khawarizmi	Dynamics of Machines and Rotating Machinery *Jarir Mahfoud (INSA, FR)*	Philip Ellis Doak			
Lunch											
14:30 - 15:10	Plenary III *Jing Tian (President of Acoustical Society of China, CN)*										Yves Rocard
15:10 - 15:50	Plenary IV - Modern Model Reduction in Dynamics - much more than just a Mathematical Toy *Peter Eberhard (University of Stuttgart, DE)*										Yves Rocard
15:50 - 16:30	Coffee break Posters session										
16:30 - 17:30	Nonlinear System dynamics *Joël Perret-Liaudet (ECL,FR)*	Yves Rocard	Flow Induced Vibrations and Noise *Lin Li (SJP, CN)*	Daa-You Maa	Vibration Field Measurements and Force Identification *Charles Pézerat (LAUM, FR)*	Al-Khawarizmi	Dynamics of Machines and Rotating Machinery *Fakher Chaari (ENIS, TN)*	Philip Ellis Doak			
19:30 - 22:00	Welcome event										

Wednesday, April 24, 2013

8:40 - 9:20	Plenary V - Nonlinearities and multifield interactions for adaptive metamaterials *Massimo Ruzzene (Georgia Institute of Technology, Atlanta, US)*										Yves Rocard
9:20 - 10:00	Plenary VI - Coupling of models and scales in the Arlequin framework *Hachmi Ben Dhia (École Centrale Paris, FR)*										Yves Rocard
10:00 - 10:30	Coffee break										
10:30 - 11:30	Nonlinear System Dynamics *Joël Perret-Liaudet (ECL,FR)*	Yves Rocard	Material & Structural Dynamics *Morvan Ouisse (FEMTO-ST, FR)*	Daa-You Maa	Smart Materials, Smart Structures and Metacomposites *Stephan Rinderknecht (TUD, DE)*	Al-Khawarizmi	Computational Methods in Vibroacoustics and Mid-Frequency *Wim Desmet (KUL, BE), Bernard Troclet (LMT, FR)*	Philip Ellis Doak			
11:30 - 12:10	Nonlinear Vibrations *Bilal Harras (FST, MA)*	Yves Rocard									
12:10 - 12:30											
Lunch											
14:30 - 15:10	Plenary VII *Goran Pavic (INSA Lyon, FR)*										Yves Rocard
15:10 - 15:50	Plenary VIII *Adnan Akay (Bilkent University, Turkey & Carnegie Mellon University, US)*										Yves Rocard
15:50 - 16:30	Coffee break Posters session										
16:30 - 17:10	Nonlinear Vibrations *Rhali Benamar (EMI, MA)*	Yves Rocard	Material & Structural Dynamics *Makrem Arfaoui*	Daa-You Maa			Friction Noise *Alain Le Bot (ECL, FR)*	Philip Ellis Doak			
17:10 - 17:30											
17:30 - 17:50											
18:50 - 19:30	Plenary IX - Numerical Design and Analysis of Flexible Structures *Eberhard Haug (ESI, DE)*										Yves Rocard
19:30 - 23:00	**Gala**										

Thursday, April 25, 2013

8:20 - 9:00	Plenary X - Nonlinear modes of vibration of structural elements *Pedro Ribeiro (University of Porto, PT)*										Yves Rocard
9:00 - 9:40	Plenary XI - New considerations on the validation and on the optimization of designs in the space domain *Jérôme Buffe (Thales Alenia Space, FR)*										Yves Rocard
9:40 - 10:10	Coffee break										
10:10 - 11:50	Nonlinear Vibrations *Rhali Benamar (EMI, MA)*	Yves Rocard	Materials for Vibroacoustics *Noureddine Atalla (GAUS, CA)*	Daa-You Maa	Robust Design under lack of knowledge *Scott Cogan (FEMTO-ST, FR)*	Al-Khawarizmi	Computational Methods in Vibroacoustics and Mid-Frequency *Mohamed Ichchou (ECL, FR)*	Philip Ellis Doak			
11:50 - 12:10											
12:10 - 12:50	Plenary XII - Synthesis of Ariane 4 & Ariane 5 vibroacoustic studies and perspectives *Bernard Troclet (EADS ASTRIUM ST, ENS Cachan, FR)*										Yves Rocard
12:50 - 13:00	Closing Ceremony - *Manuel Collet (FEMTO-ST, FR)*										Yves Rocard
Lunch											

MEDYNA 2013: 1st Euro-Mediterranean Conference on Structural Dynamics and Vibroacoustics

Tuesday, April 23, 2013

8:00 - 8:30	**Registration**				8:00 - 8:30
8:30 - 8:40	**Opening Ceremony** - ***Manuel Collet*** *(FEMTO-ST, FR)*			Yves Rocard	8:30 - 8:40
8:40 - 9:20	Plenary I - **Acoustic properties of sandwich and honeycomb panels** by ***Anders Nilsson*** *(Royal Institute of Technology, SE)* *Chair: Noureddine Atalla*				8:40 - 9:20
9:20 - 10:00	Plenary II - **Turbulent wall-pressure fluctuations: models and relation with fluid dynamics computations** by ***Daniel Juvé*** *(École Centrale de Lyon, FR)* *Chair: Lin Li*				9:20 - 10:00
10:00 - 10:30	**Coffee break**				10:00 - 10:30
Sessions	**Nonlinear System dynamics** *Mohamed Belhaq (FSAC, MA)*	**Reduced Order Models in Structural Dynamics and Vibroacoustics** *Jean-François Deü (CNAM, FR)*	**Smart Materials, Smart Structures & Metacomposites -** *Manuel Collet (FEMTO-ST, FR), Hervé Lissek (EPFL, CH)*	**Dynamics of Machines and Rotating Machinery** *Jarir Mahfoud (INSA, FR)*	Sessions
10:30 - 10:50	Vibration pumping of mdof structures using optimised multiple dynamic absorbers *Khelifi Kamel, Bouazizi Mohamed Lamjed, Nasri Rachid, Bouhaddi Noureddine*	Reduced-order model for nonlinear dynamical structures having a high modal density in the low-frequency range *Anas Batou, Christian Soize, Nicolas Brie*	Mounting Vibrational MEMS Energy Harvesters on Printed Circuit Boards for Improved Response *Mohammad Younis, David Kelemen, Abdallah Ramini*	Monitoring bearing defects by acoustic emission: application of empirical mode decomposition method for early detection *Mourad Kedadouche, Marc Thomas, Souheil-Antoine Tahan*	10:30 - 10:50
10:50 - 11:10	Effect of electromagnetic actuation on the dynamic of a forced hertzian contact oscillator *Amine Bichri, Mohammed Belhaq*	Wave propagation analysis in porous media via the Wave Finite Element Method *Quentin Serra, Mohamed Ichchou, Jean-François Deü*	Experimental investigation on adaptive shunted piezoelectric metacomposites *Flaviano Tateo, Manuel Collet, Morvan Ouisse, Mohamed Ichchou, Kenneth A. Cunefare, Philippe Abbe*	On the behavior of the flexible rotor bearing system in the vicinity of the stability threshold *Mnaouar Chouchane, Radhoine Sghir*	10:50 - 11:10
11:10 - 11:30	Dynamic friction compact model: a new multicontact tribometer *Jean-luc Dion, Gaël Chevallier, Olivia Penas, Franck Renaud*	Application of wave finite element method on reduced models for the analysis of flexural waves in periodic beams *Changwei Zhou, Mohamed Ichchou, Jean-Pierre Laine, Abdel-malek Zine*	Simple and effective friction compensation on wheeled inverted pendulum systems *Bruno Strah, Stephan Rinderknecht*	Application of Modified Modal Assurance Criteria in Mistuning Bladed Disk *Peiyi Wang, Lin Li*	11:10 - 11:30
11:30 - 11:50	Dynamic simulations of a Bouncing Ball on a randomly vibrating plat form *Chaima Zouabi, Joel Perret-liaudet, Julien Scheibert*	Vibrations of an elastic structure with shunted piezoelectric patches: efficient f.e. formulation and reduced-order models *Luciano Pereira Da Silva, Jean-françois Deü, Walid Larbi, Marcelo A. Trindade*	Analytical modeling of an unimorph multi-layer piezoelectric vibration energy harvester *Ahmed Jemai, Fehmi Najar, Moez Chafra*	Dynamic characteristics of the cyclic-periodic structure with piezoelectric networks *Pengcheng Deng, Lin Li, Yu Fan*	11:30 - 11:50
11:50 - 12:10	Free oscillations of a sliding sdof system: effect of a polynomial friction model *Fida Majdoub, Joel Perret-liaudet, Michel Belin, Jean-michel Martin*	Determining sensor locations based on model order reduction techniques *Fabio Casciati, Sara Casciati, Lucia Faravelli*	Vibration reduction of a structure by design and control of a bolted joint *Yassine Karim, Claude Blanze*	Dynamic analysis of a spur gear with active magnetic bearings in transient regime *Slim Bouaziz, Najib Belhadj Messaoud, Mohamed Mataar, Mohamed Haddar*	11:50 - 12:10
12:10 - 12:30	Bifurcation-based micro/nano-electromechanical mass detection *Van-nghi Nguyen, Sébastien Baguet, Claude-henri Lamarque, Régis Dufour*	ROM for nonlinear vibroacoustic problems with structural and acoustic nonlinearities *Youssef Gerges, Emeline Sadoulet-Reboul, Morvan Ouisse, Noureddine Bouhaddi*	Robust Active Vibration Control of Piezoelectric Flexible Structures with Probabilistic Parametric Uncertainty *Kai Zhang, Mohamed Ichchou, Scorletti Gérard*	Acoustic reconstruction of the unsteady rotating forces of fan's blade *Majdi Abid, Hassen Trabelsi, Mohamed Taktak, Mohamed Haddar*	12:10 - 12:30
12:30 - 14:30	**Lunch**				12:30 - 14:30

Yves Rocard | Daa-You Maa | Al-Khawarizmi | Philip Ellis Doak

MEDYNA 2013: 1st Euro-Mediterranean Conference on Structural Dynamics and Vibroacoustics

Tuesday, April 23, 2013

14:30 - 15:10	Plenary III - ***Jing Tian*** *(President of Acoustical Society of China, CN)* *Chair: Mohamed Ichchou*								Yves Rocard	14:30 - 15:10
15:10 - 15:50	Plenary IV - **Modern Model Reduction in Dynamics: much more than just a Mathematical Toy** by ***Peter Eberhard*** *(University of Stuttgart, DE)* *Chair: Mohamed Belhaq*									15:10 - 15:50
15:50 - 16:30	**Coffee break** **Posters session**									15:50 - 16:30
Sessions	**Nonlinear System dynamics** *Joël Perret-Liaudet (ECL,FR)*		**Flow Induced Vibrations and Noise** *Lin Li (SJP, CN)*		**Vibration Field Measurements and Force Identification** *Charles Pézerat (LAUM, FR)*		**Dynamics of Machines and Rotating Machinery** *Fakher Chaari (ENIS, TN)*			Sessions
16:30 - 16:50	Nonlinear wave propagation in post-buckled structures *Alessandro Spadoni, Florian Paul Maurin*	Yves Rocard	Turbulent wall pressure measurement in low wavenumber using the flow-induced vibrations *Damien Lecoq, Charles Pezerat, Jean-hugh Thomas, Wenping Bi*	Daa-You Maa	Model selection for the equation of motion *Michal Ruzek, Jean-Louis Guyader, Charles Pezerat*	Al-Khawarizmi	Dynamics of a horizontal axis wind turbine blade under aerodynamic, centrifugal, gyroscopic, and gravity effects *Hedi Hamdi, Charfeddine Mrad, Rachid Nasri*	Philip Ellis Doak		16:30 - 16:50
16:50 - 17:10	Non linear modal analysis of dynamic absorbers *Fathi Djemal, J. Dion, Fakher Chaari, Imad Tawfiq, Mohamed Haddar*		Detecting and Measuring Slug Velocity in Two-Phase Flows Horizontal Pipes *Muammer Alssayh, Abdulmajid Addali, David Mba, Abdelhamid Naid*		Determination of forces in risers used in the petroleum industry by indirect measurements *Alexandre Kawano, Abdel-malek Zine*		Dynamic analysis of spur gear with defected bearings *Mohamed Abbes, Taissir Hentati, Radoslaw Zimroz, Fakher Chaari, Mohamed Haddar*			16:50 - 17:10
17:10 - 17:30	Delayed feedback controller in MEMS resonators *K. Masri, M. Younis, S. Shao*		Experimental Investigation of the Equilibrium and Stability of Long Towed Cable Systems *Martin Obligado, Mickael Bourgoin*		Is high-speed digital holography the ultimate tool for vibration analysis ? *Julien Poittevin, Pascal Picart, François Gautier, Charles Pezerat*					17:10 - 17:30

19:30 - 22:00	**Welcome event**	19:30 - 22:00

MEDYNA 2013: 1st Euro-Mediterranean Conference on Structural Dynamics and Vibroacoustics

Wednesday, April 24, 2013

8:40 - 9:20	Plenary V - **Nonlinearities and multifield interactions for adaptive metamaterials** by ***Massimo Ruzzene*** *(Georgia Institute of Technology, Atlanta, US)* *Chair: Manuel Collet*			Yves Rocard	8:40 - 9:20
9:20 - 10:00	Plenary VI - **Coupling of models and scales in the Arlequin framework** by ***Hachmi Ben Dhia*** *(École Centrale Paris, FR)* *Chair: Joël Perret-Liaudet*			Yves Rocard	9:20 - 10:00
10:00 - 10:30	**Coffee break**				10:00 - 10:30
Sessions	**Nonlinear System dynamics** *Joël Perret-Liaudet (ECL,FR)*	**Material & Structural Dynamics** *Morvan Ouisse (FEMTO-ST, FR)*	**Smart Materials, Smart Structures and Metacomposites** *Stephan Rinderknecht (TUD, DE)*	**Computational Methods in Vibroacoustics and Mid-Frequency** *Wim Desmet (KUL, BE), Bernard Troclet (LMT, FR)*	Sessions
10:30 - 10:50	Bifurcation Behavior in Switching Converters Driving Other Downstream Converters in DC Distributed Power Systems Applications *Abdelali El Aroudi, Damian Giaouris, Luis Martinez-salamero, Soumitro Banerjee*	Increasing the Modal Overlap Factor of a Beam Using the Acoustic Black Hole Effect *Vivien Denis, François Gautier, Adrien Pelat*	Elastic metamaterials with local resonances for broad band vibration isolation *Gao Yan, Fusheng Sui, S. Daley*	Finite element modelling of Poroelastic-acoustic coupled problem *Walid Larbi, Jean-françois Deü, Roger Ohayon*	10:30 - 10:50
10:50 - 11:10	Chaos Control by Time-Delayed Feedback: Observing Global Properties in Electronic Circuits - *Hartmut Benner, Chol-ung Choe, Klaus Höhne, Clemens V. Loewenich, Hiroyuki Shirahama, Wolfram Just*	Scattering of flexural waves from an acoustic black hole in an infinite thin plate *Omar Aklouche, François Gautier, Adrien Pelat, Sylvain Maugeais*	Dielectric elastomer as active material in membranes for vibration-based enrgy harvesting *Emine Zaouali, Fehmi Najar, Kais Mrabet*	Prediction of random vibration and acoustic Responses by compression of the statistical Dynamical information of fem models *Gerard Borello*	10:50 - 11:10
11:10 - 11:30	Nonlinear Dynamics of A Piecewise Linear Energy Harvesting System *Abdelali El Aroudi, Hassen Ouakad, Mohammad Younis*	Fea nalysis of in-plane shear stresses of a preloded sandwich plate with a viscoelastic core – application to the disk brake systems *Mohamed Soula, T. Lazghab, M. Bouazizi*	On the radiation efficiency of local resonance stop bands *Claus Claeys, Paul Sas, Wim Desmet*	Statistical energy analysis: correlation between diffuse field and energy equipartition *Thibault Lafont, Nicolas Totaro, Alain Le Bot*	11:10 - 11:30
Sessions	**Nonlinear Vibrations** *Bilal Harras (FST Fes, MA)*				Sessions
11:30 - 11:50	Effects of constraints and stability coefficient on convergence of PSO based algorithm for impact localization *Abdelali El-bakari, Abdellatif Khamlichi, Rachid Dkiouak, Eric Jacquelin*	Wideband frequency characterization of a shape memory polymer *Pauline Butaud, Morvan Ouisse, Emmanuel Foltête, Vincent Placet, Jan Klesa, Xavier Gabrion*	Electroacoustic metamaterials with negative acoustic properties *Hervé Lissek*	A new model of improving the transmission loss of aluminium profile with corrugated cores *Shan Ouyang, Fusheng Sui*	11:30 - 11:50
11:50 - 12:10	Non-linear Free Vibration Analysis of Circular Functionally Graded Plates using a Homogenization Procedure. *Rachid El Kaak, Khalid El Bikri, Rhali Benamar*	Estimation of structural damping using an expansion in the chebyshev orthogonal basis *Catherine Chochol, Simon Chesne, Didier Remond*	Sensitivity analysis and control of a cantilever beam by mean of a shunted piezoelectric patch *Gaël Matten, Manuel Collet, Emeline Sadoulet-Reboul, Scott Cogan*	On the thermoacoustic properties of aerospace layered structures *Dimitrios Chronopoulos, Mohamed Ichchou, Bernard Troclet, Olivier Bareille*	11:50 - 12:10
12:10 - 12:30	Dynamic of a squeeze film between smooth lip seal and rough shaft *M'hammed El Gadari, Mohamed Belhaq, Mohamed Hajjam*	Guided wave propagation in uncertain elastic media through stochastic diffusion matrix *Faker Bouchoucha, Mohamed Ichchou, Mohamed Haddar*		Quantification of the power injected by acoustic sources inside a complex cavity *Fabien Ayme, Charles Cariou, Mohamed Ichchou, Daniel Juvé, Olivier Bareille*	12:10 - 12:30
12:30 - 14:30	**Lunch**				12:30 - 14:30

Yves Rocard | Daa-You Maa | Al-Khawarizmi | Philip Ellis Doak

MEDYNA 2013: 1st Euro-Mediterranean Conference on Structural Dynamics and Vibroacoustics

Wednesday, April 24, 2013

14:30 - 15:10	Plenary VII - **Virtual Noise Synthesis** by ***Goran Pavic*** *(INSA Lyon, FR)* *Chair: Charles Pézerat*			Yves Rocard	14:30 - 15:10
15:10 - 15:50	Plenary VIII - **Sound and Vibration From Friction Between Soft Materials Under Light Loads** by ***Adnan Akay*** *(Bilkent University, Turkey & Carnegie Mellon University, US)* *Chair: Alain Le Bot*			Yves Rocard	15:10 - 15:50
15:50 - 16:30	**Coffee break** **Posters session**				15:50 - 16:30
Sessions	**Nonlinear Vibrations** *Rhali Benamar (EMI, MA)*	**Material & Structural Dynamics** *Makrem Arfaoui (ENIT,TN)*		**Friction Noise** *Alain Le Bot (ECL, FR)*	Sessions
16:30 - 16:50	Vibrations of a self-excited tower under turbulent wind flow in the presence of a high frequency excitation *Ilham Kirrou, Lahcen Mokni, Mohammed Belhaq*	Propagation of deformation and strain waves in a tamping rammers springs *Anis Hamza, Sami Ayadi, Ezzedine Hadj-taieb*	Daa-You Maa	Friction noise of rough surfaces and dissipation of vibration *Alain Le Bot, Hung Dang*	16:30 - 16:50
16:50 - 17:10	Numerical simulation and experimental validation of gap supported tube subjected to fluid-elastic coupling forces for hybrid characterization tests *W. Benmalek, M. Collet, E. Foltete, M. Ouisse,*	Methodoly for robust roadside safety barrier design and certification application to steel-wood structures *M. Massenzio, C. Goubel, S. Ronel, E. Di Pasquale*		Characterization of hysteretic friction of viscoelastic joints *Hanen Jrad, Jean-luc Dion, Franck Renaud, Imad Tawfiq, Mohamed Haddar*	16:50 - 17:10
17:10 - 17:30	Taking into account of surface defects in connections in the dynamics of structures assembled *Nicolas Peyret, Gael Chevallier, Jean-Luc Dion, Pierre Argoul*			Comprehension of friction law instability: application to wiper blade squeal noise *Fabien Dalzin, Alain Le Bot, Denis Mazuyer, Julian Le Rouzic, Joel Perret-liaudet, Frédéric Bretagnol*	17:10 - 17:30
17:30 - 17:50				Direct numerical simulation of friction noise *Hung Dang, Alain Le Bot, Joel Perret-liaudet, Julien Scheibert*	17:30 - 17:50

18:50 - 19:30	Plenary IX - **Numerical Design and Analysis of Flexible Structures** by ***Eberhard Haug*** *(ESI, DE)* *Chair: Fusheng Sui*	Yves	18:50 - 19:30
19:30 - 23:00	**Gala**		19:30 - 23:00

MEDYNA 2013: 1st Euro-Mediterranean Conference on Structural Dynamics and Vibroacoustics

Thursday, April 25, 2013

8:20 - 9:00	Plenary X - **Nonlinear modes of vibration of structural elements** by ***Pedro Ribeiro*** *(University of Porto, PT)* *Chair: Rhali Benamar*			Yves Rocard	8:20 - 9:00
9:00 - 9:40	Plenary XI - **New considerations on the validation and on the optimization of designs in the space domain** by ***Jérôme Buffe*** *(Thales Alenia Space, FR)* *Chair: Scott Cogan*			Yves Rocard	9:00 - 9:40
9:40 - 10:10	**Coffee break**				9:40 - 10:10
Sessions	**Nonlinear Vibrations** *Rhali Benamar (EMI, MA)*	**Materials for Vibroacoustics** *Noureddine Atalla (GAUS, CA)*	**Robust Design under lack of knowledge** *Scott Cogan (FEMTO-ST, FR)*	**Computational Methods in Vibroacoustics and Mid-Frequency** *Mohamed Ichchou (ECL, FR)*	Sessions
10:10 - 10:30	Theory and applications of the macroscopic quantization effect in nonlinearly-coupled vibrating systems *Jonathan Tennenbaum , Danil B. Doubochinski*	Methodology using a Heat Regulated Impedance Tube for the Temperature Dependent Sound Absorption Property of Materials - *Nicolas Merlette, Christophe Gautrelet, Emmanuel Pagnacco*	On the modeling of adhesive contact and stiction failure in micro-switches *Ling Wu, Ludovic Noels, Jean-claude Golinval*	The Wave Based Method: current state of the art - *Elke Deckers, Atak Onur, Laurens Coox, Roberto D'amico, Hendrik Devriendt, Stijn Jonckheere, Kunmo Koo, Bert Pluymers, Dirk Vandepitte, Wim Desmet*	10:10 - 10:30
10:30 - 10:50	Non-linear dynamic behavior of a wind turbine system with torque limiter *Kamel Abboudi, Lassaad Walha, Yassine Driss, Mohamed Maatar, Mohamed Haddar*	Acoustics of rigid porous media with damped Helmholtz resonators *Claude Boutin*	Sensitivity analysis and optimization of sheet steel thickness for vibroacoustic behavior of enclosures - *Titouan Fourmaux, Morvan Ouisse, Scott Cogan, Emeline Sadoulet-Reboul*	Non resonant contributions in modal energy methods *Nicolas Totaro, Laurent Maxit*	10:30 - 10:50
10:50 - 11:10	Effect of high-frequency ac electromagnetic actuation on the dynamic of an excited cantilever beam - *Amine Bichri, Jarir Mahfoud, Mohammed Belhaq*	Acoustic impedance of microperforated honeycomb panels *Margaux Regniez, François Gautier, Charles Pezerat, Adrien Pelat*	Optimum shape design of incompressible hyperelastic structures with analytical sensitivity analysis *Abdessalem Jarraya, Fakhreddine Dammak*	Dynamics of stochastic and periodic structures in mid-frequency range - *Mohamed Amine Ben Souf, Olivier Bareille, Mohamed Ichchou, Bouhaddi Noureddine, Mohamed Haddar*	10:50 - 11:10
11:10 - 11:30	Internal resonances in nonlinear nanocantilever arrays under electrostatic actuation *Saoussen Souayeh, Najib Kacem*	An analytic study of the noise reduction of an infinite multi-layered cylinder *Julien Magniez, Mohamed-ali Hamdi, Jean-daniel Chazot*	Robust model calibration of a wind turbine with load uncertainties *Daniel Pereiro, Scott Cogan, Emeline Sadoulet-reboul, Felix Martinez*	SAMSARA for thin stiffened shells: first models *Sergio De Rosa, Franco Francesco*	11:10 - 11:30
11:30 - 11:50	Transverses linear vibration of cantilever beam carrying two lumped masses. Analogy between discrete models. *Ahmed Eddanguir, Rhali Benamar*	The transmission loss of sandwich-composite panels with attached noise control materials *Haisam Osman, Noureddine Attala*	Robust design of spacecraft structures under lacks of knowledge *Fabien Maugan, Scott Cogan, Emmanuel Foltête, Fabrice Buffe*	A new approach in reliability based design optimization of TMD in seismic vibration control of structures with bounded uncertain parameters - *Elyes Mrabet, Mohammed Guedri, Samir Ghanmi, Mohamed Ichchou*	11:30 - 11:50
11:50 - 12:10		Design of an Acoustic Anechoic Chamber for Application in Teaching Aid *Remram Youcef*	Real-time and in-service estimation of the degree of damage of automotive transmission parts with the aid of a torque measure *Stéphane Foulard, Stephan Rinderknecht, Mohamed Ichchou, Joel Perret-liaudet*	Detection of localized damage in rails by using elastic wave propagation *Sara Teidj, Abdellatif Khamlichi, Abdellah Driouech, Eric Jacquelin*	11:50 - 12:10
12:10 - 12:50	Plenary XII - **Synthesis of Ariane 4 & Ariane 5 vibroacoustic studies and perspectives** by ***Bernard Troclet*** *(EADS ASTRIUM ST, ENS Cachan, FR)* *Chair: Emmanuel Foltête*			Yves	12:10 - 12:50
12:50 - 13:00	**Closing Ceremony** - ***Manuel Collet*** *(FEMTO-ST, FR)*				12:50 - 13:00
13:00 - 14:30	**Lunch**				13:00 - 14:30

Yves Rocard | Daa-You Maa | Al-Khawarizmi | Philip Ellis Doak

MEDYNA 2013: 1st Euro-Mediterranean Conference on Structural Dynamics and Vibroacoustics

Posters sessions

Tuesday, April 23, 2013 / 15:50 - 16:30

Damage monitoring of trust ball bearing by a reliability approach
Mouloud Guemana, M. Boumahdi

Modelling of mechanical behaviour of bogie train
Redouane Zellagui, Ahmed Bellaouar, Salima Beleulmi

Nonlinear sloshing of two superposed immiscible liquids in a two-dimensional rectangular tank
Meziani Bachir, O Ourrad

Reconstruction of impact force via bayesian approach
Abdellatif Khamlichi, Souleymane Sammagassi, Abdellah Driouech, Eric Jacquelin

Optimization of geometrical parameters of covers & hoops of metal packaging boxes
R. Lombarkia, B. Barkat

Effect of charge polydispersity in the dynamics of a micellar system
Lamiae Talha, Mohammed Filali, Abdelhafid Azougarh, Luca Cipelletti

A method to model beams in dynamic bending under various boundary conditions
Taoufik Ayari, Charfeddine Mrad, Rachid Nasri

On the waveguide analysis of a helicopter rotor blade by the wave finite element method
Christophe Droz, Mohamed Ichchou, Jean-Pierre Laine, Grégory Balmain

Entropy solutions for nonlinear and noncoercive nonhomogeneous Neumann problems arising in the theory of electrorheological fluids
M. B. Benboubker, E. Azroul, H. Hassane, A. Touzani

Wednesday, April 24, 2013 / 15:50 - 16:30

Effect of porosity on the propagation velocities of ultrasonic waves in the trabecular bone
Abderrazek Bennamane, Boutkedjirt Tarek

Study of mechanical behavior and reliability analysis of the overhead power cables for low voltage dedicated to distribution network
Asmâa Chouairi, Abdelkader Benali, Mohamed El Ghorba, Nicolas Barbe, Anas Benouna

Experimental ajustement in real time of a semi-active numerical model suspension with a magnetorheological damper
Boukerroum Said, Hamzaoui Nacer

Elastic wave scattering by periodic cavities in backing material for ultrasound transducers
Guofeng Bai, Fusheng Sui, Jun Yang, Chengguang Zhou

Detecting dmage in mindlin plates by using the modal strain energy method
F. El Khannoussi, Abdellatif Khamlichi, A. Hajraoui, A. Liman

Non-linear free vibrations of c–c–ss–ss symmetrically laminated carbon fiber reinforced peek (as4/apc2) rectangular composite plates
Z. Zergoune, B Harras, Rhali Benamar

Geometrically non-linear free vibration of c-ss-c-ss symmetrically laminated as4/apc2 rectangular composite plates
O Baho, B Harras, Rhali Benamar

Multi-objective optimization of rail vehicle design moving in curved tracks with relatively high speed
Mohamed Nejlaoui, Ajmi Houidi, Abdelfattah Mlika, Zouhaier Affi, Lotfi Romdhane

T - p(x) Solutions for Nonlinear Elliptic Equations with an L1-Dual Datum
Elhoussine Azroul, Abdelkrim Barbara, Meryem El Lekhlifi

Table of Contents

Tuesday, April 23, 2013 - 16:30 - 17:30

Nonlinear System dynamics II

Flow Induced Vibrations and Noise

Vibration Field Measurements and Force Identification

Dynamics of Machines and Rotating Machinery II

Wednesday, April 24, 2013 - 10:30 - 12:30

Material & Structural Dynamics I

Computational Methods in Vibroacoustics and Mid-Frequency I

Wednesday, April 24, 2013 - 10:30 - 11:30

Nonlinear System dynamics III

Wednesday, April 24, 2013 - 10:30 - 12:10

Smart Materials, Smart Structures and Metacomposites II

Wednesday, April 24, 2013 - 11:30 - 12:30

Nonlinear Vibrations I

Wednesday, April 24, 2013 - 15:50 - 16:30

Posters II

Wednesday, April 24, 2013 - 16:30 - 17:10

Material & Structural Dynamics II

Wednesday, April 24, 2013 - 16:30 - 17:50

Friction Noise

Wednesday, April 24, 2013 - 16:30 - 17:30

Nonlinear Vibrations II

Thursday, April 25, 2013 - 10:10 - 12:10

Computational Methods in Vibroacoustics and Mid-Frequency II

Materials for Vibroacoustics I

Vibration pumping of mdof structures using optimised multiple dynamic absorbers

K. Khelifi[1], M.-L. Bouazizi[1*], R. Nasri[2], N. Bouhaddi [3]

[1]Preparatory Engineering Institute of Nabeul (IPEIN), Nabeul- Tunisia

khelifi_kamel72@yahoo.fr and Lamjed.Bouazizi@ipein.run.tn

[2]National School of Engineers of Tunis (ENIT), Tunis- Tunisia

Rachid.Nasri @ enit.rnu.tn

[3]FEMTO-ST Institute UMR 6174, Applied Mechanics Department, University of Franche-Comté – France :noureddine.bouhaddi@univ-fcomte.fr

ABSTRACT

The concept of energy pumping is an innovative dynamic phenomenon; it gives rise to new generation of dynamic absorbers. Theoretical studies and feasibility tests are necessary for better understanding of their dynamic behaviour and to be applied on real structures or machines.

In this paper, numerical evidence is firstly given for the passive and broadband targeted energy transfer in the case of a linear system under shock excitation with Multiple Dynamic Absorbers or Nonlinear Energy Sink (NES). Secondly, it is shown that many NES absorb shock energy in only way and dissipate this energy locally, without "spreading" it returns to the linear system. The numerical results of optimisation in the case of NES linked to a linear beam are compared to Tuned Mass Dampers (TMD) linked to the same beam.

***Keywords**: Energy pumping, dynamic absorber, Cubic non-linearity, nonlinear energy sink, tuned mass damper, Optimisation.*

1 INTRODUCTION

The phenomenon of energy pumping is an irreversible transfer of energy from a main structure to a secondary structure, as dynamic absorbers called nonlinear Energy Sink (NES) are linked to the main structure. In previous works [1-3], it has been shown that essentially nonlinear oscillators attached to linear discrete structures that act as broadband passive absorbers of vibration energy. Particularly, it has been shown that transient resonance captures of the transient dynamics may initiate one way, irreversible targeted energy transfer from a linear (main) subsystem to a local essentially nonlinear attachment, which acts, in essence, as nonlinear energy sink (NES). In this work, we propose to optimise the portion of energy damped by the linear and nonlinear dampers linked separately to a beam. The design parameters to optimise are mass ratio, linear and nonlinear stiffness and damping ratio of the dynamic absorbers. For this multi-objective optimisation we calculate the Pareto solutions using NSGA algorithm (Non-dominated Sorting Genetic Algorithm) [4, 5].

2 DYNAMIC EQUATIONS OF MOTION OF MDOF SIMPLY SUPPORTED BEAM

The studied structure consists of an impulsively forced simply supported damped linear beam, comporting multiple dynamic absorbers (Figure 1). This system was introduced in [1] with only one NES.

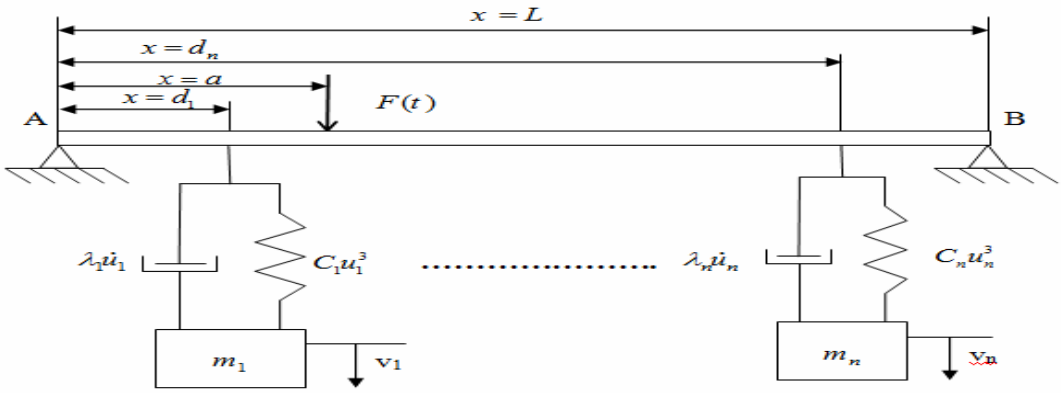

Figure 1. Simply supported beam with Multiple Dynamic Absorbers

The beam finite element model is based on the Euler-Bernoulli theory.

$$\begin{cases} EI\dfrac{\partial^4 y(x,t)}{\partial x^4}+\lambda\dfrac{\partial y(x,t)}{\partial t}+\rho A\dfrac{\partial^2 y(x,t)}{\partial t^2}+\displaystyle\sum_{i=1}^{n}\left(\left\{C_i\left[y(d_i,t)-\mathrm{v}_i(t)\right]^3+\lambda_i\left(\frac{\partial y(d_i,t)}{\partial t}-\dot{\mathrm{v}}_i(t)\right)\right\}\delta(x-d_i)\right)=F(t)\delta(x-a) \\ m_i\dot{\mathrm{v}}_i(t)+C_i\left[\mathrm{v}_i(t)-y(d_i,t)\right]^3+\lambda_i\left[\dot{\mathrm{v}}_i(t)-\dfrac{\partial y(d_i,t)}{\partial t}\right]=0 \qquad i=1,2.....n \end{cases} \tag{1}$$

The finite element model for the beam with NES is written as follow:

$$M\ddot{y}(t)+B\dot{y}(t)+K(y)y(t)=F(t) \tag{2}$$

Where M, K and B are respectively the mass, stiffness and damping matrix.

The energy dissipated by the NES and the TMD at time t is defined by the ratio:

$$\eta(t)=\frac{E_{NES\,/\,TMD}(t)}{E_{inj}}=\frac{\displaystyle\int_0^t\sum_{i=1}^{n}\lambda_i\left(\dot{\mathrm{v}}-\dot{y}\right)^2_{x=d_i}d\tau}{\displaystyle\int_0^T F(\tau)\dot{\mathrm{v}}_{(x=a)}d\tau} \tag{5}$$

Where F , λ_i , $\dot{v}$ and $\dot{y}$ represent respectively the impulse force, damping ratio and the velocity at $x = d_i$ (location of the NES and TMD).

3 OPTIMISATION STUDY

In this section, we propose the multi-objective optimisation of the linear and nonlinear dynamic dampers (TMD, NES). The NSGA genetic algorithm is used to explore the design space and exploit the whole solution of the Pareto front [4]. For this study the multi-objective optimisation is defined in the following form:

$$\begin{cases} Max(F1) = \eta \quad where\ x \in [m_i, \lambda_i, k_i, C_i] \quad i = 1, 2, \ldots n \\ x \\ Min(F2) = \dfrac{\sum_{i=1}^{n} m_i}{M} \\ x \end{cases} \tag{6}$$

Where m_i, λ_i, k_i, C_i are the coefficient of the mass, damping and stiffness of the TMD or the NES; M is the primary structure mass.

3.1 Optimisation of the beam with two TMD

In the first case of this optimisation, we consider the beam defined in section2. The parameters of the two TMD are identical: $k = 27.215N/m^3$, $m = 0.3kg$ and $\lambda = 0.057N.s/m$. These TMD are coupled in the beam at location ($d_1 = 0.25m$ and $d_2 = 0.8m$). The variation levels of the design parameters are 20% for (m, k) and 90% for λ . As a results the maximum of the F_1 is 89.04% for the minimum of $F_2 \le 0.4kg$ corresponding to the design parameters $k_{opt} = 21.7720N/m^3$, $m_{opt} = 0.2926kg$ and $\lambda_{opt} = 0.1083N.s/m$. Then, we examine the influence of variation of the optimum values of stiffness and damping ratio. The figure2 illustrates this variation. We note that a variation of 3% of k_{opt} and λ_{opt} leads to a variation of 0.03% of F_1 . This low variation shows that the optimal Cost-Function is robust to dissipate the vibration energy of the beam

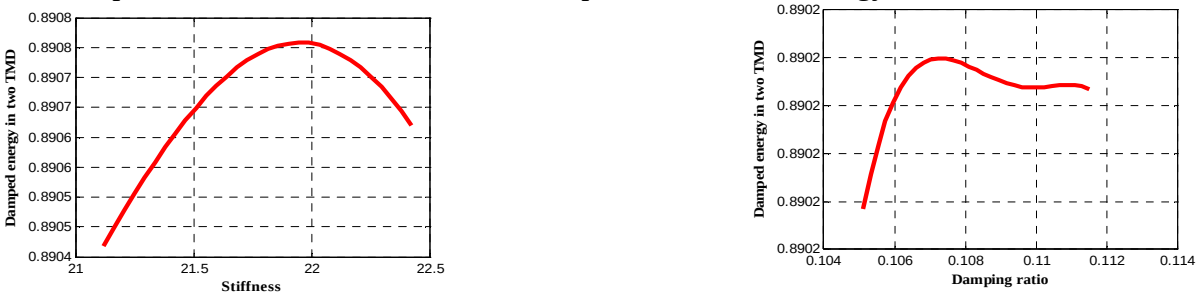

(a) **(b)**

Figure 2. Variation of dissipated energy ratio in two TMD: – (a) variation of stiffness – (b) variation of damping ratio

Finally, we examined the efficiency of the two TMD to dissipate the energy with different locations d before and after optimisation. Figure3a shows this variation, we note that the energy ratio absorbed by the two TMD before optimisation is $\eta = 89\%$ and after optimisation it becomes $\eta = 78\%$ at two locations of TMD : $d = 0.2m$ and $d = 0.8m$.

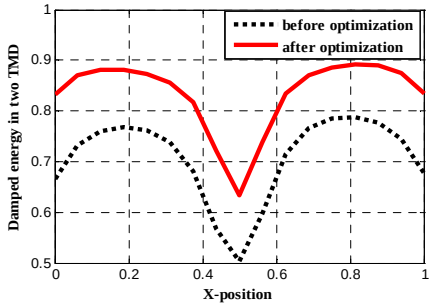

a- Dissipated energy versus X-position (TMD case)

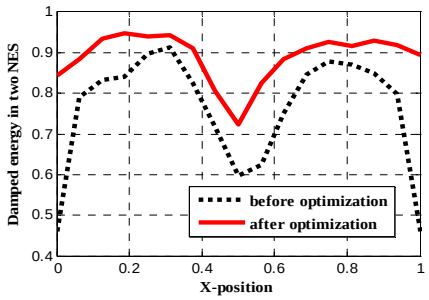

b- Dissipated energy versus X-position (NES case)

Figure 3 : Dissipated energy with optimised dynamic absorbers

3.2 Optimization of the beam with two NES

In this section, we consider the same beam with a two NES at different locations (Fig.1). The following parameters of the two NES are identical: $C_1 = C_2 = C = 1322\,N/m^3$, $m_1 = m_2 = m = 0.1kg$ and $\lambda_1 = \lambda_2 = \lambda = 0.05Ns/m$. We consider the same variation levels of the design parameters defined in the previous section except that the variation of C is 50%. As a results, the maximum of F_1 is 95% for $F_2 = 0.2kg$ and the optimum value obtained by optimisation of design parameters are: $C_{opt} = 1983N/m^3$, $m_{opt} = 0.08kg$ and $\lambda_{opt} = 0.095\,Ns/m$. Now, we examine the robustness of the optimum values (C_{opt}, λ_{opt}) by variation of 3%. We note that the variation of C_{opt} and λ_{opt} for this percentage (3%) causes a small variation of 0.04% of the cost-function F_1. So, these optimum values are robust to dissipate the maximum of energy from the beam. Then, we examine the efficiency of two NES to dissipate the shock energy before and after optimisation by varying its location on the beam. Figure3b illustrates the energy ratio dissipated by two NES for different positions on the beam. We note that this ratio reaches 95.40% after optimisation with two positions $d_1 = 0.2m$ and $d_2 = 0.8m$, whereas before optimisation this ratio is $\eta = 91\%$. As a conclusion, the variation of the position of the two NES affects its efficiency on the middle of the beam and we note that the two NES design are more efficient than two TMD design.

4 CONCLUSION

In this paper, we present a multi-objective optimisation of the dynamic absorbers (TMD and NES). In the first step of optimisation, we consider beam with two TMD the dissipated energy ratio after optimisation is 85%. On the other hand, this ratio reached 95% in the case of the beam with two NES. The robustness study with two TMD and two NES shows that the variation of the design parameters around the optimal values does not affect the dissipated energy ratio. Finally, the variation of the position of the two TMD and two NES affects its efficiency on the middle of the beam.

REFERENCES

[1] Georgiades F., Vakakis A.F., Dynamics of a linear beam with an attached local nonlinear energy sink, Communications in Nonlinear Science and Numerical Simulation 12 (2007) 643–651.

[2] Vakakis A.F., Manevitch L.I., Gendelman O., Bergman L., Dynamics of linear discrete systems connected to local,essentially non-linear attachments, Journal of Sound and Vibration 264 (2003) 559–577.

[3] Vakakis A. F., Rand R.H., Non-linear dynamics of a system of coupled oscillators with essential stiffness non-linearities, International Journal of Non-Linear Mechanics 39 (2004) 1079 – 1091.

[4] Bouazizi M.L., Ghanmi S., Nasri R., Bouhaddi N. , Robust optimisation of the non-linear behaviour of a vibrating system, European Journal of Mechanics A/Solids 28 (2009) 141–154.

[5] Bouazizi M.L., Ghanmi S., Bouhaddi N., Multi-objective optimization in dynamics of the structures with nonlinear behaviour: Contributions of the metamodels, Finite Elements in Analysis and Design 45 (2009) 612 – 623.

EFFECT OF ELECTROMAGNETIC ACTUATION ON THE DYNAMIC OF A FORCED HERTZIAN CONTACT OSCILLATOR

A. Bichri and M. Belhaq

Laboratory of Mechanics
University Hassan II-Casablanca, Morocco
Email: amine.bichri@gmail.com, mbelhaq@yahoo.fr

ABSTRACT

The effect of electromagnetic actuation (EMA) on vibroimpact dynamic in a single-sided Hertzian contact forced oscillator is investigated analytically and numerically near primary resonance. Attention is directed toward the case where the frequency of the alternative driven current in the EMA is assumed to be fast with respect to the frequency of the basic vertical harmonic load. An averaging technique based on the direct partition of motion (DPM) is first performed over the fast motion to derive the equation of the slow dynamic and then a perturbation analysis is applied on the slow dynamic to obtain the corresponding frequency response curves. It is shown that an EMA has an influence on the frequency shift in the case of DC actuation and on both the frequency shift and the nonlinear characteristic of the response in the case of fast AC actuation.

1 INTRODUCTION

Hertzian contacts are present in various mechanical devices and arise in many engineering applications, especially in mechanisms transforming movement of rotations or translations. A simple system to investigate this behavior is a moving surface subjected to a Hertzian contact force modeled by a single degree of freedom system. In [1], the vibroimpact dynamic of such a problem was studied numerically, analytically and using experimental tests in the case of a sphere-plane contact excited by a normal static and harmonic loadd. It was concluded that contact losses are provoked by jump phenomena near resonances.
The present work aims at investigating analytically and numerically the influence of EMA on the nonlinear characteristic of the frequency response and on the location of jumps near the primary resonance in a Hertzian contact oscillator. The purpose is to assess the possibility of tuning the resonance frequency values of the system by using EMA with a DC actuation or with a fast harmonic AC actuation.

2 CASE OF EMA WITH DC ACTUATION

We analyze the effect of EMA with a DC actuation on the frequency response of a forced single-sided Hertzian contact system. The schematic model of the system is shown in Fig. 1 and the equation of motion can be written in the form

$$m\ddot{\delta} + c\dot{\delta} + k\delta^{3/2} = N(1 + \sigma\cos\nu t) + F_{em} \tag{1}$$

The electromagnetic force F_{em} is given by

$$F_{em} = \frac{C_0 I^2}{(e-\delta)^2} \tag{2}$$

and I is the current induced in the magnetic circuit of the EMA which is supposed to be constant such that $I = I_0$.

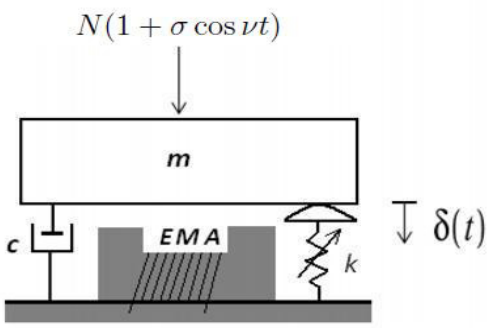

Figure 1: Schematic model of forced single-sided Hertzian contact oscillator submitted to EMA

Equation (1) can be rewritten in the following dimensionless form

$$z'' + \alpha z' + (\frac{2}{3}z + 1)^{3/2} = 1 + \sigma\cos\omega\tau + \frac{a_0}{(R - \frac{2}{3}z)^2} \tag{3}$$

where $\delta = \delta_s(\frac{2}{3}z + 1)$, $\delta_s = (\frac{N}{k})^{2/3}$, $\omega_0^2 = \frac{3k}{2m}\delta_s^{1/2}$, $\tau = \omega_0 t$, $\omega = \frac{\nu}{\omega_0}$, $\alpha = \frac{c}{m\omega_0}$, $a_0 = \frac{3C_0 I_0^2}{2m\omega_0^2\delta_s^3}$ and $R = \frac{e-\delta_s}{\delta_s}$. The nonlinear terms of Eq. (3) can be approximated using Taylor series expansion.

Expending these temes keeping only terms up to order 3 leads to

$$z^{''} + \alpha z^{'} + \omega_1^2 z + \beta_1 z^2 - \gamma_1 z^3 + G_1 = \sigma \cos \omega \tau \tag{4}$$

where $\omega_1^2 = 1 - \frac{4a_0R^{-3}}{3}$, $\beta_1 = \beta - \frac{4a_0R^{-4}}{3}$, $\gamma_1 = \gamma + \frac{32a_0R^{-5}}{27}$, $G_1 = -a_0R^{-2}$, $\beta = \frac{1}{6}$ and $\gamma = \frac{1}{54}$. Using the MMS [2], we obtain the following amplitude-frequency-response equation

$$C_1^2 r^6 + 2B_1C_1r^4 + (A_1^2 + B_1^2)r^2 - (H_1^2 + H_2^2) = 0 \tag{5}$$

Figure 2 depicts the frequency-response curve for two different values of a_0 (which is related to the current I_0).

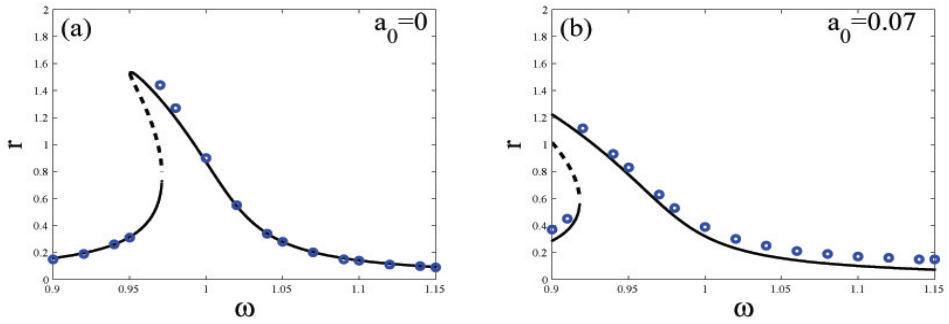

Figure 2: Amplitude-frequency response near the primary resonance. (a): $a_0 = 0$, (b): $a_0 = 0.07$; $\alpha = 0.02$, $\sigma = 0.03$ and $R = 1$. Analytical approximation (solid lines for stable and dashed lines for unstable), numerical simulation (circles).

3 CASE OF EMA WITH DC AND A FAST AC ACTUATIONS

In this section we consider that the rigid mass is excited by two EMAs, as shown in Fig. 3. The first EMA applied from above is actuated with DC debited by the current I_1 while the second actuator is actuated from below and produces AC actuation in the form $I = I_0 \cos \kappa t$, where I_0 and κ are, respectively, the intensity and the frequency of the excitation.

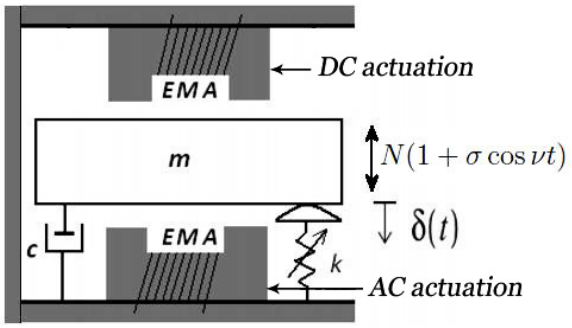

Figure 3: Schematic model of forced single-sided Hertzian contact oscillator submitted to two EMAs actuation.

Assume that the current I_1 is imposed according to the relation

$$I_1 = \frac{I_0(e + \delta)}{\sqrt{2}(e - \delta)} \tag{6}$$

the dimensionless equation of motion takes the form

$$z^{''} + \alpha z^{'} + z + \beta z^2 - \gamma z^3 = \sigma \cos \omega\tau + a_0(R^{-2} + \frac{4}{3}R^{-3}z + \frac{4}{3}R^{-4}z^2 + \frac{32}{27}R^{-5}z^3) \cos \Omega\tau \quad (7)$$

We use the method of DPM [3], we find the approximate equation of the slow dynamic

$$x^{''} + \alpha x^{'} + \omega_1^2 x + \beta_1 x^2 - \gamma_1 x^3 + G_1 = \sigma \cos \omega\tau \quad (8)$$

in which the parameters are now given by $\omega_1^2 = 1 + \frac{20a_0^2R^{-6}}{9\Omega^2}$, $\beta_1 = \beta + \frac{40a_0^2R^{-7}}{9\Omega^2}$, $G_1 = \frac{2a_0^2R^{-5}}{3\Omega^2}$ and $\gamma_1 = \gamma - \frac{400a_0^2R^{-8}}{81\Omega^2}$. Here we use the same frequency-response equation (5) obtained in the previous section but with the new definition of parameters as given in (8).
Figure 4 illustrates the frequency-response curves for different values of a_0.

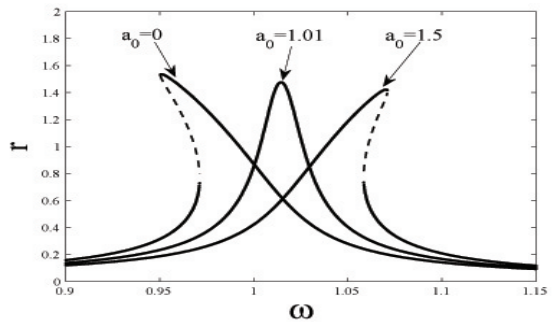

Figure 4: Frequency response near primary resonance for $\alpha = 0.02$, $\sigma = 0.03$, $\Omega = 8$ and $R = 1$. Analytical approximation (solid lines for stable and dashed lines for unstable).

4 CONCLUSION

We have studied analytically and numerically the effect of a fast harmonic EMA on vibroimpact dynamic in a single-sided Hertzian contact forced oscillator near the primary resonance. The method of DPM was applied to obtain the main equation of the slow dynamic and the MMS was implemented for obtaining the frequency response of the slow dynamic near the resonance. It is shown that adapted EMAs with DC and AC actuations not only produce a shift of the frequency response to the right, but also a change of the nonlinear characteristic of the system is obtained. Specifically, fast EMA actuation as suggested in the present study shifts the frequency response right (not left as in the case where only DC actuation is present) and changes the behavior of the system from softening.

REFERENCES

[1] J. Perret-Liaudet, E. Rigaud. "Response of an impacting Hertzian contact to an order-2 subharmonic excitation : Theory and experiments". *Journal of Sound and Vibration*, **296**: 319-333, 2006.

[2] A.H. Nayfeh, D.T. Mook. "Nonlinear Oscillations". Wiley: New York.

[3] I.I. Blekhman. "Vibrational Mechanics - Nonlinear Dynamic Effects, General Approach, Application". Singapore: World Scientific, 2000.

DYNAMIC FRICTION COMPACT MODEL : A NEW MULTICONTACT TRIBOMETER

J.L.DION, G.CHEVALLIER, O.PENAS, F.RENAUD
[1]Lab or Company Name
LISMMA- EA 2336
SUPMECA - 3 rue Fernand Hainaut 93407 Saint Ouen Cedex
France
jean-luc.dion@supmeca.fr

ABSTRACT

This paper presents an original friction measurement setup. It is designed to uncouple normal and tangential load. Friction measures acquired with this setup present a high signal to noise ratio. This friction experimental device allows characterizing various types of surfaces and several levels of excitation from static strain to dynamical motion including micro-sliding and macro-sliding. A measurement example is presented for a contact pair of Aluminum alloy starting from sticking limit until complete sliding. Finally, in order to use the results in vibration reduced models, a method is proposed to identify the compact Lugre Model from these measurements.

1 DESCRIPTION

Many previous works use or have developed tribometers ([1-11], [16-21]) The proposed test bench allow to uncouple normal and tangential loads over a wide frequency bandwidth to ensure the good quality of measurements and test conditions, as previously exposed. In order to verify this assumption and to identify state and rate models, normal force, tangential force, relative displacement and sliding velocity have to be measured over a large frequency range and with a great accuracy. Our tribometer has been so mounted on a MTS Elastomer Test System 830 which allows to obtain at 200 Hz a [1-100] µm displacement range inducing a [1.2-120] mm/s velocity range. To decouple normal and tangential load, the test setup is composed of three orthogonal symmetry-planes with four contact areas (Figure 1 and Figure 3). Each symmetry-plane allows an equal repartition of normal forces (planes P1 & P2) and tangential forces (plane P3). The complete experimental set, composed of samples in the tribometer, is iso-static. The base sample (Figure 1) is clamped on the reference frame of the hydraulic machine but the mobile sample is free in rotation around the jack displacement axis and avoids hyperstatism in the mechanism. For the same reason, the normal force (N) is performed with a flexible screw. The axis of this screw is placed along the intersection of planes P1 and P2. Moreover, the two application points of the normal force applied by the screw are symmetric on both sides of P3. These technical choices allow to assume a satisfying symmetry for three orthogonal planes, both for geometric properties of the mechanical setup and for load distributions.

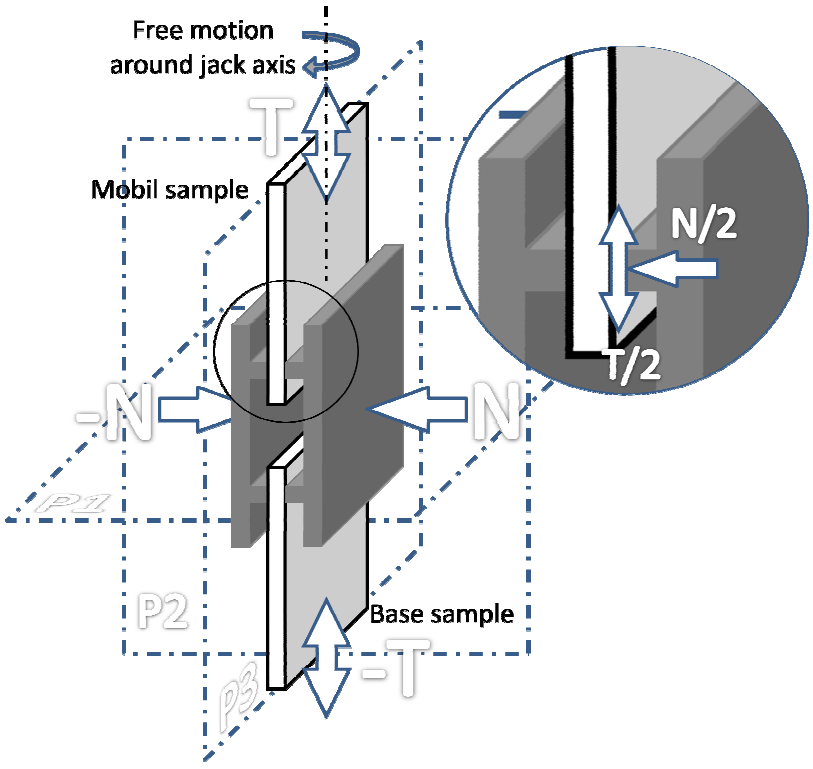

Figure 1: Principle of contact areas and normal and tangential forces The three orthogonal symmetry-planes (P1, P2 and P3) allow decoupling between normal and tangential forces and an equal repartition of these forces on each sample.

During the test, with tangential motion, static normal load is assumed to remain static. However the normal load is always measured and controlled with high frequency sampling during the test. This assumption is often not verified on other tribometers. A particular attention has been paid in the design of this tribometer in order to avoid coupling between normal and tangential load.

For all the tests, hydraulic jack movements are displacement controlled with the feed-back signal of the internal displacement transducer (LVDT). Measurements are performed with 3 force sensors (Fn, Ft, Ft2), 1 LVDT displacement sensor (X), 3 Foucault displacement sensors (xm, xh, xb) and 2 accelerometers (Ae, Af). Most of them are used in order to verify assumptions, only 3 sensors are necessary for dynamic friction measurement : 2 force sensors (Ft, Fn) and 1 displacement LVDT (X).

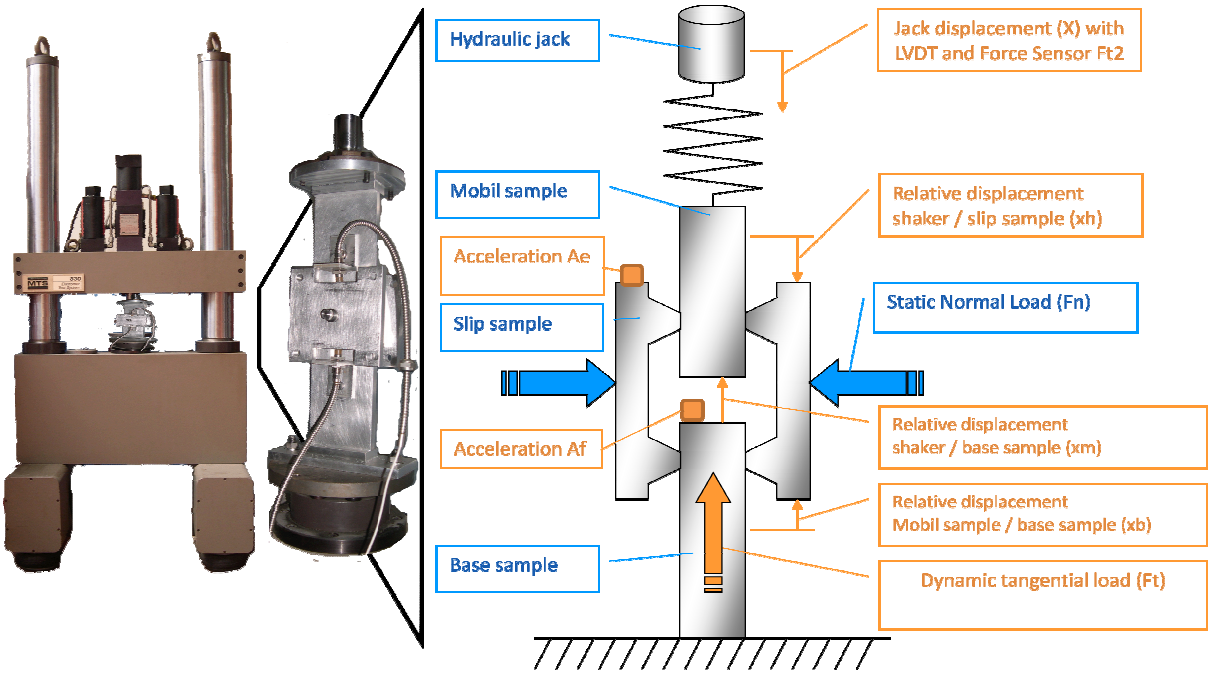

Figure 2: Schema and partial picture of the tribometer.

3 COMPACT MODEL SELECTION AND PARAMETRIC IDENTIFICATION

Many compact models have already been developed in previous works ([12]-[15], [22-29]). The LuGre model [14] can be considered as an evolution of Dahl's model with a velocity dependant friction factor introduced by the "g" function, often chosen as a Gaussian function. The LuGre model was completed in 2002 [12] and it includes elastoplastic behavior that occurs before the slipping limit has been reached.

$$\begin{aligned} F_t &= \left(K_0 z + C_0 \dot{z} + C_1 \dot{x}\right) F_n \\ \frac{dz}{dt} &= \dot{x} - K_0 \frac{|\dot{x}|}{g(\dot{x})} z \\ g(\dot{x}) &= \mu_d + \left(\mu_s - \mu_d\right) e^{-\left|\frac{\dot{x}}{V_s}\right|^{\alpha}} \end{aligned} \tag{1}$$

The proposed identification method is robust and has been applied for a very large number of tests with several frequencies and normal loads. The quality of fitting between simulation and measurements in Figure 3 is similar for most of the tests; some are better while only a few (less than 5%) are worse.

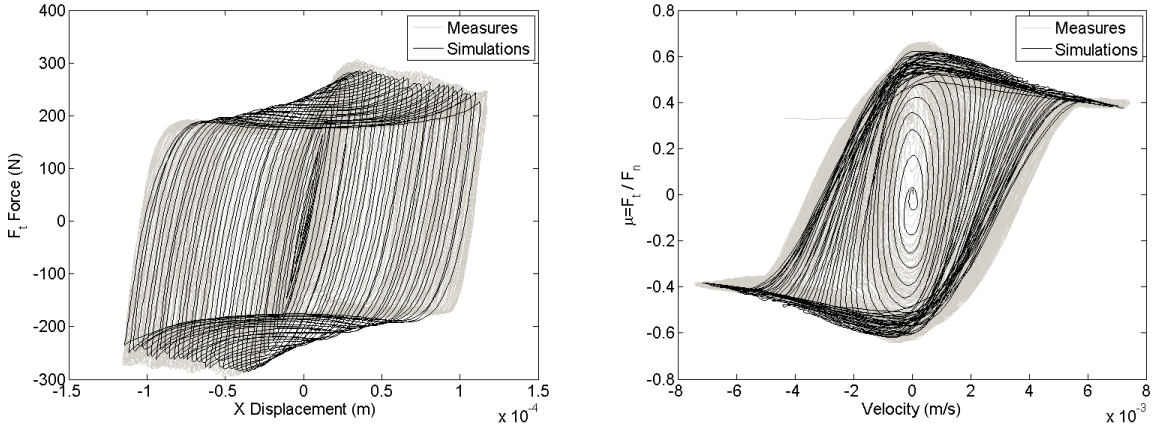

Figure 3: Comparison between measurement and simulation obtained with the proposed identification method

2 CONCLUSION

This work was performed in the field of structural vibrations. In a complex mechanism, the level of vibration strongly depends on the dissipation in the connected parts. This work presents a new test bench designed for improving the accuracy of measurements of non linear dissipative behaviors of frictional interfaces. This test bench is used for dynamic friction studies. Magnitudes of displacement have been tested from 10^{-5} m to 10^{-2}m while those of velocity have been studied from 10^{-7} m/s to 10 m/s. The tribometer design allows a very good independence between normal and tangential forces. Measurement techniques and signal processing methods highlight excellent accuracy with both direct measurements and parametric identification. As an illustration and because it is very well-formulated for vibrations problems, the LuGre Model has been identified from experimental results. An accurate method for parametric identification has been performed and a rheological description of the LuGre model has been presented. The prospects for improvement of this test means are to enable the measurements of the dissipative behavior on the scale of roughness. Thus the next test bench should make it possible to obtain measurements of displacements under 10^{-7}m.

REFERENCES

[1] Chevallier G., « Etude des vibrations de broutement provoquées par le frottement sec - application aux systèmes d'embrayage », UPMC, Paris, 2005.

[2] Camara M., Robbe-Valloire F., Gras R., Chen Y.-M. "Development of a pin-on disc type tribotester in order to study the influence of dynamic load on the tribological behaviour" Presses polytechniques et universitaires romandes, ISBN 978-2-88074-775-6, p. 65-74, 2008

[3] De Moerlooze K., Al-Bender F." On the relationship between normal load and friction force in pre-sliding frictional contacts. Part 2: Experimental investigation" Wear Vol. 269,p.183–189, 2010

[4] Mulvihill D.M., Kartala M.E., Olverb A.V, Nowella D., Hills D.A. "Investigation of non-Coulomb friction behaviour in reciprocating sliding", Wear, Vol. 271 p.802–816, 2011

[5] Eriten M., Lee C.-H., Polycarpou A. "Measurements of tangential stiffness and damping of mechanical joints: Direct versus indirect contact resonance methods" Tribology International, Vol.50, p. 35–44, 2012.

[6] Guibert M., Nauleau B. Kapsa P. Rigaud E. "Design and manufacturing of a recipocating linear tribometer", Tribologie et couplages multiphysiques, Presses polytechniques et universitaires romandes, ISBN 978-2-88074-775-6, p. 55-64, 2008

[7] Coulomb C. A., « Théorie des machines simples », in Mémoires de Mathématique et de Physique de l'Académie des Sciences, 1785, p. 161-335.

[8] Makris N. and Chang S.-P. "Effect of vscous, viscoplastic and friction damping on the response of seismic isolated structures" ISET Journal of Earthquake Technology, Paper N° 379, Vol.35, Issue N°4,pp. 113-141, 1998

[9] Adams V. and Askenazi A. "Building Better Products with Finite Element Analysis" OnWord Press, Santa Fe, N.M., 1999.

[10] Cremer L. and Heckl M., "Structure-Borne Sound", Springer-Verlag, New York,1988.

[11] Nouira H., Foltete E., Aitbrik B., Hirsinger L., et Ballandras S., « Experimental characterization and modeling of microsliding on a small cantilever quartz beam », Journal of Sound and Vibration, vol. 317, no. 1-2, p. 30-49, 2008.

[12] Almajid A., « Harmonic response of a structure mounted on an isolator modelled with a hysteretic operator: experiments and prediction », Journal of Sound and Vibration, vol. 277, no. 1-2, p. 391-403, 2004.

[13] Awrejcewicz J. et Lamarque C. H., Bifurcation and Chaos in Non-smooth Mechanical Systems. Singapore: World Scientific Publishing, J. 2003.

[14] Canudas de Wit C., Olsson H., Astrom K. J., et Lischinsky P., « A new model for control of systems with friction », IEEE Transactions on Automatic Control, vol. 40, no. 3, p. 419-425, 1995.

[15] Dahl P., « A solid Friction Model », The Aerospace Corporation, El Segundo, CA, TOR-0158H3107–18I-1, 1968.

[16] Baumerger T., Bureau L., Busson M., Falcon E., et Perrin B., « An inertial tribometer for measuring microslip dissipation at a solid–solid multicontact interface », REVIEW OF SCIENTIFIC INSTRUMENTS, vol. 69, no. 6, p. 2416-2420, 1998.

[17] Lampaert V., Al-Bender F., et Swevers J., « Experimental Characterization of Dry Friction at Low Velocities on a Developed Tribometer Setup for Macroscopic Measurements », Tribology Letters, vol. 16, no. 1/2, p. 95-105, 2004.

[18] Huang X. and Neu R.W., «High-load fretting of Ti–6Al–4V interfaces in point contact», Wear, vol. 265, no. 7–8, p 971 - 978, 2008.

[19]] Fouvry S., Duó P. and Perruchaut P. «A quantitative approach of Ti–6Al–4V fretting damage: friction, wear and crack nucleation», Wear, vol. 257, no 9–10, p 916 - 929, 2004.

[20] Guicciardi S., « On data dispersion in pin-on-disk wear tests », Wear, vol. 252, no. 11-12, p. 1001-1006, 2002.

[21] Quinn D. D., « Modal analysis of jointed structures », presented at the IDETC, Washington DC, 2011.

[22] Al-Bender F., Lampaert V. and Swevers J. "The Generalized Maxwell-Slip Model: A Novel Model for Friction Simulation and Compensation" IEEE Transactions On Automatic Control, Vol. 50, N°11, p.1883-1887, 2005

[23] Stribeck R., « Die Wesentlichen Eigenschaften der Gleit - und Rollenlager - the key qualities of sliding and roller bearings », Zeitschrift des Vereines Seutscher Ingenieure, vol. 46, no. 38-39, p. 1342-1348, 1902.

[24] Segalman D.J. "A Four-Parameter Iwan Model for Lap-Type Joints" Journal of Applied Mechanics, Vol. 72, Issue 5, p.752-760, 2005.

[25] Lampaert V., Swevers J. and Al-Bender F. "Modification of the Leuven Integrated Friction Model Structure", IEEE Transactions On Automatic Control, Vol. 47, N°4, p. 683-687, 2002

[26] Szolwinski M., « Observation, analysis and prediction of fretting fatigue in 2024-T351 aluminum alloy », Wear, vol. 221, no. 1, p. 24-36, 1998.

[27] Mo J. L., Zhu M. H., Zheng J. F., Luo J., and Zhou Z. R., « Study on rotational fretting wear of 7075 aluminum alloy », Tribology International, vol. 43, no. 5-6, p. 912-917, 2010.

[28] Liu H., « Tensile properties and fracture locations of friction-stir-welded joints of 2017-T351 aluminum alloy », Journal of Materials Processing Technology, vol. 142, no. 3, p. 692-696, 2003.

[29] Bowden F. et Tabor D., The friction and lubrication of solids. Oxford: Clarendon Press, 1950.N. Name, N. Name, and N. Name. *Book Title*. Publisher, City, 2013.

DYNAMIC SIMULATIONS OF A BOUNCING BALL ON A RANDOMLY VIBRATING PLATFORM

Chaïma Zouabi[1], Julien Scheibert[1] and Joël Perret-Liaudet[1]

[1]LTDS-UMR 5513 CNRS-Ecole Centrale de Lyon
36 Avenue Guy de Collongue, 69134 Ecully Cedex, FRANCE

Email :chaima.zouabi@ec-lyon.fr,Julien.Scheibert@ec-lyon.fr,joel.perret-liaudet@ec-lyon.fr

ABSTRACT

We study the dynamics of a bouncing ball subjected to gravity on a vibrating base platform. Contrary to popular models, we consider the case of a randomly excited system instead of a harmonically one. Then, the altitude and velocity of the plate are introduced as two stochastic independent processes known through their probability density functions. Three Poincaré maps are proposed, two of them based on the "Chirikov's assumption". The statistical properties of impact velocities and free flight duration are analyzed and compared as a function of the two control parameters, i.e. the restitution coefficient and the reduced base platform acceleration.

1 INTRODUCTION

Following the original work of Fermi in 1949 [1], the dynamic problem of a Ball Bouncing on a heavy vertically moving platform and subjected to a gravitational field has been widely studied [2-3]. Such an impacting system is commonly introduced to model many physical and engineering problems including cosmic particles in interstellar magnetic fields, vibration absorber devices, vibrated granular materials and gear rattle noise. In the deterministic case of a harmonically oscillating plate, this kind of dynamic systems exhibits a large number of interesting dynamical phenomena like chaotic behavior, global bifurcations such as crisis, period-doubling route, intermittency, stochastic gain of energy in the elastic limit case… Compared to the deterministic Bouncing Ball problem, the stochastically excited one has been much less studied [4]. The principal aim of this study is to revisit its dynamics by considering a stochastic process for the motion of the base platform instead of harmonic excitation.

2 THE BOUNCING BALL MODEL WITH A RANDOM BASE MOTION

The studied dynamic system consists of a ball that vertically bounces on a moving base platform under the action of the gravity $\boldsymbol{g}$ as shown in figure 1. The motion of the assumed infinitely massive platform is described by a stochastic continuous-time displacement process $h(t)$ of class $\mathcal{C}^1$ which is chosen so as to maintain impacts kind-motion of the ball with the base platform. With stereo-mechanical assumption for impacts, inelastic collisions are introduced via a restitution coefficient e which relates the post-impact velocity $V_{\uparrow}$ to the pre-impact ones $V_{\downarrow}$. The amount of energy dissipation is then controlled by the quantity $(1-e^2)$.

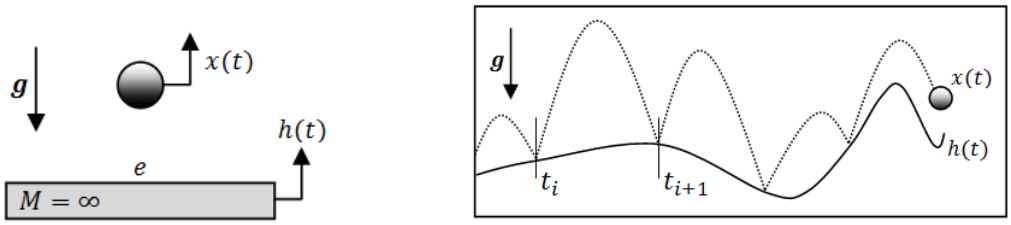

Figure 1: The Bouncing Ball system under study

Between two successive impacts occurring at times t_i and t_{i+1}, the ball follows a free flight parabolic trajectory $x(t)$ governed by the following height equation:

$$x(t) = -\frac{1}{2}g(t-t_i)^2 + V_{i\uparrow}(t-t_i) + h(t_i)$$

The pre-impact velocity at time t_{i+1} is given by $V_{i+1\downarrow} = -g(t_{i+1}-t_i) + V_{i\uparrow}$. Taking into account the restitution coefficient leads to the post-impact velocity at time t_{i+1} as follows:

$$V_{i+1\uparrow} = -eV_{i+1\downarrow} + (1+e)\dot{h}(t_{i+1})$$

These equations define the implicit mapping that describes the complete Bouncing Ball dynamics. The base displacement $h(t)$ and its time derivative $\dot{h}(t)$ will be introduced as two uncorrelated stationary ergodic random processes. In practice, random numbers are generated to simulate successive impacts. These sequences of numbers are consistent with the supposed known probability density functions (PDF).

3 THE DIMENSIONLESS POINCARÉ MAP

The dimensionless Poincaré map is obtained by introducing a frequency parameter ω defined from the two moments m_0 and m_2 of the base displacement h. More precisely, we have

$$\omega^2 = \frac{m_2}{m_0} = \frac{\int_{-\infty}^{+\infty} \Omega^2 S_{hh}(\Omega)\,\mathrm{d}\Omega}{\int_{-\infty}^{+\infty} S_{hh}(\Omega)\,\mathrm{d}\Omega}$$

where $S_{hh}(\Omega)$ is the power spectral density (PSD) of h. Expressing time in units of $1/\omega$, velocities in units of g/ω and accelerations in units of g leads to:

$$\begin{cases} \tau_{i+1} = \tau_i + \varphi_i \\ v_{i+1} = -e(v_i - \varphi_i) + (1+e)\Lambda w_{i+1} \end{cases} \quad \text{with} \quad -\frac{1}{2}\varphi_i^2 + v_i\varphi_i = \Lambda(z_{i+1} - z_i)$$

with $\tau = \omega t$, $\varphi_i = \omega(t_{i+1} - t_i)$ and $v_i = \omega V_{i\uparrow}/g$. The normalized height and velocity are given by $z = h/\sqrt{m_0}$ and $w = \dot{h}/\sqrt{m_2}$. Further, the two dimensionless control parameters of the Bouncing Ball dynamic are the restitution coefficient e and the reduced acceleration Λ given by $\Lambda = \omega\sqrt{m_2}/g = \omega^2\sqrt{m_0}/g = m_2/g\sqrt{m_0}$.

4 RESULTS

4.1 Simplified Poincaré map

In order to analyze the dynamics of our Bouncing Ball model, one can first search simplified solutions of the Poincaré map by introducing some simple assumptions. The most common one (" Chirikov assumption''[5]) is to consider that the height of the free flight is much larger than the amplitude of the base motion, so that the flight duration can be solved with $z_{i+1} \approx z_i$. In this case, $\varphi_i = 2v_i$, and the dynamics are reduced to the ones of the following simple autoregressive process: $v_{i+1} = ev_i + (1+e)\Lambda w_{i+1}$.With a normalized standard normal process for $w \sim \mathcal{N}(0,1)$, the mean value and variance of the post impact velocities are $\mathbb{E}(v) = 0$ and $\mathrm{Var}(v) = (1+e)\Lambda^2/(1-e)$, respectively. Unfortunately, this model suffers from the problem that the mean value of flight durations is equal to zero because it accepts

negative post impact velocities. In order to avoid this problem, one can retain only positive values of w by considering the random process $w = |\widetilde{w}|$ with $\widetilde{w} \sim \mathcal{N}(0,1)$. In this PDF of w is the normalized folded half-normal distribution ($\mathbb{E}(w) = \sqrt{2/\pi}$ and $\mathrm{Var}(w) = (\pi - 2)/\pi$). The mean value and variance of the post impact velocities $\mathbb{E}(v) = \sqrt{2/\pi}/(1 - e)$ and $\mathrm{Var}(v) = (1 + e)(\pi - 2)\Lambda^2/\pi(1 - e)$, respectively. From these results, one simply obtains the mean duration of flight and its variance $\varphi \sim 2v$.

4.2 Restricted Poincaré map.

In order to guarantee a physically sound behaviour, some restrictions should be applied to the generated random processes associated to both the normalized height z and velocity w. More precisely, to ensure a correct bouncing process, the sequence of z must be such that the base motion intersects the free flight, and the platform velocity w must be larger than the pre-impact velocity of the ball to ensure a correct bouncing process. These restrictions imply to solve the times t_i of the successive impacts. By solving the complete, but restricted Poincaré map, one obtains through Monte Carlo simulations the main characteristics of the random impact velocities and time duration of flight. Results concern PDF, mean values and variances of the stochastic responses as a function of the two control parameters e and Λ. These statistical results are then compared to those related to the above simplified Poincaré maps.

5 CONCLUSION

The well-known bouncing ball problem is revisited in this study by considering a stochastic base platform motion instead of a harmonic one. Statistical properties of the impact velocities and the duration of the flight motion are analysised. Three Poincaré maps are introduced to describe the dynamics, two of which built with the Chirikov assumption.

6 REFERENCES

[1] E. Fermi. On the Origin of the Cosmic Radiation. *Phys. Rev.* 75:1169-1174, 1949.

[2] P.J.J. Holmes. The dynamics of repeated impacts with a sinusoidally vibrating table. *Sound Vib.* 84(2):173-189, 1982.

[3] J.J. Barroso, M.V. Carneiro and E.E.N. Macau. Bouncing ball problem: numerical behavior characterization. *Phys. Rev. E.* 79:026206, 2010.

[4] E.D. Leonel. Breaking down the Fermi acceleration with inelastic collisions. arXiv:0903.1838, 2009.

[5] B.V. Chirikov. A universal instability of many-dimensional oscillator systems. *Phys. Rep.* 52:263, 1979.

FREE OSCILLATIONS OF A SLIDING SDOF SYSTEM: EFFECT OF A POLYNOMIAL FRICTION MODEL

F. Majdoub, J. Perret-Liaudet, M. Belin and J-M. Martin

Laboratory of Tribology and Dynamical Systems (LTDS), UMR CNRS 5513
Ecole Centrale de Lyon, Ecully, FRANCE
Email: fida.majdoub@ec-lyon.fr

ABSTRACT

This paper presents a brief study on a sliding single degree-of-freedom (SDOF) mass-spring system described by a pseudo-polynomial friction coefficient. Its oscillating free dynamic response is analyzed. The equation of motion is solved by using the Runge-Kutta Method. Furthermore, decreasing amplitudes of the damping responses are determined by using the Averaging Method. This study is concentrated on the various forms of these oscillations' envelops in relation with the polynomial expansion of the friction model.

1 INTRODUCTION

Friction is an essential aspect for different mechanical systems. Thus, many researchers have been involved in various friction models. For example, in the case of a Coulomb friction, it is modelled as a constant value independent of the sliding velocity. In other cases, viscous friction is introduced to model linear relationship with its sliding velocity. Sometimes, Stribeck effect has also been introduced [1]. In fact, friction modelling remains a challenge in mechanical systems. In order to analyze some dynamical behaviours, one of the solutions is to introduce a polynomial expansion of the friction coefficient as a function of the sliding velocity [2]. In this context, we will demonstrate a single degree-of-freedom (SDOF) mass-spring system having a pseudo-polynomial friction model. We will study the effect of this friction model on the behaviour of the free oscillatory responses by varying the constants carried in the friction coefficient.

2 THE DYNAMIC MODEL

The studied dynamic system consists of a SDOF mass-spring system (Figure 1), having a mass m and a linear spring of stiffness k. The mass can slide freely on a horizontal flat surface. The contact interface is loaded with a constant normal load N resulting in a friction force opposite to the motion represented as $\mu(\dot{x})N$.

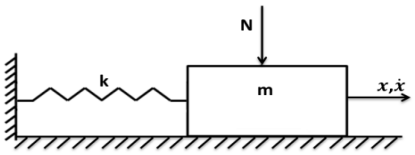

Figure 1. Mass-spring oscillating mechanical system.

The equation of motion which governs the free oscillating response of the studied dynamic system is written as follows:

$$m\ddot{x} + kx = -\mu(\dot{x})N \tag{1}$$

where $\ddot{x}$ is the acceleration and x is the displacement of the system. $\mu(\dot{x})$ is the friction coefficient as a function of the velocity $\dot{x}$. Equation (1) can be rewritten in the same form but with dimensionless parameters by performing the necessary replacements using the Vaschy-Buckingham theorem. Thus, the dimensionless equation of motion is derived to be:

$$\ddot{y} + y = -f(\dot{y}) \tag{2}$$

where $f(\dot{y})$ is the friction coefficient of the system as a function of the dimensionless velocity $\dot{y}$. The dot in this later equation (2) represents the derivative with respect to the dimensionless time τ. The initial conditions are described by: $y(0) = Y_0$ and $\dot{y}(0) = 0$. The friction coefficient $f(\dot{y})$ is defined to have a general pseudo-polynomial expansion as a function of the dimensionless velocity $\dot{y}$:

$$f(\dot{y}) = \sum_{n=0}^{+\infty} \mu_{2n} \dot{y}^{2n} \mathrm{sgn}(\dot{y}) + \sum_{n=0}^{+\infty} \mu_{2n+1} \dot{y}^{2n+1} \tag{3}$$

The sign function $\mathrm{sgn}(\dot{y})$ preserves the asymmetric property of $f(\dot{y})$. Actually, we must have $f(-\dot{y}) = -f(\dot{y})$. Furthermore, coefficients μ_m must be in such a way that $f(|\dot{y}|) > 0$ to ensure

damping behaviour. Finally, the equation of motion is directly solved using the known Runge Kutta integration time scheme.

3 THE ENVELOP OF THE DISPLACEMENT RESPONSE

As the sliding system dissipates, one observes decaying envelop of the dynamic free response. This decaying envelop can be directly obtained from the method of averaging [3]. This method assumes a slow time-variation of the amplitude $A(\tau)$ and the phase $\varphi(\tau)$ of the response compared to the period of the oscillating part of the system. Thus, using this method, the velocity response over one period is approximated by:

$$\dot{y}(\tau) = -A(\tau)\sin(\phi + \varphi(\tau)) \tag{4}$$

By averaging over one period of 2π and after the integration process, the first order derivative of the envelop is obtained as in the following:

$$\dot{A} = -\sum_{j=0}^{n}\left\{\frac{\mu_{2j+1}(2j+2)!}{\left(2^{j+1}(j+1)!\right)^2}A^{2j+1} + \frac{\mu_{2j}(-1)^j}{2^{j-1}\pi}\left[\sum_{q=0}^{q=j}\frac{(-1)^q(2q+1)!}{q!(2j+1-q)!(2j+1-2q)}\right]A^{2j}\right\} = F(A) \tag{5}$$

Sometimes, the decaying law of A can be easily obtained; however, in other cases, numerical integration is needed.

4 RESULTS AND DISCUSSION

In fact, we can analyze the properties of the amplitude by studying the first order differential equation of $A(\tau)$ denoted by $\dot{A} = F(A)$. This analysis is based on the determination of the fixed points, i.e. solution to $F(A^*) = 0$. Its stability can be discussed from the eigenvalues of the flow, i.e. $\lambda^* = dF(A^*)/dA$. Table 1 summarizes the type of the fixed point according to the sign of λ^*.

Sign of λ^*	Fixed point
$\lambda^* < 0$	Stable
$\lambda^* > 0$	Unstable
$\lambda^* = 0$	Semi-stable

Table 1. Type of the fixed points.

The fixed points can be also categorized from the potential function $G(A) = -\int F(A)dA$. Figure 2 represents all the possibilities.

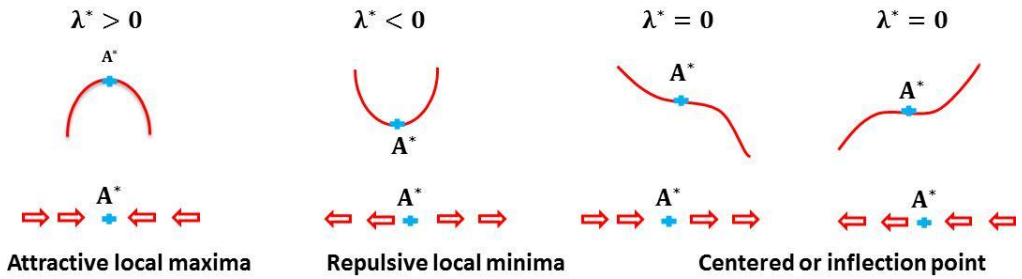

Figure 2. Determining the type of the fixed point from $G(A)$.

We can also have some information about the evolution of the envelop $A(\tau)$ by studying the second derivative d^2A/dt^2. Actually, if it is negative, the envelop is convex and if it is positive,

the envelop is concave. However, if $d^2A/dt^2 = 0$, then the envelop is a decreasing straight line. The second derivative can be found as follows:

$$\frac{d^2A}{dt^2} = F(A)\frac{dF}{dA} \tag{6}$$

For example, in the case of a constant friction model $f(\dot{y}) = \mu_0$, the amplitude A is governed by $\dot{A} = F(A) = -2\mu_0/\pi$ $(\ddot{A} = 0)$ and the evolution of the decaying envelop is linear. For viscous friction $f(\dot{y}) = \mu_1\dot{y}$, $F(A) = -\mu_1 A/2$ and the evolution of the decaying envelop is convex (the classical exponential decay). Finally, we present an example of a system having a quadratic friction model. For this example $F(A) = -0.5157 + 0.055A - 0.0209A^2$. The dimensionless displacement response is shown in figure 3 having both a concave and convex envelop form. This latter can be understood from the sign of $\ddot{A}$.

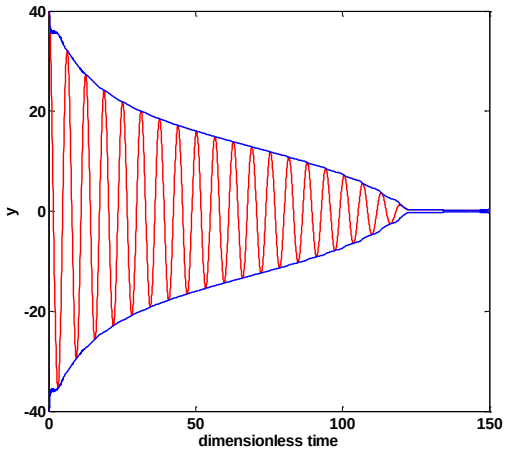

Figure 3. Dimensionless displacement response with second order pseudo-polynomial friction coefficient: $\mu(\dot{\boldsymbol{y}}) = (0.81 + 0.005\dot{\boldsymbol{y}}^2)\mathrm{sgn}(\dot{\boldsymbol{y}}) - 0.11\dot{\boldsymbol{y}}$.

5 CONCLUSION

In this study a SDOF sliding system is analyzed concerning its dynamic free response. To model the friction coefficient, a pseudo polynomial expansion is introduced. Related to this polynomial expansion, a better comprehension of the decaying amplitude of the free dynamic response is presented. From the averaging method, this amplitude is governed by a first order differential equation. Various forms of the oscillations' envelop can be shown depending on the properties of this differential equation. Currently, this kind of behaviours is confirmed by experimental work.

REFERENCES

[1] J. Awrejcewicz and P. Olejnik. Analysis of Dynamic Systems With Various Friction Laws. *Applied Mechanics Reviews*. 58: 389-411, 2005.

[2] P.L. Ko, M.-C. Taponat and R. Pfaifer. Friction-induced vibration – with and without external disturbance. *Tribology International*. 34: 7-24, 2001.

[3] A.H. Nayfeh and D.T. Mook. Nonlinear Oscillations. Wiley-Interscience Pub. 1979.

BIFURCATION-BASED MICRO/NANO-ELECTROMECHANICAL MASS DETECTION

V.-N. Nguyen[1] , S. Baguet[1], C.-H. Lamarque[2*], and R. Dufour[1]

[1]Université de Lyon, CNRS, INSA-Lyon, LaMCoS UMR5259
F-69621, Villeurbanne cedex, France
Email: Van-Nghi.Nguyen@insa-lyon.fr, Sebastien.Baguet@insa-lyon.fr, Regis.Dufour@insa-lyon.fr

[2]Université de Lyon, ENTPE, DGCB and LTDS, UMR CNRS 5513
Vaulx-en-Velin Cedex, 69518, France
Email: Claude.Lamarque@entpe.fr

ABSTRACT

When operating M/NEMS mass resonant sensors in the nonlinear regime, most of detection is based on the shift in the resonant frequency due to mass adsorption, as implemented in linear regime. This paper investigates an alternative mass detection based on the hysteretic behavior of the nonlinear frequency responses that takes advantage of bi-stability and bifurcations. A finite-degree-of-freedom reduced-order model of an electrostatically-actuated clamped-clamped microbeam is considered. Numerical results show that sudden jumps in amplitude make the detection of very small mass possible. Another interesting feature lies in the fact that the limit of detection can be set with the value of the operating frequency. However, it appears that this bifurcation-based mass detection does not exhibit the expected robustness. A possible improvement is proposed, based on the reinitialization of the system by a forced jump-down on the hysteretic response curve.

1 INTRODUCTION

Mass detection via resonant micro/nano electromechanical systems (M/NEMS) has gained a lot of interest during the last decade, and single-protein mass detection is now the state-of-the-art in terms of experimental results [1]. This higher sensitivity is achieved mostly by scaling down the devices. At micro and nano scales, devices often exhibit large amplitudes of vibration and thus operate in the nonlinear regime. The detection is traditionally based on the shift in the resonant frequency due to mass adsorption, as implemented in linear regime. Several improvements or alternatives exploiting the nonlinear behavior of the resonator have been proposed, such as the increase of the frequency shift through parametric instability [2] or pull-in phenomenon [3]. More recently, Kumar *et al.* [4] proposed a bifurcation-based detection that exploits the bi-stability of a piezoelectrically actuated microcantilever. This alternative detection principle will be computationally analysed in this paper in the case of an electrostatically-actuated clamped-clamped microbeam.

2 NONLINEAR ELECTROMECHANICAL MODEL

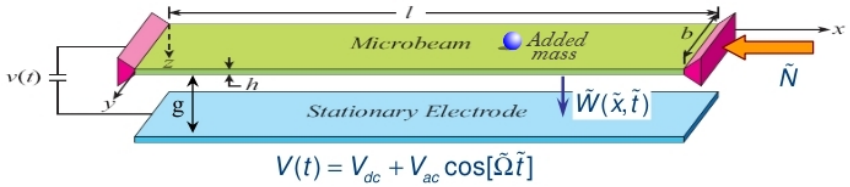

$l = 40\mu m \quad g = 0.1\mu m$
$b = 1.5\mu m \quad h = 1.5\mu m$
$Q = 10000$
$Vdc = 100 Vac = 1.9V$

Figure 1. Geometry and data of the resonant microbeam with added mass.

The model for the nonlinear electrostatically-actuated clamped-clamped microbeam with added mass of Figure 1 is based on the model developed by Kacem *et al.* for inertial resonant sensors [5].The nondimensional equation of motion is given by

$$\frac{\partial^4 w}{\partial x^4}\mathrm{d}x + \frac{\partial^2 w}{\partial t^2}\mathrm{d}x + \delta_{x_0}(x) m \frac{\partial^2 w}{\partial t^2} + c\frac{\partial w}{\partial t}\mathrm{d}x - \left(N + \alpha_1 \int_0^1 \left[\frac{\partial w}{\partial x}\right]^2 \mathrm{d}x\right)\frac{\partial^2 w}{\partial x^2}\mathrm{d}x = \alpha_2 \frac{\left[V_{dc} + V_{ac}\cos(\Omega t)\right]^2}{(1-w)^2}\mathrm{d}x \quad (1)$$

where $\tilde{w}(\tilde{x},\tilde{t})$ is the nondimensional bending displacement of the beam, m is the ratio between the added mass and the microbeam mass, i.e. $m = m_{added}/m_{beam}$ and $\delta_{x_0}(x)$ is the Dirac function used to locate the added mass. The left-hand side of Equation (1) represents the inertial, damping, elastic and geometrically nonlinear mechanical forces, whereas the right-hand side stands for the nonlinear electrostatic forces with V_{dc}, V_{ac}, Ω being the DC polarization voltage, the amplitude of the AC voltage, and the excitation frequency respectively.

A reduced-order model is generated by modal decomposition with the undamped linear mode shapes of the straight microbeam as basis functions in the Galerkin procedure. The solution of the resulting finite-degree-of-freedom nonlinear differential system is then computed by the Harmonic Balance combined with the Asymptotic Numerical Method for continuation analysis by means of the ManLab software [6].

3 DYNAMICS OF THE RESONANT SENSOR AND BIFURCATION-BASED DETECTION

The nonlinear microbeam exhibits a Duffing-like frequency response behavior, either hardening or softening depending on the dominating nonlinearity in the model (mechanical or electrostatic respectively). As shown in Figure 2a, the small amount of added mass downshifts the resonant frequency of the electromechanical resonator. This shift in frequency is commonly used to detect and measure the added mass [1]. However, the shift tends to zero as the added mass becomes smaller, thus limiting the amount of added mass which can be experimentally detected. Even if scaling down the device permits to increase the frequency shift and therefore improve the sensibility, shift-based detection shows some limitation when dealing with very small added mass such as molecules at atomic resolution.

Another approach consists in utilizing the dynamic jumps that occur in the Duffing hysteretic response. For this purpose, the resonator without added mass is operated at a constant excitation frequency Ω_{op} slightly lower than the frequency Ω_{lim} of the fold bifurcation point or limit point A_{lim}. At Ω_{op}, the frequency response curve is multi-valued (red curve of Figure 2a) with two stable solutions A_1 and A_2. In such a configuration, when a mass m is added, the response curve is shifted to the left (blue curve). At the operating frequency Ω_{op}, this curve is single-valued. As a consequence, the solution jumps from point A_1 to point B, resulting in a sudden increase in amplitude. Moreover, the smaller the added mass, the larger the increase of the response.

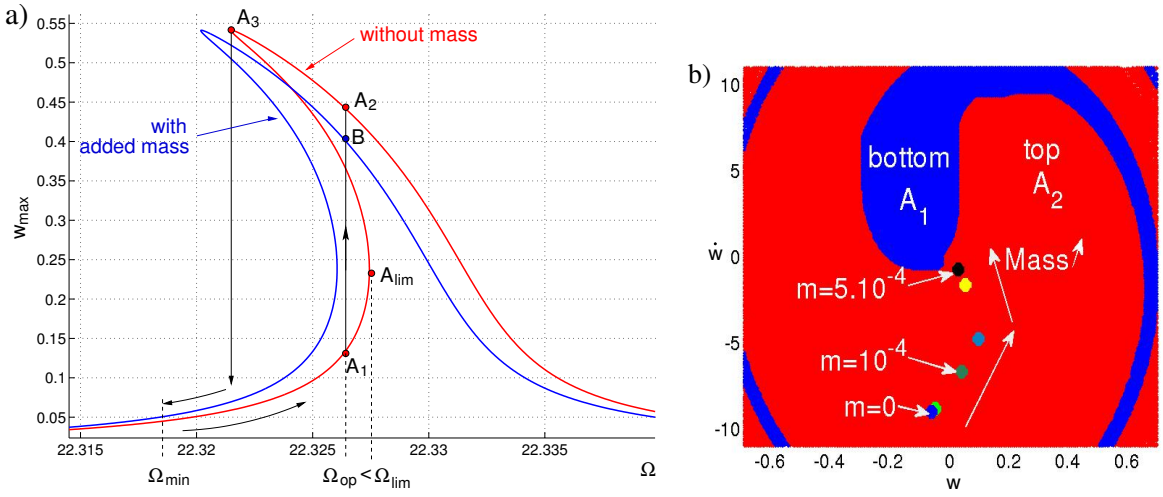

Figure 2: Softening behavior of the resonator. a) Shift in frequency of the due to added mass $m = 5.10^{-5}$ and jump phenomenon from A_1 to B. b) Basin of attraction without added mass at $\Omega_{op} = 22.3274$.

Another interesting feature is that the limit of detection can be set with the value of the operating frequency Ω_{op}. This can be useful if one wants to detect masses only above a given size. For instance, for the microbeam of Figure 1, operating at $\Omega_{op} = 22.3274$ permits the detection of masses larger than $m = 5.10^{-5}$, i.e. such that $m_{added} \geq 10^{-17}kg$, whereas operating at $\Omega_{op} = 22.325$ permits the detection of masses larger than $m \simeq 10^{-4}$, i.e. such that $m_{added} \geq 2.10^{-17}kg$. This limit of detection tends to zero as Ω_{op} approaches Ω_{lim}.

Although very promising, this bifurcation-based detection can be considered as robust only if the solution jumps back from point B to point A_1 when the added mass leaves the microbeam. On the opposite, if the solution jumps to the upper-point A_2 instead of A_1, then the next added mass will cause a jump from A_2 to B, which can be tiny and difficult to detect if the mass is very small. The value of the added mass and the moment when the added mass

leaves the microbeam lead to different initial conditions at point B, which in turn lead to a jump towards A_1 or A_2. The study of the basins of attraction of the microbeam without added mass (see Figure 2b) permits to conclude whether A_1 or A_2 will be reached. From the computations at $\Omega_{op} = 22.3274$, it turns out that for mass ratios equal or smaller than $m = 5.10^{-4}$, i.e. for physical values $m_{added} \leq 10^{-16}kg$, the jump always occurs towards the upper solution A_2 and consequently the bifurcation-based detection does not work anymore. When operating at $\Omega_{op} = 22.325$, the basin of attraction of the bottom stable solution is larger and A_1 is reached when $m > 1.5.10^{-4}$, i.e. $m_{added} > 3.10^{-17}kg$. Since the masses of interest are much lower than this value, it can be concluded that the system never returns to its initial stable position, i.e. it is not reinitialized, and thus the bifurcation-based detection only works once.

A solution for forcing the reinitialization after the added mass has left the resonator consists in decreasing the operating frequency until the point A_3 is reached and a jump-down takes place and then increasing the frequency again up to the initial operating frequency (point A_1) as depicted in Figure 2a.

4 CONCLUSIONS

An alternative mass detection based on nonlinear resonant sensors has been numerically investigated. This detection takes advantage of bistability and bifurcations of the hysteretic nonlinear responses. Contrary to the classical detection based on the shift in frequency, sudden jumps in amplitude make the detection of very small mass possible. Another interesting feature lies in the fact that the limit of detection can be set with the value of the operating frequency. However, it appears that this bifurcation-based mass detection does not exhibit the expected robustness. A possible improvement has been proposed, based on the reinitialization of the system by a forced jump-down on the hysteretic response curve.

REFERENCES

[1] M.S. Hanay, S. Kelber, A.K. Naik, D. Chi, S. Hentz, Bullard E.C., E. Colinet, L. Duraffourg, and M.L. Roukes. Single-protein nanomechanical mass spectrometry in real time. *Nat. Nanotechnol.*, 7(9):602–608, 2012.

[2] W. Zhang and K. L. Turner. Application of parametric resonance amplification in a single-crystal silicon micro-oscillator based mass sensor. *Sens. Actuators A: Phys.*, 122(1):23–30, 2005.

[3] M.E. Khater, E.M. Abdel-Rahman, and A.H. Nayfeh. Nonlinear phenomena in mems and nems - a micro sensor for measuring minute gas and biological masses. In *ENOC 2011*, Roma, Italy, July 24-29 2011.

[4] V. Kumar, Y. Yang, J.W. Boley, G.T.-C. Chiu, and J.F. Rhoads. Modeling, analysis, and experimental validation of a bifurcation-based microsensor. *J. Microelectromech. Syst.*, 21(3):549 –558, 2012.

[5] N. Kacem. *Nonlinear dynamics of M&NEMS resonant sensors: design strategies for performance enhancement*. Phd. thesis, Ecole Doctorale MEGA de Lyon, 2010-INSAL-0023, 2010.

[6] N. Kacem, S. Baguet, S. Hentz, and R. Dufour. Computational and quasi-analytical models for nonlinear vibrations of resonant mems and nems sensors. *Int. J. Nonlin. Mech.*, 46(3):532–542, 2011.

REDUCED-ORDER MODEL FOR NONLINEAR DYNAMICAL STRUCTURES HAVING A HIGH MODAL DENSITY IN THE LOW-FREQUENCY RANGE

A. Batou[1*], C. Soize[1], N. Brie[2]

[1]Laboratoire Modélisation et Simulation Multi-Echelle, MSME UMR 8208 CNRS
Université Paris-Est, 5 Boulevard Descartes, 77454 Marne-la Vallée, France
Email: anas.batou@univ-pairs-est.fr

[2]EDF R&D, Département AMA
1 avenue du général De Gaulle, 92140 Clamart, France

ABSTRACT

This research is devoted to the construction of a reduced-order computational model for nonlinear dynamical structures which are characterized by the presence of numerous local elastic modes in the low-frequency band. Therefore these structures have a high modal density in the low-frequency band and the use of the classical modal analysis method is not suited here. We propose to construct a reduced-order computational model using a small-dimension basis of a space of global displacements, which is constructed a priori by solving an unusual eigenvalue problem. Then the reduced-order computational model allows the nonlinear dynamical response to be predicted with a good accuracy on the stiff part of the structure. The methodology is applied to a complex industrial structure which is made up of a row of seven fuel assemblies with possibility of collisions between grids and which is submitted to a seismic loading.

1 INTRODUCTION

This paper is devoted to the construction of a reduced-order model for nonlinear dynamical structures having numerous local elastic modes in the low-frequency (LF) range. This paper focuses specifically on localized non-linearities such as elastic stops. We are interested in the nonlinear response of structures which are made up of a rigid master structure coupled with several flexible substructures. Such structures are characterized by the fact that they present in the LF band, both classical global elastic modes but also many local elastic modes. Moreover, the structure we consider is modelled with a large finite element model and has several localized nonlinearities (such as elastic stops). As a consequence, the non-linear transient response has to be constructed using a small time step for the integration scheme in order to correctly capture the nonlinear effects in the non-linear transient response. Then, the direct construction of the non-linear transient response is a very challenging issue and therefore the computational model has to be reduced. Due to the high modal density of the structures under consideration, the classical reduction [1] consisting in using the elastic modes of the underlying linear part of the nonlinear dynamical system is not suited here. Since we want to construct a small-dimension reduced-order computational model which has the capability to predict the nonlinear dynamical responses on the stiff part for which the local displacements are negligible, we have to construct the reduced-order computational model using a basis adapted to the prediction of the global displacements and therefore, we have to filter the local displacements in the construction of the basis.

Recently, a new method has been proposed to construct a reduced-order computational model in linear structural dynamics for structures having numerous local elastic modes in the low-frequency band [2]. In this method, a basis of the global displacements space and a basis of the local displacements space are calculated by solving two unusual eigenvalues problems. The elements of these two bases are not constituted of the usual elastic modes. The eigenvalue problem, allowing a basis of the global displacements space to be constructed, is constructed by introducing a kinematic reduction for the kinetic energy while the elastic energy is kept exact. In this paper, this method will be used to construct a basis of the global displacements space and then to deduce the reduced-order computational model of the nonlinear dynamical structure. Therefore, the contributions of the local displacements of the structure observed on the stiff part are neglected in the research presented here.

2 CONSTRUCTION OF THE REDUCED-ORDER COMPUTATIONAL MODEL

We are interested in predicting the transient responses of a three-dimensional nonlinear damped structure, with localized nonlinearities, and occupying a bounded domain Ω.

The methodology proposed in [2] consists in introducing a kinematic reduction of the structural kinetic energy. In a first step, the domain Ω is partitioned into n_J disjoint subdomains Ω_j. In a second step, this decomposition is used to construct the projection linear operator $\boldsymbol{u} \mapsto h^r(\boldsymbol{u})$ defined by

$$\{h^r(\boldsymbol{u})\}(\boldsymbol{x}) = \sum_{j=1}^{n_J} \mathbb{1}_{\Omega_j}(\boldsymbol{x}) \, \frac{1}{m_j} \int_{\Omega_j} \rho(\boldsymbol{x}') \, \boldsymbol{u}(\boldsymbol{x}') \, d\boldsymbol{x}' \,, \tag{1}$$

in which $\boldsymbol{x} \mapsto \mathbb{1}_{\Omega_j}(\boldsymbol{x}) = 1$ if $\boldsymbol{x}$ is in Ω_j and $= 0$ otherwise, where m_j is the total mass of subdomain Ω_j and where $\rho(\boldsymbol{x})$ is the mass density. This operator carries out an average of the displacements with respect to the mass density in each subdomain (kinematic reduction). We then introduce the $(m \times m)$ matrix $[H^r]$ relative to the finite element discretization of the projection operator h^r defined by Eq. (1). Then, the $(m \times m)$ projected mass matrix $[\mathbb{M}^r]$ is

constructed such that $[\mathbb{M}^r] = [H^r]^T[\mathbb{M}][H^r]$.

The basis of the global displacements space is made up of the solutions $\boldsymbol{\varphi}^g$ of the generalized eigenvalue problem

$$[\mathbb{K}]\boldsymbol{\varphi}^g = \lambda^g[\mathbb{M}^r]\boldsymbol{\varphi}^g \,, \tag{2}$$

in which the stiffness matrix is kept exact while the mass matrix is projected. The computation of the eigenvectors is carried out using an adapted subspace iteration algorithm [3]. This algorithm avoid the assembly of matrix $[\mathbb{M}^r]$ which is a full matrix. If needed, a basis of the local displacements space can also be constructed and complete the basis of global displacements (see [2]).

The reduced-order computational model is obtained using the projection of displacement vector $\mathbb{U}(t)$ on the subspace spanned by the family $\{\boldsymbol{\varphi}^g_1, \ldots, \boldsymbol{\varphi}^g_{n_g}\}$ of real vectors associated with the n_g first eigenvalues $0 < \lambda^g_1 \leq \ldots \leq \lambda^g_{n_g}$. Then, the n_g-order approximation $\mathbb{U}_{n_g}(t)$ of $\mathbb{U}(t)$ is written as

$$\mathbb{U}_{n_g}(t) = \sum_{j=1}^{n_g} \boldsymbol{\varphi}^g_j q_j{}^g(t) \quad , \tag{3}$$

in which $\boldsymbol{q}^g(t) = (q^g_1(t), \ldots, q^g_{n_g}(t))$. The vector $\boldsymbol{q}^g(t)$ is solution of the following nonlinear reduced matrix equation

$$[M]\ddot{\boldsymbol{q}}^g(t) + [D]\dot{\boldsymbol{q}}^g(t) + [K]\boldsymbol{q}^g(t) + \boldsymbol{f}^{\mathrm{NL}}(\boldsymbol{q}^g(t), \dot{\boldsymbol{q}}^g(t)) = \boldsymbol{f}(t) \quad , t \in]0\,, T]\,, \tag{4}$$

with the initial conditions $\boldsymbol{q}^g(0) = \dot{\boldsymbol{q}}^g(0) = \mathbf{0}$, in which $[M]$, $[D]$ and $[K]$ are the $(n_g \times n_g)$ generalized mass, damping and stiffness matrices, where $\boldsymbol{f}(t)$ is the vector of the generalized forces and where $\boldsymbol{f}^{\mathrm{NL}}(\boldsymbol{q}^g(t), \dot{\boldsymbol{q}}^g(t))$ is the vector of the generalized nonlinear forces. The dynamical systems we are interested in this paper are made up of few eigenvectors of global displacements. Consequently, the size of the nonlinear reduced-order computational model defined by Eq. (3) is very small.

3 APPLICATION

In this Section, we present an industrial application of the methodology which consists in the dynamical analysis of a row of seven fuel assemblies with possibility of collisions between grids and submitted to a seismic loading. A fuel assembly is a slender structure which is made up of 264 flexible fuel rods, 25 stiff guide tubes and 10 stiff grids which hold the tubes in position. The guide tubes are soldered to the grids while the fuel rods are fixed to the grids by springs. The row of assemblies is made up of seven fuel assemblies. The fuel assemblies are linked each to the others by the rigid containment building on which an homogeneous seismic displacement is imposed. The mesh of the finite element model is plotted in Fig. 1. The finite element model has $313,908$ elements and $3,147,060$ DOFs and there are $51,548$ elastic modes in the band $[0\,, 400]$ Hz. The possible contact grid/grid and grid/containment are taken into account by introducing 160 elastic stops. Each grid has a left elastic stop and a right elastic stop, the containment building has 10 elastic stops face to rightmost assembly grids and 10 elastic stops face to leftmost assembly grids.

Each fuel assembly of the row is decomposed into 100 slices yielding 700 subdomains. For the band $[0\,, 400]$ Hz, the reduced-order computational model is constructed with 245 global eigenvectors (instead of $51,548$ elastic modes which would be required with a classical modal analysis). We are interested in the nonlinear transient relative displacement of the row of assemblies.

The nonlinear relative response is calculated in the interval time $[0\,, 19.48]$ s using an explicit Euler integration scheme with an integration time step 10^{-5} s. For an observation point,

Figure 1: Finite element mesh of a row of fuel assemblies: Grids (blue) and guide tubes (red). The fuel rods are not plotted.

the relative transient displacements (for the convergence with respect to the number of global eigenvectors has been analysed) is plotted in Fig. 2.

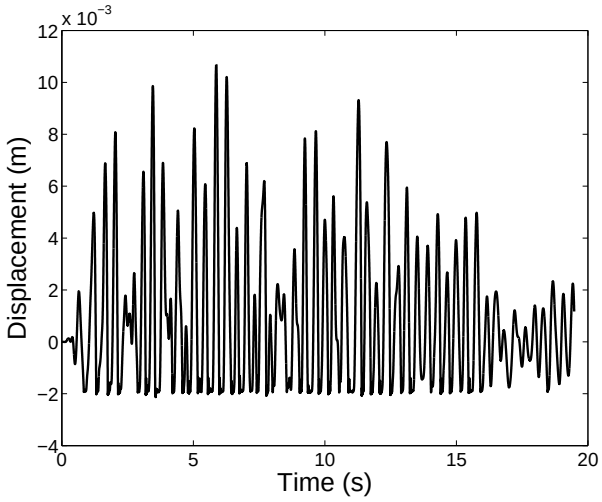

Figure 2. Relative transient displacement.

REFERENCES

[1] R.R Craig and A.J. Kurdila. *Fundmentals of Structural Dynamics*. John Wiley and Sons, New Jersey, 2006.

[2] C. Soize and A. Batou. Stochastic reduced-order model in low-frequency dynamics in presence of numerous local elastic modes. *Journal of Applied Mechanics - Transactions of the ASME*, 78(6):061003, 2011.

[3] K.J. Bathe. *Finite element Procedures, 2nd Edition*. Prentice Hall, 1996.

WAVE PROPAGATION ANALYSIS IN POROUS MEDIA VIA THE WAVE FINITE ELEMENT METHOD

Q. Serra[1,2] , M. Ichchou[1] and J-F. Deü[2]

[1]Laboratoire de Tribologie et de Dynamique des Systèmes (LTDS)
École Centrale de Lyon, Ecully, FRANCE
Email: quentin.serra@ec-lyon.fr, mohamed.ichchou@ec-lyon.fr

[2]Laboratoire de Mécanique des Structures et des Systèmes Couplés (LMSSC)
Conservatoire National des Arts et Métiers, Paris, FRANCE
Email: jean-francois.deu@cnam.fr

ABSTRACT

In this article will be presented the application of Wave Finite Element Method (WFEM) to porous media. Numerical aspects of the method such as the mode selection criterion, the influence of the formulation and the convergence of the method will be discussed. Comparison between the predicted wavenumbers and the three Biot's waves leads to physical interpretations about the propagation of energy in porous media. After its validation, this method will be used for calculating the forced response of a porous structure on a wave basis.

1 INTRODUCTION

Porous materials are used more and more often in the industry, because of their lightness and their sound absorbing properties in all the audible range. For vibroacoustic applications, the Biot-Allard model ([1]) is considered nowadays as one of the most precise ; however, because of the strong coupling within the porous medium, of the very small wavelengths and the high efficiency for reducing the sound level in the cavity, Finite Elements Method needs a large numbers of elements, and so expensive computations. Thus, such complete models are unadapted to optimization of sound absorbing layers.
Consequently, the reduction of the poroacoustic equations has been an issue in the last few years. Several strategies have been adopted: the first one is to reduce the Finite Element Model to reduce the size of matrices (e.g. with normal modes), the second one is to reduce the physic of the porous medium. In this approach can be found the Equivalent Fluid model ([1]) or the Transfer Matrix Method. These methods are very fast, but lies on assumptions (e.g. rigid skeleton) which are not in the general case perfectly justified.
In this article will be presented the application of the Wave Finite Element Method (WFEM) to porous media. WFEM is an undulatory approach based on the theory of periodic media, which can be seen as a Finite Element-based Transfer Matrix Method. It has been originally developped for slender structures which exhibit a wave guide behaviour in one direction and have uniform cross-section. It has been successfully applied to elastic beams ([2]), and adapted to bidimensional wave propagation in elastic plates ([3, 4]). Because it is based on Finite Element Matrices, all of the coupling effects within porous layers can be taken into account. From a elementary substructure, dispersion characteristics are computed, which mean wavenumbers and cross-section modes for each frequency.
In this framework, this study deals with the use of WFEM to compute the dispersion characteristics of porous media, and the wave modes deforms. These results will lead to several physical interpretations of the porous layer dynamics.

2 PRESENTATION OF WFEM

The equations of the dynamics of a free substructure can be computed by a Finite Element Method on the form :

$$\begin{pmatrix} \mathbb{D}_{LL} & \mathbb{D}_{LR} \\ \mathbb{D}_{RL} & \mathbb{D}_{RR} \end{pmatrix} \begin{pmatrix} \mathbf{q}_L \\ \mathbf{q}_R \end{pmatrix} = \begin{pmatrix} \mathbf{F}_L \\ \mathbf{F}_R \end{pmatrix} \tag{1}$$

where $\mathbb{D}_{ij} = \mathbb{K}_{ij} - \omega^2 \mathbb{M}_{ij}$, $(i,j) \in L, R$, are the ij component of the dynamic stiffness matrix, condensed on the left and right sections, and where the $\mathbf{q}_i$ are the nodal unknowns on the left and right sections.
By imposing Floquet-Bloch periodicity on the unknowns: $\mathbf{q}_R = \mu \mathbf{q}_L$, μ representing the propagation constant, the following problem can then be written ([5]):

$$\begin{pmatrix} q_R \\ F_R \end{pmatrix} = \mathbb{S} \begin{pmatrix} q_L \\ -F_L \end{pmatrix} = \begin{pmatrix} -\mathbb{D}_{LR}^{-1}\mathbb{D}_{LL} & -\mathbb{D}_{LR}^{-1} \\ \mathbb{D}_{RL} - \mathbb{D}_{RR}\mathbb{D}_{LR}^{-1}\mathbb{D}_{LL} & -\mathbb{D}_{RR}\mathbb{D}_{LR}^{-1} \end{pmatrix} \begin{pmatrix} q_L \\ -F_L \end{pmatrix} \tag{2}$$

The propagation constant μ are the eigenvalues of the Floquet propagator $\mathbb{S}$, and the cross-section modes, also called wave modes, are its eigenvalues. To avoid numerical ill-conditioning, this problem can be solved using the approach proposed by Zhong and Williams ([5]). This approach has been used here.
Because of the large number of solutions of the eigenvalue problem, equal to the size of the matrix $\mathbb{S}$, a selection criterion has to be defined to pick up only physically realistic solutions. Classically, the criterion is based on the amplitude of the imaginary part of wavenumbers or

on the ratio of imaginary part and real part of wave numbers. Finally, the unclassified selected wavenumbers at each frequency are classified following a criterion of MAC.

3 APPLICATION TO POROUS MEDIA

Application of WFEM to porous media is not just an application of a method, because two phases are present in the medium. First of all, WFEM can be applied to poroacoustic within the frame of Biot's theory. Indeed, Biot's theory is based on the hypothesis of a representative elementary volume and considers a continuum, so the medium can be considered as periodic, if the material properties and the geometry are considered to be constant in the direction of propagation. Several major differences with the elastic case might play an important role in the resolution. The presence of the fluid phase induces a strong dissipation of the energy, so imaginary part of wavenumbers are quite large (on the same order of amplitude as the real part), which creates a need to be cautious with the selection criterion. Numerical values of matrices can be quite different, because values of pressure are much bigger than displacements ; this has an influence on the conditioning of the matrices.

3.1 Convergence

Here will be presented convergence results for the mixed displacement pressure formulation, for a porous beam of lateral dimensions (3cm*2cm). The porous material is a soft acoustic foam, its parameters (Johnson-Champoux-Allard model) are given in [6].
Precision of the WFEM depends mainly on the dimension d of the substructure in the direction of propagation. Having a dimension too large will lead to errors, because the dimension will be too large compared with wavelength, and the structure will not be able to capture propagation effects precisely. However, having d too small leads to numerical errors, because the stiffness and mass matrices can be too small ([3]). The domain of validity of d has been investigated and a length of the order of $d \approx 1$mm is found to provide good results. The cross-section mesh has also an influence, having an aspect ratio $Ar = d/d_x \approx 0.2$, with d_x the element size along the transverse direction, leads also to good precision of the results. The order of shape function can be increased, but this leads to higher resolution times for no real difference in precision.

3.2 Wavenumbers and Wave Deforms

The WFEM has been applied to UP mixed formulation, and the less dissipated waves have been extracted. Classification has been made by maximizing the MAC between modes at two close frequencies. Figure 1 presents the evolution of the computed wavenumbers with frequency, together with the three analytical Biot's waves and the Johnson-Champoux-Allard equivalent fluid wave. The deform of the slow wave, computed by WFEM at 800Hz, is presented as an example Figure 2.

4 CONCLUSION

Wave Finite Element Method has been successfully applied to Biot's theory of poroelasticity. Convergence of the results has been shown. Some differences between the Biot's analytical wavenumbers and the computed wavenumbers are observed for some materials, even if cross-section deforms are coherent. This is due to an energetic coupling between the propagating waves, resulting in a difficulty to classified the modes. The visualization of cross-section modes highlights the non planeity of the cross-section. Finally this method will be used to compute the forced response of porous structures on the wave-mode basis and to compute the surface

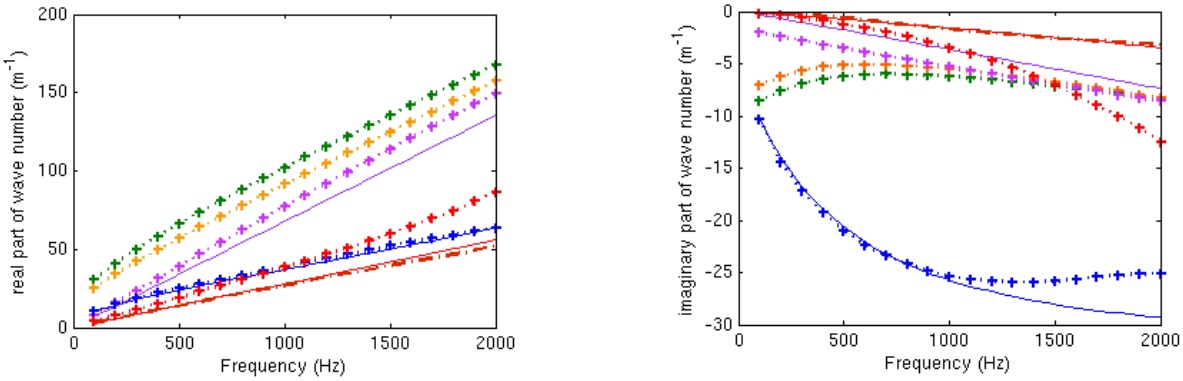

Figure 1: Dispersion Curves (UP Formulation). '.+' : WFEM results ; 'solid' Biot's analytical solutions ; '.-' : Equivalent Fluid (JCA). Left : real part ; Right : imaginary part.

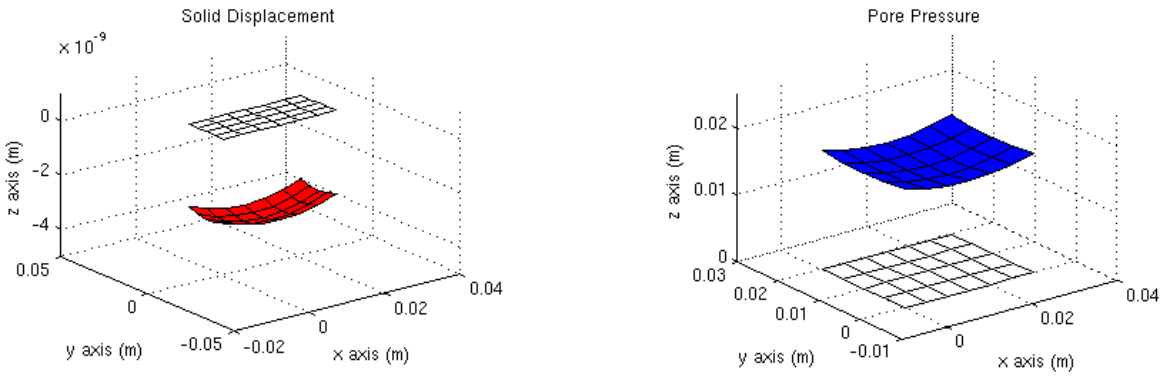

Figure 2: Wave deform at 800 Hz of the slow wave (real part). Left: Solid displacement; Right: Pressure. Initial section is plotted with transparent faces.

impedance or the transfer impedance of a structure at a lower cost than through a Finite Element analysis.

REFERENCES

[1] J.F. Allard and N. Atalla. *Propagation of sound in porous media: modelling sound absorbing materials*. John Wiley & Sons Inc, 2009.

[2] J.M. Mencik and MN Ichchou. Multi-mode propagation and diffusion in structures through finite elements. *European Journal of Mechanics-A/Solids*, 24(5):877–898, 2005.

[3] G. Inquiete. *Simulation numérique de la propagation des ondes dans les structures composites stratifiées*. PhD thesis, École Centrale de Lyon, 2008.

[4] B.R. Mace and E. Manconi. Modelling wave propagation in two-dimensional structures using finite element analysis. *Journal of Sound and Vibration*, 318(4-5):884–902, 2008.

[5] WX Zhong and FW Williams. On the direct solution of wave propagation for repetitive structures. *Journal of Sound and Vibration*, 181(3):485–501, 1995.

[6] R. Rumpler, J.F. Deü, and P. Göransson. A modal-based reduction method for sound absorbing porous materials in poro-acoustic finite element models. *The Journal of the Acoustical Society of America*, 132(5):3162–3179, 2012.

APPLICATION OF WAVE FINITE ELEMENT METHOD ON REDUCED MODELS FOR THE ANALYSIS OF FLEXURAL WAVES IN PERIODIC BEAMS

C.W ZHOU[1*] , M.N ICHCHOU[1], J.P LAINÉ[1] and A.M ZINE[2]

[1]Laboratoire de Tribologie et Dynamique des Systèmes
Ecole Centrale de Lyon, Ecully, FRANCE
Email: chang-wei.zhou@ec-lyon.fr, mohamed.ichchou@ec-lyon.fr,
jean-pierre.laine@ec-lyon.fr

[2]Institut Camille Jordan
Ecole Centrale de Lyon, Ecully, FRANCE
Email: abdel-malek.zine@ec-lyon.fr

ABSTRACT

The wave finite element (WFE) method is largely used to predict wave motion for one-dimension waveguide. In this paper, the WFE method is applied on periodic structure with sections of different impedance. The unit cell used in WFE is decomposed into sets associated with right (R) and left (L) cross-section and interior nodes. The novelty of this work lies in the integration of a model order reduction approach based on Craig-Bampton method into WFE method. The set of elastic physical coordinates of interior nodes is transformed into a set of modal coordinates, and then truncated to smaller set which takes only the low frequency modes into account. A numerical example concerning wave propagation in a periodic binary composition beam is presented. The method is validated by comparing results acquired with those obtained using the Differential Quadrature Method.

1 INTRODUCTION

The WFE method is based on finite element method and periodic structure theory. For the analysis of waveguide structures, a unit cell representative of the waveguide is extracted and analysed. The finite element formulation of this unit cell leads to an eigenvalue problem whose solution yields the wave propagation characteristics.

The WFE method is widely used to study the one-dimension homogeneous waveguide with constant cross-section. In homogeneous waveguides, the size of the unit cell in the propagation direction can be arbitrarily chosen. Usually, interior nodes in the unit cell are not necessary. But for periodic structures with a long period in the propagation direction, the interior nodes are needed to capture the local modes in medium frequency band. In the WFE formulation, the Degrees Of Freedom (DOFs) related to interior nodes are later condensed to boundary DOFs. The application of the Craig-Bampton method lies in the use of a truncated set of elastic modes expressed in modal coordinates, instead of using full mode basis expressed in physical coordinates. These matrices are easily manipulated for condensation or in the WFE formulation.

2 CRAIG-BAMPTON METHOD

The Craig-Bampton methodology is used extensively in the aerospace industry to re-characterize large finite element models into a set of relatively small matrices containing mass, stiffness and mode shape information that capture the fundamental low frequency dynamics of the structure. The primitive equation of motion for a structure is

$$\begin{bmatrix} M_{BB} & M_{BI} \\ M_{IB} & M_{II} \end{bmatrix} \begin{bmatrix} \ddot{q}_B \\ \ddot{q}_I \end{bmatrix} + \begin{bmatrix} K_{BB} & K_{BI} \\ K_{IB} & K_{II} \end{bmatrix} \begin{bmatrix} q_B \\ q_I \end{bmatrix} = \begin{bmatrix} F_B \\ F_I \end{bmatrix} \tag{1}$$

The elastic physical coordinates q_I are transformed into a set of modal coordinates P_I, then the set of modal solutions P_I is truncated to smaller set P_C. Subsequently, Craig-Bampton hybrid coordinates $[q_B \quad P_C]^t$ are related to the physical coordinates $[q_B \quad q_I]^t$ as follows:

$$\begin{bmatrix} q_B \\ q_I \end{bmatrix} = [B \quad \Phi] \begin{bmatrix} q_B \\ P_C \end{bmatrix} \tag{2}$$

The vectors in [B] are referred to as Boundary Node Functions, and those of $[\Phi]$ are referred to as Fixed Base Mode Shapes. Using reduced hybrid coordinates, the mass and stiffness matrices are changed respectively.

$$\begin{bmatrix} M'_{BB} & M_{BC} \\ M_{CB} & M_{CC} \end{bmatrix} \begin{bmatrix} \ddot{q}_B \\ \ddot{P}_C \end{bmatrix} + \begin{bmatrix} K'_{BB} & K_{BC} \\ K_{CB} & K_{CC} \end{bmatrix} \begin{bmatrix} q_B \\ P_C \end{bmatrix} = \begin{bmatrix} F'_B \\ F_C \end{bmatrix} \tag{3}$$

with

$$\begin{bmatrix} M'_{BB} & M_{BC} \\ M_{CB} & M_{CC} \end{bmatrix} = \begin{bmatrix} B & \Phi \end{bmatrix}^t \begin{bmatrix} M_{BB} & M_{BI} \\ M_{IB} & M_{II} \end{bmatrix} \begin{bmatrix} B & \Phi \end{bmatrix} \tag{4}$$

3 THE WAVE FINITE ELEMENT ANALYSIS USING THE REDUCED HYBRID COORDINATES

Consider a structural waveguide along axis x, The cross-section of the waveguide may be zero, one or two dimensional. The prediction of wave motion characteristics such as wavenumbers is targeted, which will be carried out frequency by frequency. The boundary DOFs q_B are divided

into q_L and q_R. As there are no external forces on the interior nodes, the equation of motion becomes:

$$\begin{bmatrix} M_{LL} & M_{LR} & M_{LC} \\ M_{RL} & M_{RR} & M_{RR} \\ M_{CL} & M_{CR} & M_{CC} \end{bmatrix} \begin{bmatrix} \ddot{q}_L \\ \ddot{q}_R \\ \ddot{P}_C \end{bmatrix} + \begin{bmatrix} K_{LL} & K_{LR} & K_{LC} \\ K_{RL} & K_{RR} & K_{RR} \\ K_{CL} & K_{CR} & K_{CC} \end{bmatrix} \begin{bmatrix} q_L \\ q_R \\ P_C \end{bmatrix} = \begin{bmatrix} F_L \\ F_R \\ 0 \end{bmatrix} \tag{5}$$

Without damping, the dynamic stiffness matrix are written as $\tilde{D} = K - w^2 M$

$$\begin{bmatrix} \tilde{D}_{LL} & \tilde{D}_{LR} & \tilde{D}_{LC} \\ \tilde{D}_{RL} & \tilde{D}_{RR} & \tilde{D}_{RC} \\ \tilde{D}_{CL} & \tilde{D}_{CR} & \tilde{D}_{CC} \end{bmatrix} \begin{bmatrix} q_L \\ q_R \\ P_C \end{bmatrix} = \begin{bmatrix} f_L \\ f_R \\ 0 \end{bmatrix} \tag{6}$$

$$P_C = -\tilde{D}_{CC}^{-1}(\tilde{D}_{CL} q_L + \tilde{D}_{CR} q_R) \tag{7}$$

Then the interior modal coordinates P_C are condensed to the boundary:

$$\begin{aligned} D_{LL} &= \tilde{D}_{LL} - \tilde{D}_{LI}\tilde{D}_{II}^{-1}\tilde{D}_{IL}, \quad D_{LR} = \tilde{D}_{LR} - \tilde{D}_{LI}\tilde{D}_{II}^{-1}\tilde{D}_{IR}, \\ D_{RL} &= \tilde{D}_{RL} - \tilde{D}_{RI}\tilde{D}_{II}^{-1}\tilde{D}_{IL}, \quad D_{RR} = \tilde{D}_{RR} - \tilde{D}_{RI}\tilde{D}_{II}^{-1}\tilde{D}_{IR}. \end{aligned} \tag{8}$$

Subsequently, the equilibrium equation with only the DOFs in the boundary can be written in the forme:

$$D \begin{bmatrix} q_L \\ q_R \end{bmatrix} = \begin{bmatrix} D_{LL} & D_{LR} \\ D_{RL} & D_{RR} \end{bmatrix} \begin{bmatrix} q_L \\ q_R \end{bmatrix} = \begin{bmatrix} f_L \\ f_R \end{bmatrix} \tag{9}$$

The state vector $[q_L \quad q_R]$ of $(n+1)$th unit cell and nth unit cell are related with a transfer matrix T[1]:

$$\begin{bmatrix} q_L^{n+1} \\ f_L^{n+1} \end{bmatrix} = T \begin{bmatrix} q_L^{n} \\ f_L^{n} \end{bmatrix} \tag{10}$$

The $2n$ eigenvalues λ_j of T is related to the length of the cell Δ and wave-number k_j of the j_{th} type of the wave.

$$\lambda_j = e^{-ik_j\Delta} \quad with \quad k_j = k_j^{'} - i\mu_j \tag{11}$$

μ_j and $k_j^{'}$ are real and equal to the attenuation and phase change per unit length that is associated with the j_{th} wave type.

4 NUMERICAL EXAMPLE - PERIODIC BEAM MODEL

The flexural vibration of a periodic binary composite beam with different materials is studied. The beam consists of an infinite repetition of an unit cell (see Figure 1). The unit cell is composed of two elements: one element of section A with length a_1 and one element of section B with length a_2, the periodic beam's lattice constant is then $\Delta = a_1 + a_2$.

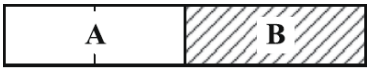

Figure 1. Unit cell of the periodic binary beam used in WFE[2]

In the WFE method, each part of the unit cell is divided into 10 elements. The reduction of the model is carried out by applying the Craig-Bampton method, the number of DOFs is reduced from 42 to less than 20. This method is validated by comparing the reduced model prediction with the study of Xiang et al.[2], which uses differential quadrature method (DQM). The dispersion relations calculated using different methods are illustrated in Figure 2. The "full

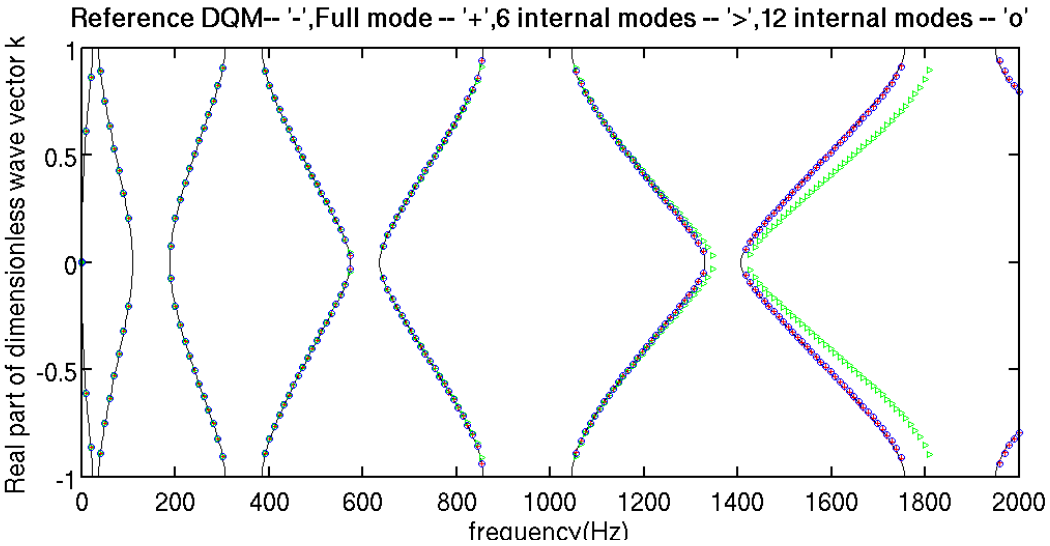

Figure 2. The dispersion relation of k using different methods

mode" refers to the WFE method without a model order reduction. If the first 12 modes shapes of the internal modes are taken into account, the wavenumber obtained conforms well with DQM result. These modes associate with the mode shapes below 6kHz, which are 3 times of the maximal frequency studied, 2kHz.

5 CONCLUSIONS

The WFE formulation with a model order reduction approach based on Craig-Bampton method is presented to analyse flexural wave propagation in a periodic beam with different section impedances. The numerical results indicate that the CraigBampton exhibits satisfying precision if modal content of the beam retains mode shapes with the frequencies at least 3 times higher than that required in the dispersion relation.

Numerous conclusions can be drawn using the dispersion relation obtained by the preceding method, such as band gap over which there can be no propagation of elastic waves in the materials, which gains insight into application such as frequency filters, noise control, absorption of vibration and so on.

Future work will be focused on the application of the reduced model for calculating the dispersion relation in 2D or 3D periodic structures, on the studies of dynamic behavior of finite periodic structures.

REFERENCES

[1] J.M. Mencik and M.N. Ichchou. Multi-mode propagation and diffusion in structures through finite elements. *European Journal of Mechanics - A/Solids*, 24(5):877–898, September 2005.

[2] Hong-Jun Xiang and Zhi-Fei Shi. Analysis of flexural vibration band gaps in periodic beams using differential quadrature method. *Computers & Structures*, 87(23-24):1559–1566, December 2009.

VIBRATIONS OF AN ELASTIC STRUCTURE WITH SHUNTED PIEZOELECTRIC PATCHES: EFFICIENT F.E. FORMULATION AND REDUCED-ORDER MODELS

L. P. da Silva[1*], J.-F Deü[1], W. Larbi[1] and M.A. Trindade[2]

[1]Structural Mechanics and Coupled Systems Laboratory
Conservatoire National des Arts et Métiers, Paris, France
Email: luciano.pereira_da_silva@cnam.fr, jean-francois.deu@cnam.fr, walid.larbi@cnam.fr

[2]Department of Mechanical Engineering, São Carlos School of Engineering at the University of São Paulo, São Carlos-SP, Brazil
Email: trindade@sc.usp.br

ABSTRACT

This work concerns the numerical modeling of the vibrations of an elastic mechanical structure equipped with several piezoelectric patches, with applications for the control, sensing and reduction of vibrations. Firstly, the validity of an original electromechanical finite element formulation, with only one couple of electrical variables per patch, namely (1) the electric charge contained in the electrodes and (2) the voltage between the electrodes, is investigated by comparison with a 3D electromechanical finite element formulation with one electrical degree-of-freedom per node (electrical potential). A clamped-free beam-like structure with a bounded piezoelectric patch is modeled and analyzed. The results demonstrate good agreement between the two formulations. The second part of the present work is devoted to the study of reduced-order models when the piezoelectric patches are shunted with special emphasis on the choice of the reduced base. Numerical examples are performed in order to evaluate several modal bases and analyze their efficiency.

1 INTRODUCTION

Since the early 70s, many finite element models have been proposed for the analysis of piezoelectric structural elements. In 2009, Thomas, Dëu and Ducarne [2] proposed an efficient finite element formulation, with only one couple of electrical variables per patch. This formulation is well adapted to practical applications due to the fact that realistic electrical boundary conditions, such as equipotentiality on the electrodes, naturally appear. The global variables are also intrinsically adapted to include any external electrical circuit into the electromechanical problem and to simulate the effect of shunt damping techniques. Thus, the first part of the present work investigates the validity of this formulation by comparison with a 3D electromechanical F.E. formulation with one electrical degree-of-freedom (dof) per node. A clamped-free beam-like structure with a piezoelectric patch is modelled and analysed.

The second part of this work is devoted to the study of reduced-order models of shunted electromechanical systems by means of modal expansion. Short-circuit and open-circuit eigenmode reduced bases are frequently used regardless of the shunt circuits type in the system [2-3]. In [1], the approach presented take-in-account the type of shunt circuits. The authors proposes the short-circuit basis for systems with resistive circuits and, for systems with resonant circuits, a modal basis, named coupled basis, obtained from the homogeneous and conservative shunted problem is suggested to be the most appropriated choice. In order to analyse the convergence of these three reduced bases, numerical examples are performed. The frequency response of the reduced order models are computed and compared to the full model response.

2 ELECTROMECHANICAL FINITE ELEMENT FORMULATION VALIDATION

This section aims to investigate the validity of the electromechanical formulation proposed in [2] by comparison with a full 3D model with one electrical dof per node [1-2]. In particular, the objective of this comparison is to show that the assumption of through-thickness linear variation of the electric potential is suitable for electromechanical systems with thin piezoelectric patches.

2.1 Electromechanical formulations

The two electromechanical finite element formulation analysed in this section are summarized in Table 1. They are applicable for the case of an elastic structure equipped with P piezoelectric patches and subjected to a prescribed displacement on a part and to a prescribed surface force density on the complementary part of its external boundary. In addition, each piezoelectric patch has its upper and lower surfaces covered with a very thin electrode and they are polarized in their transverse direction. For more details about these formulations, we refer the reader to [2].

2.2 Example of validation

The considered example consists of a clamped-free beam-like structure made of aluminium with one piezoelectric patch made of PIC-151. The thickness of the piezoelectric patch varies between 0.25 to 5 mm. To construct the two electromechanical models and solve the problems, the finite element code Nastran is used in association with Matlab software. For a complete example description (materials and geometric properties, analysis details, ...), we refer the reader to [1].

The results show that the proposed formulation is in good agreement with the full 3D standard electromechanical model, as presented in Table 2 and in [1]. Even if the difference between them increases with the thickness of piezoelectric patch, it remains small for a patch with 5 mm of thickness. So we can conclude that our formulation is validated to compute electromechanical systems with added thin piezoelectric patches bounded on a host structure.

Proposed formulation	3D standard formulation
One couple of electrical variable per patch (Q, V)	One electrical dof per node (φ)
$\begin{bmatrix}\mathbf{M}_u & \mathbf{0}\\ \mathbf{0} & \mathbf{0}\end{bmatrix}\begin{Bmatrix}\ddot{\mathbf{U}}\\ \ddot{\mathbf{V}}\end{Bmatrix}+\begin{bmatrix}\mathbf{K}_u & \mathbf{K}_{uv}\\ -\mathbf{K}_{uv}^T & \mathbf{K}_v\end{bmatrix}\begin{Bmatrix}\mathbf{U}\\ \mathbf{V}\end{Bmatrix}=\begin{Bmatrix}\mathbf{F}\\ \mathbf{Q}\end{Bmatrix}$	$\begin{bmatrix}\mathbf{M}_u & \mathbf{0}\\ \mathbf{0} & \mathbf{0}\end{bmatrix}\begin{Bmatrix}\ddot{\mathbf{U}}\\ \ddot{\boldsymbol{\varphi}}\end{Bmatrix}+\begin{bmatrix}\mathbf{K}_u & \mathbf{K}_{u\varphi}\\ -\mathbf{K}_{u\varphi}^T & \mathbf{K}_\varphi\end{bmatrix}\begin{Bmatrix}\mathbf{U}\\ \boldsymbol{\varphi}\end{Bmatrix}=\begin{Bmatrix}\mathbf{F}\\ \mathbf{q}\end{Bmatrix}$
$\mathbf{Q}$, $\mathbf{V}$: column vectors of electric charges and potential differences, of length P. $\mathbf{K}_{uv}$: electromechanical coupling matrix, of size $N_m \times P$ (N_m is the number of mechanical dofs). $\mathbf{K}_v$: diagonal dielectric matrix filled with the capacitances of the piezo. patches, of size $P \times P$.	$\mathbf{q}$, $\boldsymbol{\varphi}$: column vectors of electric charges density and potential, of length N_{el} (number of electrical dofs in the piezo. patches). $\mathbf{K}_{u\varphi}$: electromechanical coupling matrix, of size $N_m \times N_{el}$. $\mathbf{K}_\varphi$: dielectric matrix, of size $N_{el} \times N_{el}$.
Assumptions: - Equipotentiality in the electrodes; - The electric end effects for the patches are neglected; - The electric field vector is normal to the electrodes and its intensity is uniform in the piezo. patches.	**Remark:** - Equipotentiality in the electrodes enforced by assigning a single dof for voltage on all nodes of each electrode.

Table 1. Electromechanical formulations.

Effective Electromechanical Coupling Factor (EEMCF) in %						
Patch thickness (mm)	Beam Bending Vibration Modes					
	1		3		4	
	Proposed formulation	Standard formulation	Proposed formulation	Standard formulation	Proposed formulation	Standard formulation
0,25	15,36	15,36	6,98	6,98	3,47	3,46
0,5	15,88	15,91	9,02	9,02	4,69	4,67
1,00	13,00	13,18	10,46	10,50	5,74	5,69
2,00	7,81	8,15	9,54	9,71	5,36	5,25
4,00	3,75	3,96	6,48	6,53	3,17	2,89
5,00	2,99	3,10	5,68	5,58	2,48	2,16

Table 2. EEMCF: Proposed and the standard 3D electromechanical formulation.

3 REDUCED-ORDER MODELS ANALYSIS

This section is devoted to the study of reduced-order models of shunted electromechanical systems. Numerical examples are performed with special emphasis on the choice of the reduced base. The previous proposed formulation is used in this section.

3.1 Finite element model

For the cases of the piezoelectric patches are connected to the resistive shunts and to the resonant shunts, the finite element formulation of the electromechanical spectral problem writes:

$$-\omega^2\begin{bmatrix}\mathbf{M}_u & \mathbf{0}\\ \mathbf{0} & \mathbf{L}_e\end{bmatrix}\begin{Bmatrix}\mathbf{U}\\ \mathbf{Q}\end{Bmatrix}+j\omega\begin{bmatrix}\mathbf{0} & \mathbf{0}\\ \mathbf{0} & \mathbf{R}_e\end{bmatrix}\begin{Bmatrix}\mathbf{U}\\ \mathbf{Q}\end{Bmatrix}+\begin{bmatrix}\mathbf{K}_u+\mathbf{K}_{uv}\mathbf{K}_v^{-1}\mathbf{K}_{uv}^T & \mathbf{K}_{uv}\mathbf{K}_v^{-1}\\ \mathbf{K}_v^{-1}\mathbf{K}_{uv}^T & \mathbf{K}_v^{-1}\end{bmatrix}\begin{Bmatrix}\mathbf{U}\\ \mathbf{Q}\end{Bmatrix}=\begin{Bmatrix}\mathbf{F}\\ \mathbf{0}\end{Bmatrix} \quad (1)$$

where $\mathbf{R}_e$ and $\mathbf{L}_e$ are, respectively, the diagonal matrices filled with the electrical resistances R_e and the electrical inductances L_e of the shunt circuits. Note that $\mathbf{L}_e = \mathbf{0}$ for the case of resistive shunt. Moreover, depending on whether the patches are short-circuited ($\mathbf{V} = \mathbf{0}$) or in open-circuit ($\mathbf{Q} = \mathbf{0}$), the homogeneous problem associated to the Equation 1 takes the following forms:

$$[-\omega^2\mathbf{M}_u + \mathbf{K}_u]\{\mathbf{U}\} = \{\mathbf{0}\} \quad \text{short-circuit,} \quad (2)$$

$$\left[-\omega^2\mathbf{M}_u + \mathbf{K}_u + \mathbf{K}_{uv}\,\mathbf{K}_v^{-1}\,\mathbf{K}_{uv}^T\right]\{\mathbf{U}\} = \{\mathbf{0}\} \quad \text{open-circuit,} \quad (3)$$

3.2 Numerical examples

Numerical examples of shunted electromechanical problems given by Equation 1 are performed in order to evaluate the convergence of three reduced bases: short-circuit basis [2], open-circuit basis [3] and coupled basis [1]. The short-circuit and open-circuit bases can be easily computed solving Equations 2 and 3, respectively. The coupled basis is obtained by solving the conservative homogeneous problem of Equation 1. In additional, this basis can be used only for resonant shunt systems [1]. The frequency response of the reduced order models are compared to the full model response. The results show that the short-circuit and open-circuit bases need a large number of eigenvectors to converge in the resonance zones while the coupled basis demonstrate quickly and good convergence. However, combining the short-circuit and open-circuit reduced bases allows a quickly convergence of the reduced model to the full model.

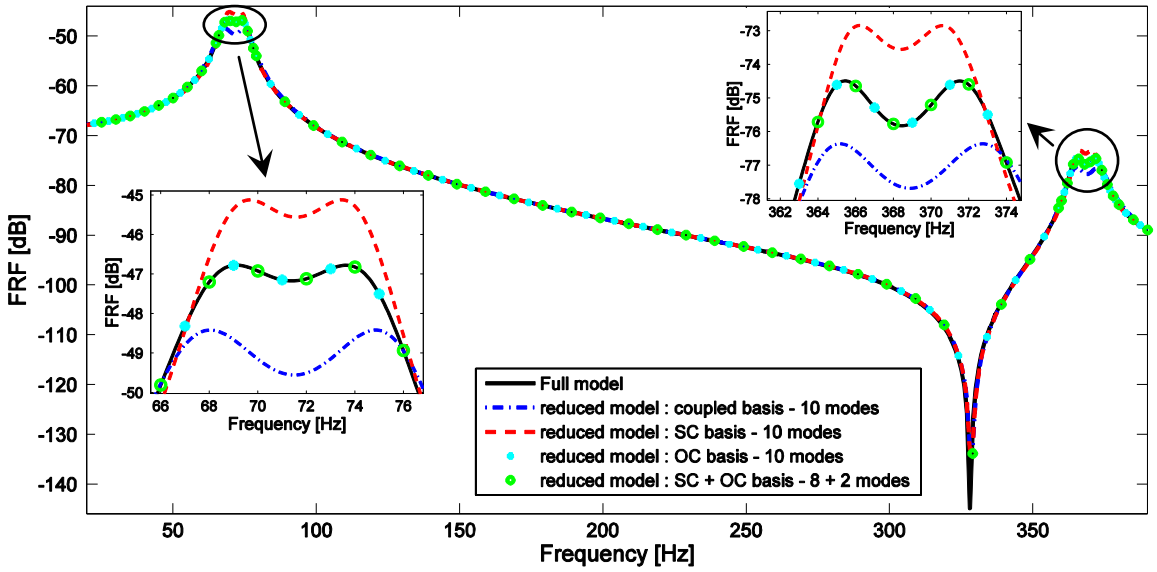

Figure 1. Frequency response functions of a clamped-free beam-like structure with two shunted piezoelectric patches – attenuation of the two first beam bending modes.

4 CONCLUDING REMARKS

In this study, an efficient electromechanical finite element formulation, adapted to any elastic structures with surface-mounted piezoelectric patches, was presented and validated. Then, reduced-order models of shunted electromechanical systems by means of modal expansion were analysed with special emphasis on the choice of the reduced base.

REFERENCES

[1] L.P. da Silva, J.-F. Deü, W. Larbi, M.A. Trindade. An efficient finite element approach for reduction of structural vibration and acoustic radiation by passive shunted piezoelectric systems. World Congress on Computational Mechanics, São Paulo, Brazil, 2012.

[2] O. Thomas, J.-F. Deü, J. Ducarne. Vibrations of an elastic structure with shunted piezoelectric patches: efficient finite elements formulation and electromechanical couplings coefficients. *International Journal for Numerical Methods in Engineering.* 80(2):235-268, 2009.

[3] T.C. Godoy de, M.A. Trindade. Modeling and analysis of la minate composite plates with embedded active-passive piezoelectric networks. Journal of Sound and Vibration. 330(2):194-216, 2011.

DETERMINING SENSOR LOCATIONS BASED ON MODEL ORDER REDUCTION TECHNIQUES

F. Casciati[1], S. Casciati[2*] and L. Faravelli[1]
[1]Department DICAr
University of Pavia, Pavia, ITALY
Email: fabio@dipmec.unipv.it, lucia@dipmec.unipv.it

[2]Department DICA
University of Catania, Siracusa, ITALY
Email: saracasciati@msn.com

ABSTRACT

In this paper how one can benefit of the Model Order Reduction theory to solve the problem of sensor placement in designing the architecture of a monitoring system is discussed.
In particular, the use of a reduced number of sensors is associated with a reduced of model and the optimal location of the sensors is pursued as the one which minimizes the deviations of the model state variables from their estimated time histories.

1 GOVERNING RELATIONS

Any discretized structural system [1] can be modeled by:

$$M\ddot{d}(t) + G\dot{d}(t) + Kd(t) = Bu(t) \tag{1}$$

$$y(t) = C_p d(t) + C_v(t)\dot{d}(t) + Du(t) \tag{2}$$

where $M, G, K \in \mathbb{R}^{n\,x\,n}$ are the mass, damping and stiffness matrices, respectively; $B = -Ma_g \in \mathbb{R}^{n\,x\,m}$ is the matrix of the input quantities; $C_p, C_v \in \mathbb{R}^{p\,x\,n}$ are the matrices of the observed variables, to be applied to $d(t)$ and $\dot{d}(t)$, respectively. In the case under investigation M is diagonal (and therefore invertible).

Let $\tilde{z}(t) = \{d(t), \dot{d}(t)\}^T \in \mathbb{R}^{2n}$. By introducing the following matrices,

$$\tilde{A} = \begin{bmatrix} 0 & I \\ -M^{-1}K & -M^{-1}G \end{bmatrix}, \tilde{B} = \begin{bmatrix} 0 & 0 \\ I & -B \end{bmatrix}, \tilde{C} = \begin{bmatrix} I & 0 \\ 0 & I \\ -M^{-1}K & -M^{-1}G \end{bmatrix} \tag{3}$$

one obtains:

$$\dot{z}(t) = \tilde{A}z(t) + \tilde{B}u(t) \tag{4}$$

$$y(t) = \tilde{C}z(t) + \tilde{D}u(t) \tag{5}$$

The order of the model can be reduced by using standard techniques, so that the minimum number of required state variables can be directly observed.

Moving from the state variables to the observed variables, the following relation holds

$$[y] = [C][z] \tag{6}$$

and the attention can be focused on accelerations and velocities at given locations

$$\begin{Bmatrix} a_t \\ v_t \end{Bmatrix} = \begin{bmatrix} C_a \\ C_v \end{bmatrix} \{z\} \tag{7}$$

To maintain a symmetric formulation, one divides $\{z\}$ into two vectors $\{z_1\}$ and $\{z_2\}$ such that

$$\begin{bmatrix} a_t \\ v_t \end{bmatrix} = \begin{bmatrix} [C_{a11}] & [C_{a12}] \\ [C_{v11}] & [C_{v12}] \end{bmatrix} \begin{bmatrix} z_1 \\ z_2 \end{bmatrix} \tag{8}$$

After the trivial kinematic reductions, further model order reductions are achieved by applying the balanced transformation method [2, 3]. For each of the studied reduced order models (which are characterized by a decreasing number of state variables), the following algebra applies:

$$[z_1] = [C_{a11}]^{-1}\{[a_t] - [C_{a12}][z_2]\} \tag{9}$$

$$[v_t] = [C_{v11}][z_1] + [C_{v12}][z_2] \tag{10}$$

where

$$[(a_{t+1} - a_t)\Delta t] = [C_{v11}][C_{a11}]^{-1}[a_t] - [C_{v11}][C_{a11}]^{-1}[C_{a12}][z_1] + [C_{v12}][z_2]$$

From the last equation, after re-arranging , one obtains:

$$[z_2]\{[C_{v12}] - [C_{v11}][C_{a11}]^{-1}[C_{a12}]\} = [(a_{t+1} - a_t)\Delta t] - [C_{v11}][C_{a11}]^{-1}[a_t]$$

and eventually

$$\begin{cases} [z_2] = \{-[C_{v11}][C_{a11}]^{-1}[C_{a12}] + [C_{v12}]\}^{-1}\{[(a_{t+1} - a_t)\Delta t] - [C_{v11}][C_{a11}]^{-1}[a_t]\} \\ [z_1] = [C_{a11}]^{-1}\{[a_t] - [C_{a12}][z_2]\} \end{cases} \quad (19)$$

.

2 SENSOR LOCALIZATION

It is assumed that the state variable model produces, at any floor, the accelerations which can be measured by suitable accelerometers. Their number is related with the minimum number of state variables that the system requires.

For each combination of the accelerometers, by using this information in Equations (19) one obtains an estimate of the state variables for the reduced models. The estimate differs from the response of the full actual model.

The deviation of these estimates form the state variables as computed by the models themselves can be evaluated by the corresponding sum-of-squares or its square-root:

$$\delta_i = \sqrt{\frac{\sum_{i=1}^{T}(z_i^* - \hat{z}_i^*)^2}{N}}$$

where the "*" denotes that each quantity is made dimensionless by dividing its value by the maximum value in the actual time history.

3 CONCLUDING REMARKS

The best location of the sensor is then assumed to be the location which minimizes the sum-of-squares. A genetic algorithm is used to drive the search problem.

REFERENCES

[1] W.H.A. Schilders, H.A. van der Vorst, and J. Rommes. *Model Order Reduction : Theory, Research Aspects and Applications*, Springer, 2008

[2] K. Calberg, C. Bou Mosleh, C. Farhat. Efficient non-linear model reduction via a least squares Petrov-Galerkin projection and compressive tensor approximations, *International Journal for numerical methods in engineering*, 86:155-181, 2011

[3] F. Casciati, S. Casciati, L. Faravelli, and M. Franchinotti, Model Order Reduction vs. Structural Control, Proceedings of 5th EACS, Genoa, July 2012.

ROM FOR NONLINEAR VIBROACOUSTIC PROBLEMS WITH STRUCTURAL AND ACOUSTIC NONLINEARITIES

Y. Gerges, E. Sadoulet-Reboul, M. Ouisse, and N. Bouhaddi

Institut FEMTO-ST, UMR 6174, Département de Mécanique Appliquée
24 Rue de l'Epitaphe, 25000 Besancon, FRANCE
Email: youssef.gerges@edu.univ-fcomte.fr, Emline-SadouletReboul / morvan.ouisse / noureddine.bouhaddi @univ-fcomte.fr

ABSTRACT

This paper presents a reduced order method dedicated to nonlinear vibroacoustic problems. Both structural and acoustics behavior are nonlinear. The structural nonlinearity is due to large displacements while the acoustic nonlinearity is due to the high intensity level in the fluid. The Kuznetsov equation is used to formulate the nonlinear acoustic problem. The reduced order model is based on the Ritz bases of the uncoupled linear problem. Nonlinear behavior is considered as a perturbation of the linear model so that the resolution is compared to a reanalysis problem. The Combined Approximation method dedicated to reanalysis problems is used to enriche the Ritz reduced basis.

1 INTRODUCTION

In this work, structural large displacements nonlinearties are considered. This type of nonlinearity is commonly encountered for thin structures as beams or plates [1]. The linear model yields to decoupling of inplane and bending movement while large displacements hypothesis involve a coupling between both displacements. On the other hand, acoustics become nonlinear with high pressure level ($> 130dB$). For low levels of nonlinearities where the pressure fluctuation remain small compared to the static pressure, Kuznetsov [2] proposed a formulation describing the fluid movement in term of velocity potential.

Modal superposition principle commonly used in linear cases to build on the reduced order model can not be used in nonlinear problems. The most common reduced order models in nonlinear problems are based on the proper orthogonal decomposition (POD) or the nonlinear normal modes (NNM). Both techniques have been compared in fluid-structure interaction [3]. In this paper, the combined approximation method (CA) [4] developed for reanalysis problems is used.

2 PROBLEM FORMULATION

Let us consider a fluid filled domain Ω_f bounded by a rigid boundary Γ_{fr} and a flexible boundary Γ_{fs}, coupled with a thin structure filling the domain Ω_s. The structure is holded on the boundary Γ_{sr}.

The three equations describing the fluid behavior are the momentum conservation, the mass conservation and the isentropic equation of state. Linearizing those equations at the first order leads to the wave equation where the fluid behavior is described with a single variable In the case of nonlinear behavior, the linearization step is no more admitted but we always aim to get an equation with one variable describing the fluid behavior. Kuznetsov has proposed a formulation with the velocity potential (Φ) as a state variable. The nonlinear wave equation is written as follow:

$$\Delta\phi - \frac{1}{c_0^2}\frac{\partial^2\phi}{\partial t^2} = \frac{1}{c_0^2}\frac{\partial}{\partial t}\left[(\nabla\phi)^2 + \frac{1}{c_0^2}\frac{(\gamma-1)}{2}\left(\frac{\partial\phi}{\partial t}\right)^2\right], \tag{1}$$

where γ is the ratio of the heat capacities.

Using the finite element method, the coupled problem can be written as follows:

$$\begin{bmatrix} \frac{1}{\rho_f}M_s & 0 \\ 0 & -M_f - \Delta M_f \end{bmatrix}\begin{bmatrix}\ddot{U}\\ \ddot{\Phi}\end{bmatrix} + \begin{bmatrix} 0 & C^T \\ C & -\Delta B_f \end{bmatrix}\begin{bmatrix}\dot{U}\\ \dot{\Phi}\end{bmatrix} + \begin{bmatrix} \frac{1}{\rho_f}K_s + \Delta K_s & 0 \\ 0 & -K_f \end{bmatrix}\begin{bmatrix}U\\ \Phi\end{bmatrix} = \begin{bmatrix}\frac{1}{\rho_f}F\\ 0\end{bmatrix}. \tag{2}$$

M_s, K_s are the mass and stiffness structure matrices, M_f, K_f are the mass and stiffness fluid matrices, C is the coupling matrix, ΔK_s is a nonconstant matrix describing the nonlinear effect of the structure, ΔM_f and ΔB_f are a nonconstant matrices describing the nonlinear effect in the fluid.

3 REDUCED ORDER METHOD

The combined approximation method (CA) was developed for reanalysis problems with reduced order models. It can be applied to nonlinear problems if the nonlinearity can be separated in a linear term and nonlinear term. Reduced order basis is written as follow:

$$T_{CA} = \left(I - B_0 + B_0^2 + \cdots + (-B_0)^{\nu-1}\right) r_0. \tag{3}$$

I is the identity matrix, r_0 and B_0 are the parameters of the reduction written as follow:

$$\begin{cases} r_0 = K_0^{-1} \left(M_0 + \Delta M \right) \varphi_0, \\ B_0 = K_0^{-1} \Delta K. \end{cases} \tag{4}$$

φ_0 is the modal basis of the initial problem.

The starting point or the reduced model is the modal basis verifying the eigenvalue problem of the uncoupled fluid-structure model (T_0). This initial basis is composed of two sub-bases representing the structural basis (T_0^s) and the fluid basis $\left(T_0^f\right)$. In order to take into account the coupling effect and the nonlinear behavior, these bases should be enriched by informations that are detailed hereinafter:

- The combined approximation method is applied to the structural basis where $\varphi_0 = T_0^s$ and $\Delta K = \Delta K_s$. For thin structures, T_0^s should include inplane and bending modes.
- Considering that the acoustic fluctuation still small compared to the static case, T_0^f can be used to predict the nonlinear uncoupled acoustic problem. With the coupling case, this basis is enriched by the static response of the fluid due to the structural contribution so that $T^f = \left[T_0^f | \Delta T_{fs}\right]$, where :

$$\Delta T_{fs} = \left(K_f - \omega^2 M_f\right)^{-1} C T_0^s. \tag{5}$$

Finally, the reduced order basis can be written as follow:

$$T = \begin{bmatrix} T_{CA}^s & 0 \\ 0 & T^f \end{bmatrix}. \tag{6}$$

4 APPLICATION

Let us consider a thin plate supported on a parallelepiped air filled cavity. The structure is excited with a harmonic excitation near the first acoustic mode. A temporal response is computed to illustrate the method. The full model (**FEM**) is compared to the reduced model using different reduced method:

- a reduced order model using the modal bases T_0^s and T_0^f of uncoupled problems (**MB**),
- a reduced order model using the modal basis T_0^s and enriching T_0^f by the structure contribution (cf. equation (5), **EMB**),
- a reduced order model using the CA for T_0^s and enriching T_0^f by the structure contribution (**CA**).

Figure 1a shows the displacement on the center of the structure for different models and figure 1b shows the pressure of different models at the corner of the cavity near the structure. To quantify the error, the energy of each signal is calculated. The relative error amplitude of the reduced order models are compared to the full model. Let $x(t)$ be a signal, the energy of $x(t)$ is written as:

$$E = \int_{-\infty}^{+\infty} x(t)^2 dt. \tag{7}$$

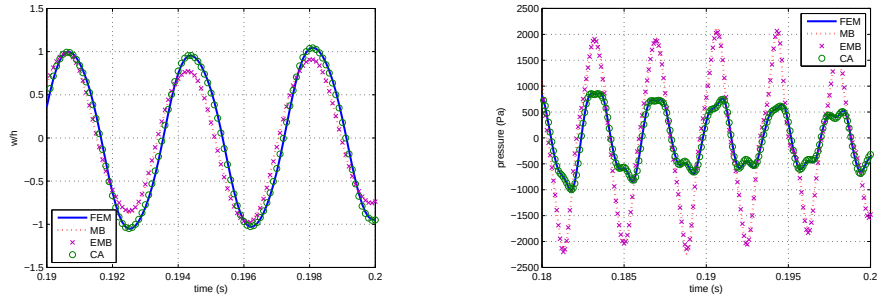

(a) Relative displacements (b) Pressure

Figure 1: Response of the cavity.

Model	U	$\dot{U}$	Φ	P
MB	26.5	27.1	12.9	22.4
EMB	26.9	27.6	13.4	22.9
CA	0.2	0.4	2.9	3.1

Table 1: Amplitude relative error (%)

Table 1 shows the displacements, the velocity,the velocity potential ant the pressure relative errors of the reduced order models. The **MB** and the **EMB** models predict badly both structure and fluid behavior. This is explained by the fact that the response is dominated by the nonlinear behavior that is neglected in the reduced order models. Using the combined approximation method and taking into account the structure contribution on the fluid describe with a high precison the structure behavior. Nevertheless, the fluid prediction can not be considered as optimum, this is due to the reduced order basis that does not take into account the nonlinear behavior.

5 CONCLUSION

A reduced order model dedicated to nonlinear vibroacoustic problems has been presented. It is based on the combined approximation method enriched by the structure contribution on the fluid. The application shows a good prediction on the structure behavior but the fluid behavior need a better prediction. A reduced order method taking into account the nonlinear fluid behavior should improve this estimation.

REFERENCES

[1] O.C. Zienkiewicz and R.L. Taylor. *The Finite Element Method: Solid Mechanics*, volume 2. Butterworth-heinemann, 2000.

[2] V.P. Kuznetsov. Equations of nonlinear acoustics. *Sov. Phys. Acoust*, 16(4):467–470, 1971.

[3] M. Amabili and C. Touzé. Reduced-order models for nonlinear vibrations of fluid-filled circular cylindrical shells: comparison of pod and asymptotic nonlinear normal modes methods. *Journal of fluids and structures*, 23(6):885–903, 2007.

[4] U. Kirsch. Combined approximations–a general reanalysis approach for structural optimization. *Structural and Multidisciplinary Optimization*, 20(2):97–106, 2000.

Mounting Vibrational MEMS Energy Harvesters on Printed Circuit Boards for Improved Response

David T. Kelemen, Mohammad I. Younis, and Abdallah H. Ramini

Department of Mechanical Engineering
State University of New York at Binghamton, UNITED STATES
Email: myounis@binghamton.edu

ABSTRACT

MEMS-scale vibration energy harvesters have gained attention as an energy source for low-power electronics. These could reduce or eliminate the need for batteries in powering remote devices. A great deal of research focuses on increasing the amount of power generated from energy harvesters. This paper proposes the idea of mounting a MEMS energy harvester on a printed circuit board (PCB) for improved performance. One idea that is investigated is to design the MEMS to resonate with the higher-order modes of the PCB to better interact with low frequency vibrations. System design is presented along with a power generation model and analysis strategies. We found that while the MEMS response does improve due to the PCB motion, at low frequencies, the higher-order modes are not active and do not contribute to the MEMS response. Accordingly, we investigate another idea of matching the fundamental natural frequency of the MEMS to that of the PCB. We found that response improves drastically in this case. By applying this concept to future designs, it may be possible to improve the response of MEMS and generate more power.

1 INTRODUCTION

Improving vibrational energy harvesters has been the focus of much research [1]. One method is to couple the MEMS with a larger structure that will have a better response in the anticipated frequency range [2],[3]. This paper proposes the use of a printed circuit board (PCB) to match one of its natural frequencies to that of the MEMS structure. It is convenient to use a PCB because the MEMS energy harvester can be mounted easily onto the structure [4].

2 PROBLEM FORMULATION

To analyze a MEMS energy harvester mounted on a PCB, a combination of a beam model coupled to a lumped-parameter model (beam-lumped model) is used. The model is illustrated in Figure 1, where the parameters of subscript 1 refer to the PCB and those of subscript 2 refer to the MEMS. Here $w(x,t)$ is the motion of the PCB relative to the base, $z_2(t)$ is the motion of the MEMS relative to the PCB, $m_{1,2}$ is mass, $k_{1,2}$ is equivalent stiffness, $c_{1,2}$ is a damping coefficient, a is the location of the MEMS on the PCB, and L_1 is the length of the PCB.

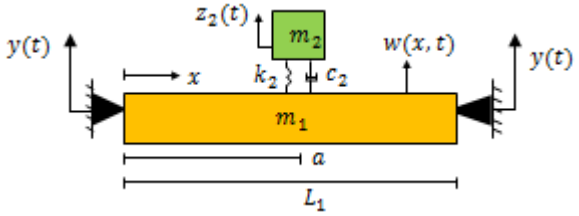

Figure 1. Model of energy harvester mounted on top of a PCB.

For this study, vibrations of a clothes dryer are chosen as a source although other values could be used per application. The input base excitation is modeled as a sinusoidal acceleration in Equation (1) with magnitude $A_s = 3.5\ m/s^2$ and frequency Ω [5]:

$$\ddot{y}(t) = -A_s \cos(\Omega t). \tag{1}$$

The governing equations for the system of Figure 1 are determined from the free-body diagrams as Equations (2) and (3), where $E_{1,2}$ is Young's Modulus, $\rho_{1,2}$ is density, and $A_{1,2}$ is area.

$$E_1 I_1 w_{xxxx} + \rho_1 A_1 \ddot{w} + c_1 \dot{w} = -\rho_1 A_1 \ddot{y}. \tag{2}$$

$$m_2 \ddot{z}_2 + c_2 \dot{z}_2 + k_2 z_2 = m_2 A_s \cos(\Omega t) - m_2 \ddot{w}(a,t). \tag{3}$$

Power generation from the damping forces due to a transduction method, such as piezoelectric and electromagnetic are estimated. The average rate at which energy is dissipated from damping forces per cycle can be estimated by [6]:

$$P_{avg} = \frac{1}{2} c_e \cdot \dot{Z}^2. \tag{4}$$

Here c_e is the damping coefficient representing the transduction method and $\dot{Z}$ is the steady-state velocity of the microstructure relative to the PCB.

3 RESULTS

3.1 Matching the fundamental frequency of a microstructure to the third of the PCB.

The first model in this study looks at exciting higher-order responses from the PCB to increase power generated. The MEMS was designed to match the third natural frequency of the PCB, or

$f_{MEMS1} = f_{PCB3} = 1091\ Hz$. Relative MEMS response and average power generation are shown in Figures 2a and 2b, respectively. These graphs show increased response as f_{MEMS1} approaches f_{PCB1}. Also, the figures suggest that response at the chosen low frequency is dominated by the fundamental mode rather than higher-order mode since the assumed excitation frequency is much lower than the higher order one.

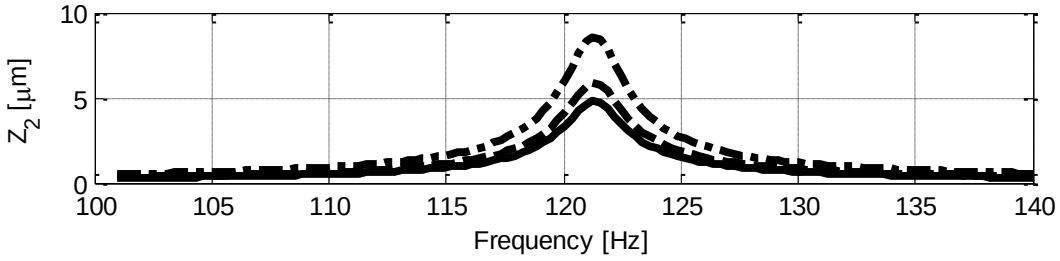

(a)

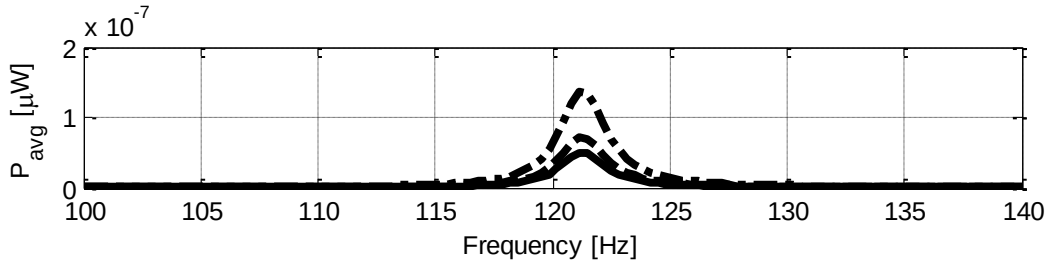

(b)

Figure 2. Frequency mismatch analysis when $f_{MEMS1} = f_{PCB3}$ around $f_{PCB1} = 121\ Hz$. (——— $f_{MEMS1} = f_{PCB3}$), (— — $f_{MEMS1} = 0.90 f_{PCB3}$), (— · - $f_{MEMS1} = 0.75 f_{PCB3}$)

The mounted energy harvester is next compared to an identical structure that is mounted directly on a source without a PCB. Using the same MEMS design, a comparison is made and illustrated in Figure 3 below.

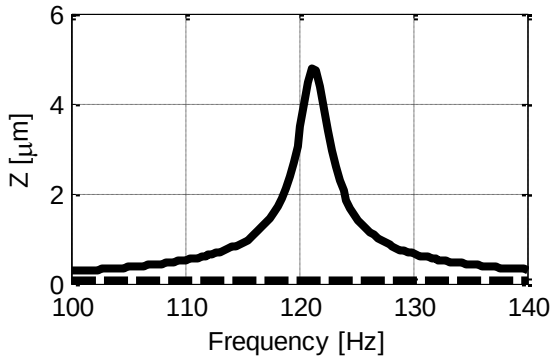

(a)

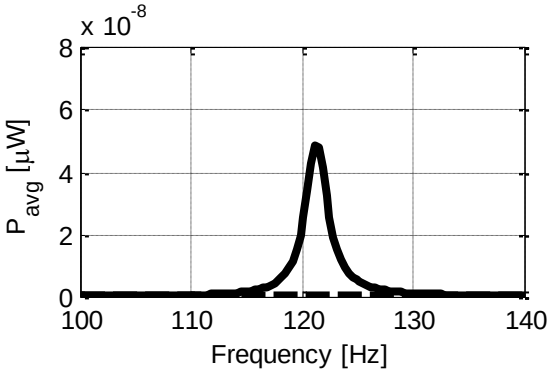

(b)

Figure 3. Comparison of mounted MEMS on PCB to that of identical unmounted MEMS. (——— MEMS mounted on PCB), (— — Unmounted MEMS)

The graphs in Figure 3 show a larger MEMS response and harvested energy when mounted on a PCB compared to its response alone.

3.2 Matching the fundamental frequency of a microstructure to that of the PCB.

Next, the system is redesigned so that $f_{MEMS1} = f_{PCB1}$ and results shown in Figure 4. The response is greatly improved and as well as power generation. Therefore, for the purpose of energy harvesting, this arrangement is more effective than the higher-order response setup.

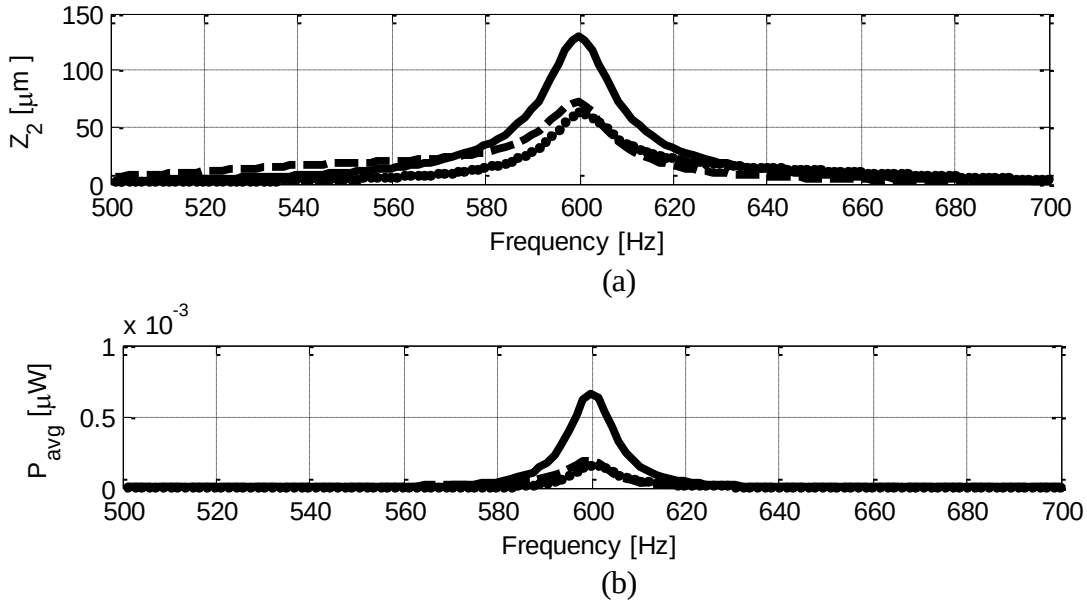

Figure 4. Frequency mismatch analysis for when $f_{MEMS1} = f_{PCB1} = 600\ Hz$.
(——— $f_{MEMS1} = f_{PCB1}$), (— — $f_{MEMS1} = 0.90 f_{PCB1}$), (····· $f_{MEMS1} = 1.10 f_{PCB1}$)

4 CONCLUSIONS

Several design ideas for a MEMS device mounted on top of a PCB were analyzed and compared in this study. It was shown that when mounted on the printed circuit board, a MEMS energy harvester has a better response than when on its own. We found that the higher-order modes do not contribute at the low frequency ranges of the energy harvesting source excitation. We found on the other hand that it is more effective to match the fundamental natural frequencies of the MEMS and the PCB. Although it is difficult to design a true microstructure of very low resonance frequency, such as that of typical ambient sources, approaching this goal could lead to significant improvement in the power output.

REFERENCES

[1] Zhu, Tudor, and Beeby. Strategies for increasing the operating frequency range of vibration energy harvesters: a review. *Measurement Science and Technology.* 21: 1-29, 2010.

[2] O. Aldraihem and A. Baz. Energy Harvester with a dynamic magnifier. *Journal of Intelligent Material Systems and Structures.* 22: 521-530, 2011.

[3] J. Rategar, C. Pereira, and H. Nguyen. Piezoelectric-based power sources for harvesting energy from platforms with low frequency vibration. *SPIE.* 6171: 617101-1 – 617101-7, 2006.

[4] A. Ramini, M. Younis, and R. Miles. Modeling the effets of PCB motion on the response of microstructures under mechanical shock. *Journal of Vibration and Acoustics*. 133: 061019-1 – 061019-9, 2011.

[5] S. Roundy, P. Wright, and J. Rabaey. A study of low level vibrations as a power source for wireless sensor nodes. *Computer Communications.* 26: 1131-1144, 2003.

[6] W. Thomson and M. Dahleh. *Theory of Vibration with Applications.* Prentice Hall, 1997.

Experimental characterization of a bi-dimensional array of negative capacitance piezo-patches for vibroacoustic control

F.Tateo[a], M. Collet[a], M. Ouisse[a], M.N. Ichchou[b] and K.A. Cunefare[c]

[a]Femto-st, 24 rue de l'Epitaphe, Besancon, France
[a]LTDS, 36 avenue Guy de Callongue, Lyon, France
[b]G.W. Woodruff School of Mechanical Engineering, 113 Erskine Love Building, Atlanta, GA

ABSTRACT

A recent technological revolution in the fields of integrated MEMS has finally rendered possible the mechanical integration of active smart materials, electronics and power supply systems for the next generation of smart composite structures. Using a bi-dimensional array of electromechanical transducers, composed by piezo-patches connected to a synthetic negative capacitance, it is possible to modify the dynamics of the underlying structure. In this study, we present an application of the Floquet-Bloch theorem for vibroacoustic power flow optimization, by means of distributed shunted piezoelectric material. In the context of periodically distributed damped 2D mechanical systems, this numerical approach allows one to compute the multi-modal waves dispersion curves into the entire first Brillouin zone. This approach also permits optimization of the piezoelectric shunting electrical impedance, which controls energy diffusion into the proposed semi-active distributed set of cells. Furthermore, we present experimental evidence that proves the effectiveness of the proposed control method. The experiment requires a rectangular metallic plate equipped with seventy-five piezo-patches, controlled independently by electronic circuits. More specifically, the out-of-plane displacements and the averaged kinetic energy of the controlled plate are compared in two different cases (open-circuit and controlled circuit). The resulting data clearly show how this proposed technique is able to damp and selectively reflect the incident waves.

Keywords: negative capacitance, smart materials, metacomposite, Bloch theorem, experiment.

1. INTRODUCTION

The design of innovative structures having new physical functionalities represents a big challenge for both industrial and academic communities. In the vibration domain a very important issue is the capacity of controlling the dynamic behavior of a structure by acting on the mechanical power flow in terms of transmitting and absorbing properties. Among all proposed solutions, distributed control system integrating shunted piezoelectric patches represents an interesting solution[9] . Different circuit's layouts can be considered, for example a control strategy based on resonant circuit where the modification of the external circuit's parameters allows the suppression of a resonant peak.[8] A different approach based on negative capacitance circuit allows a widening of the control frequency band. In order to magnify this effect a lattice of actuators connected to the circuits is introduced. Up to now this technique has been mainly applied to mono-dimensional structures such bars and beams[1] or bi-dimensional structures such plates and shells.[3] The aforementioned works are characterized by the presence of multiple actuators placed over the entire surface of the controlled structure. In this work the previous idea is modified introducing the concept of active interface which is the part of the plate containing the actuators that allows the modification of the system's response.

2. THE BLOCH THEOREM APPLIED TO THE ELASTODYNAMIC

In this section, the application of the Floquet-Bloch theorem is presented for piezoelastodynamic problems. Based on the results obtained by Floquet (Floquet,[4] 1883) for monodimensional problems and later rediscovered by Bloch (Bloch,[2] 1928) in multidimensional problems, an original application to bidimensional visco-elasto-dynamic problem has been proposed recently (Collet et al.,[6] 2011) and extended to piezo-elasto-dynamic problem (Collet et al.,[7] 2012).

Further author information: (Send correspondence to Flaviano Tateo)
Flaviano Tateo: E-mail: flaviano.tateo@femto-st.fr

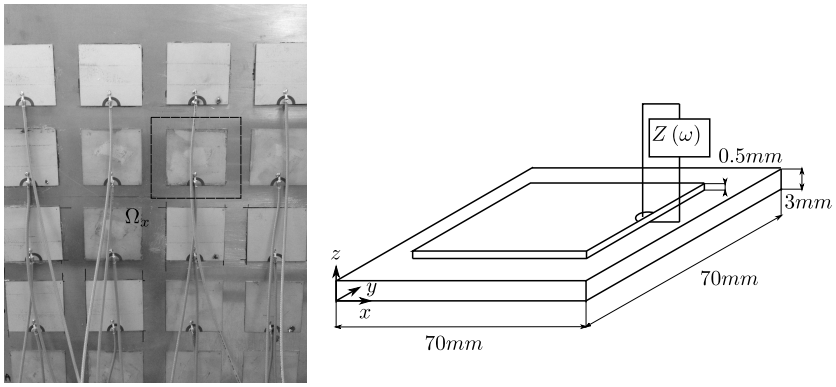

Figure 1. Actuators periodic lattice and its primitive cell Ω_x.

2.1 The Bloch theorem

The Bloch Theorem stipulates that any function $u(x) \in L^2\left(R^3, C^n\right)$ can be expressed as

$$u(x) = \int_{\Omega_k} e^{ikx} u(x,k)\, dk \tag{1}$$

where the Bloch amplitude $u(x,k)$ is Ω_x-periodic and has the representations

$$u(x,k) = \sum_n u(k+Gn)\, e^{iGnx} = \frac{\Omega_x}{(2\pi)^3} \sum_n u(x+Rn)\, e^{ik(x+Rn)} \tag{2}$$

where $u(k)$ stands for the Fourier transform of $u(x)$. It can also be demonstrated that the mean value of the Bloch amplitude is the Fourier amplitude of $u(x)$ for the corresponding wave vector.
Based on that theorem, the expansion functions $v_m(x,k)$ can be defined. They are called the Bloch eigenmodes and can be used to represent the Bloch amplitudes of any solution of periodic problem as

$$u(x,k) = \sum_m u_m(k)\, v_m(x,k) \tag{3}$$

and at the same time diagonalize the partial derivative operator.

2.2 Application to piezoelastodynamic

Let us consider a piezoelastodynamic problem made of infinite periodic distribution of unitary cell. The harmonic homogeneous dynamical equilibrium of system is driven by the following partial derivative equations

$$\begin{array}{ll} \rho\ddot{w} - \nabla\cdot\sigma = 0 & \forall x \in \Omega_x \\ -\nabla\cdot D = 0 & \forall x \in \Omega_x \end{array} \tag{4}$$

where w is the displacement vector, σ represents the Cauchy stress tensor and D the electric displacement. The linear constitutive material behavior relationships can be written as

$$\begin{array}{l} \sigma = C_E\varepsilon - e^T E \\ D = e\varepsilon + \epsilon_S E \end{array} \tag{5}$$

where $E = -\nabla V$ is the electric field vector (V being the voltage), C_E the elasticity tensor at constant electrical field, ε the Green strain tensor, e^T the piezoelectric coupling tensor, and ϵ_S the dielectric permittivity at constant strain. We add to this set of equilibrium equations an output expression

$$q_{app} = -\int_{S_t} D\cdot n dS \tag{6}$$

allowing the introduction of the charge measurement on the piezoelectrics top electrode and hence the dual counterpart of the imposed electrical Dirichlet boundary condition for applying the shunt impedance operator. The equations above are consistent for each kind of material to the extent that null piezoelectric and permittivity tensors can be used when passive materials are considered. All these tensors also depend on the spatial location vector x and are Ω_x periodic. As the problem is 2D infinitely periodic, mechanical boundary conditions are included in the formulation, while electrostatic boundary conditions have to be considered on each cell

$$\begin{array}{ll} V = 0 & \forall x \in S_b \\ V = V_{app} & \forall x \in S_t \\ D \cdot n = 0 & \forall x \in S_l \end{array} \tag{7}$$

where S_b is the grounded bottom electrode of the piezoelectric layer, S_t is the top electrode connected to the external shunt, and S_l the lateral electrode. The top electrode applied feedback voltage V depends on the shunt characteristic and on the collected charges q_{app} and can be expressed in the Fourier space by

$$V_{app} = Z q_{app} \tag{8}$$

The proposed formulation is then based on the computation of the Floquet vectors, instead of computing the Floquet propagators commonly used for elastodynamic applications. The full 2D wave dispersion functions can then be obtained, while damping and electrical impedances can clearly be introduced into the piezoelastodynamic operator. The adopted methodology allows the computation of the complete complex map of the dispersion curves incorporating computation of evanescent waves and allowing the introduction of damping and shunt operator if any.

2.3 Numerical computation of the Blochs waves

Replacing the solution expressed in term of the Bloch modes the problem 4 assume the following discretized form:

$$\left[K\left(Z\left(\omega\right)\right) + \lambda_n\left(\omega,\theta\right) L\left(\theta, Z\left(\omega\right)\right) - \lambda_n^2\left(\omega,\theta\right) H\left(\theta, Z\left(\omega\right)\right) - \omega^2 M\right] u_n\left(\omega,\theta\right) = 0 \tag{9}$$

where the angular frequency ω is a real parameter corresponding to the harmonic frequency. Wave numbers and Floquet vectors are then computed. This approach allows one to easily take into account the frequency dependency of various system's terms (i.e. damping and electric impedance). An inverse Fourier transformation in the k-space domain can lead us to evaluate the physical wave displacements and energy diffusion operator when the periodic distribution is connected to another system as described in Collet et al.[5] (2009). Another temporal inverse Fourier transformation can furnish a way to access spatio-temporal response for nonhomogeneous initial conditions.

2.4 Computation of the evanescence and damped power flow criteria

One aim of this article is to provide a numerical methodology for optimizing the piezoelectric shunt impedance $Z\left(\omega\right)$ for controlling energy flow into the periodically distributed piezocomposite structure. The first criterion which is considered for describing the capability of the metacomposite for transmitting structural energy is based on the computation of the wave group velocities. Indeed, they indicate how energy is transported into the considered system and allow to distinguish the propagative and evanescent waves.
If a Bloch eigensolution is considered, the associated group velocity vector is given by

$$C_{g_n} = \nabla_k \omega = \frac{\langle\langle S \rangle\rangle}{\langle\langle e_{tot} \rangle\rangle} = \frac{\langle I \rangle}{\langle E_{tot} \rangle} \tag{10}$$

where $\langle\langle . \rangle\rangle$ is the spatial and time average, respectively, on one cell and one period of time; S is the density of energy flow; I is the mean intensity; and e_{tot} and E_{tot} are the total piezomechanical energy and its time average, respectively, on a period. The intensity vector I is expressed as

$$\langle I_n \rangle = real\left(-\frac{\omega}{2}\int_{\Omega_x} C_E\left(\varepsilon_n + ik\Xi_n\right) \cdot w_n^* \frac{d\Omega}{Vol}\right) \tag{11}$$

Plate	Value	Unit
Length	2100	mm
Height	1050	mm
Thickness	3	mm
Mass density	2700	kg/m^3
Young's modulus	$70 \cdot 10^9$	N/m^2
Poisson's ratio	0.33	–
Piezo	**Value**	**Unit**
Length	50	mm
Height	50	mm
Thickness	0.5	mm
Mass density	7650	kg/m^3
Poisson's ratio	0.31	–
Dielectic loss	< 0.05	%
Coupling factor	0.51	–

Table 1. Geometry and physical properties of the system.

where * is the complex conjugate, *real* stands for real part, and Vol the domain volume.
As the spatio-temporal average of the system Lagrangian is null (see Maysenholder,[10] 1994), the total energy average is approximated by only computing the kinetic energy average

$$\langle E_{tot} \rangle = \frac{1}{2Vol} \left(\int_{\Omega_x} \rho \omega^2 w_n \cdot w_n^* d\Omega \right) \tag{12}$$

The group velocity vectors $C_n^g(\omega, \Phi)$ are computed for all wave numbers at each frequency. In order to focus our analysis on only flexural modes (S and SH ones), we introduce an indicator allowing to select them by computing the ratio of kinetic energy average on out-of-plane displacement as

$$Ind(n, \omega, \theta) = \frac{\frac{1}{2Vol} \left(\int_{\Omega_x} \rho \omega^2 w_{zn} \cdot w_{zn}^* d\Omega \right)}{\langle E_{tot} \rangle} \tag{13}$$

$w_{zn}(x)$ being the component of vector $w_n(x)$ on z direction. Optimization of the shunt impedance $Z(\omega)$ is based on the minimization of the maximal group velocity collinear to the wave number vector for waves having a ratio of transported flexural kinetic energy greater than the threshold value of 0.8. The criterion can then be written as

$$Crit_1(Z(\omega), \theta) = \max(C_n^g \cdot \Phi) \quad \forall p \in n / Ind(n, \omega, \Phi) > 0.8. \tag{14}$$

2.5 Optimization of the flexural energy flow inside the shunted periodic piezocomposite

The considered piezocomposite cell is presented in Figure 1. The supporting plate material is standard aluminum with 0.1% of hysteretic damping ratio, and the piezoelectric material characteristics are given in Table 1. The optimization of the transmission capability of the designed adaptive metacomposite is considered by using $Crit_1$. The objective is to avoid any energy transportation when flexural waves are excited into the periodically distributed shunted piezocomposite cells. The numerical optimization procedure is based on a multidimensional unconstrained nonlinear minimization algorithm (NelderMead). The optimization is done by considering an active/reactive electronic circuit represented by its impedance $Z(\omega)$.
The analysis is initialized with an arbitrary complex value of the shunt impedance. Optimization steps are then proceeded using $Crit_1$ and lead us to obtain frequency-dependent complex impedance for describing the circuit behavior. The real and imaginary parts of the optimal impedance are plotted in Figure 2 for all angles θ. The optimal impedance values almost correspond to a constant negative capacitance in all directions. Equivalent resistances corresponding to the active part of the shunt impedance are negative which indicates that the optimization leads to provide energy to the system for controlling mechanical damping effects introduced by hysteretic terms in the model.

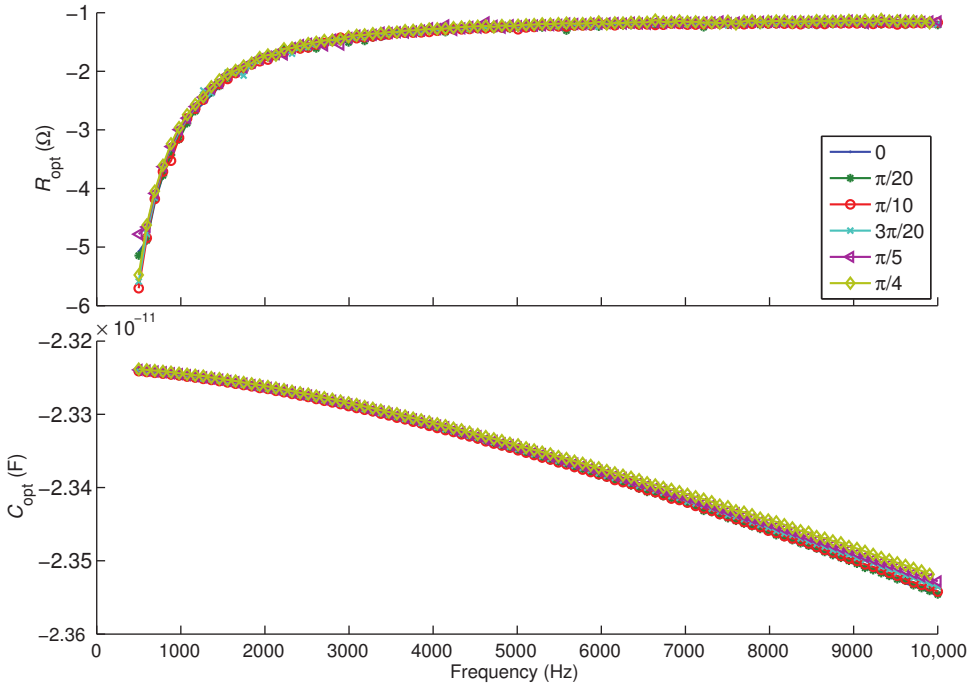

Figure 2. Optimal electric impedance using $Crit_1$.

3. EXPERIMENTAL TEST

This section introduces the design and testing of the smart metacomposite.

3.1 Periodic Lattice design

An aluminum plate with the geometric properties listed in Table 1 is suspended to a rigid frame through metallic wires. The plate is equipped with 75 piezoelectric patches from $PZ26$ series (Ferroperm industries) arranged in a regular 15×5 array. The dimension of the piezoelectric ceramics are listed in Table 1 and are justified by the following assumptions: the plate's dispersion relation of the flexural mode at 5000 Hz has a wavelength of 30 cm. This value imposes a lenght constraint of the piezoceramic in the propagation direction, the best coupling is obtained when the length of the ceramics and the wavelength of the targeted mode respect the ratio of $1/4$. The thickness of the actuator was finally defined considering the restraints of the electric circuit and the nature of the control technique. Different authors argued that the best controlling effect is obtained when the circuit is tuned in correspondence of the biggest ceramic's capacitance value. This property strongly depend on the material properties and the geometry. Once the material properties and the two dimension of the piezoelectric actuator are chosen the only parameter which may be amended is the thickness. Small thicknesses correspond to larger values of the intrinsic capacitance, however, this parameter can not be reduced indefinitely due to the weakening of the piezoelectric ceramic itself. For these reasons a thickness of 0.5 mm was adopted.

3.2 Shunt circuit design

The results derived from the optimization of the external circuit permit to design it in term of real and imaginary part of a general impedance. In Figure 4 is depicted the actual circuit used during the experiment. This circuit contains some passive components such as the resistances R_s, R, R_{tot}, the capacitance C and an active component, namely an operational amplifier that actually allows the circuit to reproduce the intended behavior. This control technique requires a tuning of the synthetic capacitance around the capacitance value of the piezoelectric ceramic, this value is intrinsic and depends upon the material properties and the geometry. The intrinsic capacitance of the piezoelectric ceramic can be easily estimated measuring the capacitance observed by an RLC-meter when the specimen is free of stresses. In the present case the measured value was $52nF$. The actual circuit

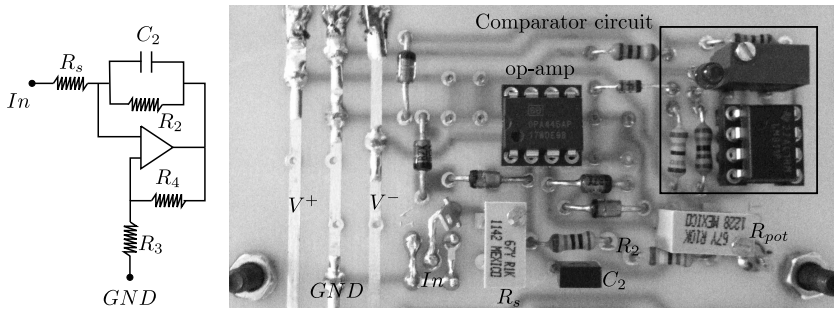

Figure 3. Layout of the electric circuit. Schematic (left), real-life circuit (right).

was tuned varying the position of the potentiometer R_{tot} with small increments. The variation of this parameter determine a variation in the synthetic capacitance according to the formula:

$$C_{eq} = -\alpha C_2 \tag{15}$$

where α is defined as R_4/R_3 and R_{pot} is the resistance of the potentiometer and it represents the sum of R_3 and R_4. The use of the potentiometer simplifies the layout of the circuit because it permits to reproduce the capacitive effect with just one component.
The regulation phase starts setting the synthetic capacitance for very high values and then slowly decreasing it until the desired value is reached. During this phase some problems can occur because of the limitation connected to the nature of the analog circuit. When the external circuit approaches the set-point the system tend to be unstable, an increase of voltage is observed. The operational amplifier is therefore saturated. In order to mitigate this effect the circuit's layout proposed by Beck[1] were modified adding a complementary circuit able to detect this specific instability. Basically a comparator was introduced in correspondence of the op-amp output in order to identify these voltage overloads. This circuit is based on a comparator that measures the differential input between the positive component of the voltage delivered by the operational amplifier in correspondence of the output gate and a reference DC signal from the power supply circuit. Whenever the differential signal results bigger than zero the gate is opened, delivering a current able to illuminate a light emitting diode (LED). This simple solution is very helpful since it allows one to detect this source of instability avoiding the use of the oscilloscope. This feature becomes very useful in this context where a huge number of actuators are involved. For example when several piezoelectric patches are excited a loss of performance can be observed due to the electromechanical coupling occurring between adjacent actuator. In this case, observing the state of the LEDs on the control panel is possible to correctly reset each external circuit.

4. EXPERIMENTAL RESULTS

The experimental procedure involves the measurement of the mobility

$$Y(\omega) = \frac{\dot{w}}{F} \tag{16}$$

where $\dot{w}$ represent the out-of-plane velocity of the controlled plate measured by means of a laser vibrometer and F the shaker's force signal.
In figure 5 the mobility FRF is provided in term of the average of the magnitude using third octave bands, in order to estimate the response reduction of the control system compared with the reference measure made on the same structure without activating the electronic circuit. On the frequency range of interest, it is possible to reduce the transmitted energy of at least 5 dB. However, this is an averaged information, it is possible to obtain, locally, even better results, for example a 15 dB reduction around 2 kHZ. The figure presents two diagrams: the first on the top is related to a measurement made at the excitation point P_1 and the other corresponds to measurements made in the opposite corner of the plate and therefore located downstream with respect the active interface, point P_2. Comparing the two diagrams, an interesting property can be deduced: the plate impedance

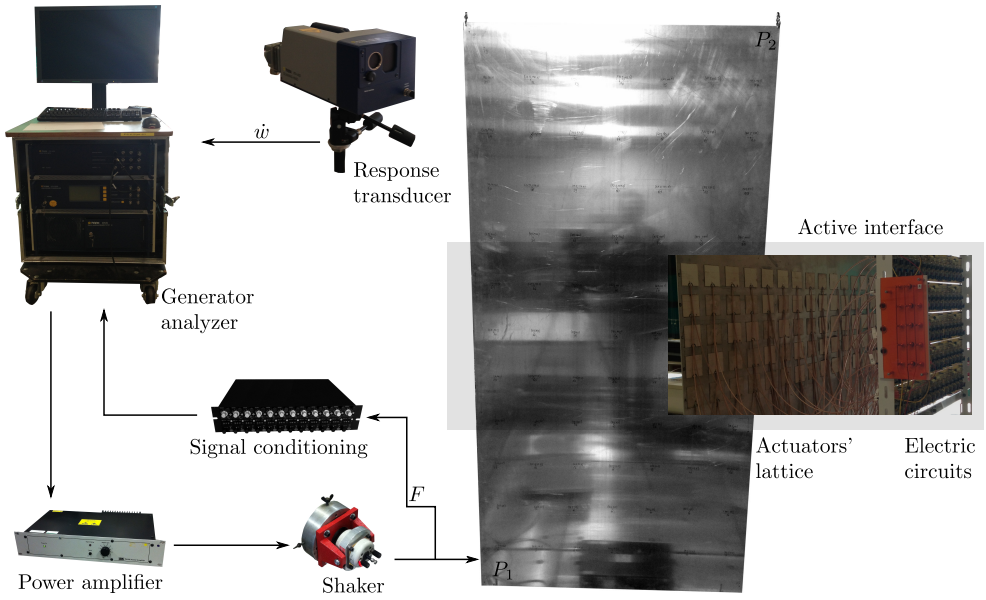

Figure 4. Layout of FRF measurement system.

seen by the excitation is not modified by the control system whereas the part of the plate beyond the active interface acts as the structure would be strongly damped. This effect can be used with profit in case one wants to isolate a source of disturbance.

These results show the effectiveness of the proposed control strategy, it is clear that in the frequency band of $50 - 5000\ Hz$ the control system properly works, reducing the magnitude of the vibrations. However for low frequency values the system seems to be unable to correctly control the underlying structure: the response is amplified during the control phase, this is only due to the deterioration of the measured data, the coherence function shows a poor quality. In order to clarify the system's behavior at low frequency other measurements

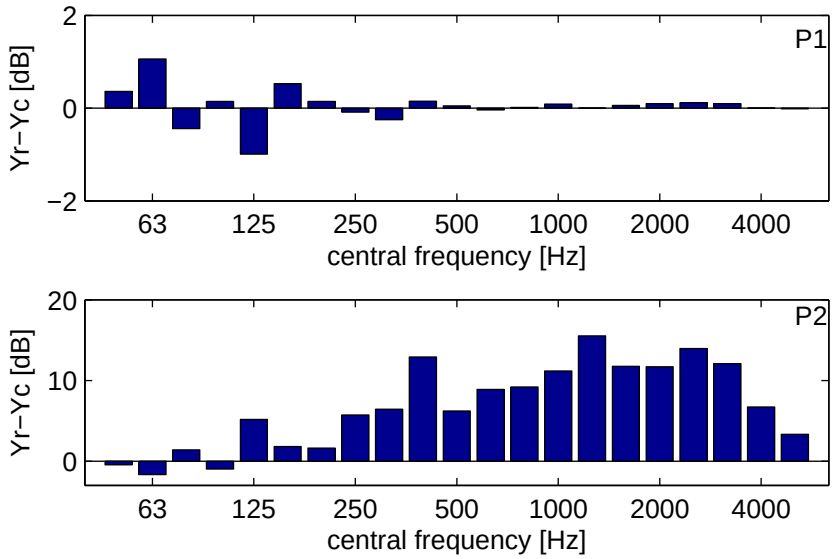

Figure 5. FRF plot comparison between the uncontrolled Y_r and controlled system Y_c expressed in third of octave band.

were performed. In Figure 6 is depicted the plate's frequency response function measured at point P_1 and P_2 of the controlled plate. The mobility function is measured over the frequency range of $0 - 5000\ Hz$, in each row, however, is presented just a small portion of the total FRF in order to point out all the details connected to the dynamics of the system, keeping the best possible values for the coherence function.
In the low frequency range $(0 - 500\ Hz)$ the system cannot be very effective for both positions upstream and downstream, however, beyond 200 Hz the control system is activated, causing an appreciable vibration reduction. On this frequency band the response of the controlled system is constantly smaller than the reference measurement: the control system's main function is to reduce the vibrations adding a certain amount of damping.
In Figure 7 a measurement of the plate's velocity distribution is provided. In the top of the image is presented the velocity field of the plate of the reference measurement (control off) against the controlled one in the frequency range where the system is not effective (low frequencies). As a consequence, the control system can not influence the plane and the response level are comparable. The slight modification of the shape of the mode observed can be justified as follows: the controlled plate in this case is experiencing a stiffness properties' modification (frequency shifting). In the active frequency band the response level are decreased in a uniform fashion over the whole region. In this case the wave confinement effect is still present demonstrated by an increase of response level in the portion of the plate behind the active interface delimited by the two horizontal lines.

5. CONCLUSIONS

This article presents a numerical procedure able to compute the damped wave dispersion functions in the whole first Brillouin domain of multidimensional damped piezoelastodynamical wave guides. The method was applied for determining the optimal shunt impedance allowing the minimization of the group velocities of the flexural waves and the damping capability of the distributed system. The proposed methodology can also be used for studying particular dissipation phenomenon such as those induced by complex shunted piezoelectric patches or even foams or complex polymers behaviors.
From the experimental point of view, we showed how it is possible to modify the dynamics of the plate equipped by a series of piezoelectric actuators shunted to negative capacitance circuits and arranged in a periodic fashion. The aim of the project was achieved overcoming several difficulties such as the circuit instability around the set point and the electrical coupling between the different piezoelectric actuators.
These preliminary results are encouraging, however further analysis will be required in order to thoroughly understand the mechanisms related to this control technique. In particular it will be necessary to better match the theoretical results with the experimental measurements.

ACKNOWLEDGMENTS

This study is a collaborative effort supported by the French Research Agency under grant number NT09-617542.

REFERENCES

[1] Beck B., Cunefare K.A., and Ruzzene M. Broadband vibration suppression assessment of negative impedance shunts. In ASME, editor, *Conference on smart materials, adaptive structures and intelligent systems*, Ellicott City, October 2008.

[2] Bloch F. Über die quantenmechanik der electron in kristallgittern. *Zeitschrift für Physik*, 52:550–600, 1928.

[3] Casadei F., Beck B., Ruzzene M., and Cunefare K.A. Vibration control of plates featuring periodic arrays of hybrid shunted piezoelectric patches. In SPIE, editor, *Conference on smart structures and materials*, San Diego, March 2009.

[4] Floquet G. Sur les équations différentielles linéaires à coefficients périodiques. *Annales Scientifiques de l'École Normale Supérieure*, 12:47–88, 1883.

[5] Collet M., Cunefare K.A., and Ichchou M.N. Wave motion optimization in periodically distributed shunted piezocomposite beam structures. *Journal of Intelligent Material Systems and Structures*, 20:787–808, 2009.

[6] Collet M., Ouisse M., Ruzzene M., and Ichchou M.N. Floquet-bloch decomposition for the computation of dispersion of two-dimensional periodic, damped mechanical systems. *International Journal of Solids and Structures*, 48:2837–2848, 2011.

[7] Collet M., Ouisse M., and Ichchou M.N. Structural energy flow optimization through adaptive shunted piezoelectric metacomposites. *Journal of Intelligent Material Systems and Structures*, 23:1661–1677, 2012.

[8] Hagood N.W. and Von Flotow A. Damping of structural vibrations with piezoelectric materials and passive electrical networks. *Journal of Sound and Vibration*, 146:243–268, 1991.

[9] Reza Moheimani S.O.R. and Fleming A.J. *Piezoelectric transducers for vibration control and damping.* Springer, 2010.

[10] Maysenholder W. *Körperschallenergie.* Hirzel, 1994.

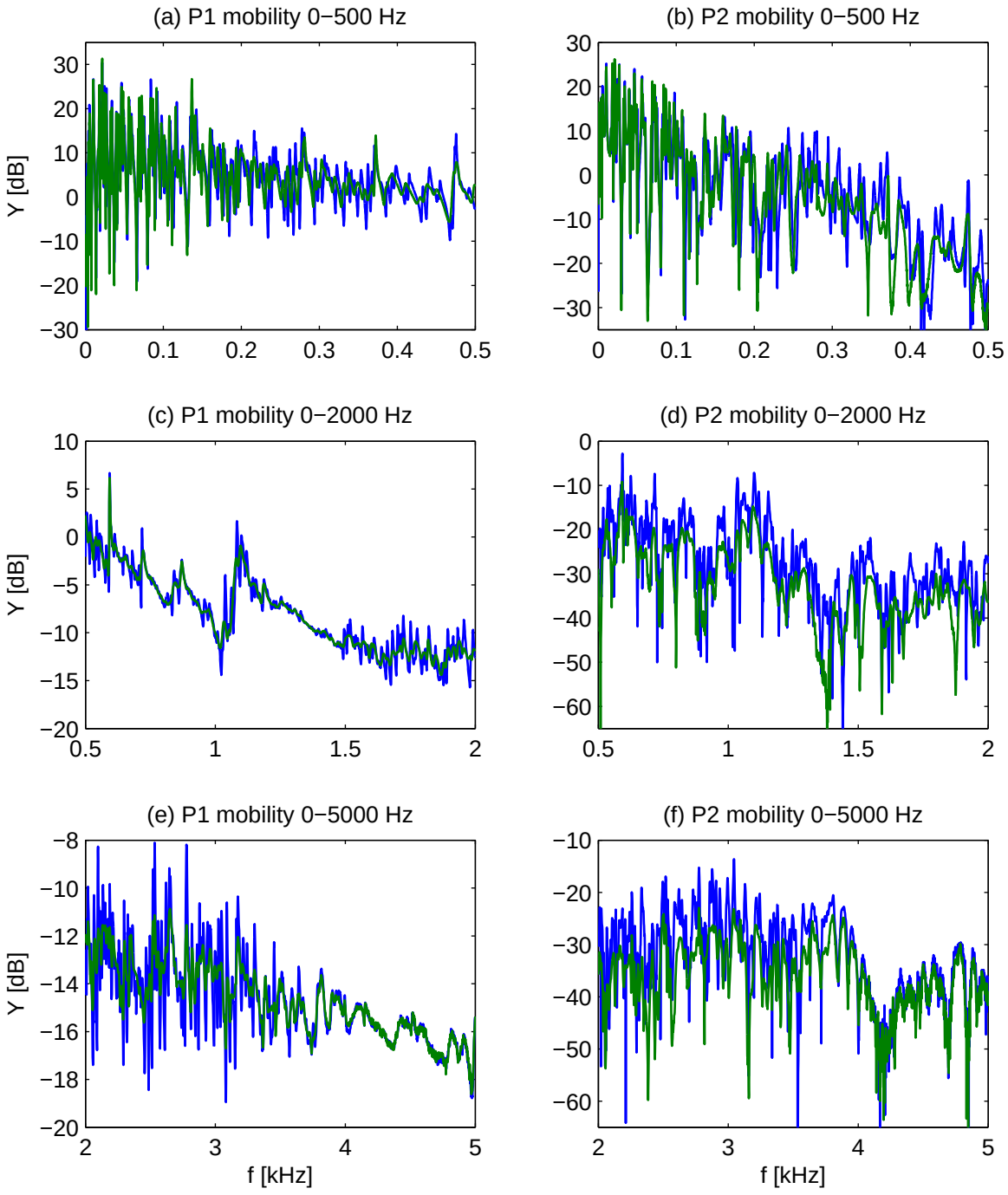

Figure 6. FRF plot comparison between the uncontrolled (blue line) and controlled system (green line). P1 measurement (left column), P2 measurement (right column).

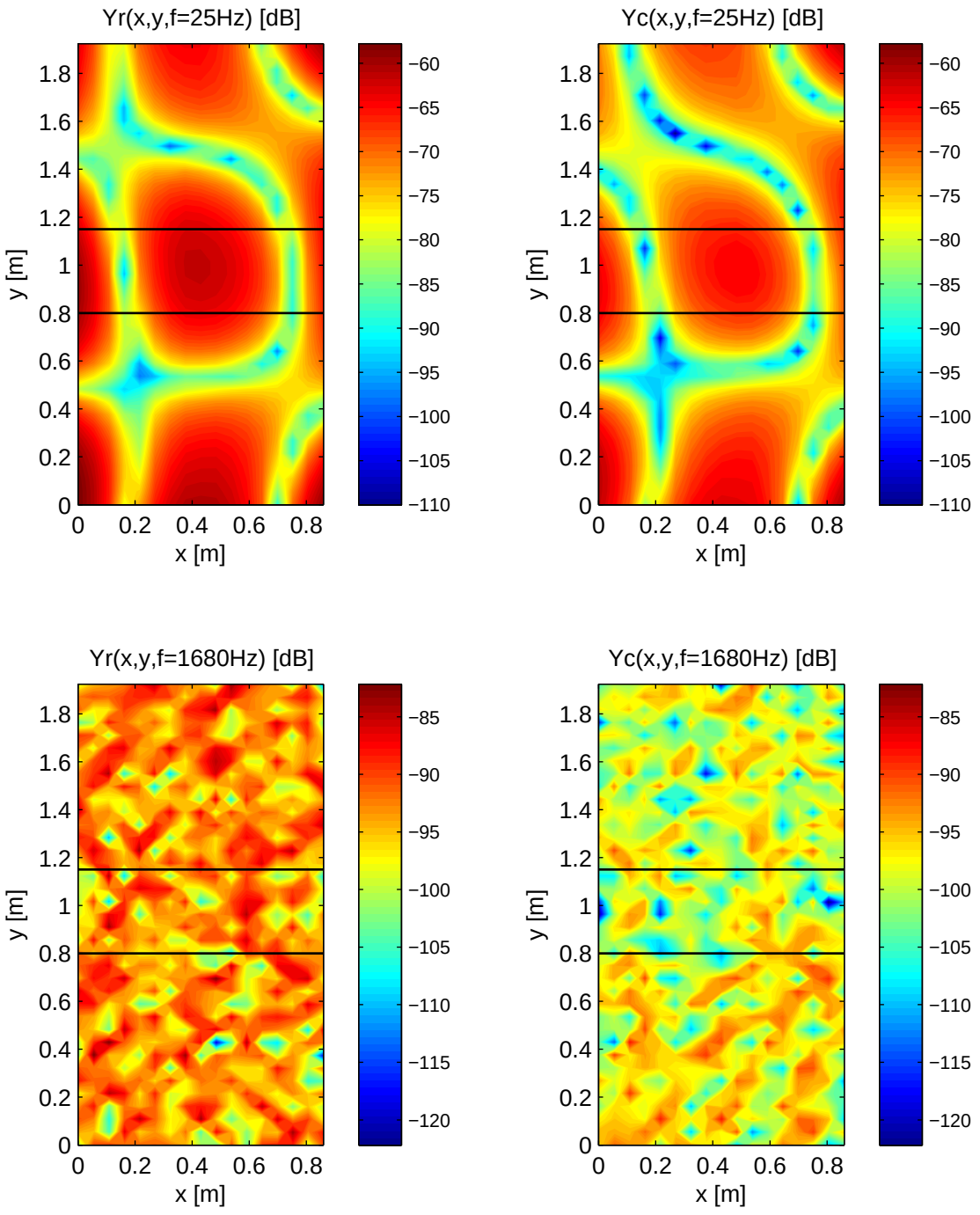

Figure 7. FRF velocity field comparison. Top: inactive region for the control system. Bottom: active region for the control system.

SIMPLE AND EFFECTIVE FRICTION COMPENSATION ON WHEELED INVERTED PENDULUM SYSTEMS

S. Rinderknecht[1*], B. Strah[1]

[1]Institute for Mechatronic Systems in Mechanical Engineering
Technische Universität Darmstadt, Darmstadt, GERMANY
Email: strah@ims.tu-darmstadt.de, rinderknecht@ims.tu-darmstadt.de

ABSTRACT

Positioning performance in mechatronic systems often suffers from negative influence of Coulomb friction. The reason is the non-smooth characteristics of this type of friction. A simple friction compensator is used to diminish the negative influence of the Coulomb friction in two considered wheeled inverted pendulum systems as an example. While the first system is a simple inverted pendulum which can move on a plane ground, the second one is a double inverted pendulum capable to climb stairs autonomously. The friction compensator is applied to the wheel drives to diminish the amplitude of the limit cycles of the system position, which exist due to Coulomb friction. Regarding the system relative drive velocity and the stabilizing smooth controller output, a compensating torque is determined and added to the smooth controller output. The decision fuzzy logic within the compensator is empirically parameterized, based on real system noise influenced signals. The presented results of the positioning performance show significant improvement due to decrease of the limit cycle amplitude.

1 INTRODUCTION

To study stair climbing with a wheeled device, a stair climbing device (SCD) (Figure 1, (c)) was built as an experimental setup. The motivation comes from enhancing autonomous stair-climbing for wheelchair drivers or wheeled robots. The reason for using a wheeled vehicle is a lower energy consumption and higher motion velocity compared to legged robots or tracked vehicles [1]. The stair climbing principle is shown in Figure 2 as a sequence of different situations. To isolate some specific issues, a simple inverted pendulum (Figure 1, (a)) was studied [2] as a predecessor of the SCD. Some issues are common for both systems: nonlinear unstable continuous-time property, non-holonomic constraints due to wheels moving in planar space, Coulomb friction influence, inclination determination and control design. Additionally, the SCD underlays discontinuous dynamics, due to activation or deactivation of wheel-to-ground contacts. Together with the continuous-time dynamics, it forms hybrid dynamics [3].

To deal with Coulomb friction is a common issue in both presented systems and often in general mechatronic systems. A simple and effective Coulomb friction compensation is the topic of this paper. Coulomb friction is a non-smooth function from system point of view. Since the common control design methods assume smooth non-linearity (continuous and differentiable) system properties, it is of high interest to actively compensate the Coulomb friction. After doing this, the resulting system in ideal case behaves as a system with smooth linear or non-linear behavior and the common control design methods can be applied.

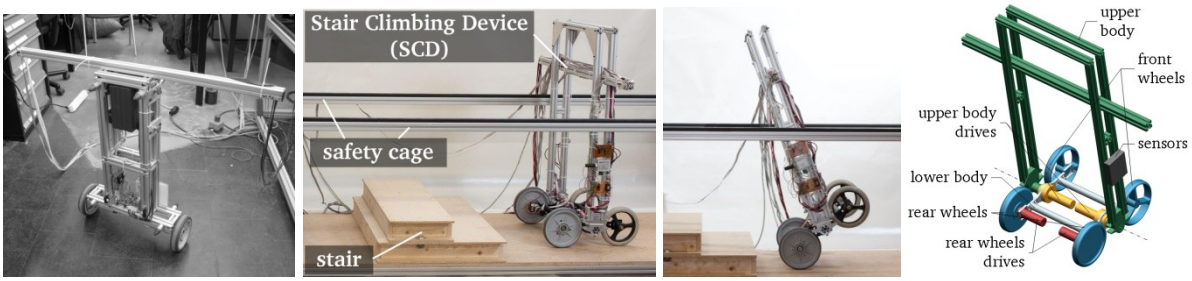

Figure 1. Inverted pendulum (a), SCD in test environment (b), SCD at stair climbing (c) and CAD model of the SCD (d).

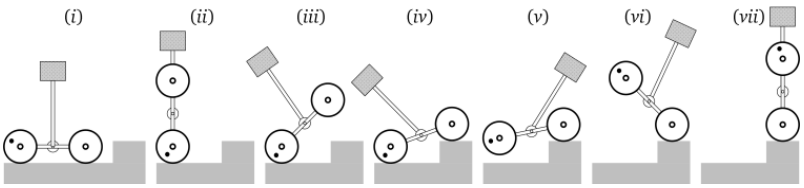

Figure 2. Sequence of situations at stair climbing of the SCD.

2 SYSTEM DESCRIPTION

Both considered mechatronic systems consist of a mechanical part which can be controlled due to drive torques. Current controlled DC-Motors with planetary gears are used as wheel drives. The SCD has additional body drives with harmonic drive gears. Incremental encoders are integrated in all drives. An inclinometer and gyroscope are used in a sensor data fusion scheme to estimate the tilt with high dynamics.

The stabilization of the simple inverted pendulum was fulfilled using a state-space control which acts on wheel drive torques. Differently, in case of the SCD there are two kinds of drives

which can stabilize the system: the wheel drives and the body drives. While both drives are used for stabilization, the weighting of the particular drive participation can be adjusted. Owing to the body drive torque limitation, the stabilization is fulfilled with higher participation of the wheel drives. Thus, the body angle stays almost constant during stabilization actions.

The friction is present in all drives as well as between the wheels and the ground. The wheel-ground-contact friction enables moving along some definite trajectory and fulfils the system functionality. Less valuable, the drive friction causes energy losses. Furthermore, consisting of a viscous and Coulomb part, especially the last part causes disturbed control system behaviour if only a smooth system model is considered.

3 FRICTION COMPENSATION

There exist different types of friction models which are used for simulation and control design purposes [4]. To implement simple and effective wheel drives friction compensation which is common for both considered systems, it was sufficient to model the friction as a superposition of the Coulomb and viscous friction. This model is qualified as a static friction model regarding [4].

The measurements of the wheel drive friction were done at different constant velocities, starting at almost zero velocity and continuing into the working velocity range. The friction torque can be determined by measuring the motor current at each velocity point and knowing the torque constant of the motor. The measurements done by this procedure fitted well into the simple static friction model mentioned above. As result of the fitting, the viscous $B_v = 0.0173$ Nm/rad/s and the Coulomb friction $B_c = 0.212$ Nm parameter were determined.

The viscous part of the friction is taken into account by the smooth controller. What is left out of the consideration is the step-like Coulomb friction M_{fr}, which can be represented with a *sign* function depending on the relative drive velocity $\dot{\alpha}$, $M_{fr} = B_c sign(\dot{\alpha})$.

Not considering the Coulomb friction M_{fr} in the control design results in stable limit cycles of position in both considered systems. The control objective is to suspend or at least to suppress this persistent oscillation behaviour.

This task could be fulfilled by using the additional control element "friction compensator" in the control loop (Figure 3, left) for both considered positioning control systems. The system position x is fed back to the stabilizing smooth (linear or non-linear) controller, which influences the controlled system with the output torque M_s considering the set position x_{set}. The additional friction compensation control torque M_c is superposed to fulfil the control objective.

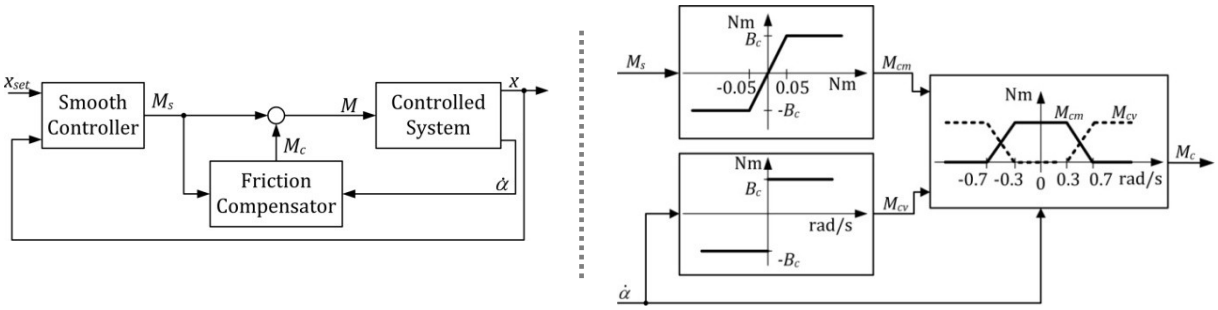

Figure 3. Control system (left) and the friction compensator principle (right).

Considering Coulomb friction M_{fr} makes reasonable at first instance, to build the friction compensation torque M_c as the function of relative drive velocity $\dot{\alpha}$. The problem using this concept arises at zero velocities (stiction). Adding no compensation torque M_c at zero velocity would be incomplete since friction is present in the system also at zero velocity. To overcome the

stiction problem, a compensation torque at zero velocity should be added as soon as moving is intended. This intention can be detected from the smooth controller output M_s and has a predictive character to the influence on the controlled system.

Following this description, the friction compensator is built as shown in Figure 3 (right). To diminish negative noise influence, the friction compensation torque to overcome stiction M_{cm} is smoothened by a definite gain at zero velocity. Together with the friction compensation torque M_{cv} at non-zero velocity, the value M_{cm} is then fed into the fuzzy decision logic block. Depending on the velocity $\dot{\alpha}$, this block provides both values to the output. The numerical parameters were empirically determined. The resulting friction compensator function is shown in Figure 4 (left). The achieved results in positioning (Figure 4, right) show successful diminishing of the limit cycles amplitude.

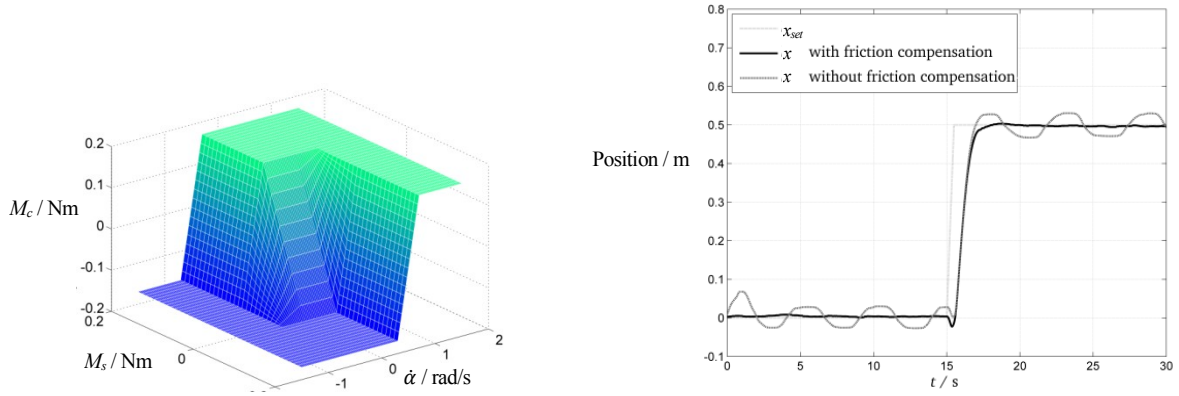

Figure 4. Friction compensator function (left) and results with simple inverted pendulum (right).

4 CONCLUSION AND OUTLOOK

The simple friction compensation implemented on considered real systems can effectively diminish the limit cycle oscillation amplitude.

To extend the SCD body dynamics, drives with higher torque are necessary. Since higher body dynamics would increase the negative influence of the Coulomb friction, the presented friction compensation should be also applied on the body drive. In that case, the attention should be paid on two distinctions. Firstly, applying compensation torques on body drive leads to reaction torques on the SCD lower body. Secondly, the smooth controller torque output cannot directly be used as moving intention information because there is in general no sign change when the body drive direction is reversed.

REFERENCES

[1] B. Siciliano and O. Khatib, Handbook of Robotics. Berlin: Springer-Verlag, 2008.

[2] B. Strah, S. Kern, T. Felzer, R. Nordmann, and S. Rinderknecht, "Mobile Inverse Pendulum Modeling and Control," in 2010 8th IEEE ICCA, Xiamen, China, 2010, pp. 1133-1138.

[3] B. Strah. (2012) Control of a wheeled double inverted pendulum considering hybrid dynamics (in German). [Online]. http://tuprints.ulb.tu-darmstadt.de/3050/

[4] H. Olsson, K. J. Åström, C. Canudas de Wit, M. Gäfvert, and P. Lischinsky, "Friction Models and Friction Compensation," European Journal of Control, vol. No. 4, pp. 176-195, 1998.

ANALYTICAL MODELING OF AN UNIMORPH MULTI-LAYER PIEZOELECTRIC VIBRATION ENERGY HARVESTER

A. Jemai[1] , F. Najar[1] and M. Chafra[1]

[1]Applied Mechanics and Systems Research Laboratory
Tunisia Polytechnic School, BP 743, La Marsa 2078, University of Carthage, TUNISIA
Email: fehmi.najar@gmail.com

ABSTRACT

The use of multi-layer cantilever beam represents a potential method to increase the performance of the structure. Generally, researchers have concentrated their efforts to study a multi-layer actuators, which show a large developed displacement for the same applied voltage compared to a single-layer actuator. Nevertheless, the multi-layer energy harvester is not very investigated. In fact, most of modeling found in the literature for multi-layer harvester is based on finite element methods and experimentation. In this paper, we propose an analytical model for multi-layer energy harvester with parallel and series connection cases. In fact, we develop a reduced-order model of the harvester, which we use in turn to obtain closed-form expressions for the tip displacement and the power output generated by the structure, which are validated with finite element simulations using ANSYS.

1 INTRODUCTION

Over the past decade, the need for alternative energy sources for wireless electronic devices has led to a considerable amount of research in the area of energy harvesting in order to replace disposable chemical batteries. The use of piezoelectric devices has received significant attention because its simplicity of integration in self-powered system. Researchers provided efforts to increase the electrical output of energy harvesters. Using piezoelectric multi-layer is an efficient method to increase the electrical performance of the harvester. Few numerical and analytical models have been reported on multilayered energy harvesters. Song et al. [1] compared the output voltage and the electrical power of piezoelectric energy harvesters with single, two and five layers for parallel connection case. Zhu et al. [2] numerically and experimentally investigated a bimorph multi-layer cantilever configuration with parallel connection and with the same total thickness of PZT. Zhu et al. [3] numerically investigated a bimorph multi-layer cantilever beam with parallel and series connections. In this paper, we seek a parameterized mathematical models of an unimorph multi-layer cantilever beam with parallel and series connections and compares different configurations with a FE validation in ANSYS.

2 ENERGY HARVESTING SYSTEM MODELING AND ANALYTICAL SOLUTION

We consider an unimorph multi-layer cantilever beam , excited by a transverse harmonic displacement $Y(t) = Y_0 \cos(\Omega t)$ ($Y_0 = 0.1\ mm$), with series and parallel connections, which is shown in figure 1. The subscript S refers to the series connection and the subscript P refers to the parallel connection.

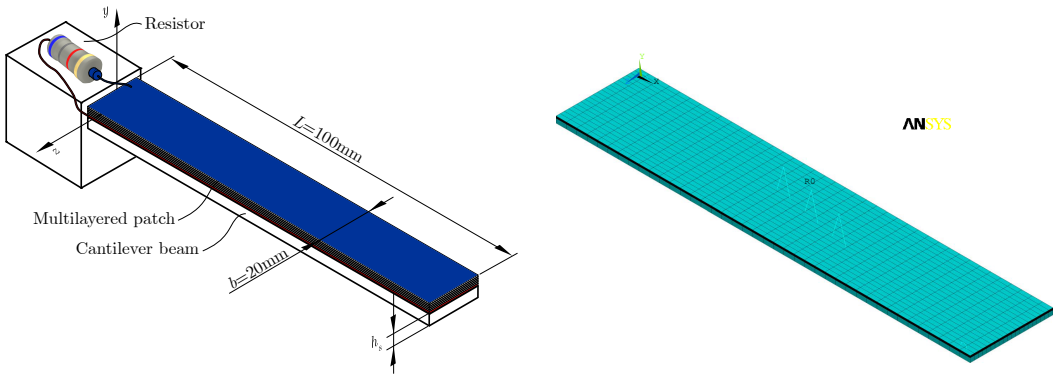

Figure 1. (a)Multilayered cantilever beam. (b) FE of the system.

Applying the Galerkin procedure and the Hamilton's principle, we obtain the following set of ordinary differential equations of a harvester with two connection cases

$$M_r \ddot{\eta}_r^n(t) + C_r \dot{\eta}_r^n(t) + K_r \eta_r^n(t) + f_r^n\ V^n(t) + m_r\ \ddot{Y}(t) = 0, \quad n = P\ or\ S \tag{1}$$

where $V^n(t)$ and $\eta_r^n(t)$ are the voltage and the mechanical responses, respectively, for the parallel and the series connection cases and the modal electrical forcing term is expressed as

$$f_r^n = \int_0^L \upsilon_n \frac{d^2\phi_r(x)}{dx^2} dx = \upsilon_n \frac{d\phi_r(x)}{dx}\bigg|_{x=L}, \quad n = P\ or\ S \tag{2}$$

where the coupling term υ_n for the parallel connection case can be written as, respectively

$$\upsilon_P = -b\, N \frac{\bar{e}_{13}^e}{2h_p} \left({y_2}^2 - {y_1}^2\right), \quad n = P \tag{3}$$

where y_0, y_1 and y_2 represent the positions of layers.

Note that the modal damping term (Q=500) and the other terms for multi-layer harvester with series connection are expressed identically as a single layer harvester [4]. Using the Gauss's law and noting that the output voltage $V(t)$, which is measured at an external resistor R, represent the harvested voltage from the proposed system, we can derive the governing circuit equation for the parallel and the series connection cases based on the Kirchhoff laws as follows

$$C_p^n \dot{V}^n(t) + \frac{V^n(t)}{R} = I^n(t), \quad n = P \text{ or } S \tag{4}$$

where the equivalent internal capacitance C_p^P and the equivalent current source $I^P(t)$, respectively, are expressed as

$$C_p^P = N^2 \bar{\epsilon}_{33}^e \frac{b}{h_p} (y_2 - y_1) \tag{5}$$

$$I^P(t) = \sum_{r=1}^{\infty} k_r^P \dot{\eta}_r^P(t), \quad \mathrm{k}_r^P = \int_0^L \sum_{i=0}^{N-1} \int_{y_1+i\frac{h_p}{N}}^{y_1+(i+1)\frac{h_p}{N}} N \bar{e}_{13}^e \frac{b}{h_p} y \, \phi_r{}''(x) \, dy \, dx \tag{6}$$

where k_r^P is the modal coupling term for the parallel connection case.

Note that the equivalent internal capacitance C_p^S and the equivalent current source $I^S(t)$ for series case are expressed identically as a single layer harvester [4]. Based on the linear system assumption and Solving the previous system analytically (1-4), we obtain the modal mechanical response ${\eta_r}^0$ and the voltage V_0 amplitudes for two connection cases [4].

3 TYPICAL RESULTS

We start by plotting in Figure 2 the numerical and analytical results of the electrical power $P_{\max}$ and the maximum normalized tip deflection v_{max} of the cantilevers having different number of layer ($N = 1$, $N = 3$, $N = 5$ and $N = 7$), for the various external resistances R. Figure 2 represents excellent agreement with the analytical and numerical models. Figure 3 represents

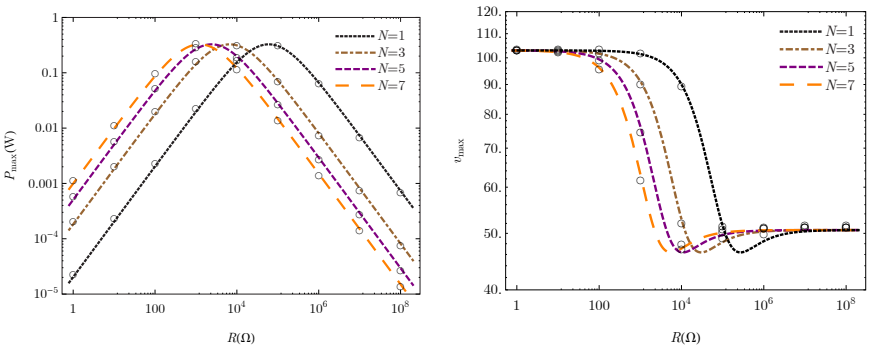

Figure 2: Analytical (dashed lines) and numerical (circles) harvested power and tip displacement at the short circuit resonance frequency for different N ($h_p = 0.5mm$ and $h_s = 1mm$).

the analytical and the numerical variation of the electrical power and the tip displacement with thickness ratio λ of the PZT to Aluminum layers at the short circuit resonance frequency for parallel and series connections (For $R = 10^3\,\Omega$), when $N = 3$. We observe good agreement between the analytical and numerical. Indeed, when the thickness of the piezoelectric layer becomes more larger, the linear voltage assumption will be not validated [5].

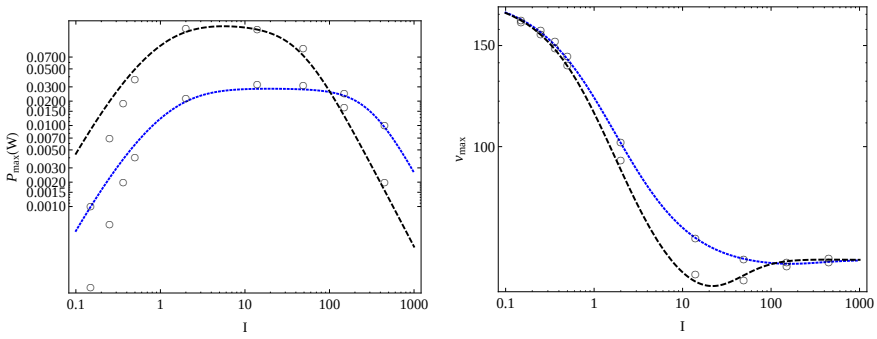

Figure 3: Variation of harvested power and tip displacement with λ at the short circuit resonance frequency for series and parallel configuration.

4 CONCLUSION

In this paper, an analytical model of a vibrating structure, composed of a substrate layer on top of which a piezoelectric multi-layer has been attached, is derived and a closed-form solution is proposed. A numerical study using FE analysis was used to validate the analytical generated power and the tip displacement for parallel and series connections. The simulations indicated that the analytical model is in good agreement with the numerical one.

ACKNOWLEDGMENTS

The first three authors are grateful for the funding provided by the Tunisian Ministry of Higher Education. This work was performed under the framework of the NSF International Institute for Multifunctional Materials for Energy Conversion (Grant DMR-0844082).

REFERENCES

[1] H.-C. Song, H.-C. Kim, C.-Y. Kang, H.-J. Kim, S.-J. Yoon and D.-Y. Jeong. Multilayer piezoelectric energy scavenger for large current generation. *Journal of Electroceramics,* 23:301-4, 2009.

[2] D. Zhu , A. Almusallam , S.P. Beeby , J. Tudor and N.R. Harris. A bimorph multi-layer piezoelectric vibration energy harvester. *Proc. PowerMEMS,* 2011.

[3] D. Zhu, S. Beeby, J. Tudor, N. White and N. Harris. Improving Output Power of Piezoelectric Energy Harvesters using Multilayer Structures. *Procedia Engineering,* 25:199-202, 2011.

[4] A. Jemai, F. Najar, M. Chafra and Z. Ounaies. Mathematical Modeling of an Active-Fiber Composite Energy Harvester with Interdigitated Electrodes. *Journal of Intelligent Material Systems and Structures,* submitted.

[5] S. V. Gopinathan, V. V. Varadan and V. K. Varadan. A review and critique of theories for piezoelectric laminates. *Smart Materials and Structures,* 9:24-48, 2000.

VIBRATION REDUCTION OF A STRUCTURE BY DESIGN AND CONTROL OF A BOLTED JOINT

Y.KARIM[1] , C.BLANZE[1]

[1]Structural Mechanics and Coupled Systems Laboratory
CNAM Paris France
Email: yassine.karim@cnam.fr, claude.blanze@cnam.fr

ABSTRACT

Control of vibration and noise can be considered as one of the most relevant technological challenges for the designer. Systems based on vibration control such as piezoelectric materials can reduce vibrations and noise. Structural joints are a primary source of energy dissipation as compared to material. To influence the vibration amplitude in a specific structure at the joints, we propose to design and integrate piezoelectric devices in this type of connection in order to reduce the amplitude of the overall structure. Moreover, joints and jointed structures exhibit uncertainties, which have to be taken into account to ensure confidence in the obtained results. Considering assemblies of various components using connections (bolts, screws, joints, etc.), a decomposition can be introduced. The components are separated, and the interfaces thus generated serve to model the connections existing between these elements: contact, friction force due to the integration of piezoelectric elements. The study of the sensitivity of the response to perturbations of the input variables is done via a confidence interval of a quantity of interest to the designer.

1 INTRODUCTION

Noise and vibration are often limiting factors in the performance of many industrial systems. The conventional method of treatment is to redesign the system in order to avoid exciting a structure at its natural frequencies or to use passive damping. Generally, designers use different strategies to control vibration such as avoiding exciting a structure at its natural frequencies or increasing damping in the structure when resonance cannot be avoided. Damping in a structure can be obtained by using materials having a large structural damping or by introducing specific equipments increasing the energy dissipation such as piezoelectric shunt[1] or viscoelastic materials [2].

In structural systems, joints and fasteners are used to transfer loads from one structural element to another. Structural joints are regarded as a source of energy dissipation between contacting surfaces in contact undergoing relative motion. Many studies [3] indicate that a joint friction has a great potential to reduce the levels of vibration of a structure.

The normal force, due to the tightening of the screw, is of great importance to control the vibration of the structure as shown in previous studies [4] . This is possible by the introduction of a piezoelectric disc between the screw and the bolt.

In addition to the energy dissipation aspect, the variable normal force is used in order to change the stiffness of the structure, and therefore to get out of the critical zones where the structure vibrates at one of its eigenfrequencies.

2 ASSOCIATION OF A FRICTIONAL CONTACT ASSEMBLY WITH PIEZOELECTRIC ELEMENT

In this section we propose to reduce the vibration amplitude of a given structure (FIG.1).

2.1 Set-up

For this purpose, a bolted joint is added to the main structure (FIG. 2) in order to change its global stiffness, and therefore to change its eigenfrequencies. The friction joint uses Coulomb type law, establishing a difference between two types of behaviour: sticking-type and sliding-type.

This shear force will not exceed a shear force limit value otherwise sliding-type behaviour will occur between surfaces in contact. The structure responses depending on the two types of behaviour are plotted on figure 3: the continuous line corresponds to the sticking-type condition when the shear force is transmitted without sliding between surfaces and the dotted line corresponds to the sliding-type condition when the shear force is equal to zero.

The idea of this work is to use a piezoelectric washer to control the normal force, and therefore to swap between a sliding and a sticking behaviour of bolted joint. If the excitation frequency is outside the critical zone, the connection remains locked (stick). Otherwise the rigidity of the structure is modified by a change of behaviour of the connection (slip).This device helps to change the structure stiffness according to excitation frequency , in order to prevent critical vibration magnitude near the structure eigenfrequencies.

2.2 Normal force control law

The proposed control law of the normal force needs the critical frequencies of the structure as input parameters. The critical frequency bandwidths around the critical frequencies are determined. When the frequency of the excitation is inside the critical frequency domain, a driving

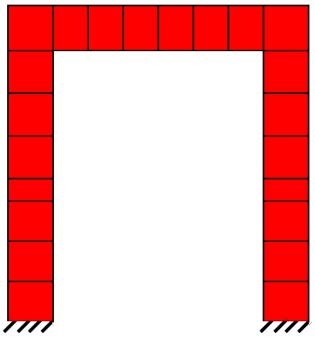

Figure 1. Structure to be damped

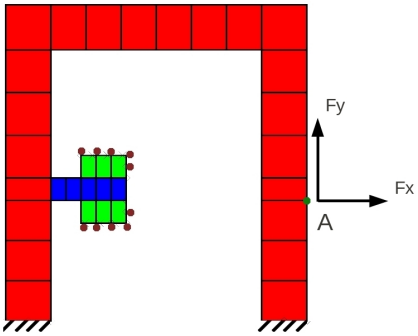

Figure 2: Structure with a added bolted joint

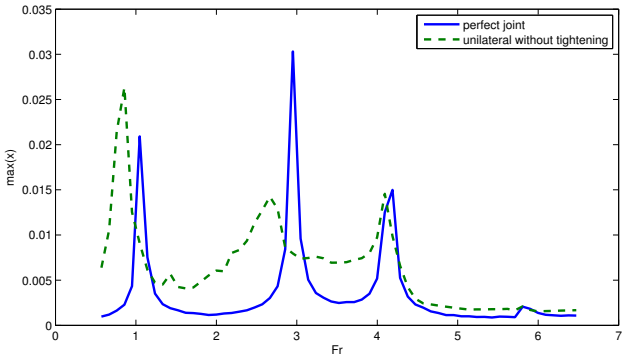

Figure 3. comparison of FRF with and without tightening

electrical value commands the piezo disc extension which increases the normal force on the assembly.

The control law could be formulate as:

$$\begin{cases} F_N = 0 & \text{if} \quad \Omega \in \Psi \\ F_N = F_{max} & \text{if} \quad \Omega \notin \Psi \end{cases} \qquad \text{with} \quad \Psi = \bigcup_{i=1}^{P} \Psi_i \tag{1}$$

where F_N is the normal force, P is the number of critical frequencies to be avoided, Ψ is the set of critical frequency bandwidths in which it is needed to change the rigidity of the structure, F_{max} is the magnitude of the normal force required to prevent the joint sliding.

The resolution of the non-linear frictional contact problem is made with the LATIN method described in [5]. This method is implemented under COFAST (an extension of the finite element software CAST3M) which is able to perform numerical simulations of contact problems with friction [6].

The graph above of Fig 4 shows a comparison of the frequency response of the structure with and without control, and the two graphs below represent a temporal response of the structure at the two first critical frequencies (FR1 and FR2)to be reduce. We can see that the control law is able to reduce the vibration amplitude at several critical frequencies.

3 CONCLUSION

In this paper we show that in the case of bolted joints the screw tightening (active control) can be controlled by a piezo-electric device and can limit the vibration amplitudes of the structure.

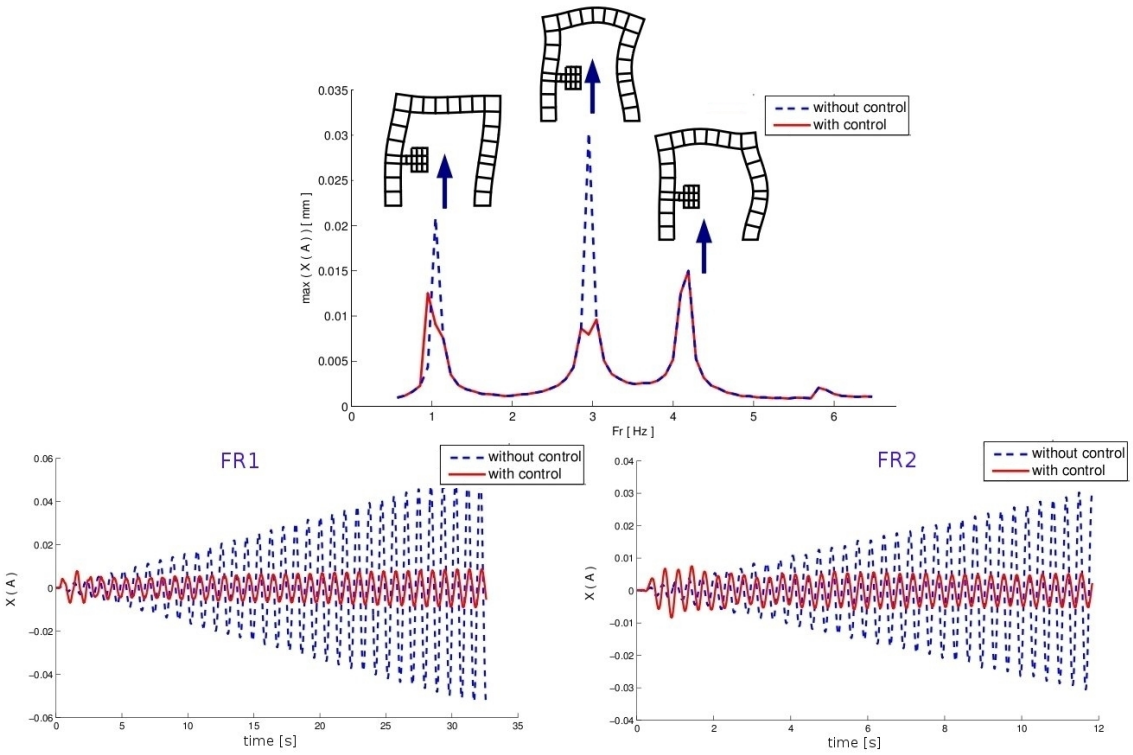

Figure 4. comparison of FRF with and without control

As an extension of this work, we also propose a more complex control law which does not require given eigenfrequency as input of the law. The robustness of proposed models was studied by a probabilistic approach, the friction coefficient and the normal force are modelled as random variables.

REFERENCES

[1] Julie-Anne Ranger Ayech Benjeddou. Use of shunted shear-mode piezoceramics for structural vibration passive damping. *Computers and Structures*, 2006.

[2] A.M. Horr and L.C. Schmidt. Modelling of nonlinear damping characteristics of a viscoelastic structural damper. *Engineering Structures*, 18(2):154 – 161, 1996.

[3] S. Bograd, P. Reuss, A. Schmidt, L. Gaul, and M. Mayer. Modeling the dynamics of mechanical joints. *Mechanical Systems and Signal Processing*, 2011.

[4] L. Gaul and R. Nitsche. friction control for vibration suppression. *Mechanical Systems and Signal Processing*, 14(2):139 – 150, 2000.

[5] P. Ladevèze and J.G. Simmonds. *Nonlinear computational structural mechanics: new approaches and non-incremental methods of calculation*. Mechanical engineering series. Springer, 1999.

[6] L. Champaney, J.Y. Cognard, and P. Ladevèze. Modular analysis of assemblages of three-dimensional structures with unilateral contact conditions. *Computers & Structures*, 73(15):249–266, October 1999.

ROBUST ACTIVE VIBRATION CONTROL OF PIEZOELECTRIC FLEXIBLE STRUCTURES WITH PROBABILISTIC PARAMETRIC UNCERTAINTY

K. Zhang[1] , G. Scorletti[2] and M.Ichchou[1*]

[1]Laboratory of Tribology and Systems Dynamics
Ecole Centrale de Lyon, Ecully, France
Email: kai.zhang@ec-lyon.fr, mohamed.ichchou@ec-lyon.fr

[2]Laboratory Ampère
Ecole Centrale de Lyon, Ecully, France
Email: gerard.scorletti@ec-lyon.fr

ABSTRACT

The main objective of this article is to develop a general and systematic robust control methodology for active vibration control of piezoelectric flexible structures. For this purpose, the propagation of uncertainty in material properties is investigated by generalized polynomial chaos (gPC) framework and traditional Monte Carlo Simulation is used as a reference solution. Phase and gain control policies based H_∞ output feedback control is used for the controller design considering a set of control objectives simultaneously. The probabilistic information of parametric uncertainty is investigated with risk-adjusted trade-off using suitable weighting functions in H_∞ control. Deterministic and probabilistic robustness analysis are conducted to verify the robust properties of the closed-loop system from both worst-case and probabilistic points of view. The deign process and effectiveness of the proposed methodology are illustrated via active vibration control of a piezoelectric cantilever beam.

1 INTRODUCTION

Flexible structures are extensively employed for many applications. They are susceptible to vibration due to their flexibility and recently active vibration control using piezoelectric materials is widely investigated in literature and practice [1]. However, no matter which kind of modeling methods is used, the obtained dynamic models always have certain level of parametric and dynamic uncertainties. In the presence of these uncertainties, a systematic control methodology is proposed in [2] for robust active vibration control of piezoelectric flexible structures, where a set of control objectives can be considered simultaneously. However, the robust properties of the closed-loop system can only be qualitatively ensured with phase and gain control policies and no probabilistic information of parametric uncertainty is considered. In this article, the general polynomial chaos(gPC) framework [3] is employed to have probabilistic information of parametric uncertainty from distributed structural property such as Young's Modulus E. This information can be investigated with probabilistic robustness analysis and the robust properties are quantitatively verified both in worst-case and probabilistic senses [4, 5]. The design process and effectiveness of the proposed control methodology is illustrated with active vibration control of a piezoelectric cantilever beam.

2 PROBABILISTIC ROBUST CONTROL METHODOLOGY

For sake of simplicity, only Young's Modulus E of the cantilever beam is assumed to follow Gaussian distribution, $i.e.$ $E \sim N(\mu_E, \sigma_E^2)$. Therefore, the corresponding natural frequency ω_i can be expanded using orthogonal Hermite polynomials [3],

$$\omega_i = \beta_0 + \beta_1\xi_1 + \beta_2(\xi_1^2 - 1) + \beta_3(\xi_1^3 - 3\xi_1) + \beta_4(\xi_1^4 - 6\xi_1^2 + 3) + \dots \tag{1}$$

where $\xi_1 = \frac{E-\mu_E}{\sigma_E} \sim N(0,1)$ is a normalized random variable, β_i the coefficient to determine with the regression and analysis of variance (ANOVA). Monte Carlo Simulation (MCS) is used to verify the effectiveness of gPC framework. The detailed procedure of this method can be found in [6] and references therein. Obviously, from gPC framework the distribution of interested ω_i is reflected by $|\delta_E| \leq 1 \sim N(0,1)$. Additionally, uniformly distributed damping ratio ζ_i is assumed to have 20% variation about its nominal values and an additive dynamic uncertainty is used to represent high-frequency neglected dynamics,

$$\begin{aligned} \omega_i &= \omega_{i0} + \omega_{i1}\delta_E;\ |\delta_E| \leq 1 \\ \zeta_i &= \zeta_{i0} + \zeta_{i1}\delta_{\zeta_i};\ |\delta_{\zeta_i}| \leq 1 \\ G_a(s) &= G(s) + W_{\text{Dyn}}(s)\Delta_{\text{Dyn}}(s),\ ||\Delta_{\text{Dyn}}(s)||_\infty \leq 1 \end{aligned}$$

Phase and gain control policies based H_∞ output feedback control is used to design a robust controller in the presence of parametric and dynamic uncertainties. The details of this method can be found in [2]. The robust properties of the closed-loop system are qualitatively ensured. Furthermore, μ/ν analysis are conducted to quantitatively verify deterministic robustness margin $k_{\text{DRM}} = \frac{1}{\max \mu}$ and worst-case performance. As accurate calculation of μ is usually NP-hard, upper and lowers bounds of μ are used to estimate μ. With upper bound of μ we can have k_{DRM} within which the system remains stable for any uncertainty. Lower bound of μ reveals the conservation in μ estimation. For flexible structures, there normally exist narrow and high peaks on μ plot with normal frequency gridding methods [7]. To have reliable estimation of μ, the frequency interval method [8] is also used in this article. MCS based probabilistic robustness is applied to investigate the probabilistic information of ω_i and calculate probabilistic robustness margin k_{DRM} and probabilistic worst-case performance. The sampling number N required by MCS is determined by Chernoff bound or Log-over-log bound [5], which does not

depends on the number of controller and uncertainty. With these analysis, robust properties of the closed-loop system are numerically verified both in deterministic and probabilistic senses. If any property is not satisfied, the weighting functions in H_∞ can be retuned to make a trade-off among various control objectives.

3 A NUMERICAL CASE STUDY

The proposed probabilistic robustness margin is illustrated with active vibration control of a non-collocated piezoelectric cantilever beam as shown in Fig. (1). The controller is designed to consider a set of control objectives with suitable weighting function in H_∞ control. With assumed uncertainties, the results of deterministic robustness analysis using both frequency gridding and interval methods are shown in Fig. (2), which demonstrate that $k_{\text{DRM}} = 4.755$ is reliable and the specification of vibration reduction is satisfied even in the worst case. With probabilistic robustness analysis, we have that, with probability 98% for either uniformly or Gaussian distributed ω_i,

$$|p_N(k_{\text{PRM}\leq 4.76}) - 100\%| \leq 0.01$$

where $\hat{p}_N$ is empirical probability estimated with N sampling numbers. This verifies that $k_{\text{DRM}} = 4.755$ is also reliable from probabilistic point of view. Furthermore, at the expense of some risk of stability violation we have that, with probability 98%,

$$\begin{aligned} |p(k_{\text{PRM}} = 4.98) - 98.20\%| &\leq 0.01, \text{Uniformly distributed } E \\ |p(k_{\text{PRM}} = 4.98) - 98.12\%| &\leq 0.01, \text{Gaussian distributed } E \end{aligned}$$

This implies that for uniformly distributed E if a 1.80% loos of probabilistic robustness is tolerated, the risk adjusted k_{PRM} may be increased by approximately 5.957% with respect to its deterministic counterpart k_{DRM}. Probabilistic worst-case performance analysis demonstrates that, with probability 98%,

$$\begin{aligned} P_R\{||G_{d2}(s)||_\infty \leq 47.17\text{dB}\} &\geq 99.9\%, \text{Uniformly distributed } E \\ P_R\{||G_{d3}(s)||_\infty \leq 50.74\text{dB}\} &\geq 99.9\%, \text{Uniformly distributed } E \\ P_R\{||G_{d2}(s)||_\infty \leq 47.08\text{dB}\} &\geq 99.9\%, \text{Gaussian distributed } E \\ P_R\{||G_{d3}(s)||_\infty \leq 50.66\text{dB}\} &\geq 99.9\%, \text{Gaussian distributed } E \end{aligned}$$

Above analysis demonstrate that the proposed control methodology is effective for active vibration control of the flexible structure and the robust properties of the closed-loop system are satisfied both in deterministic and probabilistic senses.

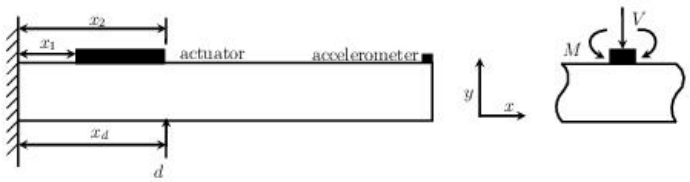

Figure 1. The piezoelectric cantilever beam

4 CONCLUSIONS AND PERSPECTIVES

This article focus on a general and systematic probabilistic robust control methodology for active vibration control of piezoelectric flexible structures such that the probabilistic information of parametric uncertainty can be considered and the robust properties are guaranteed both in

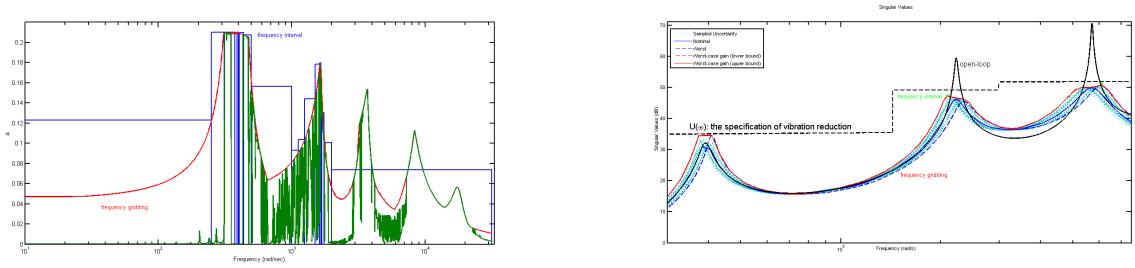

Figure 2. Deterministic robustness analysis

deterministic and probabilistic senses. With this control methodology, a definitely robust controller can be achieved with assumed parametric and dynamic uncertainties and, if necessarily, a less conservative controller is also provided by making a risk-adjusted trade-off in H_∞ control. The generality and effectiveness of the proposed methodology is illustrated by active vibration control of a piezoelectric cantilever beam. It can also been applied to more complicated and practical structures with more sources of uncertainties including time-varying uncertainties.

REFERENCES

[1] Z. Qiu, J. Han, X. Zhang, Y. Wang, and Z. Wu. Active vibration control of a flexible beam using a non-collocated acceleration sensor and piezoelectric patch actuator. *Journal of Sound and Vibration*, 326(3):438–455, 2009.

[2] K. Zhang, G. Scorletti, M. Ichchou, and F. Mieyeville. Phase and gain control policies for robust active vibration control of flexible structures using smart materials. Submitted to Smart Materials and Structures, 2012.

[3] D. Xiu and G.E. Karniadakis. The wiener-askey polynomial chaos for stochastic differential equations. *SIAM Journal on Scientific Computing*, 24(2):619–644, 2002.

[4] K. Zhou and J.C. Doyle. *Essentials of Robut Control*. Prentice Hall, 1999.

[5] R. Tempo, G. Calafiore, and F. Dabbene. *Randomized Algorithms for Analysis and Control of Uncertain Systems*. Communications and Control Engineering Series. Springer Verlag, London, 2004.

[6] S.K. Choi, R.V. Grandhi, R.A. Canfield, and C.L. Pettit. Polynomial chaos expansion with latin hypercube sampling for estimating response variability. *AIAA Journal*, 42(6):1191–1198, 2004.

[7] P.M. Young, M. Newlin, and J.C. Doyle. Practical computation of the mixed μ problem. In *Proceedings of the American Control Conference*, pages 2190–2194, Chicago, 1992.

[8] G. Ferreres, J.M. Biannic, and J.F. Magni. Robustness analysis of flexible structures: practical algorithms. *International Journal of Robust and Nonlinear Control*, 13(8):715–733, 2003.

MONITORING BEARING DEFECTS BY ACOUSTIC EMISSION: APPLICATION OF EMPIRICAL MODE DECOMPOSITION METHOD FOR EARLY DETECTION

M. Kedadouche, M. Thomas et A. Tahan

Department of Mechanical Engineering, École de Technologie Supérieure
1100, Notre-Dame West Street, Montréal (Quebec) H3C 1K3

mourad.kedadouche@hotmail.fr, marc.thomas@etsmtl.ca, antoine.tahan@etsmtl.ca

ABSTRACT

Rolling element bearing is a major cause of defects in rotating machinery and is considered as one of the key components for rotating machinery such as machine tools, motors, gearboxes, and turbo-machinery. Bearing diagnostic has been a topic of research interest for over 20 years. The most widely used technique for monitoring and diagnosing bearings is vibration analysis (≤ 20 kHz), which has conducted to many developments in improved methods for signal processing, as well as improvements in algorithms for anomaly detection, classification and failure prediction. There are several signal processing techniques that can be used for diagnosing bearing defects by vibration measurements. Actually, the most often descriptors used to describe the signals are usually based on the use of scalar statistical descriptors on the raw signal. Envelope techniques and advanced signal processing techniques around the natural frequencies may be used. Nevertheless, early defect detection is difficult and the detection becomes easy when the bearing frequencies can be easily identified which happens when the bearing is an advanced stage of degradation. At this stage of degradation, the residual life of exploitation becomes relatively short.

This motivated the aeronautic industry to investigate the potential of a detection method based on acoustic emission measurements for an early detection of bearing defects rotating at very high speeds. In this study, we propose to use the empirical mode decomposition (EMD) technique to see its efficiency on acoustic emission signals greater than 20 kHz. We use an industrial sensor UE10 000, which is a sensor of acoustic emission (AE) with an electrical circuit that converts the signal into an audible signal AE (<20 kHz) by a technique called the heterodyning. The advantage of this sensor is that it allows saving the signal on multiple frequency bands of 5 kHz bandwidth, from 20 kHz to 100 kHz with an increment of 1 kHz. Then the signals are saved for these frequency bands whose center of the band is: 20 kHz, 24 kHz, 28 kHz, 30 kHz, 36 kHz and 40 kHz.

Empirical Mode Decomposition is one of the techniques whose proved his capability for an early detection of defects for many mechanical applications like bearing, gear, etc….. The EMD methodology developed in this paper decomposes the original times series data in intrinsic oscillation modes, using the empirical mode decomposition. The well established scalar statistical parameters such as the crest factor and the distribution of moments including kurtosis and skew are utilised in the study. These statistical descriptors are calculated for each intrinsic mode function (IMF).

The technique is validated by experiments on a test bench with a very small crack (40µm) on the outer race of a ball bearing. The application of time descriptors to different IMF decomposition levels gives good results for early detection of defects in comparison with the original time signal and with the wavelet decomposition.

Keyword: Acoustic Emission, Rolling element bearings, Empirical Mode Decomposition (EMD), Intrinsic Mode Function (IMF), Early Detection, Scalar Statistical Parameters.

ON THE BEHAVIOR OF THE FLEXIBLE ROTOR BEARING SYSTEM IN THE VISCINITY OF THE STABLITY THRESHOLD

M. Chouchane[1] and R. Sghir[1*]

[1]Laboratory of Mechanical Engineering
National Engineering School of Monastir
University of Monastir, Monastir, Tunisia
Email: manouar.chouchane@enim.rnu.tn, sghirradhoineim@yahoo.fr

ABSTRACT

A four degree of freedom model of a symmetrical balanced flexible rotor supported by two identical short journal bearings is considered. The model is nonlinear owing to the nonlinear relationship of bearing forces with journal position and velocity. The dynamic model in a nondimensional form comprises six first order differential equations and depends only on three nondimensional parameters: the normalized rotor speed, the bearing modulus and the rotor stiffness. At low rotor speeds, both journal center and disk center exhibit a stable equilibrium point. Increasing the rotor speed a stability threshold speed is reached at which the equilibrium point undergoes a Hopf bifurcation and either branch of stable or unstable limit cycles emerges. The continuation of the limit cycles beyond the stability threshold reveals one or more limit point of cycle bifurcations. Several important system behaviors near the stability threshold are thus predicted such as bi-stability domains, potential jumping to large limit cycles and rubbing between the journal and the bearing so that potential bearing failure is prevented.

1 INTRODUCTION

Journal bearings are commonly used in rotating machines because of their reliability and inherent damping. Journal bearings, however, may undergo unstable motion and large oscillations causing rubbing and potential bearing premature failure. In a typical linear analysis, the stability threshold speed is predicted and a safe operating speed domain is determined. Numerical simulation and experiments have highlighted several phenomena not predicted by linear analysis such as possible operation with stable limit cycle motion and jumping from small to large unsafe limit cycles.

Early nonlinear analysis approaches, such as the methods of multiple scales, the method of averaging and the analytical Hopf bifurcation [1,2], typically predict only the Hopf bifurcation and the limit cycles in its vicinity. In recent published research work [3], numerical continuation is used to accurately predict branches of limit cycles and their successive bifurcations which are essential to explain important phenomena exhibited by rotor bearing systems near the stability threshold. This paper applies numerical continuation to determine the bifurcations of a flexible rotor supported by two hydrodynamic bearings in the neighbourhood of the stability threshold.

2 NONLINEAR DYNAMIC MODELING OF THE FLEXIBLE ROTOR-BEARING SYSTEM

A flexible rotor bearing system is considered and shown in figure 1.a. The rotor is composed of a flexible shaft of stiffness $2k$ supporting at the middle a rigid and perfectly balanced disk of mass $2m$. The rotor is supported by two identical and aligned short hydrodynamic bearings. Both bearings are assumed to have the same motion. Referring to figure 1.b, the position of the journal center O_j with respect to the bearing journal O_b is defined by the polar coordinates $(c\varepsilon, \phi)$; where c is the bearing clearance, ε is the journal eccentricity and ϕ is the attitude angle. The position of the disk center O_d with respect to the bearing center O_b is defined by the two cartesian coordinates (x, y). The system has thus four degrees of freedom.

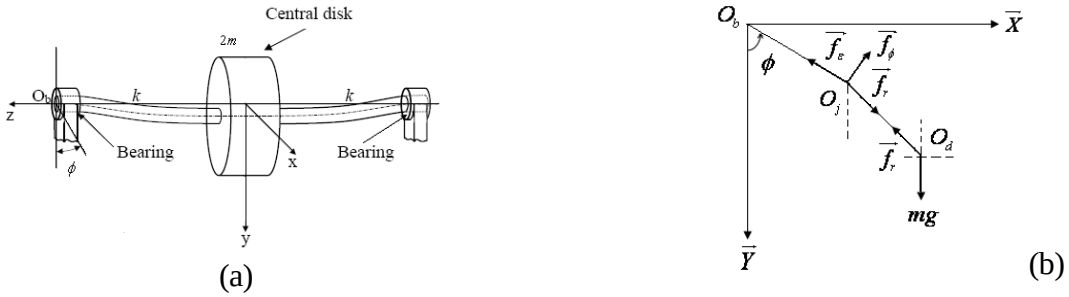

Figure 1. (a) The model of the symmetrical flexible rotor
(b) Forces applied on the journal and the disk

Applying Newton's second law to the journal and the disk yields the following four nondimensional dynamic equations

$$\begin{cases} \bar{f}_\varepsilon + \dfrac{\bar{K}}{\bar{\omega}^2}\bar{x}\sin\phi - \dfrac{\bar{K}}{\bar{\omega}^2}\bar{y}\cos\phi - \dfrac{\bar{K}}{\bar{\omega}^2}\varepsilon = 0 \\ \bar{f}_\phi + \dfrac{\bar{K}}{\bar{\omega}^2}\bar{x}\cos\phi + \dfrac{\bar{K}}{\bar{\omega}^2}\bar{y}\sin\phi = 0 \end{cases} \qquad \begin{cases} \ddot{\bar{x}} + \dfrac{\bar{K}}{\bar{\omega}^2}\bar{x} - \dfrac{\bar{K}}{\bar{\omega}^2}\varepsilon\sin\phi = 0 \\ \ddot{\bar{y}} + \dfrac{\bar{K}}{\bar{\omega}^2}\bar{y} + \dfrac{\bar{K}}{\bar{\omega}^2}\varepsilon\cos\phi + \dfrac{1}{\bar{\omega}^2} = 0 \end{cases} \tag{1}$$

where $$\bar{f}_\varepsilon = \frac{f_\varepsilon}{m\omega^2 c} = -\frac{\Gamma}{\bar{\omega}}\left[\frac{2\varepsilon^2(1-2\dot{\phi})}{(1-\varepsilon^2)^2} + \frac{\pi(1+2\varepsilon^2)\dot{\varepsilon}}{(1-\varepsilon^2)^{2.5}}\right]; \quad \bar{f}_\phi = \frac{f_\phi}{m\omega^2 c} = \frac{\Gamma}{\bar{\omega}}\left[\frac{\pi(1-2\dot{\phi})\varepsilon}{2(1-\varepsilon^2)^{1.5}} + \frac{4\varepsilon\dot{\varepsilon}}{(1-\varepsilon^2)^2}\right] \tag{2}$$

The fluid film forces f_ε and f_ϕ are shown in figure 1.b. Their expressions given in equation (2) are derived from the short bearing theory and Half Sommerfeld assumption. The system (1) consists of four differential equations for the nondimensional coordinates ε, ϕ, $\bar{x} = x/c$ and $\bar{y} = y/c$ and depends only on three nondimensional parameters $\bar{\omega} = \omega / \sqrt{g/c}$, $\bar{K} = k/(mg/c)$ and the bearing modulus $\Gamma = \mu R L^3 / (2mc^{2.5} g^{0.5})$; where μ, R and L are respectively the oil viscosity, the bearing radius and the bearing length.. The derivatives in equations (1) and (2) are with respect to nondimensional time $\tau = \omega t$.

Let $\mathbf{x} = (x_1, x_2, x_3, x_4, x_5, x_6)^T = (\varepsilon, \phi, \bar{x}, \dot{\bar{x}}, \bar{y}, \dot{\bar{y}})^T$, the system of equations (1) can thus be rewritten in the following state space form

$$\dot{\mathbf{x}} = \mathbf{f}(\mathbf{x}, \bar{K}, \bar{\omega}, \Gamma) \tag{3}$$

The steady state equilibrium position $\mathbf{x}_s = (\varepsilon_s, \phi_s, \bar{x}_s, 0, \bar{y}_s, 0)^T$ can be determined from the solution of the system of equations : $\dot{\mathbf{x}}=\mathbf{0} = \mathbf{f}(\mathbf{x}_s, \bar{K}, \bar{\omega}, \Gamma)$.

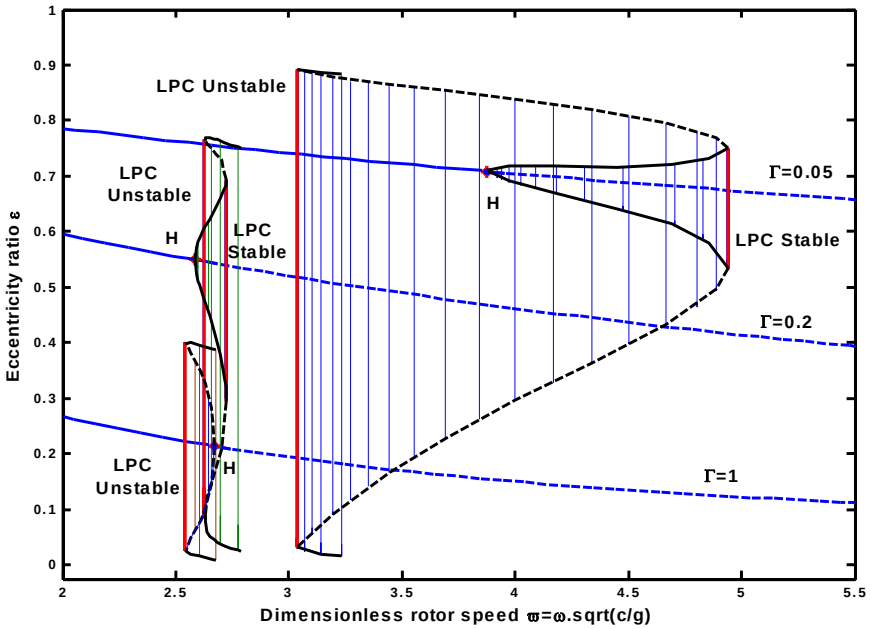

Figure 2. Bifurcation diagrams for a stiff rotor, $\bar{K}$ =1000, and for three selected bearing parameters Γ =0.05; 0.2 and 1.

3 RESULTS

The system of differential equation (3) depends on three nondimensional parameters $\bar{K}$, $\bar{\omega}$ and Γ. To apply a single parameter continuation analysis, two of the three parameters have to be fixed. In the following, both parameters $\bar{K}$ and Γ are fixed and the parameter $\bar{\omega}$ is used as a bifurcation parameter. Typically, the systems of equations (3) admits a stable steady state equilibrium point for low values of $\bar{\omega}$. Equilibrium point continuation is applied first to predict the position of the equilibrium point for an increasing value $\bar{\omega}$ until a Hopf bifurcation point is detected at a rotor speed $\bar{\omega}_H$. At this point, the equilibrium point becomes unstable. The continuation from the Hopf bifurcation point gives either a branch of stable limit cycles for $\bar{\omega} > \bar{\omega}_H$ or a branch of unstable limit cycles for $\bar{\omega} < \bar{\omega}_H$. The size of the limit cycles typically increases as rotor speed $\bar{\omega}$ is shifted away from $\bar{\omega}_H$. The limit cycles may undergo Limit Point of Cycle bifurcations (LPC) as long as the journal does come into contact with the bearing.

Continuation analysis has been performed for a highly stiff rotor and a highly flexible rotor. A value of $\bar{K}$ =1000 is chosen for the former and $\bar{K}$ =1 for the latter. Figure 2 shows the bifurcation diagrams for the highly rigid rotor, $\bar{K}$ =1000 and for three selected bearing parameters Γ =0.05; 0.2 and 1. The Hopf bifurcation is supercritical for Γ =0.05 and 0.2 and subcritical for Γ =1. Two successive LPC bifurcations have been predicted following the supercritical Hopf bifurcation and only a single LPC bifurcation is detected following the subcritical Hopf bifurcation. The continuation is stopped when the eccentricity ratio reaches zero as the system (3) is only defined for positive eccentricities. A similar analysis has been carried out for the flexible rotor, $\bar{K}$ =1. Figure 3 summarises the results for both cases. Stability boundaries occurring at Hopf bifurcation are shown along with LPC bifurcations in the $(\Gamma, \bar{\omega})$ plane. The bifurcations diagrams in figure 2 corresponds to sections a, b and c of the upper curves in figure 3.

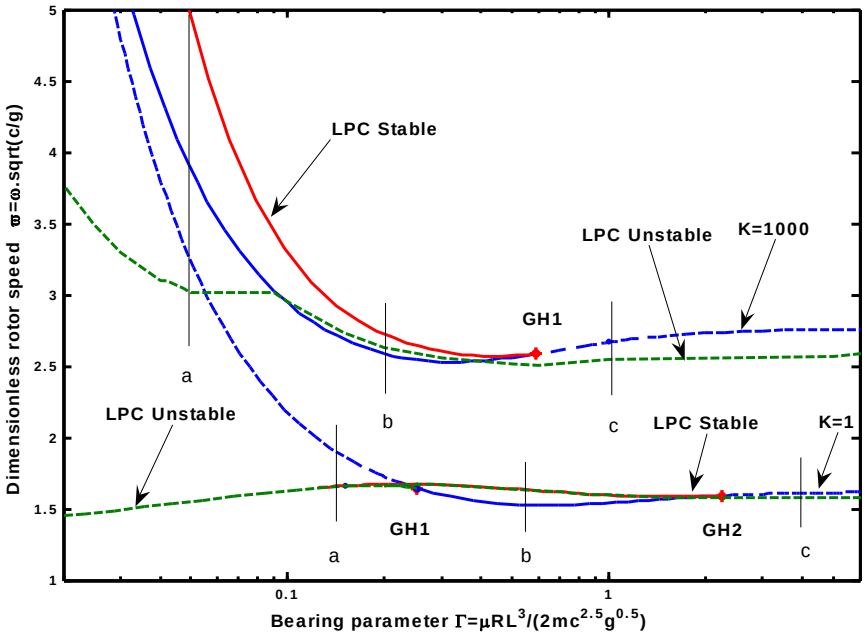

Figure 3. Extended stability charts for $\bar{K}$ =1000 and $\bar{K}$ =1.

4 CONCLUSION

Numerical continuation has been applied in the nonlinear analysis of the stability and bifurcation of a balanced flexible rotor bearing system. Using the rotor speed as a continuation parameter, we predicted the steady state equilibrium point and its bifurcation into limit cycles as well as the successive bifurcations of the limit cycles. Important phenomena required for understanding the behavior of the rotor bearing system in the vicinity of the stability critical speed are thus elucidated.

REFERENCES

[1] Lund, J. W., 1967. Oil Whip Whirl Orbit of a Rotor in Sleeve Bearings. ASME J. Eng. Ind. Vol. 89, pp. 813-823.

[2] Wang, J.K., Khonsari, M.M., 2006. Bifurcation analysis of a flexible rotor supported by two fluid film journal bearings. Journal of Tribology, Vol. 128, issue 3, pp. 594-603.

[3] Chouchane, M., Amamou A., 2011. Bifurcation of Limit Cycles in Fluid Film Bearings. International Journal of Non-Linear Mechanics. Vol. 46, pp. 1258-1264.

Application of Modified Modal Assurance Criteria in Mistuning Bladed Disk

Peiyi Wang*[1],Lin Li[1]

[1]405 Vibration Group, School of Energy and Power Engineering
Beihang University, Beijing, CHINA
Email: wangpeiyi01@163.com ,feililin@buaa.edu.cn,

ABSTRACT

The MMAC(modified modal assurance criterion) is proposed to replace the amplification factor in mistuning bladed disk research. The amplification factor has been widely utilized to measure the severity of the consequences of the mistuning. It is normally defined as the ratio of the highest forced vibration response level found in a given mistuned bladed disk to the highest forced vibration response level found in a tuned counterpart, under the same excitation pattern. However in order to obtain an accurate amplification factor, it always costs excessive computational resources, specially dealing with random mistuning bladed disk. The advantage of MMAC is that it reveals vibration amplification of the mistuned bladed disk, without frequency sweeping neither calculation of inverse matrix, the only computational cost is the eigenvalue solution, which could be time saving for design in early stages. An improved Monte Carlo method based on MMAC has been suggested to give a stochastic evaluation of a random mistuning bladed disk. The accuracy and efficiency of the proposed method has been demonstrated on a two-DOFs-per-sector lumped bladed disk model. The conclusion is obtained that the application of MMAC could be precise and more economic compared with the traditional method.

INTRODUCTION

The consequences of mistuning can be quantified by the 99.9 percentile of the probability density function, and this value is usually found by Monte Carlo simulation [1].Though the classical method has been performed more than 14 years [2], it is still quite time consuming for a stochastic solution of mistuned bladed disk. An improved MC method was developed to solve this problem.

1 LUMPED BLADED DISK

A typical 2-DOF-per-sector lumped bladed disk is shown in Figure 1. The governing equation of the i[th] sector is given below:

$$\begin{cases} m_i\ddot{X}_i + C_i(\dot{X}_i - \dot{Y}_i) + k_i(X_i - Y_i) = 0 \\ M\ddot{Y}_i + C_i(\dot{Y}_i - \dot{X}_i) + k_i(Y_i - X_i) + K_i(Y_i - Y_{i-1}) + K_{i+1}(Y_i - Y_{i+1}) + k_g Y_i = 0 \end{cases} \quad (1)$$

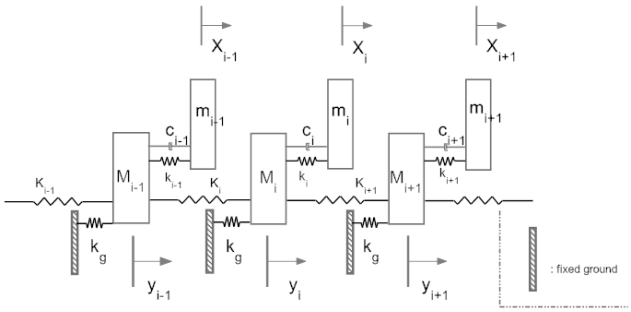

Figure 1. **Lumped Bladed Disk**

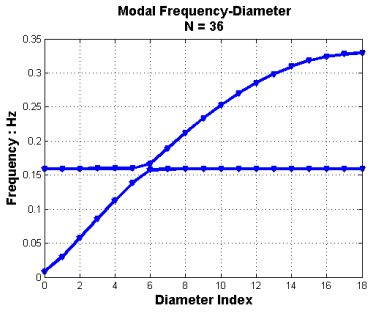

Figure 2 Frequency-Nodal Diameter

The equation of motion of whole bladed disk could be derived from Eq.(1), which is omitted due to simplification. A lumped model with 36 sectors was developed to conduct numerical research. Figure 2 shows the frequency-nodal diameter plot of it. The modes with nodal diameter equal 6 within frequency veering are sensitive to mistuning [3]. The mistuning is considered by Eq.(2),

$$k_i = k*(1+\delta_i) \quad (2)$$

In which δ_i is a sample taken from a normally distributed random variable with zero mean.

2 DEFINITION OF MMAC

Generally the resonant response of a linear structure under sinusoidal excitation can be expressed as in Eq.(3)

$$\boldsymbol{X}_s = \boldsymbol{\phi}_s \frac{\boldsymbol{\phi}_s^T \cdot F}{2\xi_s\omega_s^2} \cdot \sin(\omega_s t - \frac{\pi}{2}) \quad (3)$$

Eq.(3) shows that, the resonant response level is proportional to the generalized force $\boldsymbol{\phi}_s^T \cdot F$, the reciprocal of modal damping ratio $1/\xi_s$ and reciprocal of square of the resonant frequency $1/\omega_s^2$, which represents the modal stiffness. When there is a structural perturbation Δ, the maximum response of the bladed disk would vary, the ratio of maximum response of after and before the perturbation, is defined as the amplification factor τ,

$$\tau = \frac{\|\boldsymbol{X}_{s,\Delta}\|_\infty}{\|\boldsymbol{X}_s\|_\infty} = \frac{\xi_s\omega_s^2}{\xi_{s,\Delta}\omega_{s,\Delta}^2} \cdot \frac{\boldsymbol{\phi}_{s,\Delta}{}^T \cdot \boldsymbol{F}}{\boldsymbol{\phi}_s^T \cdot \boldsymbol{F}} \cdot \frac{\|\boldsymbol{\phi}_{s,\Delta}\|_\infty}{\|\boldsymbol{\phi}_s\|_\infty} \quad (4)$$

In turbo machine, if the wake excitation is parallel with the modal vector ϕ_s, which could essentially maximize the projection of excitation, q is a constant as in

$$\boldsymbol{F} = q \cdot \phi_s \quad (5)$$

Substitute Eq.(5) into Eq.(4), and take the norm of τ we could obtain the definition of modified modal criterion as the following,

$$MAC_{\text{mod}} = \|\tau\| = \chi_f \cdot \chi_\infty / (\chi_\xi \cdot \chi_\omega) \tag{6}$$

In which, the following quantities are defined:

Relative modal damping ratio defined in Eq.(7), reflects the change of modal damping.

$$\chi_\xi = \xi_{s,\Delta} / \xi_s \tag{7}$$

Modal stiffness ratio defined in Eq.(8), reflects the change of modal stiffness.

$$\chi_\omega = \omega_{s,\Delta}^2 / \omega_s^2 \tag{8}$$

Generalized force ratio defined in Eq.(9), reflects the change of generalized force.

$$\chi_f = \left\| \boldsymbol{\phi}_{s,\Delta}{}^T \cdot \boldsymbol{F} / (\boldsymbol{\phi}_s^T \cdot \boldsymbol{F}) \right\| = \left\| \boldsymbol{\phi}_{s,\Delta}{}^T \cdot \boldsymbol{\phi}_s / (\boldsymbol{\phi}_s^T \cdot \boldsymbol{\phi}) \right\| \tag{9}$$

Modal infinite norm ratio defined in Eq.(10), reflects the change of modal shape.

$$\chi_\infty = \left\| \boldsymbol{\phi}_{s,\Delta} \right\|_\infty / \left\| \boldsymbol{\phi}_s \right\|_\infty \tag{10}$$

As defined in Eq.(7)-Eq.(10), the quantities tell that the amplification of the forced amplification of bladed disk depends on the multiplication of them. When mistuned and tuned bladed disks are compared, these four quantities reflect the changes of dynamic characters.

The traveling wave mode vector has been provided as a proper orthogonal basis to illustrate the topologic character of the mode vectors when the bladed disk was mistuned. If any mode vector could be given as followed,

$$\boldsymbol{\Phi}_m = \sum_{i=1}^{N} \alpha_i \boldsymbol{\phi}_i \tag{11}$$

In which $\boldsymbol{\phi}_i$ is a traveling wave mode vector, $\boldsymbol{\Phi}_m$ represents mode vector of the perturbed bladed disk. If we let $\boldsymbol{\Phi} = [\boldsymbol{\phi}_1 \quad \cdots \quad \boldsymbol{\phi}_N]^T$ represent the blocked mode matrix, the coefficients α_i could form a vector, we define it as the Nodal Diameter Spectrum(NDS) in Eq.(12),

$$\boldsymbol{\alpha} = [\alpha_1 \quad \cdots \quad \alpha_N] \tag{12}$$

If let $\boldsymbol{\phi}_s = \alpha \cdot \Phi \quad \boldsymbol{\phi}_{s,\Delta} = \beta \cdot \boldsymbol{\Phi} \quad \boldsymbol{\Phi}^T \cdot \boldsymbol{\Phi} = \boldsymbol{I}$, the Generalized forced ratio could be rewritten ,

$$\chi_f == \left\| (\beta \cdot \boldsymbol{\Phi})^T \cdot (\alpha \cdot \boldsymbol{\Phi}) / (\alpha \cdot \boldsymbol{\Phi})^T \cdot (\alpha \cdot \boldsymbol{\Phi}) \right\| = \left\| \beta^T \cdot \alpha \right\| / \left\| \alpha \right\|_2 \tag{13}$$

Eq.(13) actually shows that, χ_f reflects the similarity between mistuned and tuned corresponding modes. If the stiffness of blades were perturbed by random mistuning with a standard deviation which equals to 0.01, the significant change of nodal diameter spectrum of the mistuned bladed disk can be observed from Figure 3 and Figure 4. Figure 5 shows that the discrepancies of natural frequencies are clustered within the modes dominated by blade-motion. Figure 6 tells us that the damping ratio could be altered greatly due to mistuning. In Figure 7, it can seen that, the modal infinite norm varies with mode indexes. Figure 5-Figure 7 show that contributions to amplification come from different quantities.

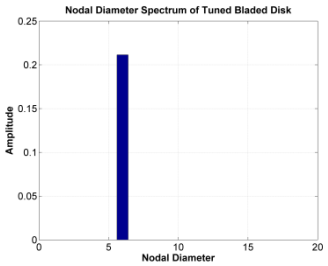

Figure 3 NDS of tuned bladed disk

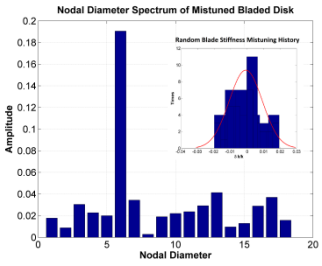

Figure 4 NDS of mistuned bladed disk

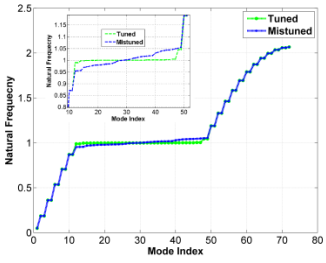

Figure 5 Tuned and mistuned natural frequency

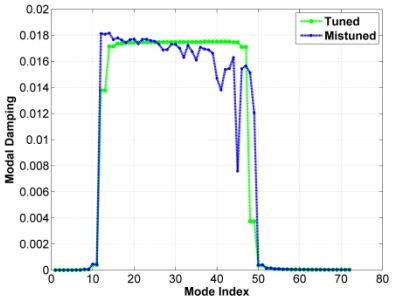

Figure 6 The change of modal damping vs modes

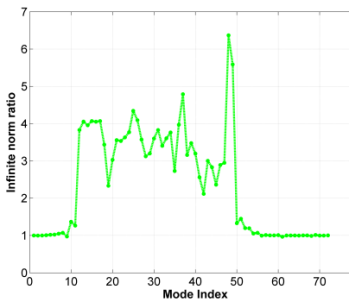

Figure 7 The change of modal infinite norm ratio

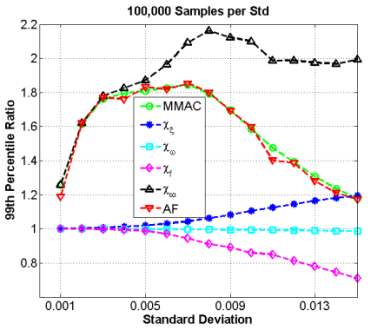

Figure 8 Improved MC simulation

3 IMPROVED MONTE CARLO SIMULATION

Thanks to MMAC, an improved Monte Carlo simulation procedure is proposed to study the dynamics of mistuned bladed disk: first, the mistuned coupling stiffness between blades and disk are assigned by a pseudo-random generator. Second, the eigenvalue problem is solved and the MMAC is calculated. Third, the process is repeated for many realizations, and then the distribution of the MMAC is estimated by using classical technique of statistics. The procedure is much more economic than classic MC simulation based on amplification factor. A numerical case is taken to examine its accuracy and efficiency. The travelling wave excitation is parallel with mode 12 (of which the nodal diameter equals 6 within frequency veering region) as shown in Eq.(5), which likely leads to response amplification due to mistuning. 100,000 samples for each standard deviation are performed. It can be seen from Figure 8, the MMAC line and AF (Amplification Factor) line are coincide with each other, which shows the accuracy of MMAC method. The χ_ω stays unchanged due to small mistuning. The damping ratio and infinite norm provide positive contribution to the increase of response while mistuning strength is increased, the generalized force ratio are reduced as the mistuning strengthened, which leads to a reduction in MMAC when mistuning strength gets lager.

4 CONCLUSION

It is shown that the MMAC factor proposed in the paper could provide the essential mechanism of response amplification of mistuned bladed disk. Meanwhile great computational benefit could be obtained in the improved MC simulation. Furthermore, if the MMAC method could be combined with reduced order model, the evaluation on random mistuned bladed disk could be more efficient.

REFERENCES

[1] Yum Ji Chan. Variability of blade vibration in mistuned bladed discs. *Doctoral Thesis*. Imperial College London.Otctober,2009

[2] Matthew P.Castanier, Christophe Pierre. Investigation of the combined effects of intentional and random mistuning on the Forced response of bladed disks. AIAA-98-3720

[3] Li Lin, Wangpeiyi. Evaluation of High-Order Resonance of Bladed Under Wake Excitation. GT2010-23148. June 14-18, 2010, Glasgow, UK

[4] Rotea M., Fernando D.A. New tools for analysis and optimization of mistuned bladed disks [R].AIAA-2002-4081, 2002.

DYNAMIC CHARACTERISTICS OF THE CYCLIC-PERIODIC STRUCTURE WITH PIEZOELECTRIC NETWORKS

Lin Li[1], Pengcheng Deng[1*] and Yu Fan[1]

[1]School of Energy and Power Engineering
Beihang University, Beijing, CHINA
Email: feililin@buaa.edu.cn, dpcking@163.com, fanyu.buaa@gmail.com

ABSTRACT

The paper deals with a cyclic-periodic system with piezoelectric (PZT) network. In such system, between periodic sectors there is not only mechanical connection but also electrical connection. The system is simulated by a lumped parameter model. The dynamical equations of the system are derived. The analytical solution of the eigenvalue problem correspondent is given. The forced vibration is researched based on certain special cases. The result shows that the presence of PZT network would change the natural frequencies of the system. The change depends on the mechanical coupling between sectors. The forced response has a sensibility to the connection and elements of the network and it is influenced also by mechanical coupling between sectors.

1 INTRODUCTION

The term 'PZT network' was used and studied firstly by K.W.Wang. In the literature published in 2003 [1], the PZT material was introduced into a quasi-periodic symmetric structure, and connected together with the inductance and capacitance in the circuit. The result showed that there will be no localized modes if suitable circuit parameters are selected. In subsequent literatures, they tried to strength the electromechanical coupling characteristics with the negative capacitance [2], and focus in the suppression of PZT networks to mistuning response [3, 4]. It is indicated that the electromechanical coupling characteristic among the mistuned sectors, can effectively suppress vibration localization and response localization.

Based on the study of Wang, literature [5] studied the possibility to change the vibration energy propagation path in order to improve the system dynamics and to reduce vibration through the design of PZT networks. In order to highlight this point, in their research it is assumed that, there is no mechanical coupling among the substructures. However, for the background of blade disk structure research, it must be taken into consideration.

2 RESEARCH OBJECTIVE

The presented work is a development based on the research work of Li and Fan [5]. The studied system is a cyclic-periodic system with PZT network. The difference from that of Li and Fan is that in such system, between periodic sectors there is not only electrical connection but also mechanical connection. But in the system studied by Li and Fan there is no connection between sectors. These structures or components are independent mechanically. The presented research objective is demonstrating that the presence of the PZT network makes mechanical energy propagate through not only mechanical connection but also electric connection, which changes the inner energy distribution of the system and could improve the dynamical behaviour of the system.

3 DYNAMICAL EQUATIONS OF THE CYCLIC-PERIODIC WITH PZT NETWORK SYSTEMS

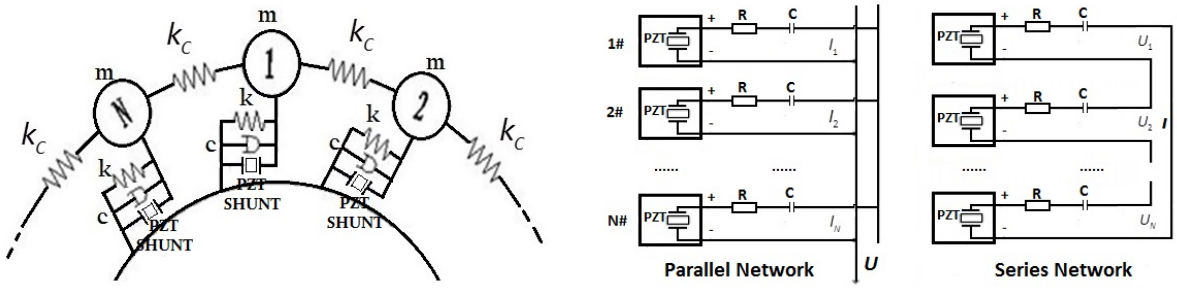

(a) (b)

Figure 1. The lumped parameter model and the PZT network

In this study, the cyclic-periodic structure is modelled by a simple lumped parameter model (shown in Figure 1 (a)). Every substructure is represented by a spring-mass lumped parameter oscillator connected with the foundation. There is a spring between two adjacent oscillators, which simulates the mechanical coupling. Values of the inertial term, damping term and stiffness term are derived from some assumptions of the whole structure. On each sector, a PZT shunt is set. The PZT shunt of each sector is connected to each other to form a network. Two types of PZT

network are considered: parallel connection and series connection (shown in Figure 1 (b)), referred by MP and MS respectively in following text.

The corresponding equations are derived and given below in non-dimensional form.

$MP(N)$:

$$\begin{cases} \lambda^2 y_i'' + 2\xi\lambda y_i' - \gamma_C y_{i-1} + \left(1+\gamma_{SC}+\gamma_{PM}+2\gamma_C\right) y_i - \gamma_C y_{i+1} - q_i = p_i(\tau) \\ \dfrac{\lambda}{2\xi\varepsilon_{RM}} q_i' + \left(\dfrac{1}{\gamma_{EM}} + \dfrac{1}{\gamma_{PM}}\right) q_i - y_i + \dfrac{1}{N}\sum_{k=1}^{N} y_k = 0 \end{cases} \quad ,1 \le i \le N. \tag{1}$$

$MS(N)$:

$$\begin{cases} \lambda^2 y_i'' + 2\xi\lambda y_i' - \gamma_C y_{i-1} + \left(1+\gamma_{SC}+\gamma_{PM}+2\gamma_C\right) y_i - \gamma_C y_{i+1} - q = p_i(\tau) \quad ,1 \le i \le N. \\ \dfrac{\lambda}{2\xi\varepsilon_{RM}} q' + \left(\dfrac{1}{\gamma_{EM}} + \dfrac{1}{\gamma_{PM}}\right) q - \dfrac{1}{N}\sum_{k=1}^{N} y_k = 0 \end{cases} \tag{2}$$

In which:

N : The number of sectors

$\tau = \omega t$: Non-dimensional time

$\omega_n^2 = k/m$: Natural frequency

$\lambda = \omega/\omega_n$: Non-dimensional frequency

$\gamma_C = k_C/k$: Non-dimensional coupling stiffness

$\varepsilon_{RM} = \eta^2/\omega_n^2 Rc$: Non-dimensional resistant

$\xi = c/\sqrt{km}/2$: Mechanical damping ratio

$\delta = f_1/k$: Stationary response

$q_i = \eta Q_i / f$: Non-dimensional electrical charge

$y_i = x_i/\delta$: Non-dimensional displacement

$p_i(\tau) = f_i(\tau)/E_1$: Non-dimensional excitation

$\gamma_{SC} = k_{SC}/k$: Non-dimensional short-circuit stiffness of PZT materials

$\gamma_{PM} = \eta^2 C_P/k$: Non-dimensional intrinsic capacitance of PZT materials

$\gamma_{EM} = \eta^2 C/k$: Non-dimensional capacitance of common capacitor

The signification of m, k, c, k_c is illustrated in Figure 1.

4 MODAL ANALYSIS OF THE CYCLIC-PERIODIC WITH PZT NETWORK SYSTEMS

Solution of the eigenvalue problem of equations (1) (2) gives natural frequencies of these two systems:

$MP(N)$:

$$\lambda_1 = \sqrt{1+\alpha+\beta}\ ,\quad \lambda_i = \sqrt{1+\alpha+\mu_i\cdot\gamma_C} \quad 2 \le i \le N \quad \left(\alpha = \gamma_{SC} + \frac{\gamma_{PM}^2}{\gamma_{PM}+\gamma_{EM}}\ ,\ \beta = \frac{\gamma_{PM}\gamma_{EM}}{\gamma_{PM}+\gamma_{EM}}\right).$$

$MS(N)$:

$$\lambda_1 = \sqrt{1+\alpha+\beta}\ ,\quad \lambda_i = \sqrt{1+\alpha+\mu_i\cdot\gamma_C} \quad 2 \le i \le N \qquad \left(\alpha = \gamma_{SC}+\gamma_{PM}\ ,\ \beta = -\frac{\gamma_{PM}\gamma_{EM}}{\gamma_{PM}+\gamma_{EM}}\right).$$

In these formulations, the letter μ_i will change according to the number N of the substructures of the system with the subscript 'i' and μ_i may be multiple-roots. However, If N is known, all μ_i of these systems are equal respectively.

Taking $\gamma_{SC}=0.8$, $\gamma_{PM}=0.1$, $\gamma_{EM}=+\infty$ and $\varepsilon_{RM}=\xi=0$,the Figure 2 in schema gives the distribution of the natural frequencies of different systems for $\gamma_C=0$ (no mechanical coupling between sectors) and $\gamma_C\neq 0$ respectively. It can be observed that with PZT network the natural frequencies of the system are increased and that with the mechanical coupling between sectors the distribution of the natural frequencies of the system is more decentralized. The result means that with the network the natural frequencies can be changed by adjusting the electrical parameters and its connected type.

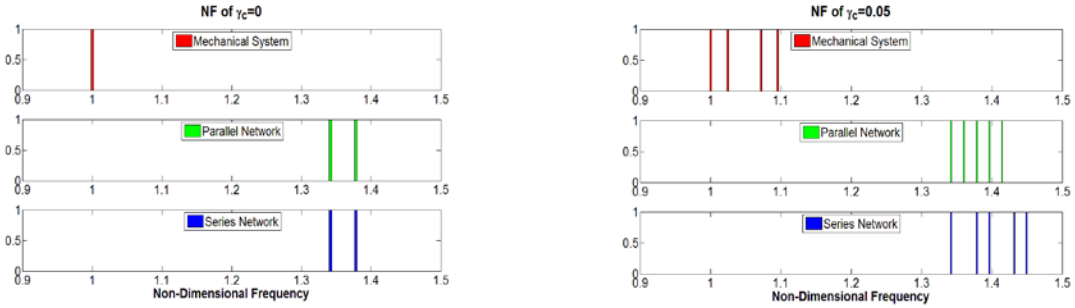

(a) $\gamma_C=0$ (b) $\gamma_C=0.05$

Figure 2. The influence of γ_C to the natural frequency

5 RESPONSE BEHAVIOR OF THE CYCLIC-PERIODIC WITH PZT NETWORK SYSTEMS

To harmonic excitations: $p_i(\tau)=B_i e^{j\tau}$, $1\le i\le N$

The response of the system (1) and (2) can be obtained by using U-transform. Their expressions are as the following:

$$\begin{cases} y_i = Y_i e^{j\tau} \\ q_i = Q_i e^{j\tau} \end{cases} \quad ,1\le i\le N. \tag{3}$$

For MP: $$Y_i=\frac{1}{N}\sum_{n=1}^{N}\frac{H_E\sum_{k=1}^{N}B_k e^{(n-1)(i-k)j\theta_N}-\bar{B}\sum_{k=1}^{N}e^{(n-1)(i-k)j\theta_N}/H_M}{H_M H_E-1+2\gamma_C H_E-\gamma_C H_E e^{(n-1)j\theta_N}-\gamma_C H_E e^{-(n-1)j\theta_N}} \quad ,1\le i\le N. \tag{4-1}$$

$$Q_i=\frac{1}{H_E}(Y_i-\sum_{k=1}^{N}Y_k/N) \quad ,1\le i\le N. \tag{4-2}$$

For MS: $$Y_i=\frac{1}{N}\sum_{n=1}^{N}\frac{H_E\sum_{k=1}^{N}B_k e^{(n-1)(i-k)j\theta_N}+H_E\bar{B}\sum_{k=1}^{N}e^{(n-1)(i-k)j\theta_N}/(H_M H_E-1)}{H_M H_E+2\gamma_C H_E-\gamma_C H_E e^{(n-1)j\theta_N}-\gamma_C H_E e^{-(n-1)j\theta_N}} \quad ,1\le i\le N. \tag{5-1}$$

$$Q=\frac{1}{H_E}(\sum_{k=1}^{N}Y_k/N) \tag{5-2}$$

$$j=\sqrt{-1}\,,\ \theta_N=\frac{2\pi}{N}\,,\ H_M=-\lambda^2+2\xi\lambda j+(1+\gamma_{SC}+\gamma_{PM})\,,\ H_E=\frac{\lambda j}{2\xi\varepsilon_{RM}}+(\frac{1}{\gamma_{EM}}+\frac{1}{\gamma_{PM}})\,,\ \bar{B}=\sum_{k=1}^{N}B_k/N$$

Where Y_i and Q_i represent amplitudes of mechanical displacement and of charge response of the i th sector.

Considering the amplitude of the excitation $B_i=e^{j\cdot(i-1)\theta}$ (6)

The case can simulate the order excitation in aero-engine. The expression means that the harmonic excitation has the same amplitude on each sector and has the same phase difference between every adjacent sectors.

The response to excitation with two kinds of phase difference: $\theta = \theta_N (= 2\pi / N)$ and $\theta = 0.1\theta_N$ are studied for systems with and without mechanical coupling between sectors respectively.
The calculated response curves are given in the figure 3. The parameters of the configuration are taken as $\gamma_{SC} = 0.8, \gamma_{PM} = 0.1, \gamma_{EM} = +\infty, \xi$=0.005 and $\varepsilon_{RM} = 100$ in the calculation.
From the figure 3 it can be observed that the charge response to order excitation ($\theta = \theta_N$) is much bigger than that to non-order excitation ($\theta = 0.1\theta_N$) in parallel network. But the mechanical response is opposite. The similar case occurs in the system with series network but the charge response to order excitation ($\theta = \theta_N$) is smaller (equal to zero) than that to non-order excitation ($\theta = 0.1\theta_N$) and the mechanical response is opposite also. The phenomena show that with PZT network a part of response energy to order excitation is translated to electric circuit. The translation depends on the phase difference of the excitation and on the connection type of the network. As a result, with a good design for the PZT network more response energy could be translated to the PZT network and the efficient reduction of the mechanical response to order excitation of engine could be obtained.

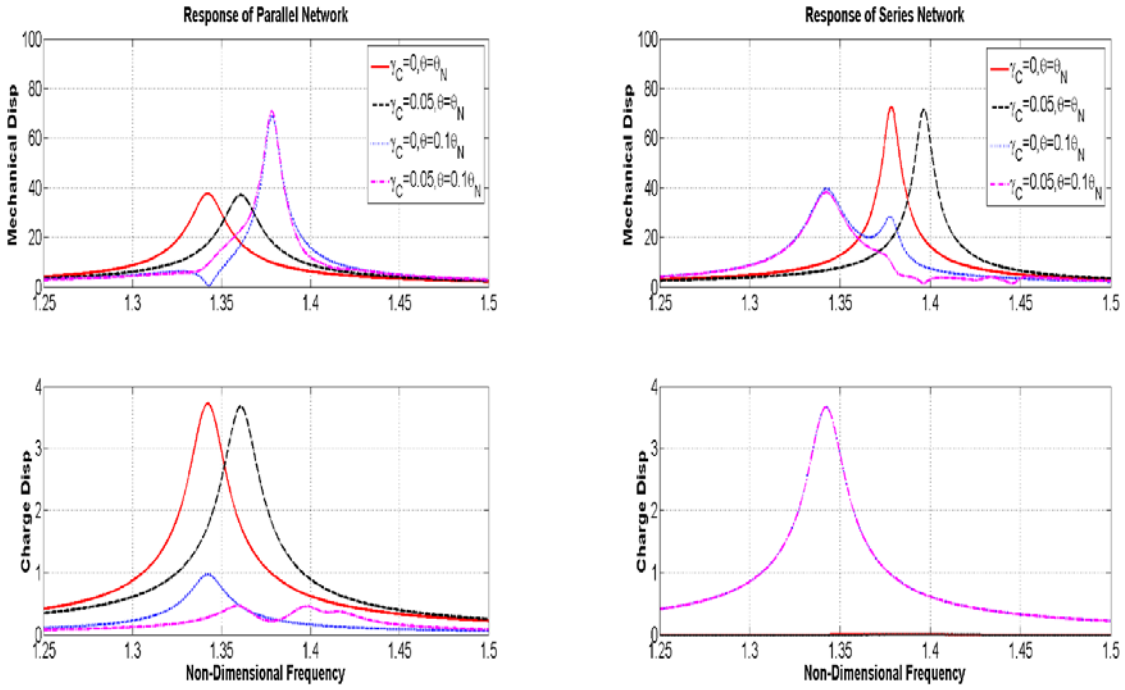

(a) (b)

Figure 3. The response of the excitation of $\theta = \theta_N$ and $\theta = 0.1\theta_N$

6 CONCLUSION

The dynamical behaviour of the cyclic-periodic system with PZT network has been studied. The natural frequencies and the forced responses before and after introducing the PZT network are compared. The mechanical coupling between periodic sectors is taken as an influence parameter in the study. The obtained result shows that the presence of PZT network would change the natural frequencies of the system. The change depends on the mechanical coupling between sectors. The forced response has a sensibility to the connection of the network. The mechanical response to order excitation of an engine could be reduced by translating the vibration energy to the electrical circuit through a good design of PZT network.

REFERENCES

[1] J. Tang and K. W. Wang. “Vibration Delocalization of Nearly Periodic Structures Using Coupled PZT Networks”, Journal of Vibration and Acoustics, vol.125, no.1, 2003.

[2] Hongbiao Yu, K. W. Wang and Jianhua Zhang. “PZT Networking with Enhanced Electromechanical Coupling for Vibration Delocalization of Mistuned Periodic Structures – Theory and Experiment”, Journal of Sound and Vibration, vol.295, no.1-2, 2006.

[3] Hongbiao Yu and K. W. Wang. “PZT Networks for Vibration Suppression of Mistuned Bladed Disk”, Journal of Vibration and Acoustics, vol.129, no.129, 2007.

[4] Hongbiao Yu and K. W. Wang. “Vibration Suppression of Mistuned Coupled-Blade-Disk Systems Using PZT Circuitry Network”, Journal of Vibration and Acoustics, vol.131, no.2, 2009.

[5] Lin Li and Yu Fan. “Vibration Dissipation Characteristics of Symmetrical PZT Networks with Passive Branches”, Proceedings of ASME Turbo Expo, 2012.

DYNAMIC ANALYSIS OF A SPUR GEAR WITH ACTIVE MAGNETIC BEARINGS IN TRANSIENT REGIME

Slim BOUAZIZ[1,3*], Najib BELHADJ MESSAOUD[1,3], Mohamed MATAAR[1], Mohamed HADDAR[2]

[1]Dynamic of Mechanical Systems Unit (UDSM), University of Sfax

[2]Mechanics Modelling and Production Unit, (U2MP), University of Sfax

[1,2]National School of Engineers of Sfax (ENIS), BP.1173, 3038, University of Sfax-Tunisia

[3]Higher Institute of Industrial Systems (ISSIG), 6032, University of Gabes-Tunisia

*Corresponding author: Tel.: +216 74 274 088, Fax: +216 74 275 595
E-mail addresses: slim.bouaziz1@gmail.com; slim_u2mp@yahoo.fr

ABSTRACT

The non-linear dynamic behavior of a single stage spur gear reducer in transient regime is investigated. Driving and driver rotors are, respectively, powered by a motor torque C_m and loaded by a resistive torque C_r. They are supported by two identical Active Magnetic Bearings (AMBs). Gear excitation is induced by the motor torque and load variation in addition to the fluctuation of meshing stiffness due to the variation of input rotational speed. Three models of AMBs were used with four, six and eight magnets. They are operated by PD controller and powered by control and bias currents. The dynamic parameters of the AMBs are modeled by stiffness and damping matrices computed by the derivation of the electromagnetic forces. The equations of motion are solved iteratively using Newmark time integration method. In the first part of the study, the model is powered by an electric motor and by a four strokes four cylinders diesel engine in the second part. The numerical results of the dynamic responses of the system come to confirm the significant effect of the transient regime on the dynamic behavior of a gear set, particularly in the case of engine acyclism condition. Results also confirm the influence of the magnet number by AMBs on the dynamic behavior of the system. Indeed, vibrations were more important in the case of gear reducer supported by AMBs with four magnets.

1 INTRODUCTION

Varieties of studies have been conducted over the last two decades on the Active Magnetic Bearings (AMBs). They have many advantages over the conventional bearings. Because of the contact less, the lubrication less, the friction less and the higher level of the temperature and the rotational speed of use. A parametric study on the effect of the geometrical parameters of the AMBs on the dynamic behavior is made by Belhadj Messaoud et al. [1]. The influence air gap and the variation of the speed on the electromagnetic forces is investigated. To survey the vibratory response of the receptor shaft, a numerical simulation of a mechanical AMBs model is analyzed by Bouaziz et al. [2]. A mathematical model of an AMB-rotor system is presented by Inayat-Hussain [3]. The rotor dynamic responses are observed for exhibit a rich variety of dynamical behaviour with synchronous, sub-synchronous, quasi-periodic and chaotic vibrations. The same author [4] has developed, in another paper, a numerical investigation on the dynamic non-linearity due to the geometric coupling of the magnetic actuators. Determined results show that the actuating forces are a nonlinear function of the coil current and the air gap. The catastrophic phenomena for the transient nonlinear oscillations amplitude are observed in AMBs-rotor system with 8-pole legs and the time-varying stiffness. The dynamic behavior from the transient state chaotic motion to the steady state periodic and quasi periodic motions is also established by Zhang et al. [5].

This paper is made to study the dynamic behaviour of a spur gear reducer with AMBs powered, at a first stage, by an electric motor, then at a second stage, by four strokes four cylinders diesel engine. A numerical study of the dynamic responses of the AMBs system are made to reveal the effect of the transient regime on the dynamic behavior of a gear set, particularly in the case of engine acyclism condition. Three models of AMBs are used in this study where four, six and eight magnets are powered by control and bias currents.

2 MODEL OF A SINGLE STAGE SPUR GEAR TRANSMISSION

A single stage spur gear model with eight degrees of freedom is presented in figure 1. It is composed by two rotors supported by AMBs. The driving rotor (Part 1: P1) has a pinion with Z1 teeth, mass m1 and moment of inertia J11. The driven rotor (Part 2: P2) has a wheel with Z2 teeth, mass m2 and moment of inertia J_{22}. The system is sought by motor torque Cm and load torque Cr. The gear mesh stiffness ke(t) and damping kc(t) are modelled by linear spring and damping acting on the line of meshing teeth action. The displacement λ along the line of action is expressed by:

$$\lambda(t) = (x_1 - x_2)\sin\alpha + (y_1 - y_2)\cos\alpha + \theta_{12} r_{b12} + \theta_{21} r_{b21} \quad (1)$$

x_i and y_i The translations of the pair of gearing (i=1, 2). θ_{ij} is the angular displacement of the component. α is the pressure angle. r_{b12} and r_{b21} are the base radius of, respectively, the pinion and the wheel. The rotational speed of the pinion is N_1. The mesh period can be defined by:

$$T_e = \frac{60}{N_1 Z_1} \quad (2)$$

The vector of degrees of freedom can be expressed by:

$$\{q\} = \begin{bmatrix} \theta_{11} & x_1 & y_1 & \theta_{12} & \theta_{21} & x_2 & y_2 & \theta_{22} \end{bmatrix}^T \quad (3)$$

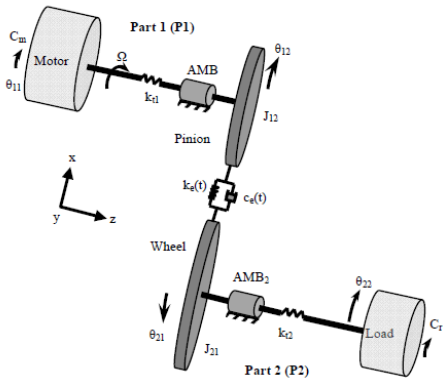

Figure 1. Systems modeling of a single stage spur gear.

3 EQUATIONS OF MOTION

The system differential equation of motion the is so determined, it has the following expression

$$[M]\{\ddot{q}\} + [C(t)]\{\dot{q}\} + [K(t)]\{q\} = \{F_{ext}(t)\} \quad (17)$$

[M] represents the mass matrix, $k_e(t)$ and $C_e(t)$ represent respectively the time varying gear mesh stiffness and damping. The external vector is given by:

$$\{F_{ext}(t)\} = \{C_m, 0, 0, 0, 0, 0, -C_r\}^T \quad (18)$$

4 NUMERICAL SIMULATIONS

The mechanical transmission is loaded by a pump having an inertia moment $J_{22}=45\times10^{-4}$ Kgm^2. The evolution of the meshing stiffness in transient regime is shown in figure 2; numerical results show that it is modeled as a non-periodic function. It should be noted that the meshing period decreases when the speed increases.

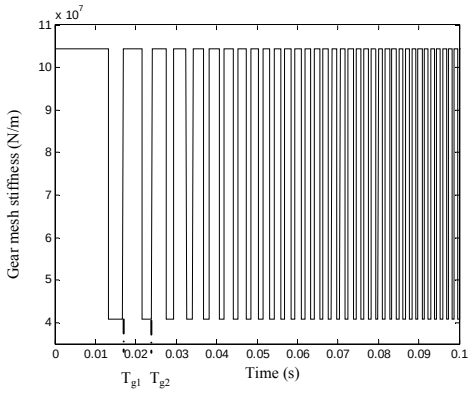

Figure 2. Non-periodic evolutions of the gear mesh stiffness.

The dynamic response registered on the pinion AMB_1 is presented in figure 3 a). Two different behaviors are determinate: The first period (P_1) corresponding to the interval of time [0;0.23s] in which the displacement is variable and non-periodic with high vibration amplitudes (figure 3 c)). The second period (P_2) is observed in time interval [0.23s;0.4s] in which the displacement is periodic with period T_1 (figure 3 b)). The spectrum (figure 3 d))indicate the presence of the meshing frequency F_{g1}=480Hz and its harmonics $n\times F_{g1}$ encircled by side-bands. The system eigenfrequencies are also shown. The presence of side-bands is caused by the transient regime behavior.

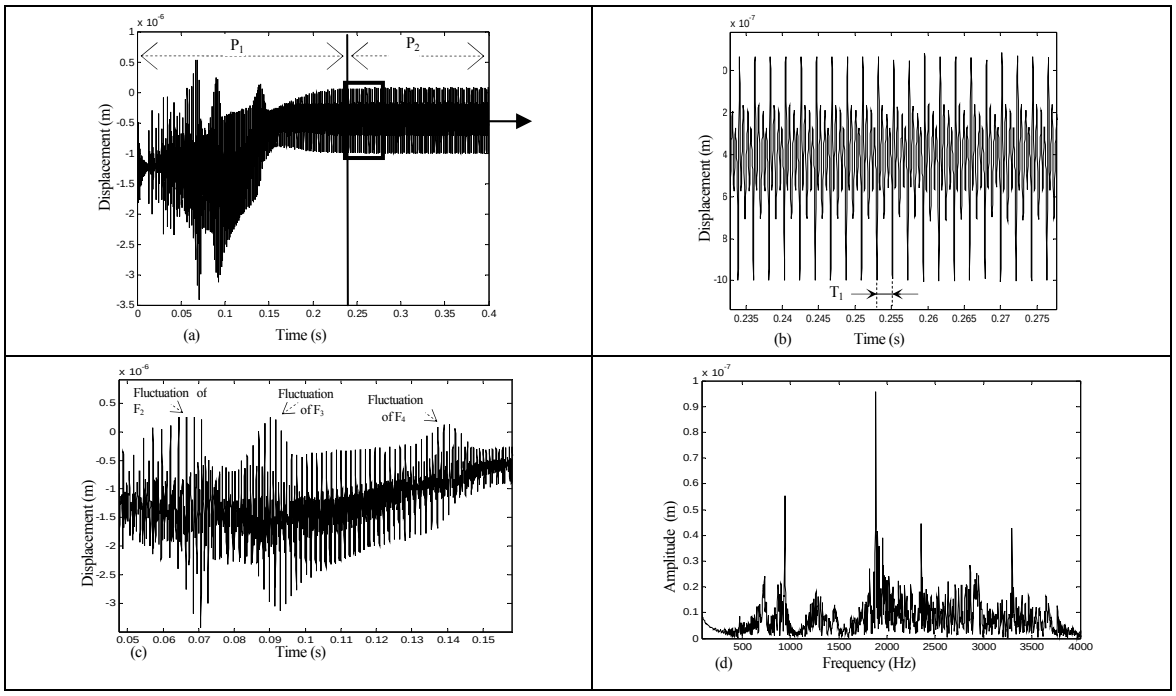

Figure 3. A numerically simulations of the displacement and its spectrum (AMB_1).

5. Conclusion

In this study, the dynamic response of a pair of single stage spur gear reducer system is analyzed in the transient and the steady state regimes. Two cases were considered in the first part with an electric motor and a diesel engine in the second part. The equations of motion of the studying model are derived from the eight dof of the system. After deriving nonlinear equations of motion for the gear set, the dynamic responses are computed by applying the Newmark time integration method. The excitation of the gear pair is caused by the variation of the motor torque and the meshing stiffness fluctuation caused by the variation of the input rotational speed. The numerical results of the dynamic responses of the mechanical system come to confirm a significant effect of the transient regime on the dynamic behavior of a gear set.

6. References

[1] N. Belhadj Messaoud, S. Bouaziz, M. Mataar, T. Fakhfakh, M. Haddar, Dynamic behaviour of active magnetic bearings in presence of angular misalignment defect, *Int J. of Appl. Mech.(IJAM)*,Vol. 3, N°. 3 1-15, 2011.

[2] S. Bouaziz, N. Belhadj Messaoud, M. Mataar, T. Fakhfakh, M. Haddar, A Theoretical Model for Analyzing the Dynamic Behaviour of Spatial Misaligned Rotor with Active Magnetic Bearings, *Mechatronics,* 21 899-907, 2011.

[3] J. I. Inayat-Hussain, Chaos via torus breakdown in the vibration response of a rigid rotor supported by active magnetic bearings, *Chaos, Sol. and Frac.,* 31, 4, 912-927, 2007.

[4] J. I. Inayat-Hussain, Geometric coupling effect on the bifurcations of a flexible rotor response in active magnetic bearings. *Chaos, Sol. and Frac*, 41, 5, 2664-2671, 2009.

[5] Wei Zhang, Jean W. Zu, Transient and steady nonlinear responses for a rotor-active magnetic bearings system with time-varying stiffness, *Chaos, Solitons and Fractals* 38 1152–1167, 2008.

ACOUSTIC RECONSTRUCTION OF THE UNSTEADY ROTATING FORCES OF FAN'S BLADE

M. ABID, H. TRABELSI, M. TAKTAK and M. HADDAR

Unit of Dynamics of Mechanical Systems
National School of Engineers of Sfax, University of Sfax, Sfax, TUNISIA
Emails: majdiab@yahoo.fr, htrabels@gmail.com, mohamed.taktak@fss.rnu.tn, mohamed.haddar@enis.rnu.tn

ABSTRACT

This paper deals with noise sources in a cooling fan. The aim of this paper is to investigate the aero acoustic forces on the fan's blade. A simple model based on the tonal noise produced by an axial fan is used in the direct problem. First the model is validated with a directivity experience. Validated model is then used to simulate acoustic pressure at known spatial positions in the radiated field. The discretized direct problem is associated with a regularization technique for inverse problem to estimate the unsteady rotating forces. Tikhonov regularization can provide an appropriate regularization parameter to improve reconstruction accuracy. The simulation reveals the possibility to reconstruct fan noise sources even with a perturbed measured acoustic signal. Obstacle on the fan suction mouth can be detected since it affects the aerodynamic forces.

1 INTRODUCTION

Sources reconstruction using acoustic signal is a promising technique in fault diagnosis and in understanding the source behaviour. The well known direct problem is discretized and written in a matrix form relating the aerodynamic forces to the acoustic pressure. The inverse problem consists in inversing this matrix.

The dominant tonal noise in small axial fan under investigation was studied by many authors. The first model was written by Gutin [1] in 1936. Lowson [2] studied the sound from singularities in motion and applied it to the aerodynamic forces. Ffowks Williams and Hawking [3] extended the Lighthill [4] theory to take into account the presence of rigid corps in the fluid.

The source reconstruction was treated by Li and Zhou [5] who inverse the Farassat integral. Luo and Li [6] used the Fredholm integral equation of the first kind for his inverse method. Anthony et al. [7] proposed theoretical and experimental results for source reconstruction of axial fan based on dipole source distribution.

In this paper, the experimental validation of the adopted direct model is presented in the following section. Then, simulated acoustic pressure on a measure plane is used as input for the inversion algorithm. Finally, the results of the proposed method are presented and discussed.

2 DIRECT MODEL FOR AXIAL FAN NOISE PREDICTION

2.1 Theoretical formulation

In this section a model for fan noise prediction is presented, this model is used to calculate the acoustic pressure emitted by the fan at any point in space. Parameters of the fan like hub and blade tip radius, power of the motor, rotating speed and aerodynamics forces are the inputs of this model. By considering a well designed fan with thin blades and sharp edge and with a low Mach number on blade tip, only the dipole term of the fowks Williams and Hawkings equation is taken into account [8]:

$$p(t) = -\frac{1}{4\pi}\iint \frac{r_i}{c_0.Dop.r^2}\frac{\partial}{\partial\tau}\left(\frac{F_i}{Dop}\right)dS \tag{1}$$

where t and τ are respectively observer and source relative times. F_i the components of the force $\vec{F}$ exerted by the blade on the medium, r_i is the components of the source-observer vector $\vec{r}$ with $r = \|\vec{r}\|$, $Dop = 1 - \frac{\vec{r}}{r}\vec{M}$ is the Doppler factor, $\vec{M} = \frac{\vec{V}}{c_0}$ and $\vec{V}$ is the source speed. After mathematical treatment the following equation is obtained:

$$P_s = \frac{is\omega}{4\pi c_0 r_0} e^{is\omega\frac{r_0}{c_0}} \sum_{q=-\infty}^{+\infty} (-i)^q J_q\left(s.\omega.\sin\theta.\frac{r_s}{c_0}\right) e^{iq\varphi}\left(\cos\theta.T_{s-q} + \frac{q.c_0}{s.\omega.r_s}D_{s-q}\right) \tag{2}$$

2.2 Experimental validation

After model calibration using a reference experience [9], directivities experiences were carried out in an anechoic chamber. The acoustic pressure was measured at sixteen points equally separated over a circle of radius 0.55m in the middle plan of the fan.

Figure 1 shows a good agreement between theoretical and experimental directivities. The model is validated and can be used to simulate acoustic pressure on an antenna of sensors for inverse problems.

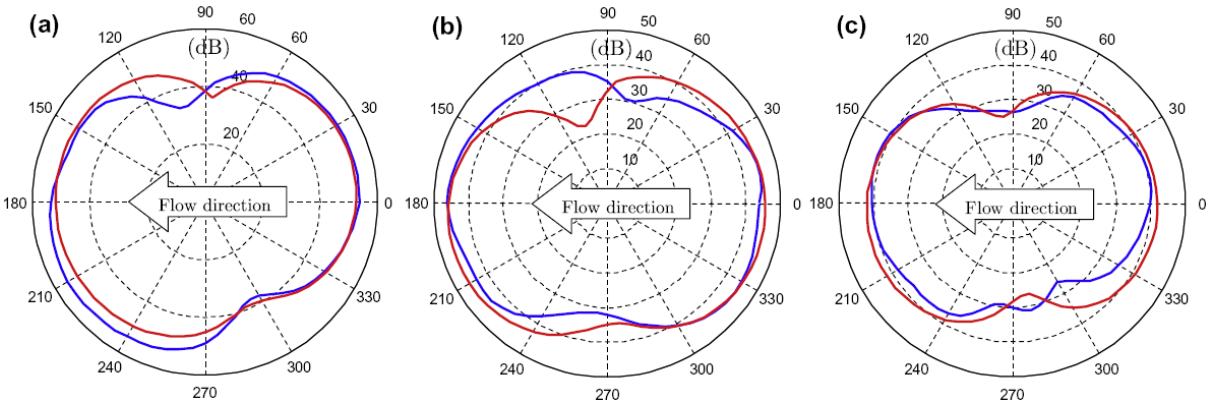

Figure 1. Calculated (Red) and experimental (Blue) directivities of the fan in dB (a) 332.7Hz (b) 665.4Hz (c) 998.2 Hz.

3 INVERSE MODEL

3.1 Model discretization

In the following, trust and drag forces in Equation (2) are related by the parameter γ that depends on the geometry of the fan blade and the summation over q is truncated between q_{min} and q_{max}. Therefore, the acoustic pressure is given by the following equation:

$$P(s,r_o,\theta,\varphi)=\frac{is\omega}{4\pi c_0 r_0}e^{is\omega\frac{r_0}{c_0}}\sum_{q=q_{\min}}^{q_{\max}}(-i)^q J_q\left(s.\omega.\sin\theta.\frac{r_s}{c_0}\right)e^{iq\varphi}\left(\cos\theta+\frac{q.c_0}{s.\omega.r_s}\gamma\right)T_{s-q} \tag{3}$$

For different measurements at the same frequency, Equation (3) can be written in matrix notation as:

$$\begin{pmatrix}P_s^1\\P_s^2\\\vdots\\P_s^m\end{pmatrix}=\left[H_{mq}\right]\begin{pmatrix}T_{s-q_{\min}}\\\vdots\\\vdots\\T_{s-q_{\max}}\end{pmatrix}\Rightarrow\{P\}=\left[H_{mq}\right]\{T\}\Rightarrow\{T\}=\left[H_{mq}^{-1}\right]\{P\} \tag{4}$$

P_s^m is the s^{th} Fourier coefficient of the far field acoustic pressure at the m^{th} location, and T_{s-q} represents the $(s\text{-}q)^{th}$ Fourier coefficient of the aerodynamic force. The source vector T is determined by inversing the matrix H_{mq}. Tikhonov regularization and L-curve can help to stabilize this ill-conditioned inversion.

3.2 Inversion simulation

In this section, an imposed force on the blade surface is inserted in the direct model to compute acoustic pressure at different positions. These positions simulate the distribution of sensors on the antenna used in experience and allow the calculation of the [H_{mq}] matrix coefficients. Therefore, by the inversion of this matrix, the imposed force can be reconstructed.
A Gaussian random noise is added to the computed pressure to simulate the experience environment.

Figure 2 shows the very good agreement between the imposed and reconstructed aerodynamic force. This result illustrates the capability of the inverse model to reconstruct the spectra of the aerodynamics forces on the fan's blade.

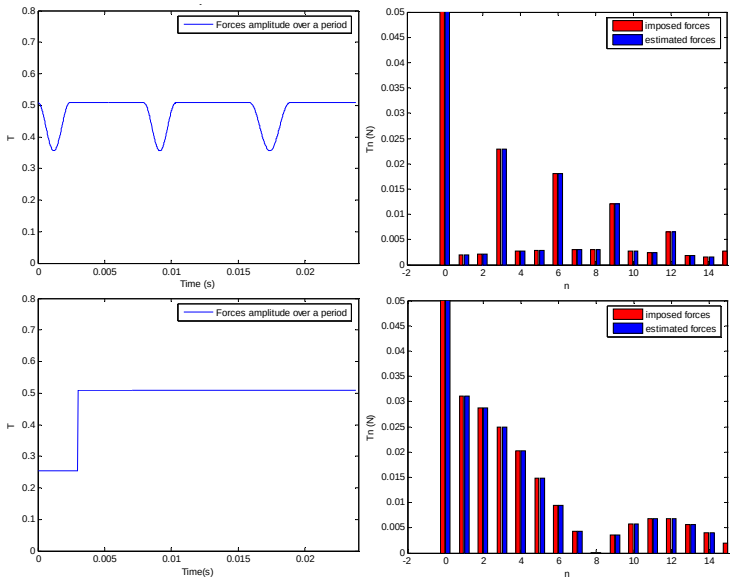

Figure 2. Simulation of the inversion problem

4 CONCLUSION

In this work, the proposed direct model was validated by directivity experience. The numerical simulation of inverse problem is well stabilised with Tikhonov regularization and L-curve technique. Thus, the inverse model works well even with a noisy measurement.

5 REFERENCES

[1] L. Gutin. On the sound field of a rotating propeller. *Translated in 1948 from Physikalische Zeitschrift der Sowjetunion*. NACA TM 1195, 1936

[2] M.V. Lowson. The sound field for singularities in motion. *Proceeding of the Royal Society of London.* A286:559-572, 1965

[3] J.E. Ffowcs Williams and D.L. Hawkings. Sound generation by turbulence and by surfaces in arbitrary motion. *Philosophical Transaction of the Royal Society of London.* 264:321-342, 1969

[4] M.J. Lighthill. On sound generated aerodynamically. *Proceeding of the Royal Society of London.* A211:564-587

[5] X.D. Li and S. Zhou. Spatial transformation of the discret sound fiel from a propeller. *American Institute of Aeronautics and Astronautics Journal.* 34(6):1097-1102, 1996

[6] J. Luo and X.D. Li. An inverse aeroacoustic problem on rotor wake/stator interaction. *Journal of sound and vibration.* 254:219-229, 2002

[7] G. Anthony, B. Alain, and M. Patrice. Control of tonal noise from subsonic axial fan PART 1 : reconstruction of aeroacoustic sources from far-field sound pressure. *Journal of sound and vibration.* 288:1049-1075, 2005

[8] S. Khelladi, S.Kouidri, F.Bakir and R. Rey. Predicting tonal noise from a high rotational speed centrifugal fan. *Journal of sound and vibration.* 313:113-133, 2008

[9] M. Abid, H. Trabelsi, M. Taktak, J. Antoni, J.M. Ville, T. Fakhfakh and M. Haddar. Tonal prediction of a faulty axial fan. *Applied Acoustics*. 73:1022-1028, 2012

A METHOD TO MODEL BEAMS IN DYNAMIC BENDING UNDER VARIOUS BOUNDARY CONDITIONS

A. Taoufik AYARI[1], B. Charfeddine MRAD[2*], and C. Rachid NASRI[3]

[1,2,3]Laboratoire de Recherche Mécanique Appliquée et Ingénierie
Ecole Nationale d'Ingénieurs de Tunis
Université Tunis El Manar
Tunis, TUNISIA
Email: ayaritaoufik10@yahoo.fr, Charfeddine.Mrad@enit.rnu.tn, Rachid.Nasri@enit.rnu.tn

ABSTRACT

The work consists on developing a discrete method to model beams in dynamic bending under various boundary conditions. The method consists on dividing the beam into rigid-bar elements, linked between themselves by spiral springs. A static study of the beam was done to determine the stiffness of the spiral springs, it is followed by a kinetic study to determine the inertia of the elements. A library of the mass and stiffness matrices in the general case and for diverse boundary conditions was then elaborated. A dynamic study allowed obtaining the modal characteristics of the beam, and an application of the method on a real beam was conducted. The modal characteristics of the considered beam were then determined using two other methods: the analytical method and the numerical method (FEM-Abaqus); and the results, in natural frequencies and modal shapes, of the three methods were illustrated. The comparison of the results, for the used different methods, permitted to confirm the proposed method for its accuracy and simplicity, to constitute a very good alternative to analytical and numerical methods in simply taken practical industrial cases where the numeric means are useless and the analytic computing becomes complex.

INTRODUCTION

The modelling of beams in dynamic bending under different boundary conditions, was the subject of many works which permitted to propose discrete and continuous methods. The analytic approach is very interesting for the modal characterization of beams, but it is too complicated. Discrete approaches were proposed by Rayleigh and Ritz, but remain not much practical. The numeric approach is very useful, especially with the commercialization of specialized software, but it is too thorough for certain applications.
The proposed method consists of modelling the beam into elements linked between themselves by springs. Static, kinetic, and dynamic studies allowed determining the modal characteristics of the beam, which were compared later to results obtained by two other methods, analytical and numerical. The comparison of the three results shows clearly that the proposed method is enough simple and precise to constitute an alternative to analytical and numerical methods in simply taken practical industrial applications [1], [2].

1 FORMULATION

After dividing the beam into rigid elements linked by springs, a parameterization is elaborated, an example is presented in Figure 1. A static study is conducted to determine the springs stiffness, and a kinetic study is done to determine the elements inertia. The mass and stiffness matrices are defined in the general case, according to the boundary conditions (BC).

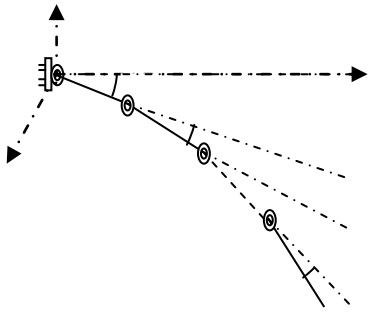

Figure 1. Beam modelling, Fixed-Free

2 RESULTS

A dynamic study permitted to determine the modal characteristics of the beam, and an application of the method, said discrete (D), on a real beam was conducted. The real beam was then considered using the analytical method (AN) and the numerical method (FEM-Abaqus; AB), to determine its modal characteristics.
Figure 2, compares the natural frequencies of the considered beam, obtained through the discrete and analytical methods; BC: Fixed-Free. Natural frequencies: First-Second-Third-Fourth.
Figure 3, compares the natural frequencies of the considered beam, obtained through the discrete and numerical methods; BC: Fixed-Free. Natural frequencies: First-Second-Third-Fourth.
Figure 4, compares the natural frequencies of the considered beam, obtained through the discrete and analytical methods; BC: Fixed-Fixed. Natural frequencies: First-Second-Third.
Figure 5, compares the natural frequencies of the considered beam, obtained through the discrete and numerical methods; BC: Fixed-Fixed. Natural frequencies: First-Second-Third.
Figure 6, compares the modal shape of the considered beam, obtained by the different methods; BC: Fixed-Free. Modal shapes: AN-D-AB.

Figure 7, compares the modal shape of the considered beam, obtained by the different methods; BC: Hinged-Hinged. Modal shapes: AN-D.
Figure 8, compares the modal shape of the considered beam, obtained by the different methods; BC: Fixed-Hinged. Modal shapes: AN-D.
Figure 9, compares the modal shape of the considered beam, obtained by the different methods; BC: Fixed-Fixed. Modal shapes: AN-D-AB.

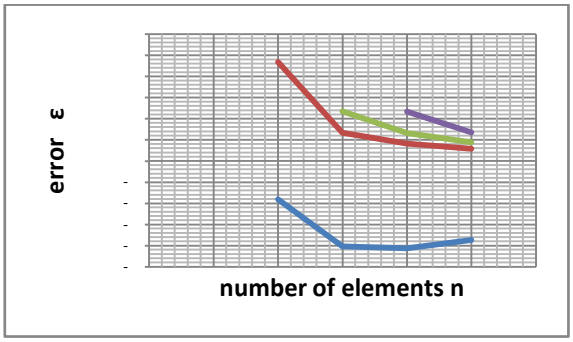

Figure 2. D-AN Error, Fixed-Free

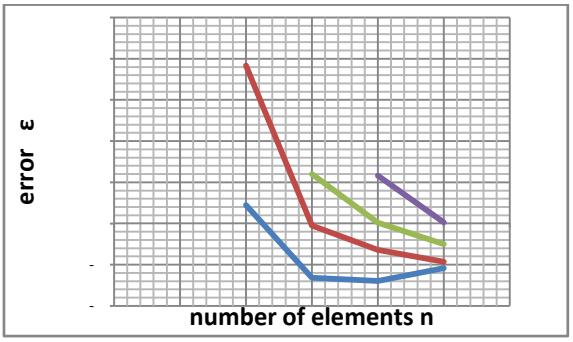

Figure 3. D-AB Error, Fixed-Free

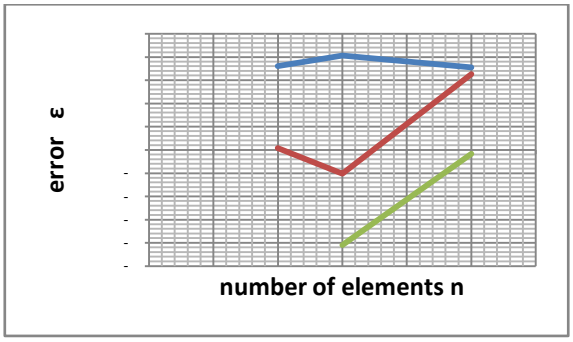

Figure 4. D-AN Error, Fixed-Fixed

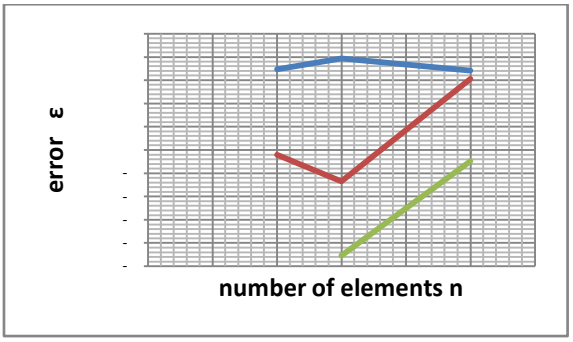

Figure 5. D-AB Error, Fixed-Fixed

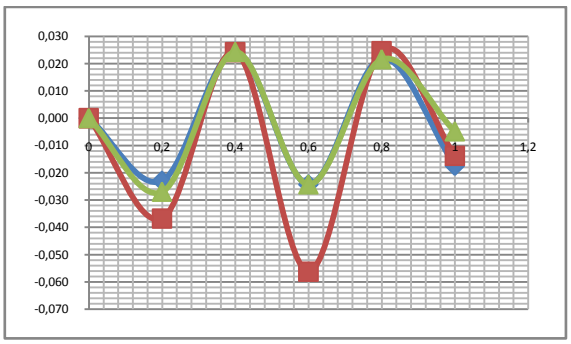

Figure 6. Modal shape, Fixed-Free

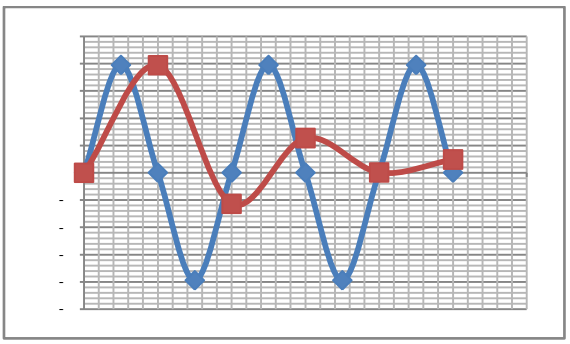
Figure 7. Modal shape, Hinged-Hinged

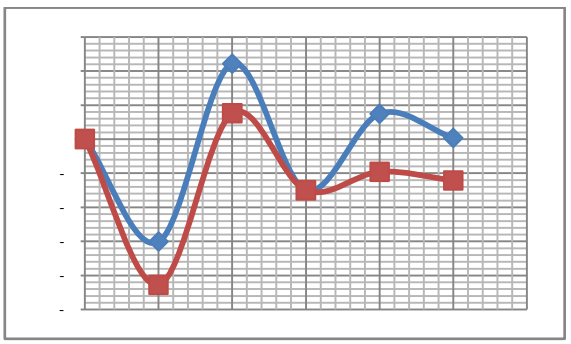
Figure 8. Modal shape, Fixed-Hinged

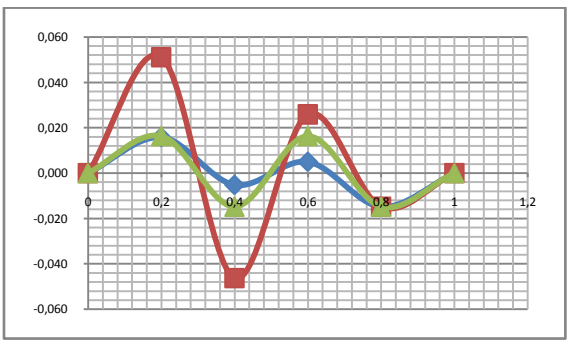

Figure 9. Modal shape, Fixed-Fixed

CONCLUSION

The comparison of the results of the tackled different methods, in natural frequencies and modal shapes, permits to confirm the proposed method for its accuracy and simplicity, to constitute a very good alternative to analytical and numerical methods in simply taken practical industrial cases where the numeric means are useless and the analytic computing becomes complex.

REFERENCES

[1] B. Corves, A. F. Ahmed, and F. Allmendinger. Dynamic modeling of a flexible manipulator with minimum and finite degrees of freedom and comparison of modeling methods. *CMSM'2011*, Sousse, Tunisia.

[2] L. Ben Fekih, G. Kouroussis, and O. Verlinden. Development of a user–friendly and open–source multi-body framework with the help of symbolic tools. *CMSM'2011*, Sousse, Tunisia.

DAMAGE MONITORING OF TRUST BALL BEARING BY A RELIABILITY APPROACH

M. BOUMAHDI[1] and M. GUEMANA[1]

[1]Department of mechanical engineering,
University of MEDEA, Ain-dheb 26000, MEDEA, Algeria
Email: boumahdi_m@yahoo.fr, guemana_m@yahoo.fr,

ABSTRACT

The monitoring damaged component state in the rotating machinery has always been an important aspect in the assessment of their remaining useful life. The components reliability is conditioned by their specific characteristics, use conditions, environment and damage process. The traditional reliability approach analyses the event data only. In the condition monitoring of rotating machinery, additional information, condition monitoring data, is available. This paper presents the use of proportional hazards model to predict the evolution of trust ball bearing damage by combining the above two data type. Experiments have been performed on rig test to calculate and to validate the proposed model. The results are encouraging .They indicate that the proposed model can be used to effectively predict the remaining useful life of trust ball bearing.

1 INTRODUCTION

Trust ball bearings are among the most widely used machine elements and are critical to almost all forms of rotary machinery. These elements produce vibrations when they are partially or completely degraded. The vibration analysis is the most suitable and effective [1]. The setting up of a conditional maintenance based on the vibratory analysis allows to obtain an increased availability of these machines and to avoid not planned shut down due to the breakdowns.
In conditional maintenance, there are two important aspects: diagnostic and prognostic. The goal of prognostic is to predict defects before they occur. To fulfill this goal, three crucial steps are needed. First, the defect should be able to be detected at an early stage. Second, the machine performance should be assessed robustly and tracked continuously. Finally, the remaining useful life RUL and possible failure mode of the machine should be effectively predicted [2].

In the following sections, we focus on RUL estimation using proportional hazards model PHM developed by COX [3]. The aim of this approach is to combine traditional reliability model (Weibull distribution) and condition monitoring data (indicators calculated from vibration signals).

An experimental application on a fatigue test rig, is designed to expose the trust ball bearing to operating loads is performed.

2 COX PRORPORTIONAL HAZARD MODEL

The proportional hazards model PHM (Cox 1972) is commonly used to characterize the relationship between failure time and covariates. It was successfully used for survival analyses in medical areas and reliability predictions in accelerated life testing. The assumption of PHM is that the hazard rate of a system is the product of a baseline hazard rate function $h_0(t)$, depending on time to failure, and a positive function Ψ depending only on the values of a set of diagnostic variables. Thus, if Z is the vector of diagnostic variables, the hazard rate function is defined as follows:

$$h(t) = h_0(t).\Psi\big(Z(t)\big) \tag{1}$$

The most common form for $\Psi\big(Z(t)\big)$ is

$$\Psi\big(Z(t)\big) = exp(\gamma.Z) = exp(\sum \gamma_i.Z_i) \tag{2}$$

Where $Z(t) = [Z_1, Z_2, \dots, Z_n]$ consists of n variables at given time t,
$\gamma = [\gamma_1, \gamma_2, \dots, \gamma_k]$ is the coefficients vector of Cox model.
The construction of proposed model is to determine the parameters of function Z and the parameters of baseline function $h_0(t)$.According to reference [4] the Weibull distribution is suitable for mechanical components. In this paper, We propose a modeling by Weibull distribution with two parameters. The failure rate base is then expressed as follows:

$$h_0(t) = \frac{\beta}{\eta}\left(\frac{t}{\eta}\right)^{\beta-1} \tag{3}$$

where β is the shape parameter and η is the scale parameter. Once the underlying model of a system is defined, we can easily derive the other reliability functions. As shown in Eqs. 4-5, where *R(t)* is the reliability and RUL is the remaining useful life:

$$R_0(t) = exp\left[-\left(\frac{t}{\eta}\right)^{\beta}\right] \tag{4}$$

$$RUL(t) = \frac{1}{R(t)}\int_t^{\infty} R(x)dx \tag{5}$$

Cox suggests estimating the parameters of $\Psi(Z(t))$ by maximizing an expression he calls partial likelihood. Thus, the partial likelihood function for Weibull-PHM is given by Eq.6.

$$L(\beta,\eta,\gamma)=\left[\prod_i\left(\frac{\beta}{\eta}\left(\frac{t_i}{\eta}\right)^{\beta-1}\exp\left(\gamma.z_i\right)\right)\right].\ .\left[\prod_j\exp\left(-\left(\frac{t_j}{\eta}\right)^{\beta-1}\exp\left(\gamma.z_j\right)\right)\right]. \quad (6)$$

3 DATA COLLECTION (BOLD, 12 POINT, ALL CAPS)

3.1 Experimental set-up and procedure (bold)

A fatigue tests for monitoring of trust ball bearing (TBB) faults on the platform test "SURVIB" are undertaken. Tests were performed to validate the proposed methodology. The experimental set-up, as shown in Fig. 1, had two thick plates, four amounts and a press which slides on the amounts. The TBB on which tests are conducted is mounted between the press and the TBB holder. The TBB type is SKF51207 consist of a shaft washer, a housing washer and a ball and cage thrust assembly. The bearings are separable so that mounting is simple as the washers and the ball and cage assembly can be mounted separately. An axial load is provided by a hydraulic jack. The fatigue tests are performed to an axial load of 3000daN and a rotational speed of 1800 r / min. For each new TBB, the system is rotated until the degradation of the TBB. Two accelerometers were installed on the press. One accelerometer is fixed in axial position and the other in radial position. Measurements were taken broad band [0–20 kHz] in root mean square of acceleration.

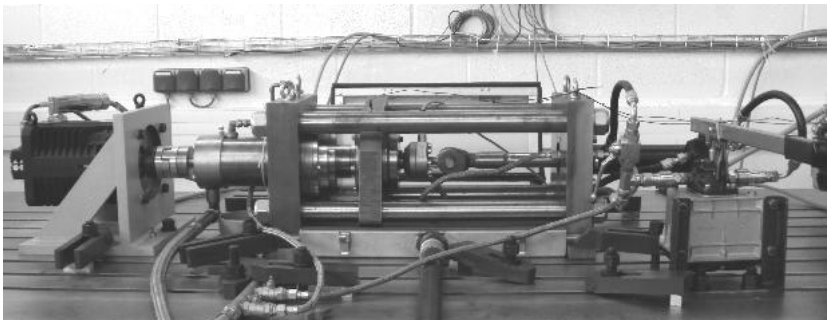

Figure 1. Test rig

4 RESULTS AND DISCUSSION

From the signals analysis obtained by axial accelerometer, various indicators have been calculated, namely, root mean square, crest factor, kurtosis, etc. The figures 2, show that the curves of the RMS is most representatives the evolution of vibratory level. Furthermore, the crest factor CF curve is fewer representatives the evolution of vibratory level, because this indicator is very sensitive to shock, to noise and to defects size.

The parameters of proportional hazard model are estimated from the dataset collected on test rig (time to failure and the vibratory indicator values). Figure 3 (a) shows the evolution of the indicator RMS in time for a set of TBBs. the hazard rate function of Cox PHM for all these TBBs, is given by Eq. 7.

$$h=\frac{2.86}{78.12}\left(\frac{t}{78.12}\right)^{1.86}.\exp\left(0.0067.RMS\right) \quad (7)$$

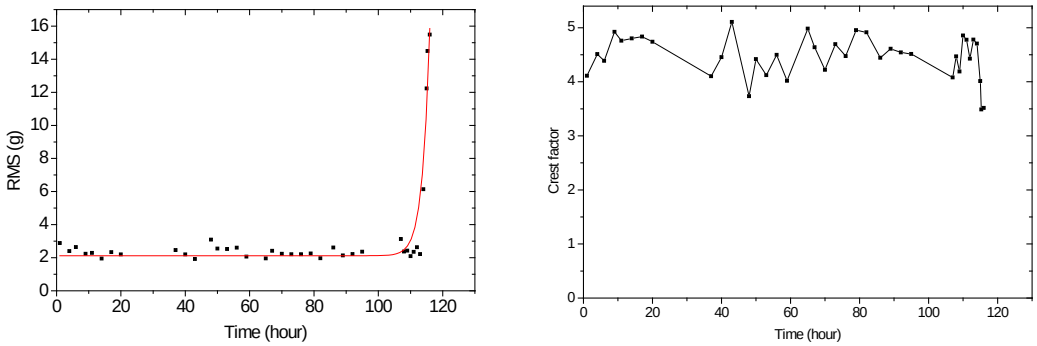

Figure 2. RMS and Crest factor indicators

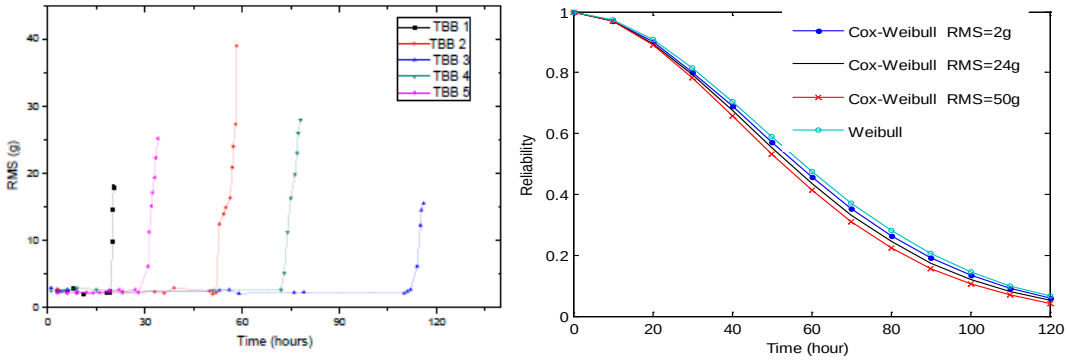

Figure 3 (a) RMS, (b) Reliability

Figure 3 (b) presents the curve of reliability function, obtained from Eq. 7, corresponding to three value of RMS. The figure shows that the reliability of TBB decreases when the RMS value increases. In this study, the results obtained shows that the RMS indicator is more important compared to the other indicators (kurtosis, CF, CV) to estimate the reliability and then the RUL.

5 COCLUSIONS

This paper presents the Cox- proportional hazards model to predict the defects evolution. This model allowed to express the reliability function the service time and the vibration indicators and on the other to estimate the remaining useful life of TBB. The results revealed that the introduction of the vibrations indicators, especially RMS, is necessary to estimate the component reliability. Further research is necessary to study the effect of other indicators and operation conditions, such as load and speed.

6 REFERENCES

[1] N. Gebraeel, M. Lawley, R. Liu, V. Parmeshwaran, Residual life predictions from vibration-based degradation signals: A neural network approach, IEEE Transactions on Industrial Electronics 51 694–700, 2004.

[2] H. Qiu, J. Lee, J. Lin, G. Yu, Robust performance degradation assessment methods for enhanced rolling element bearing prognostics, Advanced Engineering Informatics 17 127–140, 2003.

[3] D.R Cox. Regression models and life tables. J R Stat Soc B.**26**:187-220, 1972.

[4] B. Lanternier, P. Lyonnet et R .Toscano. Modèle à hasard proportionnel pour la fiabilité des composants mécaniques. Mécanique et industries. **9**, 397–405, 2008.

EFFECT OF CHARGE POLYDISPERSITY IN THE DYNAMICS OF A MICELLAR SYSTEM

Lamiae Talha[1], Mohammed Filali[1], Abdelhafid Azougarh[1], Luca Cipelletti [2, 3]

[1]Laboratoire de Physique théorique et appliquée (LPTA),
Université Sidi Mohamed Ben Abdellah Faculté des Sciences Dhar El Mahraz BP 1796
Fes, Atlas, Maroc.
Lamiae.1984@yahoo.fr, filali_mohammed@yahoo.fr
[2]Université Montpellier 2, Laboratoire Charles Coulomb
UMR 5221, F-34095, Montpellier, France.
[3]CNRS, Laboratoire Charles Coulomb UMR 5221,
F-34095, Montpellier, France.
Luca.Cipelletti@univ-montp2.fr

ABSTRACT

We use dynamic light scattering to investigate a surfactant systems composed of neutral spherical micelles, to which electric charges may be added in a controlled way. The neutral system exhibits one single relaxation mode, due to diffusion. By contrast, two relaxation modes are observed in the charged system. The fast one corresponds to collective diffusion due to fluctuations of the number density of micelles. Following Appell *et al.* [1], we attribute the slow mode to self diffusion associated with local fluctuations of charge density. Our results support the existence of two relaxation modes in diluted suspensions of weakly charged colloids, in contrast to previous findings.

1 INTRODUCTION

Surfactant systems are of great importance in various industrial fields, such as painting, coating, adhesion, water purification, paper manufacturing, food processing and drug delivery

Typical structural length scales in surfactant systems range from 1 nm to several tens of nm, depending on composition. Scattering methods are thus well suited for their characterization. While neutron or X-ray scattering are used for structural characterization, valuable information on the dynamical properties can be obtained by dynamic light scattering (DLS).

Dynamic light scatttering (DLS) explores the relaxation of the fluctuations of polarization from which light scattering originates. For suspensions of particles in a solvent (colloidal dispersions, macromolecules or polymers in solution, microemulsions etc...) these fluctuations are essentially due to the fluctuations of concentration. The DLS spectra is a single exponential for dilute dispersions of one species of particles [2,3] reflecting a single relaxation mode (Brownian motion of the particules) . However in many different experimental situations the DLS spectra is more complicated. For polydisperse suspensions, the spectra is found to be the sum of two exponentials described theoretically [4,5,6] in terms of the collective and self diffusions respectively . These two modes have been oberved in concentrated colloidal dispersions [7,8]and in charged dispersions.

2 DYNAMIC LIGHT SCATTERING

Dynamic light scattering experiments are performed on a standard set up (AMTEC Goniometer and Brookhaven BI-9000AT correlator), using as a source an argon ion laser with *in-vacuo* wave length λ = 514.5 nm.

In a DLS experiment, one measures the normalized temporal autocorrelation function of the scattered intensity: $g_2(q,t) = \dfrac{\langle I(q,o)\, I(q,t)\rangle}{\langle I(q,0)\rangle^2}$ (1)

Using the Siegert relation: $g_2(q,t) = 1 + B\,|\, g_1(q,t)\,|^2$ (2)

For monodisperse spherical particles the decay of $g_1(q,t)$ is a simple exponential:

$$g_1(q,t) = \exp\left[-\frac{t}{\tau}\right] \quad (3)$$

With $\Gamma = \tau^{-1} = D_c q^2$ (4)

Dc, is the collective translational diffusion coefficient.

3 RESULTS

In this present paper, we investigate a water-based, micellar system comprising a neutral surfactant, Triton X-100 (TX_{100}), and a cosurfactant (octanol). We focus on the dynamical behavior, as measured by DLS, in the dilute regime, measuring the average size. After, we investigate the effect of charges on the dynamics of dilute neutral system by addition of a cationic surfactant, Cetylpyridinium chloride (CPCl).

3.1 Neutral micelles composed of TX100 and octanol

We find a classical sequence in aggregate morphology (Fig 1). A closely similar phase behavior found by Oberdisse et al. [9]. We focus on the dynamics of the micellar phase in the range $\Omega < 0.05$, we observe a single diffusive mode (Fig2) .

3.2 Charged micelles composed of TX100, Octanol, and CPCl.

The phase diagram of the charged system is significantly different from that for the neutral system .Two different phases are observed: a viscoelastic phase in the region [Φ > 4%, 0.4< Ω < 0.58], and an isotropic fluid phase (IFP in the region[Φ < 2%, 0 <Ω<0.6] and [0 < Φ <10%, 0< Ω <0.2] (Fig5)

We study by DLS the dynamics of the micellar phase at low Ω (0< Ω <0.2 Φ < 10%) [10]. Two relaxation modes are observed for the charged system (Fig6), similarly to Ref. [1] and in contrast to Ref. [11], thus supporting the notion that weakly charged colloids exhibit multistep dynamical relaxations even in the diluted regime.

4 FIGURES AND FIGURE CAPTIONS

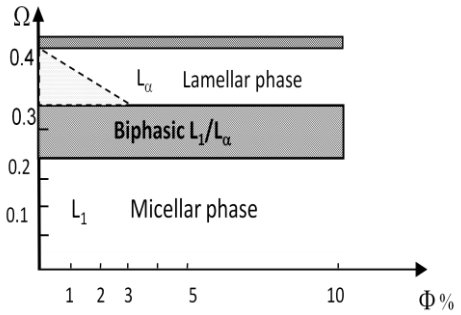

Figure 1: Phase diagram of the neutral system

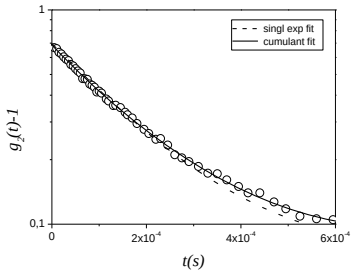

Figure2: Normalized intensity autocorrelation function measured at θ = 30 degrees for the diluted neutral system

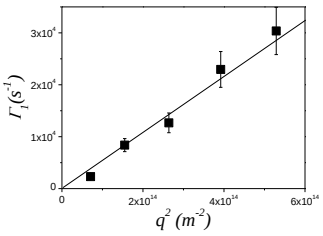

Figure 3: Mean decay rate Γ_1 *vs* q^2 for the neutral system

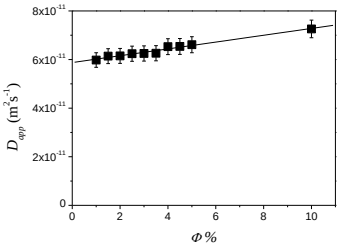

Figure 4: D_{app} *vs* Φ for the neutral system

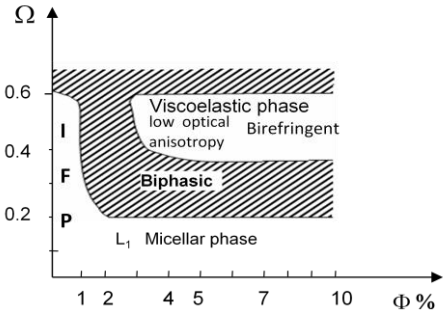

Figure 5: Phase behavior of the charged system with γ = 3.84%.

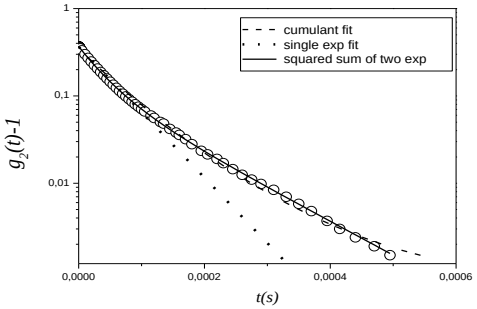

Figure 6: normalized intensity autocorrelation function measured at θ = 60° for the charged system with γ = 3.84%

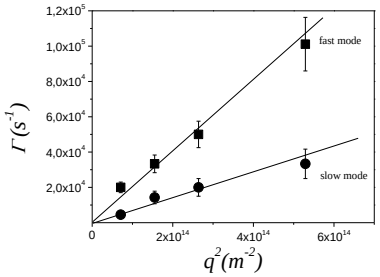

Figure 7: Decay rates Γ_f and Γ_s as a function of squared scattering vector, for the charged system.

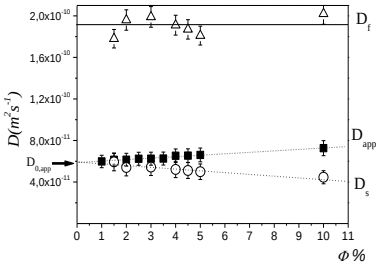

Figure 8: Concentration dependence of the diffusion coefficients D_f and D_s for the charged system

5 CONCLUSION

We have studied two different systems: neutral and charged. In the diluted regime, the systems neutral show one mode diffusive. But, the charged system presents two modes diffusive: the first mode corresponds to fluctuations in the number density of the micelle (fast mode), the second mode is associated with fluctuations in the mean number of charges $\overline{p}$ per micelle

REFERENCES

[1] J.Appell, G.Porte, E.Buhler,J Phys Chem B, 109 : 13 186 (2005)

[2] Berne, B. J.; Pecora, R. Dynamic light Scattering; Wiley: New York, 1976.

[3] Pusey, P. N. Dynamic Light Scattering. In *Neutrons, X-rays and Light*; Lindner, P., Zemb, T., Eds.; Elsevier Science B.V.: Amsterdam NL, **2002**

[4] Pusey, P. N.; Fijnaut, H. M.; Vrij, A. *J. Chem. Phys.* **1982**, *77*, 4270.

[5] Pusey, P. N.; Tough, R. J. A. *Adv. Colloid Interface Sci.* **1982**, *16*, 143.

[6] Yan, Y. D.; Clarke, J. H. R. *J. Chem. Phys.* **1990**, *93*, 4501.

[7] Pusey, P. N.; Segre, P. N.; Behrend, O. P.; Meeker, S. P.; Poon, W. C. K. *Physica A* **1997**.

[8] Segre, P. N.; Pusey, P. N. *Physica A* **1997**, *235*, 9.

[9] J.Oberdisse,C.Couve,J.Appell,J.F.Berret,C.Ligoure G.Porte,Langmuir, 12, 1212-1218 (1996)

[10] J. Oberdisse, O. Regev, G. Porte*J. Phys. Chem. B, 102* (7), pp 1102–1108 (1998)

[11] M. Gradzielski, H.HoffmannJ.Phys.Chem 98, 2613 (1994)

MODELLING OF MECHANICAL BEHAVIOUR OF BOGIE TRAIN

R. Zellagui[1], A. Bellouar[1*] and **S.** Beleulmi[1].

[1]Transportation Engineering Laboratory and Environment
University of Constantine Mentouri 25000 Algeria
Email:Zellagui_redouane@yahoo.fr, bellaouar_ahmed@yahoo.fr, salima_b05@yahoo.fr

ABSTRACT

This study is on the modeling the bogie auto rail in order to highlight certain shortcoming. Indeed, during the operation it was noticed premature deterioration of bogie axles. The purpose of this model is to present a numerical model to predict the mechanical behavior under various loads. The numerical model and geometry will be achieved by Ansys software.

1 INTRODUCTION

The mechanical power transmission should be more reliable, this trend is true for all transport systems, materials handling equipment etc.. Consulting firms are sometimes faced with problems of design and integration; operate more results from numerical models. Today, we talk about digital model of mechanical behavior overall. Numerical modeling has become an essential tool to gain more time and to facilitate the formatting of complex systems. Our work is in this logic. Studied the mechanism is a train bogie in which certain elements, such as pins, exhibit premature cracking. It comprises components that contribute to the torque transmission to the wheels. The truck is a mechanical device of great importance in the architecture of train. From a functional point of view, the bodies that constitute it are the following: the chassis, the two sets (axles, wheels), three sets (spring axle boxes, brake discs). According to references [4], [5], [6], [7], the bogie axis is the element that undergoes more loads where the premature appearance of cracks. The study is focused on determining the trend of the crack under the influence of lubrication.

2 FUNCTIONAL DECOMPOSITION MECHANISM:

The numerical model of the bogie study shows in figure 1. It is composed of main components (chassis, axle-wheel sets spring axle boxes, brake discs) [1] that contributes to the transmission of movement and effort to the wheels. To simplify the study, we isolated some routes to make the numerical model easier to study. Figure 2 shows the separate organs. Each member will be modeled according to the loading conditions throughout the digital model. In this study, we considered a first axis bogie shown in figure 2.

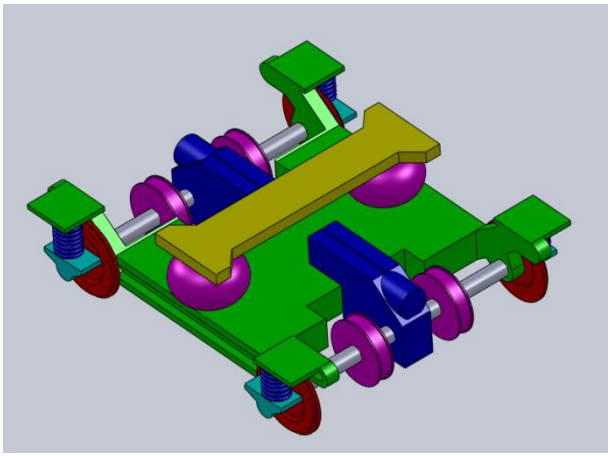

Figure 1: A bogie of train.

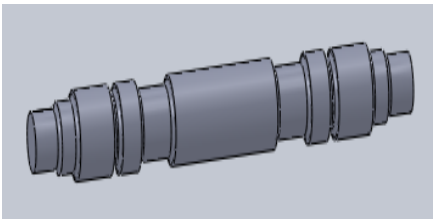

Figure 2: Axle.

The danger zone of the axle is modeled in Figure 3.

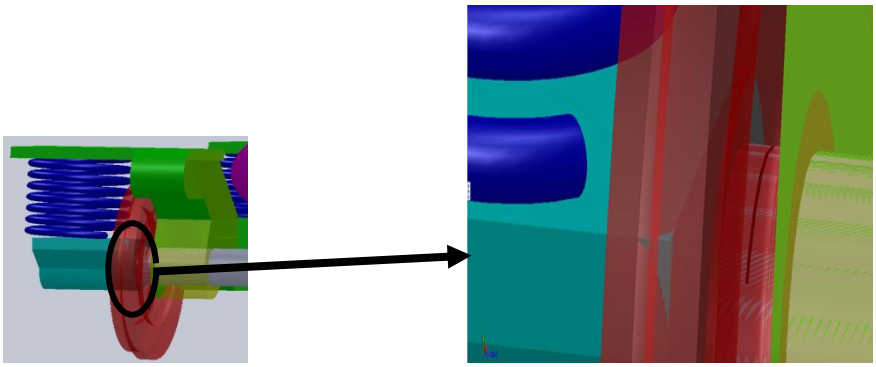

Figure 3: The dangerous area in the axle.

3 NUMERICAL MODEL

The numerical model generated in ANSYS software shows in Figure 4. We modeled a section of the axle shaft of the engine as a two-dimensional structures (185 * 135mm^2) having a crack (plane strain) [3]. In Table 1 are presented the essential features of the XC38 nuance in the normalized condition. The shaft is subjected to rotary bending stress where there is a risk of rupture propagation of fatigue crack.

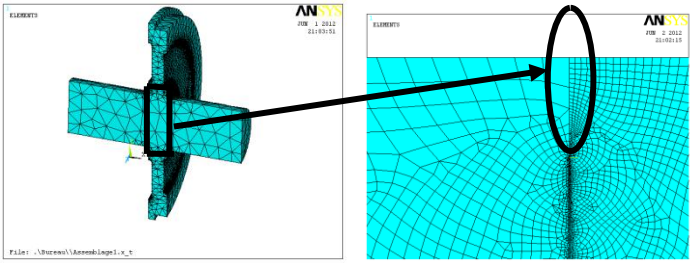

Figure 4: Representation of the critical region (a), Creation of the crack (b).

4 RESULTS AND DISCUSSION

The results presented are obtained by varying certain parameters cited in the references as follows:

1. The effect of the inclination angle of the crack and its length (Figure 5).
2. The influence of a failure of 1mm diameter in different positions (Figure 6).

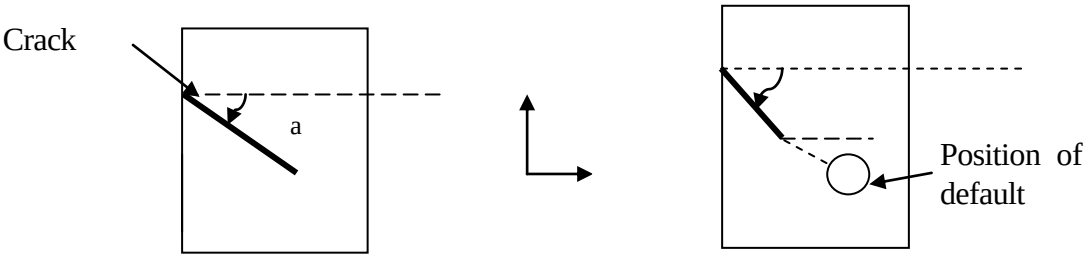

Figure 5: Representation of incline crack. Figure 6 : Représentation of positon défaut.

Figure 7 shows the influence of the angle of inclination without default initiation in both directions X (direction of the crack) and Y where we can see that the larger the angle is large

strain is more important in the sense crack and vice versa in the opposite direction. This is confirmed by Von mises stress in Figure 8 where it increases along the X direction.

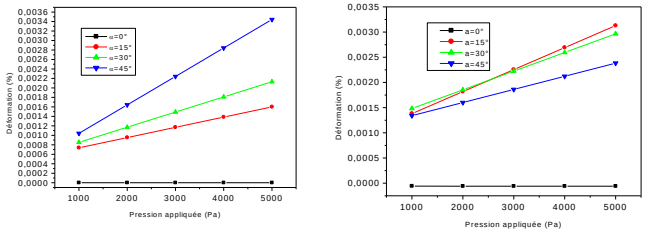

Figure 7: Evolution of strain in X and Y axels.

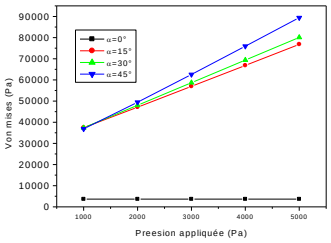

Figure 8: Evolution of Von mises stress.

Figure 9 shows the strain in the angle β = 45 ° since this is the worst case with the creation of a default around the crack tip and change in the position angle of the default (0°, 30°, 60° 90°). We note that the values of stress and strain decrease away from the crack tip, which is logical. Figure 10 present the evolution of the Van Misses stress for the same event of removal of the default.

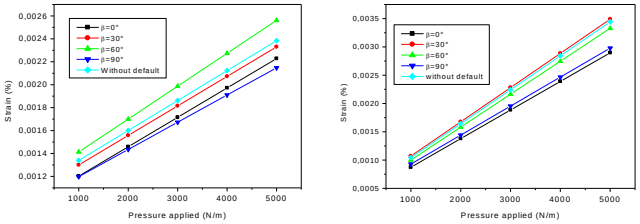

Figure 9: evaluation strain in X and Y axels.

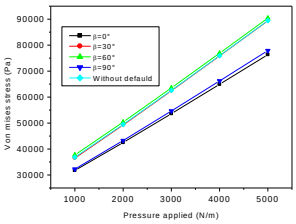

Figure 10: Von mises stress.

5 CONCLUSION

The axes of the bogie are important elements in the operation of the transmission of forces to the wheels. The numerical approach presented in this study is a predictive character. The onset of the crack could be avoided if it works on a numerical model can determine optimal operating conditions and loading. The mechanical behavior (stress and strain) shows at what level we can observe the triggering of the crack and its trend. Early detection of crack initiation probably avoids a lot of damage.

REFERENCES

[1]. J. Campedlli. *Modélisation globale statique des systèmes mécaniques hyperstatiques pre-charges (application a un bogie de train)*2005.

[2]. J.Rice, R.Rosengren. *Plain strain deformation near a crack-tip in a power-law hardening material*.1968.

[3]. R.Smith, S.Hillmansen. *Monitoring Fatigue in Railway Axles*.2001.

[4]. A. Carpinteri , R. Brighenti, A. Spagnoli. *Fatigue growth simulation of part through flaws in thick walled pipes under rotary bending*.2000.

[5]. H. Weixing. *Calculation and analysis of expanding fatigue cracks on axle*.1992.

[6]. A. Bower. *The influence of crack face friction and trapped fluid in surface initiated rolling contact fatigue cracks*.1988.

NONLINEAR SLOSHING OF TWO SUPERPOSED IMMISCIBLE LIQUIDS IN TWO DIMENSIONAL RECTANGULAR TANK

B. MEZIANI[1] and O. OURRAD[1*]

[1]Theoretical Physics Laboratory
University Of Bejaia Targua Ouzemour Campus, 06000 Bejaia, ALGERIA
Email: bachirdidih@yahoo.fr, omeziani@yahoo.fr

ABSTRACT

Sloshing is a physical phenomenon of great importance in technology. In particular, the two layer sloshing encountered in many industrial processes: engines developed with dual fuel tanks, condensers of thermodynamic systems with two fluids and installations of oil-water separators that increase annually due to the growing interest in water pollution. Although the problem is generally nonlinear, linearization of this problem yields satisfactory results in many cases. However, it is recognized that it does not reflect the true shape of the surface profile. Moreover, experience shows that when steepness of the wave becomes sufficiently large, the peak break and flow: this is called breaking. Movement of the free surface in a tank was originally studied by ***Poisson(1831)*** *[1] and* ***Rayleigh(1876)*** *[2] by examining the movement of a liquid in cylindrical and rectangular rigid uniform depth with linearized boundary conditions. Their works are presented in* ***Lamb(1932)*** *[3]. The latter also studied linear oscillations of the of the two superposed liquids interface and free surface in open environment. One of the nonlinear important method is the modal approach to develop the unknown free surface elevation and the velocity potential of the liquid in generalized Fourier series. With respect to nonlinear modal theories, a significant modal theory was established by* ***Faltinsen et al.(2000)*** *[4] where the transient effects can be described. This theory is derived from the variational principle of* ***Bateman(1944)****[5] and* ***Luke(1967)*** *[6]. Recently,* ***Hara and Takahara(2008)*** *[7] studied the linear sloshing of two immiscible perfect fluids by using a Hamiltonian formulation of this system. The influence of surface tension on the natural frequencies and the elevation of the free surface is considered. The same authors,* ***Hara and Takahara(2008 b)*** *[8] have applied the same method, by considering the Hamiltonian at third order to explore the nonlinear problems. We propose in this paper a perturbation method, which can take into account the non-linear effects, the sloshing of two superposed immiscible liquids in rectangular fixed tank. The asymptotic expansion of the interaction modes implies the existence of a dominant single mode and the second-order solution can be determined analytically. This method builds a bridge between the completely non-linear numerical methods and linear methods.*

REFERENCES

[1] S. D. Poisson. Mémoire sur les équations générales de l'équilibre et du mouvement des corps solides élastiques et des fluides. *Journal de l'École polytechnique*, 13(20):1–174, 1831.

[2] L. Rayleigh. On waves. *Phil. Mag.*, 5(1):257–276, 1876.

[3] H. Lamb. *Hydrodynamics*. Cambridge University Press, Cambridge, 1932.

[4] O. M. Faltinsen, O. F. Rognebakke, I. A. Lukovsky, and A. N. Timokha. Multidimensional modal analysis of nonlinear sloshing in a rectangular tank with finite water depth. *J. Fluid Mech.*, 407:201234, 2000.

[5] H. Bateman. *Partial Differential Equations of Mathematical Physics*. Dover Publications, Inc., New York, 1944.

[6] J. C. Luke. A variational principle for a fluid with free surface. *J. Fluid Mech.*, 27:395–397, 1967.

[7] K. Hara and H. Takahara. Hamiltonian formulation of surface and interface sloshing in a tank containing two immiscible fluids. *J. of System Design and Dynamics*, 2(1):299–310, 2008a.

[8] K. Hara and H. Takahara. Hamiltonian formulation for nonlinear sloshing two immiscible fluids. *J. of System Design and Dynamics*, 2(5):1183–1193, 2008b.

ON THE WAVEGUIDE ANALYSIS OF A HELICOPTER ROTOR BLADE BY THE WAVE FINITE ELEMENT METHOD

C. Droz[1,2*] , M.N. Ichchou[1], J-P. Lainé[1] and G. Balmain[2]

[1]Laboratoire de Tribologie et Dynamique des Systèmes
Ecole Centrale de Lyon, 36 Avenue Guy de Collongue, 69134 Ecully Cedex, FRANCE
Email: Christophe.Droz@ec-lyon.fr, Mohamed.Ichchou@ec-lyon.fr

[2]EADS Eurocopter
Aéroport International de Marseille-Provence,
13725 Marignane Cedex, FRANCE
Email: Gregory.Balmain@eurocopter.com

ABSTRACT

Delaminating ice layers from helicopter rotor blades using selected propagating waves requires a wave dispersion analysis of the structure to be performed. Due to their main direction uniformity, rotor blades can be regarded as one-dimensional waveguides. Then, periodic structure theory can be applied from conventional finite element models. This short paper addresses the wave dispersion curves computation for the leading edge of a helicopter rotor blade. Propagating waves in the main axis of the blade are analysed and selected with respect to the stress repartition induced by their deformed shapes. Such wave modes are then expected to promote an efficient de-icing when generated by appropriate actuators. Another concern is due to the important cross-section complexity of the waveguide, which can involve important computation time for broadband frequency analysis. A model order reduction based on a reduced set of basis functions is investigated for the waveguide finite element method.

1 INTRODUCTION

When helicopters fly through icing environments, microscopic cooled water droplets can impact rotor blades and freeze instantaneously on their leading edge (see Figure 1). Such accreted ice have high adhesion strength and its accumulation can lead to performance degradation as far as sizeable accidents. Ice protection and prediction techniques are a concern since the mid-twentieth and inspired several systems such as anti-icing fluids, pneumatic boots, microwaves de-icing or icephobic materials. However, the most commonly used de-icing method, based on electro-thermal system, tends to be outdated due to its high energy consumption and incompatibility for polymer blades.

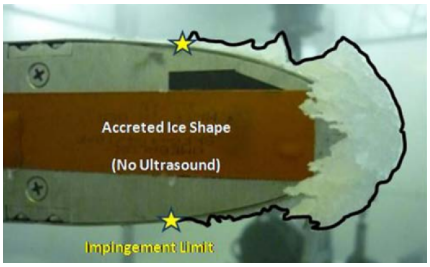

Figure 1. Ice accretion on a rotating leading edge [1].

Mid-frequency waves are mainly known for their applications to nondestructive evaluation (NDE) and structural health monitoring (SHM). These waves can also be considered as potential candidates for delaminating accreted ice layers from substrates as rotor leading edges or an entire helicopter blade. Recent investigations [1, 2] tend to prove that PZT actuators driven at their radial resonant frequencies can generate high enough ice-interface stresses to produce ice delamination on a leading edge sample.

Notwithstanding, a propagative approach is required to extend these results to general cases. In this research work a propagative analysis of rotor blades and leading edges waveguides is provided. Predicted strains and dispersion properties gives critical informations about de-icing potential and expectable wave range through dissipative structures.

2 WAVEGUIDE FINITE ELEMENT METHOD

2.1 Free wave propagation in periodic structures

Rotor blades can be considered as 1-dimensional waveguides, whose large dimensions and complex cross-section tends to disqualify for conventional finite element analysis (FEA) beyond lower frequencies. Considering structure homogeneity along its main direction, periodic structure theory can be used. Wave finite element method (WFE) is thus an appropriate solution providing dispersion relations for free wave propagation, considering commercial FEA packages can be applied.

A representative cross-section of the waveguide is meshed using classical finite elements and shown Figure 2. The equation of motion in terms of dynamic stiffness matrix $\mathbf{D}$ for time harmonic motion is written Equation 1.

$$\begin{bmatrix} \mathbf{D}_{LL} & \mathbf{D}_{LR} \\ \mathbf{D}_{RL} & \mathbf{D}_{RR} \end{bmatrix} \begin{Bmatrix} \mathbf{u}_L \\ \mathbf{u}_R \end{Bmatrix} = \begin{Bmatrix} \mathbf{f}_L \\ \mathbf{f}_R \end{Bmatrix}. \tag{1}$$

Vectors $\{\mathbf{u}\}$ and $\{\mathbf{f}\}$ contain nodal degrees of freedom and forces and the subscripts L, R denote the left and right sides of the cross-section element. Cells periodicity condition and forces

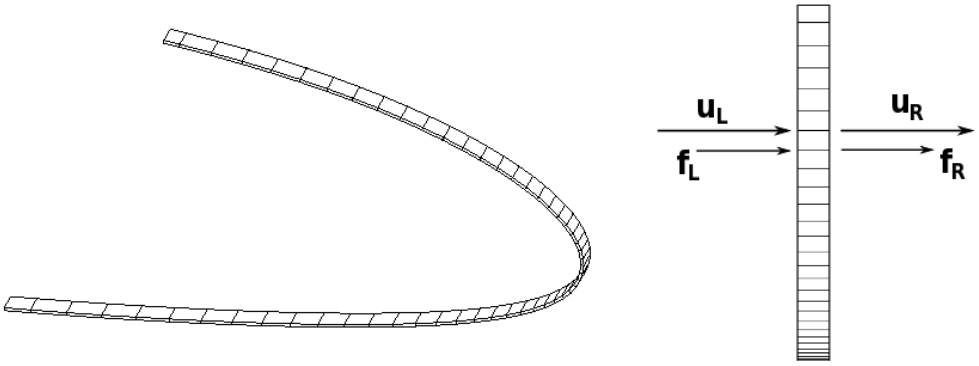

Figure 2. Example of a meshed rotor blade leading edge cross-section

equilibrium statements lead to the eigenproblem Equation 2.

$$\mathbf{T} \left\{ \begin{array}{c} \mathbf{u}_L \\ \mathbf{f}_L \end{array} \right\} = \lambda \left\{ \begin{array}{c} \mathbf{u}_R \\ \mathbf{f}_R \end{array} \right\}. \tag{2}$$

Where **T** is the transfer matrix between forces and displacements in both faces of the section, its eigenvalues are the propagation constants which can be written $\lambda = e^{-jkd_x}$, d_x and k denoting the cross-section length and wavenumber.

2.2 Wave analysis of a leading edge section

The results in wavenumbers for propagative waves are shown Figure 3.a for a 0.6mm thick rotor blade leading edge. Flexural waves are identified as well as their conversions with similar shaped waves at higher frequencies. De-icing system requires that propagative waves can be found at higher frequencies in order to induce local strains. Figure 3.b shows a flexural wave deformed section.

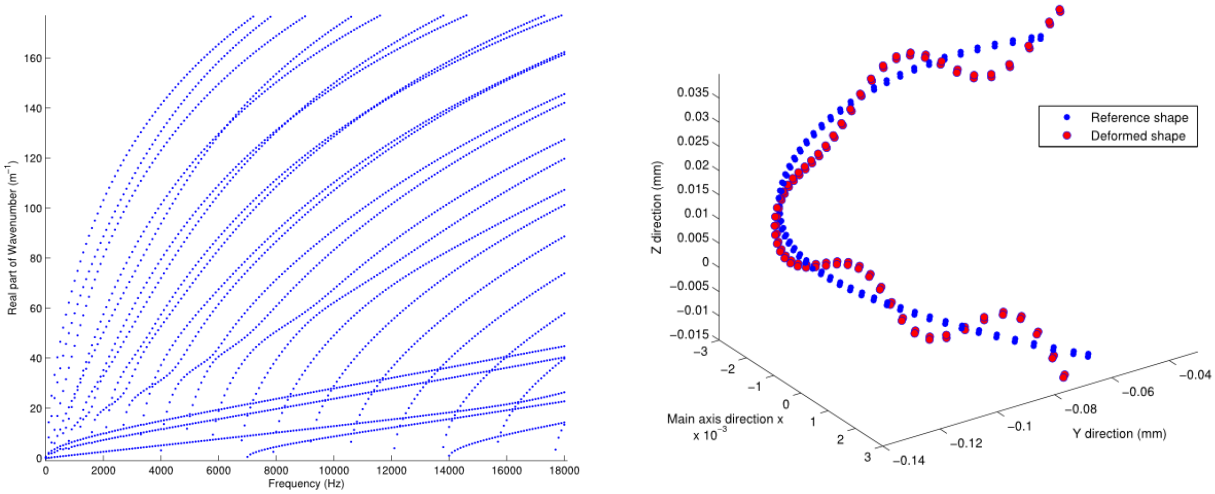

Figure 3: (a) Real part of the wavenumbers for propagative waves (b) Deformed section for 8th flexural wave.

3 PROJECTION ON A REDUCED BASIS

3.1 Interest of model reduction

Despite an important system reduction along the waveguide main axis, the WFE method supposes to take into consideration the whole cross-section complexity while solving the eigenproblem in Equation 2. Moreover, an accurate computation of normalized stresses associated to the deformed wave shapes requires refined meshing of the finite element section. The idea is to approximate displacements on the section boundaries u_L and u_R by using a projection on the reduced modal basis containing relevant cross-section modes.

3.2 Calculation of a reduced basis

We denote $\tilde{\mathbf{\Phi}}_m = \begin{bmatrix} \tilde{\mathbf{\Phi}}_m^{(u_L)} & \tilde{\mathbf{\Phi}}_m^{(u_R)} \end{bmatrix}^T$, where $\tilde{\mathbf{\Phi}}_m^{(u_i)}$ are to be understood as the projection matrices of displacements over boundary i on a reduced basis build with m selected modes of the full modal basis $\{\mathbf{\Phi}_j\}_{j=1,\dots,n}$, and $\tilde{\boldsymbol{\psi}}_m = \begin{bmatrix} \tilde{\boldsymbol{\psi}}_L & \tilde{\boldsymbol{\psi}}_R \end{bmatrix}^T$, the reduced modal displacements.

Propagation constants and deformed shapes, initially computed through a $2n * 2n$ eigenproblem (using Zhong [3] formulation with $\mathbf{T} = \mathbf{N}\mathbf{L}^{-1}$) can now be approximated by solving reduced $m * m$ system Equation 3.

$$\tilde{\mathbf{\Phi}}_m^T \mathbf{N} \tilde{\mathbf{\Phi}}_m \tilde{\boldsymbol{\psi}}_m = \lambda \tilde{\mathbf{\Phi}}_m^T \mathbf{L} \tilde{\mathbf{\Phi}}_m \tilde{\boldsymbol{\psi}}_m. \tag{3}$$

with explicit deformed shapes written Equation 4.

$$\begin{Bmatrix} \tilde{\boldsymbol{u}}_L \\ \tilde{\boldsymbol{u}}_R \end{Bmatrix} = \begin{Bmatrix} \tilde{\mathbf{\Phi}}_m^{(u_L)} \tilde{\boldsymbol{\psi}}_L \\ \tilde{\mathbf{\Phi}}_m^{(u_R)} \tilde{\boldsymbol{\psi}}_R \end{Bmatrix}. \tag{4}$$

Investigations regarding modal selection relevance and propagation constants sensitivity to system reduction are carried out and applied to the rotor blade leading edge presented above.

REFERENCES

[1] A. Overmeyer, J. Palacios, E. Smith, and R. Royer. Rotating testing of a low-power, non-thermal ultrasonic de-icing system for helicopter rotor blades. *SAE 2011 International Conference on Aircraft and Engine Icing and Ground Deicing*, doi:10.4271/2011-38-0098, 2011.

[2] J. Palacios, E. Smith, and J. Rose. Instantaneous de-icing of freezer ice via ultrasonic actuation. *AIAA*, 49(6):1158–1167, 2011.

[3] W.X. Zhong and F.W. Williams. On the direct solution of wave propagation for repetitive structures. *Journal of Sound and Vibration*, 181(3):485–501, 1995.

Optimization of geometrical parameters of covers & hoops of metal packaging boxes

April 23, 2012

R. Lombarkia[1] & B. Barkat[2].
[1, 2] University of Batna, lab. LRP.
1 Rue Chahid Bouhklouf Mohammed El-Hadi.
05000 Batna, Algeria.

Keywords: Metal packaging, sequential quadratic programming (SQP), ABAQUS, Finite Elements.

Finding the best compromise between economic, mechanic and technologic imperatives is still being one of the most important goal for the engineer. Working methods to achieve this goal of excellence have advanced considerably in recent years. Nowadays, optimization programs are included in many commercial codes of finite elements (ANSYS, LS-DYNA, Msc-Marc,...), so that optimization can be made from the design phase. Therefore, it may be a part of an integrated design process.

In this work we try to find the ideal geometric parameters of covers and hoops of metal packaging boxes. A similar approaches were introduced in the past, we can presents the following example: To minimize the weight of can ends of beverage cans, K.Yamazaki *et al*. (2006). (Yamazaki. [1]). applied the method of response surface approximation to develop the can ends. The geometric parameters of the sheet metal are considered as design variables to optimize. The strategy is to combine between the design of experiments using orthogonal arrays and a series of simulations with the finite elements code Msc Marc to approximate the expression of stresses and displacements at the center of can end according to design variables. Finally a numerical optimization program, in this case, DOT from Vanderplaats, is used to minimize the weight, under three constraints.

In our study, we have shape optimization of metal boxes under internal pressure, with the condition to avoid opening the cover, the objective function to optimize is

difficult to interpret analytically, we opted for an approximation method based on design of experiments coupled with the finite elements code ABAQUS.

The optimization method applied is hybrid in a way because it use both the response surfaces methodology and nonlinear constrained optimization algorithm (SQP). It is divided into two steps:

A first step will allow us to express the objective function which is the contact pressure between the lid and hoop by a quadratic polynomial formula with the Box-Behnken method. A second step is to maximize under constraints, the contact pressure at the last increment before final opening of the cover, this maximization is solved by the SQP algorithm.

The contribution of this paper is to find the optimal values of geometric variables of metal packaging boxes to ensure a better quality of service of the product, optimum closing and lightweithing.

References

[1] Yamazaki, K., Itoh, Watanabe, M., Han, J. & Nishiyama, S., Applications of structural optimization techniques in light weighting of aluminum beverage can ends. *Journal of food engineering*, 81(2), pp. 341-346, 2007.

RECONSTRUCTION OF IMPACT FORCE VIA BAYESIAN APPROACH

S. Sammagassi[1], A. Khamlichi[1], A. Driouech[1*] and E. Jacquelin[2]

[1]Laboratory Communication systems
Abdelmalek Essaâdi University, Tetouan, MOROCCO
saora82@yahoo.fr, khamlichi7@yahoo.es, adriouach@hotmail.com

[2]Laboratory LMM
University of Lyon, Villeurbanne, FRANCE
eric.jacquelin@univ-lyon1.fr

ABSTRACT

In this work, reconstruction of pressure signal developed during non punctual impact occurring on elastic beams has been achieved through using Bayesian approach. This was performed by mans of an a posteriori density of probabilities function that takes into account both the likelihood and a priori random information. The a priori density of probabilities that was incorporated enabled, through a hierarchical model, to reduce uncertainty on pressure signal to only that affecting its amplitude. It was found that reconstruction functions very well in this situation as the obtained reconstructed pressure was very close to the original pressure taken at input of the system.

1 INTRODUCTION

Knowledge of a force exerted on a mechanical system constitutes very important information in various applications dealing with dynamics of structures. However, direct measure of the force by transducers is so difficult in practice, and even impossible in many situations. This is why indirect methods are preferred in this field. These consist in reconstruction of the force by solution of the inverse problem. Various methods have been developed during last decades which enable identification of force characteristics through measuring the response in some locations of the elastic structure [1]. Considering the time domain approach to the problem, great attention has been paid to the stability issue of inversion operation like for instance applying singular value decomposition followed by Tikhonov regularisation [2].

In this work, force reconstruction is considered within the context of Bayesian approach which considers the unknowns as random variables [3-5]. This approach provides a rigorously probabilistic framework which incorporates all sources of uncertainties such as those resulting from the actual model used or those associated to noise during measurement. Bayesian reconstruction of the force is conducted through Markov Chain Monte Carlo sampling method (MCMC). The Bayesian based incorporates both the a priori available information and the a posteriori information provided by the measured response. Estimation of the inverse problem solution can then be obtained by the conditional mean of the a posteriori density of probabilities.

The Bayesian algorithm for reconstruction is applied in the following to recover the impact pressure developed during a non punctual impact occurring on an elastic beam.

2 IMPACT WITH UNIFORM PRESSURE ON AN ELASTIC BEAM

A planar beam having a symmetric section and loaded orthogonally to its mean fibre in its plane of symmetry is considered. It is assumed to be made from a homogeneous elastic material and having a uniform cross section. The beam is subjected to a force resulting from a non punctual impact where the acting pressure is assumed to be uniform on the whole impact zone which is considered to be perfectly known. The inverse problem is then only about reconstruction of the pressure time signal from the measured strain. The impact pressure is of the form $p(x_0,\eta,t)$ where x_0 designates the center of the impact zone, η its longitudinal extension $[x_0-\eta/2, x_0+\eta/2]$ and t the time. The measured longitudinal normal strain $y(x_c,t)$ corresponds to a measurement point of abscissa x_c located on the upper beam fiber.

Let p and y denote respectively the vector containing the unknown discrete values of the pressure and measured strain, the a posteriori density of probabilities according to Bayes writes

$$\pi(p/y)=\frac{\pi(y/p)\pi_{pr}(p)}{\pi(y)} \tag{1}$$

where $\pi_{pr}(p)$ is the a priori density of probabilities rending some available information about the unknown pressure p, $\pi(y/p)$ is the likelihood density of probabilities giving the probability that observation be y when the pressure is p and $\pi(y)$ is the density of probabilities of observations.

The beam model that integrates the presence of some additive measurement noise is considered under the following linear form

$$Y=GP+E \tag{2}$$

where E a random vector representing measurement noise. E and P are assumed to be distributed according to multi-variable Gaussians: $P \sim N(\bar{p},\sigma^2 I)$ and $E \sim N(0,\upsilon^2 I)$ with known σ

and υ while the expectation $\bar{p}$ is assumed to be a hyper-parameter. The a posteriori density of probabilities takes then the following hierarchical form

$$\pi(x/y) \propto \exp\left(-\frac{1}{2\upsilon^2}(y-Gx)^t(y-Gx)\right)\pi_{pr}(x/\bar{x})\pi_{hpr}(\bar{x}) \tag{3}$$

Toeplitz like matrix G giving the discrete time response in terms of longitudinal axial strain of the upper fibre, as function of the discrete vector P representing the pressure of impact, writes $G(k,j) = \sum_{m=1}^{M}\left[\sin\left(\frac{m\pi x_c}{L}\right)\sin\left(\frac{m\pi x_0}{L}\right)\sin\left(\frac{m\pi\eta}{2L}\right)g(\omega_m,\xi_m,(j-k)\Delta T)\right]$ with $g(\omega_m,\xi_m,(j-k)\Delta T)=0$ if $j<k$

and $g(\omega_m,\xi_m,(j-k)\Delta T) = \left[-\frac{mh\pi}{2\omega_m\sqrt{1-\xi_m^2}}\sin\left(\omega_m\sqrt{1-\xi_m^2}(j-k)\Delta T\right)\exp\left(-\xi_m\omega_m(j-k)\Delta T\right)\right]$ if $j \geq k$,

$\omega_m = \frac{m\pi}{L}\sqrt{\frac{EI}{\rho S}}$, and where E is the Young's modulus, ρ the density, I the moment of inertia, S the cross section area, L the beam length, Let h be the height of the beam cross section, ξ_m the modal damping associated to mode number m, Δt le the time step and M the total number of selected first modes.

The applied pressure is assumed to be $p(t) = at^2e^{-bt}$. It reaches the maximum $p_{max} = 4a/(b^2e^2)$ for $t_{max} = 2/b$. Parameters a and b are then given by $a = p_{max}e^2/t_{max}^2$ and $b = 2/t_{max}$.

By examining the assumed expression of pressure one can see that the discrete pressure writes $p = ap_0$, where vector p_0 depends only on parameter b, the selected time step Δt and time duration T_c. As $P \sim N(\bar{p},\sigma^2 I)$ and $\bar{p} = \overline{ap_0}$, one obtains $AP_0 \sim N(\overline{ap_0},\sigma^2 I)$. If the information available a priori enables to know exactly the time instant t_{max} where the pressure is p_{max} so that only parameter a is random, p_0 is deterministic and $A \sim N\left(\bar{a},\frac{\sigma^2}{\|p_0\|^2}\right)$. Assuming that $\bar{a}$ is uniformly distributed over the interval $[a_1,a_2]$, which is expected to contain the expectation of the random variable A almost surely, one can simplify the conditional density of probabilities, equation (3), under the following form

$$\pi(p/y) \propto \exp\left(-\frac{1}{2\upsilon^2}(y-Gp)^t(y-Gp) - \frac{\|p_0\|^2}{2\sigma^2}(a-\bar{a})^2\right)\prod[a_1,a_2] \tag{5}$$

Estimation of the inverse problem solution can then be performed through the conditional mean $\tilde{p}$ of pressure p knowing the measured response y, as given by equation (5). Evaluation of this expectation can be performed through the ergodic mean of a homogeneous Markov chain process $\{p_j\}$ [5]. Such a process can be generated by operating Hastings-Metropolis algorithm on the density of probabilities function, hence $\tilde{p} = \int_{\mathbb{R}^n} p\pi(p/y)dp = \lim_{N\to\infty}\frac{1}{N}\sum_{j=1}^{N}\pi(p_j/y)$.

3 CASE STUDY

Let's consider a beam for which $E = 2.1\times10^{11}\,Pa$, $\rho = 7800\,kg.m^{-3}$, $L = 1\,m$, $h = 10^{-2}\,m$. $\xi_m = 0.5\%$, $x_0 = 5L/6$, $\eta = L/6$ and $x_c = L/3$. The 5 first frequencies of the pinned-pinned beam are : $f_1 = 7.49\,Hz$, $f_2 = 15Hz$, $f_3 = 22.5\,Hz$, $f_4 = 30Hz$ and $f_5 = 37.5Hz$. The first 5 modes are selected in the following so $M = 5$. The total duration of calculation is taken to be $T_c = 0.08\,s$ and

the time step is $\Delta t = 2.125\times10^{-3}\,s$. Length of the unknown vector p is then 38. The pressure signal considered is that for which $a = 10^8$ and $b = 1000$.

Applying statistical inversion by means of the Bayesian approach when using the a posteriori density of probabilities function defined in equation (5) and et Hasting-Metropolis algorithm enables to estimate the conditional mean of pressure signal amplitude. The following data has been used for the complete description of the a posteriori density of probabilities: $a_1 = 10^7$, $a_2 = 10^9$, $\upsilon = 100$ and $\sigma = 2$. In the actual version of Hastings-Metropolis algorithm, the proposition density of probabilities is taken to be a multivariable Gaussian having zero average and uniform diagonal covariance matrix of standard deviation $\sigma' = 2$. Figure 1 shows superposition of both reconstructed and original pressure signals. This figure shows that reconstruction of impact pressure achieves remarkable accuracy

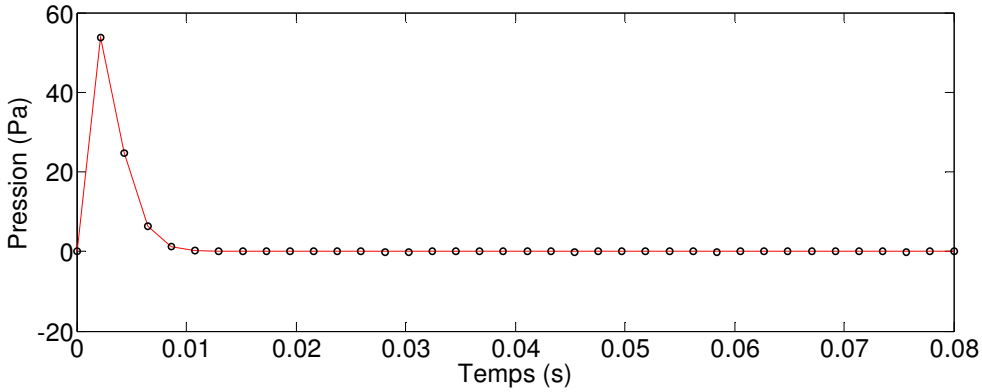

Figure 1. Pressure signal, as reconstructed by the Bayesian approach, superposed to the original pressure signal (The dot-line curve corresponds to the reconstructed pressure)

4 CONCLUSION

In this work, reconstruction of pressure developed during non punctual impact occurring on elastic beams has been achieved through using the Bayesian approach. This was performed through using an a posteriori density of probabilities that takes into account both the likelihood and a priori densities of probabilities. The a priori information used enabled to reduce uncertainty on the pressure amplitude alone. It would be interesting considering more general situations through using more hyper-parameters to represent the a priori information for the pressure random variable.

REFERENCES

[1] H. Choi, A. Thite, D. Thompson, Comparison of methods for parameter selection in Tikhonov regularization with application to inverse force determination, Journal of Sound and Vibration 304: 894-917, 2007.

[2] E. Jacquelin, A. Bennani, P. Hamelin, Force reconstruction: analysis and regularization of a deconvolution problem, *Journal of Sound and Vibration* 265: 81-107, 2003.

[3] P. Lee, Bayesian Statistics: An Introduction, Arnold Publication, 1997.

[4] W. Hastings, Monte Carlo sampling methods using Markov chains and their applications, *Biometrika* 57: 97–109, 1970.

[5] W. Gilks, S. Richardson, D. Spiegelhalter, Markov Chain Monte Carlo in Practice, Chapman and Hall, 1995.

NONLINEAR WAVE PROPAGATION IN POST-BUCKLED STRUCTURES

A. Spadoni[1*] , F. P. Maurin[1]

[1]Laboratory of Wave Mechanics and Multifield Interactions (LOMI)
École Polytechnique Fédérale de Lausanne (EPFL)
Email: alex.spadoni@epfl.ch

ABSTRACT

Nonlinear wave propagation in solids and material structures provides a physical basis to derive canonical equations which govern disparate phenomena such as vortex filaments, plasma waves, and traveling loops. Solids and structures furthermore provide a medium were wave processes are relatively simple to measure, and this allows validating various theoretical aspects. Nonlinear waves in solids however remain a challenging proposition since nonlinearity is often associated with irreversible processes. Reversible nonlinear behavior is usually obtained employing hyperelastic materials, and this is balanced with dispersive effects. We introduce an additional state for slender structures with presents both intrinsic dispersion and nonlinear behavior. Namely, we consider wave propagation in initially post-buckled structures with linear-elastic material behavior. We find that dispersion is strongly dependent on pre-compression and we compute waves with a dispersive front or tail. Post-buckled structures with large initial pre-compression instead are well described by the KdV equation. We employ finite-element, difference-differential, and analytical models to support our conclusions.

Nonlinear wave propagation in solids and material structures provides a physical basis to derive canonical equations which govern disparate phenomena such as vortex filaments [1], plasma waves [2], and traveling loops [3]. Continuous solids and material structures are also convenient test beds to investigate nonlinear processes as they may be easier to measure and validate against appropriate mathematical models than other realms. Nonlinear waves in solids however remain a challenging proposition since nonlinearity is often associated with irreversible processes. Shock waves [4] and buckle waves [5] are two examples. Reversible nonlinear processes, on the other hand, have been reported in media with hyperelastic behavior. If the nonlinear kinematic behavior is balanced by dispersion nonlinear-stable waves are possible. In waveguides like rods and plates made of nonlinear-elastic materials like Mooney or Murnaghan materials[6] stable nonlinear waves result from dispersion introduced by geometric properties of the waveguides and nonlinear material behavior. A particular type of nonlinear waves, solitons, has also been demonstrated in thin-film-like coatings resting on a nonlinear substrate made of lithium niobate [7]. Stable nonlinear waves are also predicted as bulk waves in general hyperelastic, power-law solids [8]: in this case nonlinearity is induced by material behavior and dispersion arises from coupling of deformation components. Slender structures such as rods also allow reversible nonlinear processes such as propagating curves or loops with the same characteristics as solitons [3, 9].

We introduce an additional state for continuous, slender structures with presents both intrinsic dispersion and nonlinear behavior. Namely, we consider wave propagation in initially post-buckled structures. In such domain, nonlinear behavior arises from large deformations while dispersion in naturally introduced by the bifurcated configuration. Proper selection of boundary conditions determines lengthscales in the buckled configuration. Dispersion in such a medium can be adapted to promote or inhibit certain wave characteristics. We consider linear-elastic material behavior and we demonstrate that the interaction of geometric nonlinearities and bifurcation-induced dispersion lead to various types of nonlinear waves. Furthermore, the characteristics of wave propagation in post-buckled structures strongly depend upon the level of pre-compression and the frequency regime. We consider three levels of initial deformations and we show that the strength of nonlinear behavior decreases with increasing pre-compression while dispersion can both accelerate and decelerate wave packets of increasing frequency. In all cases, we restrict ourselves to the low-frequency regime, where deformation potentials can be described by the static response of the medium.

REFERENCES

[1] R. E. Goldstein and D. M. Petrich. The korteweg–de vries hierarchy as dynamics of closed curves in the plane. *Physical review letters*, 67(23):3203–3206, 1991.

[2] N.J. Zabusky and M.D. Kruskal. Interaction of "solitons" in a collisionless plasma and the recurrence of initial states. *Physical Review Letters*, 15(6):240–243, 1965.

[3] B. D. Coleman, E. H. Dill, and D. Swigon. On the dynamics of flexure and stretch in the theory of elastic rods. *Archive for rational mechanics and analysis*, 129(2):147–174, 1995.

[4] W. K. Nowacki. *Stress waves in non-elastic solids*. Pergamon Press, 1978.

[5] D. G. Vaughn and J. W. Hutchinson. Bucklewaves. *European Journal of Mechanics-A/Solids*, 25(1):1–12, 2006.

[6] A. M. Samsonov. *Strain solitons in solids: and how to construct them*. Chapman & Hall/CRC Monographs and Surveys in Pure and Applied Math. Taylor & Francis Group, 2001.

[7] G. A. Maugin. *Nonlinear Waves in Elastic Crystals*. Oxford Mathematical Monographs. Oxford University Press, 1999.

[8] M Destrade and G Saccomandi. Nonlinear transverse waves in deformed dispersive solids. *Wave Motion*, 45(3):325–336, 2008.

[9] K. Nishinari. Nonlinear dynamics of solitary waves in an extensible rod. *Proceedings of the Royal Society of London. Series A: Mathematical, Physical and Engineering Sciences*, 453(1959):817–833, 1997.

NON LINEAR MODAL ANALYSIS OF DYNAMIC ABSORBERS

F. DJEMAL[1,2*], J. DION[2], F. CHAARI[1], I. TAWFIQ[2], M. HADDAR[1],

[1]Unit of Mechanics, Modeling and Manufacturing
National School of Engineers of Sfax, BP1173-3038 Sfax, Tunisia
Email: fathidjemal@yahoo.fr, fakher.chaari@gmail.com

[2]Engineering Laboratory of Mechanical Systems and Materials
Higher Institute of Mechanics of Paris, Paris, France.
Email: jean-luc.dion@supmeca.fr

ABSTRACT

Isolation of mechanical systems is widely adopted in several engineering applications such as space or automotive fields. Linear absorbers allow reducing vibration only around resonance frequency. Non linear absorbers are much more interesting since they attenuate vibration on a large band of frequency.
In this paper, a non-linear two degrees of freedom (DOF) model is developed. A cubic non-linearity is considered, it is induced by a gap. The objective of the paper is to characterize nonlinear vibration of the system by applying explicit formulation (EF). This is a direct-path method based in physical coordinates, which uses the linear coefficients stored in the system's matrices to represent the nonlinear frequency response function (FRF).

1 INTRODUCTION

In this work, we study a two DOF the system with stops submitted to a harmonic force as shown in "Figure 1". It has a nonlinear behavior due to the gap between the mass M_2 and the two stops. To investigate the dynamics of this model, a non linear formulation is presented. The dynamic responses of the linear and nonlinear systems are compared by means of FRF and non linear normal modes (NNM).

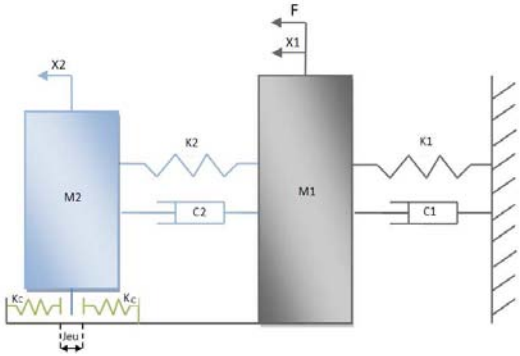

Figure 1. A two DOF system with stops.

2 NON LINEAR FORMULATION

The matrix form describing the motion of a linear undamped mass-spring system is given by:

$$[M]\{\ddot{X}(\omega)\}+[K]\{X(\omega)\}=\{F\}e^{i\omega t} \tag{1}$$

[*M*] and [*K*] are the mass and stiffness matrices respectively. {*F*} is the harmonic excitation vector operating at frequency ω.

The mathematical model of a cubic stiffness element can be expressed as [2]:

$$\tilde{g}(\tilde{x})=k\tilde{x}+\beta\tilde{x}^3 \tag{2}$$

$\tilde{g}(\tilde{x})$ is the force induced by the tension of a spring by a distance $\tilde{x}$. The coefficient *k* represents the linear component of the spring and the coefficient β accounts for the nonlinear effects due to the term $\tilde{x}^3$.

By introducing (2) in (1), we obtain

$$[M]\{\ddot{\tilde{X}}(\omega)\}+[K]\{\tilde{X}(\omega)\}+\{\tilde{G}(\tilde{x}^3)\}=\{F\}e^{i\omega t} \tag{3}$$

$\{\tilde{X}\}$ is the vector of generalized coordinates of the nonlinear system.

$\{\tilde{G}(\tilde{x}^3)\}$ is a nonlinear vector defined by:

$$\{\tilde{G}(\tilde{x}^3)\}=\begin{Bmatrix}\tilde{g}_{11}+\tilde{g}_{12}+\ \dots\ +\tilde{g}_{1N}\\ \tilde{g}_{21}+\tilde{g}_{22}+\ \dots\ +\tilde{g}_{2N}\\ \vdots\\ \tilde{g}_{N1}+\tilde{g}_{N2}+\ \dots\ +\tilde{g}_{NN}\end{Bmatrix} \tag{4}$$

Each component $\tilde{g}_{ij}$ describes the presence or not of non-linearity between DOFs *i* and *j*. It can be expressed as:

$$\tilde{g}_{ij}(\tilde{x}^3_{i,j})=\beta\tilde{x}^3_{i,j} \tag{5}$$

Linearization of $\tilde{g}_{ij}$ yields to the following equation :

$$\tilde{g}_{ij}(\tilde{x}_{i,j}^3) = \tilde{v}_{ij}(\tilde{x}_{i,j}^2).\tilde{x}_{i,j} = \left[\frac{3}{4}\beta_{ij}\left|\tilde{X}_{i,j}\right|^2 \quad -\frac{3}{4}\beta_{ij}\left|\tilde{X}_{i,j}\right|^2\right]\begin{Bmatrix}\tilde{X}_i\\ \tilde{X}_j\end{Bmatrix} \tag{6}$$

Using equation (6), the nonlinear equation of motion in the frequency domain can be written as:

$$\left(-\omega^2[M]+[K]+\left[\tilde{v}(\tilde{x}_{i,j}^2)\right]\right)\left\{\tilde{X}(\omega)\right\} = \{F\} \tag{7}$$

The resolution of this type of system is accomplished through the Newton-Raphson method. The nonlinear eigenvalue problem is given by:

$$\left(-\omega^2[M]+[K]\right)\left[\tilde{\Phi}\right]\left\{\tilde{P}\right\} + \left\{\tilde{G}(\tilde{x}_{i,j})\right\} = 0 \tag{8}$$

where $\left[\tilde{\Phi}\right]$ is the nonlinear modal matrix depends on the amplitude and frequency. This matrix can be decomposed into two matrices as:

$$\left[\tilde{\Phi}\right] = \left[\Phi + \Delta\tilde{\Phi}\right] \tag{9}$$

The system response can be obtained by solving (9):

$$\left\{\tilde{X}\right\} = \frac{\left[\tilde{\Phi}\right]\left[\tilde{\Phi}\right]^T\{F\}}{\left[\tilde{\lambda}^2-\omega^2\right]} \tag{10}$$

Where $\tilde{\lambda}$ are the nonlinear eigenvalues. They are defined by:

$$\tilde{\lambda}^2 = \lambda^2 + \Delta\tilde{\lambda}^2 \tag{11}$$

For each mode, the variation $\Delta\tilde{\lambda}_r$ is defined by:

$$\Delta\tilde{\lambda}_r^2 = \frac{\left(\Phi^T\tilde{G}\right)_r + \left((\lambda^2-\omega^2)\Phi^{-1}\Delta\tilde{\Phi}\left\{\tilde{P}\right\}\right)_r + \left(\Delta\tilde{\Phi}^T F\right)_r}{\left\{\tilde{P}\right\}_r} \tag{12}$$

3 NUMERICAL SIMULATIONS

The frequency response for the first DOF of the non-linear model is shown in Figure 2. It is characterized by the presence of peaks corresponding to two resonance frequencies of the linear model.

The nonlinear frequency response is also characterized by jump phenomenon (discontinuity of responses). This jump is in the vicinity of the two eigenfrequencies of the system for two DOFs.

We note that the amplitudes of the frequency response near the natural frequencies are significantly attenuated.

Figure 3 shows the discontinuities of the eigenvalues in the vicinity of the two natural frequencies of the structure. These discontinuities are caused by non-linearity introduced into cubic stiffness model. Indeed, these modes were constant when the system is completely linear.

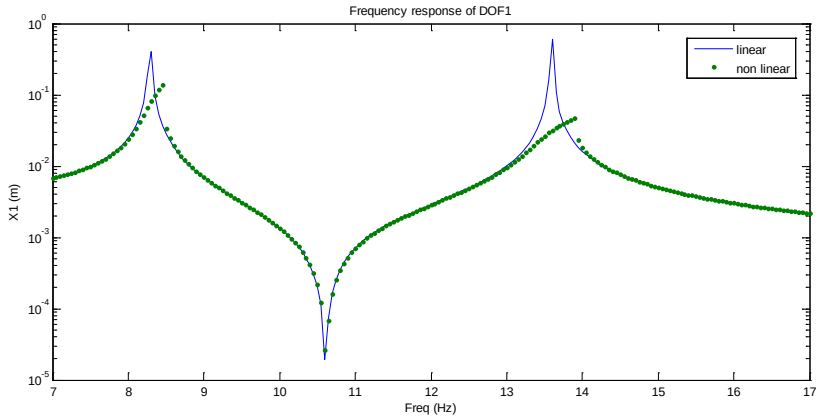

Figure 2. Frequency response at the first degree of freedom.

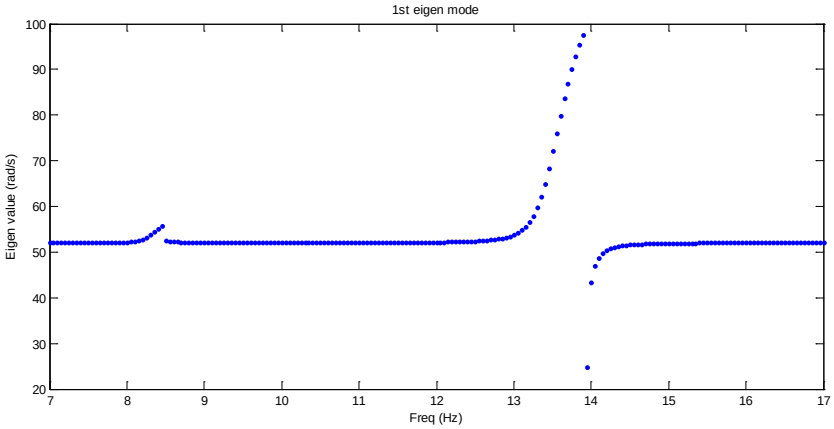

Figure 3. Discontinuity of the first nonlinear mode.

4 CONCLUSION

In this works, we presented the EF method to investigate the non linear dynamics of a two DOF system with a non linear cubic stiffness. The results showed that the natural frequencies of the system vary with the excitation motion. It is also observed the existence of the jump phenomenon which characterizes the non linear behaviour of the system.

REFERENCES

[1] G. Kerschen, K. Worden, A. F. Vakakis, and J. C. Golinval, “Past, present and future of nonlinear system identification in structural dynamics,” Mechanical Systems and Signal Processing,vol. 20, no. 3, pp. 505–592, 2006.

[2] H. R. E. Siller, Non-linear modal analysis methods for engineering structures [Ph.D. thesis], Imperial College London/University of London, 2004.

[3] A. F. Vakakis. Nonlinear normal modes (NNMs) and their applications in vibration theory: an overview. Mechanical Systems and Signal Processing, 11(1):3–22, 1997.

[4] S. W. Shaw and C. Pierre. Normal modes for nonlinear vibratory systems. Journal of Sound and Vibration, 164(1):85–124, 1993

[5] N. Barbieri and R. Barbieri. Dynamic analysis of stockbrige Damper. Advences in Acoustics and Vibration, volume 2012, article ID 659398.

DELAYED FEEDBACK CONTROLLER IN MEMS RESONATORS

K. Masri, M. Younis, and S. Shao

Department of Mechanical Engineering, State University of New York at Binghamton, Binghamton, NY 13902, USA
E-mail: myounis@binghamton.edu

ABSTRACT

Controlling mechanical systems is an important branch of mechanical engineering. Several techniques have been used to control Microelectromechanical systems (MEMS) resonators. In this paper, we study the effect of a delayed feedback controller on stabilizing MEMS resonators. A delayed feedback velocity controller is implemented through modifying the parallel plate electrostatic force used to excite the resonator into motion. A nonlinear single degree of freedom model is used to simulate the resonator response. Long time integration is used first. Then, a finite deference technique to capture periodic motion combined with the Floquet theory is used to capture the stable and unstable periodic responses. We show that applying a suitable positive gain can stabilize the MEMS resonator near or inside the instability dynamic pull in band. We also study the stability of the resonator by tracking its basins of attraction while sweeping the controller gain and the frequency of excitations. For positive delayed gains, we notice significant enhancement in the safe area of the basins of attraction.

1 INTRODUCTION

Delayed Feedback Control (DFC) [1] is a simple algorithm that has been used to stabilize the unstable periodic orbits in nonlinear dynamical systems. It controls the system by feeding the system with a signal, which is a difference between the current state of the system and the state of the system delayed by a specific period. This method was introduced by Pyragas [1] and it has been successfully applied to various nonlinear and chaotic systems.

The delayed feedback controller has been successfully applied to different mechanical systems. Alsaleem and Younis [2] conducted an experimental and theoretical study on stabilizing a capacitive MEMS resonator using the Pyragas [1] delayed feedback controller; however using the velocity instead of displacement as the feedback signal. Hikihara *et al.* [3] and Christini *et al.* [4] used it to stabilize the UPOs of the mechanical pendulums. Sieber [5], and Landry *et al.*[6] used the displacement delayed feedback controller to balance an inverted pendulum.

Here, a single degree of freedom model is used to model the capacitive resonator of [2] under a delayed feedback velocity controller. The equation of motion can be expressed as

$$m\,\ddot{\hat{x}}(\hat{t}) + \hat{c}\,\dot{\hat{x}}(\hat{t}) + k\,\hat{x}(\hat{t}) = \varepsilon\,A\frac{(V_{DC} + V_{AC}Cos(\Omega\,\hat{t}) + G[\dot{\hat{x}}(\hat{t}-\hat{\tau}) - \dot{\hat{x}}(\hat{t})])^2}{2(d-\hat{x}(\hat{t}))^2} \tag{1}$$

where $\hat{x}$ is mass deflection, A is upper electrode area, $\hat{c}$ is a damping coefficient, k is the resonator stiffness, ε is the dielectric constant, V_{DC} is the DC voltage, V_{AC} is the AC voltage, Ω is the excitation frequency, $\hat{G}$ is the controlling gain, $\hat{\tau}$ is the time delay, which is here chosen is half the natural period, d is the distance between the upper and lower electrodes , and $\hat{t}$ is time.

2 RESULTS

We demonstrate how delayed feedback control can stabilize MEMS resonators by applying suitable positive gain. We use velocity DFC and long-time integration of Eq. (1) to examine and show the effect of DFC on the MEMS resonator. In the following, we show results of $x = \hat{x}/d$, where d is the gap width of the capacitor electrode =38 μm. Figure 1 shows the time history of the capacitive resonator. It shows the effect of small positive gain on stabilizing the MEMS resonator, which was initially undergoes unstable motion without the controller.

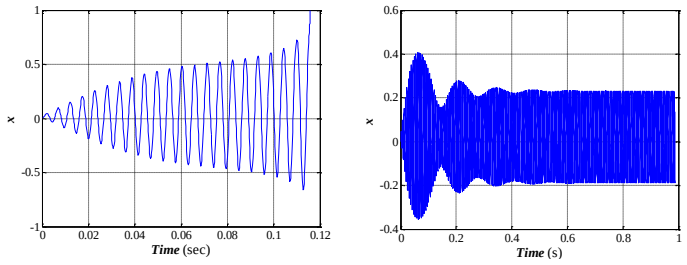

(a) (b)

Figure 1. Time history curve of the capacitive resonator when its actuated with V_{DC} =40.2 V, V_{AC} =20.1 V, and Ω=183 Hz (a) without the delayedfeedback controller, (b) with the delayed feedback controller of G=75 V.s/m and $\tau = T/2$.

The effect of DFC in decreasing the steady-state deflection is shown in Figure 2. It also shows that it requires at least G=180 V.s/m to stabilize the resonator. This DFC effect is noticeable on frequencies (187.5 Hz- 195 Hz) and it has a minimal effect away from the pull-in band (instability band) at frequencies lower 185 Hz and higher 197.5 Hz.

Next we show frequency response of the resonator using finite difference method combined with the Floquet theory [7] and the long-time integration method (LTI). Figure 3 shows that positive gain can stabilize the response of the uncontrolled system. Accordingly in Figure 3, it is obvious to see the systems with G=200 V.s/m and 250 V.s/m yield stable response under frequencies where uncontrolled system generate unstable response. One can see that the finite difference method is able to catch both stable and unstable periodic motions.

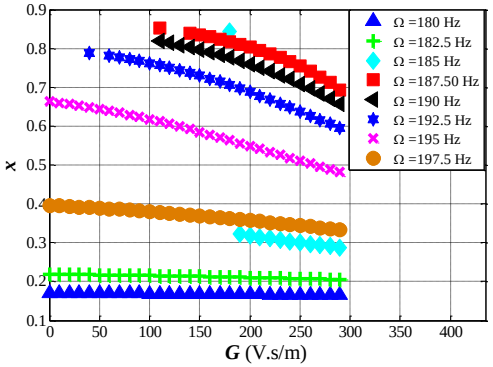

Figure 2. The effect of DFC gain on the resonator steady state response

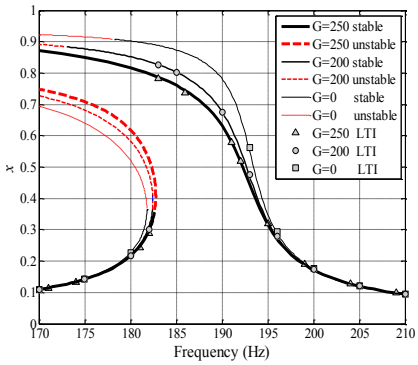

Figure 3. Comparison between the responses under positive gain delayed controllers for various values of gain. Solid lines and dash lines are finite difference method results.

In order to better understand the effect of the delayed feedback controller on the capacitive resonator, we calculate its basin of attraction (initial conditions leading to stable state [8]) with and without the controller. Figure 4 shows the results for different DFC gain values. For G=0, it is almost unstable except for very few initial conditions (the safe area is very small). There is a small increase in the safe area for G=50 V.s/m. The area increases for G =150 V.s/m and the erosion of the safe area disappears totally for G=200V.s/m.

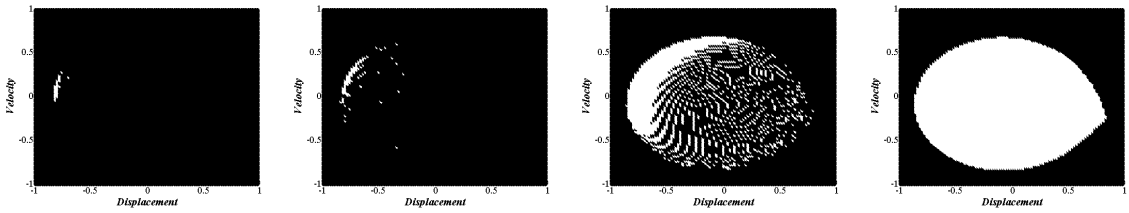

G=0 V.s/m . G=50 V.s/m. G=150 V.s/m. G=200 V.s/m.

Figure 4. Basins of attraction at Ω =186 Hz when the resonator is actuated with V_{DC} = 40.2 V and V_{AC} = 20.1 V with $\tau = T/2$ with DFC.

For more quantitative stability study, we determine the Normalized Safe Area (NSA), which is calculated by finding the ratio between the white (safe) areas to the total basin of attraction area (the total grid points). Figure 5 shows the safe areas at different gains. We can

notice the increase in the safe area ratio at every frequency when the applied delayed gain is increased. Using low gain (up to G=100 V.s/m) enhances the stability but does not stabilize the resonator at frequencies 185 Hz and 186 Hz. However, using high gain (G=150 V.s/m - G=200 V.s/m) yields stable response at almost all frequencies. Using a very high gain (G=300 V.s/m) gives the same safe area for all frequencies.

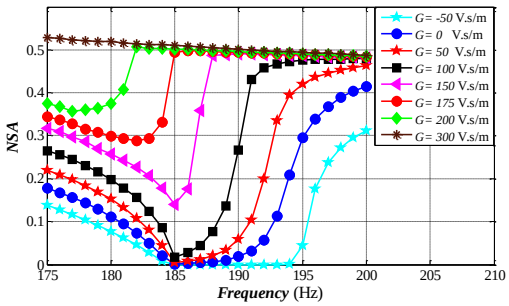

Figure 5**.** The normalized safe areas at different gains when the resonator is actuated with V_{DC} = 40.2 V and V_{AC} = 20.1 V with $\tau = T/2$.

3 CONCLUSIONS

We studied the effect of delayed feedback velocity controllers to stabilize the response of electrostatically actuated MEMS resonators. We demonstrated the effect of positive gains on the dynamical behavior of the resonator through the combined use of long-time integration of the equation of motion, the finite difference to find periodic motion combined with the Floquet theory, and through a basin-of-attraction analysis. We found that increasing the delayed gain, the system tends to stabilize faster and there is a slight decrease in the steady state value. It was shown that increasing the positive gain will increase the system stability by increasing the safe area. As a result, such a controller can be used to achieve high vibration amplitudes, compared to noise levels, of MEMS resonators while keeping them in robust stable state.

REFERENCES

[1] Pyragas K., Pyragas N., and Benner H., "Delayed feedback control of dynamical systems at a subcritical Hopf bifurcation," Physical Review E, p. 056222, 2004.

[2] Alsaleem F. M. and Younis M. I., "Stabilization of electrostatic MEMS resonators using a delayed feedback controller," *Smart Materials and Structures,* vol. 19 , p. 035016, 2010.

[3] Hikihara T. and Kawagoshi T., " Experimental study on stabilization of unstable periodic motion in magneto-elastic chaos," *Phys. Lett,* vol. 211A, p. 29–36, 1996.

[4] Christini D.J, In V, Spano M.L, Ditto W.L, Collins J.J, "Real-time experimental control of a system in its chaotic and nonchaotic regimes.," *Phys. Rev. E,* vol. Phys. Rev. E, p. R3749–R3752., 1997.

[5] Sieber J. and Krauskopf B., "Complex balancing motions of an inverted pendulum subject to delayed feedback control.," *Physica D* , vol. 197, no. 3-4, pp. 332-345, 2004.

[6] Landry M., Campbell S. A., Morris K., and Aguilar C. O., "Dynamics of an Inverted Pendulum with Delayed Feedback Control," *SIAM J. APPLIED DYNAMICAL SYSTEMS,* vol. 4, no. 2, pp. 333-351, 2005.

[7] A. Nayfeh and B. Balachandran, Applied Nonlinear Dynamics, Wiley, New York, 1995.

[8] Younis M. I., MEMS Linear and Nonlinear Statics and Dynamics, Springer, 2011.

TURBULENT WALL PRESSURE MEASUREMENT IN LOW WAVENUMBER USING THE FLOW-INDUCED VIBRATIONS

D. Lecoq[1*] , C. Pézerat[1], J.-H. Thomas[1] and W. Bi[1]

[1] LUNAM Université, Université du Maine, CNRS UMR 6613, Laboratoire d'Acoustique de l'Université du Maine (LAUM), Avenue Olivier Messiaen, 72085 Le Mans Cedex 9, FRANCE
Email: damien.lecoq @univ-lemans.fr

ABSTRACT

The purpose of this study is to see how to measure aeroacoustic sources responsible for noise inside a vehicle especially the low wavenumbers of low Mach-number flows. It is proposed to realize this identification with an inverse problem by calculating the wall pressure from vibration measurements. To do this, it is chosen to test the Corrected Force Analysis Technique which consists in calculating the force distribution verifying locally the motion equation of the structure. Two cases are studied. The first is a simulation of a plate excited by a Turbulent Boundary Layer with an aerodynamic part and an acoustic component that is much smaller in energy. The second is an experimental validation in a wind tunnel where a structure is excited by turbulences generated by a Forward-Facing Step and by an additional acoustic source. In the two cases, even if the excitation contains a very high aerodynamic component, it is found that the inverse method identifies the acoustic part of the excitation. Indeed, this component is located in the low wavenumbers and coincides with the flexural wavenumber of the structure.

1 INTRODUCTION

Turbulent wall pressures are vibration sources composed of two components: the aerodynamic part due to the pressure fluctuations of the turbulences and the acoustic part corresponding to the radiation of the turbulences (Figure 1). In the wavenumber plan (k_x,k_y), the first is localized in the high wavenumbers around the convection wavenumber $k_{conv} = \omega/U_c$ linked to the convection velocity U_c [1]. The acoustic component excites wavenumbers within the circle of radius $k_{ac} = \omega/c_0$, which corresponds to the acoustic wavenumber and where c_0 is the sound speed. Although it depends on the studied cases, the acoustic component has always an energy much smaller than that of the aerodynamic part [2, 3]. However, the vibration and the acoustic radiation of the plate are more sensitive to the acoustic component because the acoustic wavenumber k_{ac} is closer to the flexural wavenumber. In other words, the acoustic wavelengths are very close to the natural wavelength of the structure over a wide frequency range.

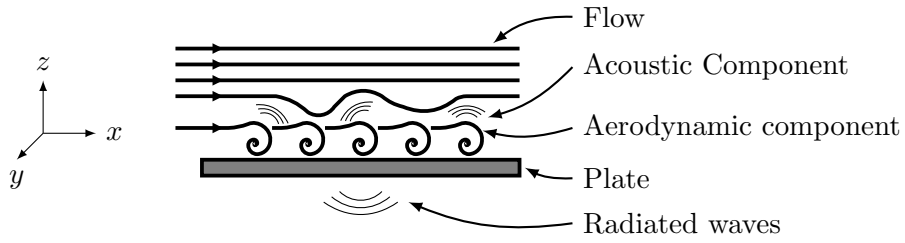

Figure 1. Plate excited by a turbulent flow.

The aim is to identify the low wavenumbers of turbulent wall pressures which are very difficult to assess by measurement because of their low level. As show in a first study [4], the idea is to use the plate as a sensor of the acoustic energy since the vibrations of this latter are very sensitive to these wavelengths. For this, it is proposed to apply the Force Analysis Technique [5], which allows to identify the force distribution exciting the plate from the measurements of its vibration. In this paper, the Corrected Force Analysis Technique (CFAT) is proposed [6, 7]. This improvement allows one to identify the acoustic pressure at one point with a restrictive number of measurement.

2 THE CORRECTED FORCE ANALYSIS TECHNIQUE (CFAT)

The motion equation which gives the displacement w at one angular frequency ω for a given pressure field p can be written:

$$D\left(\frac{\partial^4 w}{\partial x^4} + \frac{\partial^4 w}{\partial y^4} + 2\frac{\partial^4 w}{\partial x^2 \partial y^2}\right) - \rho h\, \omega^2 w = p(x, y, \omega), \tag{1}$$

with $D = \frac{Eh^3}{12(1-\nu^2)}$ and where ρ, E, ν are respectively the mass density, the Young's modulus, the Poisson's ratio of the material and h is the thickness of the plate. The discretized equation of motion given by FAT with a spatial step Δ between the measurement points is:

$$p^{\text{FAT}}(x, y, \omega) = D\left(\delta_\Delta^{4x} + \delta_\Delta^{4y} + 2\delta_\Delta^{2x2y}\right) - \rho h \omega^2 w, \tag{2}$$

where δ_Δ^{4x}, δ_Δ^{4y} and δ_Δ^{2x2y} are given in [5]. It requires 13 points of measured displacement around the point (x, y) to compute them. This inverse problem usually requires a regularization to avoid different problems of sensitivity to noise measurement. This involves applying the method on many points of the plate. An alternative, CFAT [6], is to use the discretization of the array of

13 sensors to automatically regularize when the measurement is realized at a single point. To optimize this regularization, we add two additional coefficients μ^4 and ν^4 [6] in Equation (2):

$$p^{CFAT}(x,y,\omega) = D\left(\mu^4\delta_\Delta^{4x} + \mu^4\delta_\Delta^{4y} + 2\nu^4\delta_\Delta^{2x2y}\right) - \rho h\omega^2 w. \quad (3)$$

3 SIMULATION: TURBULENT BOUNDARY LAYER

In this simulation, an automotive windshield is excited by a TBL generated by a flow of 50 m/s. A diffuse acoustic field with a low amplitude is artificially added to the Corcos model. The direct problem of vibration is computed and CFAT is applied (Figure 2). In the domain of validity of CFAT, from 400 Hz to 2 kHz (respectively from $n = 4$ to $n = 2$ with n the number of points per natural wavelength λ_f), the method allows to identify exclusively the acoustic component. Indeed, for these frequencies, the plate and the method constitute low-pass wavenumber filterings, with cutoff wavenumbers equal to the flexural wavenumber k_f, which are smaller than the convection wavenumber k_{conv}.

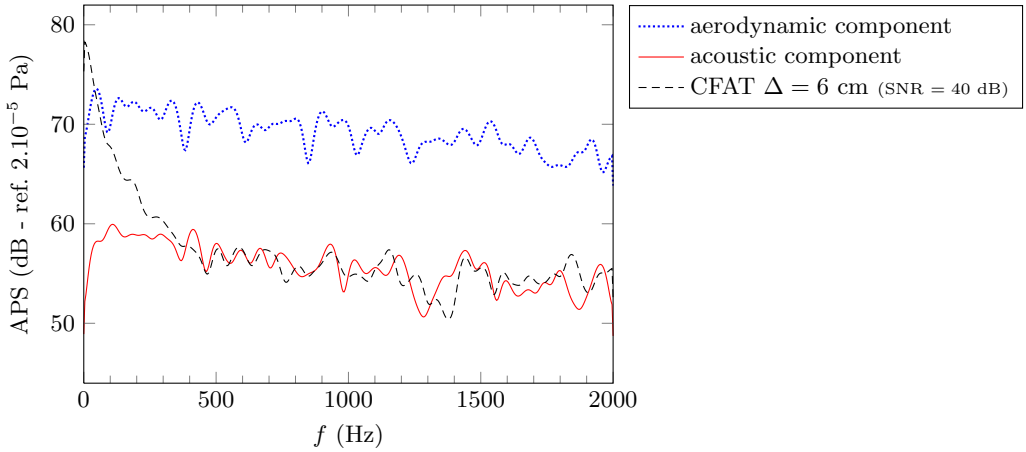

Figure 2: Frequency spectra of the identified pressures by CFAT where a noise is added to the displacement field (SNR = 40 dB).

4 EXPERIMENTATION: FORWARD-FACING STEP (FFS)

For the experimental validation, a small plate (automative windshield) is placed in a wind tunnel. The turbulences are generated by a FFS and the surface pressure measurement is made with an insert of 1.3 mm diameter. This measurement is realized with an additional acoustic source that is a loudspeaker placed above the flow which generates a 1500 Hz sine (Figure 3). Thanks to the coincidence between the acoustic wavelength and the natural wavelength of the structure, CFAT identifies precisely the acoustic sine whereas the classical surface pressure measurement is not able to extract this low component. Apart from the frequency corresponding to the acoustic sine, CFAT identifies an intermediate level between the isolated acoustic source and the flow which corresponds to sources in the low wavenumbers, below the flexural wavenumber k_f. We hypothesize that these low-wavenumber excitations correspond to the acoustic component of the flow and to the acoustic radiation of the plate.

5 CONCLUSION

In our study, the use of vibration data for the turbulent wall pressure measurement has two advantages. First, the plate is very sensitive to the low wavenumbers, so the SNR is better than

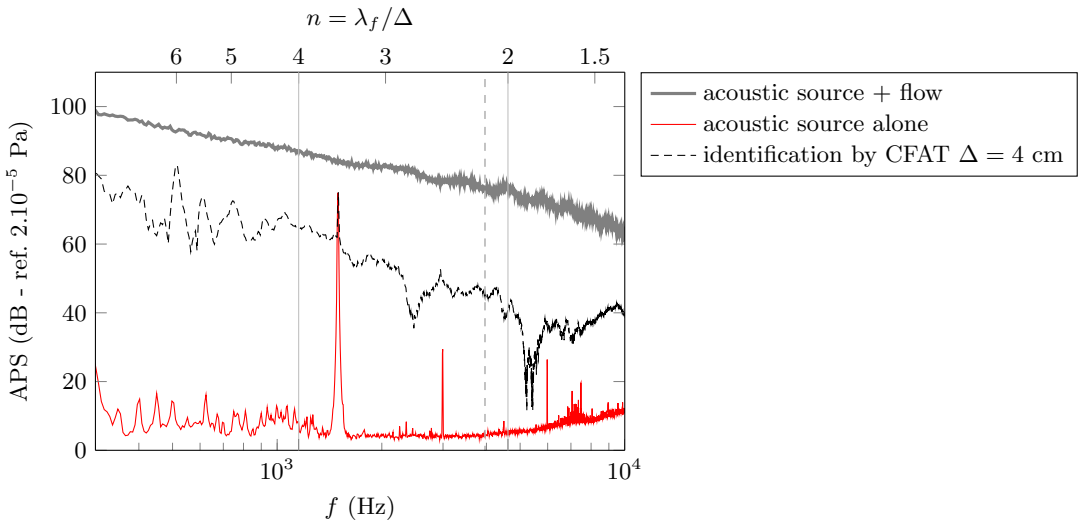

Figure 3: APS of the wall pressure for the plate excited by the sinusoidal acoustic source and by the flow of 40 m/s, and APS of the pressure identified by CFAT. Vertical solid lines indicate the frequency limits of the inverse problem, and the vertical dashed line corresponds to the acoustic coincidence.

in the classical surface pressure measurement for the identification of these large wavelengths. Then, it identifies the main source of vibration and acoustic radiation of the plate because of the coincidence between the flexural and acoustic wavelengths. In addition, this method does not affect the flow, since one can place the 13 sensors on the side of plate without flow.

REFERENCES

[1] W. K. Blake. *Mechanics of Flow-Induced Sound and Vibration, Vols. 1 and 2*. Academic Press, New York, 1986.

[2] M.S. Howe. Surface pressures and sound produced by turbulent flow over smooth and rough walls. *The Journal of the Acoustical Society of America*, 90:1041–1047, 1991.

[3] B. Arguillat, D. Ricot, C. Bailly, and G. Robert. Measured wavenumber: Frequency spectrum associated with acoustic and aerodynamic wall pressure fluctuations. *The Journal of the Acoustical Society of America*, 128:1647–1655, 2010.

[4] D. Lecoq, C. Pézerat, J.-H. Thomas, and W. Bi. Identification of the acoustic component in the turbulent boundary layer excitation by the force analysis technique. Acoustics 2012, 23-27 april 2012, Nantes, France.

[5] C. Pézerat and J.-L. Guyader. Force analysis technique: reconstruction of force distribution on plates. *Acta Acustica united with Acustica*, 86(2):322–332, 2000.

[6] Q. Leclère and C. Pézerat. Vibration source identification using corrected finite difference schemes. *Journal of Sound and Vibration*, 331:1366–1377, 2012.

[7] D. Lecoq, C. Pézerat, J.-H. Thomas, and W. Bi. How an inverse vibration method can be used for the extraction of the acoustic component of a turbulent boundary layer? Internoise 2012, 19-22 august, New-York, USA.

Detecting and Measuring Slug Velocity in Two-Phase Flows Horizontal Pipes

Alssayh Muammer, Addali Abdulmajid [1], Mba David [1], Naid Abdelhamid [,2]

1 : Cranfield University
2 : Azzaytuna University

Two phase flow is a common phenomenon in petroleum and chemical engineering. An important feature used to describe two phase flow is the flow regime which varies depending on the individual velocities of the components within the two-phase flow. One of these regimes, the slug regime, can create significant pressure fluctuations that compromise the integrity of the transporting structure (pipes, separators, etc.). This is in addition to other unwanted effects such as flooding at the receiving end, an increase in deposits of hydrates and corrosion. Under such circumstances the detection of the slug and its associated characteristics are vitally important to the operator.
This experimental study investigates the application of Acoustic Emission (AE) technology for detecting slug velocity in two phase (gas/liquid) flow. It is demonstrated that slug velocity can be determined using acoustic emission sensors.

EXPERIMENTAL INVESTIGATION OF THE EQUILIBRIUM AND STABILITY OF LONG TOWED CABLE SYSTEMS

M. Obligado[1*] and M. Bourgoin[1]

[1]Laboratoire des Ecoulements Geophysiques et Industriels, CNRS/UJF/G-INP UMR 5519, BP53, 38041, Grenoble, France
Email: Martin.Obligado@legi.grenoble-inp.fr, Mickael.Bourgoin@legi.grenoble-inp.fr

ABSTRACT

The dynamics of towed objects in a fluid environment is of interest for many practical situations. In this work, an experimental investigation of the Lagrangian dynamics of a spherical object towed at the tip of a cable is proposed. The cable has a length-to-diameter ratio of $5 \cdot 10^4$*, several orders of magnitude higher than previous studies and similar to the value needed for applications. The towing configuration is artificially obtained by considering a steady cable (with one fix end and a free one to which a sphere is attached) in a low turbulence wind-tunnel. This reproduces the situation of an object towed at constant speed. Three different configurations of cable tip are considered: (i) the cable free end by itself ; (ii) a light millimetric towed sphere made of expanded polystyrene and (iii) a denser millimetric towed sphere made of lead. For each situation a systematic study of the influence of Reynolds number is done by varying the mean velocity of the surrounding flow. For the free end and light sphere case, the tip of the cable is stable only below a critical towing velocity. Above this threshold, a monotonic increase of fluctuation levels with increasing towing velocity is observed. No such threshold is observed for the heavy particle, for which the velocity and acceleration fluctuations remain two order of magnitudes below that of the light particle and the free end.*

1 INTRODUCTION

The dynamics of towed objects in a fluid environment is of interest for many practical situations, such as acoustic streamers [1] and aerial systems towed by aircrafts [2], among others. In the context of these applications, it is of crucial importance to warrant the stability of the trajectory of the towed object (at the tip of the cable) what turns to be an interesting and complex fluid-structure interaction problem. The case of very long cylinders is of particular interest because most of the mentioned practical applications of towed systems do use long cables where the length-to-diameter ratio is large. Several types of instability have been reported, including mainly divergence (which corresponds to a non-oscillatory motion with growing amplitude) and flutter (oscillatory motion), where the instability is relatively well predicted numerically from the coupling between the fluid and the cylinder (via inviscid terms and friction) [3]. However, the study of the stability of such long cylinders in a flow remains an open field of theoretical and numerical research. On the experimental side, characterization of the dynamics of long cylinders remains scarce, probably due to the difficulty of achieving appropriate conditions in laboratory facilities. The main avaiable works are those realized by Ni & Hansen [4] and by Sudarsan [5] (with a length to diameter ratio of the cable of 500 and 150 respectively) for cylinders submerged in water. Both studies report *divergence* and *flutter* of the cylinders.

In the present article is considered a towed system where the length-to-diameter ratio of the cable is of $5 \cdot 10^4$, hence several orders of magnitude higher than previous studies. The focus is put on the analysis of the Lagrangian dynamics of the tip of the cable. The towing configuration is artificially obtained by considering a steady cable (with one fix end and a free tip end to which a sphere is eventually attached) in a horizontal low turbulence wind-tunnel (see figure 1). This reproduces the situation of an object towed horizontally at constant speed (therefore the terminology *wind velocity* or *towing velocity* in the subsequent will be indifferently used). Three different configurations of cable tip are considered: (i) just the free end by itself (without any sphere attached) ; (ii) a light millimetric sphere made of expanded polystyrene and (iii) a denser millimetric towed sphere made of lead. For each situation a systematic study of the influence of the towing velocity on the equilibrium and stability of the cable extremity is performed.

2 EXPERIMENTAL SETUP

The experiment has been run in a large wind tunnel (figure 1), with a measurement section of 0.75 m x 0.75 m. The towing cable is a thin Polyamide-Nylon fiber, with a lineal density of order 17 mg/m, made of three stranded filaments with a diameter of 25μm each (giving an equivalent diameter for the stranded cable of $a_c = \sqrt{3} \cdot 25\mu\text{m} \simeq 43\mu\text{m}$). One extremity of the cable is fixed at the entrance of the test section at the center of the tunnel, while the other end is free to move. The fixed extremity of the cable is attached at the middle of a transverse horizontal *support* cable tensed across the tunnel at mid-height and located at the entrance of the test section (see figure 1). The support cable is made with the same fiber and no measurable increase of the natural fluctuation level of the flow in the wind-tunnel was detected downstream due to the presence of it (with such natural fluctuations always below 0.5%). The length of the towing cable is $L = 2.08$ m, what places the free tip nearly at mid-distance between the entrance and the exit of the 4 m long test section. Considering this length, which is significantly longer than the maximum transverse displacement of the tip (which does not exceed a few centimeters), the motion of the moving extremity of the cable is essentially two-dimensional, in a transverse xOy plane. The light sphere has a diameter of 6.3 mm and a density of 13.35 Kg/m^3 while the heavy particle has a diameter of 1.7 mm and a density of 9130 Kg/m^3. For the case of the free end, a small single knot (with effective diameter $d_k \simeq 2a_c$), colored with red varnish, was made at the

tip of the cable to improve its visualization.

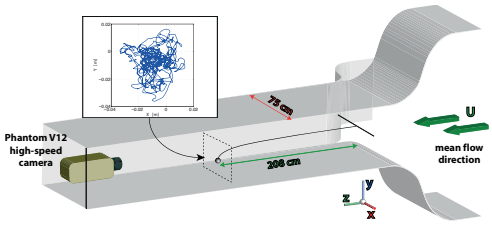

Figure 1: Sketch of the experimental setup. The inset shows an example of fluctuating trajectory of the tip of the cable, recorded using a high speed camera.

3 RESULTS AND DISCUSSION

Figure 2a shows the velocity standard deviation (STD) of the three configurations in the horizontal coordinate. As similar results are obtained for the vertical coordinate, all the results will be analyzed for this component. Interestingly, the level of fluctuations remains almost null below a threshold of wind velocity of the order of $U^* \simeq 6-7$ m/s. Above this threshold the tip of the cable becomes unstable and fluctuations of velocity are observed to grow as the mean wind speed is increased. The light sphere shows an almost identical scenario, although the instability threshold might be slightly lower. For this last case, the STD also seems to be higher for large enough velocities. The dynamical behavior of the heavy sphere is clearly different than the previous cases. The fluctuation level is about two orders of magnitude lower than that of the polystyrene sphere or the free end (and also one order of magnitude below the natural fluctuation level of the flow). It is therefore concluded that the heavy sphere is always towed in stable conditions.

Further insight can be obtained on the dynamics of the towed system by exploring the Lagrangian power spectral density (PSD) of the velocity as a function of the frequency component f for each configuration. Figure 2b shows the velocity power spectral density (PSD) of the cable tip. A remarkable feature in (figure 2b) is the trend of the spectra to exhibit a clear maximum as the wind velocity U increases. It can also be observed that the first hint of emergence of the spectral peak appears for a mean wind velocity between 6 m/s and 7 m/s, what is comparable to the threshold velocity U^* for which the standard deviation of velocity for the free end was previously noted to start growing. The low frequency f^2 regime holds all the way below the maximum ($f < f_{pk}$). Above the peak ($f > f_{pk}$), the spectral power density decreases rapidly as f^{-4}, indicating an efficient dissipative mechanisms of high frequency fluctuations. Therefore, this broad spectral peak does not correspond to an oscillatory mode of the cable tip. Indeed, the corresponding spectra for the particle displacement remains flat for ($f < f_{pk}$) and is damped as f^{-6} for ($f > f_{pk}$). Hence at the instability onset, the cable tip simply wiggles randomly with no characteristic frequency and the peak frequency f_{pk} is simply related to the high-frequency dissipative cut-off, consistenly with a divergence instability.

The light towed sphere (figure 2c) shows some similarities but also clear distinctions compared to the free end case. The same regimes as for the free end case are observed. It can also be appreciated the growth of a clear peak above a threshold mean wind velocity of the order of 5-6 m/s. However, the peak is much sharper and clearly defines a resonant frequency f_{pk}. On the other hand, the spectral analysis of the velocity of the heavy sphere reveals a completely different landscape (figure 2d). The dynamics is clearly dominated by slow fluctuations with a resonant frequency peak f_{pk} around 1 Hz, which increases with the mean towing velocity U. While at low frequencies the spectra follows a f^2 regime, the high frequency damping seems less steep than for the free end and light sphere cases and roughly follows a f^{-3} regime. Several

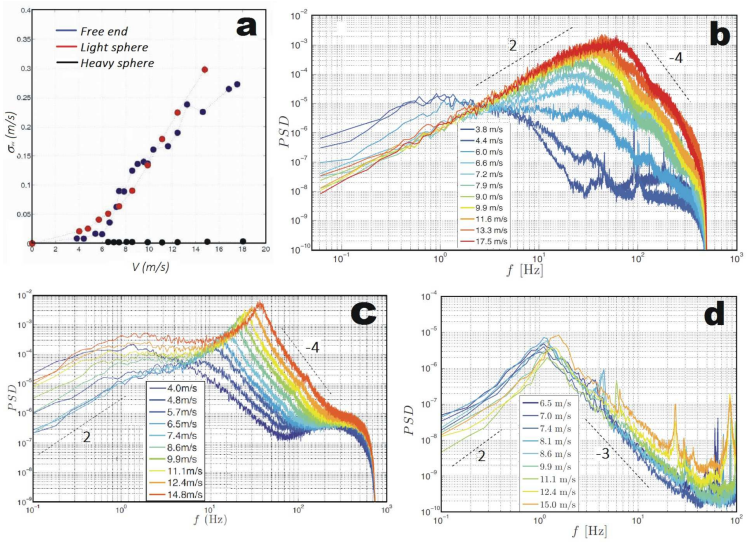

Figure 2: Velocity STD's for the thre configurations (a). Velocity PSD for the free end (b), the light sphere (c) and the heavy sphere (d).

narrow peaks are also observed for frequencies above f_{pk} which are probably to be related to spurious noise.

With the fluctuations and spectral analysis is now possible to make some concluding remarks. Though the standard deviations of the velocity of the free end and the light particle were found to be of the same order of magnitude in figure 2a, the PSDs in figure 2b&c show that this results from a spurious compensation effect: slow fluctuations are order of magnitude larger for the light sphere, while rapid fluctuations are stronger for the free end. It is conluded from this work that there is a *flutter* type instability for the sphere, with a dominant oscillatory motion, while the cable alone develops a *divergence* type instability with random fluctuation. The heavy sphere remained stable for all the towing velocities. A remarkable result of this work, is that depending on the type of the sphere towed, the fluctuations level of the tip may be enhanced (light sphere) or drastically reduced (heavy sphere), a fact of extreme importance considering applications.

REFERENCES

[1] A P Dowling. The dynamics of towed flexible cylinders Part 1&2. Journal of Fluid Mechanics, **187:507–571**, 1988.

[2] Y. W. Jun, K. R. Hall, A. G. Bennett, and P. D. Bridges. Optimal guidance for airborne cable pickup system. In Proceedings of the guidance and control conference, pages 379–384, Seattle, Washington, 1984.

[3] M. P. Paidoussis. Fluid-Structure Interactions: Slender Structures and Axial Flows - Vol. 2. Elsevier, 2003.

[4] C. C. Ni and R. J. Hansen. An experimental study of the flow-induced motions of a flexible cylinder in axial flow. Journal of Fluids Engineering, **100(4):389–395**, 1978.

[5] K. Sudarsan, S. K. Bhattacharyya, and C. P. Vendhan. An experimental study of hydroelastic instability of flexible towed underwater cylindrical structures. In ASME, editor, Proc. 16th OMAE Conf., pages 73–80, Yokohama, Japan, 1997.

MODEL SELECTION FOR THE EQUATION OF MOTION

M. Ruzek[1*] , J.-L. Guyader[1] and C. Pézerat[2]

[1]Laboratoire Vibrations Acoustique
INSA Lyon, 25 Jean Capelle, 69621 Villeurbanne, France
Email: michal.ruzek@insa-lyon.fr, jean-louis.guyader@insa-lyon.fr

[2]LUNAM Université, Université du Maine
CNRS UMR 6613, LAUM, ENSIM,
avenue Olivier Messiaen 72085 LE MANS cedex 9, France
Email: charles.pezerat@univ-lemans.fr

ABSTRACT

This paper deal with the problem of model selection applied to the vibration. The goal of this research is to identify the most appropriate model (represented by its equation of motion) for given experimental measurements. This research is motivated by a necessity to describe the behaviour of structures whose model is either not known, or there may be more candidate models. Model selection techniques do some trade-off between the model precision and complexity. Two model selection techniques are investigated: Akaike information criterion (AIC) and cross validation technique. Every one of them is associated with a particular inverse problem. Experimental example of stretched paper membrane is examined and appropriate model is identified. It is shown that the natural choice of a membrane model is by far less adequate than Kirchhoff model. The best model is identified as Kirchhoff model with membrane effects.

1 INTRODUCTION

Model selection is a relatively new discipline in the applied statistics. Its goal is to choose an appropriate mathematical model from given experimental measurement. There is no unique criterion for a model selection in general. A suitable technique used in the model selection depends largely on the mathematical nature of the studied problem.

A typical model selection problem is schematically shown in Figure 1. After having chosen a finite set of candidate models $\mathbf{M}$=[M_1,M_2,...,M_n] we apply some inverse technique to fit the experimental measurements with each model. The resulting fit of these models is then processed by some model selection criterion which chooses the appropriate model based on the experimental data. It should be noted that the initial selection of the set of candidate models is of principal importance, however, there exist no general rule how to make this choice. It is always based upon preliminary experience (for example [1]).

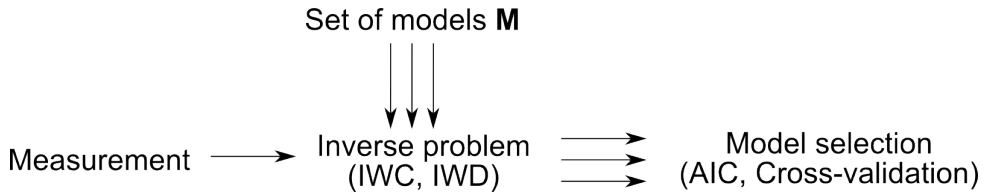

Figure 1. General scheme of the model selection chain.

A standard example of a model selection problem would be to choose an optimal fitting curve to some data. In this case we have some discrete data obtained by measurement and several possible fitting curves in the set **M**. The inverse problem is represented by the method of the least squares. The model selection then examines the residuals of the fitted models and the complexity of the models. The aim of the model selection would be to choose a model which is the sufficiently precise without being unstable.

In this paper the measurement is represented by a steady-state vibration field of some 2D structure like a plate or membrane. The candidate models **M** are different equations of motion. Two inverse techniques are considered: *Inverse wave correlation* and *Inverse wave decomposition*. Each method leads to a different model selection technique. The first is associated with Akaike information criterion (AIC) and the second with a cross validation.

2 INVERSE METHODS

Two different inverse methods are employed. Their similitude is they can both be applied on a semi-local vibration field and the knowledge of the boundary conditions and geometry is not necessary.

2.1 Inverse wave correlation (IWC)

The *Inverse wave correlation* was developed in the PhD thesis of Berthaut (for reference see for example [2]). This method estimated the natural wave number from finite vibration field (see Fig.2A). The idea is to correlate the vibration field with a plane wave travelling in some direction (see Fig.2B above). The coefficient of this correlation is called IWC. This coefficient should be maximal when the wave number of the plane wave equals the natural wave number of the equation of motion which is associated with the vibration field (see Fig.2C above). Although this is true only asymptotically when the vibration field is infinite, the method can be used with some caution on finite fields if there are sufficient number of waves. The result of this inverse method is the dispersion curve of the measured structure.

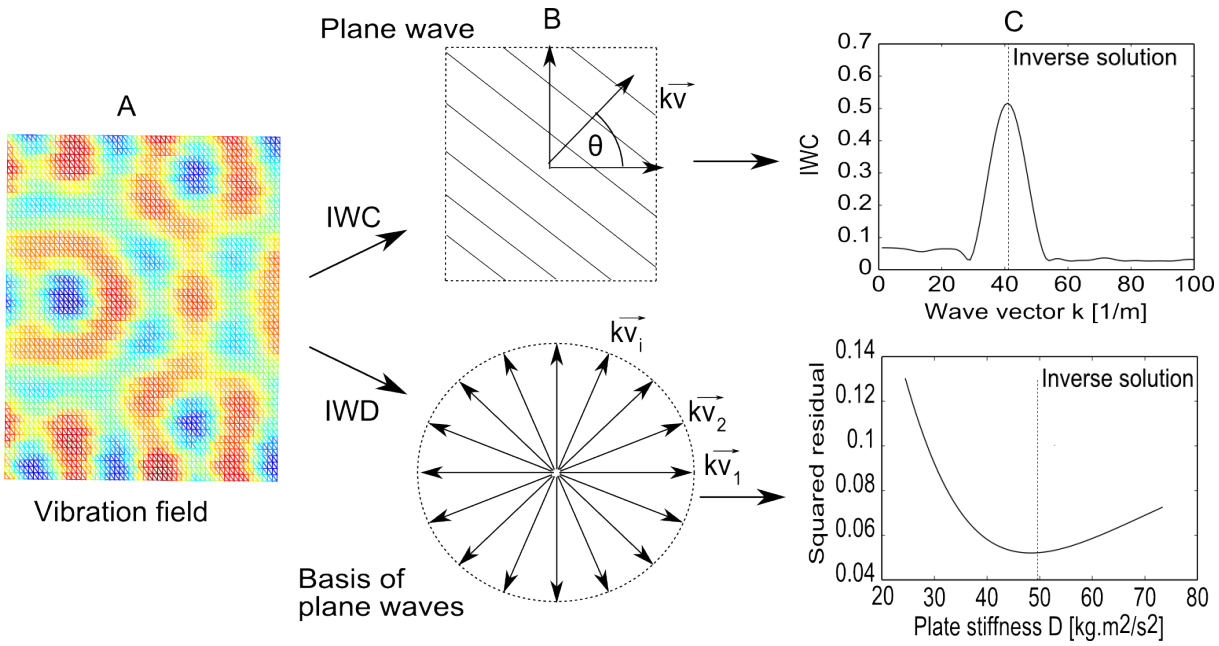

Figure 2. Principle of the IWC and IWD methods.

2.2 Inverse wave decomposition (IWD)

The *Inverse wave decomposition* is based upon the decomposition of the vibration field into a basis of plane waves. It is largely inspired by works of Chardon et al.[3].The difference between IWD and the IWC is that while the field is decomposed to *one* plane wave at a time for the IWC, in the IWD method the field is decomposed to a *linear space* spanned by a number of plane waves (see Figure 2B below). In this linear spaces there are plane waves representing particular solutions of the equation of motion in question. There are propagating as well as evanescent waves. The wave numbers of these waves **k** depend on the parameters of the equation of motion. These parameters are iterated until the minimal residual between the measured field and the plane wave space is found (Figure 2C below). The solution of the IWD inverse method is the optimal parameter of the equation of motion considered. With this parameter the plane wave solutions fit the best the measurement.

3 MODEL SELECTION

Both inverse methods are applied to the vibration measurement of the uniformly stretched paper (see Figure 3 left). Three models (equations of motion) are considered: membrane, Kirchhoff plate and the Kirchhoff/membrane mixed model.

3.1 Akaike information criterion (IWC)

Akaike information criterion or AIC (see [4] for reference) is the model selection criterion based on information theory. It chooses asymptotically the best model in terms of minimizing the modelling error. It can be applied as a post processing of the IWC inverse method. If we suppose that the residuals $\mathbf{r}^{(i)}$ of the i-th IWC model defined as $\mathbf{r}^{(i)} = \mathbf{k}_{IWC} - \mathbf{k}^{(i)}$ are identically independently distributed then $AIC = N \ln \sigma^2 + 2K$. N is the number of measurements and K is number of parameters of i-th model. A model with lower value of AIC is chosen. The absolute value of AIC does not matter, it is only the difference which has statistical importance. In Figure 3 middle we can see the fit of the dispersion curve by the three models and the values of their

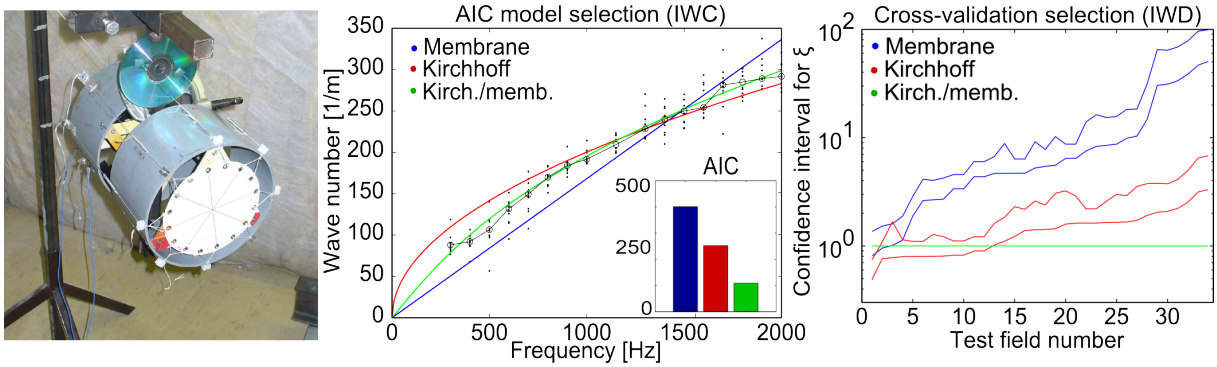

Figure 3: Example of a model selection applied to a thick paper membrane under tension (left).

AIC. The Kirch./membrane model is by far statistically best according to the AIC criterion.

3.2 Cross validation (IWD)

A cross-validation technique is very general method of selecting models. The measurement is divided into two pairs: *training* and *testing* samples. The training sample serves for identification of the model parameter. Then this identified model is tested on the testing sample. This technique is suitable for model selection using the IWD method. Certain vibration fields are used to identify the model parameters and the other are decomposed on the basis wave basis corresponding to the identified model. The goodness of this decomposition indicates how adapted is the model. On Figure 3 right we can see the confidence intervals of $\xi = \mathrm{var}(y)/\mathrm{var}(x)$ where x stands for the IWD residuals of the Kirchhoff/membrane model (which is the best) and y are the residuals the other two models. We can see that for a large majority of fields these residuals are statistically important and $\xi \neq 1$.

4 CONCLUSION

We have introduced the usage of two statistical techniques used in model selection problems in vibration. Each technique is used with appropriate inverse problem. The methodology is demonstrated by identifying the appropriate model for vibration of a stretched paper. Both model selection techniques favour the mixed Kirch./membrane model. It is quite surprising that the membrane model is very little adapted (it is third after the Kirchhoff plate model). This conclusion shows the interest of model selection in the cases where we are not sure about which model is to be used.

REFERENCES

[1] W. Zucchini. An introduction to model selection. *Journal of Mathematical Psychology*, 44(1):41–61, 2000.

[2] J. Berthaut, M.N. Ichchou, and L. Jezequel. K-space identification of apparent structural behaviour. *Journal of sound and vibration*, 280:1125–1131, 2005.

[3] G. Chardon, A. Leblanc, and L. Daudet. Plate impulse response spatial interpolation with sub-nyquist sampling. *Journal of sound and vibration*, 330:5678–5689, 2011.

[4] K.P. Burnham and D.R. Anderson. *Model selection and multimodel inference*. Springer, New York, 2002.

DETERMINATION OF FORCES IN RISERS USED IN THE PETROLEUM INDUSTRY BY INDIRECT MEASUREMENTS

A. Kawano[1] , A. Zine[2]

[1]Escola Politécnica
Universidade de São Paulo (USP), São Paulo, USP
[2]Institut Camille Jordan
Ecole Centrale Lyon, Eculy, France
Email: Abdel-Malek.Zine@ec-lyon.fr

ABSTRACT

Risers are long tubes used to convey fluids, in particular oil, from the sea bottom to the vessel at the water surface. They are subject to several kinds of forces, that are difficult to calculate, for besides the great uncertainties involved, there are no simple mathematical models to predict them. The determination of the loading on the riser is important for model calibration purposes and to estimate remaining fatigue life. In this article we propose a method to infer the spatial distribution of forces acting upon a portion between two sections of a riser from the measurement of the displacement of one of its points and the curvature of the riser at the end points of the portion considered.

1 INTRODUCTION

One of the most challenging problems we currently face is how to produce the huge amount of energy that is required to support human needs with less risk of damaging our planet. After the recent nuclear accidents, the option for petroleum is favored again, since in the near future alternative sources can not supply all the energy we consume.

In particular, about 65% of the area encompassed by the Brazilian Oil Company Petrobras' exploratory blocks are located offshore and at water depths of more than 400 m. For this reason, research is necessary to understand the mechanics of the tubes used to bring oil and gas to the surface. The part of a tube that is not permanently in contact with the sea bottom is called riser. A riser is subjected to many kinds of forces. They may originate from the movements of the production vessel or from sea currents and waves. To have an idea of the complexity of calculating the induced forces, it suffices to mention the vortex induced vibration effect. For Reynolds numbers greater than 40, a cylinder subject to a transverse fluid flow starts to exhibit the vortex shedding effect which induces vibration in the structure, that in its turn changes the flow around the cylinder in a non-linear interaction. Other important forces are those due to the contact of the riser with the bottom and in the region that it is connected to the surface vessel.

A riser moves, vibrates and this causes fatigue of the material, which is the main cause of riser failures, that may lead to an ecological disaster. To keep the risks low and reliability high, basically there are two interrelated measures. The first is to monitor the level of loading which generates mechanical stress, and the second is to use the collected data to improve future designs by improving future design codes. The ideas contained in this paper can be applied to both measures. Here we present a method to determine the loading that acts over a span of a riser. The information gathered can be used to validate fatigue life prediction analysis, or to infer the remaining fatigue life.

A portion of a riser that spans some meters long can be modeled as a Euler-Bernoulli beam under tension. The load determination is viewed as an inverse problem related to vibrating beams. Damage detection in beams has been studied, among others, by Barcilon [1], Mclaughlin [2], Morassi [3], and Nicaise and Zair [4]. Here we employ a new method based on almost periodic distributions [5].

The central equation in this inverse problem is

$$\begin{cases} \rho\dfrac{\partial^2 w}{\partial t^2} + \nu\dfrac{\partial w}{\partial t} + EI\dfrac{\partial^4 w}{\partial x^4} - T\dfrac{\partial^2 w}{\partial x^2} = g(t)f(x), & \text{in }]0,T_0[\times]0,L[\\ w(0,x) = \frac{\partial w}{\partial t}(0,x) = 0, & \forall x \in]0,L[\\ w(t,x) = \frac{\partial^2 w}{\partial x^2}(t,x) = 0, & \forall t \in]0,T_0[,\ \forall x \in]0,L[, \end{cases} \tag{1}$$

where $g \in \mathcal{C}^1([0,T_0])$ is a given function with $g(0) \neq 0$ and w is the displacement. The physical parameters are: E is the Young Modulus, I is the moment of inertia of the cross section, ρ is the material's linear density, ν is the damping coefficient, and T is the tension force along the cable. The Young Modulus and the material's density must be calculated and used as equivalent values, for in general a riser comprises several layers of steel and plastic.

We are interested in determining $f \in \mathrm{H}^{-1}(]0,L[)$. The data available in this inverse problem is the set

$$\Gamma_{T_0,x_0} = \{w(t,x_0) \,:\, t \in]0,T_0[\}\,, \tag{2}$$

where $]0,T_0[$ is an arbitrary non empty open set and $x_0 \in \{x \in]0,L[: \sin(n\pi x) \neq 0,\ \forall n \in \mathbb{N}\}$.

2 THE DIRECT PROBLEM

Consider the set of functions $\{S_n \,:\, n \in \mathbb{N}\}$, $S_n : [0,L] \to \mathbb{R}$, defined by $S_n(x) = C_n \sin(\frac{n\pi x}{L})$, $C_n \in \mathbb{C}$. We know that $\{S_n \,:\, n \in \mathbb{N}\}$ is orthogonal and dense in $\mathrm{H}_0^1(]0,L[)$, as well as or-

thonormal in $\mathrm{L}^2(]0,L[)$. It follows easily that $\| S_n \|_{\mathrm{H}^1_0(]0,L[)} = \frac{n\pi}{L} \| S_n \|_{\mathrm{L}^2(]0,L[)} = \mathcal{O}(n)$.

The set $\left(\frac{S_n}{n}\right)_{n\in\mathbb{N}}$ forms an orthonormal Hilbert basis of $\mathrm{H}^1_0(]0,L[)$, and any function in $\mathrm{H}^1_0(]0,L[)$ can be expressed as $\sum_{n=1}^{+\infty} \frac{A_n}{n} S_n$, with $(A_n)_{n\in\mathbb{N}} \in \ell^2$. From duality pairing, we see that Any distribution $h \in \mathrm{H}^{-1}(]0,L[)$ can be represented uniquely as $h = \sum_{n=1}^{+\infty} \tilde{A}_n n S_n$, with $(\tilde{A}_n)_{n\in\mathbb{N}} \in \ell^2$. Now we use $\{S_n : n \in \mathbb{N}\}$ to represent the spatial distribution $f \in \mathrm{H}^{-1}(]0,L[)$ as $f = \sum_{n=1}^{\infty} A_n S_n$, with $(A_n/n)_{n\in\mathbb{N}} \in \ell^2$.

By the method of separation of variables, after some manipulation, we obtain that

$$w(t,x) = \int_0^t g(t-\tau) \left[\mathrm{e}^{-\frac{1}{2}\frac{\nu}{\rho}\tau} \sum_{n=1}^{\infty} \frac{A_n}{\omega_n} \sin(\omega_n \tau) S_n(x) \right] \mathrm{d}\tau, \tag{3}$$

for $t \in [0,T_0]$ and $x \in [0,L]$, where $\omega_n = \sqrt{\beta_n - \left(\frac{\nu}{2\rho}\right)^2}$, $\beta_n = \frac{EI}{\rho}\left(\frac{n\pi}{L}\right)^4 + \frac{T}{\rho}\left(\frac{n\pi}{L}\right)^2$. Moreover, it can be proved that for any $t \in [0,T_0]$, the traces of ω at the boundaries are well defined, and that $w \in \mathcal{C}([0,T_0], \mathrm{H}^1_0(]0,L[)) \cap \mathcal{C}^1([0,T_0], \mathrm{H}^1_0(]0,L[))$.

3 THE INVERSE PROBLEM

By using a result found in [4], it can be proved that (3) together with the data $\Gamma_{T_0,x_0} = \{0\}$ implies that

$$\sum_{n=1}^{\infty} \frac{A_n}{\omega_n} \sin(\omega_n \tau) S_n(x_0) = 0, \quad \forall \tau \in [0,T_0[. \tag{4}$$

Now we invoke a theorem for the uniqueness of the sequence of coefficients in an almost periodic distribution posed in a form like (4). The following result is from [5]. We recall that a sequence $(\lambda_n)_{n\in\mathbb{N}} \subset \mathbb{C}$ is uniformly discrete if there is an $\epsilon > 0$ such that $p \neq q \Rightarrow |\lambda_p - \lambda_q| > \epsilon$, and s' is the space of slowly growing sequences. That is, if $(a_n)_{n\in\mathbb{N}} \in s'$, then $\exists q \in \mathbb{Z}_+$ such that $(n^{-q} a_n)_{n\in\mathbb{N}} \in \ell^1$.

Theorem 1. Given $\Lambda = (\lambda_n)_{n\in\mathbb{N}}$, uniformly discrete, is such that $\exists n_0 \in \mathbb{N}$, $\exists C \in \mathbb{R}_+$ such that $n > n_0 \Rightarrow |\lambda_n| > C n^\alpha$, if $\alpha > 1$ and $(a_n)_{n\in\mathbb{N}} \in s'$, that is $\exists q \in \mathbb{Z}_+$ such that $(n^q a_n)_{n\in\mathbb{N}} \in \ell^1$, then if there is a $\tau > 0$ such that $\sum_{n\in\mathbb{N}} a_n \mathrm{e}^{i\lambda t} = 0, \forall t \in [-\tau,\tau]$, then $(a_n)_{n\in\mathbb{N}} = \{0\}$.

Now apply theorem 1 to (4) to conclude that $A_n = 0$. We conclude that the data $\Gamma_{T_0,x_0} = \{0\}$ is enough to determine uniquely $(A_n)_{n\in\mathbb{N}}$, and consequently the distribution $f \in \mathrm{H}^{-1}(]0,L[)$ in (1).

To summarize, we have just proved the following uniqueness result.

Theorem 2. In problem (1), with $g \in \mathcal{C}^1([0,T_0])$, $T_0 > 0$, $g(0) \neq 0$, the data $\Gamma_{T_0,x_0} = \{w(t,x_0) : t \in]0,T_0[\}$ is enough to determine uniquely $f \in \mathrm{H}^{-1}(]0,L[)$ in (1).

To illustrate the theory above we show some numerical experiments. Consider a span of $L = 100m$ of a riser that can be modeled as a beam under traction with the following parameters (all values are in the metric system, SI): $EI = 2.7 \times 10^7$, $\rho = 1.3 \times 10^1$, $T = 5.0 \times 10^5$, $\nu = 0.1$. The excitation force used to simulate the dynamics of the riser is $\cos(\tilde{\omega}_1) g(x)$, with $g(x) = \sum_{j=1}^{15} A_n \sqrt{2/L} \sin(\pi j x/L)$, $(A_n)_{n=1,\ldots 15} = (3.64186, -2.94632, -0.463688, 2.03586, -0.900316, -0.143288, -0.198724, 0.388815, 0.404651, -0.900316, 0.331078, 0.25921, -0.107005, -0.061409, -0.300105)$.

Function g is an approximation for an unit uniformly distributed load spanning from $x = 0.5L$ and $0.8L$. Of course, since the problem is linear, it suffices to multiply the excitation

by a constant factor to obtain more realistic displacement values. The measurements are done in intervals of time of $T_0 = 10$, $T_0 = 30$ and $T_0 = 60$ seconds at point $x_0 = 0.31L$. The function $w(t, x_0)$ generated with the data above is shown in figure 3. A random noise uniformly distributed over $[-\epsilon, \epsilon]$, $\epsilon = 0.01$ was added to $w(t, x_0)$. This disturbed data is used for the recovery of the first five elements of (A_n). The results from the recovery process are shown in figures 2(a) and 2(b).

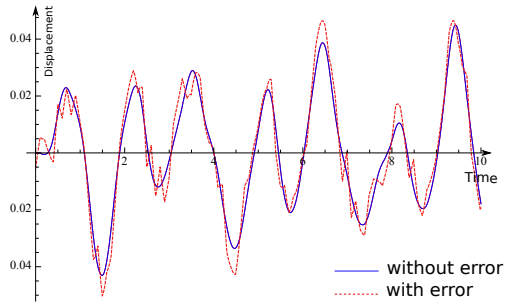

Figure 1. Displacement $w(t, x_0$ without and with error.

REFERENCES

[1] V. Barcilon. Inverse Problem for the Vibrating Beam in the Free–Clamped Configuration. *Philosophical Transactions of the Royal Society of London. Series A, Mathematical and Physical Sciences (1934-1990)*, 304(1483):211–251, February 1982.

[2] Joyce R Mclaughlin. An Inverse Eigenvalue Problem of Order Four. *SIAM Journal of Mathematical Analysis*, 7(5):646–661, 1976.

[3] Antonino Morassi. Damage detection and generalized Fourier coefficients. *Journal of Sound and Vibration*, 302(1-2):229–259, 2007.

[4] Serge Nicaise and Ouahiba Zair. Determination of point sources in vibrating beams by boundary measurements: Identifiability, stability, and reconstruction results. *Electronic Journal of Differential Equations*, 2004(20):1–17, 2004.

[5] A Kawano and A Zine. Uniqueness and nonuniqueness results for a certain class of almost periodic distributions. *SIAM Journal of Mathematical Analysis*, 43(1):135–152, 2011.

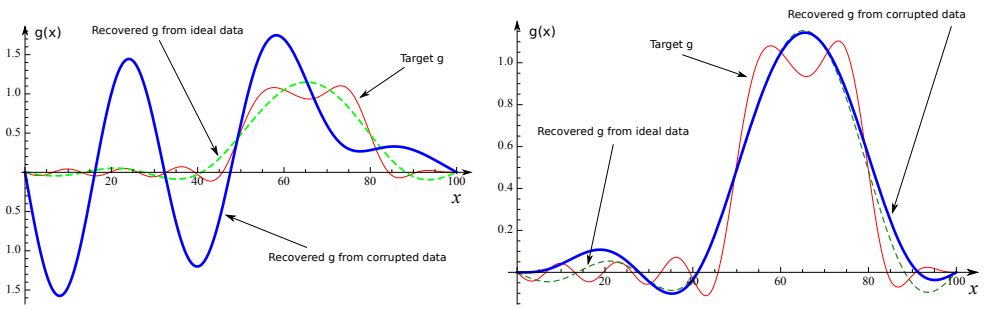

(a) Recovered g with $T_0 = 10$ seconds. (b) Recovered g with $T_0 = 60$ seconds.

Figure 2. Recovery of f.

IS HIGH-SPEED DIGITAL HOLOGRAPHY THE ULTIMATE TOOL FOR VIBRATION ANALYSIS?

J. POITTEVIN[1,2], P. PICART[1], F. GAUTIER[1] , C. PEZERAT[1],

[1]L'Université Nantes Angers Le Mans, Université du Maine,
CNRS UMR 6613, Laboratoire d'Acoustique de l'Université du Maine
Avenue Olivier Messiaen, 72085 LE MANS, FRANCE

[2]Institut de Recherche Technologique Jules Verne
Chemin du Chaffault, 44340 BOUGUENAIS, FRANCE

Email: julien.poittevin@univ-lemans.fr, julien.poittevin@irt-jules-verne.fr
pascal.picart@univ-lemans.fr
francois.gautier@univ-lemans.fr
charles.pezerat@univ-lemans.fr

ABSTRACT

Structural vibration can be measured with optical digital holography. Such a technical provides measurements with very high spatial resolution. Using high speed camera, it can also be implemented in the time domain to investigate non stationary problem. Four different regimes can be found in the literature for the digital holography : the time averaging regime, the pulse regime, the pseudo-pulse regime and the quasi-time averaging. Parameters constraining the design of the set-up are listed and a discussion on how the set-up can be optimized is provided.

1 STATE OF THE ART

Structural vibrations are usually measured using accelerometers or laser-vibrometers. Accelerometer is an intrusive sensor as vibrometer doesn't. Both provide point-wise measurements. To avoid the need for scanning other measurement points, optical digital holography is useful and allow to provide full-field measurements. However, this method is mainly limited to stationary vibratory fields.

In 1948, Dennis GABOR [1] invented a method for recording and reconstructing the full amplitude of a wave-field. He called his method "holography". Historically, vibration analysis with optical holographic techniques started with the works of Powell and Stetson [3], which first established the principle of time-averaging and the possibility of studying vibrations. A full bibliographical review is provided in [3]. The first applications were described, showing a large variety of possibilities: tympanic investigations, vibration measurements of plates, mode discrimination or study of loudspeaker membranes. Hybrid techniques combining heterodyne holography with time-averaging or frequency shifting were also proposed recently [3]. At LAUM, digital holographic methods for vibration analysis has been investigated. Illustrative examples are given : Fig.1a) shows the time averaging method applied to detect default in the resonant mode of a dome loudspeaker [4]; Fig.1b) illustrates the stroboscopic pulsed regime applied to the investigation of high amplitude auto oscillation of a clarinet reed under playing conditions [4]; Fig.1c) shows the measurement of the amplitude of a loudspeaker using the pseudo-pulsed regime [5]. Fig.1d) shows application of the quasi-time averaging regime to the visualization of acoustic waves propagating at the surface of human skin [3]). Simultaneous multidimensional vibration measurements are also possible [6].

The stationary regime is a particular case which is useful for investigating the structure vibratory behaviour. Usually, characterisation of structures under operational or real functioning conditions requires analysis in the time domain. As examples, problems that can not be addressed by a stationary approach are : vibrations of panels induced by hydro or aeroacoustic sources, structural vibration induced by squeak and rattle noise. Nowadays, performances of high power continuous wave lasers (>6W) and high speed CMOS sensor (rate up to 100kHz) have been improve in a very significant way since 10 years. These new technologies give the opportunity of bringing back digital holography and vibration analysis. We would like to take the opportunity of the MEYDINA meeting to discuss about the capability of high speed digital holography to investigate non stationary vibration problems.

2 PRINCIPLE OF HOLOGRAMS RECORDING

Basically, digital holography consists in recording an interference pattern using a sensor arranged as a matrix of pixels. In the set-up, the structure under interest is illuminated by a laser beam, which is scattered by the object. This laser beam interferes with a reference beam at the sensor plane. Then, the hologram is reconstructed by numerically calculating diffraction propagation, and the optical phase of the numerically diffracted field are the purpose of this metrology. The main parameter for vibration analysis is related the exposure time during which the sensor is accumulating photons from the surface of the object. The cyclic ratio defined by $R_c = T/T_0$, which is the ratio between the exposure time T and the vibration period T_0 of the stationary vibration. The cyclic ratio influences the error-free vibration reconstruction from a digital holographic sequence [2]. Three cases of regime have to be distinguished.

Now, the Stroboscopic Pulsed regime or Pseudo-Pulsed regime ($R_c << 1$), the recording regime uses light pulses and is equivalent to a freezing of the object at the instant at which the recording is performed ("impulse regime") [4]. This regime enables the vibration amplitude

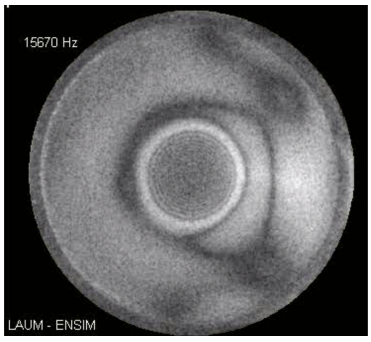

(a) Time-Averaging Regime

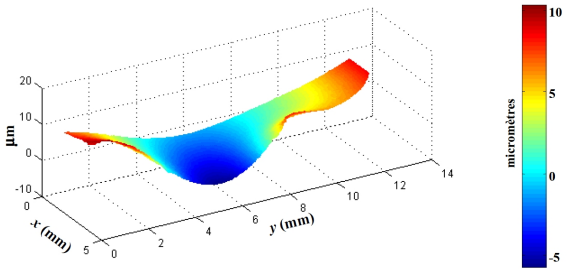

(b) Pulsed Regime

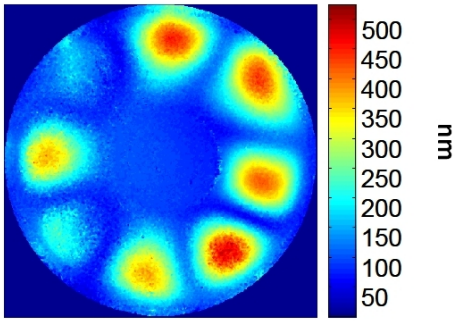

(c) Pseudo-Pulsed Regime

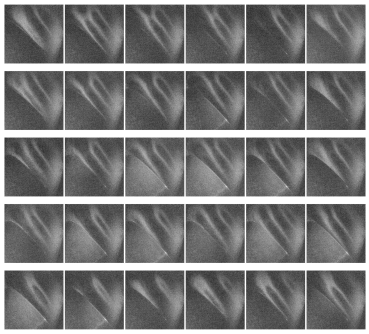

(d) Quasi-Time-Averaging Regime

Figure 1: Illustration of holograms result. (a) Vibration mode of a loudspeaker (from [6]). (b) Amplitude auto oscillation displacement of a clarinet reed (from [4]). (c) Amplitude displacement of a loudspeaker (from [5]). (d) Sequence of 30 successive images over time of surface acoustic waves on the human skin (from [3]).

to be measured with high precision. The regime is based on synchronization between the acquisition and the excitation (see illustrations in fig 1b and fig 1c).

The intermediate case, Quasi-Time-Averaging Regime, for which $0 << R_c < 1$. The cyclic ratio is too high to be classified as "impulse" and too short to be considered as "time-averaging". The vibration amplitude can be measured using some assumption [3]; illustration on the visualisation of the mechanical behaviour is given in fig 1d).

3 HOW TO DESIGN A METROLOGICAL TOOL FOR VIBRATION ANALYSIS?

The design of an optical set-up for vibration analysis depends on the regime chosen for the holograms recording. Assuming that the frequency band of the vibration signal has an upper limit, f_{max}, the type of regime is given by $R_c = T \times f_{max}$. A pulse regime would be the best configuration, implying $T < 1/f_{max}$. Such a condition depends on numerous parameters which are listed in Table 1.

These parameters are closely correlated one with each other. The frame rate of the sensor is strongly influencing the time resolution but it also influences the exposure time, the min/max cyclic ratio, spatial resolution, so the mechanical wave number, the laser power and then the object size, distance to sensor and pixel surface.

A detailed analysis explaining how the cyclic ratio is depending on the parameters is necessary to design the set-up which should be able to work in the complete audio range [20 Hz - 20 kHz].

We aim at presenting useful relationships for designing the optical set up. Preliminary

	Parameters	Influence
Sensor	bit number	Detection sensitivity, measurement noise
	Pixel surface	Spatial resolution, recording distance
	Frame rate	Time resolution, spectral aliasing
	Exposure time	Frame rate, maxi/min cyclic ratio, Spectral aliasing, measurement errors
	pixel number	Spatial resolution, maximum frame rate
Laser	Power	recording distance, spatial resolution
	wavelength	Spatial resolution, vibration sensitivity, measurement dynamics
Object	surface	Laser power, recording distance, spatial resolution
	sensor distance	Spatial resolution, detection sensitivity
	albedo	Detection sensitivity, laser power
	mechanical wave-number	Spatial resolution, pixel surface, pixel number
	spectrum	Max frame rate, cyclic ratio, spectral aliasing
	amplitude	frame rate, spatial resolution, vibration sensitivity

Table 1. Parameters constraining the design of recording holograms.

experimental results demonstrating the feasibility of high speed digital holography for vibration measurements will be shown.

4 CONCLUSION

This paper presents a brief state of the art of the different optical holographic methods existing in literature for the measurement of vibrations. The methods are based on stationary recordings and are suitable only for vibration measurements in stationary regime. So as to pave the way to full-field contact-less vibration investigations in transient regime, we have targeted the set of influence parameters that need to be taken into account to develop the next generation tool for vibration analysis.

REFERENCES

[1] D. Gabor et al. A new microscopic principle. *Nature*, 161(4098):777–778, 1948.

[2] T. Kreis. Holographic interferometry: Principles and methods. 1996.

[3] M. Leclercq and al. Evaluation of surface acoustic waves on the human skin using quasi-time-averaged digital fresnel holograms. *Appl. Opt.*, 52(1):A136–A146, Jan 2013.

[4] J. Leval. *Etude et développement de capteurs holographiques numériques pour l'analyse des vibrations*. PhD thesis, Université du Maine, Le Mans, 2006.

[5] J. Leval, P. Picart, J.P. Boileau, and J.C. Pascal. Full-field vibrometry with digital fresnel holography. *Applied optics*, 44(27):5763–5772, 2005.

[6] P. Tankam. *Méthodes d'holographie numérique couleur pour la métrologie sans contact en acoustique et mécanique*. PhD thesis, Université du Maine, 2010.

DYNAMICS OF A HORIZONTAL AXIS WIND TURBINE BLADE UNDER AERODYNAMIC, CENTRIFUGAL, GYROSCOPIC, AND GRAVITY EFFECTS

A. Hedi HAMDI[1], B. Charfeddine MRAD[2], and C. Rachid NASRI[3*]

[1,2,3]Laboratoire de Recherche Mécanique Appliquée et Ingénierie
Ecole Nationale d'Ingénieurs de Tunis
Université Tunis El Manar
Tunis, TUNISIA
Email: hedi_hamdi@yahoo.fr, Charfeddine.Mrad@enit.rnu.tn, Rachid.Nasri@enit.rnu.tn

ABSTRACT

This work presents an analytic and numeric study of the dynamic response of a horizontal axis wind turbine blade, under aerodynamic and gravitational forces. The blade supposed deformable, is assimilated to a wiry beam of variable section in homogenous and isotropic material, and is discretized in multiple beam elements of constant section. The assembly of these elements constitutes the approximate model of the blade to which the finite element method is applied. The analytic study consists on defining the elementary matrices of mass, stiffness, and gyroscopic coupling, in addition to the elementary vector of applied forces. The numeric study consists on solving the linear system of the vibration of the blade for a practical case, and plotting its dynamic response under the aerodynamic and gravitational forces. The results show that the gyroscopic coupling and the own weight give alternating deformations to the blade, which cause fatigue for the blade and turbulence for the wake.

INTRODUCTION

In [1], we studied the free vibration of a short blade under a sudden variation of the wind speed, and we want in this work to expand the study to the forced vibration of a long blade, thus of non negligible weight. [2] uses the 3D beam theory with transverse shear and the membrane effect to write the vibration equations of the blade. [3] utilises the thin shell theory to write the motion equations of the blade and studies the effect of the column vibration on the blade dynamic behaviour. [4] proposes a procedure to analyse the vibration of a blade in the case of linear deformation with transverse shear. [5] studies the effect of gravitational forces with centrifugal hardening on a blade and proposes a technologic solution to control this type of vibration. [6] presents an approach to study the gyroscopic effect on the dynamic response of a floating wind turbine blade. In this work, we wish to study the effect of the gyroscopic coupling and the own weight on the dynamics of a blade.

1 FORMULATION

Figure 1, the blade rotation speed Ω, and the inclination angle δ of the wind turbine rotor relatively to a horizontal reference.
Figure 2, referring to an Euler description of the displacement of a blade element of length *dx* and situated at a distance *x* of the rotor rotation axis, u is the lengthening, v et w are the bending, α is the rotation, β is the precession, and γ is the nodding, of this element.
Figure 3, further to the incidence angle *i* , the relative speed of the air flow V_r is, *V* is the absolute speed:

$$V_r = \sqrt{V^2(1-a)^2 + x^2\Omega^2(1+a')^2}$$

The blade vibration is governed by the following equation:

$$\boldsymbol{M_e}\ddot{\boldsymbol{q}} + \boldsymbol{C_e}\dot{\boldsymbol{q}} + \boldsymbol{K_e}\boldsymbol{q} = \boldsymbol{P_e}(\boldsymbol{t}) + \boldsymbol{F_a} + \boldsymbol{F_c}$$

We obtain the displacement vector $\boldsymbol{q}$ of the blade related to the nodal displacement, after discretization and interpolation.
We determine the mass matrix, the stiffness matrix, and the gyroscopic coupling matrix.
We determine the aerodynamic forces: Lift, Drag, and Pitch. Last, we determine the gravitational forces: Centrifugal and Gravity.

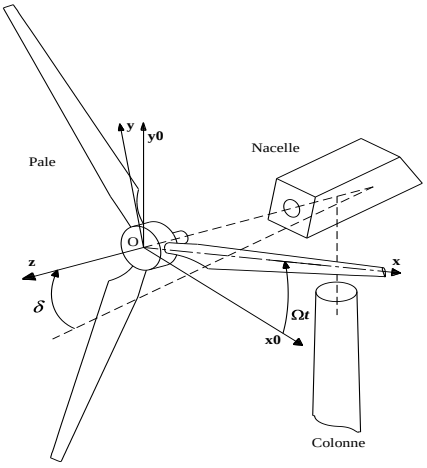

Figure 1. Wind turbine parameterization

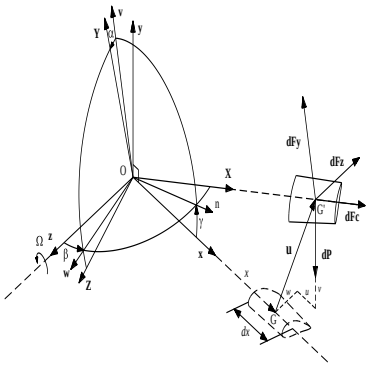

Figure 2. A blade element

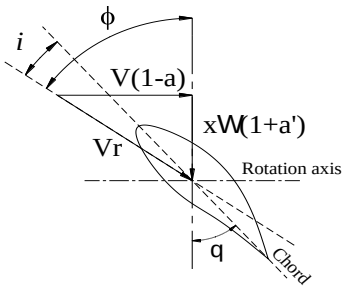

Figure 3. Air flow

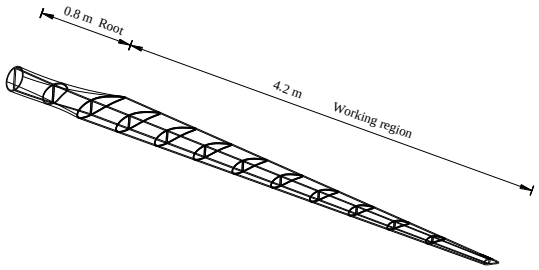

Figure 4. Studied blade

The elementary aerodynamic forces are expressed as:

$$dF_y = \frac{1}{2}\rho_a C_y c V_{\mathbf{r}}^2 dx \;;\; dF_z = \frac{1}{2}\rho_a C_z c V_{\mathbf{r}}^2 dx \;;\; dM = \frac{1}{2}\rho_a C_x c^2 V_{\mathbf{r}}^2 dx$$

The elementary centrifugal force is defined as:

$$dF_x = \rho S x \Omega^2 dx$$

The weight vector ***dP*** of an element of the blade of chord c , is composed of three components: dP_x, dP_y, and dP_z; and taking into account the wind turbine rotor inclination:

$$\boldsymbol{dP} = -\rho g S^{\;T}\ \cos\delta\sin(\Omega t),\quad \cos\delta\cos(\Omega t),\quad \sin\delta\ \ dx$$

2 RESULTS

Figure 4, the studied blade has a length of 5m, the skin thickness is 8mm, it is the element of a three bladed turbine of a radius R=5.45m, and a maximum electric power 15kW.
Figure 5: The blade is deforming under alternating Traction-Compression, relatively to (O,x).
Figure 6: The blade is deforming under alternating bending, relatively to (O,y).
Figure 7: The blade is deforming under alternating bending, relatively to (O,z).
Figure 8: The blade is deforming under alternating torsion, relatively to (O,x), without gyroscopic coupling.
Figure 9: The blade is deforming under alternating torsion, relatively to (O,x), with gyroscopic coupling.
Figure 10: The blade is deforming under alternating torsion, without and with the gyroscopic coupling.
The contribution of the gyroscopic coupling is clearly visible.
A frequency analysis (FFT) of the obtained results is useful to identify the present frequencies.

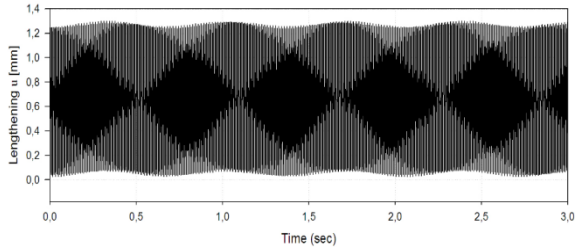

Figure 5. Blade lengthening

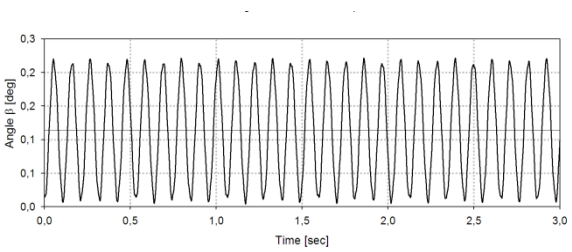

Figure 6. Blade bending, around Oy

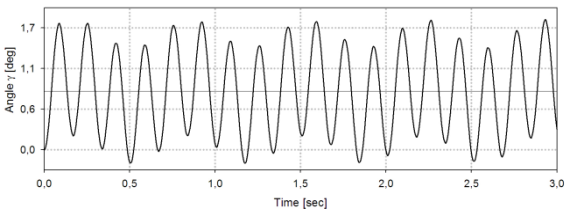

Figure 7. Blade bending, around Oz

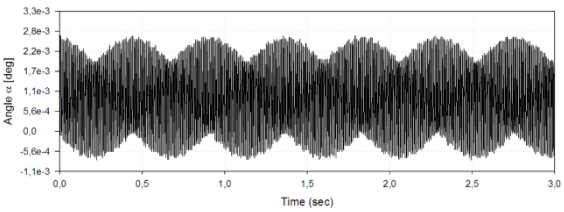

Figure 8. Blade torsion, without Coupling

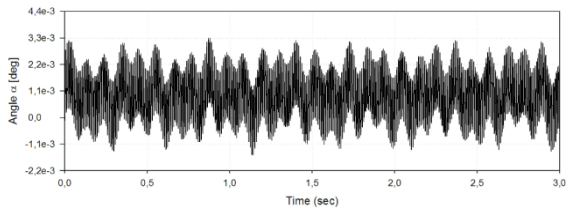

Figure 9. Blade torsion, with Coupling

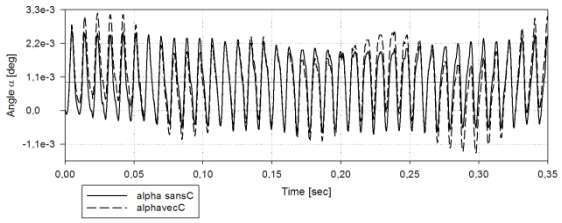

Figure 10. Blade torsion, without and with Coupling

CONCLUSION

The gyroscopic coupling and the own weight generate, during the blade rotation, vibrations of low amplitudes but which persist, which poses the problem of the blade fatigue.
On the other hand, these alternating deformations of the blade affect the air flow, the wake trajectory is no more perfect and becomes snaky helical, which poses the problem of the air flow turbulence.
Some technologic solutions may be considered, as installing an absorber into the blade, to reduce the vibrations and thus their effects.

REFERENCES

[1] H. Hamdi, C. Mrad, R. Nasri, and A. Hamdi. Static and dynamic study of a wind turbine blade with horizontal axis. *Journal of Environmental Science and Engineering*. 5: 1167–1174, 2011.

[2] R. Younsi, I. El Batanony, J. B. Tritsch, H. Naji, and B. Landjerit. Dynamic study of a wind turbine blade with horizontal axis. *European Journal of Mechanics A/Solids*. 20: 241–252, 2001.

[3] W. Jianhong, Q. Datong, and C. L. Teik. Dynamic analysis of horizontal axis wind turbine by thin-walled beam theory. *Journal of Sound and Vibration*. 329: 3565–3586, 2010.

[4] J. H. Park, H.Y. Park, S. Y. Jeong, S. Lee, Y. H. Shin, and J. P. Park. Linear vibration analysis of rotating wind turbine blade. *Current Applied Physics*. 10: 332–334, 2010.

[5] A. Staino, B. Basu, and S. R. K. Nielsen. Actuator control of edgewise vibrations in wind turbine blades. *Journal of Sound and Vibration*. 331: 1233–1256, 2012.

[6] P. Blusseau, and H. P. Minoo. Gyroscopic effects on a large vertical axis wind turbine mounted on a floating structure. *Renewable Energy*. 46: 31–42, 2012.

DYNAMIC ANALYSIS OF SPUR GEAR WITH DEFECTED BEARINGS

Taissir Hentati [1], Mohamed Slim Abbes [1], Radoslaw Zimroz[2], Fakher Chaari [1] and Mohamed Haddar [1]

[1] Dynamics of Mechanical Systems Research Unit.
National Engineering School of Sfax, BP 1173, 3038 Sfax, Tunisia University
Email: taissirhentati@yahoo.fr, slim.abbes@enis.rnu. tn

[2] Wroclaw University of Technology - Poland
Email: radoslaw.zimroz@gmail.com

ABSTRACT

The main idea of this paper is to develop an original modelling of a gear transmission taking into account the time varying gear mesh stiffness and the nonlinear forces exerted by defected ball bearings supporting the transmission. Backlash default realized on the input rolling bearing is considered. The Hertzian contact theory is applied to calculate the elastic deflection and the non linear contact force exerted by the totality of bearings balls on the input and output shafts. The equation of motion is written and solved using the Newmark method coupled with Newton Raphson iterative method (the implicit Newmark-β numerical integration technique). A case study of a single stage spur gear transmission system is presented and analyzed. Parametric studies are performed to show the effect of bearing backlash default on the dynamic behavior of the mechanical system.

1 INTRODUCTION

In rotating machines, rotating contact bearings can operate in several conditions such as bad lubrication and manufacturing or installation problems. Coupled with additional defect, contact bearings are a source of internal excitation. Many researches, in this context, have shown that the nonlinear Hertzian contact forces generate vibrations and noise.

Abbes et al. [1], have developed a theoretical study of the dynamic behavior of helical gears supported by defect element bearings. The performed model is derived to observe the effect of the internal excitation sources such as the gear mesh stiffness fluctuation and the ball bearing waviness on the vibration characteristics of the machine elements.

Sawalhi N. and Randall R.B. [2] have developed a lumped mass parameter model of 34-dofs for a gearbox test rig in order to study the dynamic interaction between gears and defect bearings.

Harsha S.P. [3] theoretically studied the speed effects of a rotor supported by rolling bearings with geometrical imperfections. The results show the manifestation of instability and chaos in the dynamic behaviour as the speed of the rotor-bearing system is modified.

The objective of this study is to perform a theoretical investigation on the dynamic behaviour of spur gears supported by defected element bearings. A global model predicting dynamic behaviour of a gear transmission is developed based on lumped mass parameters. The Hertzian contact theory is applied to calculate the elastic deflection and the non linear contact force exerted by the totality bearings balls on the input and output shafts.

2 MODELLING OF GEAR TRANSMISSION SYSTEM

The study consists in analyzing dynamic behavior of a single stage spur gear transmission supported by two identical ball bearings. Bearings outer races are fixed in the rigid support and the inner races are rigidly assembled to the rotating shafts. The dynamic response will be analyzed in order to show the impact of the bearing backlash on the dynamic behavior of the transmission.

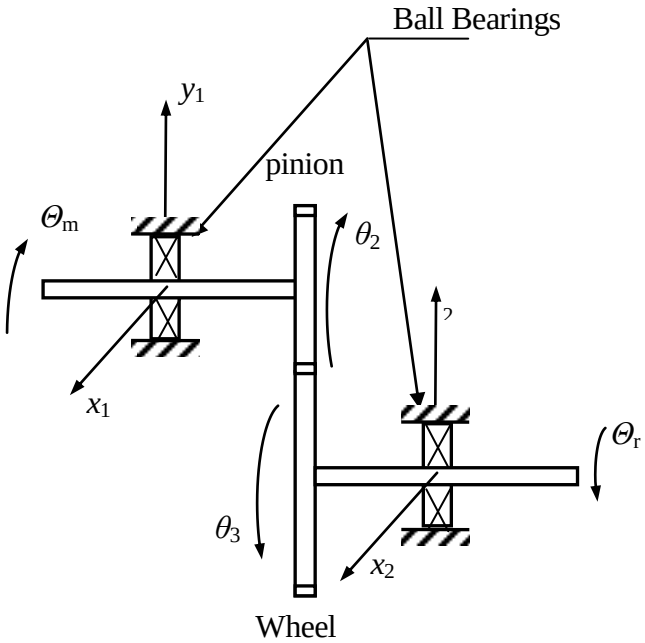

Figure 1. Studied single stage gear transmission.

Lagrange formalism is used to describe the non-linear dynamic behavior of the mechanical system by the following equation of motion.

$$M\ddot{q} + C\dot{q} + \left[K_p + Kg(t)\right] q + Fnlb = Fext(t) \tag{1}$$

where $q = \{x_1, y_1, \theta_m, \theta_1, x_2, y_2, \theta_2, \theta_r\}^T$ is the vector of the degrees of freedom of the system, M represents the mass matrix.
K_p is the bearing torsional stiffness matrix and Kg represents the time-varying gear mesh stiffness matrix given by:

$$Kg(t) = k(t) \cdot G \tag{2}$$

where $k(t)$ is the periodic mesh stiffness obtained through measurement or calculation. For helical gears, trapezoidal waves are often used to approximate the mesh stiffness alternating between n and $n+1$ pairs of teeth in contact. The geometric characteristics matrix G is derived from of the gear pair characteristics:

$$G = \langle X \rangle^t \cdot \langle X \rangle \tag{3}$$

where: $\langle X \rangle = \left[\sin\alpha \quad \cos\alpha \quad 0 \quad r_{b1} \quad -\sin\alpha \quad -\cos\alpha \quad r_{b2} \quad 0\right]$
r_{b2} and r_{b1} denotes the base circle radii of gear and pinion, α is the pressure angle
C is the proportional damping matrix given by :

$$C = a\,M + b\,K_p \tag{4}$$

$Fext(t)$ is the external applied torques vector given by:

$$Fext(t) = \{0 \;\; 0 \; C_m(t) \;\; 0 \; 0 \; 0 \; 0 \; -C_r(t)\}^T \tag{5}$$

in which $C_r(t)$ is the loading torque and $C_r(t)$ the driving torque.
$Fnlr$ represent the nonlinear forces exerted by the rolling bearings given by:

$$Fnlb = \left\{ \sum_{j=1}^{N_b} -K\,\Delta_{1_j}^{1,5} \cdot \cos\psi_j \quad \sum_{j=1}^{N_b} -K\,\Delta_{1_j}^{1,5} \cdot \sin\psi_j \quad 0 \quad 0 \quad \sum_{j=1}^{N_b} -K\,\Delta_{2_j}^{1,5} \cdot \cos\psi_j \quad \sum_{j=1}^{N_b} -K\,\Delta_{2_j}^{1,5} \cdot \sin\psi_j \quad 0 \quad 0 \right\}^T \tag{6}$$

where K is the Hertz contact constant, ψ_j is the ball angular position and Δ_{BBNB_j} represents the elastic deformation of the j^{th} rolling element of the *BBNB* ball bearing. A negative elastic deformation means that no contact occurs between ball and the two races. In this case the elastic deformation is considered as null. The radial elastic deformations can be written as following:

$$\Delta^*_{BBNB_{ij}} = \left(x_{1,2} + x_{backlash}\right)\cos\psi_j + \left(y_{1,2} + y_{backlash}\right)\sin\psi_j + d_{BBNB_0} \tag{7}$$

Each of the ball bearings has two radial degrees of freedom called $\{x_1, y_1\}$ for the input bearing and $\{x_2, y_2\}$ for the output one. $x_{backlash}$ and $y_{backlash}$ denotes backlash default realized on the input or output rolling bearing.

3 NUMERICAL SIMULATIONS

The system investigated in this paper is shown in fig. 1. We are interested to analyze vibrations generated by a gear coupled to two shafts bearing system in the presence of faults.

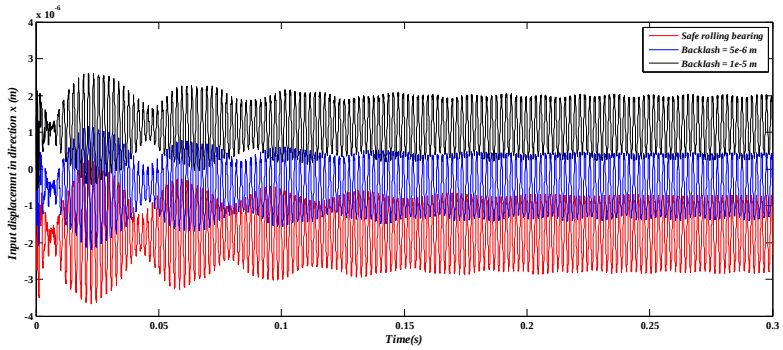

Figure 2. Input and output displacements in direction *x*

Output displacements in direction *x* are given in figure 2 for the defected rolling bearing. We note that the input displacement (corresponding to the defected bearing) increase with respect with the backlash value, where the output displacement is unchanged.

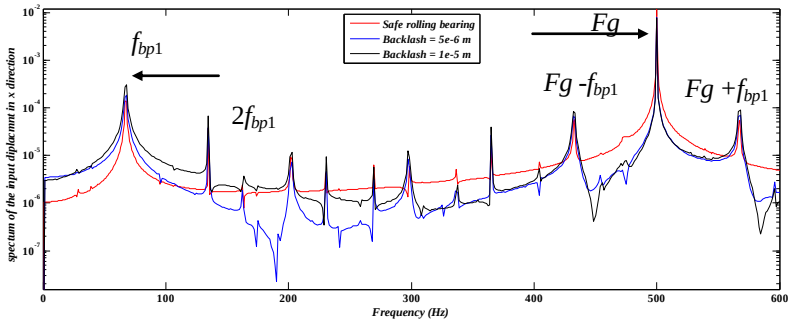

Figure 3. Spectrum of the output displacements in direction *x*

Figure 3 presents the spectrum of the input and output displacements in direction x. We note the presence of the gearmesh frequency F_g occurring at *500 Hz* and their harmonics. We note also the presence of the ball passage frequency corresponding to the input f_{bp1}, and the output f_{bp2} rolling bearings and their harmonics. When we introduce a backlash, an increase in the vibratory level is observed.

4 CONCLUDING REMARKS

In this paper a spur gear transmission is modelled including bearing and backlash incidence. For safe pinion, the vibration spectra are dominated by mesh frequency and harmonics induced by the mesh stiffness variation; we note also the presence of ball passage frequency and harmonics and a modulation between mesh frequency and ball passage frequency. The influence of the ball bearing backlash on the system transmission dynamic behaviour is also studied. The presented simulated signals can be very valuable to develop diagnostic and prognostic techniques for rolling element bearings in real systems.

5 REFERENCES

[1] Abbes M. S., Hentati T., Maatar M., Fakhfakh T. and Haddar M. 'Dynamic analysis of helical gears supported by rolling elements bearings', *Journal of Theoretical and Applied Mechanics*, Vol. 41, No. 1, pp. 33–50, 2011.

[2] Sawalhi, N. Randall, R. B. Simulating Gear and Bearing Interactions in the Presence of Faults. Part I. The Combined Gear Bearing Dynamic Model and the Simulation of Localised Bearing Faults, *Mechanical Systems and Signal Processing*, 22, No. 8, 1924-1951, 2008.

[3] Harsha, S. P. Nonlinear Dynamic Analysis of a High-speed Rotor Supported by Rolling Element Bearings. *Journal of sound and vibration*. 290, No. 1-2, 65-100, 2006.

INCREASING THE MODAL OVERLAP FACTOR OF A BEAM USING THE ACOUSTIC BLACK HOLE EFFECT

V. Denis[1*], F. Gautier[1] and A. Pelat[1]

[1]Laboratoire d'Acoustique de l'Universite du Maine
Avenue Olivier Messiaen, Le Mans, FRANCE
Email: vivien.denis@univ-lemans.fr, francois.gautier@univ-lemans.fr,
adrien.pelat@univ-lemans.fr

ABSTRACT

Acoustic Black Hole (ABH) effect is a passive vibration reduction technique which takes advantage of properties of wave propagation in thin structures of varying thickness in order to reduce the reflexion coefficient of an edge. A practical implementation of ABH on a conventional beam consists in an extremity whose thickness follows a power-law profile covered by a very thin layer of additional damping material. An observation using a High Resolution technique shows that the ABH significantly increases the modal overlap factor (MOF) of the beam, and thus reduces the overall level of vibration. Further investigations, including a two-dimensions numerical model of the structure, show that this MOF can be explained by an increase of the modal density and a high damping of a number of modes of the structure due to the ABH.

1 INTRODUCTION

Acoustic Black Hole (ABH) effect is a passive vibration reduction technique. It is based on the fact that flexural waves in beams and plates slow down if their thickness decreases. Mironov [1] establishes a power-law relationship between local thickness h and the distance from the edge x

$$h(x) = \epsilon x^m \qquad (m \geq 2),$$

that provides an infinite travel time for a wave to reach the edge of a structure whose truncated thickness tends to zero. The flexural waves then stop propagating and never reflect back. However, practical implementations of such a power-law profile always exhibit a non-zero thickness; this is why a reflected wave always occurs. Krylov *et al.* [2] shows that a truncated power-law profile covered by a thin layer of damping material could overcome this effect and provide an important reduction of the theoretical reflexion coefficient. Further work from Gautier *et al.* [3] apply the effect on elliptical plates and Georgiev *et al.* [4] attempts to model the ABH effect on 1D-structures and evaluate it on 1D or 2D-structures.

This work focuses on 1D-structures and aims to explain by a modal approach why the ABH effect works so well in practice. The first section describes what can be said from a modal analysis of a practical ABH beam. The second section attempts to provide a numerical model that is correlated with the experimental results. Some conclusions are drawn in the final section.

2 EXPERIMENTAL OBSERVATIONS

In order to show the smoothing of the mobility curve induced by the ABH effect, two structures are observed: the first is a reference beam, made of aluminium and of dimensions 0.89 m x 20 mm x 1.5 mm; the second is a similar beam having an extremity following a parabolic profile on a length of 60 mm. The thickness of the extremity is approximately 30 μm. This extremity is covered by a very thin layer of damping material on a length of 50 mm. The two beams are suspended vertically. The experimental setup is made of a hammer, an accelerometer and a National Instrument acquisition card, in order to acquire the time signals of force and acceleration. The impact takes place on the centerline of the beam, and is supposed to excite only the flexural modes.

The mobility curves on Figure 1 show that above a certain frequency, the level of vibration is considerably reduced due to the ABH effect, as previous works showed [2, 4]. A modal analysis permits to know more on the peaks of these two curves.

The High-Resolution ESPRIT (Estimation of Signal Parameters by Rotational Invariance Technique) [5] technique is used for the identification of parameters of the resonance peaks, such as frequencies, amplitudes and dampings. With these parameters, one is able to estimate the Modal Overlap Factor (MOF), which the product of the frequency, the dampings and the modal density.

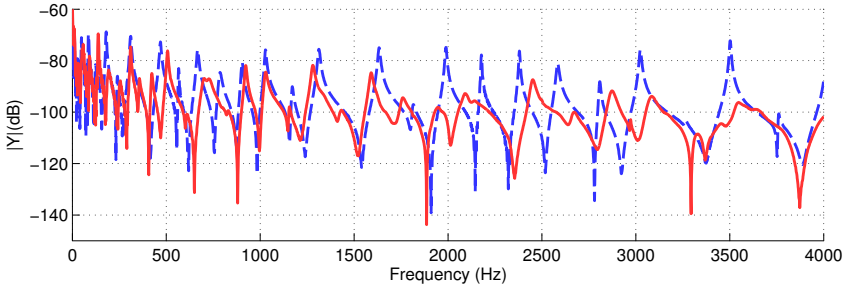

Figure 1: Compared mobilities of the reference beam (dashed) and the ABH beam (solid).

Figure 2 presents the results obtained computing the MOF of the beams. The quantities used to compute the MOF can also be studied. While the reference beam has a low MOF on the considered frequency band, the ABH beam presents the same MOF in the low frequency band then an unusually high MOF which can reach values as high as 60 %. Similar observations can be made on the modal density which is higher than the modal density for the flexural vibration of a beam and on the modal damping factors that are mostly much higher than in the reference beam.

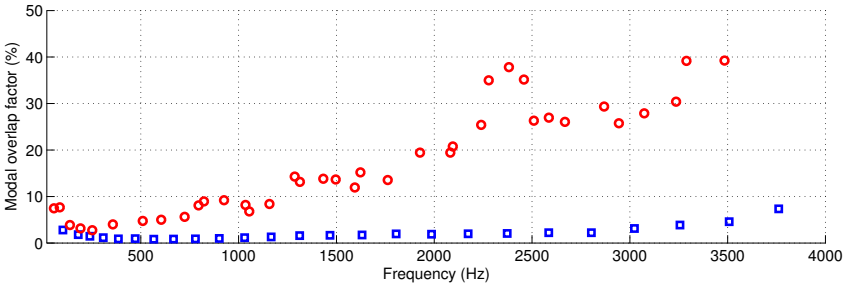

Figure 2: Compared Modal Overlap Factor of the reference beam (□) and the ABH beam (○).

3 MODELLING THE ABH STRUCTURE

A model is proposed to explain the experimental MOF. the local wavelength at the very end of the ABH profile can be of the order of magnitude of the width of the beam suggesting that a 2D (i.e. plate-like) behaviour at rather low frequencies. This is the reason why a 2D-model of the structure is built, using the Kirchoff plate theory with a variable thickness in the x-direction; this is well described in [6]. The plate is considered under free conditions on all edges and corners. The eigenvalue problem is considered and solved using a finite difference method on a stretched grid, in order to accommodate changes in the wavelength; this method is described by Bilbao [7]. This allows to obtain the eigenfrequencies and the eigenmodes of the beams used in the experiment. The eigenfrequencies permit to estimate the modal density of the structure. Modal loss factors can be found using the local equivalent loss factor of the structure [2] and the local strain energy.

The observation of the eigenmodes shows flexural modes presenting a transverse behaviour in the ABH region; this is a proof that even if the reference structure could be well represented by a 1D-model, the ABH makes it a 2D structure.

Figure 3a represents experimental and numerical modal densities for the two structures. The model of the reference beam presents a good correlation with the experiment, and shows that only flexural modes have been excited. The model of ABH shows a surprisingly good correlation with the practical structures, except in the 400-500 Hz band. It shows that torsional modes have indeed been excited while hitting the centerline; this behaviour is rather surprising, but may be explained by defects of the extremity of the ABH, due to the cumbersome manufacturing process. Nevertheless, considering torsional modes for both, the modal density is slightly higher for the ABH; it is a consequence of the lower phase velocity in the decreasing thickness profile.

Results for the modal loss factors (see Figure 3b) show that most of the ABH modes have a significantly high loss factor compared to the reference. It can be explained by a localized strain energy in a region that is highly damped due to the damping material. The high MOF is mainly due to these high loss factors.

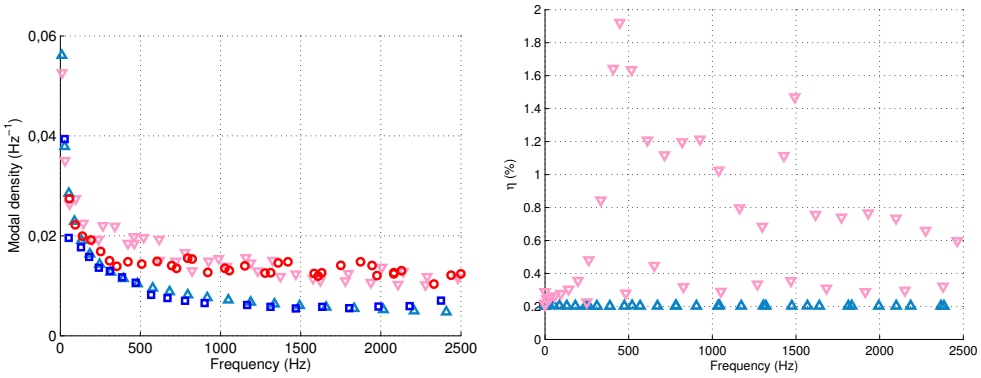

(a) (b)

Figure 3: (a) Modal densities for experimental reference beam (□), the simulated reference beam (△), the experimental ABH beam (○) and the simulated ABH beam (▽).(b) Modal loss factor for the simulated reference beam (△) and ABH beam (▽)

4 CONCLUSIONS

The ABH effect is indeed an efficient passive vibration reduction method. The mobility drop can be explained by an increase of the Modal Overlap Factor. This MOF is due to a higher modal density and higher values for most of the modal damping factors. Only a 2D-model is able to correctly represent the practical ABH beam, which has modes presenting a locally transverse behaviour.

REFERENCES

[1] M.A. Mironov. Propagation of a flexural wave in a plate whose thickness decreases smoothly to zero in a finite interval. *Soviet Physics: Acoustics*, 34(3):318–319, 1988.

[2] V.V. Krylov and F.J.B.S. Tilman. Acoustic 'black holes' for flexural waves as effective vibration dampers. *Journal of Sound and Vibration*, 274(3-5):605–619, July 2004.

[3] F. Gautier, J. Cuenca, V.V. Krylov, and L. Simon. Experimental investigation of the acoustic black hole effect for vibration damping in elliptical plates. In *Acoustic'08, Paris*, 2008.

[4] V.B. Georgiev, J. Cuenca, F. Gautier, L. Simon, and V.V. Krylov. Damping of structural vibrations in beams and elliptical plates using the acoustic black hole effect. *Journal of Sound and Vibration*, 330(11):2497–2508, May 2011.

[5] K. Ege, X. Boutillon, and B. David. High-resolution modal analysis. *Journal of Sound and Vibration*, 325(4-5):852–869, September 2009.

[6] A. Leissa. *Vibration of plates*. Acoustical society of America, London, 1993.

[7] S. Bilbao. *Numerical sound synthesis finite difference schemes and simulation in musical acoustics*. John Wiley & Sons,, Hoboken, 2009.

SCATTERING OF FLEXURAL WAVES FROM AN ACOUSTIC BLACK HOLE IN AN INFINITE THIN PLATE

O. AKLOUCHE[1,2], A. PELAT[1], S. MAUGEAIS[3], F. GAUTIER[1]

[1]Laboratoire d'Acoustique de l'Université du Maine. UMR CNRS 6613
Avenue Olivier Messiaen, 72085 LE MANS, FRANCE

[2]Institut de Recherche Technologique Jules Verne
Chemin du Chaffault, 44340 Bouguenais, FRANCE

[3]Laboratoire Manceau de Mathématiques
Avenue Olivier Messiaen, 72085 LE MANS, FRANCE

Email: omar.aklouche@univ-lemans.fr, omar.aklouche@irt-jules-verne.fr
adrien.pelat@univ-lemans.fr
sylvain.maugeais@univ-lemans.fr
francois.gautier@univ-lemans.fr

ABSTRACT

*The **ABH** (Acoustic Black Hole) is a passive method of reducing vibrations, it acts as a trap for flexural waves. ABH effect has been demonstrated experimentally in LAUM[1] for beams and plates.*

The work presented in this paper consists in modeling of the vibrational behavior of an infinite thin plate with an ABH. The calculation of the scattered field and the vibrational field in the black hole allows the analysis of the black hole mechanism.

This model is a preliminary modeling of propagation in periodic media, and multiple scattering of flexural waves by a periodic lattice of black holes.

[1]Laboratoire d'Acoustique de l'Université du Maine

1 STATEMENT OF THE PROBLEM

We consider a plane wave propagating toward an acoustic black hole in Kirchhoff's plate (Fig.1-(a)).
Studying the propagation in this plate, involves solving of two coupled problems. One concerns propagation in plates of constant thickness and scattering by a circular inclusion, the other concerns propagation in plates of variable thickness.

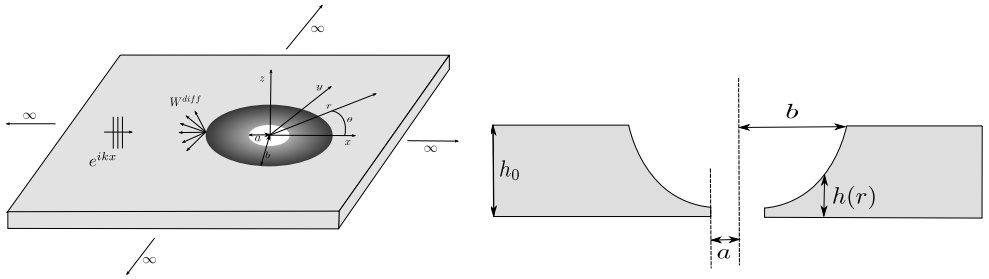

(a) (b)

Figure 1. (a): Infinite thin plate with ABH. (b): Thickness profile of the ABH plate.

2 ABH SCATTERING MODEL

The general equation governing the transverse motion in a plate of variable thickness is given in [1] as

$$\rho h(r)\frac{\partial^2 W(r,\theta,t)}{\partial t^2} = (1-\nu)\diamondsuit^4\{D(r),W(r,\theta,t)\} - \nabla^2\left[D(r)\nabla^2 W(r,\theta,t)\right], \qquad (1)$$

where

$$\diamondsuit^4\{D^{int}(r),W^{int}(r,\theta)\} = \frac{\partial^2 D^{int}(r)}{\partial r^2}\left[\frac{1}{r}\frac{\partial W^{int}(r,\theta)}{\partial r}+\frac{1}{r^2}\frac{\partial^2 W^{int}(r,\theta)}{\partial\theta^2}\right]+\frac{\partial^2 W^{int}(r,\theta)}{\partial r^2}\left[\frac{1}{r}\frac{\partial D^{int}(r)}{\partial r}\right]$$

2.1 External field ($r > b$)

Outside the black hole ($r > b$), the thickness is constant. The total field outside the black hole (Fig.1-(a)) is assumed to be composed of two terms (Eq.2) representing respectively the incident wave $W_0 e^{ikr\cos(\theta)}$ and the scattered field, where $k = \sqrt[4]{\frac{\rho h}{D^{ext}}}\sqrt{\omega}$ is the wave number outside the black hole, ρ is the density, h is the thickness and D^{ext} represents the flexural rigidity outside the black hole. The Fourier series expansion $W(r,\theta) = \sum_{n=0}^{\infty} W_n(r)\cos n\theta$ allows to write,

$$W^{ext}(r,\theta) = \underbrace{W_0\sum_{n=0}^{\infty}\varepsilon_n i^n \boldsymbol{J}_n(kr)\cos(n\theta)}_{\text{incident field}} + \underbrace{\sum_{n=0}^{\infty}\left[A_n\boldsymbol{H}_n^{(1)}(kr)+B_n\boldsymbol{K}_n(kr)\right]\cos(n\theta)}_{\text{scattered field}}, \quad r > b. \qquad (2)$$

The amplitude W_0 is assumed to be known. Amplitudes A_n and B_n will be determined from the continuity conditions which will be specified later. In the formula (Eq.2), $\boldsymbol{J}_n$ is the Bessel function of the first kind, $\boldsymbol{H}_n^{(1)}$ is the Hankel function of the first kind, and $\boldsymbol{K}_n$ is the modified Bessel function of the second kind.

2.2 Internal field ($a < b < r$)

Inside the black hole (Fig.1-(b)), the thickness varies according to the power law $h(r) = \xi r^m$, whence the variation of the bending stiffness. Equation (1) can also be written as,

$$\rho h(r)\frac{\partial^2 W^{int}(r,\theta)}{\partial t^2} = (1-\nu)\diamondsuit^4\{D^{int}(r), W^{int}(r,\theta)\} - \nabla^2\left[D^{int}(r)\nabla^2 W^{int}(r,\theta)\right]. \quad (3)$$

To solve this equation, we assume that the black hole profile is quadratic (m = 2), then we use the change of variable $r = e^z$ [2], [3]. Substituting the development $W(r,\theta) = \sum_{n=0}^{\infty} W_n(r)\cos n\theta$ in the equation (3), the solution can be written

$$W^{int}(r,\theta) = \sum_{n=0}^{\infty}\left\{\sum_{p=1}^{4}\left[C_{p,n}r^{k_{p,n}}\right]\right\}\cos(n\theta). \quad (4)$$

With

$$k_{p,n} = -2 \pm \sqrt{7 - 3\nu + n^2 \pm \sqrt{8n^2(3\nu-1) + 9(1-\nu)^2 + \left[\frac{12\rho\omega^2(1-\nu^2)}{E\xi^2}\right]}} \quad ; \quad p = 1,\ 2,\ 3,\ 4. \quad (5)$$

3 DISPERSION CURVES

The dispersion relation (Eq.5) predicts the presence of four evanescent waves into the black hole. In case of frequencies which are upper than the cutoff frequency (f_c), two waves become propagative (Fig.2).

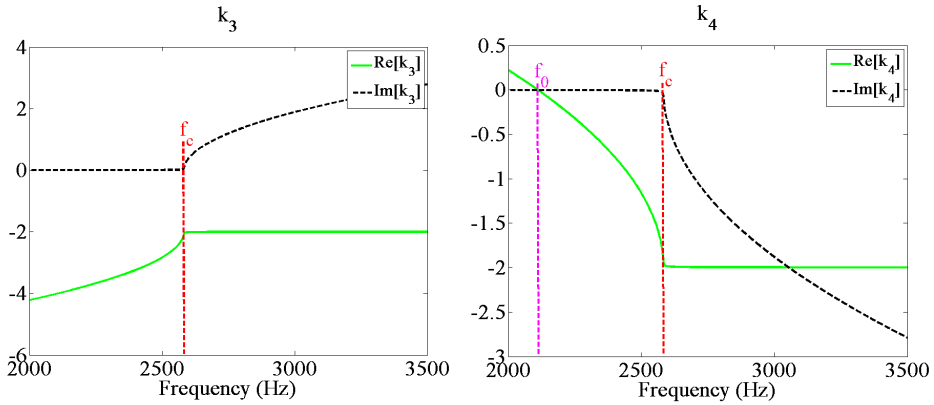

Figure 2: Example of k_3 and k_4 dispersion curves of bending waves in acoustic black hole , for the circumferential order n = 4.

4 DIFFUSED FIELD AND SCATTERING DIAGRAMS

The edge $r = a$ of the black hole is free, and the vibrational field is continuous in $r = b$. The first condition impose the cancellation of the bending moment and shear force at $r = a$. The second reflects the continuity of displacements, slopes, bending moments and shear forces at

the boundary $r = b$ of the black hole. The six conditions allow the calculation of the constants A_n, B_n, $C_{1,n}$, $C_{2,n}$, $C_{3,n}$ and $C_{4,n}$. The figure below shows the vibrational field and scattering diagrams of a plane wave from an ABH in an infinite thin plate. These results show that the ABH effect in plates is more important at high frequencies.

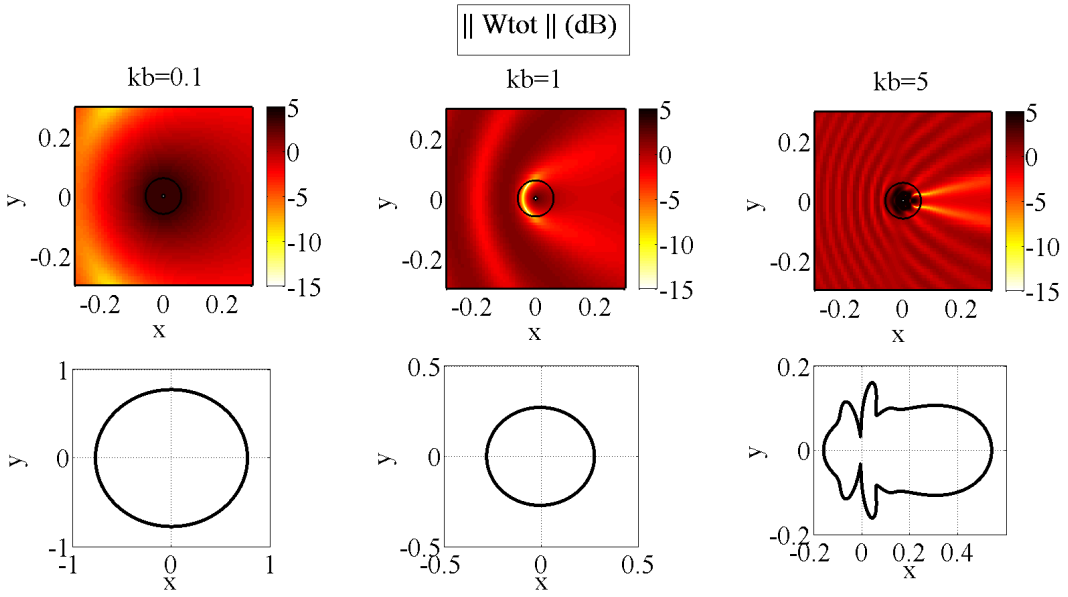

Figure 3: Vibrational field of thin infinite plate with an acoustic black hole, and directivity patterns of scattering of bending waves from an acoustic black hole. kb=0.1, kb=1 et kb=5.

CONCLUSION

This document is a summary of modeling of the propagation of flexural waves in an infinite thin plate with an ABH. The model allows to quantify the dispersion and study the behavior of bending waves inside the ABH. It provides the scattered field and directivity patterns associated. This model is the preliminary step to describe the propagation in structure with periodic lattice of acoustic black holes.

REFERENCES

[1] Arthur W Leissa. Vibration of plates. Technical report, DTIC Document, 1969.

[2] DJ O'Boy and VV Krylov. Damping of flexural vibrations in circular plates with tapered central holes. *Journal of Sound and Vibration*, 330(10):2220–2236, 2011.

[3] HD Conway. Some special solutions for the flexural vibration of discs of varying thickness. *Archive of Applied Mechanics*, 26(6):408–410, 1958.

[4] P.M.C. Morse and H. Feshbach. *Methods of theoretical physics*, volume 1,2. McGraw-Hill, 1953.

[5] C.C. Mow and Y.H. Pao. The diffraction of elastic waves and dynamic stress concentrations. 1971.

FEA NALYSIS OF IN-PLANE SHEAR STRESSES OF A PRELODED SANDWICH PLATE WITH A VISCOELASTIC CORE – APPLICATION TO THE DISK BRAKE SYSTEMS

M. Soula[1] T. Lazghab[2] M. Bouazizi[3]

[1] Laboratoire de Mécanique Appliqué et Ingénierie - ENIT, ESSTT, 5, Avenue Taha Hussein 1008 Tunis – Tunisia
Soulamed2003@Yahoo.fr
[2] Laboratoire de Mécanique Appliqué et Ingénierie - ENIT, IPEI El-Manar, P.O. Box 244, El Manar, Tunis 2092, Tunisia.
lazghabt@yahoo.com
[1] Laboratoire de Mécanique Appliqué et Ingénierie - ENIT, ESSTT, 5, Avenue Taha Hussein 1008 Tunis – Tunisia
bouazizi_maher@yahoo.fr

ABSTRACT

In this work a study of the response of sandwich plates with a viscoelastic core used in brake systems is presented. These plates attenuate the squealing noise due to friction between the disk and the pads. A finite element analysis is conducted to determine the in-plane shear stress distribution in the sandwich plate under various operating conditions. The effects of braking pressure, coefficient of friction between the disk and brake pads and angular speed of the disk on the in-plane shear stress are analyzed and compared. Results show that the coefficient of friction and braking pressure are the most influential factors.

1 INTRODUCTION

Automotive disk brake systems produce a noise known as brake squeal. It is an undesirable phenomenon often associated with braking performance even though it has very little to do with it. One solution to mitigate brake squeal is to insert a sandwich plate behind the brake pads. The three-layer sandwich plate (metal/elastomer/metal) will dissipate the noise that would be generated from brake squeal during braking. Gacem et al. [1] have studied the nonlinear dynamic behaviour of a preloaded thin sandwich plate incorporating visco-hyperelastic layers used to attenuate noise in brake systems. Triches et al. [2] have studied the effect of adding a sandwich plate with a viscoelastic core on brake squeal and showed this approach to be effective in reducing brake squeal occurrence. However, the sandwich plate is subjected to a combination of high shear stresses from braking friction and normal stresses from braking pressure. Under these conditions the sandwich plate may be damaged, especially during the braking phase. These loading conditions are not typical of sandwich plates. A review of the theoretical and experimental investigations of sandwich plate behaviour from the past few decades is provided [3]. Several authors have studied the behaviour of sandwich plates with a viscoelastic core. In most cases, sandwich plates are subjected to flexural loads, transverse shear in addition to in plane loading [4,5].

2 MODEL DESCRIPTION

2.1 Geometry

The simplified model of the brake system consists in a disk confined between two pads as shown in figure 1. A viscoelastic sandwich plate is attached to the back of each pad as shown in figure 2; it is composed of two thin steel layers and a viscoelastic core (steel/viscoelastic core/steel).

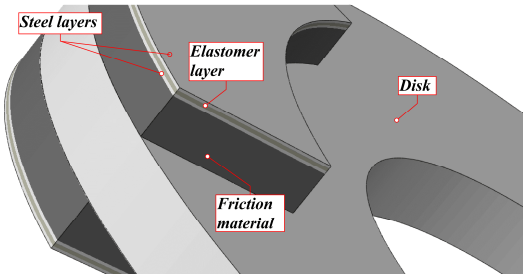

Figure 1: Simplified model of a disk brake model.

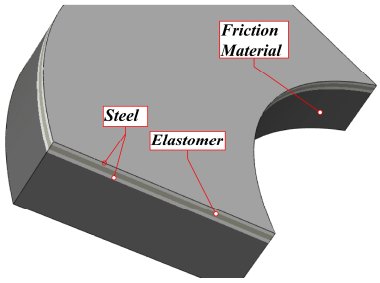

Figure 2: Brake pad details.

2.2 Materials

The materials used for the components of the brake system are elastic isotropic steel for the disk and external layers of the sandwich plate. The pads are made from brake shoe material essentially. The sandwich plate is made from steel layers and a viscoelastic polymer core. The polymer material behaves as a viscoelastic material with a shear stress relaxation modulus $G(t)$ given in terms of a Prony series as:

$$G(t) = G_0\left(1-\sum_{i=1}^{N} g_i\left(1-e^{-t/\tau_i}\right)\right) \tag{1}$$

Where $G_0 = G(0)$; $G_\infty = \lim_{t\to\infty} G(t)$; g_i and τ_i are material parameters.

2.3 Finite element model

2.3.1 Mesh

A finite element model of the brake system assembly was built. It consists of two brake pads and the steel disk as shown in figure 3 .The friction material of the brake pads is modeled using C3D8R type elements (linear 8-noded continuum reduced integration brick elements with hourglass control). The sandwich plate is modeled using SC8R type elements (linear 8 noded continuum shell elements with reduced integration) for the three layers (metal/elastomer/metal). The disk is also modeled using continuum brick elements of type C3D8R. The general purpose finite element software package ABAQUS was used to conduct the simulations.

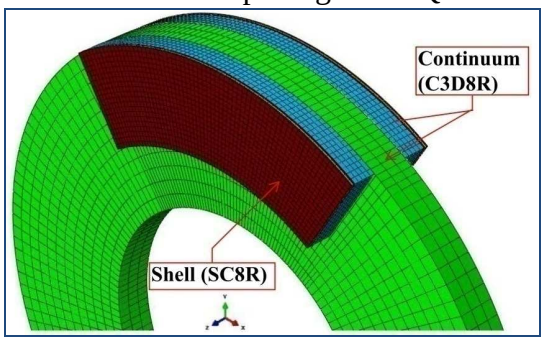

Figure 3: Element types used in the finite element model

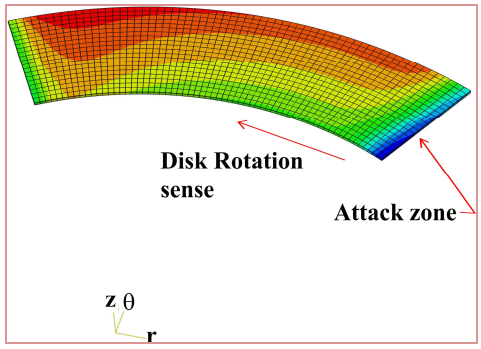

Figure 4: Location of the attack zone in the viscoelastic core layer

3 NUMERICAL RESULTS AND ANALYSIS

In figure 5 are presented the shear stress distributions in the viscoelastic layer under severe and moderate braking conditions. The disk is rotating around the positive Z direction and the stresses are represented in a cylindrical coordinate system (r,θ, z) with origin at the center of the disk.

The shear stress maximum value increases with μ and its location drifts towards the attack zone of the pad as μ increases as shown figure 4 and figure 5 The distribution of the shear stress is clearly non symmetric and depends on r and θ.

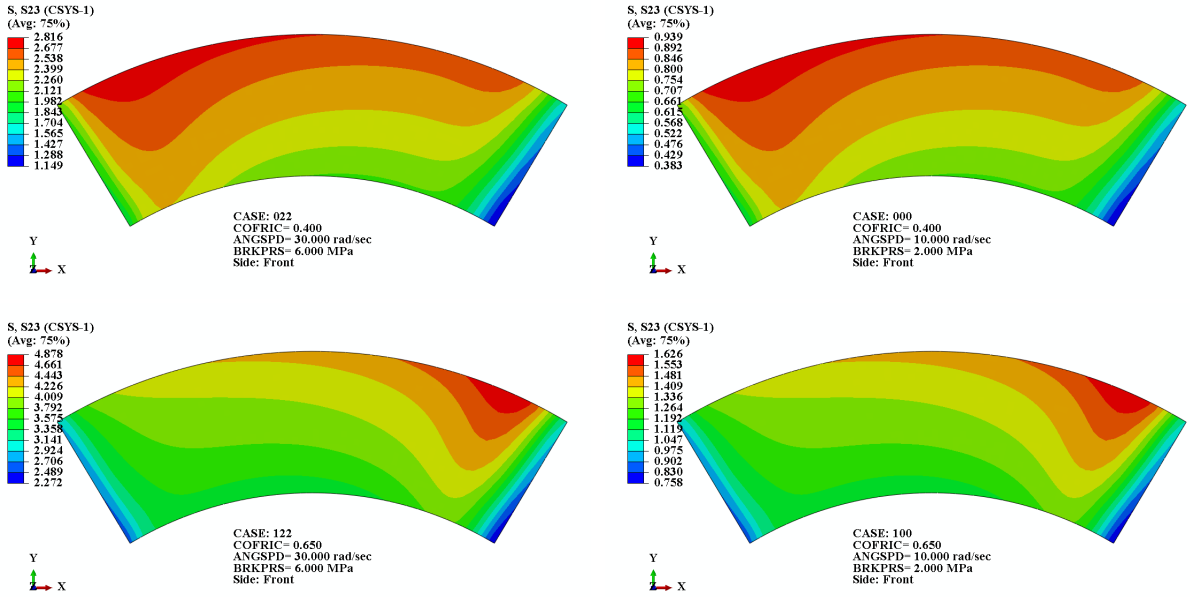

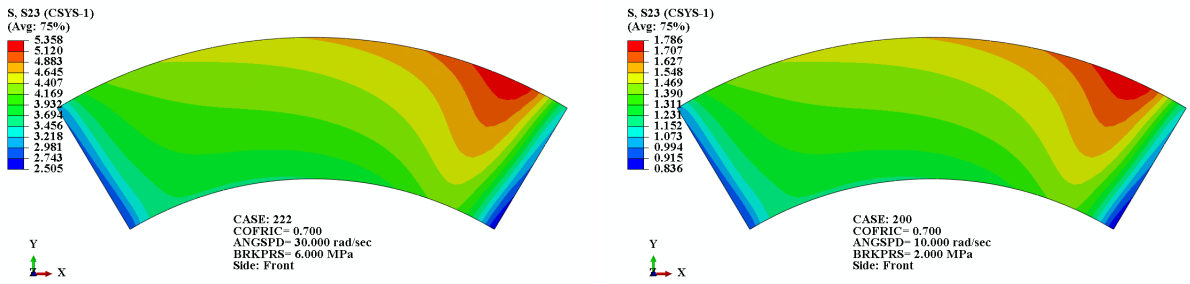

Figure 5: The effects of coefficient of friction on shear stress in severe and moderate conditions at several values of the coefficient of friction

4 CONCLUSION

In this work a parametric study was conducted to determine shear stresses in the sandwich plate for various coefficients of friction, angular speed of the disk and breaking pressure. A finite element model was used to calculate the shear stresses of the model using the general purpose finite element software ABAQUS [11].The numerical results show that the shear stresses in the viscoelastic layer of the sandwich plate are dependent on the coefficient of friction and the brake pressure and are independent of the angular speed of the disk. This is due to the assumption that the coefficient of friction is not dependent on angular speed. Variations in the coefficient of friction affect the amplitude of the shear stresses in the viscoelastic layer of the sandwich plate as well as there through the thickness distribution and the location of the maximum shear stress which drifts towards the attack zone as the coefficient of friction increases. Variations in the braking pressure affect the levels of the shear stresses without affecting their distribution

5 REFERENCES

[1] Gacem H, Chevalier Y, Dion J, Soula M, Rezgui B. Nonlinear dynamic behaviour of a preloaded thin sandwich plate incorporating visco-hyperelastic layers. Journal of Sound and Vibration. 2009;322(4-5):941-53.

[2] Triches Jr M, Gerges S, Jordan R. Reduction of squeal noise from disc brake systems using constrained layer damping. Journal of the Brazilian Society of Mechanical Sciences and Engineering. 2004;26(3):340-8.

[3] Herakovich CT. Mechanics of composites: A historical review. Mechanics Research Communications. 2012;41(0):1-20.

[4] Moita JS, Araújo AL, Martins P, Mota Soares CM, Mota Soares CA. A finite element model for the analysis of viscoelastic sandwich structures. Computers & Structures. 2011;89(21–22):1874-81.

[5] Ćetković M, Vuksanović D. Bending, free vibrations and buckling of laminated composite and sandwich plates using a layerwise displacement model. Composite Structures. 2009;88(2):219-27.

WIDEBAND FREQUENCY CHARACTERIZATION OF A SHAPE MEMORY POLYMER

P. Butaud[1*], M. Ouisse[1] , E. Foltête[1], V. Placet[1], J. Klesa and X. Gabrion[1]

[1]Département de Mécanique Appliquée
Femto-St 25000 Besançon FRANCE
Email: pauline.butaud@femto-st.fr

ABSTRACT

This study is an experimental evaluation of the mechanical properties of shape memory polymer Veriflex® under different tests conditions. Veriflex® was chosen because of its easy accessibility and its properties similar to epoxy resins which make it very suitable for use in a wide variety of technical applications. Dynamic mechanical analysis (DMA) has been used to determine the evolution of the viscoelastic properties versus temperature and frequency under harmonic loading. The time-temperature superposition principle has been found to be valid for this material. This is illustrated here through the use of the master curves. Furthermore a modal analysis on a Veriflex® rectangular plate has been performed in order to reach higher frequencies than the DMA, and a finite element model was employed to find the viscoelastic properties of the material. A correlation between these two experimental methods allowed to highlight a disparity of results explained by the deterioration of the Veriflex® over time.

1 INTRODUCTION

Shape memory polymers (SMP) have the capability of changing their shape in response to an external stimulus [1]. The glass transition temperature Tg, is the reference point where the higher temperature component starts to melt. When the SMP is heated above Tg, it is soft and rubbery and it is easy to change its shape. When subsequently cooled below Tg, it retains the given shape (shape fixing characteristic). When heated again above Tg, the material autonomously returns to the original permanent shape [2]. The shape-memory effect is in principle a behavior inherent to all polymers. However, polymers that exhibit a useful shape-memory effect must demonstrate a sharp transition temperature and a rubbery plateau, along with relatively large strain capacity without local material damage [3]. Only a few polymers that satisfy these criteria are described in the literature [4]. The characterization of these materials is necessary over a wide frequency band for their current and future applications [5]. For this, a dynamic mechanical analysis and a modal analysis have been performed in order to determine as well as possible a law of time-temperature equivalence [6].

2 DYNAMIC MECHANICAL ANALYSIS

Dynamic mechanical analysis (DMA) of Veriflex® has been performed using BOSE Electro Force equipment. The Veriflex® sample is tested from 0.01 Hz to 10 Hz (from static to dynamic), a sinusoidal force is applied, while viscoelastic properties (storage modulus E', loss modulus E'' and loss factor $tan\ \delta$) are measured every 2°C in isothermal conditions between 25°C and 90°C. Veriflex® shows huge loss of storage modulus while the temperature is increasing, from about 1000 MPa at 25°C to 1 MPa at 90°C. Curves of E' vs. frequency at one temperature (Figure 2) can be shifted to overlap with adjacent curves (Figure 1). The time superposition shift factor a used for E' must be the same for $tan\ \delta$ to get a time-temperature equivalence. In our case, the shift factors a are obtained through an optimisation procedure, and are equivalent for both E' and $tan\ \delta$, in coherence with the time-temperature equivalence. The master curve of the storage modulus is given in Figure 1.

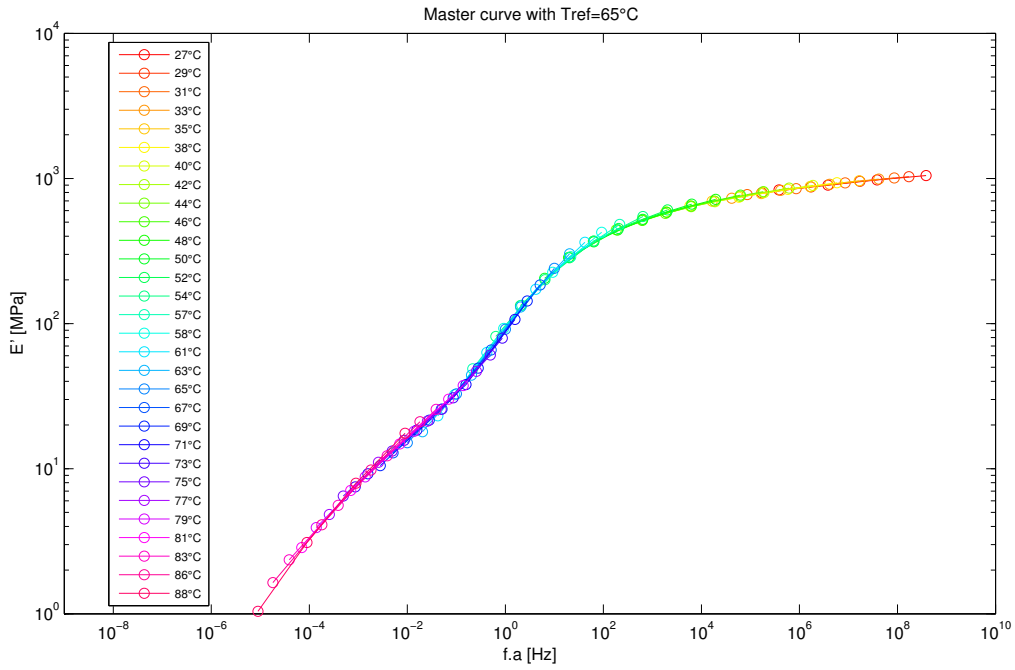

Figure 1. Veriflex® master curve for the storage modulus (E')

3 MODAL ANALYSIS

A modal analysis on a Veriflex® rectangular plate has been performed in free-free conditions, with a temperature control between 20°C and 50°C every 10°C. Contactless actuators and sensors have been used to avoid undesirable effects on the structural behaviour. Experimental modal analysis allowed to obtain modal frequencies (ten frequencies are identified between 100 Hz and 700 Hz), modal damping and mode shapes. At the same time, a finite element model of this plate was established with the same conditions as in experimental (free-free conditions, elastic homogeneous) and a presumed Young's modulus. Numerical modal analysis gives modal frequencies and mode shapes, and mechanical parameters are obtained through the use of model-test correlation and model updating. Just as dynamical mechanic analysis, the obtained Young's modulus of Veriflex® (taken for the storage modulus) depends on the temperature and the frequency as shown in Figure 2.

4 CORRELATION BETWEEN DMA AND MODAL ANALYSIS

This study intends to compare the results obtained with the DMA and those collected by the modal analysis. In both cases, according to the time-temperature equivalence detected by the DMA, the storage modulus should be the same. However the storage modulus for the modal analysis is around 2000 MPa contrary to only 1000 MPa for the DMA at the same temperature, this is a huge gap between these two experimental methods (Figure 2). The possible explanation is that these tests were performed with a time lag of two years. Specifically, Veriflex® samples were elaborated and tested on the DMA in the same year, while the modal tests were performed on these same samples two years later.

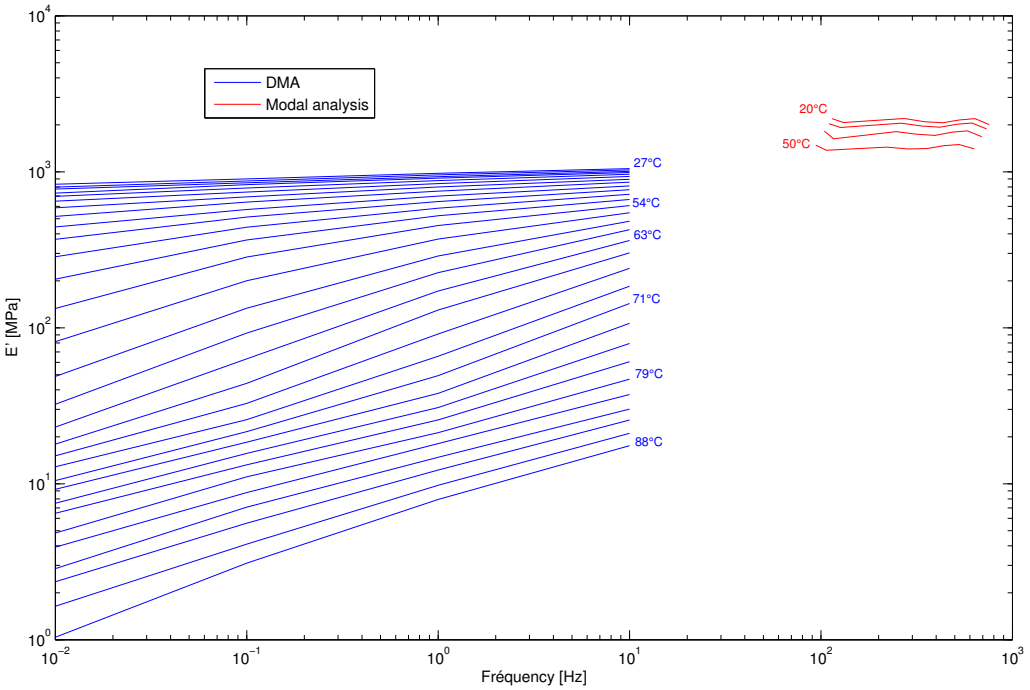

Figure 2. Correlation plot between DMA (blue) and modal analysis (red)

5 CONCLUSION

The objective of this study was to highlight the time-temperature equivalence by comparing two experimental methods allowing the identification of the storage modulus over frequency and temperature. This equivalence has been checked on a sample tested at a given moment with the DMA. However, the deterioration over time of the Veriflex® was not foreseen. Thus, the modal analysis, which has been performed at a later time, could not conclude on the validity of this equivalence over a wide frequency band. Indeed, the material stiffness increased, the Veriflex® storage modulus doubled over two years. Further investigations are needed to clarify the Veriflex® behaved. The age of the material should be taken into account by conducting a series of test runs at the same year. The correlation between DMA and modal analysis remains to be carried out.

REFERENCES

[1] A. Lendlein and S. Kelch. Shape-memory polymers. *Angewandte Chemie International Edition*, 41(12):2034–2057, 2002.

[2] S.A. Wilson, R.P.J. Jourdain, Q. Zhang, R.A. Dorey, C.R. Bowen, M. Willander, Q.U. Wahab, S.M. Al-hilli, O. Nur, E. Quandt, et al. New materials for micro-scale sensors and actuators: An engineering review. *Materials Science and Engineering: R: Reports*, 56(1):1–129, 2007.

[3] B. Sillion. Shape memory polymers. *Acta Chim*, 3:182–188, 2002.

[4] J.M. Shaw, J.D. Gelorme, N.C. LaBianca, W.E. Conley, and S.J. Holmes. Negative photoresists for optical lithography. *IBM Journal of Research and Development*, 41(1.2):81–94, 1997.

[5] M. Behl and A. Lendlein. Shape-memory polymers. *Materials Today*, 10(4):20–28, 2007.

[6] Julie Diani, Pierre Gilormini, Carole Frédy, and Ingrid Rousseau. Predicting thermal shape memory of crosslinked polymer networks from linear viscoelasticity. *International Journal of Solids and Structures*, 49(5):793–799, 2012.

ESTIMATION OF STRUCTURAL DAMPING USING AN EXPANSION IN THE CHEBYSHEV ORTHOGONAL BASIS

C. Chochol, S. Chesne and D. Remond[1]

[1]LaMCoS, INSA-Lyon, CNRS UMR5259
18, rue des Sciences, F69621 Villeurbanne, France
Email: catherine.chochol@insa-lyon.fr

ABSTRACT

The aim of this study is to estimate structural parameters such as material properties (density, Young Modulus...) or geometrical properties (inertia, cross-section...) and structural damping. The identification method is based on a three steps process. Firstly, the recorded displacement field is recorded an expanded on the Chebyshev orthogonal basis. Thanks to this expansion the partial derivatives of the signal are computed. Finally, the partial derivatives are used to reconstruct the partial differential equation of motion of the structure.
The three steps process will be directly illustrated by an example, even if this method could be applied to any kind of structure. The example is a simply-supported bar. The free response of this bar is the input signal used in our identification process. The identification process will be tested by simulation in noisy condition through a Monte Carlo test. The influence of the truncation order and the wave number will be discussed. With 5% *of noise the structural damping is estimated with an error smaller than* 0.001%

1 INTRODUCTION

Continuous Time (CT) methods have been developed to allow identification with unequally sampled signals. One of the main applications of this method is to transform the dynamic equations of the system behaviour into an algebraic equation set, generally in order to estimate directly mechanical parameters such as mass, stiffness, damping, etc.
In the approach proposed for example in [1], orthogonal functions are frequently used in an integral formulation of differential equations. As proposed in [2], the differential equations governing the system's behaviour to be identified can be transformed into algebraic equations. Nevertheless, the differentiation step involves a biased derivative matrix (as shown by [3]).
The purpose of this study is to adapt and to improve a continuous time identification method to discrete-space signals and partial differential equations. In this study, a novel differentiation tool is presented. This approach is then adapted to the computation of partial derivatives.

2 MODEL

The longitudinal motion in a bar is described by

$$\frac{\partial^2}{\partial t^2}v(x,t) = \frac{E}{\rho}\frac{\partial^2}{\partial x^2}v(x,t) + \delta\frac{\partial}{\partial t}v(x,t) \tag{1}$$

where ρ is the density, E the Young modulus of the material, and δ the structural damping a of the beam. t is the time variable, x the space variable and v is the longitudinal displacement.
For this study the particular case of free response of the simply supported bar will be treated. However the method proposed in the next section can be applied to every kind of structure (beam, bar, plate...), response (forced, transient, ...) or boundary condition (clamped-free, clamped-clamped, simply supported, ...).

3 IDENTIFICATION PROCESS

3.1 Preliminaries

3.1.1 Expansion

Every functions f can be expanded on an orthogonal basis P. f can be approximated by

$$\begin{aligned} f(x) &\simeq \sum_{i=0}^{N} \lambda_i P_i(x) \\ &\simeq \{\lambda\}_N \{P\}_N^T \end{aligned} \tag{2}$$

where N is the truncation order, $\{\lambda\} = \begin{pmatrix}\lambda_0 & \cdots & \lambda_N\end{pmatrix}$ and $\{P\} = \begin{pmatrix}P_0 & \cdots & P_N\end{pmatrix}$. The λ_i are the expansion coefficients. With i growing, the λ_i are decreasing. The λ_i coefficients are computed using the integral form of the scalar product which is defined in [4]. The exact value of λ_i (even with discrete data) can be computed using the Gauss points as explained in [4].

3.1.2 Differentiation

The traditional $[D]$ operator developed by [2] can be expressed as:

$$\frac{d^q f(x)}{dx^q} \approx \{\lambda\}[D]^q\{P\}^T \tag{3}$$

where $[D]$ is a square matrix made of scalars computed analytically. As explained in [3], this estimation of the derivative is corrupted by bias term errors that originate from the truncation of the expansion of f.
The aim of our novel differentiation tool is to eliminate the bias term by integrating the expression of the scalar product, as proposed in [5]. Using the integration by parts and a weighting function $u_\gamma(x) = (1-x^2)^\gamma$, we can compute an exact derivative of the signal f by:

$$u_\gamma(x)\frac{d^q f(x)}{dx^q} \approx \{^{\gamma-q}\tilde{\lambda}_k\}[\Delta_q]\{P\}^T \tag{4}$$

with $\{^{\gamma-q}\tilde{\lambda}\} = \begin{pmatrix}^{\gamma-q}\tilde{\lambda}_0 & \cdots & ^{\gamma-q}\tilde{\lambda}_N\end{pmatrix}$, $^{\gamma-q}\tilde{\lambda}_k$ being the expansion of $f(x)\cdot u_{\gamma-q}(x)$ and $[\Delta]$ is a square matrix whose terms are made of the scalars computed analytically (see [6] for further explanations). Here the approximation is only due to the truncation of $f^{(q)}$. For first kind polynomials, the operator is named $[\Delta]_1$ (and $[\Delta]_2$ for second kind).

3.2 Three steps process

3.2.1 STEP 1: Expansion

If we consider in the second step the novel differentiation method, we need to multiply the recorded signal v by the appropriate function $u_{\gamma-q}$. Then, in a two dimensional case we have :

$$u_{\gamma_x-q_x}(x)u_{\gamma_t-q_t}(t)v(x,t) \approx \{P(x)\}[^{\gamma_x-q_x,\gamma_t-q_t}\tilde{\lambda}]\{P(t)\}^T \tag{5}$$

3.2.2 STEP 2: Differentiation

The q_x partial derivative in space and the q_t partial derivative in time are obtained using $[\Delta_{q_x}]$ and $[\Delta_{q_t}]$ respectively (see 4). Then we have :

$$\begin{aligned} u_{\gamma_x}(x)u_{\gamma_t}(t)\frac{\partial^{q_x+q_t}}{\partial x^{q_x}\partial t^{q_t}}(x,t) &\approx \{P(x)\}[\Delta_{q_x}][^{\gamma_x-q_x,\gamma_t-q_t}\tilde{\lambda}][\Delta_{q_t}]\{P(t)\}^T \\ &\approx \{P(x)\}[^{\gamma_x,\gamma_t}_{q_x,q_t}\tilde{\lambda}]\{P(t)\}^T \end{aligned} \tag{6}$$

3.2.3 STEP 3: Equation of motion reconstruction

If we use a unique couple (γ_x,γ_t) for all partial derivatives computation, we can rewrite (1) as :

$$[^{\gamma_x,\gamma_t}_{0,2}\tilde{\lambda}] = \frac{E}{\rho}[^{\gamma_x,\gamma_t}_{2,0}\tilde{\lambda}] + \delta[^{\gamma_x,\gamma_t}_{0,1}\tilde{\lambda}] \tag{7}$$

with $\gamma_x > 2$ and $\gamma_t > 2$. We have three N_x-by-N_t matrices. Depending on the signal shape (symmetric or not) and its richness (frequency range), only a few components of these matrices will be relevant (significantly greater than the other). Choosing only the s relevant values, we have s equations and 2 unknowns : $\theta_1 = \frac{E}{\rho}$ and $\theta_2 = \delta$. The least square estimate of (θ_1,θ_2) can be easily computed.

4 SIMULATION RESULTS AND DISCUSSION

In this simulation the wavelength varies for $k = 1$ to 12 (Y-axis in fig. 1). The truncation order varies from $N = 6$ to 60 (X-axis in fig. 1). The error (in dB) is plotted and varies from -3 (error : 0.001%) to 3 (error : $10^3\%$). The figures located on the top (left to right) present the estimation of θ_1. The figures located on the bottom (left to right) present the estimation of θ_2. We see clearly in fig. 1 for each parameter estimation three zones:

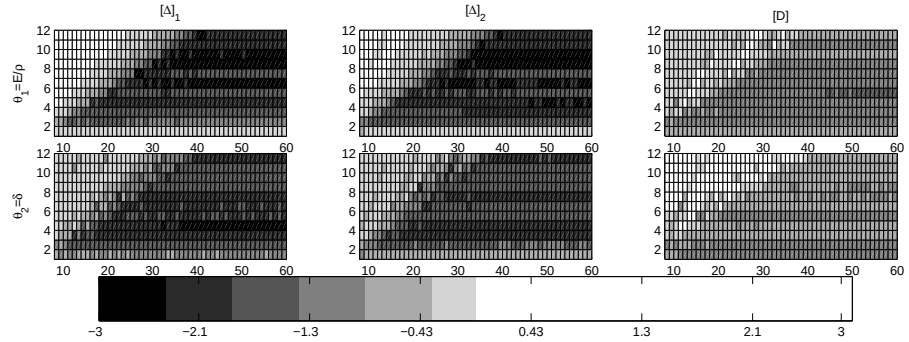

Figure 1. Error(dB) on the estimation of θ_1 and θ_2 by 3 different operators : $[\Delta]_1$,$[\Delta]_2$ and $[D]$

- In the upper left triangle, (small N, big k) the truncation order N is too small to describe correctly the signal v. The parameter estimation is not accurate.
- In the lower zone,(big N, small k) the amount of information brought by the bar response is not sufficient for the identification. Indeed for $k \approx 1$, the space signal is only a single period of a sine function. Therefore the expansion in the orthogonal basis gives only a few non null λ_i coefficients which are more sensitive to noise.
- For bigger N, the signal is well described by the polynomial expansion. The signal is rich enough for the computation of both θ_1 and θ_2.The precision goes up to $10^{-3}\%$. The precision on θ_1 is better than the one for θ_2 It must be also noticed that $\frac{\theta_1}{\theta_2} \approx 10^2$. θ_2 is therefore more sensitive to noise. Furthermore, with the biased operator $[D]$, the error is around 10 times greater than with $[\Delta]_1$ or $[\Delta]_2$.

5 CONCLUSION

This paper develops an original and efficient identification method for the estimation of material properties and damping. A significant enhancement is provided by the novel differentiation operator. The structural damping of a bar was estimated with an error smaller than 0.001%

REFERENCES

[1] E.K. Larsson and T. Söderström. Continuous-time AR parameter estimation by using properties of sampled systems. In *Proc. of the 15th IFAC world congress*, 2002.

[2] D. Remond, J. Neyrand, G. Aridon, and R. Dufour. On the improved use of chebyshev expansion for mechanical system identification. *Mechanical Systems and Signal Processing*, 22(2):390 – 407, 2008.

[3] Lui D-Y., O. Gibaru, and W. Perruquetti. Error analysis of jacobi derivative estimators for noisy signals. *Numerical Algorithms*, 58:53–83, 2011. 10.1007/s11075-011-9447-8.

[4] J.C. Mason and D.C. Handscomb. *Chebyshev polynomials*. Chapman & Hall/CRC, 2003.

[5] M. Mboup, C. Join, and M. Fliess. Numerical differentiation with annihilators in noisy environment. *Numerical Algorithms*, 50(4):439–467, 2009.

[6] C Chochol, S Chesne, and D Remond. An original differentiation tool for identification on continuous structures. *Journal of Sound and Vibration*, NA, 2013.

GUIDED WAVE PROPAGATION IN UNCERTAIN ELASTIC MEDIA THROUGH STOCHASTIC DIFFUSION MATRIX

F. BOUCHOUCHA[1*], M. N. ICHCHOU[2] and M. HADDAR[1]

[1]Unit of Dynamics of the Mechanical Systems (UDSM)
National School of Engineers of Sfax. BP. W3038 Sfax, TUNISIA
Email: fakersbouchoucha@yahoo.fr, mohamed.haddar@enis.rnu.tn

[2]Laboratory of Tribology and Dynamics of Systems (LTDS)
Ecole Centrale de Lyon – 36 Avenue Guy de Collongues 69130 Ecully. France
Email: Mohamed.Ichchou@ec-lyon.fr

ABSTRACT

In this paper, the authors present a numerical approach to study Defect detection through Stochastic Wave Finite Element Method. The uncertain material properties are modeled as a set of random fields. The structure is presented considering two waveguides connected through a stochastic coupling element, simulated as the defect (crack). Diffusion matrix for uncertain media through stochastic wave finite element method is studied in this paper. The forced response following a vibratory excitation is computed to investigate the defect detection. The computational efficiency of the method is demonstrated by comparison with MC simulation.

1 INTRODUCTION

Many researchers proposed some structural health monitoring (SHM) techniques in order to carry out the monitoring and the diagnosis of the risks [1, 2]. SHM is among the fields of application of guided wave propagation. Wave finite element method (WFEM) can be used for wave propagation predictions and wave scattering estimations. The WFEM regards the waveguide structure as a periodic system assembled by identical substructures, the dispersion curves and the mode shapes are among the primary properties to be given [3, 4].
In the literature, however, most of founded numerical issues of wave propagation simulations are mainly limited to deterministic media. Numerical guided wave techniques characterization in spatially homogeneous random media is investigated in this paper. The uncertainties are often present in geometric properties, material characteristics and boundary conditions of the model. These variables are taken into account in models according to the both parametric [5] and non-parametric [6] approaches. Ichchou et al [7] considered the wave propagation features in random guided elastic media through the Stochastic Wave Finite Element Method (S.W.F.E.M) using a parametric probabilistic technique. Bouchoucha et al [8] presented in their paper a numerical approach to study the guided elastic wave propagation in uncertain elastic media. Stochastic Wave Finite Element Method (S.W.F.E.M) formulation with consideration of spatial variability of material and geometrical properties is developed for probabilistic analysis of structures. They extended their work in [9] to the diffusion matrix for uncertain media through stochastic wave finite element method (SWFEM). The stochastic diffusion relationship allows evaluating the statistics of reflection and transmission coefficients under structural uncertainty.

This paper will extends mentioned works in order to provide a full numerical description of the stochastic problem of the wave propagation in uncertain damaged structure. The main contribution of this paper seems the calculation of the stochastic forced response of the uncertain waveguide with defect.

2 GUIDED WAVE PROPAGATION IN UNCERTAIN ELASTIC MEDIA THROUGH STOCHASTIC DIFFUSION MATRIX

The damaged structure is modelled by 2 periodic waveguides connected through a coupling element assimilated as a defect (figure 1). The stochastic parameters have a Gaussian distribution through the first order perturbation.

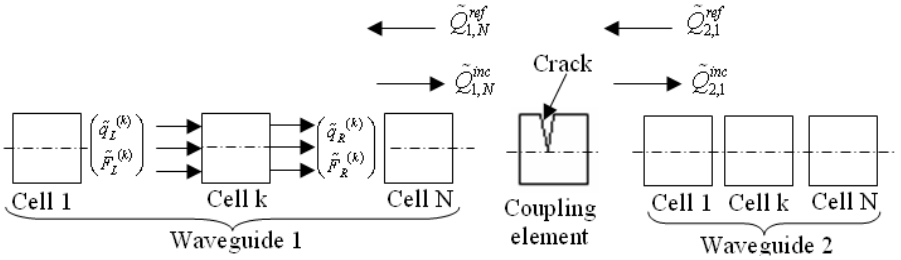

Figure 1. An illustration of the damaged structure

We consider the stochastic state vectors: $\tilde{u}_L = (\tilde{q}_L^T - \tilde{F}_L^T)^T$ and $\tilde{u}_R = (\tilde{q}_R^T \ \tilde{F}_R^T)^T$, we have:

$$\tilde{u}_R = \tilde{S}.\tilde{u}_L \tag{1}$$

Using a modal decomposition [8], the state vectors can be projected on the wave mode base as:

$$\tilde{u}_L^{(k)} = \tilde{\varphi}\,\tilde{Q}^{(k)}, \tilde{u}_R^{(k)} = \tilde{\varphi}\,\tilde{Q}^{(k+1)} \tag{2}$$

$$\begin{pmatrix} \tilde{Q}_{1,N}^{inc} \\ \tilde{Q}_{1,N}^{ref} \end{pmatrix} = \tilde{\lambda}^{N-1} \begin{pmatrix} \tilde{Q}_{1,1}^{inc} \\ \tilde{Q}_{1,1}^{ref} \end{pmatrix} \text{ and } \begin{pmatrix} \tilde{Q}_{2,N}^{inc} \\ \tilde{Q}_{2,N}^{ref} \end{pmatrix} = \tilde{\lambda}^{N-1} \begin{pmatrix} \tilde{Q}_{2,1}^{inc} \\ \tilde{Q}_{2,1}^{ref} \end{pmatrix} \tag{3}$$

Where $\tilde{Q}^{(k)}$ is the vector of the stochastic wave mode amplitude, $\tilde{\varphi}$ is the matrix of the stochastic

eigenvectors, $\tilde{\lambda}$ is a diagonal stochastic eigenvalue matrix. Using the wave/defect interaction, the diffusion matrix is written as [9]:

$$\begin{pmatrix} \tilde{Q}_{2,1}^{inc} \\ \tilde{Q}_{2,1}^{ref} \end{pmatrix} = -\begin{pmatrix} \tilde{D}_{LR}^{c}\tilde{\varphi}_{q}^{inc} & \tilde{D}_{LR}^{c}\tilde{\varphi}_{q}^{ref} \\ \tilde{D}_{RR}^{c}\tilde{\varphi}_{q}^{inc} - \tilde{\varphi}_{F}^{inc} & \tilde{D}_{RR}^{c}\tilde{\varphi}_{q}^{ref} - \tilde{\varphi}_{F}^{ref} \end{pmatrix}^{-1} \begin{pmatrix} \tilde{D}_{LL}^{c}\tilde{\varphi}_{q}^{inc}\tilde{\lambda}^{inc} + \tilde{\varphi}_{F}^{inc}\tilde{\lambda}^{inc} & \tilde{D}_{LL}^{c}\tilde{\varphi}_{q}^{ref}\tilde{\lambda}^{ref} + \tilde{\varphi}_{F}^{ref}\tilde{\lambda}^{ref} \\ \tilde{D}_{RL}^{c}\tilde{\varphi}_{q}^{inc}\tilde{\lambda}^{inc} & \tilde{D}_{RL}^{c}\tilde{\varphi}_{q}^{ref}\tilde{\lambda}^{ref} \end{pmatrix} \begin{pmatrix} \tilde{Q}_{1,N}^{inc} \\ \tilde{Q}_{1,N}^{ref} \end{pmatrix} \quad (4)$$

Where $\tilde{\mathbf{D}}^{c}$ is the stochastic dynamic stiffness matrix of the coupling element.
The stochastic displacement $\tilde{q}_{L}^{(k)}$ can be calculated as follows:

$$\tilde{q}_{L}^{(k)} = \tilde{\varphi}_{q}^{inc}\left(\tilde{\lambda}^{inc}\right)^{(k-1)}\tilde{Q}^{inc(1)} + \tilde{\varphi}_{q}^{ref}\left(\tilde{\lambda}^{ref}\right)^{(k-1)}\tilde{Q}^{ref(1)} \quad (5)$$

Where $\tilde{Q}^{(1)}$ is already calculated by adopting the appropriate boundary conditions.

3 NUMERICAL RESULTS AND DISCUSSION

In this section, we study the longitudinal vibration of the structure in order to validate the SWFEM. We consider the following boundary conditions:

$$\tilde{F}_{L}^{(1)} = \tilde{F}\ (\text{excitation}) \text{ and } \tilde{F}_{R}^{(N)} = 0\ (\text{free end}) \quad (6)$$

The excitation has a Gaussian distribution $\tilde{F} = \overline{F} + \sigma_{F}.\varepsilon$ when $\sigma_{F} = 0.05.\overline{F}$.

We introduce the uncertainty in the structural parameters to study their effects on the wave propagation. These parameters were a Gaussian distribution (standard deviation = 0.05.mean).

We study the forced response of the structure with defect for the longitudinal mode. Monte Carlo simulations are used to validate the SWFEM results. The mean of the stochastic forced response with defect is presented in figure 2. The effect of the structural parameter perturbations in presence of defect is presented in figure 3. In figure 4, we present the mean and the standard deviation of the forced response with defect following uncertainty introduced in Young modulus in order to demonstrate the efficiency of the proposed method. In fact, the wave propagation isn't affected by the perturbation of the structural parameters. Figure 5 illustrates the competence of the SWFEM as a tool for the defect detection through the comparison between the forced response with and without defect.

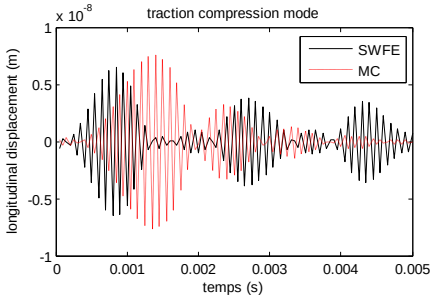

Figure 2. Mean of the forced response of the waveguide with defect

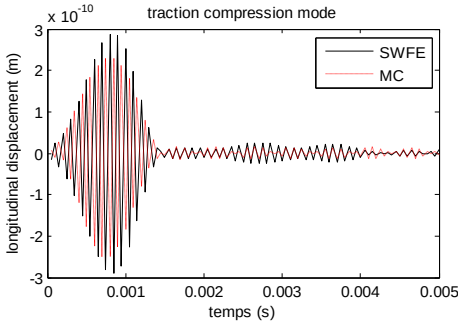

Figure 3. Standard deviation with defect (E stochastic)

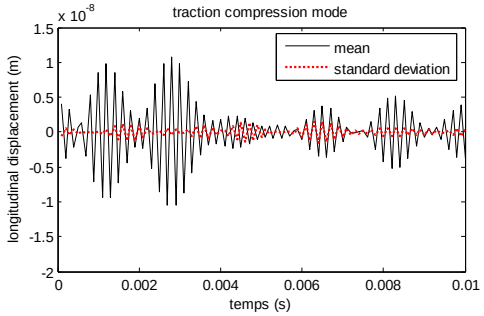

Figure 4. The forced response with defect (E stochastic)

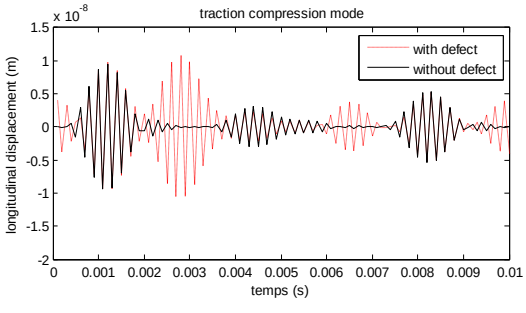

Figure 5. The defect detection for the traction compression mode

4 CONCLUSION

In this paper, the subject of forced response in uncertain structure with defect was dealt with. The structure is presented considering two waveguides connected through a stochastic coupling element, simulated as the defect (crack), the stochastic diffusion relationship is used to study the wave/defect interaction following an uncertainty introduced in the structure parameters. The stochastic wave finite element method is used for the defect detection in uncertain structure. The main paper finding can be extracted as follows:

1. Stochastic forced response associated to stochastic wave propagation is given.
2. Stochastic diffusion matrix associated to damage front is given. This paper provides a numerical investigation of guided waves and defect interaction.
3. The defect detection in uncertain structure is offered.

The SWFE offers some interesting research perspectives. The use of SWFE for energy issues in complex wave guide is an important task. Among the investigations in progress, the mid and high frequencies behavior is the main target in this case. Further investigations are under progress in order to use such numerical methods in the context of smart materials and structures.

REFERENCES

[1] DN. Alleyne, MJS. Lowe, P. Cawley. The reflection of guided waves from circumferential notches in pipes. *Journal of Applied Mechanics* 65: 635-641, 1998.

[2] F. Bouchoucha, M. Akrout, T. Fakhfakh, MN. Ichchou, M. Haddar. Detection of the defects in cylindrical pipes: Application to the Wave Finite Element Method. *International journal of Modeling, identification and control (IJMIC)* 9(4): 336-349, 2010.

[3] JM. Mencik, MN. Ichchou. Multi mode propagation and diffusion in structures through finite element. *European journal of Mechanics/ A: Solid* 24(5): 877–898, 2005.

[4] D. Duhamel, BR. Mace, MJ. Brennan. Finite element analysis of the vibrations of waveguides and periodic structures. *Journal of Sound and Vibration* 294: 205–220, 2006

[5] M. Pellissetti, E. Capiez-Lernout, H. Pradlwater, C. Soize, GI. Schueller. Reliability analysis of a satellite structure with a parametric and a non-parametric probabilistic model. *Comput. Methods appl. Mech. Engrg.* 198: 344-357, 2008.

[6] C. Soize. A nonparametric model of random uncertainties in linear structural dynamics. *ISBN* 152: 109–138, 1999.

[7] MN. Ichchou, F. Bouchoucha, MA. Ben Souf, M. Haddar, O. Dessombz. Stochastic wave finite element for random periodic media through first-order perturbation. *Comput. Methods appl. Mech. Engrg.* 200: 2805-2813, 2011.

[8] F. Bouchoucha, MN. Ichchou, M. Haddar. Guided wave propagation in uncertain elastic media. *Ultrasonics* 53: 303–312, 2013.

[9] F. Bouchoucha, MN. Ichchou, M. Haddar. Diffusion matrix through stochastic wave finite element method. *Finite Elements in Analysis and Design* 64: 97–107, 2013.

BIFURCATION BEHAVIOR IN SWITCHING CONVERTERS DRIVING OTHER DOWNSTREAM CONVERTERS IN DC DISTRIBUTED POWER SYSTEMS APPLICATIONS

A. El Aroudi[1], D. Giaouris[2], L. Martinez-Salamero[1], S. Banerjee[3], S. Voutetakis[2] and S. Papadopoulou[2,4]

[1]Department of Electronics,
Electrical Engineering and Automatic Control
Universitat Rovira i Virgili, Tarragona, Spain,
Email: {abdelali.elaroudi,luis.martinez}@urv.cat

[2]Chemical Process Engineering Research Institute,
Centre for Research and Technology Hellas, Thermi-Thessaloniki, Greece
Email: damian.giaouris@ncl.ac.uk

[3]IISER-Kolkata, Mohanpur Campus,
Nadia 741252, India,
Email: soumitro.banerjee@gmail.com

[4]Department of Automation,
Alexander Technological Educational Institute of Thessaloniki, Thessaloniki, Greece

ABSTRACT

This paper presents a study of nonlinear dynamics of switching converters feeding other downstream converters for distributed power electronics systems. It is observed that these systems can exhibit some interaction of different kind of instabilities that give rise to complex bifurcation behavior. Although this interaction has been already observed in stand-alone converters, the mechanism of its creation is quite different. The complete system can be modeled with high order nonlinear model. However, in order to study these complex phenomena, a simple still accurate model is needed. First, using some physical insights, a simple equivalent system is obtained and then, a simplified reduced-order model is derived. Numerical simulations shows a good agreement between the full-order and the reduced-order models[1].

[1]This work has been partially supported by the Spanish Ministry of Science and Innovation by projects DPI2010-16481, DPI2010-16084 and CSD2009-00046 and National Strategic Reference Framework (NSRF) 2007-2013 of Greece and the European Union, research program “SYNERGASIA" (SUPERMICRO).

1 INTRODUCTION

During the two last decades, much effort has been devoted to the study of nonlinear behavior in switching converters [1]. A large variety of complex nonlinear instability phenomena, such as period doubling leading to subharmonic oscillations, and Hopf or Neimark-Sacker bifurcations leading to slow scale instabilities have been studied. These studies, which are mostly based on *exact* discrete-time models, allow a deep understanding of the fundamental properties which describe the nonlinear dynamic behavior of these systems. Another technique based on Floquet theory and *Filippov's method* together with the *saltation matrix*, which is inspired from mechanics community, has been recently used in [2] for analyzing the bifurcation behavior in dc-dc converters and similar results to those obtained from the discrete-time approach have been obtained. In practice, it is desirable that the system operates periodically with a constant switching frequency $f_s = 1/T$ equal to that of an external clock signal. However, under parameter changes, the stability of this operating mode can be lost resulting in bifurcation phenomena [1]. Theoretically, three different kinds of smooth bifurcations can occur in a switched-mode dc-dc power converter, namely: period-doubling bifurcation, Neimark-Sacker bifurcation and saddle-node bifurcation [1]. The two first kinds of bifurcations result in the lost of the stability of the stable T-periodic orbit. The last one corresponds to the collision and anhilation of two different T-periodic orbits. Interaction of more than one instability has also been reported in [3, 4] where different interaction mechanisms can be identified. There have been hitherto many research efforts devoted to stand-alone converters *ended by a constant resistance load*. In distributed power electronics applications, switching converters are loaded by other converters and if the input current in the second stage is tightly regulated to its desired value, the first stage see this converter as a *constant current sink*. The current mode operation in DPS provides fast transient response, eases loop stabilization and cycle-by-cycle current limitation and thermal shutdown protection [5]. However, their dynamics will be quite different than those converters whose load is a constant resistance. Due to its superiority over voltage mode control, current mode control (CMC) is used in DPS line conditioners which provides a regulated voltage at the first stage (Bus voltage) [5]. The rest of this work is organized as follows: Section II deals with the description of the system under study which consists of a cascade connection of two switching converters. In Section III, some bifurcation phenomena exhibited by the system are shown and then explained in terms of Floquet multipliers, corresponding to both $T-$periodic and $2T-$periodic, obtained from a reduced-order Poincaré map. Finally, some conclusions are given in the last section.

2 SYSTEM DESCRIPTION

The CMC two stage dc-dc converter considered in this study is shown in Fig. 1-a. It is assumed that both converter stages operate in continuous conduction mode (CCM). In this case, the inductor currents are always positive Both switch and diode are considered ideal and the Equivalents Series Resistance (ESR) of inductors and capacitors are included in the circuit. The system is controlled by comparing the input currents of the first and the second stages i_{L1} and i_{L2} with their reference values i_{ref1} and i_{ref2}. The second stage is a boost converter with tightly regulated input current using a very fast controller. A hysteretic comparator, with a hysteresis width h, is used for the second stage. The inductor current in the first stage, which consists of a buck converter, is controlled by a typical peak CMC with an external $T-$periodic ramp compensator $v_r(t)$. Therefore, at the beginning of the cycle in the first stage, the switch S_1 is turned on. The controlled current i_{L1} increases until it reaches the signal $i_{ref1} - m_{a1}(t \bmod T)$, the switch S_1 is then turned off, and remains off until the next cycle begins. During this time, the diode D_1 is on. m_{a1} is the slope of the $T-$periodic ramp compensator. The second stage is

regulated by a very fast controller in such a way that the inductor current in this stage is equal to its reference value, i.e., $i_{L2} = i_{ref2}$. Therefore, as shown in Fig. 1-b, the second stage can be considered as a current source feeding the load resistance R in parallel with the filtering capacitor C_2 while the first stage can be seen as a buck converter with a constant current sink as a load [6].

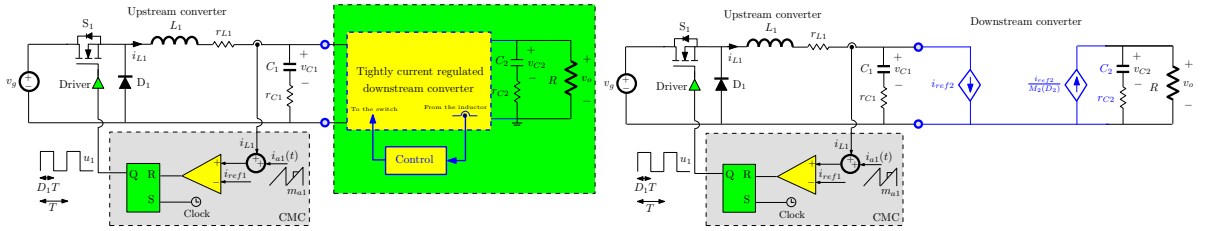

(a) (b)

Figure 1: Schematic diagram of a buck converter loaded by another switching converter. (a) General scheme, (b) Simplified diagram.

3 BIFURCATION BEHAVIOR

The parameters used are shown in Table 1 and they are selected as practical values for a typical DPS [5]. Let us consider the demanded current i_{ref1} in the first stage as a bifurcation parameter. This parameter is varied within the range (40, 54) A and the bifurcation diagram of the full-order and the reduced-order system are plotted. The results are shown in Fig. 2. In the case of the reduced-order model, the $T-$periodic, $2T-$periodic branches and and the borderline defined by $I_{\mathrm{BL}} = i_{ref1} - m_{a1}T$ obtained all analytically are also plotted. In both cases, in order to illustrate how the trajectory of the system is evolving, the samples $i_{L1}(2nT)$ and $i_{L2}(2nT)$ at even multiples of the switching period are plotted in dark color while those at odd multiples of the switching period, $i_{L1}((2n+1)T)$ and $i_{L2}((2n+1)T)$, are plotted in light color. It can be observed that for $i_{ref1} < 46.1$ A, the system presents a stable periodic behavior. At $i_{ref1} \approx 46.1$ A, the dynamic behavior of the system becomes suddenly quasiperiodic. It can be believed that a Neimark-Sacker or Hopf bifurcation takes place at $i_{ref1} \approx 46.1$ A. However a careful examination of the bifurcation diagrams reveals that at this critical point, a saddle-node bifurcation takes place and just very close to this point, an unstable $2T-$periodic orbit is born. The Floquet multipliers of the $2T$-periodic orbit are complex conjugates with modulus larger than 1 giving rise to a quasiperiodic behavior. As a consequence, for $46.1 < i_{ref1} < 54$, the Poincaré section is formed by two loops. As the parameter i_{ref1} is decreased, the loops become closer and closer till they collide at $i_{ref1} \approx 46.1$ A. For values of i_{ref1} smaller than this critical value, the system desired periodic regime is stable.

Table 1. The used parameter values for this study.

v_g	L_1 and L_2	C_1 and C_2	R	h	i_{ref2}	f_s	m_{a1}
120 V	37.5 and 100 μH	420 and 100 μF	10 Ω	1 A	38 A	50 kHz	10^3A/s

4 CONCLUSIONS

In this work, we have studied the nonlinear dynamics of a cascaded two stage switching converter for distributed power electronics applications. The different behaviors exhibited by the

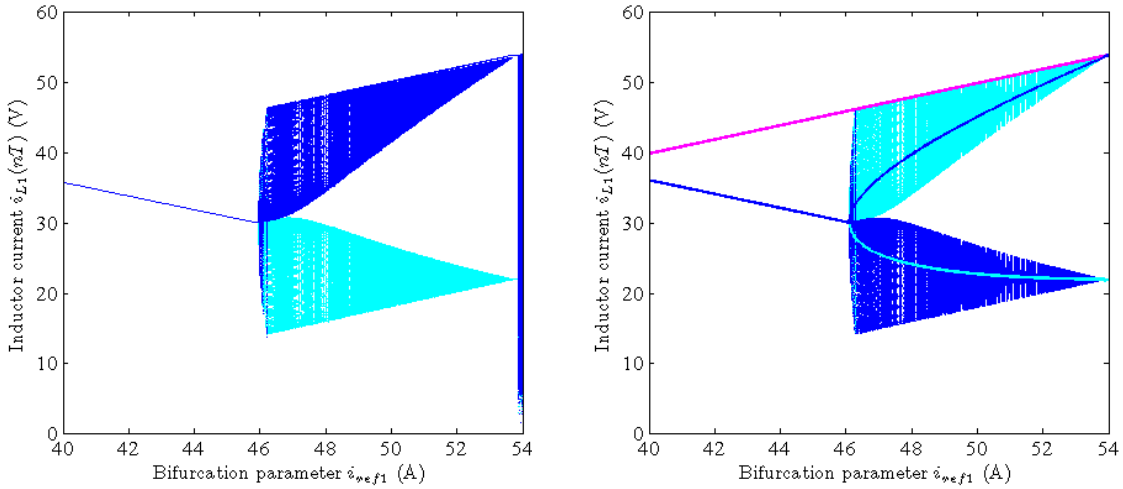

Figure 2: Bifurcation diagrams from the full-order (left) and reduced-order (right) model. The resemblance between the results is remarkable.

system are unfolded. A reduced-order equivalent circuit has been used to derive a simplified reduced-order model for the system. Bifurcation diagrams show that the full-order and the reduced-order models exhibit qualitatively very similar behaviors. In particular, it has been shown that the system exhibits an interaction between a period doubling bifurcation of the first order Poincaré map and a Neimark-Sacker bifurcation of its second iterate. This has been proved by computing the Floquet multipliers of $T-$periodic and $2T-$periodic orbits.

REFERENCES

[1] A. El Aroudi, M. Debbat, G. Olivar, L. Benadero, E. Toribio and R. Giral, "Bifurcations in DC-DC Switching Converters Review of Methods and Applications," *International Journal of Bifurcation and Chaos,* Vol. 15, No 5, pp. 1549-1578, May 2005.

[2] D. Giaouris, S. Banerjee, B. Zahawi, V. Pickert, "Stability Analysis of the Continuous-Conduction-Mode Buck Converter Via Filippov's Method," *IEEE Transactions on Circuits and Systems I: Regular Papers,* Vol. 55, No. 4, pp. 1084 - 1096, 2008.

[3] Y. Chen, C. K. Tse, S. S. Qiu, L. Lindenmuller, and W. Schwarz, "Coexisting fast-scale and slow-scale instability in current-mode controlled DC/DC converters: Analysis, simulation and experimental results," *IEEE Transactions on Circuits and Systems I: Regular Papers,* Vol. 55, No. 10, pp. 3335-3348, 2008.

[4] D. Giaouris, S. Banerjee, O. Imrayed, K. Mandal, B. Zahawi, and V. Pickert: "Complex interaction between tori and onset of 3-frequency quasiperiodicity in a current mode controlled boost converter," *IEEE Transactions of Circuits and Systems-I,* Vol. 59, No. 1, pp. 207-214 , Jan. 2012.

[5] B. Choi, B. H. Cho, and S.-S. Hong, "Dynamics and Control of DC-to-DC Converters Driving Other Converters Downstream," *IEEE Transactions on Circuits and Systems I: Fundamental Theory and Applications*, Vol. 46, No. 10, pp. 1240-1248, Oct. 1999.

[6] G.-H. Zhou , J.-P Xu, B.-C, F. Bao and X.-S Liu, " Fast-Scale and Slow-Scale Subharmonic Oscillation of Valley Current-Mode Controlled Buck Converter," *Chin. Phys. Lett,* vol. 27. No. 9, 090504-1-090504-4, 2010.

CHAOS CONTROL BY TIME-DELAYED FEEDBACK: OBSERVING GLOBAL PROPERTIES IN ELECTRONIC CIRCUITS

H. Benner[1*], C.-U. Choe[1], K. Höhne[1], C. v.Loewenich[1]. H. Shirahama[1,2], and W. Just[3]

[1]Institute of Solid State Physics, TU Darmstadt, Darmstadt, GERMANY
Email: benner@physik.tu-darmstadt.de

[2]Faculty of Education, Ehime University Matsuyama, JAPAN
Email: jyuichiro@yahoo.co.jp

[3]School of Math. Sciences, Queen Mary/University of London, London, UK
Email: w.just@qmul.ac.uk

ABSTRACT

Delayed feedback control is a convenient tool to stabilize unstable periodic orbits embedded in strange attractors of chaotic systems. We review recent developments for the control of chaos by time-delayed feedback methods. The essential ideas for a general theoretical approach are sketched , and the results are compared with experiments on electronic circuits. In particular, we focus on two topical problems: (i) We show, both analytically and experimentally, that the success of control is not only determined by the change of local stability of the unstable orbit but depends sensitively on the continuous or discontinuous type of transitions at the control boundaries. A subcritical transition at the control boundary gives rise to small basins of attraction and limits the control scheme considerably. (ii) We demonstrate the feasibility of an unstable control loop to stabilize torsion-free orbits not accessible by standard delayed-feedback control. Analytical normal form calculations and numerical simulations reveal a severe dependence of the control performance on the coupling scheme of the control force. These predictions are confirmed by the experiments and emphasize the importance of the coupling scheme for the global control performance.

1 INTRODUCTION

Time-delayed feedback control introduced by Pyragas in the early '1990s is a simple, robust and efficient method to control unstable periodic orbits in chaotic systems [1]. To apply this method one only needs a scalar output signal s(t) of the dynamical system and the period τ of the unstable periodic orbit (UPO) to be stabilized. The control force, which is fed back to the dynamical system, has the form

$$F(t)=K[s(t)-s(t-\tau)], \tag{1}$$

where K is the control amplitude. The control is non-invasive, i.e. once the periodic orbit is reached, we have s(t) = s(t +τ), and the control force vanishes. Local properties of time-delayed feedback control, i.e. the stability of the target orbit, are meanwhile well understood by local theory. Linear stability analysis reveals several restrictions for successful control: (i) a limited control interval, (ii) an upper limit for the maximal Lyapunov exponent and (iii) the necessity of finite torsion. These limitations have been derived under quite general conditions and are in very good qualitative and quantitative agreement with experimental findings [2]. However, from a practical point of view global properties, like the basin of attraction of the controlled state or the robustness against external perturbations, are of similar importance and may strongly affect the control performance.

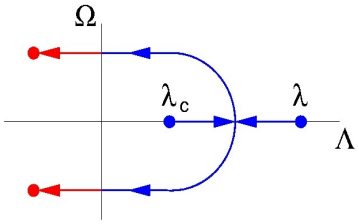

Figure 1. Mechanism of time-delayed feedback control by means of an unstable controller. The real Floquet exponents of the unstable system, λ, and of the unstable controller, λ_c, collide under the influence of the control force, and a Hopf bifurcation occurs.

Early analytical investigations indicated that unstable orbits with an odd number of real unstable modes cannot be stabilized by this method [3]. To overcome this limitation the counter-intuitive idea of an unstable control loop has been proposed [4]. By including an additional unstable mode into the control loop one artificially enlarges the set of real multipliers greater than unity to an even number (see Figure 1). We demonstrate the feasibility of an unstable control loop to stabilize such torsion-free orbits in an electronic circuit experiment. Analytical normal form calculations and numerical simulations reveal a severe dependence of the control performance on the coupling scheme of the control force. These predictions are confirmed by the experiment and emphasize the importance of the coupling scheme for the global control performance [5].

2 THEORETICAL APPROACH

2.1 Unstable van der Pol oscillator

A prominent paradigmatic system showing such torsion-free unstable orbits is the unstable van der Pol oscillator which is described by the following equations of motion:

$$\begin{aligned} \dot{x}(t) &= -y(t) + \varepsilon\, x(t) + x^3/3 \\ \dot{y}(t) &= x(t) \end{aligned} \tag{2}$$

Here, ε is the bifurcation parameter of the system, and the time scale is normalized to the inverse oscillator frequency. For $\varepsilon < 0$, this equation has two coexisting solutions, a stable fixed point at the origin $x = y = 0$, and an unstable limit cycle with period $\tau = 2\pi + O(\varepsilon)$, amplitude $2\sqrt{-\varepsilon}$ and a real positive Floquet exponent $\lambda = -\varepsilon$. For $\varepsilon > 0$ the limit cycle disappears, and the fixed point at the origin becomes unstable. Thus at $\varepsilon = 0$ we have a subcritical Hopf bifurcation. The real positive Floquet exponent indicates that the limit cycle is unstable and shows no torsion. In such a case any attempt to stabilize the unstable orbit by conventional time-delayed feedback control would fail.

2.2 Applying the concept of an unstable controller

We assume that x is an observable accessible in experiment. To stabilize the unstable periodic orbit appearing for $\varepsilon < 0$ we consider the following control algorithm:

$$\begin{aligned} \dot{x}(t) &= -y(t) + \varepsilon\, x(t) + x^3/3 + w(t) f(x(t)) \\ \dot{y}(t) &= x(t) \\ \dot{w}(t) &= \lambda_c w(t) - K(x(t) - x(t-\tau)) f(x(t)) \end{aligned} \tag{3}$$

The term $w\,f(x)$ in the top line is the control signal perturbing the x-variable. The specific form of this coupling is given by the smooth function $f(x)$ and will be specified later. The bottom line describes an unstable delayed feedback controller with $\lambda_c > 0$. Here w is the dynamical variable of the controller and K determines the feedback strength. Note that the control scheme does not change the solution of the free system corresponding to the unstable orbit of period τ, since for $x(t) = x(t-\tau)$ Equation (3) is satisfied by $w = 0$ and the control signal $w(t)\, f(x(t))$ vanishes. The possibility to stabilize such an orbit was explored both analytically and by means of numerical simulations [5], and successful control was achieved.

3 EXPERIMENT

We now apply the concept of an unstable controller to an experimental situation where e.g. limited sensitivity, drifting parameters and noise may severely hamper the control performance.

3.1 Design of the electronic circuit

We designed an autonomous electronic circuit along the lines of Equation (3). A block diagram of this setup is shown in Figure 2. Besides the van der Pol oscillator circuit, the diagram includes the unstable controller as well as elements for defining the experimental initial condition. The bifurcation parameter ε, the control amplitude K, and the positive exponent λ_c are determined by the gain of electronic amplifiers. It turned out that small internal offset voltages at the electronic multipliers could affect the size, symmetry, and position of the target orbit. For defining the initial conditions we introduced switches which allowed to apply adjustable constant voltages x_0, y_0, and w_0, respectively. Thus, when switching on the system at t=0, the variables $x(t)$ and $y(t)$ start from a well-defined state. At about two cycles later, the feedback loop which generates the control signal and the controller variable $w(t)$ are switched on. Such a time-lag is necessary to fill the memory with the history of the uncontrolled dynamics.

3.2 Experimental Results

Our experimental results underline that the success of control depends sensitively on the specific form of the coupling function $f(x)$. When applying a linear coupling $f(x) = x$ successful control was obtained, as expected from our numerical simulations, only for a small range of initial conditions close to the target orbit. Starting from initial conditions outside this small range the

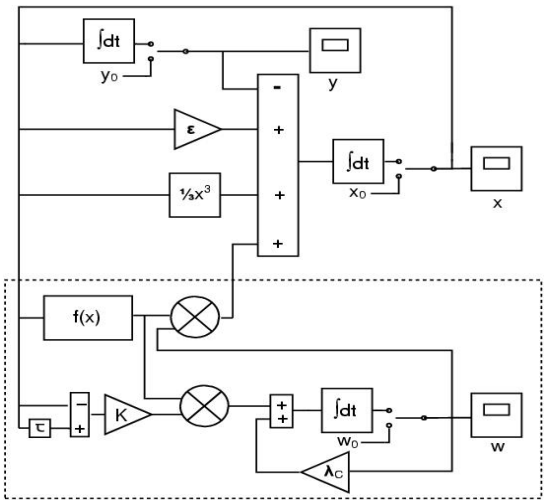

Figure 2: Block diagram of the van der Pol oscillator with control loop.

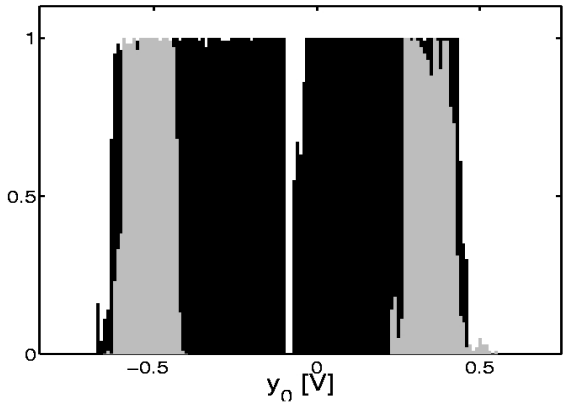

Figure 3: Experimentally obtained histograms for successful control as a function of the initial condition y_0. Grey: linear coupling $f(x) = x$ ($K = 0.4$), black: sigmoidal coupling $f(x) = \mathrm{sign}(x)$ ($K = 0.15$).

controller variable $w(t)$ immediately escaped to infinity while $x(t)$ and $y(t)$, after some irregular transient, either approached the center of the orbit or ended up in high amplitude oscillations. When replacing the linear coupling $f(x) = x$ by a sigmoidal one, e.g. $f(x) = \mathrm{sign}(x)$, the situation changed considerably. A quantitative estimate of the control performance was obtained by varying both the control amplitude and the initial conditions at a fixed value of $\varepsilon = -0.1$. In the case of linear coupling control was achieved in the range $K \in [0.28, 0.67]$ with shortest transient behaviour at about $K = 0.4$ while for the sigmoidal case control was observed in the range $K \in [0.12, 0.16]$. We fixed the initial conditions x_0 and w_0 at zero and changed y_0 from −0.8 V to +0.8 V in steps of 10 mV. For each set of initial values we repeated the control experiment about 100 times. The fraction of successful attempts is shown in a histogram, Figure 3, in dependence of y_0. For linear coupling successful control was merely achieved for values of y_0 slightly below the radius of the unstable orbit. For the sigmoidal coupling the 'basin of attraction' of the controlled orbit was found to be much larger than before. Apart from a narrow gap at the centre, the basin now covers the full range of y_0 inside the orbit.

We have studied in detail the implementation of an unstable controller to stabilize periodic orbits with a single real unstable Floquet mode by time-delayed feedback control. Our setup provides the first experimental proof of the feasibility of such a concept. We therefore conclude that unstable controllers are a suitable tool to broaden the scope of time-delayed feedback techniques. Furthermore, our analysis highlights the importance of suitable coupling schemes to improve the overall control performance, in particular with regards to basins of attraction.

REFERENCES

[1] K. Pyragas, *Phys. Lett. A,* 170: 421-428 (1992).

[2] W. Just, T. Bernard, M. Ostheimer, et al., *Phys. Rev. Lett. 78*, 203-206 (1997).

[3] H. Nakajima, *Phys. Lett. A*, 232: 207-210, 1997.

[4] K. Pyragas, *Phys. Rev. Lett.*, 86(11): 2265-68, 2001.

[5] K. Höhne, H. Shirahama, C.-U. Choe, et al. , *Phys. Rev. Lett.*, 98: 214102, 2007.

DYNAMICS OF A PIECEWISE LINEAR ENERGY HARVESTING SYSTEM

A. El Aroudi[1], H. Ouakad[2] and M. Younis[3]

[1] Department of Electronics, Electrical Engineering and Automatic Control
Universitat Rovira i Virgili, Tarragona, Spain, Email: abdelali.elaroudi@urv.cat

[2]Mechanical Engineering Department,King Fahd University of Petroleum and Minerals, Dhahran, PO Box. 31261, Saudi Arabia, Email: houakad@kfupm.edu.sa

[3]Physical Sciences and Engineering Division, King Abdullah University of Science and Technology KAUST, Suadi Arabia
Email: mohammad.younis@kaust.edu.sa

ABSTRACT

Recently, nonlinearities have been shown to play an important role in increasing the extracted energy of vibration-based energy harvesting systems. In this paper, we study the dynamical behavior of a piecewise linear (PWL) spring-mass-damper system for vibration-based energy harvesting applications. After a frequency response analysis, we show that the harvested energy could be larger at low frequencies as compared to an equivalent linear system. This could be an advantage for potential use of this system in low frequency vibrational-based energy harvesting. First, we present a continuous time single degree of freedom PWL dynamical model of the system. From this PWL model, different configurations of the system and their corresponding state space regions can be identified. Then, extensive numerical simulations are carried out by computing time domain series, state space trajectories and frequency responses under a deterministic harmonic excitation for different sets of system parameter values[1].

[1]This work has been partially supported by the Spanish Ministry of Science and Innovation under grant DPI2010-16481 and the Deanship of the Scientific Research (DSR) at KFUPM through project No. JF111011.

1 INTRODUCTION

Recently, there has been a lot of interest in self-powered devices in remote environment applications where the use of rechargeable batteries becomes inviable or problematic such as in hard-to-access locations. Some approaches have been investigated in the literature to solve this problem by using energy harvesting techniques [1]. Among the commonly used energy sources, vibrational kinetic energy is the most used for applications such as development of micro generators and noise harvesters [1]. In most of the reported studies, the energy harvesters are designed as linear resonators by matching the resonant frequency of the harvester with that of the external excitation to extract maximum power. This maximum power extraction depends on the quality factor (Q factor) of the linear resonator but it is viable only when the excitation frequency is known a priori. Moreover, a maximum energy extraction with a high Q factor will paradoxically imply a limited and narrow frequency range within which energy can be harvested. The performances of these systems are therefore rapidly degraded if the excitation frequency is far from the resonant one and being therefore only effective when an optimum design is performed by tuning the resonance frequency to match with the ambient source vibrations frequency. However, in environments where no single dominant frequency exists, these performances can be lowered significantly as the excitation frequency moves away from the designed frequency. Some solutions have been reported recently to remedy these problems. Among them, we can quote resonance tuning, frequency up-conversion techniques and nonlinear wide bandwidth energy harvesting [1]. Traditionally, nonlinearities are to be avoided in device design. However, recently these nonlinearities have been shown to have a potential to allow designers to take advantages of nonlinear behavior in certain applications [2]. In the nonlinear energy harvesting approach, rather than resonance frequency tuning, the nonlinearity of the system is exploited to improve the performances of the energy harvester within a wide frequency range outperforming, in this way, classical resonant energy harvesters [2], [3].

The ultimate aim of this work is to study the dynamical behavior of a PWL system proposed recently for energy harvesting applications [4]. The rest of the paper is organized as follows. In Section 2, a brief description of the system is provided. In Section 3, the dynamical model of the PWL model is presented and its different configuration are unfolded. The dynamics of the system is studied in Section 4 when the external force intensity and frequency together with other system parameters are varied. Finally, conclusions are presented in the last section.

2 SYSTEM DESCRIPTION

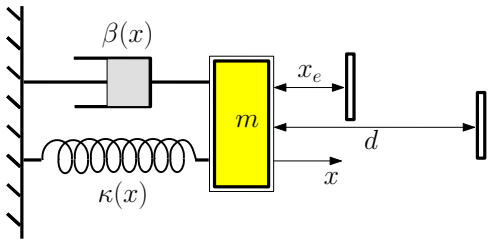

Figure 1. Schematic diagram the spring-mass-damper system with spatial limitations.

In the present work we study the dynamical behavior of a PWL energy harvester first considered in [4]. The schematic diagram of the system is shown in Fig. 1. It consists of

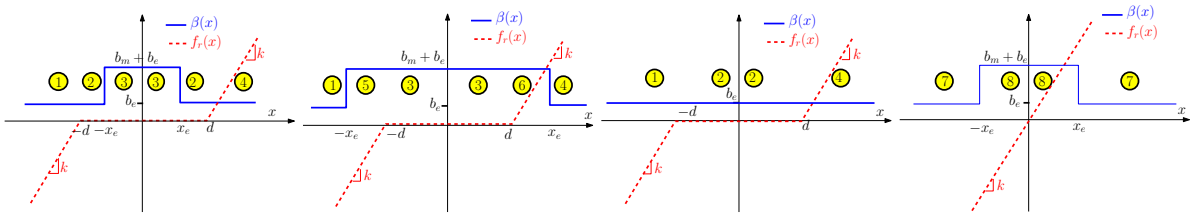

(a) $d > x_e$ (b) $d < x_e$ (c) $b = 0$ (d) $d = 0$

Figure 2. Functions $\beta(x)$ and $f_r(x)$ for different cases.

a spring-mass-damper system for vibration-based energy harvesting applications [4] where a piecewise linear (PWL) model for the friction and the stiffness is considered which models spatial limitations [4]. The piecewise linearity comes from the fact that the electromechanical coupling is assumed to be significant only over a finite interval for the displacement x of the mass m. Moreover, the restoring force $f_r(x) := \kappa(x)x$ acting on the inertial mass is assumed to contain an interval of zero stiffness, with a linear term outside this region. In particular, the state dependent mechanical damping factor $\beta(x)$ can be expressed as the sum of an electromechanical damping term $\beta_e(x)$ depending on the state and a purely mechanical constant term b_m, i.e., $\beta(x) = \beta_e(x) + b_m$, where the term $\beta_e(x)$ and the restoring force $f_r(x)$ are expressed as follows

$$\beta_e(x) = \begin{cases} b_e & \text{if} \quad |x| \leq x_e \\ 0 & \text{if} \quad |x| > x_e \end{cases} \tag{1}$$

$$f_r(x) = \begin{cases} k(x+d) & \text{if} \quad x < -d \\ 0 & \text{if} \quad |x| \leq d \\ k(x-d) & \text{if} \quad x > d \end{cases} \tag{2}$$

Note that the stiffness corresponding to a linear spring can be restored from (2) by just putting $d = 0$. Similarly, making $b_e = 0$ in (1), one has the linear mechanical damping case.

3 DYNAMICAL MODEL

Let us consider that the system is driven harmonically with an external force $f(t) = F\sin(\omega_f t)$. By applyig Newton's law, the system can be described by the following set of differential equations

$$\ddot{x} + \frac{1}{m}\left[\beta(x)\dot{x} + \kappa(x)x\right] = \frac{F}{m}\sin(\omega_f t) \tag{3}$$

where x is the mass displacement, ω_f is the harmonic forcing angular frequency, and the overdot stands for differentiation with respect to time. The dynamics of the system is highly dependent on the system parameters. In particular, depending on the values of parameters d and x_e, different sequences and configurations can take place. Figure 2 shows the possible cases depending on whether $d < x_e$ or $x_e < d$, $b \to 0$ or $d \to 0$.

4 NUMERICAL SIMULATIONS

The same set of parameter values considered in [4] are used in this study. These are: $b_m = 0.1$, $\beta = 0.05$, $m = 0.1$, $k = 1$, $d \in (0, 5)$, $x_e = 1$. The excitation angular frequency is swept in the range $(0.1, 2\pi)$ rad/s and the steady-state solution are computed. The corresponding frequency response is then obtained. The results are shown in Fig. 3 for different values of force intensity

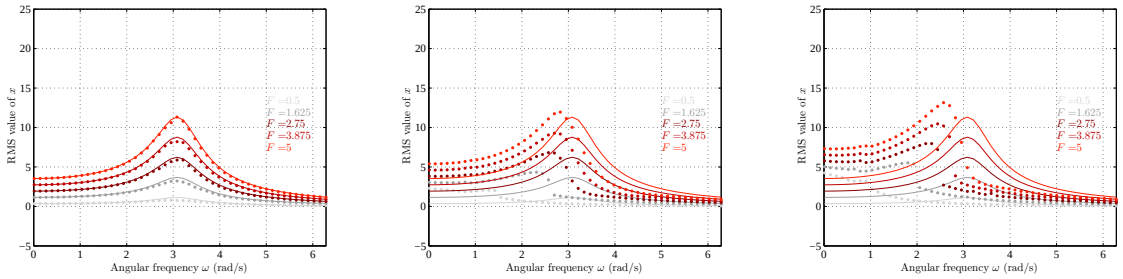

(a) $d = 0$ (b) $d = 2$ (c) $d = 4$

Figure 3: Numerically obtained frequency responses (dots) of the PWL system and the analytical frequency response (solid) of the linear equivalent system for different values F and d.

F and distance d. For comparison, the frequency response of an equivalent linear system ([5]) is also plotted in the same figure for the same value of parameters. One can observe that the system with PWL stiffness and damping factor has much more amplitude of displacements for low values of external forcing frequencies ω. This could be an advantage for potential use of this system in low frequency vibrational-based energy harvesting.

5 CONCLUSIONS

We studied the dynamics of a PWL spring-mass single degree of freedom system for energy harvesting applications. It was shown through steady-state time domain simulations of the dynamical model and the corresponding frequency response, that the harvested energy could be larger than that obtained from a linear equivalent system. In particular, we found that at low frequency ranges of the energy harvesting source excitation, the PWL system presents a better performance as compared to the linear equivalent system. This could be an advantage for potential use of this system in low frequency ambient vibrational-based energy harvesting. Future works will deal with stability analysis of the PWL system.

REFERENCES

[1] T. J. Kaźmierski and S. Beeby (Eds), “Energy Harvesting Systems. Principles, Modeling and Applications," Springuer, 2011.

[2] L. Gammaitoni, H. Vocca, I. Neri, F. Travasso and F. Orfei, “Vibration Energy Harvestng: Linear and Nonlinear Oscillator Approaches," in *Sustainable Energy Harvesting Technologies-Past, Present and Future*, pp. 171-190, 2007.

[3] C. Trigona, N. Dumas, L. Latorre, B. Andò, S. Baglio and P. Nouet, “Exploiting Benfits of a Periodically-Forced Nonlinear Oscillator for Energy Harvesting from Ambient Vibration," *Procedia Engineering*, pp. 2-4, 2011.

[4] A. Triplett, J. Linton and D. D. Quinn, “Electromagnetic Energy Harvesting," ENOC 2011, 24-29 July 2011, Rome, Italy.

[5] N.G. Stephen, “On energy harvesting from ambient vibration," *Journal of Sound and Vibration*, vol. 293, No. 1-2, pp. 409-425, May 2006.

FINITE ELEMENT MODELLING OF POROELASTIC-ACOUSTIC COUPLED PROBLEM

W. Larbi, J.-F. Deü and R. Ohayon

Structural Mechanics and Coupled Systems Laboratory
Conservatoire National des Arts et Métiers (Cnam), 292 rue Saint-Martin, case 353,
75141 Paris Cedex 03, France
Email: (walid.larbi, jean-francois.deu, roger.ohayon)@cnam.fr

ABSTRACT

We propose in this paper to investigate and compare finite element formulations for acoustic problems with soundproofing materials. The coupled system consists of an acoustic cavity (described by its pressure field) coupled with a porous material. This material can be modeled by a tridimensional poroelastic finite element based on the Biot-Allard theory. Another approach consists of using acoustic normal impedance for modeling the wall absorption. Through an approximation of this impedance by a Kelvin-Voigt rheological model and using a new scalar unknown in the finite element formulation, the coupled problem can be written directly in time and frequency domains. Numerical example is presented in order to illustrate and compare the proposed approaches.

1 INTRODUCTION

During the last decades, many studies have focused on passive damping techniques for noise and vibration reduction. Within this context, we propose to investigate and compare finite element modeling of soundproofing material in acoustic internal problems. The system under study consists of an acoustic cavity coupled with a porous sound absorbing material. For modeling the porous domain, two approaches are analysed: (i) a local wall impedance model and (ii) a more refined approach based on poroelasticity theory.

When acoustic wall impedance is used for modeling the absorbing material, the problem becomes strongly frequency dependent. In this work, a simplified but rather general constitutive model of Kelvin-Voigt type is used, through the introduction of a scalar interface variable (fluid normal displacement at the interface) which allows the problem to be reduced to a classical vibration damping problem. This impedance model, though local, may represent relatively satisfactory soundproofing materials. The acoustic impedance parameters can be determined starting from intrinsic characteristics of the porous medium by a numerical approach or by an analytical solution. The latter can be obtained by considering a laterally infinite poroelastic materials excited by normal incidence plane wave. The proposed formulation is then compared with a more refined approach consisting in a three-dimensional description of the poroelastic medium through the Biot-Allard model.

2 FE MODELLING OF POROELASTIC-ACOUSTIC COUPLED PROBLEM

Consider an inviscid compressible barotropic fluid contained in a rigid cavity, with some of its walls covered by a porous treatement in order to absorb a part of the acoustic energy of the fluid. Let us denote by Ω_F the domain occupied by the fluid and by Ω_P the domain occupied by the poroelastic material. The boundary of Ω_F is noted $\partial\Omega_F = \Sigma_F + \Sigma_P + \Sigma_R$, with Σ_P the part covered by the poroelastic material and called absorbing boundary, Σ_R the rigid part and Σ_F the part where a given displacement $\mathbf{u}^d$ is applied (Fig. 1). The unit outer normal vector along $\partial\Omega_F$ is denoted by $\mathbf{n}$. The following notations are used for the quantities associated with the fluid: p for the pressure, ρ_0 for the mass density, and c_0 for the celerity of the sound in the fluid.

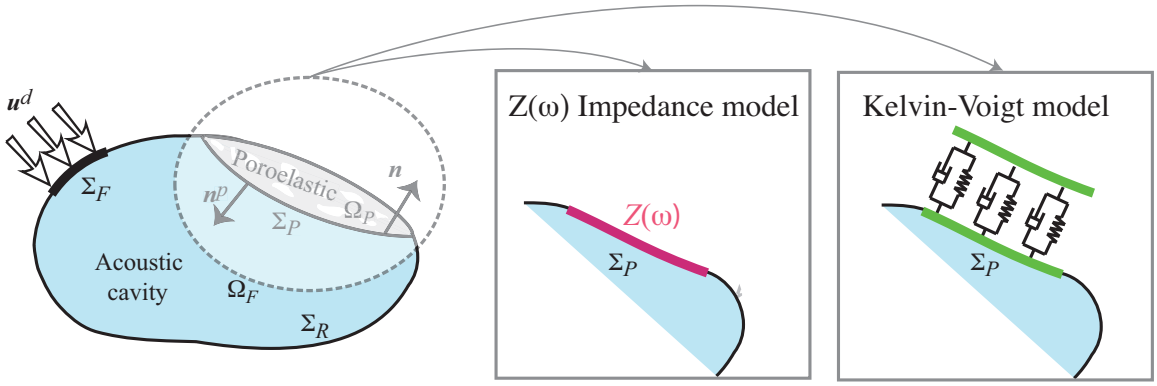

Figure 1. Poroelastic-acoustic coupled problem.

In the literature, the poroelastic materials can be modeled by several tridimensional finite elements model based on Biot-Allard theory [1] or by impedance approach ($Z(\omega)$). Both of these formulations can be written only in frequency domain and allows to nonlinear system in terms of angular frequency ω. To avoid this problem, a new finite element formulation based on the introduction of an additional scalar unknown, namely the normal fluid displacement field η at the dissipative interface, has been presented by the authors in [2]. In this case, the acoustic

wall impedance $Z(\omega)$ is approximated by a Kelvin-Voigt rheological model, i.e. sum of constant real part and an imaginary part inversely proportional to the frequency: $Z(\omega) = d^I - ik^I/\omega$. The local equations of the acoustic problem with absorbing material can then be written in terms of fluid pressure p and normal fluid displacement at the absorbing interface η.

$$\Delta p + \frac{\omega^2}{c_0^2} p = 0 \qquad \text{in} \quad \Omega_F \tag{1a}$$

$$\nabla p \cdot \mathbf{n} = \rho_0 \omega^2 \mathbf{u}^d \cdot \mathbf{n} \quad \text{on} \quad \Sigma_F \tag{1b}$$

$$\nabla p \cdot \mathbf{n} = -\rho_0 \omega^2 \eta \qquad \text{on } \Sigma_P \tag{1c}$$

$$p = k^I \eta + i\omega d^I \eta \quad \text{on } \Sigma_P \tag{2}$$

Using the test function method, the corresponding variational formulation is obtained:

$$\frac{1}{\rho_0 \omega^2} \int_{\Omega_F} \nabla p \cdot \nabla\, \delta p \, \mathrm{d}x - \frac{1}{\rho_0 c_0^2} \int_{\Omega_0} p\, \delta p \, \mathrm{d}x - \int_{\Sigma} \eta\, \delta p \, \mathrm{d}\sigma = \int_{\Sigma_F} \mathbf{u}^d \cdot \mathbf{n} \delta p \, \mathrm{d}s \tag{3}$$

$$\int_{\Sigma} p\, \delta\eta \, \mathrm{d}\sigma - k^I \int_{\Sigma} \eta\, \delta\eta \, \mathrm{d}\sigma - i\omega d^I \int_{\Sigma} \eta\, \delta\eta \, \mathrm{d}\sigma = 0 \tag{4}$$

After discretizing by the finite element method the bilinear forms in equations (3) and (4), we obtain the following matrix equation:

$$\left[\begin{pmatrix} k^I \mathbf{G}_\eta & -\mathbf{C}_{\eta p} \\ \mathbf{0} & \frac{1}{\rho_0} \mathbf{K}_p \end{pmatrix} + i\omega \begin{pmatrix} d^I \mathbf{G}_\eta & \mathbf{0} \\ \mathbf{0} & \mathbf{0} \end{pmatrix} - \omega^2 \begin{pmatrix} \mathbf{0} & \mathbf{0} \\ \mathbf{C}_{\eta p}^T & \frac{1}{\rho_0 c_0^2} \mathbf{M}_p \end{pmatrix} \right] \begin{pmatrix} \mathbf{H} \\ \mathbf{P} \end{pmatrix} = \omega^2 \begin{pmatrix} \mathbf{0} \\ \mathbf{F} \end{pmatrix} \tag{5}$$

where $\mathbf{H}$ and $\mathbf{P}$ are the vectors of nodal values of η and p respectively. This unsymmetric formulation can be solved in frequency and in time domain by introducing only one unknown per node on the damping interface (normal fluid displacement η).

3 NUMERICAL EXAMPLE

We consider in this example a three-dimensional cubic enclosed cavity of 1 m^3 filled with air (density $\rho_0 = 1$ kg/m^3, speed of sound $c_0 = 340$ m/s). A poroelastic material of size $60 \times 60 \times 0.0762$ m^3 is embedded to one wall of the cavity. The cavity is excited by a volume velocity source placed in one corner (x, y, z)=$(0, 0, 0)$ (see Fig. 2). Fig. 3 (a) shows the pressure level

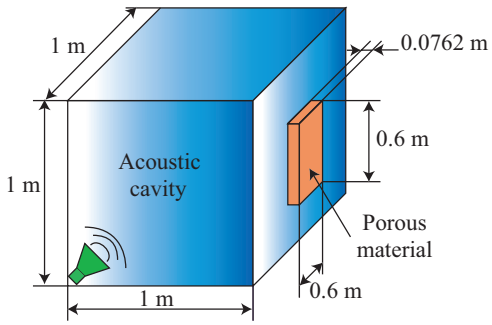

Figure 2. Geometry of the 3D rigid cavity problem with porous absorbing material.

in the acoustic cavity with an without poroelastic treatment. The peaks observed in this figure

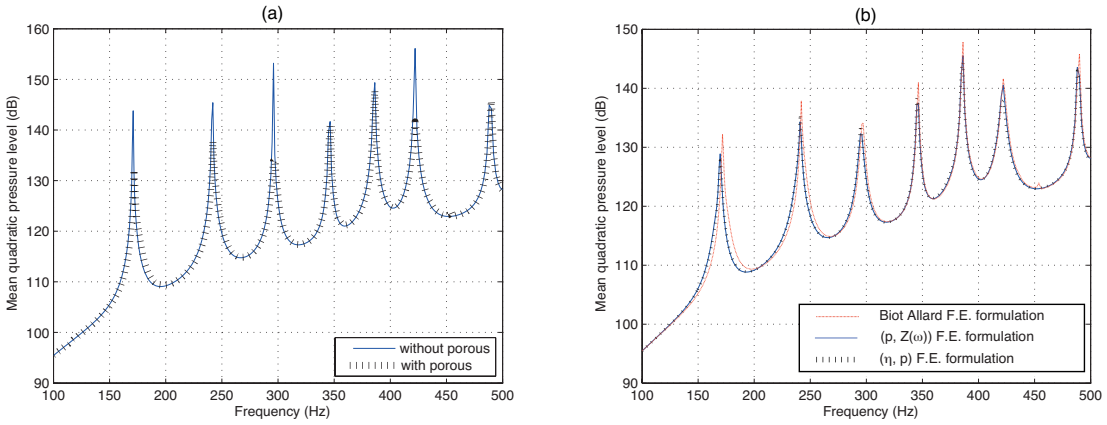

Figure 3. Pressure level in the acoustic cavity with poroelastic treatment

correspond to the frequencies of the rigid acoustic cavity. Thus, this figure clearly shows that there is a substantial reduction in pressure level due to the addition of the poroelastic material.

The results obtained with Biot-Allard FE formulation for the acoustic cavity with poroelastic treatment is compared in Fig. 3 (b) to those obtained from two approaches: (i) a general impedance $Z(\omega)$, and (ii) a simplified impedance using the Kelvin-Voigt model. An excellent agreement between the three methods is obtained. This test validate the proposed approximations of the poroelastic medium by an acoustic impedance in low frequency range. It is worth noting that, in comparison with the Biot-Allard finite element formulation, the acoustic impedance approach (in general form or using Kelvin-Voigt approximation) is more efficient in term of computational time and complexity. Indeed, with the impedance or Kelvin-Voigt approach, only the cavity needs to be discretized with acoustic elements. Moreover, with the Kelvin-Voigt formulation, the problem can be solved directly in time domain without any specific treatment. However, the impedance approach has some performances limitations. For example, if the poroelastic material is linked to a flexible wall, the use of localized normal incidence impedance can lead to significant discrepancies. In contrast, the Biot-Allard FE formulation can handle such situations upon its coupling with elastic domains.

4 CONCLUSION

Finite element formulations for interior acoustic problems with poroelastic treatments have been proposed in this work. Two approaches are compared for modeling the porous material: (i) a three dimensional Biot-Allard model and (ii) a localized normal impedance technique. We have shown that this impedance can be approximate by a Kelvin-Voigt model in the low frequency range. In this case, an original acoustic-poroelastic coupled finite element formulation has been developed. It is based on the introduction of a new scalar unknown field and allows solving the dissipative acoustic problem in frequency and time domains.

REFERENCES

[1] J.-F. Allard, *Propagation of Sound in Porous Media: Modelling Sound Absorbing Materials*, Elsevier Applied Science, London (1993).

[2] W. Larbi and J.-F. Deü and R. Ohayon, A new finite element formulation for internal acoustic problems with dissipative walls, *International Journal for Numerical Methods in Engineering*, **68**(3), 381–399 (2006).

PREDICTION OF RANDOM VIBRATION AND ACOUSTIC RESPONSES BY COMPRESSION OF THE STATISTICAL DYNAMICAL INFORMATION OF FEM MODELS

Dr. G. Borello

InterAC
10 impasse Borde-Basse, L'Union, FRANCE
Email: gerard.borello@interac.fr

ABSTRACT

Prediction of random responses over broadband frequency range (including acoustically driven vibrations) requires more computational power than deterministic cases and a lot more information on sources such as cross-correlation data from force field.
Statistical Energy Analysis (SEA) is an alternate technique for running such a prediction but extra assumptions and expertise are required to build-up models with "regular" SEA software. Then despite a very sober usage of computational resources, SEA models may still be too long to set-up regarding project constraints.
From the last past decade, the virtual SEA (VSEA) technique has been developed for fastening random response prediction in the MF range on complex dynamical systems such as a car, a spacecraft or an aircraft.
VSEA uses the SEA power balanced equations formalism to create a compressed "picture" of the statistical dynamical information included in the FEM model. Generated VSEA models are in band-integrated format and are run interactively thanks to their 'SEA format'. VSEA models can be coupled with classical SEA models and with other methods such as the transfer matrix method or ray-tracing. A review of applications through a set of industrial examples from aerospace, automotive and building industries will be presented.

1 INTRODUCTION

FEM tools provide detailed models but slow to run and to implement as soon as inputs are random with large frequency bandwidth. SEA [1] contrarily provides fast to solve models directly shaped for random prediction but generally too coarse based on their internal analytic formulations which cannot capture the details of a complex geometry. The Virtual SEA (VSEA) method [4][5], derived from experimental SEA [2][3], overcomes both previous limitations by authorizing random prediction combining accuracy of FEM and SEA calculation speed. Results are directly provided in band-integrated format for fulfilling project needs.

2 VIRTUAL SEA METHOD

2.1 VSEA analysis steps

VSEA is capturing the statistical dynamical behavior contained in a FEM model and compressed it into a few number of SEA subsystems cross-coupled by a small parametric loss factor matrix compatible with classical definition of SEA loss factors [1].

VSEA steps are given in Figure 1. A standardized computational process generates related SEA representation for the original FEM model. SEA subsystems are described by parametric spectra (modal density, coupling loss factors and mass). VSEA may be seen as a compression algorithm working on the dynamic FEM information with subsystem number as key parameter for compression quality. Latest version of VSEA algorithm is automated to reduce the loss of information to 1 or 2 dB during compression by performing multi-scale subsystem decompositions over the whole frequency range.

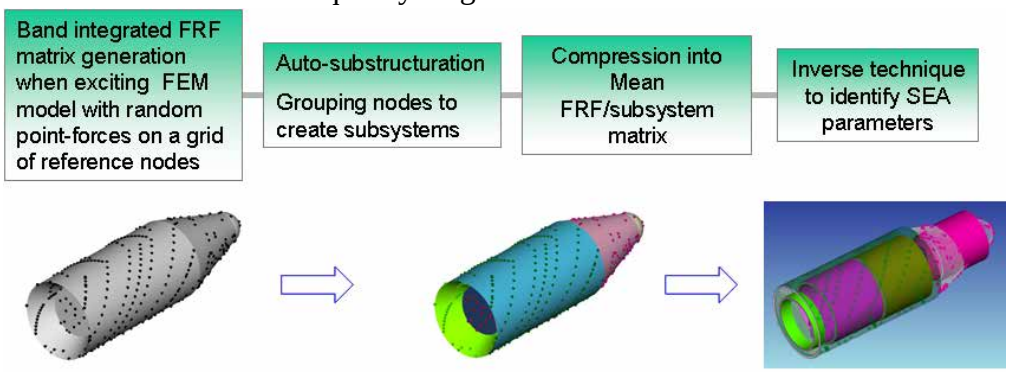

Figure 1. The VSEA analysis process for deriving SEA model from FEM

2.2 VSEA 3D reconstruction

Contrarily to classical SEA, VSEA preserves local information on reference nodes. The model may then include specific nodes, for easier load definition and more comprehensive correlation with tests. The 3D field reconstruction is based on the physical system behavior in the MF range: Long-distance transfers are becoming smooth operators of frequency and resonant modal behavior is localized in the input mobility terms.

3 APPLICATIONS TO RANDOM PREDICTION

Random vibration prediction involves solving the matrix problem: $X^2 = \mathbf{H}^T F^T F^* \mathbf{H}^*$ where F is the nodal force vector, X^2 the autospectrum of the response vector, $\mathbf{H}$ is the transfer matrix between FEM dofs. $F^T F^*$ is the cross-spectral load matrix and in the general case of correlated forces, $F^T F^*$ is full and frequency dependant and difficult to handle in FEM.

3.1 Response to Turbulent Boundary Layer (TBL) of structures in SEA

TBL is an example of distributed correlated random loads applied to a structure, induced by a flow of given velocity undertaking turbulent behavior from a given distance to some obstacle. SEA+ software provides predictions in the energy domain of structural responses through the calculation of TBL injected power given by:

$$P_{in} = \frac{S}{4m} \left\langle G_{pp}(\omega) \right\rangle N(f) \left\langle j_n{}^2(\omega) \right\rangle_{n,\omega} \quad (1)$$

with N the modal density of the structure, S its "wet" surface area, m the mass density, $\left\langle j_n{}^2(\omega) \right\rangle_{n,\omega}$ the band-averaged TBL joint acceptance, G_{pp} the mean autospectrum of applied TBL pressure.

3.2 Underwater vehicle submitted to TBL

The FEM model represents the structure of a simple underwater vehicle and is shown in Figure 2. This model is transformed into hybridized VSEA model up to 1250 Hz (1/3rd octave band central frequency) after adding acoustic cavities and TBL loads for 10 m/s stream velocity.

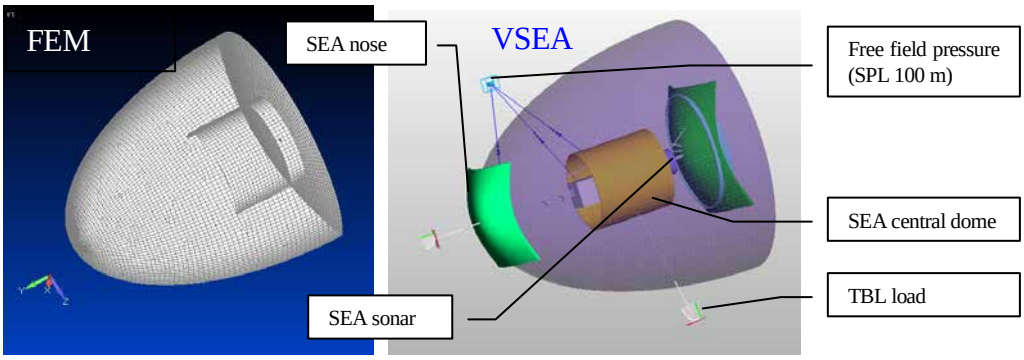

Figure 2. FEM underwater vehicle model and related VSEA model

TBL VSEA calculation provides power flow between the various subsystems and ranks propagation paths, providing comprehensive outputs (Figure 3): Internal SPL (sound pressure level) driven by central dome radiation and sound radiated pressure in free field driven by non-resonant mass of the central dome.

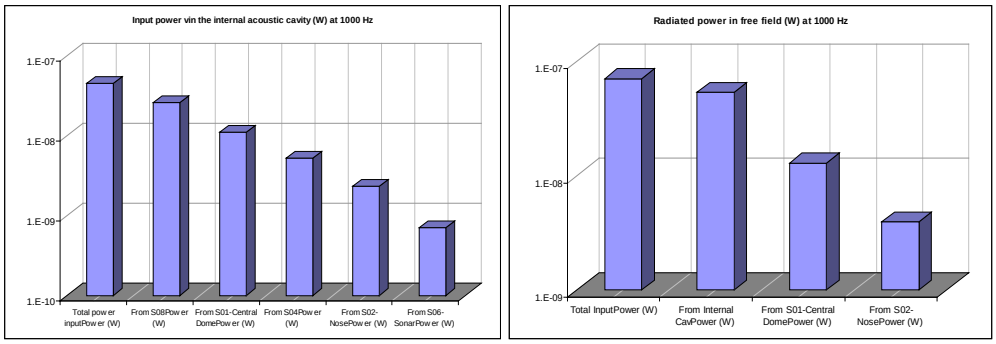

Figure 3. Input power in internal cavity from subsystems (left) and radiated power in free field (right) at 1000 Hz

3.3 Response to acoustic noise of payload antenna

The acceleration PSD (power spectral density) of a spacecraft antenna under diffuse acoustic pressure is simulated by a hybrid SEA+ model (Figure 4) with structural behavior obtained from FEM model. The structure is made of sandwich (composite skin and honey al core) and VSEA

parameters are processed from FEM up to 2000 Hz then extrapolated above by analytical sandwich plates. Four subsystems are found which are coupled to two reverberant cavities in SEA+ with diffuse related pressure constrained to 1 pa. Acceleration is thus provided as mean per subsystem in g²/Hz/Pa in Figure 5-left for baffled radiation conditions and as local PSD at reference nodes in Figure 5-right.

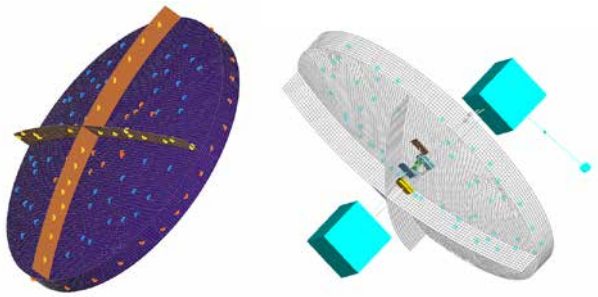

Figure 4. VSEA model of spacecraft antenna under diffuse acoustic loads

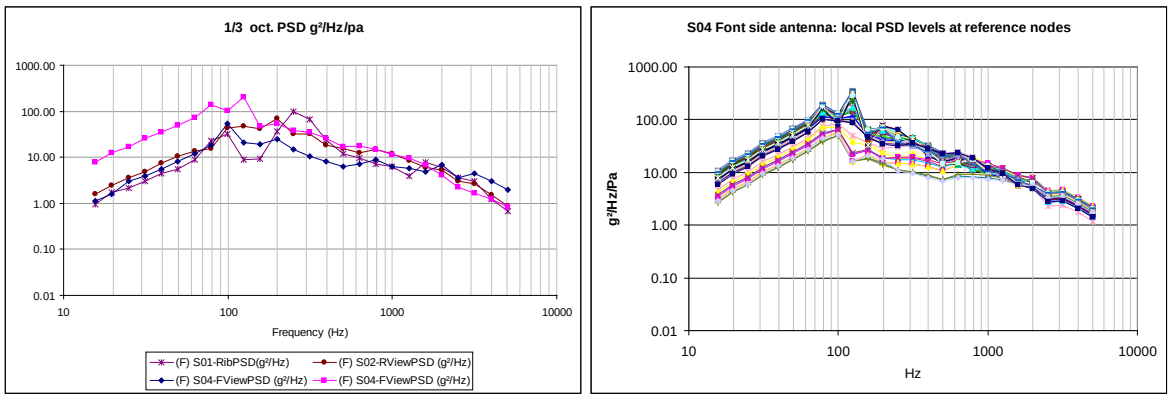

Figure 5. PSD acceleration response of antenna subsystem (left) and local responses predicted in front side face (right)

4 CONCLUSION

Virtual SEA provides an efficient way of predicting random vibrations with the benefit of SEA fast-to-solve interactivity and the quality of FEM for structural transfers. More examples will be given in the presentation as well as comparisons with test.

REFERENCES

[1] R. H. Lyon. *Statistical Energy Analysis of Dynamical Systems*. MIT Press, 1975.

[2] N. Lalor. The Experimental Determination of Vibrational Energy Balance in Complex Structures. *Proc. SIRA Conf. on Stress & Vibration*, Paper 108429, London, GB, 1989.

[3] B.P. Cimerman, T. Bharj, and G. Borello. Overview of Experimental Approach to Statistical Energy Analysis. *Proc. SAE Noise & Vibration Conf.*, Paper 97NV169, Traverse City, MI, USA, 1997.

[4] L. Gagliardini, L. Houillon, L. Petrinelli, G. Borello. Virtual SEA: mid-frequency structure-borne noise modeling based on Finite Element Analysis. *Proc. SAE Noise & Vibration Conf.*, Paper 03NVC-94, Traverse City, MI, USA 2003.

[5] G. Borello, L. Gagliardini. Virtual SEA: towards an industrial process. *Proc. SAE Noise & Vibration Conf.*, Paper 2007-01-2302, St Charles, IL, USA, 2007.

STATISTICAL ENERGY ANALYSIS: CORRELATION BETWEEN DIFFUSE FIELD AND ENERGY EQUIPARTITION

T. Lafont[1*], A. Le Bot[1] and N. Totaro[2]

[1]Laboratoire de Tribologie et Dynamique des Systèmes
Ecole Centrale de Lyon, Ecully, FRANCE
Email: thibault.lafont@ec-lyon.fr, alain.le-bot@ec-lyon.fr

[2]Laboratoire Vibrations Acoustique
INSA de Lyon, Villeurbanne, FRANCE
Email: nicolas.totaro@insa-lyon.fr

ABSTRACT

This paper studies two concepts used in Statistical Energy Analysis (SEA): the diffuse field and the energy equipartition. To study the equivalence between these concepts the example of a simply supported plate is taken. First, the degree of diffuseness of the field is quantified by a simple criterion. Then, extracting information from an analytical model, the standard deviation of modal energies is evaluated. Two maps are drawn on the frequency-damping plane in both cases. These maps allow correlating concepts of diffuse field and energy equipartition and validity diagrams defined by Le Bot.

1 INTRODUCTION

Using the statistical energy analysis (SEA) method introduced by Lyon and DeJong [1] requires some specific assumptions which limit its range of application. These fundamental requirements have been clearly highlighted in the literature. Burroughs [2] summarised them: broadband excitation, conservative coupling, light damping loss factor, equipartition of energy, large number of modes and light coupling. Many authors have studied these hypotheses individually and proposed solutions to enhance the validity of SEA. For example Goyder [3] on power flow, Wöhle [4] on coupling.

The concept of diffuse field comes out with its assumptions even if it is not clearly mentioned. Indeed, broadband power flow and high modal overlap suggest diffuseness. Defining from a raw acoustical point of view, an ideal diffuse sound field is homogeneous and isotropic or, in other words, it is assumed that independent sound of equal strength arrives at a receptor from all directions. In the literature, Langley [5] presents several approaches when talking about diffuse field, the wave approach and the modal approach. It thus can lead to different types of definitions. As an example, Fahy [6] employs one using the energy density: “the average energy density is the same throughout the volume of the enclosure”. The computation of a diffuse field criterion in the next section is based on this latter definition.

Equipartition of the energy is another assumption used in SEA. Lesueur [7] proposed a clear definition in his chapter dedicated to SEA. Each subsystem has a finite number of modes and the coherent effect between them is ignored. In addition, each mode of subsystem A is coupled with all of the modes of subsystem B. Calling $<E_{A,i}>$ and $<E_{B,k}>$ the average energies of the mode i in subsystem A and mode k in subsystem B; E_A and E_B the global energies of subsystem A and B; N_A and N_B the number of modes in each subsystem, energy equipartition assumption can be written as

$$< E_{A,\,i} >= \frac{E_A}{N_A}; < E_{B,\,k} >= \frac{E_B}{N_B} \tag{1}$$

In the study, for each frequency band and with a varying damping coefficient, the modal energies are computed in order to analyse the energy distribution over all of the modes.

Alongside, recently A. Le Bot [8] proposed validity diagrams which leaned on some specific parameters: the number of modes, the modal overlap of the subsystem, the attenuation factor of wave per meter and the coupling strength. It permits to have an idea of how well the SEA method could be applied to a system. In this paper, a correlation is made between the validity diagrams and the assumptions of diffuse field and energy equipartition for a simply supported plate.

2 DEFINING A CRITERION

2.1 Diffuse field criterion

The example of a simply supported plate excited by a random point force F(t). The power spectral density (PSD) of such a force is equal to the PSD of a white noise S_0 confined to a specified frequency band $\Delta\omega_i$. The energy expectation $W(x,y,\omega_i)$ of a receptor $R(x,y)$ for a frequency band ω_i, is given by

$$W(x,y,\omega) = m < \dot{u}^2 >= \frac{mS_0}{2\pi} \int_{\Delta\omega i} \omega^2 \left|H_{rs}\right|^2(\omega) d\omega \tag{2}$$

Where u is the deflexion, m the specific basis weight and H_{rs} the frequency response function (FRF) calculated between the excitation source s and a receiver r.

The definition of the criterion is based on the energy expectation distribution. For that, several energy receptors are placed on the plate. For each frequency band, a comparison is done between the values of all receivers.

The criterion is defined as the standard deviation normalized by the average,

$$\sigma_{diffuse} = \frac{\sqrt{\overline{W^2} - \overline{W}^2}}{\overline{W}}. \tag{3}$$

Where S is the surface of the plate, the average is defined by $\bar{f} = \int_S f(x,y) dxdy.$

When the criterion tends to zero, the field can be considered perfectly diffused. All of the energy densities are equal over the plate.

2.2 Energy equipartition criterion

A similar method is used to define the energy equipartition criterion. The deflexion $u(x,y,t)$ at a receiver $R(x,y)$ at a specific time t is given by

$$\begin{aligned} u(x,y,t) &= \sum_k A_k(t)\psi_k(x,y) \\ E(t) &= m\int \dot{u}^2 dxdy \Leftrightarrow E = \sum_k m < \dot{A}_k^2 > \Leftrightarrow E_k = m < \dot{A}_k^2 > \end{aligned} \tag{4}$$

Where A_k is the modal energy and ψ_k the eigenfunction of mode k. The criterion is defined as follow

$$\sigma_{equi} = \frac{\sqrt{\overline{E_k^2} - \overline{E}_k^2}}{\overline{E}_k}. \tag{5}$$

3 RESULTS

For the numerical simulation, several parameters must be fixed (number of modes, frequency step and number of receptors for spatial discretization). For that, a preliminary study on the convergence of these parameters is done. Then, two maps presenting the criterion of the diffuse field versus the validity diagrams of SEA and the computation of modal energies are showed.
On one hand, the validity domain of SEA defined by A. Le Bot and the mapping of the criterion fit well. On the other hand, a strong correlation between the two maps is done. Some conclusions on the SEA assumptions finally closed the presentation.

REFERENCES

[1] R. H. Lyon, G. DeJong. *Theory and application of Statistical Energy Analysis*. Buttersworths-Heimann, 1995.

[2] C. B. Burroughs, R.W. Fischer and F. R. Kern. An introduction to statistical energy analysis. *J. Acoustic. Soc. Am.* 101(4):1779-1789, 1997.

[3] H. G. D. Goyder. Vibrational power flow from machines into built-up structures. *Journal of Sound and Vibration.* 68(1):59-75, 1980.

[4] W. Wöhle. Coupling loss factors for statistical energy analysis of sound transmission at rectangular structural slab joints. *Journal of Sound and Vibration.* 77(3):335-344, 1981.

[5] R. S. Langley and P. J. Shorter. Diffuse wavefields in cylindrical coordinates. *J. Acoustic. Soc. Am.* 112(4):1465-1470, 2002.

[6] F. J. Fahy. *Sound and structural vibration.* Academic, 1985

[7] C. Lesueur. *Rayonnement acoustique des structures*. Eyrolles, 1988.

[8] A. Le Bot. Validity diagrams of statistical energy analysis. *Journal of sound and vibration*. 329(6):221-235, 2010.

A NEW MODEL OF IMPROVING THE TRANSMISSION LOSS OF ALUMINIUM PROFILE WITH CORRUGATED CORES

SHAN OUYANG[1], FUSHENG SUI[1*]
[1]Key Laboratory of Noise and Vibration Research, Institute of Acoustics,
Chinese Academy of Sciences, Beijing, China
Email: ouyangshan@mail.ioa.ac.cn , sui@mail.ioa.ac.cn

ABSTRACT

Abstract: An experimental and simulation study of the sound transmission loss of Aluminum profile with corrugated cores has been performed. Firstly, modal frequencies and boundary conditions of the aluminum profile mounted on the reverberation-anechoic chamber are determined by modal test. Secondly, followed by sound transmission loss measurement, the mechanism of how the structure modes influence transmission loss is analyzed. Finally, the transmission loss of the profile model is simulated using FEM, the experimental boundary conditions with some appropriate modification are taken into account, of course. Simulation results show good agreement with experimental results. As the sound insulation performance is poor, a new Aluminum profile model is proposed here, and by the same simulation method as mentioned above, the simulation results indicate that, sound insulation effect of the new model is better than that of the original structure without increasing total weight.

ON THE THERMOACOUSTIC PROPERTIES OF AEROSPACE LAYERED STRUCTURES

D. Chronopoulos[1,2*] , M. Ichchou[2], B. Troclet[1] and O. Bareille[2]

[1]EADS Astrium ST
66 Route de Verneuil, BP3002, 78133 Les Mureaux Cedex, France
Email: chronopoulos.dimitri@gmail.com

[2]Ecole Centrale de Lyon
36 Avenue Guy de Collongue, 69134 Ecully Cedex, France

ABSTRACT

The temperature dependent material characteristics of a layered panel are experimentally measured using a Thermal Mechanical Analysis (TMA) configuration. The temperature dependent wave dispersion characteristics of the panel are subsequently computed using a Wave Finite Element Method (WFEM). The WFEM predictions are eventually used within a wave context SEA approach in order to calculate the temperature dependent Sound Transmission Loss (STL) of the layered panel. Results on the STL for temperatures varying between -100 ^oC to 160 ^oC are computed for a structure operating at sea level. The importance of the glass transition region on the panel's vibroacoustic response is exhibited and discussed.

1 INTRODUCTION

An aerospace structure operates within a broad temperature range, typically varying between -100 ^{o}C to 200 ^{o}C for launch vehicles. With regard to aircrafts, their mission usually involves narrower temperature ranges (typically -60 ^{o}C to +50 ^{o}C) as is the case for automotive structures. A very little amount of research has been conducted on predicting the effect of temperature on the vibroacoustic behaviour of layered structures. Hereby, an attempt is made in order to exhibit the sensitivity of the vibroacoustic behaviour of a composite structure to the ambient flight temperature.

The main novelty of the work hereby presented is the investigation of the impact of temperature dependent parameters on the acoustic performance of a layered aerospace structure. The mechanical characteristics of an orthotropic sandwich panel comprising carbon epoxy facesheets and a honeycomb core are experimentally measured using a Thermal Mechanical Analysis (TMA) configuration. The STL of the structure is calculated within a wave context SEA approach and the impact of the temperature dependent parameters on the STL is investigated.

2 CALCULATION OF THE TEMPERATURE DEPENDENT WAVE PROPAGATION CHARACTERISTICS

2.1 Measurement of the thermomechanical characteristics

An orthotropic sandwich panel is hereby used for experimentation purposes. Its facesheets are made of a 1mm thick carbon epoxy composite comprising four layers of 1-1 twilled weaves. Its core is made of an orthotropic 12.7mm thick Nomex honeycomb material. During the fabrication process the carbon fabric is impregnated in the resin and draped over the mould. The honeycomb material is then added and the system is put in vacuum. The polymerization takes place and the honeycomb absorbs some of the resin included in the tissues and thus adheres thereto. The same kind of resin therefore serves as the facesheets matrix and as an adhesion agent. The measured thermomechanical properties for the facesheets and the core of the panel are exhibited in fig.1,2.

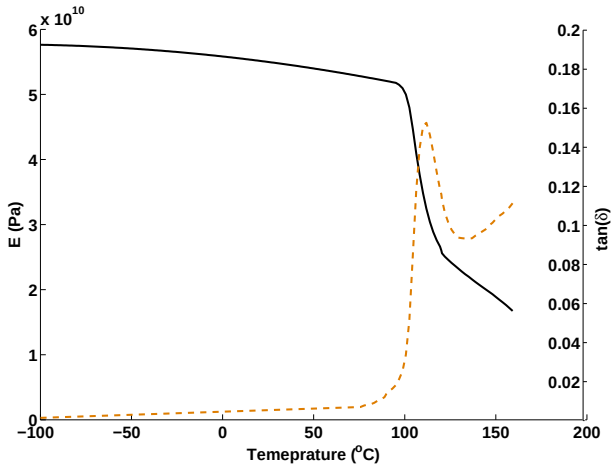

Figure 1: The experimentally obtained temperature dependent Young modulus and the corresponding tan(δ) for the facesheet of the sandwich panel: Young modulus (–), tan(δ) (- -)

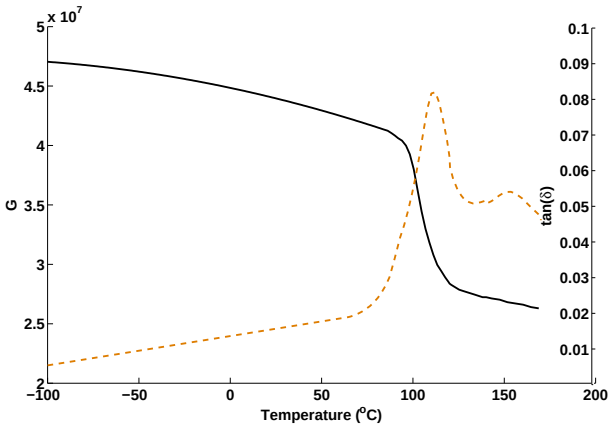

Figure 2: The experimentally obtained temperature dependent shear modulus and the corresponding tan(δ) for the core of the sandwich panel: shear modulus (–), tan(δ) (- -)

3 PREDICTING THE VIBROACOUSTIC RESPONSE OF A LAYERED PANEL

3.1 An SEA wave-context approach

The approach that will be hereby emplyoed for the prediction of the vibroacoustic response of a layered panel is a wave-context SEA approach and is detailed in [1]. The acoustic transmission coefficient is written as:

$$\tau = \frac{P_{23} + P_{13}}{P_{\mathtt{inc}}} = \frac{P_{23}}{P_{\mathtt{inc}}} + \frac{P_{13}}{P_{\mathtt{inc}}} \tag{1}$$

After writing the energy balance equations and some algebraic manipulation the resonant contribution is written as:

$$\frac{P_{23}}{P_{\mathtt{inc}}} = \frac{8\rho^2 c^4 \pi \sigma_{\mathtt{rad}}^2 n_2}{\rho_s \omega^2 A(\rho_s \omega \eta_2 + 2\rho c \sigma_{\mathtt{rad}})} \tag{2}$$

with ρ_s the surface density of the panel, n_2 its modal density, η_2 its damping loss factor, $\sigma_{\mathtt{rad}}$ its radiation efficiency. The non-resonant contribution can be expressed as:

$$\frac{P_{13}}{P_{\mathtt{inc}}} = \frac{\int_0^{2\pi}\int_0^{\theta_{\mathtt{max}}} \frac{4Z_0^2\sigma(\theta,\phi,\omega)\sin\theta\cos^2\theta}{|\mathtt{i}\omega\rho_s + 2Z_0|^2}\mathrm{d}\theta\mathrm{d}\phi}{\pi(1-\cos^2\theta_{\mathtt{max}})} \tag{3}$$

4 PREDICTING THE TEMPERATURE DEPENDENT STL OF A LAYERED STRUCTURE

The Leppington's set of asymptotic formulas is initially used in order to calculate the radiation efficiency of the sandwich panel for each considered temperature. The resulting radiation efficiencies are presented in fig.3.

It is observed that temperature has a significant impact on the radiation efficiency of the structure. The coincidence frequency utterly depends on the flexural wave phase velocity inside the acoustic medium and the the structure. When temperature increases, phase velocity in the acoustic medium increases, while the one of the waves propagating inside the layered panel decreases, which results in a higher coincidence frequency. Thus, at lower frequencies a 'cold' panel behaves as more damped compared to a 'hot' one. The temperature dependent TL is shown in fig.4.

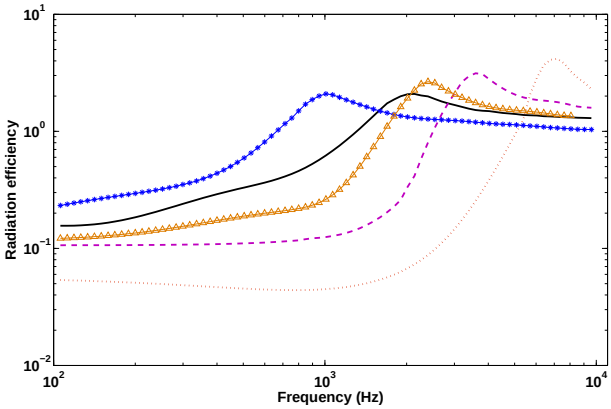

Figure 3: Temperature dependent acoustic radiation efficiency of the sandwich panel: -100 ^{o}C ($*$), 25 ^{o}C (–), 90 ^{o}C ($\triangle$), 110 ^{o}C (- -), 160 ^{o}C ($\cdots$)

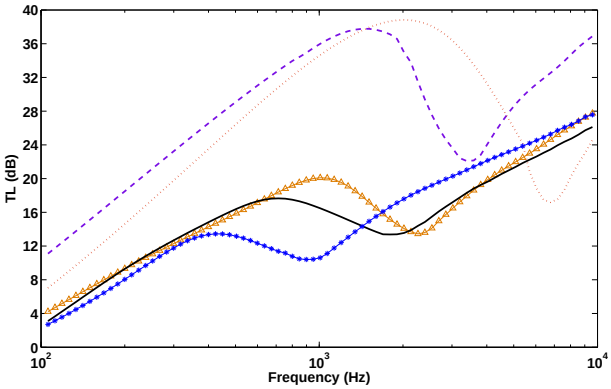

Figure 4: Temperature dependent Transmission Loss of the sandwich panel at sea level: -100 ^{o}C ($*$), 25 ^{o}C (–), 90 ^{o}C ($\triangle$), 110 ^{o}C (- -), 160 ^{o}C ($\cdots$)

It can generally be concluded that operation within or above the T_g of the panel can result in improved acoustic insulation performance. Once more it is observed that the mechanical and acoustic performances of the structure need to be compromised.

5 CONCLUSIONS

The presented work exhibited the impact of the thermomechanical characteristics of a layered aerospace structure on its vibroacoustic performance: 1) The thermomechanical properties of a sandwich structure were measured separately for its facesheets and the honeycomb core. The results exhibited a large divergence of the modula and the damping loss factor especially near and above the glass transition temperature of the resin. 2) An approach for predicting the STL of layered panels within a wave-context SEA approach was briefly described and used in order to calculate the temperature dependent SEA quantities of a layered orthotropic structure. 3) A great impact of the temperature dependent parameters was observed on the radiation efficiency, the coincidence frequency and the STL of the panel.

REFERENCES

[1] D. Chronopoulos. *Prediction of the vibroacoustic response of aerospace composite structures in a broadband frequency range*. PhD thesis, Ecole Centrale de Lyon, 2012.

QUANTIFICATION OF THE POWER INJECTED BY ACOUSTIC SOURCES INSIDE A COMPLEX CAVITY

F. Ayme[1,2,3] , C. Cariou[1*] , M. Ichchou[2] , D. Juvé[3] and O. Bareille[2*]

[1]Airbus - Acoustic tests lab
316 route de Bayonne, 31016 Saint Martin du Touch Cedex 9, FRANCE
Email: fabien.ayme@airbus.com, charles.cariou@airbus.com

[2]Ecole Centrale de Lyon, Laboratoire de Tribologie et Dynamique des Systèmes
36 avenue Guy de Collongue, 69134 Ecully Cedex, France
Email: mohammed.ichchou@ec-lyon.fr, olivier.bareille@ec-lyon.fr

[3]Ecole Centrale de Lyon, Laboratoire de mécanique des fluides et d'acoustique
36 avenue Guy de Collongue, 69134 Ecully Cedex, France
Email: daniel.juve@ec-lyon.fr

ABSTRACT

To find efficient solutions to reduce the noise inside aircraft cavities, aircraft manufacturers need to localize the acoustic sources and also quantify the power injected. The identification method used in this paper is based on an energy flow method : the Simplified Energy Method (MES). To run the inverse problem, the method needs energy density measurements. An acoustic energy probe has been designed and manufactured in metallic stereo-lithography. From four pressure measurements performed with thin tubes around a small hard sphere, the probe can provide in one measurement the needed previous energy quantities. To test the association between one probe and the identification method, a cockpit mock-up inspired of the A380 cockpit is set-up. A vibroacoustic test is carried out inside, and the results are presented. The sources are well located and their acoustic power level is fairly good retrieved in each third octave band, from 500Hz to 5kHz.

1 INTRODUCTION

Noise issues into aircraft cabins and especially cockpits have become real topics of research for the manufacturers. They need to localize the noise sources and to obtain a hierarchy of the acoustic power injected. A global inverse approach is often necessary in so far as the environments are large cavities. But, due to the considered frequency band $[500; 5000]$Hz, and also the size of the studied cavities, inverse methods based on FEM or BEM are excluded. Inverse energy methods like inverse SEA, or inverse local energy methods like the Inverse Simplified Energy Method (IMES) are possible alternatives to the problem [1–4]. The last one is able to retrieve the acoustic power injected into a cavity with a modeling of the direct and the reverberant acoustic fields. Such energy based method needs the acoustic energy density to be measured to run the inverse posed problem. The main addressed issue in this work is the test of the association composed of an energy probe and the IMES. The quality of the results will be assessed on the capability to localize the sources, and to retrieve their power level.

This paper is organized as follows. First, the direct and inverse formulations of the local energy method are recalled. Then, the energy probe is presented. To finish, the vibroacoustic test carried out in the mock-up with the energy probe, and the results post-processed by the inverse energy method are presented.

2 LOCAL ENERGY METHOD

The identification method used in this paper is based on a direct local energy method called Simplified Energy Method (MES)[2, 3]. This method aims at computing the energy density W field inside a cavity. To perform such calculations, the geometry of the cavity, the acoustic absorption coefficients of the materials inside, but also the position and the power injected ϕ by each source need to be known. Moreover, the method makes the hypothesis that the energy quantities are uncorrelated.

Based on the energy balance equation of the cavity, the elementary solutions describing the energy density propagation inside the cavity can be computed. Then, the method assumes the total energy density W is composed of a direct W^{dir} and a reverberant W^{rev} part. The direct part is related to the primary sources power ϕ, whereas the reverberant part is due to secondary sources power σ dispatched on the cavity boundaries. The MES predicts the energy exchanges and the dissipation inside the cavity. This leads to the determination of the power injected by those secondary sources σ as a linear function of the primary sources ϕ, the acoustic absorption coefficients and the geometry of the cavity. Then, the total energy density inside the cavity can be computed as stated by Equation (1), where all the quantities $\mathbf{W}, \mathbf{W}^{dir}, \mathbf{W}^{rev}, \phi$ and σ are vectors, except $\mathbf{Y}$ which is a matrix including the propagation terms,

$$\mathbf{W} = \mathbf{W}^{dir} + \mathbf{W}^{rev} = \mathbf{Y}\phi + \mathbf{Y}\sigma. \tag{1}$$

Once the energy density field expression is established, the inverse problem can be introduced [3, 4]. The goal is to retrieve the primary sources ϕ, starting from energy density measurements W^{meas} in the cavity. Based on the Equation (1), and with the linear relationship between the primary ϕ and the secondary σ sources, the energy density measurements can be directly related to the primary sources ϕ with a model matrix $\mathbf{S}$, as stated by Equation (2),

$$\mathbf{W}^{meas} = \mathbf{Y}\phi + \mathbf{Y}\sigma = \mathbf{Y}\left(\phi + \sigma\right) = \mathbf{S}\phi. \tag{2}$$

Thus, the acoustic sources can be retrieved in inverting the matrix $\mathbf{S}$, and with the energy density measurements. The goal is now to design a tool able to provide accurately those energy quantities.

3 ACOUSTIC ENERGY PROBE

In a previous work [5], an acoustic energy probe has been designed and manufactured in metallic stereo-lithography. It provides the acoustic pressure p_0, and the three dimensional particular velocity vector $\mathbf{V}_0$ at the center of the probe. Based on those complex quantities, the energy density can be computed as stated by Equation (3),

$$W = U + T = \frac{|p_0^2|}{4\rho c^2} + \frac{\rho}{4}\mathbf{V}_0.\mathbf{V}_0^*. \tag{3}$$

The probe is based on four pressure measurements arranged around a small sphere as the vertices of a regular tetrahedron. The measurements are performed with tiny tubes, behind which microphones are connected. In [5], this measurement technique has been studied, and the calibration, which is the key point, has also turned out to be possible and really accurate. The probe has been validated by several acoustic tests. The degree of confidence for the results, compared to three normal intensity probe measurements is almost 0.5 to 1.5 dB, depending on the test environment and the frequency band.

4 VIBROACOUSTIC TEST

4.1 Presentation

To carry out the acoustic tests, a cockpit mock-up has been designed, as shown by the Figure 1a and 1b. It is based on the A380 cockpit, with a scale ratio of 2/3. The mock-up integrates a location where an acoustic source can be inserted flush, Figure 1a. Moreover, a shaker vibrates a window of the mock-up to add a vibroacoustic source. The two sources can respectively be seen on the Figures 1a and 1b.

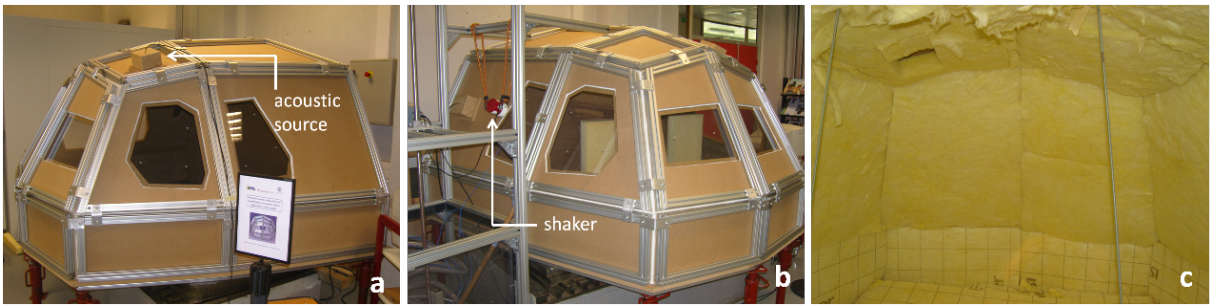

Figure 1: The cockpit mock-up : a. The acoustic source - b. The shaker on a window - c. The calibration configuration with glass wool

4.2 Sources calibration

To assess the quality of those results, the calibration of the acoustic power injected by each source is needed. To perform such calibration measurements, all the interior panels of the mock-up are covered of glass wool to create an anechoic environment, as seen on Figure 1c. Then, a source is unmasked, turned on, and intensity measurements are performed in scanning the acoustic field produced, close to the source. The acoustic power injected inside the mock-up can be computed, and the source is masked again. This process is repeated for each source.

4.3 Results

The cockpit mock-up is discretized into almost 1000 surface elements used for the computation. A measurement mesh made of 165 points positioned inside the mock-up ($45mm$ far from the surfaces) is also defined. The test consists of measuring the energy density in scanning a surface parallel to the cockpit panel around each measurement point. Then, in inverting the matrix $\mathbf{S}$ the primary sources ϕ are computed with Equation (2). The location of the sources are retrieved,

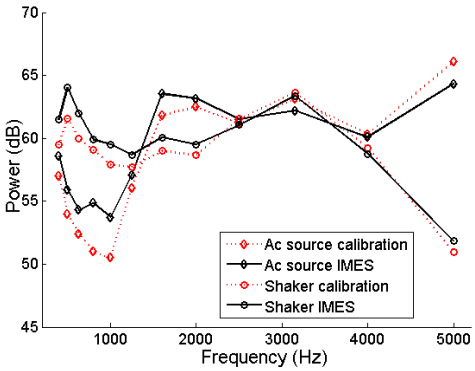

Figure 2. Acoustic power of the sources: calibrated and computed by IMES

and as can be seen on Figure 2, the acoustic power injected by each source in the mock-up computed by IMES is in fairly good agreement with the calibration measurements.

5 CONCLUDING REMARKS

In this paper, a vibroacoustic test is carried out to assess the association made of an energy probe and an energy identification method. Based on energy density scanned measurements, the inverse method allows to localize the sources, but also to retrieve the acoustic power they inject inside the mock-up with an expected averaged accuracy of almost 2dB on the third octave bands from 500Hz to 5kHz. After a few tests in the mock-up [4], the necessity to set up an array of such energy probes to scan very quickly all the surfaces of the cavity has been demonstrated.

REFERENCES

[1] R.H. Lyon. *Statistical Energy Analysis of Dynamical Systems : Theory and Application*. MIT Press, Cambridge, 1975.

[2] M. Ichchou. Formulations énergétiques pour l'étude moyennes et hautes fréquences des systèmes : théorie et applications. Ph.D. thesis, Ecole Centrale de Lyon, 1996.

[3] P. Hardy. Méthodes énergétiques simplifiées en moyennes et hautes fréquences : théorie et applications industrielles. Ph.D. thesis, Ecole Centrale de Lyon, 2005.

[4] F. Ayme, M. Ichchou, C. Cariou, D. Juvé, and O. Bareille. A new energetic acoustic probe and its association with an acoustic energetic identification method. Proceedings of ISMA 2012 (3539-3550), Leuven, Belgium, 2012.

[5] F. Ayme, C. Cariou, M. Ichchou, and D. Juvé. A new acoustic three dimensional intensity and energy density probe. Proceedings of Acoustics 2012 congress (2057-2062), Nantes, France, 2012.

ELASTIC METAMATERIALS WITH LOCAL RESONANCES FOR BROAD BAND VIBRATION ISOLATION

Y. Gao[1*], F. Sui[1*] and S. daley[2]

[1] Key Laboratory of Noise and Vibration Research
Institute of Acoustics, Chinese Academy of Sciences, 100190, P. R. China.
Email: gaoyancn@yahoo.co.uk, fs_sui@yahoo.cn

[2] Institute of Sound and Vibration Research
University of Southampton, Southampton SO17 1BJ, U.K.
Email: S.Daley@soton.ac.uk

ABSTRACT

A novel elastic metamaterial with local resonances is proposed to realize double negativity in this paper. The underlying mechanisms of the negative effective mass and stiffness required for negative refraction are investigated based on a lumped parameter model. It is demonstrated that the double negative band lies within the band gap (BG) for reducing vibration transmission. By slightly tuning the physical properties of the local resonators in different layers, the elastic metamaterial attenuates low frequencies over a broader BG to a lower transmissibility level with additional improvement on the asymmetric behaviour inherited in the conventional design of elastic metamaterials. The proposed elastic metamaterial exhibiting the double negative property is potentially useful in the application of low frequency vibration isolation over a broad frequency band.

1 INTRODUCTION

In the last decades, acoustic/elastic metamaterials have received a significant amount of interest since the concept of the electromagnetic counterpart was firstly proposed by Vesalago [1]. Like their electromagnetic counterpart, acoustic/elastic metamaterials with the presence of local resonances possess either a single negative parameter including negative effective mass/mass density and negative effective modulus or both parameters negative simultaneously, i.e., double negativity [2]. Some composite components have been grown from the raw materials in a layer-to-layer fashion with varying degree of success. For example, great interest towards negative parameter material has been induced in the phononic crystal (PC) study for attenuating the acoustic or elastic waves. Since the investigation on the local resonance (LR) mechanism induced in the PCs, some new developments have further been theoretically attempted and shown that composites with certain manmade microstructures may break the limits of the frequency range, which is of considerable interests for the design of acoustic/elastic metamaterials. Although the static material properties of the PCs are positive in nature, the dynamic effective properties can become negative at resonance. However, the promises of the current available designs of acoustic/elastic metamaterials are very limited due to the highly asymmetric nature of the BG and the property of absolute wave attenuation at the single frequency [3]. Correspondingly the effective parameters including mass/mass density and modulus, are inherently dispersive in nature and only negative over a certain frequency band.

A novel elastic metamaterial is proposed to provide both the negative effective mass and stiffness required for negative refraction. The vibration transmission is determined using the transfer matrix method and the dispersion relations are further derived by evoking the Bloch's theorem. The broad band elastic metamaterial is realized by altering the physical properties of the metamaterial in different transmission layers. Based on the previous work [4], some physical parameters are defined in the elastic metamaterial and the corresponding simulation results are presented. This provides an important basis for the experimental validation for the proposed elastic metamaterial.

2 DESIGN OF THE ELASTIC METAMATERIAL WITH DOUBLE NEGATIVITY

Consider a one-dimenational elastic metamaterial with an array of local resonators connected to the tranmission medium, as illustrated in Figure 1. A lumped parameter model as suggested in [4] is adopted to study the performance of the metamaterial for vibration isolation. The material consists of solid layers separated by a damped viscoelastic layer, represented in lumped paremater form by the tranmission masses, *m*, and the tramission stiffness and viscous damping terms *k* and *c*, respectively.

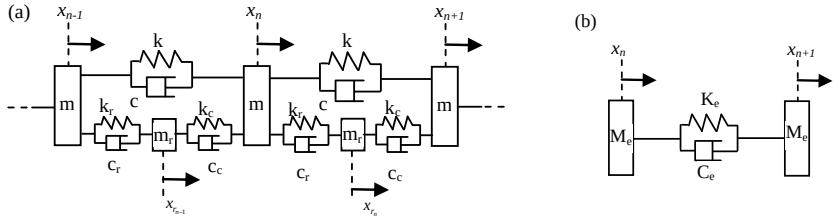

Figure 1. (a) Illustration of the lumped parameter model of an elastic metamaterial with the same physical parameters in each layer; (b) The effective system of the elastic metamaterial, where the viscoelasticity is represented using a Kelvin-Voigt model.

The effective mass and the cross coupling of the effective stiffness and damping can be derived from equation of motions, which are given by

$$M_e = m + \frac{m_r[k_r + k_c + j\omega(c_r + c_c)]}{-\omega^2 m_r + k_r + k_c + j\omega(c_r + c_c)}, \quad (1)$$

$$K_e + j\omega C_e = k + j\omega c + \frac{(k_r + j\omega c_r)(k_c + j\omega c_c)}{-\omega^2 m_r + k_r + k_c + j\omega(c_r + c_c)}, \quad (2)$$

respectively. Significant insight can be gained into vibration transmission through an infinite periodic structure by using Bloch's theorem. The current design of the metamaterial with the same physical parameters in each layer only leads to a narrow BG due to the strong dispersion inherent to the resonant elements in the transmission medium. A broader BG can be achieved by varing the configurations of the local resonators from layer to layer, for example, tuning the resonator mass m_r and/or stiffness k_r and k_c. When the physical properties of the metamaterial vary in different layers, the effective medium approach given above is not valid since the system cannot be simplified using effective elements due to the interfering effect of the adjacent layers. In this case the transfer matrix method can be adopted to study the dynamic behaviour of vibration transmission through the transmission medium.

3 SIMULATIONS AND DISCUSSIONS

In this section example results are presented for the proposed elastic metamaterial to gain the insight into the realisation of a broader BG for blocking vibration transmission. It can be seen from Figure 2 that the effective mass becomes negative in the proposed LR type BG despite the narrow frequency range of double negativity 55Hz-59Hz within the BG 55Hz-101Hz. Nevertheless, the novel behaviour of the double negativity exhibited in the BG is non-trivial, which is vital for the realisation of negative refraction.

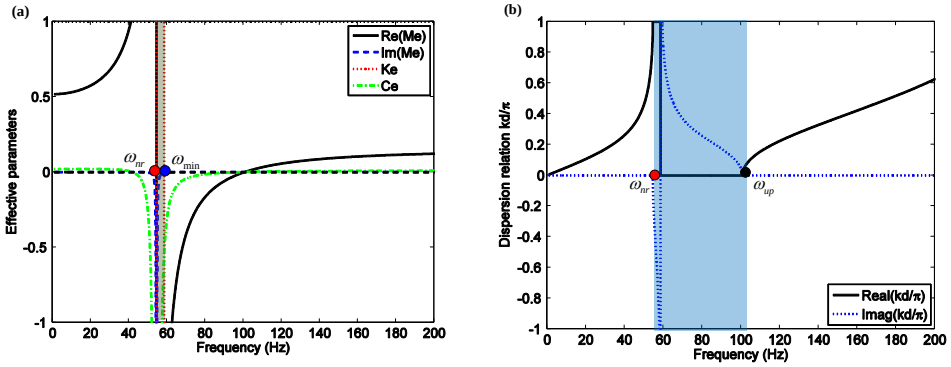

Figure 2. Comparision of the region of double negativity (marked by grey band) and the BG (marked by blue band). (a) Effective elements; (b) Dispersion curves. The physical properties of an elastic metamaterial are: m=0.15kg, m_r=0.37kg, k=7.04e4Nm^{-1}, k_r=k_c=2.15e4Nm^{-1}, c=0.01 Nsm^{-1}, and c_r=c_c=0.02 Nsm^{-1}.

A broad band metamaterial is proposed to tune the physical properties including the mass m_r and the stiffness k_r and k_c of the local resonators to achieve slightly different natural frequencies. The main advantage of the new design is to attenuate more frequencies to a lower level of transmissibility and to enhance the possibility of the achievement of a broader BG, allowing optimisation of the overall performance. Figure 3 shows that the BG of a smoother profile lies in the frequency range between 33Hz and 92Hz when $\Delta m_r = 10\%$ and $\Delta k_r = \Delta k_c = -10\%$. Particularly the transmissibility drops to a considerable lower level of roughly -40dB in the frequency band of 45Hz-59Hz. When $\Delta m_r = -10\%$ and $\Delta k_r = \Delta k_c = 10\%$, the upper edge frequency of the BG increases to 110Hz while the lower edge frequency decreases slightly to 53Hz. However, the strong interactions between the main transmission medium and the

local resonators cause amplifications at three discrete frequencies within the BG. Further extension to this work will be conducted to in-depth optimal design to eliminate the undesirable interfering effect on the LR type BG.

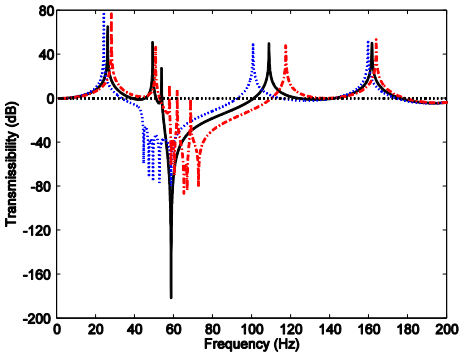

Figure 3. The transmissibility in the infinite elastic metamaterials (N=3): Black lines denote the original results for the metamaterial with the same physical properties in each layer; blue lines denote the results when $\Delta m_r = 10\%$ and $\Delta k_r = \Delta k_c = -10\%$; red lined denote the results when $\Delta m_r = -10\%$ and $\Delta k_r = \Delta k_c = 10\%$.

4 CONCLUSIONS

In the paper an elastic metamaterial with local resonances has been proposed to achieve both the negative effective mass and stiffness. It has been found that the BG has a highly asymmetric nature with the property of absolute wave attenuation at the single frequency. The limitations of the proposed double negative elastic metamaterial to operate as a useful vibration isolation device were discussed and it has been shown that the potential of slightly changing the physical properties of the local resonators in different layers of the metamaterial can lead to a broader BG and attenuate more frequencies to a lower transmissibility level in the BG. The elastic metamaterial presented in this paper will facilitate the design and understanding of the low frequency vibration isolation over a useful and broad frequency band.

5 ACKNOWLEDGEMENTS

The authors gratefully acknowledge the support provided for this research by the Engineering and Physical Science Research Council (EPSRC) and the National Natural Science Foundation of China (No. 10974217 and No. 11174317).

REFERENCES

[1] V. G. Veselago. The electrodynamics of substances with simultaneously negative vales of ε and μ. *Sov. Phys.—Usp*. 10: 509-514, 1968.

[2] X. N. Liu, G. K. Hu, G. L. Huang and C. T. Sun. An elastic metamaterial with simultaneously negative mass density and bulk modulus. *Appl. Phys. Lett.* 98, 251907, 2011.

[3] Y. Xiao, B. R. Mace, J. Wen and X. Wen, Formation and coupling of band gaps in a locally resonant elastic system comprising a string with attached resonators. *Phys. Lett. A*. 375:1485-1491, 2011.

[4] S. A. Pope and S. Daley, Viscoelastic locally resonant double negative metamaterials with controllable effective density and elasticity. *Phys. Lett. A*. 374: 4250-4255, 2010.

DIELECTRIC ELASTOMER AS ACTIVE MATERIAL IN MEMBRANES FOR VIBRATION-BASED ENRGY HARVESTING

E. ZAOUALI[1], F. NAJAR[1*] and K. MRABET[1]

[1] Applied Mechanics and Systems Research Laboratory
Tunisia Polytechnic School, BP 743, La Marsa 2078, University of Carthage, TUNISIA
Email: emine.zaouali@gmail.com, fehmi.najar@gmail.com, kais.mrabet@ipeit.rnu.tn

ABSTRACT

The main objective of this work is to develop an electromechanical model for a dielectric elastomer transducer membrane used as a vibration-based energy harvester. We use a circular membrane made of VHB4910 material, assumed as a prestretched diaphragm clamped about its outer radius, which is subjected to a timevarying displacement in the membrane-normal direction, sandwiched between two compliant electrodes. A bias voltage is also injected to accomplish the energy harvesting cycle. The problem is considered as a geometrically, materially and electrically nonlinear. We derive equations of motion according to Helmholtz energy density function for both Neo-Hookean and Mooney-Rivlin material models, added to a dielectric term. Static response of pre-stretch phase is calculated analytically using the DQM also for Neo-Hookean and Mooney-Rivlin materials. Dynamic response of harmonically excited membrane is also calculated. The time response of the membrane is found to be two-period quasi-periodic. The quantity of converted energy found is equal to 28.25 μJ, the power generated equals to 5.65mW, and the power density is equal to 2.88mW/cm^3.

***Acknowledgments**: The authors are grateful for the funding and support provided by BEBCOM Technology, Tunisia.*

1 INTRODUCTION

Nowadays, many researchers and R&D centers are focusing in the development of Wireless sensor networks. The low-power characteristics of these devices motivated researchers to seek alternate sources of power. Vibration-based energy harvesters (VEH) explore the ability of active materials (e.g., piezoelectric, dielectric elastomer…) to generate an electric energy in response to external mechanical displacements. Dielectric Elastomer (DE) belongs to the Electroactive polymer family that are light and flexible smart materials that experience shape and dimensions changes when electrically stimulated, and vice versa [1]. We aim at developing an electromechanical model for a dielectric elastomer transducer membrane used as a vibration-based energy harvester.

2 DERIVATION OF THE EQUATIONS OF MOTION

We use a circular membrane [2] made of VHB4910 material, prestretched, clamped about its outer radius and sandwiched between two compliant electrodes. The membrane is subjected to a harmonic edge displacement in the normal direction (Figure 1). Here the electrodes are omitted in the mechanical model. We use Hamilton's principle and assuming membrane deformation.

The circular membrane is considered homogeneous, isotropic, axisymmetric and hyperelastic with undeformed radius R_0, thickness H and mass density Γ. Only the radial displacement r and the transverse deflection w are allowed for a particle initially at material point P_0.

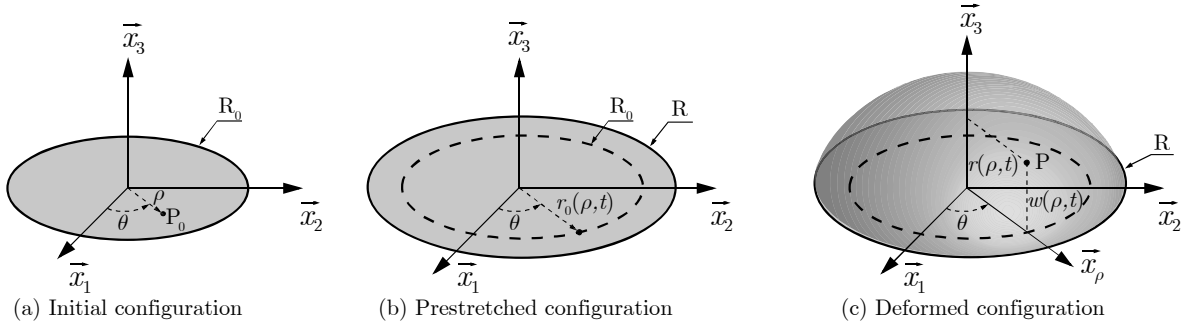

(a) Initial configuration (b) Prestretched configuration (c) Deformed configuration

Figure 1. Particle displacements in different configurations of the membrane.

The application of the Hamilton's principle and letting W be the free energy density

$$\begin{aligned} \rho\Gamma\ddot{r} + \rho\frac{\partial W}{\partial r} - \frac{\partial}{\partial\rho}\left(\rho\frac{\partial W}{\partial r'}\right) = 0 \\ \rho\Gamma\ddot{w} + \rho\frac{\partial W}{\partial w} - \frac{\partial}{\partial\rho}\left(\rho\frac{\partial W}{\partial w'}\right) = 0 \end{aligned} \tag{1}$$

The boundary conditions are given by

$$\text{at } \rho = 0 \Rightarrow\ r = 0 \text{ and } \frac{\partial W}{\partial w'} = 0 \tag{2}$$

$$\text{at } \rho = R_0 \Rightarrow\ r = 0 \text{ and } w = 0 \tag{3}$$

3 STATIC ANALYSIS OF THE PRE-STRETCH PHASE

The static solution was derived using the Differential Quadrature Method [3]. The static equation for Neo-Hookean case is

$$\begin{aligned} &\frac{2C_{10}r_0(\rho)}{\rho^2} + \frac{6\rho C_{10}}{r_0(\rho)^2 r_0'(\rho)} - \frac{6\rho^2 C_{10}}{r_0(\rho)^3 r_0'(\rho)^2} - \frac{2C_{10}r_0'(\rho)}{\rho} \\ &-2C_{10}r_0'(\rho) - \frac{6\rho^2 C_{10}r_0'(\rho)}{r_0(\rho)^2 r_0'(\rho)^4} = 0 \end{aligned} \tag{4}$$

We show the DQM static solution of the applied prestrech equals to 1.2R for different number of DQM grid points. We conclude that the solution is linear with respect to the initial

configuration. As a result, we propose the following approximated linear solution for the prestrech,

$$r_0(\rho) = \frac{R}{R_0}\rho = \delta\rho \tag{5}$$

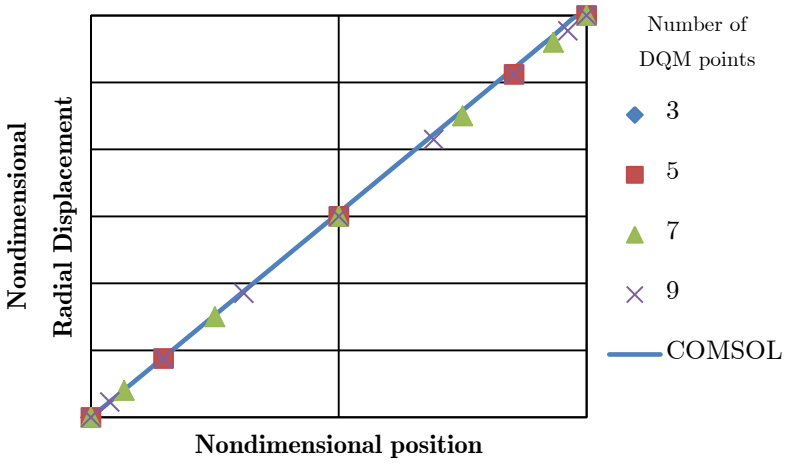

Figure 2. Static solution for the prestrech for different number of DQM grid points.

4 ENERGY HARVESTING USING HARMONIC EXCITATION

First, we solve for the mode shapes and natural frequencies using ABAQUS for the prestretched membrane with δ=1.2. The natural frequencies of the stretched hyperelastic membrane are given by [2]

$$f_{mn} = \frac{\alpha_{mn}}{2\pi}\sqrt{\frac{2C_{10}\left(\delta^6 - 1\right)}{R_0^2\,\delta^6\,\Gamma}} \tag{6}$$

where α_{mn} are the mth zero of the Bessel function of order *n*. We validate the results given by the proposed model concerning the natural frequencies of the system using free vibrations analysis in Table 1.

Table 1. Natural frequencies associated to the first 4 mode shapes using different methods.

	1st (1,0)	2nd (1,1)	3rd (1,2)	4th (2,0)
Neo-Hookean (ABAQUS)	218.18	347.54	465.66	500.46
Neo-Hookean (Analytical)	234.97	374.39	501.79	539.35
Neo-Hookean (DQM n=7)	235	-	-	539

Next, we solve the equation of motion discretized using different DQM grid point number *n* at a fixed applied DC voltage equals to 50V, when a non-dimensional (with respect to membrane thickness) displacement excitation $Z(t)=Z_0\,\mathrm{Sin}(2\pi\, f\, t)$ is applied at the boundaries for Neo-Hookean model. It is found that the solution is convergent even for low number of grid points.

In Figure 3 we plot the time response and phase portrait. We found that a quasiperiodic solution is obtained.

To estimate the amount of electrical energy that can be extracted from the system, we use the following estimation of the stored energy into the membrane supposed to be an electrical capacitance [4]

$$E_{converted} = \frac{1}{2}V^2\left(C_{\max} - C_{\min}\right)\frac{C_{\max}}{C_{\min}} \tag{7}$$

We calculate the maximum and minimum capacities as

$$C_{\max} = \frac{\varepsilon_0 \varepsilon_r \pi R_0^2 \delta^2}{H \lambda_{3\min}} \text{ and } C_{\min} = \frac{\varepsilon_0 \varepsilon_r \pi R_0^2 \delta^2}{H \lambda_{3\max}} \quad (8)$$

where $\lambda_3 = \frac{1}{\lambda_1 \lambda_2}$, $\lambda_1 = \sqrt{\delta^2 + w'(R_0,t)^2}$ and $\lambda_2 = \delta$.

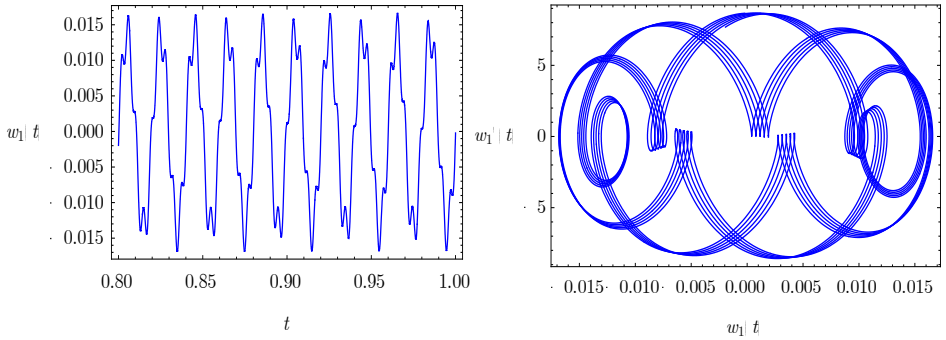

(a) (b)

Figure 3. Deflection of the membrane at the center (a) and its corresponding phase plot (b) using Neo-Hookean model when n=3, V=50V, Z_0=0.005, f=50Hz.

From the equation (8) we deduce that the minimum of transversal stretch ratio $\lambda_{3\min}$ (minimum of thickness), which corresponds to the maximum slope of the membrane located at the boundary, $w'_{\max}(R_0,t)$. For $\lambda_{3\max}$ (maximum of thickness), it corresponds to $w'(R_0,t)=0$. From simulated results, we deduce that $\lambda_{3\min} = 0.6217$ and $\lambda_{3\max} = 0.694444$.

Putting these values in the equation (8), we end up with the quantity of converted energy $E_{converted}$= 28.25 µJ, which corresponds to energy density equal to 14.4 µJ/cm^3.

The power generated in the active phase

$$P = \frac{E_{converted}}{t_{CD}} \quad (9)$$

Where P is the instantaneous mean power generated by the elastomer and t_{CD} is the required time to go from $C_{\min}$ to $C_{\max}$.

The equation (9) becomes

$$P = 4f\ E_{converted} \quad (10)$$

Taking f =50Hz, we get P=5.65 mW corresponding to 2.88mW/cm^3.

5 CONCLUSIONS

In this work, an electromechanical model for a dielectric elastomer transducer membrane used as a vibration-based energy harvester was developed. Static response of pre-stretch phase was calculated analytically and validated with FE. Dynamic response of harmonically excited membrane was also calculated using the DQM, were two-period quasi-periodic solution are identified. The proposed system was able to generate 28.25 µJ, corresponding to a power density of 2.88mW/cm3.

REFERENCES

[1] C. Jean-Mistral, *Récupération d'énergie mécanique par polymères électroactifs pour microsystèmes autonomes communicants*, Université Joseph Fourier, France, Phd-thesis, octobre 2008.

[2] P. B. Gonçalves, R. M. Soares, D Pamplona, Nonlinear vibrations of a radially stretched circular hyperplastic membrane, *J. of Sound and Vibration*, vol. 327, pp. 231–248, 2009.

[3] F. Najar, Choura, S., El-Borgi, S., Abdel-Rahman, E.M., Nayfeh, A.H. Modeling and design of variable-geometry electrostatic microactuators. *J. of Micromechanics and Microengineering* 15, 419–429, 2005.

[4] S Roundy, P K Wright, K S J Pister, Micro-Electrostatic Vibration-to-Electricity Converters, IMECE2002 Engineering Congress & Exposition, New Orleans, Louisiana 17-22, 2002.

ON THE RADIATION EFFICIENCY OF LOCAL RESONANCE STOP BANDS

C.C. Claeys[1] , P. Sas[1] and W. Desmet[1]

[1]Department of Mechanical Engineering
KU Leuven, Celestijnenlaan 300B, B-3001 Heverlee (Leuven), Belgium
Email: claus.claeys@mech.kuleuven.be

ABSTRACT

The application of stop bands, i.e. frequency zones in which no free wave propagation is possible, is emerging as a novel way of creating periodic structures with good vibrational behaviour. In recent literature examples are shown in which good vibrational attenuation is possible in those stop bands. The radiation efficiency of those zones with good vibrational attenuation is often not investigated. This paper formulates an uncoupled vibro-acoustic unit cell model of a plate with local resonant stop band behaviour. It is shown that the beneficial vibration reduction that is achieved in a stop band can be counteracted by an increase in radiation efficiency. When care is taken in the design of the stop band, the vibration reduction can be combined with a decrease in acoustic radiation efficiency, leading to a stop band with good vibro-acoustic behaviour.

1 INTRODUCTION

In recent literature the application of stop bands emerges as a novel method with good prospects for periodic light weight structures [1–5]. Stop bands are zones with no free wave propagation in a certain frequency range of interest and this stop band behaviour can be achieved through different mechanisms. Previous work of the authors [6] indicated that especially local resonance based stop bands are promising for achieving vibration reduction. This paper continues this work and investigates the potential for creating panels with good vibro-acoustic properties.

2 ACOUSTIC RADIATION ON DISPERSION CURVES

2.1 Dispersion curves

Application of the Bloch's theorem allows modeling infinite periodic structures by considering only a unit cell. The equation of motion of the unit cell can be reduced by writing the boundary conditions based on the wave vector propagating in the equivalent infinite structure. For 2D systems, this approach enables obtaining the dispersion curves: the frequencies of unattenuated wave propagation as a function of the direction and magnitude of the propagating wave vector [7]. Solving this problem for all wave vectors on the first irreducible Brillouin contour allows investigation of stop band behaviour. In this paper, the unit cell will be limited to a square unit cell, the corresponding Brillouin contour is known to have the corner points (0;0), (π;0), (π;π), (0;0) in the wave domain [8].

2.2 Acoustic radiation

The efficiency of flexural vibration transmission into an acoustic medium depends on the efficiency of the coupling between acoustic and flexural waves. The dispersion equation governs the relation between wave propagation and wave speed in an acoustic medium, when considering an ideally compressible, linear fluid and neglecting viscosity and thermal effects;

$$c_{ac} = 2\pi f / k_{ac} \tag{1}$$

with k_{ac} the acoustic wave vector length, f the frequency of propagation and c_{ac} the wavespeed in the acoustic medium.

The acoustic wave radiated from the structure has an in-plane ($k_{\_}$) component in the coupling plane between the structure and the acoustic domain and an out-of-plane component ($k_\perp$) in to the acoustic domain $k_{ac} = \sqrt{k_\perp^2 + k_{\_}^2}$. The flexural structural wave (k_{str}) lies in the coupling plane and acts as a boundary condition for the acoustical wave; meaning $k_{\_} = k_{str}$. The structure-acoustic coupling is efficient if the acoustic wave vector is equal or larger than the structural wave vector [9]. Mathematically this condition is expressed as;

$$\Rightarrow k_\perp = \sqrt{(2\pi f / c_{ac})^2 - k_{str}^2} \tag{2}$$

where $k_\perp$ needs to be real for efficient acoustic radiation. The frequency for which $k_\perp = 0$ is the most efficient frequency of acoustic radiation and is called the coincidence frequency.

2.3 Acoustic radiation on dispersion curve

Each dispersion branch on the Brillouin contours obtained from the structural model, links a certain structural wave vector with a frequency of free wave propagation. Combination of the dispersion curve and Equation 2 allows indicating which points on the Brillouin contour will have an efficient vibro-acoustic coupling.

3 APPLICATION ON A STEEL PLATE

An infinite steel plate (Young's modules 210GPa, density 7800$\frac{\text{kg}}{\text{m}^3}$, Poission's ratio 0.3) of 5mm thickness serves as a test case. To introduce stop bands, tuned vibrators are added on a periodic grid. The length of repetition in x and y direction equals 50mm, so that the unit cell (Figure 1) is symmetrical and square. The mass (m) of the tuned vibrator is 20$\%$ of the mass of the unit cell, the stiffness (k) is changed throughout the examples.

According to the Kirchoff-plate-theory the dispersion relationship between frequency and wave vector for bending waves in an infinite plate is given by:

$$f = \frac{1}{2\pi k^2}\sqrt{\frac{t^2 E}{12(1-\nu^2)\rho}}. \tag{3}$$

From Equations 1 and 3 it can be derived that the coincidence frequency, for which $k_\perp = 0$, is 2343Hz.

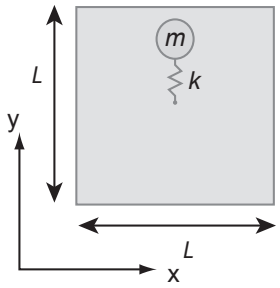

Figure 1: Unit cell of a plate with a periodic tuned vibrator.

To asses the effect of stop bands on the radiation efficiency, three different cases are investigated; plates with tuned resonator resonances of 1171, 2343 and 3514Hz. From [6] it is known that each case has a stop band in the region of the tuned resonator resonance.

From inspection of Figure 2 it is clear that the stop band has a huge impact on the zone of efficient radiation. In the case without resonator, the efficient radiation zone starts at 2343Hz as predicted. In the case with a resonator at half the coincidence frequency (1171Hz) a second zone of efficient radiation is created for frequencies just above the stop band zone. The case of a tuned resonator frequency at the coincidence frequency or 150$\%$ of the coincidence frequency (2343 and 3514 Hz resp.), the zone of efficient radiation is shifted to higher frequencies.

4 CONCLUSION

Although stop bands improve the vibrational behaviour, care should be taking in making statements about the acoustic behaviour. This is a crucial insight since an improved vibro-acoustic coupling can counteract the vibration attenuation of the stop band from an acoustic point of view. This paper shows that by careful design of the stop band, attenuated vibrational behaviour as well as a decrease in acoustic coupling can be combined, leading to a double advantage.

5 ACKNOWLEDGEMENTS

The research of Claus Claeys is funded by a Ph.D. grant of the Institute for the Promotion of Innovation through Science and Technology in Flanders (IWT-Vlaanderen). The IWT Flanders within the ASTRA project and the EC within the FP7 eLiQuiD Marie Curie European Industry Doctorate (GA 316422) are also gratefully acknowledged for their support.

REFERENCES

[1] L. Brillouin. *Wave propagation in periodic structures*. McGraw-Hill Book Company, New York, 1946.

[2] Z. Liu, X. Zhang, Y. Mao, YY Zhu, Z. Yang, CT Chan, and P. Sheng. Locally resonant sonic materials. *Science*, 289(5485):1734–1736, 2000.

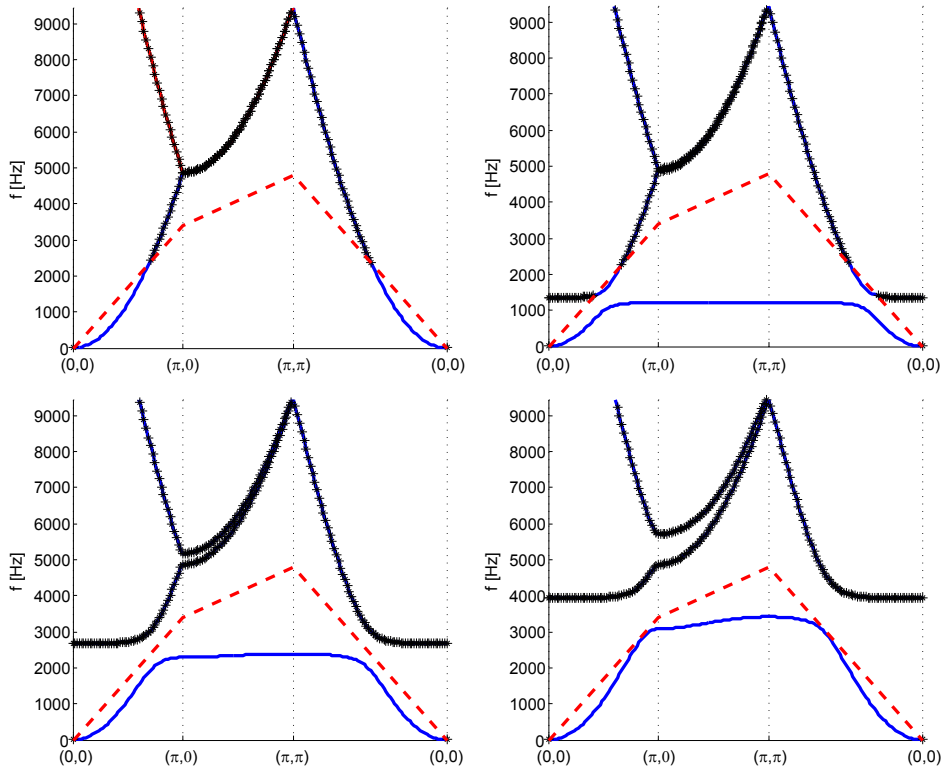

Figure 2: Comparison between dispersion diagrams for an infinite steel plate (upper left) and the same plate with a periodic grid of tuned resonators; the resonance frequencies of the tuned resonators are 1171, 2343 and 3514Hz for the upper right, lower left and lower right figure respectively. The black stars ($*$) indicate the structural travelling waves that will radiate efficiently. The red dashed lined indicates the dispersion curve for air.

[3] F. Casadei, L. Dozio, M. Ruzzene, and K.A. Cunefare. Periodic shunted arrays for the control of noise radiation in an enclosure. *Journal of Sound and Vibration*, 329(18):3632–3646, 2010.

[4] Y. Xiao, J. Wen, D. Yu, and X. Wen. Flexural wave propagation in beams with periodically attached vibration absorbers: Band-gap behavior and band formation mechanisms. *Journal of Sound and Vibration*, 332:867–893, 2012.

[5] M. Collet, M. Ouisse, M.N. Ichchou, and R. Ohayon. Semi-active optimization of 2d wave dispersion into shunted piezo-composite systems for controlling acoustic interaction. *Smart Materials and Structures*, 21:094002, 2012.

[6] C.C. Claeys, K. Vergote, P. Sas, and W. Desmet. On the potential of tuned resonators to obtain low-frequency vibrational stop bands in periodic panels. *Journal of Sound and Vibration*, 332:1418–1436, 2012.

[7] RS Langley. A note on the force boundary conditions for two-dimensional periodic structures with corner freedoms. *Journal of Sound and Vibration*, 167:377–381, 1993.

[8] A.R. Diaz, A.G. Haddow, and L. Ma. Design of band-gap grid structures. *Structural and Multidisciplinary Optimization*, 29(6):418–431, June 2005 2005.

[9] F. Fahy and P. Gardonio. *Sound and structural vibration: radiation, transmission and response*. Academic Press, 2007.

ELECTROACOUSTIC METAMATERIALS WITH NEGATIVE ACOUSTIC PROPERTIES

H. Lissek[1]

[1]Lab. d'Electromagnetisme et d'Acoustique
Ecole Polytechnique Federal de Lausanne, Lausanne, SWITZERLAND
Email: herve.lissek@epfl.ch

ABSTRACT

Acoustic metamaterials are physical structures that exhibit acoustic properties not readily available in nature. These properties can be a negative mass density (expressing the opposition of the acceleration of a particle to the application of pressure), or a negative bulk modulus (rarefaction of the particle in reaction to a compression, or condensation in reaction to a depression). However, these artificial behaviors result from a periodic arrangement of unit-cells, and not from individual meta-properties of each unit-cell. It is however possible to observe such intrinsic metamaterial properties out of active electroacoustic resonators. This concept encompasses a loudspeaker, connected to a closed-loop active electronic control device, altering the acoustic dynamics of the loudspeaker diaphragm when subject to an exogenous sound source. It is then possible to achieve negative acoustic impedance at its diaphragm. This paper aims at highlighting the metamaterial nature of such electroacoustic resonators.

1 INTRODUCTION

The "Acoustic metamaterial" label represents physical structures that exhibit acoustic properties not readily available in nature. These properties can be a negative mass density, or a negative bulk modulus, or more generally a negative acoustic impedance (either negative resistance or reactance). Recent publications [1, 2] report the achievement of simultaneous negative mass density (eg. acoustic mass) and bulk modulus (eg. acoustic compliance), based on the design of acoustic transmission lines periodically loaded with elastic membranes along the duct, and side holes ("stubs"). Looking at the unit-cell and deriving the equivalent lumped-element components of the transmission-line yields frequency-dependent acoustic equivalents (series acoustic mass and shunt acoustic compliance), taking successively negative and positive values as frequency increases.

The electroacoustic resonator describes a closed-loop acoustic impedance control concept, allowing the achievement of either total absorption, but also potentially negative absorption (through the obtention of negative acoustic impedance) [3]. This specific feature reveals the capability of a loudspeaker to reflect more sound energy than it receives from the field (negative resistance), but also to act as a negative acoustic reactance. This property reveals similarities with the concept of metamaterial with negative mass density or negative bulk modulus. However, rather than achieving these meta-properties from a distribution of passive acoustic impedances, this active concept presents intrinsic metaproperties, allowing to describe the individual active loudspeaker as a metamaterial by itself. This paper describes a reproducible example of such active impedance control concept, highlighting the achievement of electroacoustic metamaterial with both negative acoustic mass and compliance.

2 THE ELECTROACOUSTIC RESONATOR CONCEPT

Let us consider an electrodynamic loudspeaker, disposed transversally to a cylindrical duct of cross section S and infinite length, as depicted in Figure 1, connected to a amplifier delivering voltage e. The total pressure at the loudspeaker diaphragm (of surface S) is denoted p and represents the sum of the pressure generated by the speaker (towards the speaker front) and the action of an exogenous sound source propagating along the duct filled of air (mass density ρ, celerity of sound c). In the following development, we consider as a convention that the sound source is located at the left side of the loudspeaker, the right side being practically terminated by a layer of absorbent material (eg. assuming the termination specific impedance $Z_l = \rho c$). The diaphragm velocity is denoted v and represents the dynamic response of the speaker to the total pressure force (output). From a control perspective the electroacoustic resonator dynamics can then be characterized by the normalized acoustic admittance in the Laplace domain $Y(s) = \rho c(V(s)/P(s))$. In this work, we consider the loudspeaker as part of a direct impedance control

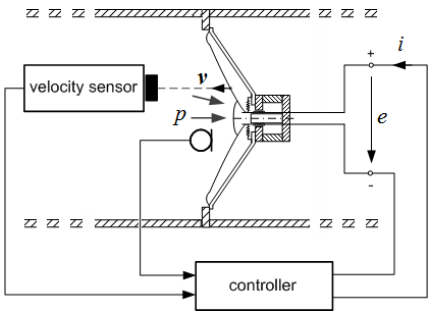

Figure 1. Electroacoustic resonator.

setup, the whole being entitled an active electroacoustic resonator [4]. In this case, the amplifier is fed back with a combination of two voltages, one emanating from a velocity sensor (eg. laser velocimeter) and the other from a microphone, sensing pressure p at the diaphragm of the loudspeaker. We denote here Γ_p and Γ_v the feedback gains applied to velocity v and pressure p signals. Then, the total voltage delivered by the amplifier can be expressed in the Laplace domain as (capital letters represent the Laplace transform of minuscule letters):

$$E(s) = \Gamma_p P(s) - \Gamma_v V(s) \tag{1}$$

It can be shown that the resulting acoustic admittance $Y(s)$, characterizing the velocity response of the closed loop loudspeaker to the external sound pressure, can be written as [4]:

$$Y(s) = \rho c S \frac{s^2 L_e + s(R_e + \Gamma_p \frac{Bl}{S})}{s^3 M_{ms} L_e + s^2(M_{ms} R_e + R_{ms} L_e) + s(R_{ms} R_e + \frac{L_e}{C_{ms}} + Bl(Bl + \Gamma_v)) + \frac{R_e}{C_{ms}}} \tag{2}$$

where (R_{ms}, M_{ms}, C_{ms}) are respectively the mechanical resistance, mass and compliance of the mobile equipment of the loudspeaker, (R_e,L_e) are the electric resistance and inductance of the coil, and Bl is the force factor of the electromechanical driver. The two feedback gains Γ_p and Γ_v allow then to modify the dynamics of the feedback controlled loudspeaker, through poles/zeros placement, specifically around resonance frequency $\omega_s = \sqrt{M_{ms} C_{ms}}^{-1}$.

As a low-frequency approximation, let us neglect the influence of the inductance L_e of the loudspeaker in the frequency range of interest (around the resonance frequency), which is legitimate since the inductance is generally dominating above $\omega_c = R_e/L_e$ which is of the order of 1kHz for most electrodynamic loudspeakers, whereas resonance generally occurs around some tens of Hertz. Then it is possible to derive the low-frequency equivalent acoustic impedance of the electroacoustic resonator as:

$$z(\omega) \approx r_a + j\omega m_a + \frac{1}{j\omega c_a} = r_a + j x_a \quad (\omega \ll \omega_c) \tag{3}$$

$$\tag{4}$$

where

$$r_a = \frac{R_{ms} R_e + Bl(Bl + \Gamma_v)}{\rho c S \left(R_e + \Gamma_p Bl/S\right)}$$

$$m_a = \frac{M_{ms} R_e}{\rho c S \left(R_e + \Gamma_p Bl/S\right)} \tag{5}$$

$$c_a = \frac{C_{ms} \left(R_e + \Gamma_p Bl/S\right)}{\rho c S R_e} \tag{6}$$

$$\tag{7}$$

For feedback gain values $\Gamma_p < -\frac{S R_e}{Bl}$, equivalent acoustic mass and compliance are negative.

3 EXAMPLE OF NEGATIVE ACOUSTIC REACTANCE

In this work, a VISATON AL170 loudspeaker has been employed as an electroacoustic resonator, the Thiele-Small parameters of which are given in Table 1. We have chosen to illustrate this work with control gain Γ_p=-0.024 V/Pa (and Γ_v=0 V.s/m), which satisfies the Nyquist criterion relative to the closed-loop stability of the electroacoustic resonator. The equivalent normalized resistance, mass and compliance become $r_a = -1.4$, $m_a = -0.002$ and $c_a = -0.008$, as depicted in Figure 2.

Label	Description	Value	Unit
L_e	electrical inductance of the coil	0.9 10^{-3}	H
R_e	electrical resistance	5.6	Ω
M_{ms}	moving mass	13 10^{-3}	kg
R_{ms}	mechanical resistance	0.8	N s m^{-1}
C_{ms}	mechanical compliance	1.2 10^{-3}	m N^{-1}
Bl	force factor	6.9	N A^{-1}
S	diaphragm area	133 10^{-4}	m^2

Table 1. Thiele Small parameters of the loudspeaker

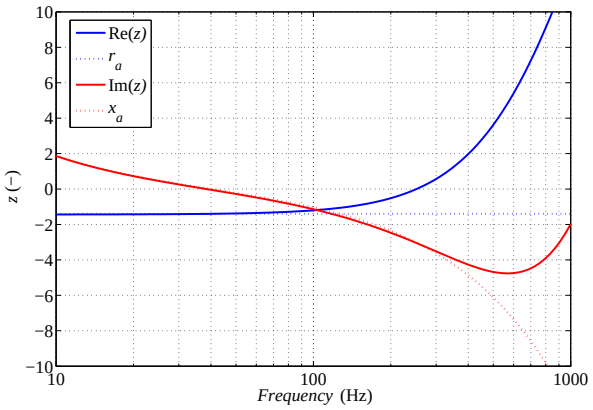

Figure 2: Simulated normalized acoustic impedance with feedback gains Γ_p=-0.024 V/Pa and Γ_v =0 V.s/m. The real part (blue line) is compared to the equivalent normalized resistance r_a and the imaginary part (red line) is compared to the equivalent normalized reactance x_a

.

4 CONCLUSIONS

This work presents a closed-loop active control concept allowing the achievement of negative reactance, namely an equivalent negative compliance and mass, out of a loudspeaker diaphragm. Such properties can be identified as negative (electro-)acoustic metamaterials.

REFERENCES

[1] F. Bongard, H. Lissek, and J.R. Mosig. Acoustic transmission line metamaterial with negative/zero/positive refractive index. *Phys. Rev. B*, 82(16):094306, 2010.

[2] Yong Mun Seo, Jong Jin Park, Seung Hwan Lee, Choon Mahn Park, Chul Koo Kim, and Sam Hyeon Lee. Acoustic metamaterial exhibiting four different sign combinations of density and modulus. *J. App. Phys.*, 111(2), JAN 15 2012.

[3] H. Lissek, R. Boulandet, and R. Fleury. Electroacoustic absorbers, bridging the gap between shunt loudspeakers and active sound absorption. *J. Acoust. Soc. Am.*, 129(5):2968–2978.

[4] Romain Boulandet. *Tunable Electroacoustic Resonators through Active Impedance Control of Loudspeakers*. PhD thesis, EPFL, Lausanne, 2012.

SENSITIVITY ANALYSIS AND CONTROL OF A CANTILEVER BEAM BY MEANS OF A SHUNTED PIEZOELECTRIC PATCH

G. Matten[1] , M. Collet[1], E. Sadoulet-Reboul[1] and S. Cogan[1]

[1]Applied Mechanics Department
Femto-ST Institute
24 Chemin de l'Epitaphe, Besançon, FRANCE

ABSTRACT

In this paper, a sensitivity analysis of a beam controlled with a shunted piezoelectric patch is presented. A negative capacitance controller is implemented and a study of stability and performance is performed. Besides, the effects of the technological aspects such as the variability in the material properties or in the position of the piezoelectric patch is evaluated through a finite element simulation.

1 INTRODUCTION

During the last thirty years, vibration control using piezoelectric materials such as lead zirconate titanate (PZT) or polyvinylidene fluoride (PVDF) has been proven to be efficient. Indeed, these materials produce a voltage when strained and conversly strain when exposed to a voltage. Therefore, the mechanical energy can be converted into electrical energy and can be dissipated through a circuit [1]. This technique is called shunted piezoelectric damping. Researches have been led concerning passive shunt [2] or active shunt [3]. The most recent works have shown the efficiency of distributed piezoelectric tranducers [4].

Although, the robustness of such systems, especially the sensitivity of the performances to variations in the material properties in the position of the tranducers, has not been studied. Moreover, the implementation constraints and the nonlinearities of the electronic shunt have not been taken into account during the modelization of the mechanical system. This paper aims at studying the effects of technological aspects such as variability in the material properties or in the position of the piezoelectric patch.

2 SENSITIVITY ANALYSIS

2.1 The mechanical problem

If the design of shunt damping technics has been extensively studied [5–7], the behaviour of the controlled systems in presence of model variations is still unknown. The objective of the sensitivity analysis is to identify which parameter is the more critical when it comes to insure the robustness of the system. We will present here a sensitivity analysis of a 3D cantilever beam controlled by a shunted piezoelectric transducer fixed on one of the surface (see figure 1(a)). The uncertainties considered are :

- the Young modulus of the beam material
- the position of the piezoelectric tranducer
- the thickness of the glue layer

To do so, a multiphysics finite element simulation piloted by a matlab program is performed. Thus, specific functions are built where the entries are the parameters mentioned before and the outputs are the eigenfrequencies and the frequency response. The beam is fixed at one of its end and excited by an harmonic force applied on the other. It is in steel, 1 mm long, 10 mm wide and 5 mm thick. A piezoelctric transducer in PZT-5A is attached on the upper face of the beam, 20 mm long, 10 mm wide and 0.5 mm thick, according to [8].

The tranducer is shunted by a negative capacitance C in serial with a resistor R. With u the voltage between the two faces of the piezoelectric patch, the electric charge applied q applied at a pulsation ω is then :

$$q = \frac{uC}{1 + jRC\omega}$$

2.2 Control sensibility

The choice of C and R has been optimized according to [8] to damp the first bending mode of the beam. By shunting the transducer with a negative capacitance controller, a displacement attenuation of 20 dB is achieved (see figure 2). The damping performances of the first bending mode are found to be robust to a 10% variation of the Young modulus and a 1 mm shift in the position of the tranducer. The induced loss in attenuation does not exceed one decibel *i.e.* 5 %

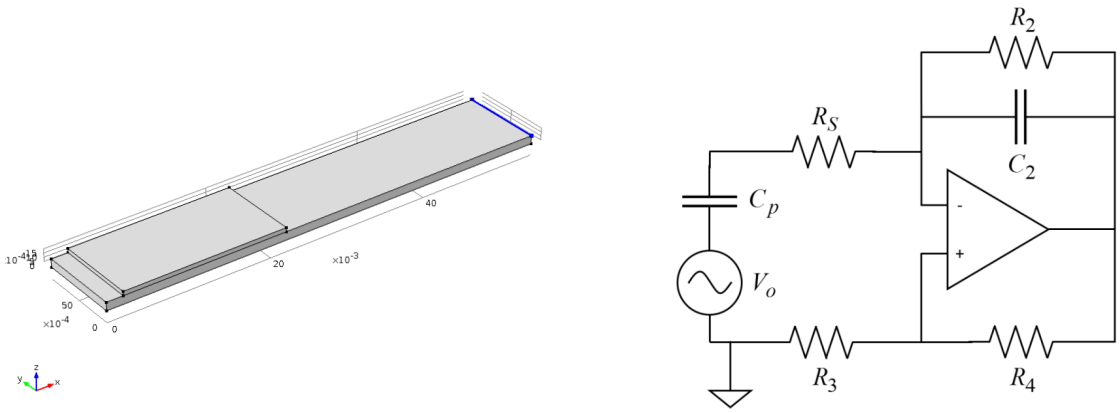

(a) Geometry of the beam (b) Shunt circuit

Figure 1. Analog implementation of the negative capacitance controller

of the nominal attenuation. Recent works have been led using a negative capacitance controller. For now the implementation is fully analogic, as proposed in [9]. The electric scheme is given on figure 1(b). Although, the stability of the circuit is hard to insure. Moreover, the damping performances are very sensitive to the variations of the negative capacitance. Indeed, as shown on figure 3, a variation of 10% of the capacitance leads to a 2dB loss in damping.Experimentally, a potentiometer is used for the tuning. This operation is manual and has to be performed for every circuit.

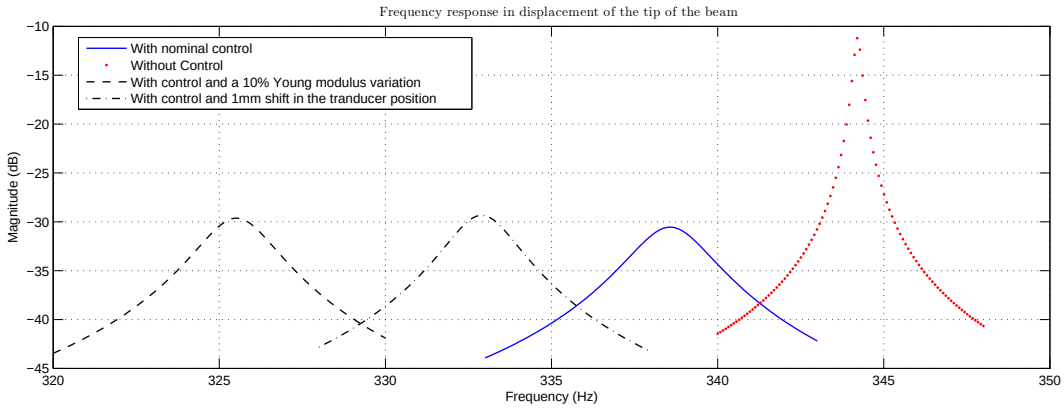

Figure 2. Frequency response in displacement of the tip of the beam

3 CONCLUSION

The performances of the negative capacitance controller appears to be quite robust to a variation of the system properties. Indeed, when controling the first bending mode of the beam, large variation in the material properties and in the position of the tranducer induce a loss of damping of at most one decibel. The electronic circuit has been designed to implement a negative capacitance impedance. However, the damping efficiency relies on a fine tuning of the capacitance. In addition, it is possible to synthetize any king of circuit or filter. By knowing the influence

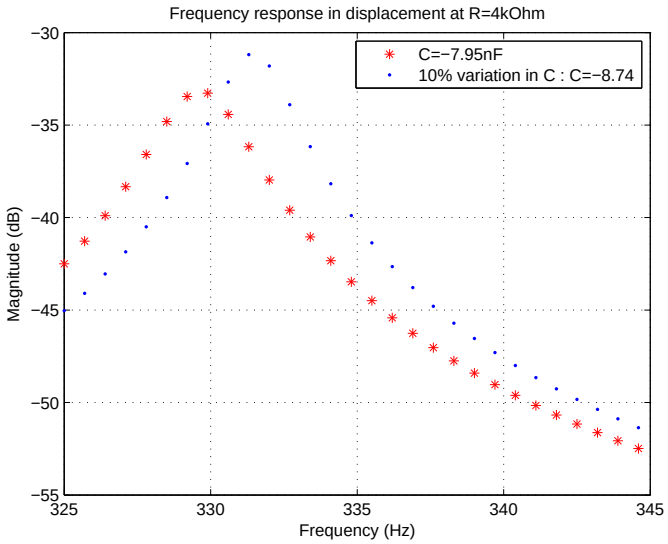

Figure 3. Effects of a capacitance variation

of the technological aspects and the uncertainties on the system performances, an adaptative controller could be implemented to optimize the damping performances in real time.

REFERENCES

[1] R. L. Forward. Electronic damping of vibrations in optical structures. *Applied optics*, 18(5):690–7, March 1979.

[2] S. Behrens, A. J. Fleming, and S. O. R. Moheimani. Passive Vibration Control via Electromagnetic Shunt Damping. *IEEE/ASME Transactions on Mechatronics*, 10(1):118–122, 2005.

[3] D. R. Browning and W. D. Wynn. Vibration damping system using active negative capacitance shunt circuit with piezoelectric reaction mass actuator. *EPO Patent 0715092*, Mai 1996.

[4] M. Collet and K. A. Cunefare. Modal Synthesis and Dynamical Condensation Methods for Accurate Piezoelectric Systems Impedance Computation. *Journal of Intelligent Material Systems and Structures*, 19(11):1251–1269, April 2008.

[5] J. J. Hollkamp and R. W. Gordon. An experimental comparison of piezoelectric and constrained layer damping. *Smart Materials and Structures*, 5(5):715–722, October 1996.

[6] J. Kim and J-H. Kim. Multimode shunt damping of piezoelectric smart panel for noise reduction. *The Journal of the Acoustical Society of America*, 116(2):942, 2004.

[7] S. Behrens, A. J. Fleming, and S. O. R. Moheimani. A broadband controller for shunt piezoelectric damping of structural vibration. *Smart Materials and Structures*, 12(1):18–28, February 2003.

[8] S. Livet, M. Collet, M. Berthillier, P. Jean, and J-M. Cote. Structural multi-modal damping by optimizing shunted piezoelectric transducers. *European Journal of Computational Mechanics/Revue Europenne de Mcanique Numrique*, 20(1-4):73–102, 2011.

[9] B. S. Beck. *Negative capacitance shunting of periodic arrays for vibration control of continuous flexural systems*. PhD thesis, Georgia Institute of Technology, 2012.

EFFECTS OF CONSTRAINTS AND STABILITY COEFFICIENTS ON CONVERGENCE OF PSO BASED ALGORITHM FOR IMPACT LOCALIZATION

A. El-Bakari[1], A. Khamlichi[2], R. Dkiouak[1] and E. Jacquelin [3]

[1]Mechanics and Civil Engineering Laboratory, Faculty of Sciences and Techniques
Ancienne Route de l'Aéroport, Km 10, Ziaten. BP : 416. Tangier – Morocco
Email: ab_elbakari@yahoo.fr, rdkiouak@hotmail.com

[2]Telecommunications Systems Laboratory, Faculty of Sciences
Avenue de Sebta, Mhannech II 93002 - Tetouan – Morocco
Email: khamlichi7@yahoo.es

[3]Mechanics and Materials Laboratory, Department of engineering Civil and Urbanism, INSA Lyon
Avenue Albert Einstein Avenue, Villeurbanne 69662, French
Email: eric.jacquelin@univ-lyon.fr

ABSTRACT

This paper analyzes some parameters that govern convergence of an adapted version of Particle Swarm Optimization (PSO) algorithm which is used for identifying location of an impact occurring on an elastic beam structure. The problem takes the form of a constrained non linear mathematical program for which the fitness function is obtained through Maxwell-Betti theorem. Sensors are assumed to be implemented in judiciously chosen locations and emphasis is done on the geometrical constraints that are introduce to limit the possible domain of impact location as well as on the stability coefficients that are specified in PSO algorithm. It was found that both the chosen constraints and stability coefficients control to large extent performance of this algorithm.

1 INTRODUCTION

Identifying the characteristics of the force generated by impact can be used to better assess in real time the health of a structure that was impacted by a projectile. This enables to reduce favourably the required experimental effort and thus the derived cost of diagnosis. In case of simple linear elastic structures with homogeneous geometric and material properties such as beams or plates, identification of impact characteristics can be implemented through using a structural model [1,2].

When the impact location is known, the impulse response functions between the impact zone and the sensors placed at known positions, allows by using a regularized deconvolution to reconstruct the force signal. When the impact location is unknown, the inverse formulation uses a minimization technique between the measured and calculated responses to iteratively reconstruct the impact characteristics: point location and force time evolution.

Doyle et al. [3,4] described a method to determine the location of an impact force. Yen and Wu et al. [5,6] have analyzed two-dimensional plate-like structures. They have identified force locations with multiple strain responses on isotropic plates from a mutuality relationship based on Green's functions and measured strains.

Here, a variant of Yen and Wu approach is implemented. Localization is expressed as a non linear mathematical problem with some geometrical constraints that fixes the domain where impact is expected to happen. Solution of this mathematical program is searched by means of a modified PSO algorithm. The purpose is to analyse the effect on convergence that are resulting from the considered constraints as well as the effect due to some choice of the stability coefficients in the PSO algorithm. The study is performed by fixing the population size at 200 and by assuming on the other hand that the sensors implementation configuration is given.

2 DIRECT PROBLEM

An elastic beam is considered. The beam having the length L is assumed to be pinned - pinned. It is assumed to be impacted by a non punctual object such that a uniform pressure develops over an interval having the form $[s_0 - u/2; s_0 + u/2]$ where s_0 is the centre of the impact domain and u is the extent of the impact zone. The temporal approach to inverse problem is considered. It is based on the analytical expression of the transfer function between the impact zone and the sensors placed at known points. Solving the equation of motion of the beam yields a linear system of the form.

$$Y_k = G_k P \quad k = 1, 2, \dots, N. \tag{1}$$

$$\begin{aligned} Y &= \left[y(1) \quad y(2) \quad \cdots \quad y(N) \right]^t. \\ P &= \left[p(1) \quad p(2) \quad \cdots \quad p(N) \right]^t. \end{aligned} \tag{2}$$

$$G = \begin{bmatrix} g(1) & 0 & \cdots & 0 \\ g(2) & g(1) & \ddots & \vdots \\ \vdots & \vdots & \ddots & 0 \\ g(N) & g(N-1) & \cdots & g(1) \end{bmatrix}. \tag{3}$$

where G is a Toeplitz like matrix between the pressure P and the measured signal Y, and N the size of the sample determined by the choice of the increment ΔT of time discretisation and the calculation time T_c .

3 INVERSE LOCALIZATION PROBLEM

If $k = i$ and $k = j$ are substituted in equation (1), the following equations are obtained:

$$Y_i = G_i(s_0, u_0)P \qquad Y_j = G_j(s_0, u_0)P. \tag{4}$$

The commutative property and the writes the Maxwell-Betti theorem yield

$$G_i(s_0, u_0)Y_j = G_j(s_0, u_0)Y_i \tag{5}$$

This equation does not involve the force history vector P, enabling thus to decouple localization and pressure signal reconstruction. Knowing the measured responses $\tilde{Y}_i$ and $\tilde{Y}_j$, the tow parameters that define the impact location: s_0 and u_0, can be found by minimizing the following fitness function

$$(s_0, u_0) = \underset{(s,u)}{Arg\,min}\left\{\phi(s,u) = \sum_{i=1}^{N_s}\sum_{\substack{j=1 \\ j\neq i}}^{N_s} \alpha_{ij}\left\|G_j(s,u)\tilde{Y}_i - G_i(s,u)\tilde{Y}_j\right\|^2\right\} \tag{6}$$

PSO algorithm can be used to perform this minimization. The stability coefficients denoted c_0, c_1 and c_2 proper to this algorithm should then be specified [7]. The effect of these coefficients on convergence depends on the problem under consideration. To accelerate convergence, their values should be determined by a parametric study.

4 RESULTS AND DISCUSSION

Let's consider a beam having length $L = 0.5\,m$ and the following sets of domains containing respectively s_0 and u_0: constraints 1: $[0, L]$, $[0, L]$; constraints 2: $[0, L/2]$, $[L/10, L - L/10]$, and constraints 3: $[-\infty, +\infty]$, $[-\infty, +\infty]$. In parallel, let's consider the following two sets of stability coefficients: case 1: $c_1 = 2.5$; $c_2 = 0.5$; $c_0 = 0.4$, and case 2: $c_1 = 2.5$; $c_2 = 1$; $c_0 = 0.8$.

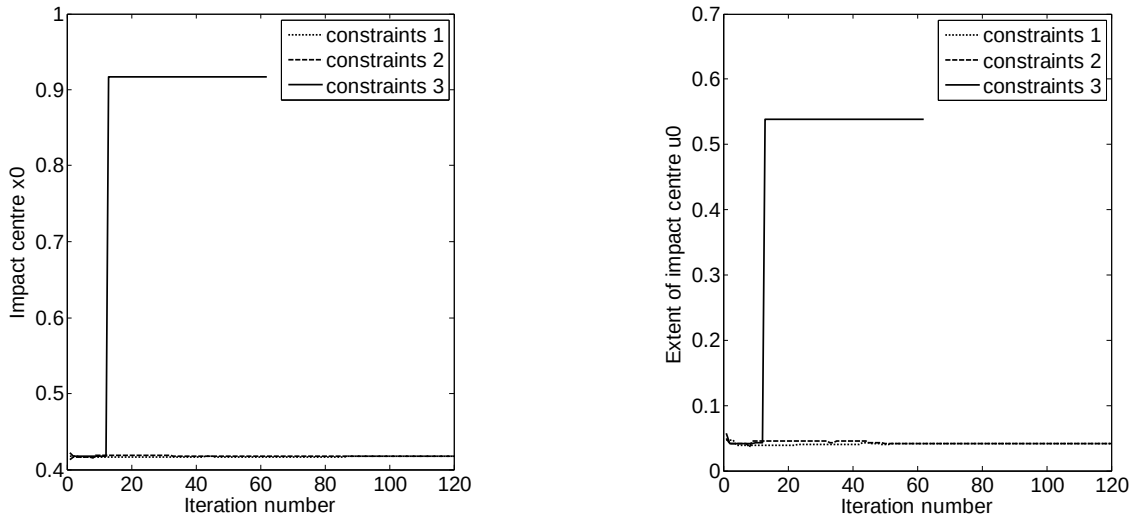

Figure 1. Variation of impact characteristics as function of constraints; case 1

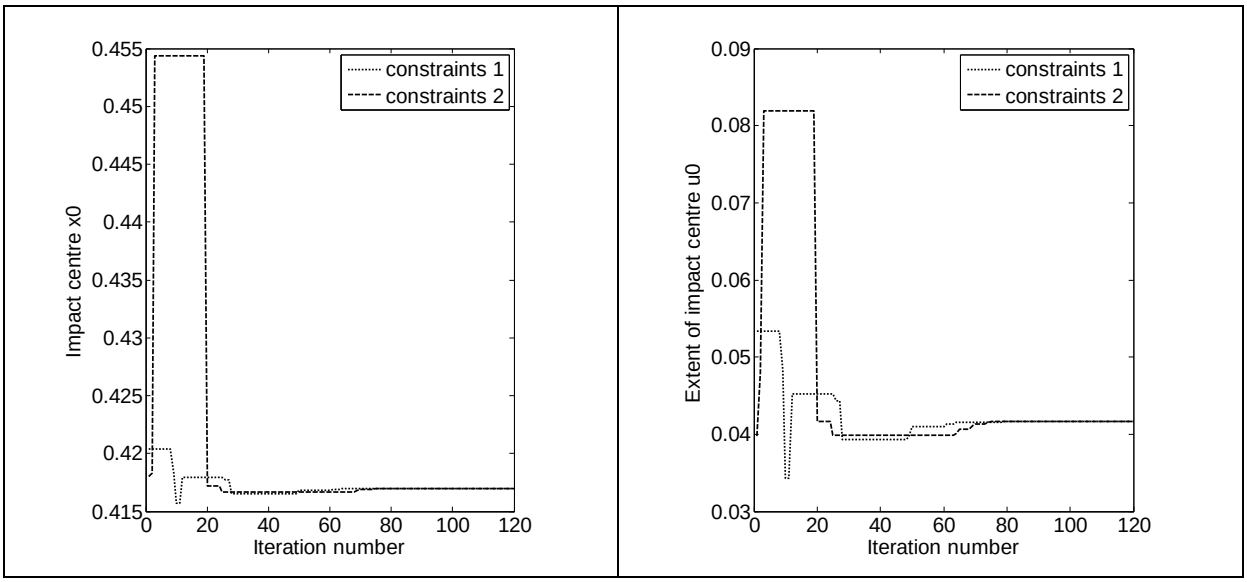

Figure 2. Variation of impact characteristics as function of constraints type; case 2.

From figure1, one can see that if no constraints are imposed on the impact characteristics convergence is not reached. Figures 1 and 2 show that convergence is obtained for both constraints 1 and 2. Convergence is however better for constraints 2. The two sets of stability coefficients yield almost the same result but convergence is quicker with case 1.

REFERENCES

[1] M. Tracy, and F.K. Chang. Identifying Impacts in Composite Plates with Piezoelectric Strain Sensors. Part 1: Theory. *Journal of Intelligent Material Systems and Structures*, 9(11): 920-928, 1998.

[2] M. Tracy, and F.K. Chang. Identifying Impacts in Composite Plates with Piezoelectric Strain Sensors. Park 2: Experiments. *Journal of Intelligent Material Systems and Structures*, 9(11): 929-937, 1998.

[3] J.F. Doyle. An experimental method for determining the location and time of initiation of an unknown dispersing pulse. *Exp. Mech*. vol. 27: 229–33, 1987.

[4] M.T. Martin, and J.F. Doyle. Impact force location in frame structures, International *journal of impact engineering*, vol.18, 79-97, 1996.

[5] C.S. Yen, and E. Wu. On the Inverse Problem of Rectangular Plates Subjected to Elastic Impact, Part I: Method Development and Numerical Verification. *Journal of Applied Mechanics*, vol. 62: 692-698, 1995.

[6] C.S. Yen, and E. Wu. On the Inverse Problem of Rectangular Plates Subjected to Elastic Impact, Part II: Experimental Verification and further Applications. *Journal of Applied Mechanics*, vol. 62: 699-705, 1995.

[7] A. El-Bakari, R. Dkiouak, A. Khamlichi, E. Jacquelin, A. Limam. Influence of mesh size and truncation order on reconstruction of impact force on composite elastic beams. International Review of Applied Sciences and Engineering, 3(2): 105-111, 2012.

Non-linear Free Vibration Analysis of Circular Functionally Graded Plates using a Homogenization Procedure

A. EL KAAK Rachid[1], B. EL BIKRI Khalid[1*] and C. BENAMAR Rhali[2]

[1] Université Mohammed V-Souissi. ENSET- Rabat, LaMIPI
B.P. 6207, Rabat Instituts. Rabat, Morocco
Email: rachidkhinto@gmail.com , k.elbikri@um5s.net.ma

[2] Université Mohammed V- Agdal.
Ecole Mohammadia d'Ingénieurs, LERSIM
Av. Ibn Sina, Agdal Rabat, Morocco
Email: rbenamar@emi.ac.ma

ABSTRACT

In the present study, the problem of geometrically nonlinear free vibrations of functionally graded circular plates (FGCP) is studied. An homogenization procedure (HP) has been developed to reduce the problem under consideration to that of isotropic homogeneous circular plate. The material properties of the functionally graded composites examined are assumed to be graded in the thickness direction of the plate and estimated through the rule of mixture. The theoretical model is based on the classical Plate theory and the Von Kármán geometrical nonlinearity assumptions. Hamilton's principle is applied and a multimode approach is derived to calculate the fundamental nonlinear frequency parameters, which are found to be in a good agreement with the published results dealing with the problem of functionally graded plates.

1 INTRODUCTION

In recent years, functionally graded materials (FGMs) have gained much popularity as materials to be used in structural components such as nuclear reactors and high-speed spacecraft industries. FGMs are composite materials with mechanical properties varying smoothly or continuously from one surface to the other. Numerous studies have been reported in open literature dealing with the geometrically non linear vibration of functionally graded and isotropic circular plates [1, 2].

In the present work, large axisymmetric free vibration amplitudes of clamped immovable thin functionally graded circular plates are investigated by proposing an homogenization procedure, which reduces the above problem to that of homogeneous isotropic circular plate, previously studied by Haterbouch and Benamar [1]. By assuming harmonic motion and expanding the transverse displacement in the form of finite series of basic functions, obtained in terms of Bessel's functions, the discretized expressions for the total strain energy and kinetic energy have been derived. In these expressions, in addition to the classical mass and rigidity tensors, a fourth order tensors appear due to the non-linearity. The application of Lagrange's equations and Harmonic balance method reduce the large amplitude free vibration problem to a set of non-linear algebraic equations, which have been solved numerically.

2 FONCTIONALLY GRADED MATERIALS

In this study, the properties of the plate are assumed to vary through the thickness of the plate with a power-law distribution of the volume fractions of the two materials in between the two surfaces. The top surface (z = h/2) of the plate is assumed metal-rich whereas the bottom surface (z = -h/2) is ceramic-rich. Poisson's ratio ν is assumed to be constant, equal to 0.28 throughout the analysis.

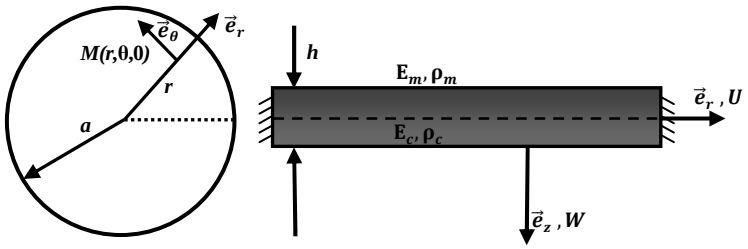

Figure 1. Geometry of a FG clamped circular plate.

The material properties P are given by [3]:

$$P(z) = (P_m - P_c)\left(\frac{Z}{h} + \frac{1}{2}\right)^k + P_c. \quad (1)$$

In which the subscripts m and c represent the metallic and ceramic constituents, respectively.

3 GENERAL MATHEMATICAL MODEL

Consider a fully clamped thin circular plate as shown in figure 1. Considering axisymmetric vibrations of the circular plate, the expression for the total strain energy V, and the kinetic energy T are given by:

$$V = \pi \int_0^a D_{11} \left[\left(\frac{\partial^2 W}{\partial r^2} \right)^2 + \frac{1}{r^2} \left(\frac{\partial W}{\partial r} \right)^2 + 2 \frac{\vartheta}{r} \frac{\partial W}{\partial r} \frac{\partial^2 W}{\partial r^2} \right] + \frac{A_{11}}{4} \left(\frac{\partial W}{\partial r} \right)^4 r \, dr. \quad (2)$$

A, *B* and *D* are the stiffness matrices, the expression of which is given in [4].

$$T = \pi \int_{-h/2}^{h/2} \rho(z) \, dz \int_0^a \left(\frac{\partial W}{\partial t} \right)^2 r dr. \quad (3)$$

By considering the following change of variable z'=z-d, with $d=B_{11}/A_{11}$, then B_{11} vanishes and D_{11} becomes $(D_{11} - B_{11}^2)/A_{11}$, whereas A_{11} does not change in this new coordinate system. Consequently, the total strain energy takes the following new expression, involving the effective bending stiffness: $D_{eff} = (D_{11} - B_{11}^2/A_{11})$ and the effective axial stiffness $A_{eff} = A_{11}/4$.

$$V = \pi D_{eff} \int_0^a \left[\left(\frac{\partial^2 W}{\partial r^2} \right)^2 + \frac{1}{r^2} \left(\frac{\partial W}{\partial r} \right)^2 + 2 \frac{\vartheta}{r} \frac{\partial W}{\partial r} \frac{\partial^2 W}{\partial r^2} \right] r \, dr + \pi A_{eff} \int_0^a \left(\frac{\partial W}{\partial r} \right)^4 r dr \, . \quad (4)$$

Applying Lagrange's equations and Harmonic Balance Method and expanding the displacement W in the form of a finite series, the following set of nonlinear algebraic equations is obtained:

$$2 a_i \, k_{ir}^* + 3 a_i a_j a_k \, b_{ijkr}^* - 2 \, \omega^{*2} a_i \, m_{ir}^* = 0. \quad (5)$$

The m^*_{ij}, k^*_{ij} and b^*_{ijkl} terms are non-dimensional tensors given by the following relationships:

$$k_{ij}^* = \int_0^1 \left(\frac{\partial^2 w_i^*}{\partial r^{*2}} \frac{\partial^2 w_j^*}{\partial r^{*2}} + \frac{1}{r^{*2}} \frac{\partial w_i^*}{\partial r^*} \frac{\partial w_j^*}{\partial r^*} + + 2 \frac{\vartheta}{r^*} \frac{\partial w_i^*}{\partial r^*} \frac{\partial^2 w_j^*}{\partial r^{*2}} \right) r^* dr^* \, . \quad (6)$$

$$b_{ijkl}^* = \alpha \int_0^1 \left(\frac{\partial w_i^*}{\partial r^*} \frac{\partial w_j^*}{\partial r^*} \frac{\partial w_k^*}{\partial r^*} \frac{\partial w_l^*}{\partial r^*} \right) r^* \mathrm{d}r^*. \quad (7)$$

$$m_{ij}^* = \int_0^1 w_i^* w_j^* r^* dr^* \, . \quad (8)$$

With: $\alpha = \dfrac{h^2 A_{eff}}{D_{eff}}$, $w_i^* = \dfrac{w_i}{h}$ and $r^* = \dfrac{r}{a}$

4 NUMERICAL RESULTS AND DISCUSSIONS

In the problem considered here, the top surface of the plate is ceramic rich (E_c=384.43e9GPa, υ_c=0.24, ρ_c=2370Kg/m^3), whereas the bottom surface of the plate is metal rich (E_m=201.04e9GPa, υ_m=0.3177ρ_m=8166 Kg/m^3).

W^*_{Max}	Present Work 2013	[2] 2008	[1] 2003
0.2	1.0108	1.0075	1.0072
0.4	1.0421	1.0296	1.0284
0.8	1.1560	1.1135	1.1073
1.0	1.2318	1.1724	1.1615

Table 1. Frequency ratio $\omega^*_{nl} / \omega^*_{l}$ of a clamped circular isotropic plate.

In table 1, the first nonlinear frequency ratios ω^*_{nl}/ω^*_l, calculated in the present work at various vibration amplitudes, is compared with the results obtained in [2]. It is noted that the solution given in the present work overestimates the frequencies of the clamped circular isotropic plate, especially for high values of dimensionless amplitude. This discrepancy is mainly due to the fact that the axial displacements have been neglected in the expression of the axial strain energy.

W^*_{Max}	Present Work 2013	From graph [2] 2008
0.2	1.0110	1.0068
0.4	1.0430	1.0275
0.8	1.1593	1.1034
1.0	1.2363	1.1586

Table 2. Frequency ratio ω^*_{nl}/ω^*_l of a clamped circular FG plate.

The same comparison has been conducted in the case of circular functionally graded plate. As expected, the frequency ratios obtained with the present model are higher than those obtained in [2].especially for large vibration amplitudes for which the contribution of axial displacement becomes significant.

5 CONCLUSION

The present study deals with the problem of geometrically nonlinear free vibrations of FG circular plate with immovable ends. An homogenization procedure has been proposed which reduces the problem studied to that of isotropic homogenous plate. Nonlinear frequency ratios ω^*_{nl}/ω^*_l have been compared to the results published in the case of isotropic circular plate [1] and in the case of FG circular plate in [2]. A good agreement is obtained, with however increasing discrepancy when the amplitude grows, which is mainly due to the fact that the axial displacements have been neglected in the expression of the axial strain energy.
The main feature of the present contribution is the fact that the existing analytical solutions, numerical techniques and software developed over the years for the nonlinear analysis of isotropic circular plates can be easily used for FG circular plates.

REFERENCES

[1] M. Haterbouch, R. Benamar. The effects of large vibration amplitudes on the axisymmetric mode shapes and natural frequencies of clamped thin isotropic circular plates, part I: iterative and explicit analytical solution for non-linear transverse vibrations. *Journal of sound and vibration*, 265(2003)123-154.

[2] A. Allahverdizadeh, M.H. Naei, and M. Nikkhah Bahrami. Nonlinear free and forced vibration analysis of thin circular functionally graded plates. *Journal of Sound and Vibration*, 310 (2008) 966-984.

[3] H. Shen Shen. *Functionally graded materials: nonlinear analysis of plates and shells*. Taylor & Francis Group, LLC. 2009.

Dynamic of a squeeze film between smooth lip seal and roughshaft

M. El Gadari[1], M. Belhaq[2] andM. Hajjam[3]

[1]ENSAM, University of Moulay Ismail, Meknès, MOROCCO
Email: m.elgadari@ensam-umi.ac.ma,

[2]Laboratory of Mechanics, UniversityHassan II-Casablanca, Casablanca, MOROCCO
Email: mbelhaq@yahoo.fr

[3]D3 Department, Pprime Institute, University of Poitiers, Poitiers, FRANCE
Email: mohamed.hajjam@univ-poitiers.fr

ABSTRACT

This paper studies the dynamic behavior of a squeeze film between a rotary lip seal surface and a shaft surface taking into account the nonlinearities of the material behavior and the squeeze film. We present an analytical approach considering a mass-spring-damper systemmodeling the motion of the interacting elements of the system: thelip seal, the squeezed film and the roughness of shaft. Using the harmonic balance method, analytical prediction of the periodic response of the squeezed film is approximated, the resonance curve is obtained and the effect of the roughnessof the shaft on the jumps in the amplitudeof the film response is discussed. The influence of the nonlinearity of the viscoelastic behavior ofsqueeze film on the performance of the leap seal is manifested in shifting the resonance frequency and jumps in the film thickness response.This canhave direct applications in reducingleakage that may occurbetween a smooth lip seal and a rough shaft.

1 INTRODUCTION

The lip seal is the most used device in the family of dynamic seals that can reduce both leakage and wear caused by the high speed rotation of the shaft. To improve thelife of the seal, designers usually use the generation of hydrodynamic pressure field to separate and lubricate surfaces (lip seal / shaft). In order to explain the presence of two paradoxical phenomena (wear and leakage) in such problems, several studies have been conducted on the film behaviourby taking into consideration the factor influencing the seals work.Recently, a numerical model for the oscillatory behavior of 'squezze film' between a rubber surface and a rigid viscoelastic surface was proposed in [1] and it was shown that increasing the roughness of the surface profile leads to a significant increase of the hydrodynamic force accompanied by a slight decrease in leakage. In addition, it was shown that the spatial distribution of the roughness of the rubber has no significant effect on the leakage and the hydrodynamic force. The work performed in [1] was conducted under specific conditions where the film is squeezed between two rough surfaces,namely an elastomer surface and an oscillating rigid surface.

An important issue is the study of the roughness effect on the dynamics of the film thickness between a lip seal and the shaft. Indeed, to the best of our knowledge no model is available in the literature that deals with such a problem. Motivated by the lack of analytical study of the dynamic of the film thickness, the present work proposes an analytical approach based on a simplified mechanical model consisting in a mass-spring-damper that takes into account both the hydrodynamic behavior of the film and the dissipative character of the mechanical behavior of the lip seal. For modeling the viscoelastic behavior of the joint we adopt the Maxwell model. By using the "short bearing" theory, we can reformulate the condition of 'squeeze film' between the shaft and the seal and therefore determine the stiffness coefficients equivalent to squeezed fluid [2],[3].

2 ANALYTICAL MODEL AND EQUATION OF MOTION

The equations that model the motion of the film thickness between the lip seal and the shaft can be approximated byanonlinear mass-spring-damper system as shown in Fig. 1and can be written in the form

$$\begin{cases} m_2(\ddot{z}_1 + \ddot{z}_2) + K_r(z_1 + z_2) + \eta\dot{z}_2 = K_2(H_0 + r - z_1 - z_2) + \eta_2(\dot{r} - \dot{z}_1 - \dot{z}_2) \\ K_\infty z_1 = \eta\dot{z}_2 \end{cases} \quad (1)$$

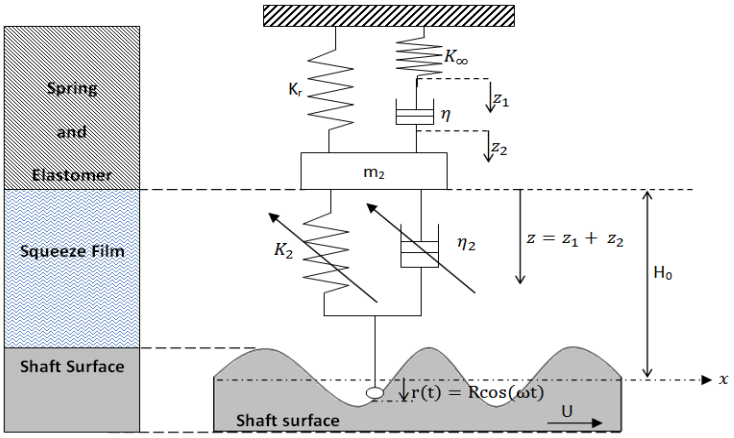

Figure 1. A schematic model of the system

where z_1, z_2 are, respectively, the elastic and the damping displacements of the elastomer, H_0 is the average thickness film, squeezed between lip andshaft, r(t) the roughness shaft

fluctuation,m_2 the weight of lip seal, K_∞, K_r, $K_2$are, respectively, the equivalent stiffnessof the elastomer, the spring and the squeeze film. The parameters η, $\eta_2$are, respectively, damping factors of elastomer and damping factor equivalent of squeeze film, U the shaft velocity,ω the pulsation of the film due to shaft roughness such that$\omega = \frac{2\pi}{\lambda}U$ where λ is theshaft roughness wavelength.

Introducing the nonlinear rheological model of the fluid as in [2], [3] such that the coefficients of stiffness and viscosity of the fluid aregiven by

$$K_2 = K.(H_0 + r - z_1 - z_2)^{-3}, \qquad \eta_2 = \eta(H_0 + r - z_1 - z_2)^{-3}$$

Considering the variable change$y_1 = r - z_1 - z_2$, expanding $K_2$and $\eta_2$in Taylor series up to order 3, and assuming

$$K_{10} = \frac{K}{H_0^3}, K_{11} = 3\frac{K}{H_0^4}, K_{12} = 6\frac{K}{H_0^5}, K_{13} = 10\frac{K}{H_0^6}, \eta_{10} = \frac{\eta}{H_0^3}, \quad \eta_{11} = 3\frac{\eta}{H_0^4}, \eta_{12} = 6\frac{\eta}{H_0^5}$$
$$\eta_{13} = 10\frac{\eta}{H_0^6}$$

the equations of motion canbe rewrittenin the form

$$\begin{aligned} &\ddot{y}_1 + 2\xi_{10}\omega_{10}\dot{y}_1 - 2\xi_{11}\omega_{11}y_1\dot{y}_1 + 2\xi_{12}\omega_{12}y_1^2\dot{y}_1 - 2\xi_{13}\omega_{13}y_1^3\dot{y}_1 + \omega_1^2.y_1 \\ &-(\omega_{11}^2 - \omega_{12}^2H_0)y_1^2 + (\omega_{12}^2 - \omega_{13}^2H_0)y_1^3 + \omega_{10}^2H_0 + 2\xi_\infty\omega_\infty\dot{z}_2 = \ddot{r} + \omega_r^2r + \omega_r^2H_0 \\ &\dot{z}_2 + \frac{1}{2}\frac{\omega_\infty}{\xi_\infty}z_2 + \frac{1}{2}\frac{\omega_\infty}{\xi_\infty}y_1 = \frac{1}{2}\frac{\omega_\infty}{\xi_\infty}r \end{aligned} \tag{2}$$

where

$$\omega_{10}^2 = \frac{K_{10}}{m_2}, \xi_{10} = \frac{\eta_{10}}{2\sqrt{K_{10}m_2}}, \omega_{11}^2 = \frac{K_{11}}{m_2}, \xi_{11} = \frac{\eta_{11}}{2\sqrt{K_{11}m_2}}, \omega_{12}^2 = \frac{K_{12}}{m_2}, r = R_2\cos(\omega t)$$

$$\xi_{12} = \frac{\eta_{12}}{2\sqrt{K_{12}m_2}}, \omega_{13}^2 = \frac{K_{13}}{m_2}, \xi_{13} = \frac{\eta_{13}}{2\sqrt{K_{13}m_2}}, \omega_r^2 = \frac{K_r}{m_2}, \omega_\infty^2 = \frac{K_\infty}{m_2}, \xi_\infty = \frac{\eta}{2\sqrt{K_\infty m_2}}$$

and$\omega_1^2 = \omega_{10}^2 + \omega_r^2 - \omega_{11}^2H_0$. We consider the following parameters (taken from literature):K_r=10^4N/m, K_∞=2.10^4N/m, η=1N.s/m, m_2=0.1Kg,z_c=10^{-5}m, K_{10}=10^6N/m, η_{10}=30N.s/m, K_{11}=3.K_{10}/z_c, K_{12}=6.K_{10}/(z_c^2), K_{13}=10.K_{10}/(z_c^3), η_{11}=3.η_{10}/z_c, η_{12}=6.η_{10}/(z_c^2), η_{13}= 10.η_{10}/(z_c^3) and H_0=10^{-6} m.

Applying the harmonic balance method[4],the first term approximation of the periodic solution of (2) can be assumed as

$$\begin{cases} y_1 = y_{10} + y_{11}\cos(\omega t) + y_{12}\sin(\omega t) \\ z_2 = z_{20} + z_{21}\cos(\omega t) + z_{22}\sin(\omega t) \end{cases} \tag{3}$$

where the coefficients y_{10}, y_{11}, y_{12}, y_{20}, y_{21} and y_{22} in (3) are to be determined and ω is the frequency of the harmonic oscillation of the squeeze film pulsation.

An approximation of such solution can be written in the polar form as

$$Y_1 = y_{10} + Y.\cos(\omega t + \phi) \tag{4}$$

where$Y = \sqrt{y_{11}^2 + y_{12}^2}$and $\phi = \text{Artang}\left(\frac{y_{12}}{y_{11}}\right)$.

Figure 2 shows the effect of roughness on the amplitude of the squeeze film oscillation. This figure indicates that the amplitude of the roughness of the shaft has a significant influence on the jumps of the oscillating film amplitude. As the roughness increases, the jump labelled H_e (occurring when sweeping speed toward lower values) shifts toward higher frequencies and the amplitude following jump H_s (occurring when sweeping toward higher speed) increases.

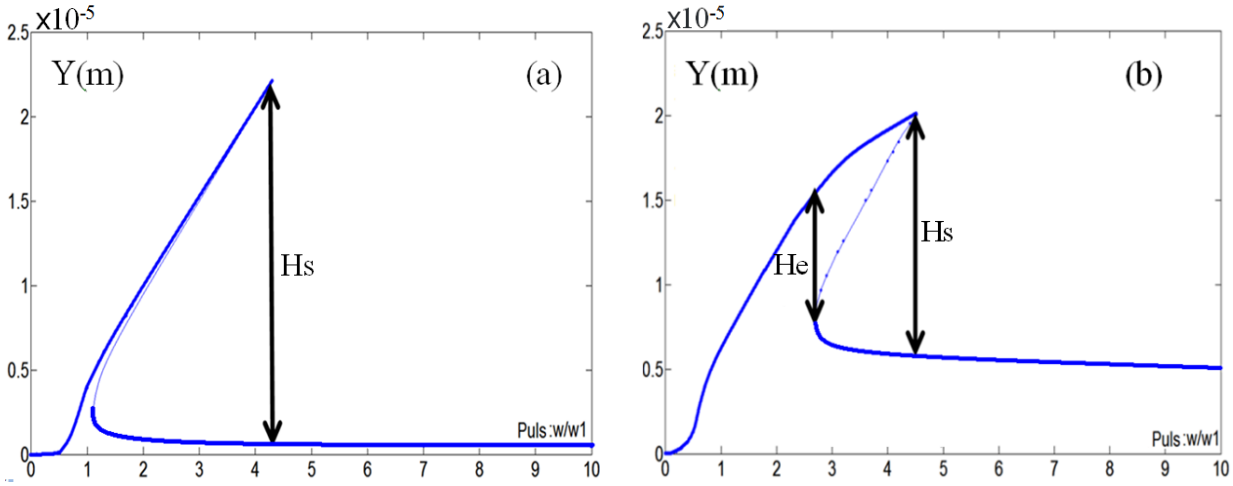

Figure.2.Squeeze film response under shaft roughnessfluctuation
(a): R_2=0.5µm , (b): R_2=5µm

Based on the short bearing theory, an approximation for the outflow of the seal is proportional to the film thickness [5]. Thus, the shaft roughness affects leakage in low and high shaft frequency. Indeed, rough surface leaks more than the smoothest one in high shaft frequency, but contributes for less leakage fluctuations (thickness film jump) in low frequency.

3 CONCLUSION

This workproposes a mass-spring-damper modelto study the dynamic of a squeeze film between a rotary lip seal surface and a shaft surface taking into account the nonlinearity of the rheological film. We have examined the influence of shaft roughness on the jumps of the perturbed squeezed film oscillation.We have shown that the frequency response of the squeeze film is bent toward higher frequencies meaning that the equivalent stiffness of the squeezed film is hardening. Moreover, increasing the shaft roughness shifts the lower jump toward higher frequencies and increases the amplitude of the response beyond the higher jump. This result indicates that theshaft roughness affects directly the lip performance, especially leakage. Therefore, a judicious choice between smooth/rough surfaces of the shaft must be done to optimize the life of rotary lip shaft.

REFERENCES

[1] M. Mustafa, N.J.Chhanda, M.M.Razzaque.A numerical model of an oscillating squeeze film between a rubber surface and a rigid surface. Tribology International 43(2010)202–209.

[2] A. Younan, P.Allaire. A review of tilting pad bearing theory timothy dimond. International Journal of Rotating Machinery 23 (2011)1-23.

[3] E.J.Gunter. Design of nonlinear squeeze film dampers for aircraft engines.Journal of Lubrication Technology 99 (1977)57-64.

[4] L.Liu, J.P.Thomas, E.H.Dowell, P.Attar , K.C. Hall. A comparison of classical and high dimensional harmonic balance approaches for a Duffing oscillator. Journal of Computational Physics 215 (2006) 298–320.

[5] H.J.Van Leeuwen, M.J.L.Stakenborg. Visco-elastohydrodynamiclubrication in radial lip seals: Part 2- Fluid film formation.Transactions of the ASME 112 (1990) 584-592.

DETECTING DMAGE IN MINDLIN PLATES BY USING THE MODAL STRAIN ENERGY METHOD

F. El Khannoussi[1], A. Khamlichi[1], A. Hajraoui[1*] and A. Limam[2]

[1]Laboratory Communication systems
Abdelmalek Essaâdi University, Tetouan, MOROCCO
Fadoua_845@hotmail.com, khamlichi7@yahoo.es, ab_hajraoui@hotmail.com

[2]Laboratory LGCIE
University of Lyon 1, Villeurbanne, FRANCE
ali.limam@insa-lyon.fr

ABSTRACT

In this work, a vibration based method is considered for detection of damage in Mindlin plates like structures. A finite element model was built and modal strain energy method was applied. A classical damage index defined through comparing the damaged and undamaged states was used in order to identify the damage location. Identification of damage severity was discussed as function of the actual damping present in the structure. It was shown that damping impedes identifying damage amplitude as the maximum value of damage index was found to be very sensitive to the damping level present in the plate.

1 INTRODUCTION

Detecting damage in real structures as earlier as possible before it reaches a critical phase of growth is an essential issue. Spectacular failures occurred in the past have focused on the need for monitoring structural health to ensure safety of structures [1].
Structural damage detection can be performed by various non-destructive testing (NDT) techniques including optical, microscopy, acoustic emission, ultrasonic, radiography, eddy-current, thermal or electromagnetic wave based methods. To use them, damage location should be already known and the damaged part of the structure accessible, so these expensive and time-consuming techniques are ineffective for complex structures with parts not easily reachable.
Vibration based methods seem to be more adequate as they are low cost and can monitor damage detection where the conventional techniques are inefficient. These approaches are initiating from the changes that occur on the commonly measured modal parameters consisting of frequencies, mode shapes and damping. Detectable changes in these modal properties under significant changes of the physical properties of the structure. Such changes can affect stiffness, due to the apparition of cracks or mass due to the effect of erosion and oxidation. Detecting damage holds then implicitly a comparison between the initial undamaged and the damaged states. Sensing these changes is not always possible within the framework of modal analysis, as there are some limitations that are inherent to this method. These consist mainly in restrictions in system identification process such as the difficulty to identify all the modes from measured time-history responses and coupling occurring between modes that are closely spaced in frequency [2].
When the modal characteristics can be measured, their changes can be used as indicators of damage. In real structures, modal changes suffer however from poor sensitivity to small damage. Vibration based methods are then fairly to be used only for damage exceeding a critical size.
Salawu [3] has performed a review on the detection of structural damages by using frequency-based methods. He has stated that 5% change of natural frequency may be necessary for damage detection. In practice, 5% of frequency change may not imply necessarily the existence of damage as system parameters can vary due to environmental conditions. It has been also found that some delamination defects in composites have no observable effects on the first global system frequencies [4]. As these defects yield more perceptible irregularity of mode shapes [5], this has motivated the development of Modal Strain Energy (MSE) based method.
MSE method is based fundamentally on comparison of modal shapes associated to damaged and undamaged states of the structure. Modal strain energy density involves the second spatial derivatives of the modal displacement, so it is much more sensitive to small deviation in the structural response than the displacement itself. MSE based method was recognized to enable better detection of the damage size and damage severity [6]. To asses the change of the MSE a damage index is defined in order to locate structural damage and quantify its level [7,8].
In this work, focus will be done on homogenous elastic plates suffering a local loss of rigidity. The MSE method will be applied to diagnose the damaged plate in order to locate the damage zone. A parametric study will be conducted on key intervening factors such as the amount of damage and the damping of the system.

2 MODAL STRAIN ENERGY AND DAMAGE INDEX

Using $N_x \times N_y$ interior points to mesh the plate, where x, y are the coordinates, the MSE density for the element centred on point number i when the impulse impact is applied on point j, and for a given mode number k, is given by

$$U_{ijk} = \frac{D_i}{2} \int_{\Omega i} \left(\frac{\partial^2 \Phi_{j,k}}{\partial x^2} \right)^2 + \left(\frac{\partial^2 \Phi_{j,k}}{\partial y^2} \right) + 2\nu \left(\frac{\partial^2 \Phi_{j,k}}{\partial x^2} \right) \left(\frac{\partial^2 \Phi_{j,k}}{\partial y^2} \right) + 2(1-\nu) \left(\frac{\partial^2 \Phi_{j,k}}{\partial x \partial y} \right)^2 dx\, dy \quad (1)$$

where D_i is the bending plate rigidity, Ωi the domain of the element centred on point i, ν the Poisson coefficient and $\Phi_{j,k}$ the j^{th} component associated to the k^{th} mode .

The MSE ratio for the undamaged and damaged plate (*) are defined respectively as

$$F_{ijk} = \frac{U_{ijk}}{U_k} \text{ and } F^*_{ijk} = \frac{U^*_{ijk}}{U^*_k} \quad (2)$$

By considering modal contributions, for a total of m modes, the global MSE ratio is defined as

$$\beta_{ij} = \sum_{k=1}^{m} F^*_{ijk} \Big/ \sum_{k=1}^{m} F_{ijk} \quad (3)$$

A normalized damage index can then be defined for each pair (i, j) by taking

$$z_{ij} = \frac{\beta_{ij} - \bar{\beta}}{\sigma_\beta} \quad (4)$$

where $\bar{\beta}$ and σ_β are respectively the mean and standard deviation for the statistics β_{ij} .

To compute effectively the MSE density as defined by equation (1), the DQM [9] is used in order to evaluate the second order derivatives.

3 PARAMETRIC STUDY

Let us consider a homogeneous and elastic plate made from steel material for which Young's modulus is $E = 2\times10^{11}$ Pa and Poisson coefficient is $\nu = 0.3$. The material density is $\rho = 7800\,kg.m^{-3}$. The plate which is assumed to be simply supported on all its boundaries has a square geometry $L_x = L_y = 1m$ with a uniform thickness $h = 10^{-2}m$. As shown in figure 1, a fixed sensor is placed in some location of the plate surface. The excitation is assumed to result from the impact of a hammer which location is varied on the considered mesh. The plate has a defect of rigidity located in a given position. A finite element was built to compute the first 12 modes using a uniform mesh of 225 Mindlin Q4 elements, with shear factor $\kappa = 5/6$.

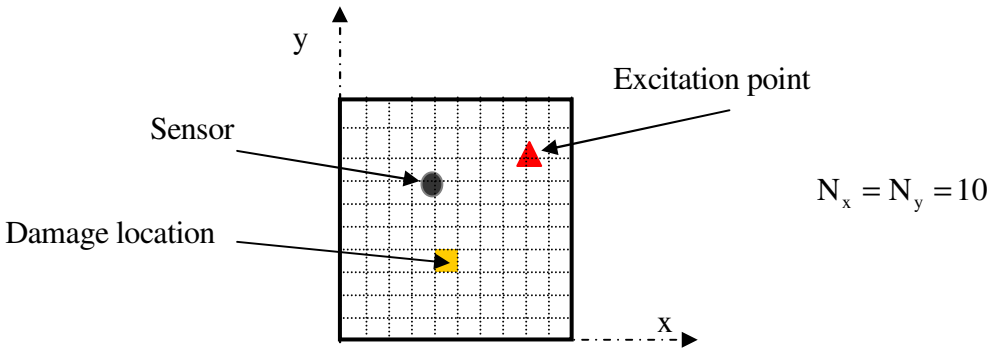

Figure 1. Plate with a localized damage, the boundaries are simply supported

The normalized damage index as defined by equation (4) is plotted for different combinations of Figure 2 shows the obtained damage index as function of the structural damping and considered amount of the localized defect. The maximum value of damage index is indicated in each case. One can observe that the pattern of damage index is very sensitive to the amount of damping. Since this can not be easily identified in real structures, the severity of damage can not be directly obtained from this index.

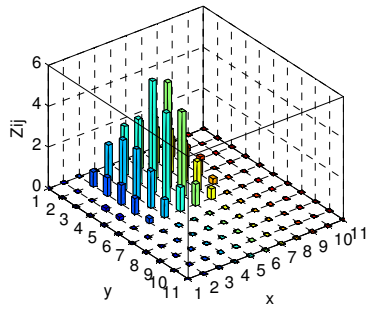

(a) $\max(z_{ij}) = 5.474$

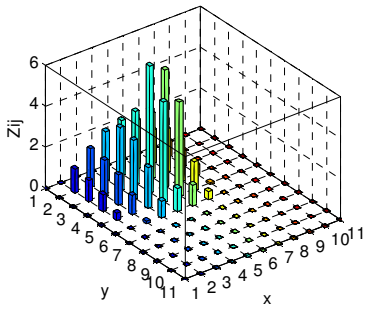

(b) $\max(z_{ij}) = 6.241$

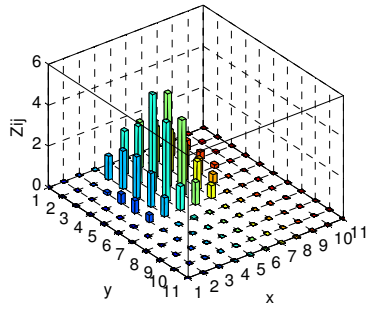

(c) $\max(z_{ij}) = 4.770$

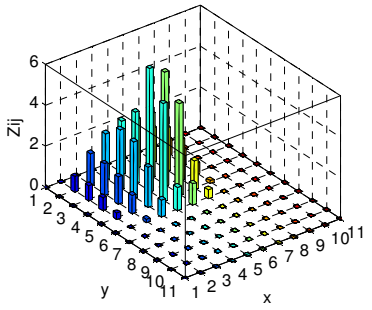

(d) $\max(z_{ij}) = 6.055$

Figure 2: Damage index z_{ij} as obtained for different combination of damage severity d and structural damping ξ; (a) $d = 2\%$; $\xi = 0.5\%$; (b) $d = 10\%$; $\xi = 0.5\%$; (c) $d = 2\%$; $\xi = 1\%$; (d) $d = 10\%$; $\xi = 1\%$

4 CONCLUSION

In this work, modal strain energy based damage detection method was considered in the case of Mindlin plates. A damage index ratio was defined to assess damage location by comparing the damaged and undamaged states of the structure. It was found that damping has a crucial effect, so damage severity could not be easily recovered from this index.

REFERENCES

[1] A. Morassi, F. Vestroni, Dynamic methods for damage detection in structures, Springer Verlag, ISBN 978-3-211-78776-2, 2008.
[2] D.J. Ewins, Modal Testing: Theory and Practice, John Wiley and Sons, New York, 1984.
[3] O.S. Salawu, Detection of structural damage through changes in natural frequency: a review, *Engineering Structures*, 19:718-723, 1997.
[4] M.H.H Shen, J.E. Grady, Free vibration of delaminated beams, *AIAA J.* 1992; 30:1361-1370.
[5] A.K. Pandey, M. Biswas, M.M. Samman, Damage detection form changes in curvature mode shapes, *Journal of Sound and Vibration*, 145:321-332, 1991.
[6] J.T. Kim, Y.S. Ryu, H.M. Chp, N. Stubbs, Damage identification in beam-type structures: frequency-based method vs mode-shape-based method, *Engineering Structures*, 25:57-67, 2003.
[7] Z.Y. Shi, S.S. Law, L.M. Zhang, Improved damage quantification from elemental modal strain energy change, *Journal of Engineering Mechanics*, 128(5):521-529, 2002.
[8] P.J. Cornwell, S.W. Dobeling, C.R. Farrar, Application of the strain energy damage detection method to plate-like structures, *Journal of Sound and Vibration*, 224(2):359-374, 1999.
[9] C.W. Bert, M. Malik, Differential quadrature method in computational mechanics: a review, *Applied Mechanics Review*, 49(1): 1-28, 1996.

Effect of porosity on the propagation velocities of ultrasonic waves in the trabecular bone

[(a)] BENNAMANE Abderrazek, [(b)] BOUTKEDJIRT Tarek

[(a)] Equipe Ondes et Acoustiques, Faculté de Physique, USTHB, BP 32, El-Alia, DZ-16111 Alger, Algérie.
benamane@yahoo.fr

[(b)] Equipe Physique des Ultrasons, Faculté de Physique, USTHB, BP 32, El-Alia, DZ-16111 Alger, Algérie.
tarek_boutkedjirt@hotmail.com

This work is a theoretical and experimental study of the influence of porosity on the propagation velocities of longitudinal ultrasonic waves through the trabecular bone. The Biot approach is used to describe the vibro-elastic behavior of the cancellous bone. By using this model, a quantitative analysis of the fast propagation velocity according to the medium porosity is performed (The porosity is directly related to the bone mineral density). Experimentally a characterization of trabecular bone samples extracted from the femoral head of bovines is conducted. The porosity of these samples lies between 50 % and 75 %. For the determination of the velocity associated with each sample, a contact pulsed measurement technique, with a pair of transducers of 500 kHz nominal frequency, has been used. The experimental results show a strong correlation between the bone density and the measured propagation velocity. The fast longitudinal velocity in trabecular bone undergoes a decrease when its porosity increases. These results corroborate the theoretical results obtained by using the Biot model. This study confirms the sensitivity of the ultrasonic propagation velocity to the change of bone porosity. The measurement of these velocities allows determining its elastic parameters. It also proves the merits of the use of the Biot model in the description of ultrasound propagation in cancellous bone. The potential of ultrasound in bone tissue characterization seems to provide interesting results and would lead to predict bone pathology and particularly to permit better diagnosis of bone fragility.

Keywords: ultrasonic propagation, Biot model, bone tissue characterization.

Elastic wave scattering by periodic cavities in backing material for ultrasound transducers*

Guofeng Bai, Fusheng Sui, Jun Yang, Chengguang Zhou
(Key Laboratory of Noise and Vibration Research, Institute of Acoustics, Chinese Academy of Sciences Beijing 100190)

ABSTRACT

The backing material of piezoelectric polymer ultrasound transducer demands careful design consideration. In order to obtain good absorption performance and low acoustic impedance matching, it is a good way to use viscoelastic material containing periodic cavities. The basic multiple scattering(MS) theory on acoustical performance of backing material is presented in this paper. The reflection, transmission and absorption performance of periodic cavity in backing materials are analyzed by MS method. The results indicate that the absorption performance of backing material depends on the cavity scattering and impedance matching.

Email: *bgf@mail.ioa.ac.cn*

*This research was supported by the National key Basic Research Program of China (973 Program) under Grant No. 2013CB632900 and the National Nature Science Foundation of China under Grant No. 11104310.

1. Introduction

The lossy backing is used to absorb the ultrasonic energy of piezocomposite transducers. In order to obtain shorter pulse at the expense of sensitivity, the acoustic impedance of the backing demands to match to the active materials. To achieve longer pulse and greater sensitivity, we may use the backing with a lower acoustic impedance[1]. Viscoelastic materials such as rubber and polystyrene have lower acoustic impedance than active materials. At the same time, the absorption performance of such cavity structure is greatly improved for energy dissipation among periodic cavities.

It is known that the MS method can be used to analyze reflection, transmission and absorption performance. The periodic structure for the spherical[2,3] and axisymmetric cavities[4] were investigated, and the results indicate that the acoustic energy dissipation depends on MS effect. In this paper, we used the MS method to analyze absorption performance of viscoelastic materials containing periodic cavities for the backing of piezocomposite transducers. The computational results indicate that the cavity scattering and impedance matching are very important for the sound absorption of backing material.

2. The multiple scattering method of periodic structures in backing materials

The displacement $\mathbf{u}$ for harmonic elastic wave propagation in a homogeneous medium can be written as a time-independent equation[3]

$$(\lambda+2\mu)\nabla(\nabla\cdot\mathbf{u})-\mu\nabla\times(\nabla\times\mathbf{u})+\rho\omega^2\mathbf{u}=0 \qquad (1)$$

where ρ is density, ω is angular frequency, and λ, μ are Lamé coefficient and shear modulus, respectively. For a viscoelastic medium containing energy losses, Lamé coefficient and shear modulus can be regarded as complex numbers.

The $\boldsymbol{a}_1, \boldsymbol{a}_2$ are lattice primitive vectors of one cavity element along in the x, y directions. The other lattice vectors in these two dimensions are obtained as follows:

$$\boldsymbol{R}_n = n_1\boldsymbol{a}_1 + n_2\boldsymbol{a}_2, \quad n_1, n_2 = 0, \pm1, \pm2, \pm3, \cdots \tag{2}$$

One of the cavity centers can be seen as the origin of the coordinate system. In spherical coordinate system, the solution can be decomposed into one longitudinal and two transverse solutions [2]:

$$\boldsymbol{u}(\boldsymbol{r}) = \sum_{lm\sigma} [a_{lm}^{\sigma} J_{lm\sigma}(\boldsymbol{r}) + b^{\sigma} H_{lm\sigma}(\boldsymbol{r})] \tag{3}$$

For solid medium, $\sigma = L$ denotes longitudinal mode, $\sigma = M, N$ denote SH and SV transverse modes, respectively. a_{lm}^{σ}, b_{lm}^{σ} are the expansion coefficients for the incident and scattered waves, respectively. $J_{lm\sigma}(r), H_{lm\sigma}(r)$ are the combined spherical Bessel function and spherical Hankel function where the subscripts are the function orders[3].

The displacement of scattered waves are given by

$$\sum_{l'm'\sigma'} [\boldsymbol{I}_{ll'}\boldsymbol{I}_{mm'}\boldsymbol{I}_{\sigma\sigma'} - \sum_{l''m''\sigma''} \boldsymbol{T}_{lm;l''m''}^{\sigma\sigma''}\boldsymbol{\Omega}_{l''m'';l'm'}^{\sigma''\sigma'}]\boldsymbol{B}_{l'm'}^{\sigma'} = \sum_{l'm'\sigma'} \boldsymbol{T}_{lm;l'm'}^{\sigma\sigma'}\boldsymbol{A}_{l'm'}^{O\sigma'} \tag{4}$$

where $\boldsymbol{I}$ is the unit matrix, $\boldsymbol{A} = [a_{lm}^{\sigma}]$, $\boldsymbol{B} = [b_{lm}^{\sigma}]$. $\boldsymbol{T}$ matrix of equation can describe the relation between the incident waves and scattered waves, both depend on the geometry of the cavity. $\boldsymbol{\Omega}$ describes the scattering effect between the total scattered waves and the sum of the waves from all the other cavities, which in turn depends on the lattice geometry, frequency and the material properties[5].

Acoustic performance of viscoelastic layers containing periodic cavities can be given from MS and sound propagation theory in the layered medium[4]. The acoustic energy of the reflection and transmission waves is associated with the displacement of the plane waves. The reflection coefficient R is defined to be the ratio of acoustic energy of the reflected waves to that of the incident waves. The transmission coefficient T is the acoustic energy ratio of the transmission waves to the incident waves, and the absorption coefficient is defined to be

$$\alpha = 1 - R - T \tag{5}$$

3. Computational results and discussions

The spherical cavities are arranged periodically in the middle of the backing, which is immersed in water. The corresponding material properties: the thickness of the viscoelastic material is 5mm， the density is 1100kg/m^3, the Poisson's ratio is 0.49, the Young's modulus is 1.5×10^{8}Pa, and its loss factor is 0.3. Other parameters: the lattice primitive vectors are (0,1) and (1,0), the lattice period is 20mm, the max order of the spherical harmonics is 3, and the radius of

the spherical cavity is 0.5mm. It can be seen from Fig.1 that the viscoelastic material has good absorption performance for its acoustic impedance closely matched to water.

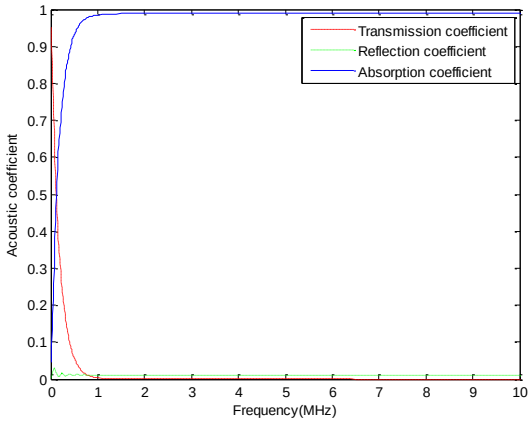

FIG.1 Acoustic coefficient curves of backing materials immersed in water

One of the faces of the backing is in contact with piezoelectric material and the other with air. The plane waves from piezoelectric material are incident normally on the backing. The sound velocity of longitudinal waves of piezoelectric material is 5660m/s and its density is 2.65g/cm^3. Other parameters are the same as mentioned above. Fig2 shows absorption coefficients of the viscoelastic material for different specific acoustic impedance Z, which is equal to the product of material density and sound velocity. The more specific acoustic impedance is, the better the absorption performance will be. It can be seen from Fig.2 that the matching impedance between active materials and the backing is very important to absorption performance.

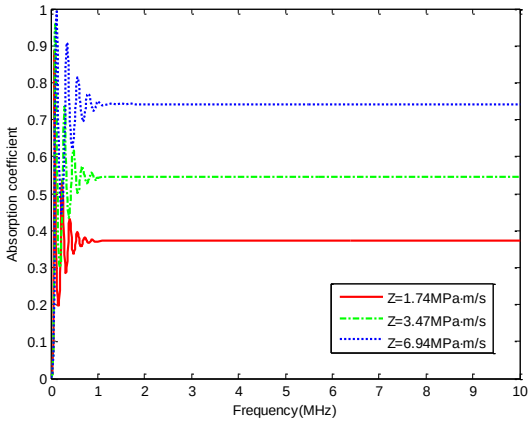

FIG.2 Absorption coefficient curves of backing materials for different specific acoustic impedance

We assume that the lattice period is 1mm and specific acoustic impedance of the viscoelastic material is 6.94MPa •m/s. Other parameters are the same as mentioned above. There are 5 layers of viscoelastic material containing spherical cavities in the backing materials. Fig.3 shows absorption coefficients of backing material for different radius of the spherical cavity. Although specific acoustic impedance of viscoelastic material is same, the densities of backing materials are different for filling cavities. The scattering of elastic wave increases number of propagation routes for sound waves travelling inside the backing. Maybe the absorption performance is reduced at lower frequencies while increased at higher frequencies for much reflections from the cavity surface.

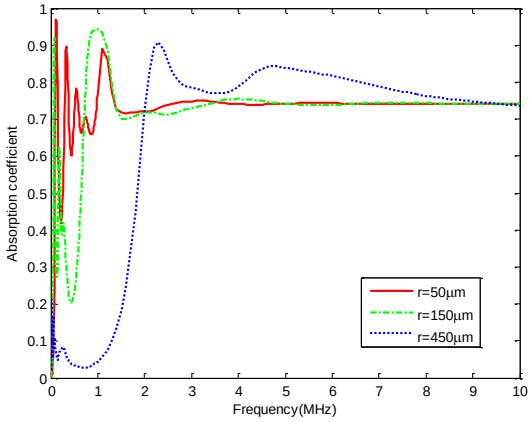

FIG.3 Absorption coefficient curves of backing materials for different cavity radius

4. Conclusions

The basic MS theory on acoustical performance of the viscoelastic materials containing periodic cavities is presented in this paper. The impedance matching and cavity scattering are initially analyzed based on the MS method. The cavity of viscoelastic material can reduce acoustic impedance and change the absorption performance of the backing. If we need to increase acoustic impedance to match the active materials and improve the absorption performance at the same time, it's a good way to fill metallic particles in the viscoelastic materials.

References

[1] Webster R A, Button T W, Meggs C, Maclennan D, Cochran S. Passive materials for high frequency ultrasound components. 2007 IEEE Ultrasonics Synposium, 1925-1928

[2] Psarobas I E, Stefanou N, Modinos A. Scattering of elastic waves by periodic arrays of spherical bodies. *Physical Review B*, 2000; 62 (1): 278-291

[3] Liu Z Y, Chen C T *et al*. Elastic wave scattering by periodic structures of spherical objects: theory and experiment. *Physical Review B*, 2000; 62 (1): 2446-2457

[4] BAI Guofeng, LIU Bilong, SUI Fusheng, LIU Ke, YANG Jun. An investigation on acoustic performance for viscoelastic coatingcontaining axisymmetric cavities using the multiple scattering method. *Acta Acustica* (In Chinese), 2012; 37(3):263-269

[5] Pendry J B. Low Energy Electron Diffraction. London: Academic Press, 1974:275-394

EXPERIMENTAL AJUSTEMENT IN REAL TIME OF A SEMI-ACTIVE NUMERICAL MODEL SUSPENSION WITH A MAGNETORHEOLOGICAL DAMPER

Said Boukerroum[1*] and Nacer Hamzaoui[2]

[1] USTHB/FGMGP, LMA, BP 32 El Allia 16111, Bab Ezouar Alger, Algérie
Email: sboukerroum@yahoo.fr

[2] INSA de Lyon, LVA, Bâtiment A de S[T] Exupéry, 25 bis avenue Jean Capelle 69621 Villeurbanne, France
Email: nacer.hamzaoui@insa-lyon.fr

ABSTRACT

The purpose of this paper is to experimentally validate the performance of a semi-active suspension incorporating a MagnetoRheological damper (MR), where the parameters of the numerical models are often poorly adapted to real responses measured experimentally. To ensure a better representation of a real semi-active suspension, we must consider the internal dynamics of the MR damper in its numerical modeling. By adopting models which demonstrate that dynamic, such as the Bouc-Wen model, we can approach the measured responses by adjusting their internal parameters. The law control introduction for feedback control of the semi-active suspension incorporating the internal dynamics of the MR damper allows, through the analysis of its robustness and response time, to better assess its performance. To validate the performance of these models, a comparative analysis was made between the experimentally measured responses by the dSPACE system used as an acquisition and control chain and the calculated or predicted responses. A rapprochement between measured responses and those calculated for the same dynamic characteristics of the test bed is possible by adjusting the most influential parameters of Bouc-Wen model.

1 INTRODUCTION

In recent years, the MR dampers are the subject of special attention because of their characteristics, including mechanical simplicity, high dynamic range, low power, high force capacity and robustness. However, and early this century, researchers began to consider the development and use of MR dampers in several areas, especially where other technologies have begun to emerge to make their use practicable. Microprocessors, sensors and controllers to increase the processing speed have created opportunities for control that did not exist before.

A wide range of applications of MR dampers has enabled researchers to improve their performances, focusing on their internal dynamics. Indeed, several mathematical models highlighting the physical and energy of MR fluids, allowed the development of several numerical models governing the internal dynamics of these shock absorbers particularly the Bouc-Wen model [1]. To obtain a more representative model of the MR damper, which can substitute for an experimental model in other studies, it is necessary to validate and adjust from a confrontation 'calculation-test', where the adjustment is one of the objectives of this confrontation for a better representation of the numerical model.

2 SEMI ACTIVE SUSPENSION OF QUARTER VEHICLE

Figure 1 shows the functional scheme of a semi-active suspension with two degrees of freedom modeling the quarter-vehicle incorporating an MR damper in the secondary suspension, and whose internal dynamics is governed in this study by the Bouc-Wen model [2] which takes into account the hysteresis.

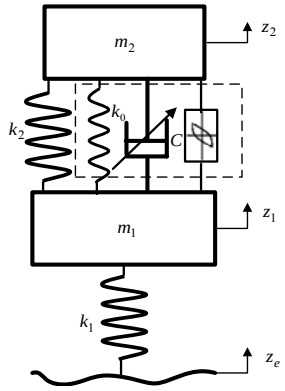

Figure1. Semi active suspension at 2dof incorporating an MR damper with Bouc-Wen model

Such a suspension differs from a conventional passive suspension by the presence of an MR damper whose internal dynamics is governed by the and Bouc-Wen model ‘’Figure 1’’. The variation of the damping in the MR damper is obtained by modification of the oil viscosity mixed with ferromagnetic nanoparticles controlled by a DC. This model, equivalent to a quarter of vehicle consists of a secondary suspension, formed by the mass m_2 (of the chassis), suspended by a k_2 spring stiffness and connected in parallel with the c variable damping coefficient of the damper. As from the measurement of acceleration by sensors placed on the two vibrating masses, we can control in real time the damping force developed by the damper, using a control algorithm deduced the control law semi-active on/off [3]. The elements of the internal dynamics of the MR damper model are described below.

3 MATHEMATICAL MODELING

The differential equations governing the motion of the model shown in Figure 1 can be written:

$$[M]\{\ddot{Z}\}+[C]\{\dot{Z}\}+[K]\{Z\}=[K_e]\{h\}. \quad (1)$$

In state space, the system (1) can be written as:

$$\dot{x} = Ax + Bxy_1 + Dh + Fy_2.$$
$$y = Cx \ . \tag{2}$$

Where **X** is the state vector, **A** is the dynamic system matrix, **B** is the control system matrix, **D** is the input matrix, **F** is the force matrix induced by inertial dynamics of the MR damper and **C** is the output matrix of the measured states. The first control variable y_1 is the signal given by the on/off law control [3] to control the damping coefficient through the current delivered to the MR damper.

$$y_1 = \begin{cases} C_{max}, & \dot{z}_2(\dot{z}_2 - \dot{z}_1) > 0 \\ C_{min}, & \dot{z}_2(\dot{z}_2 - \dot{z}_1) \le 0 \end{cases}. \tag{3}$$

In addition to the first control variable y_1, the second control variable y_2 governed by the same law, takes into account the internal dynamics of the MR damper by the Bouc-Wen model, it is written as:

$$y_2 = \begin{cases} k_0(z_2 - z_1) + \alpha.z, & \dot{z}_2(\dot{z}_2 - \dot{z}_1) > 0 \\ 0 \ , & \dot{z}_2(\dot{z}_2 - \dot{z}_1) \le 0 \end{cases}. \tag{4}$$

The force due to stiffness α generated by the fluid elasticity under magnetic field, represented by the product αz. The variable z which models the hysteresis phenomenon evolves according to the below equation [2]:

$$\dot{z} = -\gamma.|\dot{z}_r|.z.|z|^{n-1} - \beta.\dot{z}_r.|z|^{n-1} - \beta.\dot{z}_r.|z|^n + A_1.\dot{z}_r. \tag{5}$$

By adjusting the parameters β, γ, n, and A_1 of this model, we can indeed control the linearity in the transition periods pre-and post-tensioning stress of MR damper.

4 EXPERIMENTAL SETUP

The experimental setup shown in figure 2 was mounted in the LVA laboratory of INSA in Lyon. It reproduces the dynamic model elements at 2°dof represented in figure 1, incorporates an MR damper type commanded by a current controller of the acquisition system and control.

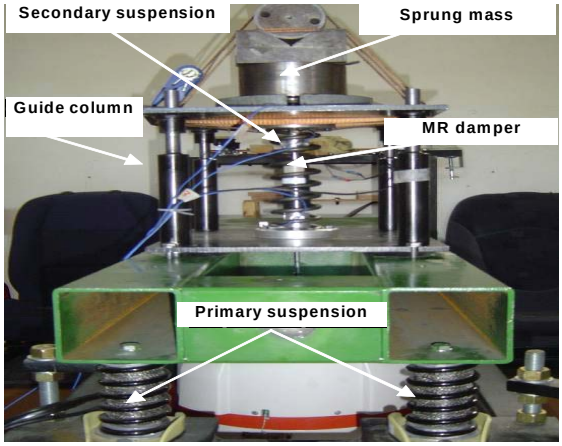

Figure 2. Experimental setup of the suspension at 2 dof

The dSPACE system is used for acquisition and control of closed loop control law governing the damping force developed by the MR damper using the current controller. We perform two programs Simulink, one dedicated to the experimental closed-loop control based on measured parameters and the other to control simulated from the calculated parameters of state equations system (2) [4].

5 RESULTS AND DISCUSSION

Figure 3 shows the permanent response curves to a sinusoidal excitation of the secondary suspension equipped with a MR damper. By adjusting the current I supplied to the damper and the damping coefficient of the numerical model via the change in current, the performance obtained by simulation calculations of the on/off law control without consideration of the internal dynamics of shock absorber ‘’figure3a’’ were experimentally validated by the dSPACE system ‘’figure3b’’.

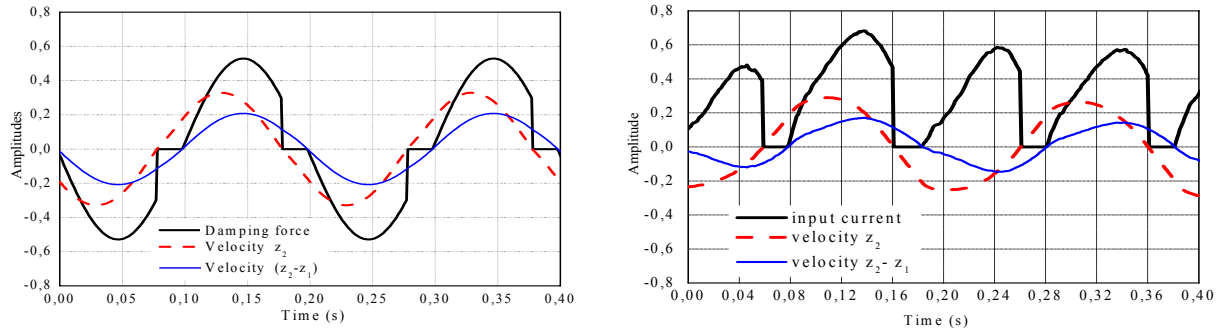

Figure 3. Responses calculated **(a)** and measured **(b)** of on/off control with sinusoidal excitation

Figures 4 shows the response curves measured and calculated of the damping force ‘’figure 4a’’ and suspension relative velocity ‘’figure 4b’’. We already noticed that the shape of this damping force calculated or measured, perfectly obeyed the on/off law control used in this study.

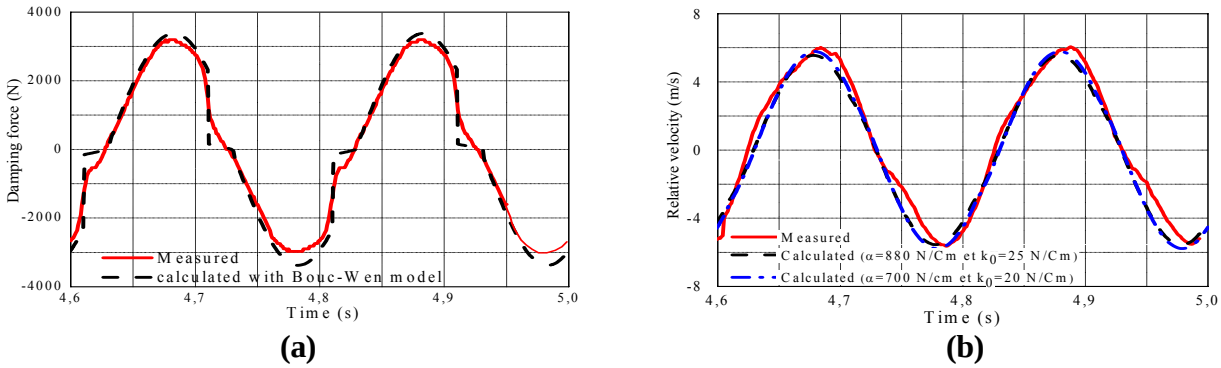

Figure 4. Responses calculates and measured of damping force **(a)** and relative velocity (**b)**

For this model, both curves are similar in terms of frequency. Note that the amplitude curves of the damping force calculated is slightly larger than that measured. This is due to the fact that we did not considered in the numerical model the nonlinearity of the forces friction in guide columns of the setup. By adjusting α and k_0 of Bouc-Wen model, the shape of the relative velocity curve, calculated approach in terms of frequency and amplitude to that of the measured response.

6 CONCLUSION

The present work has allowed us from the experimental control of a semi-active suspension incorporating an MR damper validate control programs in Matlab/Simulink executed with ControlDesk software of dSPACE. With this acquisition system and control, it is possible to control in real time a suspension, by adopting an appropriate control scheme and finely adjusting the current I supplied to the MR damper. From the results of this analysis, we have shown the rapprochement between the calculated and measured responses for the same dynamic characteristics of the test bed. By adjusting the most influential parameters of Bouc-Wen model.

7 REFERENCES

[1] B. F. Spencer. Phenomenological Model of a Magneto-Rheological Damper. *Journal of Engineering Mechanics.* ASCE, vol 123, pp. 230-238, 1997.

[2] Y.K. Wen. Method for Random Vibration of Hysteresis Systems. *Journal of Engineering Mechanics*. ASCE, vol 102, pp. 249-263, 1976.

[3] J. Alanoly and S. Sankar. A New Concept in Semi-Active Vibration Isolation. *ASME, Journal of Mechanisms Transmissions and Automation in Design.* Vol 109, pp. 242-247, 1987.

[4] L. Zhang, F. Ma and J. Wang. Study of Control System of Magnetorheological Dampers under Impact Load. *Second International Conference on Intelligent Computation Technology and Automation.* Changsha, Hunan, China October 10-October 11 2009.

GEOMETRICALLY NON-LINEAR FREE VIBRATION OF C-SS-C-SS SYMMETRICALLY LAMINATED AS4/APC2 RECTANGULAR COMPOSITE PLATES

O. Baho[1], B. Harras[1*] and R. Benamar[2]

[1]Lab Laboratoire de Génie mécanique.
FST de Fès, Route d'Immouzer, BP 2202 Fès, Morocco
Email: baho.omar@gmail.com, bharras@gamil.com

[2]Laboratoire d'Etudes et de Recherches en Simulation, Instrumentation et Mesure, LERSIM, E.G.T, Ecole Mohammadia d'Ingénieurs, Université Mohammed V, BP 765 Agdal, Rabat, Morocco
Email: rbenamar@emi.ac.ma

ABSTRACT

This paper is concerned with a new improved formulation of the theoretical model previously developed by Benamar based on Hamilton's principle and spectral analysis, for the geometrically non-linear vibrations of thin structures. The aim of this investigation is to characterize the non-linear dynamic response of Peek/carbon (AS4/APC2) unidirectional composite panels. The general formulation of the model for non-linear vibration of symmetrically laminated plates at large vibration amplitudes is presented. The clamped simply-supported clamped simply-supported (C–SS–C–SS) boundaries have been examined because they are adequate to model many real panel-type situations. The natural frequencies are determined. The first non-linear mode shape is examined. The effect of non-linearity on the non-linear resonant frequencies and the non-linear fundamental mode shape and associated bending stress patterns at large vibration amplitudes is investigated. Comparison of the change in natural frequency at large vibration amplitudes between AS4/APC2 and isotropic plates is presented.

1 INTRODUCTION

AS4/APC-2 is a high-performance thermoplastic composite material consisting of thermoplastic matrix PEEK (polyether ether ketone) reinforced with continuous AS4 graphite fibres. Compared with other types of thermoplastic matrix, PEEK has higher ductility, higher operating temperature and is unaffected by solvents. In addition, AS4/APC-2 exhibits greater plasticity.

The properties of material have been taken from references [1, 2], and the calculation was made for the plate using the present model. The plate is symmetrically laminated plates and its bending and twisting stiffness are uncoupled. Also, as in symmetric laminates, the in-plane and bending stiffness are uncoupled [3].

Regarding the geometrically non-linear vibrations analysis of laminated plate, it is not many numerical or experimental results which can be used for comparison.Besides, the validity and accuracy of this model results has been discussed largely in previous publications [4, 5-6].

2 APPLICATION TO C–SS–C–SS LAMINATED RECTANGULAR PLATE

2.1 Formulation of the problem

Consider the transverse vibration of C–SS–C–SS rectangular plate which is clamped on the two edges parallel to the y axis, and simply supported in the two other edges. This plate is shown in figure 1.

The Cartesian coordinate system (x, y, z) and let (x, y) be the in-plane coordinates of a point of the middle surface of the plate, and z be the transverse coordinate, normal to the plane middle surface (see Figure 1).

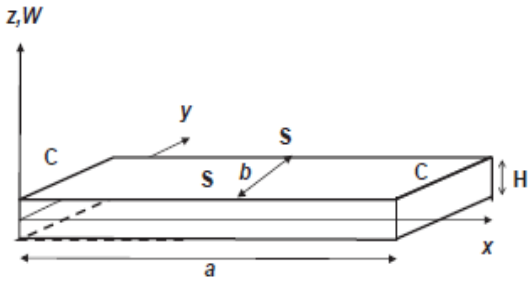

Figure 1. Plate notation

For the classical plate laminated theory, the strain-displacement relationship for large deflections are given by [7]$\{\boldsymbol{\varepsilon}\} = \{\boldsymbol{\varepsilon^0}\} + \boldsymbol{z}\{\boldsymbol{\kappa}\} + \{\boldsymbol{\lambda^0}\}$ (1)

Where $\{\varepsilon^0\}$ and $z\{\kappa\}$are the membrane and the flexural strain tensors,

The constitutive equation of a laminate expresses the resultants and the moments in a plate are given by:$\begin{bmatrix} N \\ M \end{bmatrix} = \begin{bmatrix} A & B \\ B & D \end{bmatrix} \begin{bmatrix} \varepsilon^0 + \{\lambda^0\} \\ \{\kappa\} \end{bmatrix}$ (2)

The matrix $[A_{ij}]$ is the stretching stiffness matrix, the matrix $[D_{ij}]$ is the bending-twisting stiffness matrix and the matrix$[B_{ij}]$ is the coupling stiffness matrix. The existence of the matrix$[B_{ij}]$ leads to coupling effects between stretching and bending-twisting of laminates.

A, B and D are symmetric matrices given by the following equation, B=0 for symmetrically laminated plates [8]

$$\mathbf{3a_i a_j a_k b^*_{ijkl} + 2a_j k^*_{ir} - 2a_i \omega^{*2} m^*_{ir} = 0, \quad i = 1, \dots, n.} \qquad \mathbf{(3)}$$

$$m_{ij} = \rho H^5 ab\, m^*_{ij} k_{ij} = \frac{aH^5 E}{b^3} k^*_{ij} b_{ijkl} = \frac{aH^5 E}{b^3} b^*_{ijkl}$$

$$\omega^{*2} = \frac{a_i a_j k^*_{ij} + \frac{3}{2} a_i a_j a_k a_l b^*_{ijkl}}{a_i a_j m^*_{ij}}$$

a, b: length, width of the plate,E: Young ' s modulus, H: plate thickness, a_k : contribution corresponding to the kth basic functions,ρ: mass density per unit volume of the plate

ω, and ω*: are the frequency and non-dimensional frequency parameters respectively

k^*_{ij}, m^*_{ij} and b^*_{ijkl} General term of the non-dimensional rigidity tensor, mass tensor andnon-linearity tensor respectively

2.2 Results of non-linear analysis :

The geometrical and material properties are defined in table1 and 2. The properties have been taken from references [1].

Number of layers	Orientation of principal axes	a (mm)	b(mm)	h (mm)
8	$(30, 50, 30, 50)_{sym}$	485.7	322.9	1

Table 1. Geometric properties of the plate

E_x(Gpa)	E_y(Gpa)	G_{xy} (Gpa)	ν_{xy}	ρ (kg/m^3)
131	4.7	5	0.28	1570

Table 2. Material properties of the plate

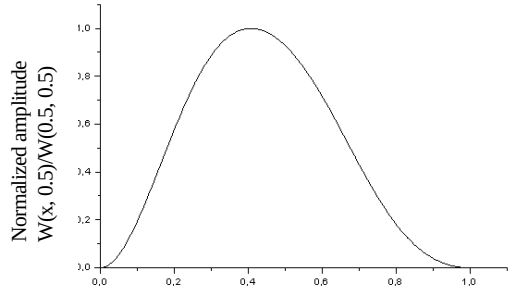

Figure 2. Normalized sections of the first shape of a C-S-C-S APC-2/ASP4 rectangular plate corresponding to y*=0.25 and α=0.66

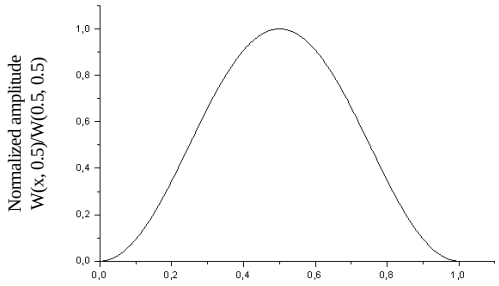

Figure 3. Normalized sections of the first shape of a C-S-C-S APC-2/ASP4 rectangular plate corresponding to y*=0.5 and α=0.66

Normalised sections of the non-linear fundamental mode shape, corresponding to y*= 0.5, and 0.25 with α=0.66 are plotted in Figures 2 and 3. All curves show the amplitude dependence of the mode shape and an increase of curvatures near to the clamped.

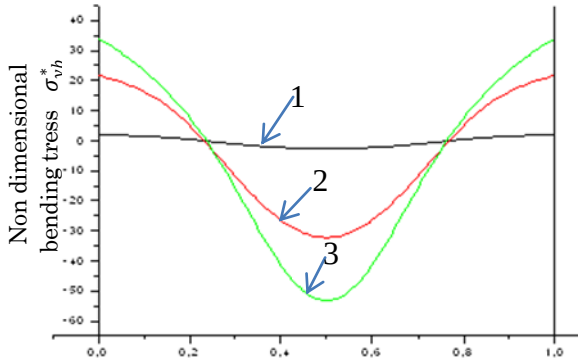

Figure 4. Non-dimensional bending stress distribution corresponding to the first non-linear mode shape of a C–S–C–S, along the section $y*$=0.5 and α=0.66. Curve 1: Lowest amplitude. Curve 3: Highest amplitude.

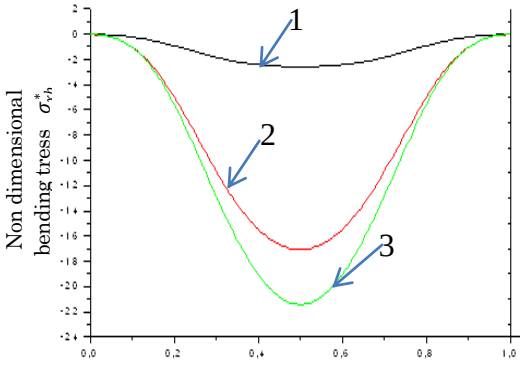

Figure 5. Non-dimensional bending stress distribution corresponding to the first non-linear mode shape of a C–S–C–S, along the section $x*$ = 0. 5 and α= 0 .66. Curve 1: Lowest amplitude. Curve 3: Highest amplitude.

The non-dimensional bending stress distribution is plotted in Figures 4 and 5, for x*= 0.5 and y* = 0.5 with α=0.66. As may be expected,It can be seen that the bending stress is equal to zero near to the simply supported edges. For the simply supported, those figures show that the bending stresses obtained in theirneighbourhoods exhibit a non-linear increase with theamplitude of vibration.

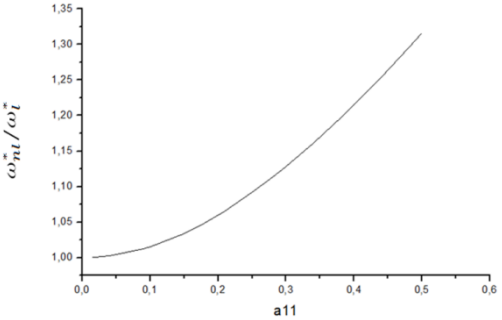

Figure 6. ω^*_{nl}/ω^*_l in terms of a_{11}

3 CONCLUSION

The free response of the C-SS-C-SS rectangular laminated plates AS4/APC2 at large amplitudes of vibration has been investigated using the non-linear model developed in [2] and used and adapted in [4, 5-6]. This model has been successfully used in the present work in order to further extend our understanding of the dynamic behaviour of the AS4/APC2 at large vibration amplitudes with C-SS-C-SS boundary conditions. The amplitude dependence of the first non-linear mode shape of C-SS-C-SS rectangular plates, for an aspect ratio $\alpha = 2/3$, has been obtained via the iterative solution of a set of non-linear algebraic equations, involving a fourth order tensor due to the geometrical non-linearity. The amplitude-dependent first non-linear mode shape was expressed as a series of plate functions obtained as products of clamped clamped–clamped and simply supported–simply supported beam functions in the x- and y-directions.

It appears from the present work that the non-linear model developed in references [2, 4] allows the estimation of the amplitude dependent first non-linear mode shape, the associated non-linear frequency, and qualitative estimation of the bending stresses associated with the first non-linear mode. Further investigations are needed in order to allow exhaustive results and comparison with isotropic plates and to find out how the estimated non-linear modes can be simply used in the non-linear forced response analysis. Also, the effects of such a non-linearity on the fatigue life of highly excited plate-type structures, working in severe environment, have to be investigated. There is considerable relevance to the acoustic fatigue problem in aircraft structures.

REFERENCES

[1]. B. HARRAS, K. C. COLE and T. VU-KHANH 1996 J. Reinf. Plast. Compo. Vol. 15, No. 2, 174-182. Optimisation of the ultrasonic welding of Peek-carbon composites

[2]. B. HARRAS, K. C. COLE and T. VU-KHANH 1997 twenty-ninth International Sampe Technical Conference, Orlando, Florida USA. Vol. 29, 475-485. Characterisation of the ultrasonically welded Peek-carbon composites.

[3]. Chia CY. Nonlinear analysis of plates. New York: McGraw-Hill, 1980

[4]. B. Harras, R. Benamar, R.G. White, Geometrically nonlinear free vibration of fully clamped symmetrically laminated rectangular composite plates, J. Sound Vib. 251 (4) (2002) 579–619.

[5]. M EL KADIRI, R. BENAMARand R. G. WHITE November 1999Journal of Sound and Vibration228 (2), 333-358., The non-linear free vibration of fully clamped rectangular plates: second non-linear mode for various plate aspect ratios.

[6]. B. HARRASand R. BENAMAR. Fourth International Conference on Applied Mathematics and Engineering Sciences, October 23, 24 and 25, Casablanca, Morocco 2002. Geometrically non-linear, steady state, forced, periodic vibration of fully clamped composite laminated rectangular plates. Part I: Semi-analytical approach using a single mode.

[7]. R. BENAMAR 1990 Ph.D. Thesis, Institute of Sound and Vibration Research. Non-linear dynamic behaviour of fully clamped beams and rectangular isotropic and laminated plates.

[8]. R. BENAMAR, M. M. K. BENNOUNA, and R. G. WHITE 1993 Journal of Sound and Vibration164 (2), 295-316. The effects of large vibration amplitudes on the fundamental mode shape of thin elastic structures, part II: Fully clamped rectangular isotropic plates.

MULTI-OBJECTIVE OPTIMIZATION OF RAIL VEHICLE DESIGN MOVING IN CURVED TRACKS WITH RELATIVELY HIGH SPEED

NEJLAOUI. M[1*], HOUIDI. A[2], MLIKA. A[3], AFFI. Z[4] and ROMDHANE. L[5]

[1]L M S, Ecole Nationale d'Ingénieurs de Monastir, Tunisia, nejlaouimohamed@gmail.com
[2] LMS, Institut Supérieur des Sciences Appliquées et de Technologie de Sousse, Tunisie, ajmi.houidi@issatso.rnu.tn
[3] LMS, Ecole Nationale d'Ingénieurs de Sousse, Tunisie, abdelfettah.mlika@eniso.rnu.tn
[4] LGM, Ecole Nationale d'Ingénieurs de Monastir, Tunisia, zouhaier.affi@enim.rnu.tn
[5] LMS, Ecole Nationale d'Ingénieurs de Sousse, Tunisie, lotfi.romdhane@enim.rnu.tn

ABSTRACT

This paper deals with the multi-objective optimization of the rail vehicle design moving in curved tracks with relatively high speed. Two criteria are considered simultaneously which are the safety and the comfort. The genetic algorithm is used to solve the problem. The obtained solutions are presented as a "Pareto front" and they are analyzed for several design parameters. The outcome of this discussion could help the designer in his selection of the satisfactory design parameters yielding the best compromise between safety and comfort.

Nomenclature:

i,j,k	Index of wheelset, wheel and bogie respectively	φ_{ki} , φ_k , $\bar{\varphi}$	Pitch motion of the wheelsets, the bogies and the carbody respectively
X_{ki} , X_k , $\bar{X}$	longitudinal displacement of the wheelsets, the bogies and the carbody respectively	e_0	Half of the track gauge
Y_{ki} , Y_k , $\bar{Y}$	Lateral displacement of the wheelsets, the bogies and the carbody respectively	C*ij*	Coefficients of Kalker
Z_{ki} , Z_k , $\bar{Z}$	Vertical displacement of the wheelsets, the bogies and the carbody respectively	F_{xij}	Longitudinal creep forces
α_{ki} , α_k , $\bar{\alpha}$	Yaw motion of the wheelsets, the bogies and the carbody respectively	F_{yij}	Lateral creep forces
θ_{ki} , θ_k , $\bar{\theta}$	Roll motion of the wheelsets, the bogies and the carbody respectively	M_{zij}	The creep moment acting in vertical direction

1 INTRODUCTION

Safety and comfort are two imperative criteria to rail vehicles (RV) circulation. Traveling on short radius curves, the RV can circulate with creep wheel-rail (WR) causing wear. Moreover, the RV circulates in general with a contact flange-rail, which can create the derailment [1].

Several works treated the effect of the designs parameters of the rail vehicle system on its behavior. He and McPhee [2] **Erreur ! Source du renvoi introuvable.**developed a mono-objective optimization of RV design parameters using Genetic Algorithms. The objective function is a weighted combination of the angle of attack and the ratio of the lateral force to the vertical force applied by each wheel on the rail. Rejeb et al. [3] optimized the critical speed as a function of the design variables of RV system in rectilinear motion using the Genetic Algorithm method. Nejlaoui et al. [4] treat the multi-objective optimization of the RV design based on safety and comfort criteria at a small RV speed. The roll motion of the RV system is not considered.

The goal of this work is the multi-objective optimization of the RV design moving with a relatively high speed. In section 2, the improved dynamic model of the RV system developed in [5] will be presented. In section 3, the safety and comfort criteria are presented in closed form and the model was solved. In section 4, the multi-objective optimization of the RV design will be developed. Some concluding remarks will be given in section 5.

2 MODEL OF THE RV SYSTEM

The RV model is composed of seven rigid body; a car body connected by 2 secondary suspension to each bogie. The bogies are connected to 4 wheelsets using 8 primary suspensions (see figure 1).

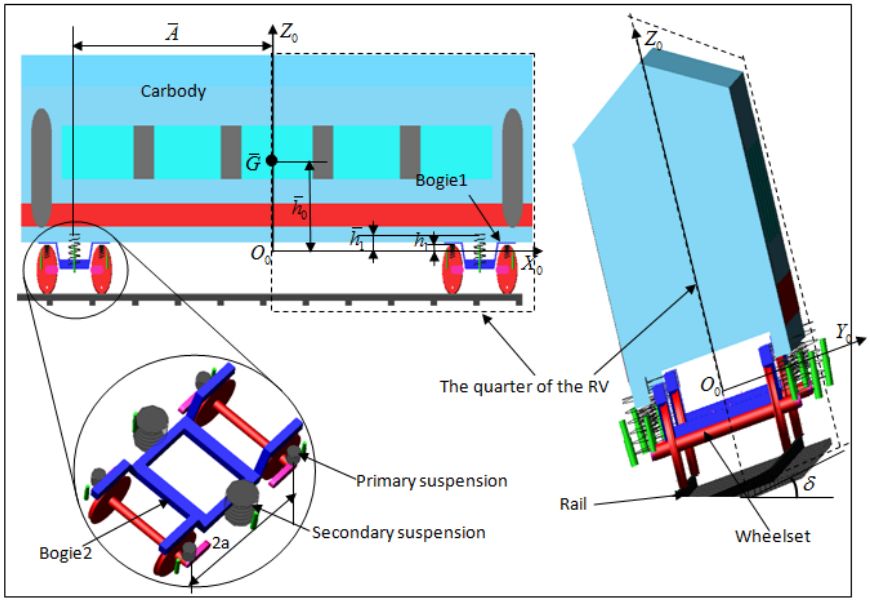

Fig. 1. The rail vehicle model

Based on the RV symmetry and due to the fact that we focus on the transversal dynamics, it is proved that the study of the dynamic modeling of the system can be reduced to the modeling of its quarter as presented by (Figure 1) [4, 6].

Thus we have a quarter vehicles with only 10 degrees of freedom given by

$$\mathbf{q} = \left[\bar{y}, \bar{\alpha}, \bar{\theta}, y_1, \alpha_1, \theta_1, y_{11}, \alpha_{11}, y_{12}, \alpha_{12} \right]^T \qquad (1)$$

The analytical model of the rail vehicle system is obtained based on the Lagrange formalism and can be expressed: $\mathbf{A}(\mathbf{q})\mathbf{q} = \mathbf{b}$ (2)

The matrix **A** and the vector **b** are given in [4, 5]. For more details see [5].

3 SAFETY AND COMFORT CRITERIA

In curved tracks with a low radius, there is usually a flange rail contact. This contact leads to a lateral force F_{1i} (Figure 2b) that if it exceeds a certain limit, it can cause the derailment of the RV system. Moreover, this kind of motion is usually accompanied by the creep of the wheel on the rail. This creep generates the wear of the WR contact surface, and it is accompanied by a high noise level. This is considered as a comfort criterion.
In what follows, we will give, in a closed form, the indicators of safety and comfort.

3.1 The derailment angle

When we have a flange – rail contact, the generalized coordinate y_{1i} becomes a known constant and the corresponding displacement appears as a reaction to force F_{1i}. These unknown forces become additional variables, instead of the corresponding displacement y_{1i}, which can be identified through the algebraic equations of the analytical model (Eq.2):

$$F_{1i} = -K_y(1+l\Gamma)y_1 + (-1)^i K_y(1+l\Gamma)a\alpha_1 - \left(K_y(1+l\Gamma)h_1 + K_z d^2\Gamma\right)\theta_1 + \left(2K_y(1+l\Gamma)\left(1+\frac{l\Gamma}{2}\right) + K_z d^2\Gamma^2\right)y_{1i}$$
$$-K_y(1+l\Gamma)^2 y_0 - K_z d^2\Gamma^2 y_0 + \chi C_{22}\left[1 - \frac{C_{22}}{3\mu N}\alpha_{1i} + \frac{{C_{22}}^2}{27\mu^2 N^2}{\alpha_{1i}}^2\right]\alpha_{1i} + \frac{m}{2}\left(\frac{V^2}{R_c} - g\delta\right) \quad (3)$$

With: $\Gamma = \frac{\gamma_0}{(e_0 - r_0\gamma_0)}$, $\chi = \frac{e_0}{(e_0 - r_0\gamma_0)}$ and C_{ij} is the Kalker's coefficient [7].

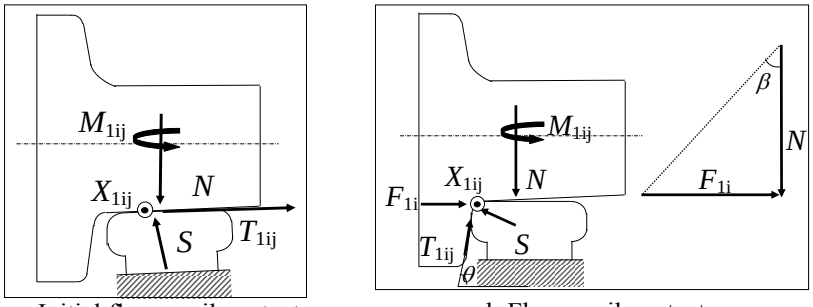

a: Initial flange rail contact b:Flange rail contact

Fig. 2. The Wheel – Rail contact forces**.**

The analysis of the equilibrium of forces in vertical and lateral directions gives:

$$\frac{F_{1i}}{N} = \frac{\tan\theta - \frac{T_{1ij}}{S}}{1 + \frac{T_{1ij}\tan\theta}{S}} \quad (4)$$

The maximum of safety is obtained when this term is (F_{1i}/N) minimal [8]. The maximum of (T_{1ij}/S) corresponds to the friction coefficient μ. At a given θ_{max}, to avoid derailment:

$$\frac{F}{N} < \frac{\tan\theta_{max} - \mu}{1 + \mu\tan\theta_{max}} \quad (F = \max(F_{1i})) \quad (5)$$

$$\tan\beta < \frac{\tan\theta_{max} - \mu}{1 + \mu\tan\theta_{max}} \quad (\tan\beta = \frac{F}{N}) \quad (6)$$

The minimization of the derailment angle β will be considered as the first objective function.

3.2 The Creep forces

In the WR interface there is a creep force in longitudinal (X_{1ij}) and lateral (T_{1ij}) directions and a torque (M_{1ij}) (see figure 2.a). The creep forces are modeled based on the analytic method [7]. The maximum of the creep resultant force is given by:

$$R = \max(R_{1ij}) = \max\left(\sqrt{{X_{1ij}}^2 + {T_{1ij}}^2}\right) \quad (7)$$

In order to reduce noise and wear, we should minimize the maximum of the creep resultant forces *R*. The second objective function will be the minimization of the force *R*.
To determine β and R, we should have the expressions of the generalized coordinates of the system. To achieve this goal, we developed an algorithm based on the Broyden's method [9]. This algorithm solves the model for q. The values of β and R are calculated using eq.6 and 7.

4 MULTI-OBJECTIVE OPTIMIZATION DESIGN OF RAIL VEHICLE

4.1 Formulation of the problem

In what follows, we will optimize the design variables (xi) that has the significant effect on the dynamic behavior of the RV system [2]. The search domain (D(xi)) of each xi are given in table 1. The other design parameters are presented in [2-6]. The RV speed is $V = 25ms^{-1}$ and the radius of curved tracks is *R*c = 280 m.

Variables x_i	D (x_i)	Variables x_i	D (x_i)
$K_x(N/m)$	$[10^6, 10^8]$	$\bar{K}_z(N/m)$	$[10^4, 10^6]$
$K_y(N/m)$	$[10^6, 10^8]$	γ_e	[0.05, 0.2]
$K_z(N/m)$	$[10^6, 10^8]$	$a(m)$	[1,2]
$\bar{K}_x(N/m)$	$[10^4, 10^6]$	$\bar{M}(Kg)$	[30000,45000]
$\bar{K}_y(N/m)$	$[10^4, 10^6]$	$M(Kg)$	[3000,3500]

Table 1: Design variables and their search domains

Thus, the optimization problem is with two objective functions:

$$\begin{cases} \text{Minimize} \quad \beta(x_i) \\ \text{Minimize} \quad R(x_i) \\ \text{under the constraints :} \\ \qquad x_i \in D(x_i) \end{cases} \tag{8}$$

Genetic algorithms method has been used to solve this problem [4].

4.2 Optimization results

The optimization results are presented in Figure 3. For $\theta_{max} = 75$ degree [8] and $\mu = 0,31$ [4]**Erreur ! Source du renvoi introuvable.**, the derailment angle β should be less than 58.8 degree (Eq.6) in order to avoid the derailment risk.

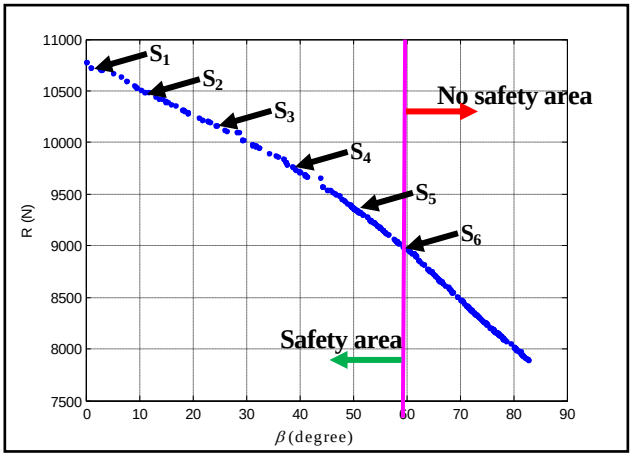

Figure 3. Optimization front

Therefore, we can define two regions in Figure 3; the safety and the non safety area.

One can note also that when the creep forces R increase the derailment angle β decreases. In fact, the increase of creep forces increases the creep area and consequently the decrease of β **Erreur ! Source du renvoi introuvable.**.

In what follows, we will study the effect of the design parameters on the evolution of the derailment angle and the creep forces in the safety zone. For this goal, we select six optimal solutions from the Pareto front (Figure 3).

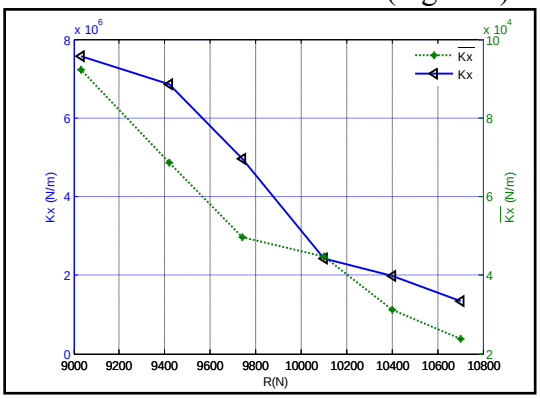

Figure 4. Effect of the longitudinal stiffness on safety and comfort

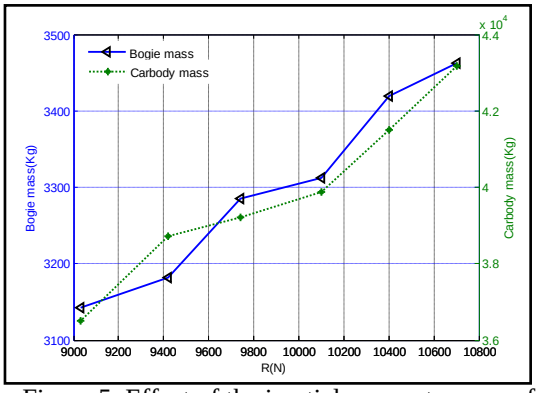

Figure 5. Effect of the inertial parameters on safety and comfort

One can notice that the increase of the suspension stiffness parameters causes the decrease of the creep force R (figure 4). In fact, if the structure is more compliant, a great part of the energy generated by the force applied by the car body, the bogies and the wheelset to the rail is converted to a potential energy which is proportional to the square of the allowable spring deformation. On the other hand the increase of carbody and bogie masses increases the creeps force R (figure 5); in fact the increase of the masses of the RV structure increases size of the ellipse of contact. This leads to an increase of the creep force.

5 CONCLUSIONS

This Work dealt with the multi-objective optimization of the RV design based on safety and comfort criteria. Based on the symmetry of the rail vehicle and on the motion nature in curves, we performed a multi-objective optimization using the genetic algorithm in which the optimization of the derailment angle and the creep forces is considered simultaneously. We showed that the design variables can have a conflicting effect on the two performances.

6 REFERENCES

[1] Majka M., Hartnett M, (2008), Effects of speed, load and damping on the dynamic response of railway bridges and vehicles, Computers and structures 86, 556-572.

[2] He Y, McPhee J (2005), Optimization of curving performance of rail vehicles, Vehicle System Dynamics 43, 895-923.

[3] Rejeb H, Affi Z, Bettaieb H, (2007), Optimization of the design variables of rail vehicles system in rectilinear motion, The Second International Congress Design and Modeling of Mechanical Systems, CMSM'2007.

[4] M. Nejlaoui, A. Houidi, Z. Affi, L. Romdhane, "Multiobjective robust design optimization of rail vehicle moving in short radius curved tracks based on the safety and comfort criteria", Simulation Modelling Practice and Theory 30 (2013) 21–34

[5] Nejlaoui M, Houidi A, Affi Z, Romdhane L (2010), An improved Analytical model of rail vehicle system moving in curved tracks, The First International Congress Passive and Active Mechanical Innovation, IMPACT'2010.

[6] Nejlaoui M , Affi Z, Houidi A, Romdhane L, (2009), Analytical modeling of rail vehicle safety and comfort in short radius curved tracks, C. R. Mecanique 337 303–311

[7] Datoussaid S, (1998), Optimisation du comportement dynamique et cinématiques des systèmes multicorps à structure cinématique complexe, Ph.D these, Service de mécanique rationnelle, dynamique et vibration, Faculté polytechniquede Mons.

[8] Elkins J, Wu H, (1999), Angle of attack and distance based criteria for flange climb derailment, Vehicle system Dynamics Supplement 33, 293-305.

[9] Nocedal J, Wright S. J, (1999), Numerical Optimization. (Springer-Verlag, New York)

NON-LINEAR FREE VIBRATIONS OF C–C–SS–SS SYMMETRICALLY LAMINATED CARBON FIBER REINFORCED PEEK (AS4/APC2) RECTANGULAR COMPOSITE PLATES

Z.Zergoune [1*], B. Harras [1], & R. Benamar [2]

[1]Laboratoire de Génie mécanique, FST de Fès, Route d'Immouzer, BP 2202 Fès, Morocco
Email: zergoune.uni@gmail.com, harrasbilal@yahoo.fr

[2]Laboratoire d'Etudes et de Recherches en Simulation, Instrumentation et Mesure, LERSIM, E.G.T Ecole Mohammadia d'Ingénieurs, Université Mohammed V, BP 765 Agdal, Rabat, Morocco
Email: rbenamar@emi.ac.ma

ABSTRACT

The aim of the work reported here is to further extend our understanding of the dynamic behavior of the clamped clamped simply supported simply supported (C-C-SS-SS) AS4/APC2 composite plates at large vibration amplitudes, via the theoretical modeling of the effect of the geometrical non-linearity on the dynamic characteristics. In a series of papers of Benamar and co-workers, a theoretical model based on Hamilton's principle and spectral analysis has been developed and used to study the non-linear free and steady state periodic forced vibration of beams, the non-linear free vibration of shells and homogeneous and composite plates. This model has been adopted and extended in this work. The model reduces the non-linear vibration problem to solution of a set of non-linear algebraic equations, performed numerically using appropriate algorithms in order to obtain a set of non-linear mode shapes for the structure considered in each case, with the corresponding amplitude dependent non-linear frequencies. Results are given for various plate aspect ratios and vibration amplitudes, showing a higher increase of the induced bending stress near to the clamps at large deflections. Comparisons with the dynamic behavior of a similar isotropic plate at large vibration amplitudes are presented and good results are obtained. The second and higher non-linear mode shapes will be presented later.

1 INTRODUCTION

The survey about geometrically non-linear vibration of structures is of continuing interest, because of wide use of the tendency to build more preferment structures, with high strength, high stiffness, and low weight, such as composites. Such new materials have a more accentuated non-linear behavior. It is then necessary to develop new design concepts, taking into account the non-linear behavior induced by large vibration amplitudes, which may occur for example when in such severe environments, the plate may be subjected to large displacement amplitudes inducing geometrical non-linearity that is mainly caused by the development of in-plane membrane stresses. In this case, one of the basic assumptions of the linear vibration theory is violated, therefore necessitating the development of a mathematical approach which takes into account the membrane effect, neglected in the classical treatment of plate vibrations. Even though the vibration of plates overall has interested researchers for a long time, the exact linear solutions are known only for the six cases having two opposite edges simply supported corresponding to a square plate or a rectangular plate [1-2]. Furthermore, in the survey made by Leissa in 1973 [1], it was pointed out that until 1954, when Warburton derived his formulae based on a single-term representation of the deflection shapes for the natural frequencies of plates with various boundary conditions, no solution, even approximate, was known for six boundary condition cases. The general accuracy of Warburton's formulae is discussed in references [1].

The purpose of this paper is to apply the theoretical model developed in references [3] in order to analyze the geometrically non-linear free dynamic response of C-C-SS-SS rectangular symmetrically laminated plates so as to investigate the effect of non-linearity on the non-linear resonance frequencies, the non-linear fundamental mode shape and associated bending stress patterns at large vibration amplitudes. Various values of the plate aspect ratio and the amplitude of vibrations will be considered, and useful numerical data will be provided.

2 GENERAL FORMULATION OF THE GEOMETRICALLY NON-LINEAR FREE VIBRATION OF C-C-SS-SS SYMMETRICALLY LAMINATED RECTANGULAR COMPOSITE PLATES

The discretization of the strain and kinetic energy expressions via the expression of the transverse displacement function W as in reference [4] can be carried out leading to:

$$V_b = \frac{1}{2} a_i a_j k_{ij} \sin^2 \omega t, \quad V_a = \frac{1}{2} a_i a_j b_{ijkl} \sin^4 \omega t, \quad T = \frac{1}{2} a_i a_j \omega^2 m_{ij} \cos^2 \omega t \quad (1, 2, 3)$$

Where m_{ij}, k_{ij}, and b_{ijkl} are respectively the mass tensor, the rigidity tensor and geometrical non-linearity tensor. The expressions for these tensors are defined as follows:

$$\mathrm{m_{ij}} = \rho \mathrm{h^5 ab\, m_{ij}^*}\ , \quad \mathrm{k_{ij}} = \frac{\mathrm{ah^5 E}}{\mathrm{b^3}}\ \mathrm{k_{ij}^*}\ , \text{and} \quad \mathrm{b_{ijkl}} = \frac{\mathrm{ah^5 E}}{\mathrm{b^3}}\ \mathrm{b_{ijkl}^*} \quad (4,5,6)$$

Where the expression of the non-dimensional tensors $\mathrm{m_{ij}^*}$, $\mathrm{k_{ij}^*}$, and $\mathrm{b_{ijkl}^*}$ have been taken from the reference [11]

Applying Hamilton's principle to the vibration problem gives:

$$3\mathrm{a_i a_j a_k b_{ijkl}^*} + 2\mathrm{a_j k_{ir}^*} - 2\mathrm{a_i \omega^{*2} m_{ir}^*} = 0, \quad \mathrm{i} = 1, \ldots, \mathrm{n}. \quad (7)$$

Where ω* is the non-dimensional non-linear frequency parameter, the expression of which can be obtained by pre-multiplying equation (7) by $[A]^T$ from the left-hand side, which leads to the following equation:

$$\omega^{*2} = \frac{\mathrm{a_i a_j k_{ij}^*} + \frac{3}{2}\mathrm{a_i a_j a_k a_l b_{ijkl}^*}}{\mathrm{a_i a_j m_{ij}^*}} \quad (8)$$

3 APPLICATIONS TO C-C-SS-SS RECTANGULAR LAMINATED PEEK CARBON (AS4/APC2) COMPOSITE PANELS

The following table 1 shows the geometric and material properties of the AS4/APC2 rectangular composite plates which they have been quoted from the reference [5].

Number of layers	**Orientation of principal axes**	**Aspect ratio**		**h (mm)**
8	$(30, 50, 30, 50)_{sym}$	0.667		1
E_x(Gpa)	**E_y(Gpa)**	**G_{xy} (Gpa)**	**ν_{xy}**	**ρ (kg/m^3)**
131	4.7	5	0.28	1570

Table 1. Geometric and material properties of the rectangular plate

The calculation was made by using 36 basic functions obtained as products of the first six clamped simply-supported beam functions, leading to square mass and rigidity matrices of dimension 25. In the table 2, the non-linear frequency parameters obtained from the non-linear analysis at too small vibration amplitudes (a_{11}=0.005) corresponding to various values of the plate aspect ratio, are compared with results obtained from linear analysis. Consequently, the results are showing the convergence of the non-linear model to the linear approach at very small vibration amplitudes.

	Aspect ratio α		
	0.4	**0.5**	**0.667**
ω^*_l	13.252	15.041	19.80
ω^*_{nl} (a_{11}=0.005)	13.30	15.11	19.92
ω^*_{nl} (a_{11}=0.1)	13.84	15.68	20.58

Table 2. Comparison of non-dimensional frequency parameters

In the figure 1 are plotted the non-linear frequency on the maximum non-dimensional amplitude for the first non-linear mode shape of C-C-SS-SS rectangular plate for various values of the plate aspect ratio. All curves are similar to that mentioned in reference [2].

The curves in figures 2, obtained via the present model, are plotted for the values of the maximum non-dimensional amplitudes W^*_{max}=0.039210739, 0.60840897, and 1.1960736, along the x-direction of the non-linear fundamental mode shape of a rectangular plate (α=1.0), corresponding to x*= 0.5. They show an increase of curvatures near to the clamped edges of the amplitude of the non-linear mode shape, on the other hand no changes concerning the simply supported ones, thereby, we suppose that the flexural stresses will increase non-linearly near to the clamped edges accompanying increase of the vibration amplitudes.

The figures 3 and 4 represent the non-dimensional flexural distributions associated to the first non linear mode shape of a C-C-SS-SS rectangular plate, which show the effect of large vibration amplitudes along the x and y directions, corresponding to x*=0.5 and y*=0.5 for α=1.0. All curves show that the flexural stress is equal to zero close to the edge where the rectangular plate is simply supported, but on the other side the flexural stress exhibit a higher increase which has been proved in the linear vibration approach.

4 CONCLUSION

The non-linear free vibrations of C-C-SS-SS rectangular symmetrically laminated plates are studied in this survey using a theoretical model developed previously in references [3] for geometrically non-linear free vibrations of thin elastic structures. The objective was to determine the effects of large vibration amplitudes on the first mode shape, the fundamental natural frequency, and the associated flexural stress distribution. The model, based on Hamilton's principle, reduces the non-linear free vibration problem to solution of a set of non-linear algebraic equations involving the classical rigidity, mass tensors and a fourth order tensor due to the

geometrical non-linearity.

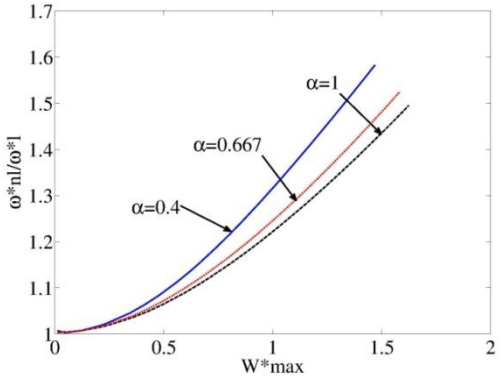

Figure1. Comparison of the change frequency of the first mode for α=0.4, 0.667, and 1.0

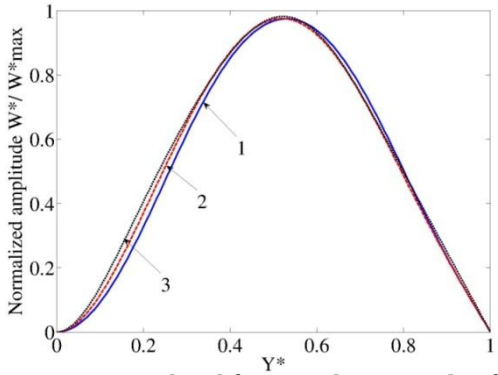

Figure 2. Normalized first non-linear mode of a C-C-SS-SS rectangular plate for Y*=0.5 and α=1.0. Curve 1, lowest amplitude ; Curve 3, highest amplitude

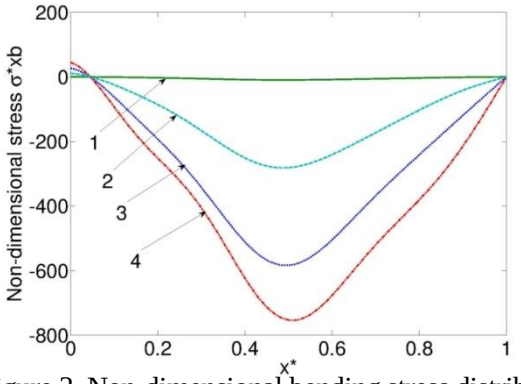

Figure 3. Non-dimensional bending stress distribution associated with C-C-SS-SS rectangular plate first non-linear mode along X*=0.5 for α=1.0. Curve 1, lowest amplitude; Curve 4 highest amplitude.

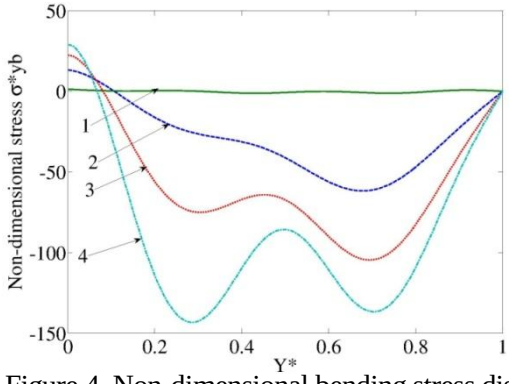

Figure 4. Non-dimensional bending stress distribution associated with C-C-SS-SS rectangular plate first non-linear mode along Y*=0.5 for α=1.0. Curve 1, lowest amplitude ; Curve 4 highest amplitude.

In the end, this present work enabled us to find out how the thin elastic structures behave at the large vibration amplitude by plotting different spectrum analysis. In addition, as far as quality is concerned, the comparison has been done with the results of an isotropic rectangular plate at the similar boundary conditions obtained in reference [2] showed good results.

REFERENCES

[1]. AW. Leissa. Vibration of plates. NASA-SP-160. Washington, DC: US Government Printing Office; 1969.

[2]. K.El Bikri, R.Benamar, and M.Bennouna Geometrically non-linear free vibrations of clamped simply supported rectangular plates. Part I: the effects of large vibration amplitudes on the fundamental mode shape. journal of sound and vibration 2003; 81 : 2029–2043.

[3]. R.Benamar, M.M.K.Bennouna, and R.G.White 1991 Journal of Sound and vibration 149, 179-195. The effects of large vibration amplitudes on the fundamental mode shape of thin elastic structures. Part I: simply supported and clamped clamped beams.

[4]. B.Harras, R.Benamar, and RG.White. Geometrically non-linear free vibration of fully clamped symmetrically laminated rectangular composite plates. Journal of Sound and vibration 2002;4: 579–619.

[5]. Daniel and Ishai, Engineering Mechanics of composite materials. Oxford university press: 1994.

STUDY OF MECHANICAL BEHAVIOR AND RELIABILITY ANALYSIS OF THE OVERHEAD POWER CABLES FOR LOW VOLTAGE DEDICATED TO DISTRIBUTION NETWORK

A. CHOUAIRI[1], A. BENALI[1], M. EL GHORBA[1], N. BARBE[2], A.BENOUNA[2]

[1] Characterization and Control Laboratory Mechanics of Materials and Structures (LCCMMS)
National School of Electricity and Mechanics (ENSEM) Oasis Route d'El Jadida, BP 8118, Casablanca, Morocco
Email: chouairi.asmaa@gmail.com

[2] Lyonnaise Des Eaux de Casablanca (LYDEC)
48 Rue Mohamed Diouri, BP 16048 Casablanca, Morocco

ABSTRACT

Today, electricity is essential and experiencing very strong growth due to the development of new technologies. In addition, incidents thereto are causing many failures each year in the world. However, mastering the reliability of overhead lines of electric power long distances through generally different parts of their relief (topography and altitude), climate (temperature, pressure, wind) their environment (industrial areas, coastal areas) has become increasingly important. Therefore, the equipment power transmission is exposed to various constraints. Among these, the degradation of connections, electrical aging weapons are recognized as major factors causing the faults stored on airlines, and thus appear as very important factors in the quality and reliability energy transport.

These defects include bad connections tightening the cable connections. They also include bad connections due to hardware that is not suitable. A connection fault generally contributes to increase the electrical resistance of connection.

The purpose of our work is to optimize the control performance of low voltage cables and their connections and specially taking into account all the constraints for hardware limitations inherent to their structures.

1 INTRODUCTION

Since the onset of electrical systems, electrical cable was the first physical media for circulating electric current. Until now, the power cable is still valid and has undergone changes intrinsic to adapt with the more severe electrical and environmental constraints.
Electrical cables are ubiquitous in many areas where the flow of energy and information is necessary to ensure the proper functioning of a system.
The cable type is different depending on the type of current that we want to convey and the environment in which the system works. Signals can be analog or digital, low or high power and low, medium and high frequencies. For example, a power grid can use three types of cable: coaxial cable, twisted pair or fiber.
Damage to drivers in service occurs at the interface between the driver and the equipment that hold (suspension clamps, pier's spacer). Tightening the cap of the suspension clamp induced contact forces between the conductor and the clamp between the wires and the driver.
Thus, in this paper we present, first, a theoretical framework, what an electrical contact with the main parameters that characterize it. Then, we will focus on the analysis of resistance of these electrical contacts.

2 TERMS OF DRIVERS AND ELECTRICAL CONNECTORS

The overhead power transmission travels long distances generally very different parts of their relief (topography and altitude), climate (temperature, pressure, and wind), environment (industrial zones, regions coastal). Therefore, the equipment power transmission is exposed to various constraints. Among these, the degradation of the aging connections and insulations which are recognized as major factors causing the faults stored on airlines, and thus appear as very important factors in the quality and reliability energy transport.

Figure 1 illustrates the formation of a typical single-phase cable. From a purely technical point of view, we can distinguish two types of cables, those paper-insulated (PILC cable) and those isolated cross linked polyethylene (XLPE cable). Inevitably, the insulation disposed around the conductor of a cable (figure 1) ages and degrades over time. Destruction, partial or complete of this insulation involves maintenance effort or worse cable replacement.

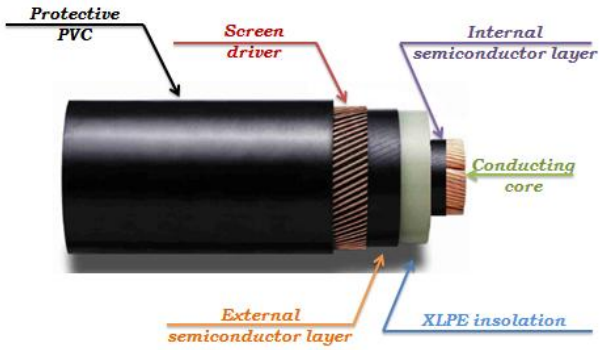

Figure 1: Formation of a low voltage cable with xlpe insulated

Cables must have a regular diagnosis whose main task is to verify the quality of their insulation faults. In this respect, the measurement of partial discharges [1][2][3] is a technique that has proven its worth for many years.

3 CONTACT AND CONNECTION ELECTRICAL OVERHEAD POWER CABLES

The electrical contacts can electrically connect two conductive elements. These elements can be bus bars, cables where equipment. Electrical contact in its simplest form is the contact surfaces of two conductive metal powers.
When you put two metal surfaces in contact, the contact between these two surfaces is never perfect. That is to say, the contact interface is not a smooth area consists of an infinite number of points, where all points would touch next. In reality the surface of a contact interface consists of a finite number of contact points called elementary contacts (Figure 2).

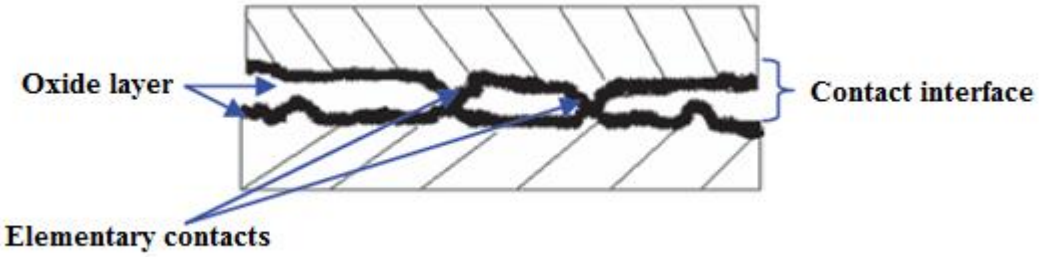

Figure 2: Appearance actual electrical contact interface close up microscopic

The number and size of elementary contacts is dependent on many parameters, the most significant are:

- The material hardness,
- The pressing force to the contact,
- The flatness of the contact surface.

Impurities such as dust, chips of all kinds can be inserted at the interface of contact, and are likely to create a discontinuity at the contact interface. This discontinuity is not only the source of additional resistance to current flow (electrical resistance) [4] [5] [6] but also a resistance to the passage of heat flow (thermal resistance) [7] [8].

4 CONCLUSION

The electrical conductors are among the most important component of overhead transmission and distribution of electrical energy they assured both the mechanical support of the parties brought to the low voltage electrical insulation with recent parts made in air or energized.
The use of lightweight cables, flexible, compact, highly reliable and resistant to various environments are the main constraints imposed by most industries.
First designed in copper and aluminum cable manufacturing has experienced through the years, a significant change, and in order to improve their performance whatever the weather and environmental conditions to which they are exposed. Indeed, disruption of electrical conductor can result in certain circumstances a major risk to the reliability and operation of the transmission of electrical energy by air.

5 REFERENCES

[1] M. HENRIKSEN Partial discharges in spherical cavities in epoxy resin Technical University of Denmark, 1982.

[2] P.H.F. MORSHUIS Partial discharge mechanism Delft University Press, 1993.

[3] F. GUTFLEISCH et L NIEMEYER Measurements and simulation of PD in epoxy voids IEEE Transaction on Dielectrics and Electrical Insulation, vol. 2(5) pp.729–743, 1995.

[4] International Electrotechnical Commission. "IEC-60943, paragraph 2.3.2 Calculation of the film resistance." 1998.

[5] International Electrotechnical Commission. "IEC-60943, paragraph 2.3.1 Calculation of the constriction resistance." 1,998

[6] Christian Ngo, HélèneNgô. "Chapter 4.7: Tunneling." Introduction Quantum Physics Ed Wiley Paris: 2000. pp. 166-171.

[7] Bernard Eyglunent. "Chapter 3.2: The issue of interfaces." Thermal Theory and Practice in the use of engineering Hermes, 1994.

[8] Ana Maria Bianchi, Yves Fautrelle, Jacqueline Etay. "Chapter 2.3.2: Thermal resistance of contact." Heat transfer polytechnic and university Romandes Press, 2004.

PROPAGATION OF DEFORMATION AND STRAIN WAVES IN A TAMPING RAMMERS SPRINGS

A. Hamza[1], S. Ayadi[1*] and E. Hadj-Taïeb [1*]

[1]Laboratory of Applied Fluid Mechanics and Modelling
University of Sfax, National Engineering School of Sfax (E.N.I.S.), B.P 1173, 3038 Sfax, TUNISIA
Email: anis7amza@gmail.com, sami.ayadi@issatgb.rnu.tn, Ezed.Hadj@enis.run.tn

ABSTRACT

In this study, the vibrations of coil, excited axially, in helical compression springs such as tamping rammers are discussed. The mathematical formulation is composed by a system of four partial differential equations of first order hyperbolic type as unknown variables are angular and axial deformations and velocities. The numerical resolution is performed by the conservative finite difference scheme of Lax-Wendroff.

The study takes into account the dynamic coupling between the axial and angular waves due to the effects of Poisson's ratio. The impedance method is applied to calculate the frequency spectrum. The results, obtained using this method, were used to analyze the evolution in time of deformations and velocities in different sections of the spring result of a sinusoidal excitation of the axial velocity applied at the end of the spring. These results clearly show the effect of the interaction between the slow axial waves and the fast angular waves, the resonance and other phenomena related to wave propagations such as wave reflections and beat.

1 INTRODUCTION

Helical springs are important mechanical components in many industrial applications. Several accidents have been explained by different forms of resonance oscillations of the springs. For this reason, the frequency study must be carefully done. In this paper, we study the numerical propagation of elastic waves in a helical compression springs such as tamping rammers following a sinusoidal excitation. The tamping rammers (See Figure 1) are equipments used for compaction in confined areas, where the utilization of similar equipments is not possible [1].

Figure 1. Helical spring description from tamping rammers.

2 MATHEMATICAL FORMULATION

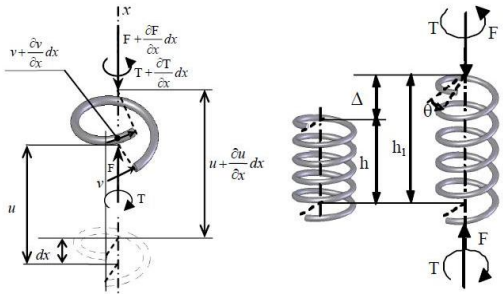

Figure 2. Helical spring description

The mathematical model [2] (See Figure 2):

$$\frac{\partial u_t}{\partial t} = a\frac{\partial u_x}{\partial x} + b\frac{\partial v_x}{\partial x} \tag{1}$$

$$\frac{\partial v_t}{\partial t} = b\frac{\partial u_x}{\partial x} + c\frac{\partial v_x}{\partial x} \tag{2}$$

$$\frac{\partial u_x}{\partial t} = \frac{\partial u_t}{\partial x} \tag{3}$$

$$\frac{\partial v_x}{\partial t} = \frac{\partial v_t}{\partial x} \tag{4}$$

3 NUMERICAL SOLUTION

3.1 Impedance method

The impedance method consists in solving the equations by the method of separation of variables $Y(x,t) = X(x)T(t)$, where $X^t(x) = (U_x \quad V_x \quad U_t \quad V_t)$ a vector of the single variable *x* and *T* is a function of the single variable *t*. By restricting the solution for *T* to the steady-oscillatory case, that is, by assuming a particular solution for *T* as a harmonic oscillation, the solution can be expressed: $T = Ce^{i\omega t}$, where ω is the angular frequency and $X(x) = [A(x)]X(0)$ [3].

3.2 Lax-Wendroff method

The numerical solution of the problem for hyperbolic partial differential equations can be obtained by the method of Lax-Wendroff which is applied to transform the system of partial differential equations into a system of finite difference equations. This method numerical scheme [4] is an explicit throw of prediction and correction and is easily applied to the resolution of conservative formulations [5].

4 APPLICATIONS AND RESULTS

4.1 System Description

Parameter	Symbol	Outside spring	Inside spring	Units
Spring free length	h	224.972	224.972	mm
Spring mounted length (Initial compression)	h_{min}	130.06	130.06	mm
Spring length at maximum load	h_{Max}	75.06 mm	75.06	mm
Helix angle	α	8° = 0.140	8.731° = 0.152	rad
Number of active coils	n_a	6	9	-
Number of end coils	n_e	1.5	2.5	-
Poisson's ratio	υ	0.29	0.29	-
Wire steel density	ρ	$7.87 .10^{-6}$	$7.87 .10^{-6}$	Kg/mm^2
Young's modulus	E	206.85	206.85	GPa
Rigidity modulus	G	78	78	GPa
Mass of the spring	M	0.951	0.309	Kg
Radius of the spring	R	39.915	24.380	mm
Wire radius	r	4.5	2.65	mm
Wire length	l	1899.4	1782.26	mm
Load at solid limit	F	3235.3	1145.24	N
Proper frequency	f	82.381	130.036	Hz

Table 1. Mechanical and geometric characteristics of the considered springs.

4.2 Initial and boundary conditions

$$u_x(x,0) = -h_{\min}/h \,,\, v_x(x,0) = \theta r/h = 0 \,,\; u_t(x,0) = 0 \text{ and } v_t(x,0) = 0 \tag{24}$$

$$u_t(0,t) = 0 \,,\; v_t(0,t) = 0 \,,\; u_t(h,t) = \psi(t) = u_{t0}\sin(\omega t) \text{ and } v_t(h,t) = 0 \tag{35}$$

4.3 Study of isolated outside spring (As an example)

4.3.1 Excitation with fast frequency ω_f

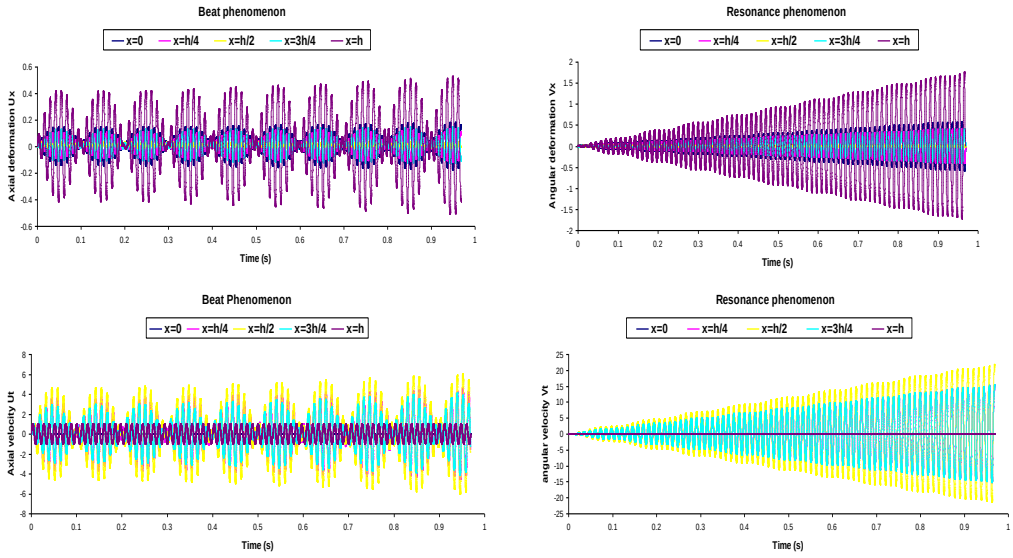

Figure 3. Evolution of deformations and strains in the outside spring with an excitation at ω_f.

4.3.2 Excitation with slow frequency ω_s

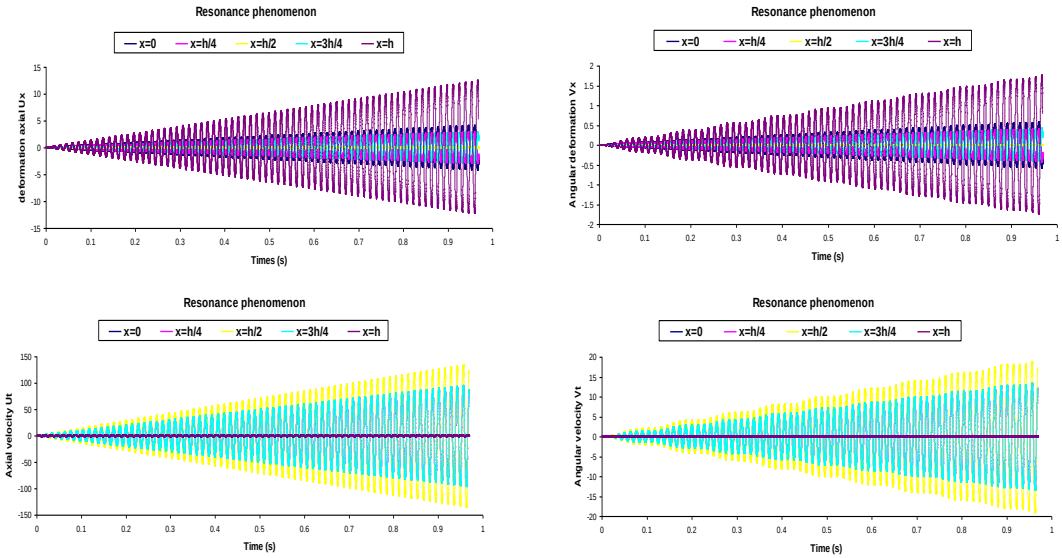

Figure 4. Evolution of deformations and strains in the outside spring with an excitation at ω_s.

5 CONCLUSION

This paper investigated resonance and beat phenomena of strains due to forced sinusoidal excitation in two different helical springs of the tamping rammers. To study vibrations in helical compression springs subjected to a sinusoidal excitation, we propose a coupled model. At first, the natural frequencies of the spring were predicted by the impedance method. The obtained results permitted to show that the natural frequencies are proportional to the tow wave speeds in the spring: the slow axial wave speed and the rapid rotational wave speed. Numerical solutions were obtained by the Lax-Wendroff scheme. The amplification was more important for the axial strain than for the rotational one which was induced by the effect of coupling Poisson. Numerical results of the example studied and simulated, have been confronted with such physical explanations regarding the phenomena of wave reflections and the dynamic coupling between the axial and angular waves on both ends of the spring. The numerical results showed that the axial and rotational strains resonated and followed the excitation for slow frequencies. For excitation with rapid natural frequencies, the resonance occurred only for rotational strains and the beat phenomenon was observed for axial strain.

REFERENCES

[1] Tudose L., R. Morariu-Gligor and S. Haragas, Optimal design of helical compression springs from tamping rammers, the 2nd International Conference of Advanced Engineering in Mechanical Systems ADEMS'09, 2009.

[2] Ayadi S., Hadj-Taieb E. and Pluvinage G., The numerical solution of strain waves propagation in elastic helical springs, *Materials and Technology*, p. 47-52, 2007.

[3] Ayadi S. and Hadj-Taieb E., Finite element solution of dynamic response of helical springs, *International Journal of Simulation and Modelling*, Vol. 7, N°1, p. 17-28, 2008.

[4] Lax P.D. and Wendroff B., Difference schemes for hyperbolic equations with high order of accuracy, *Communications on Pure and Applied Mathematics 17*, p. 381-398, 1966.

[5] Ayadi S., Hamza A. and Hadj-Taïeb E., Comportement dynamique des ressorts hélicoïdaux composites, Third International Congress Design and Modelling of Mechanical Systems CMSM'2009, 16-18 Mars 2009, Hammamet, Tunisia.

METHODOLY FOR ROBUST ROADSIDE SAFETY BARRIER DESIGN AND CERTIFICATION APPLICATION TO STEEL-WOOD STRUCTURES

M. Massenzio[1], C. Goubel[1,2], S. Ronel[1,] E. Di Pasquale[3]

[1]LBMC, UMR_T 9406
Université de Lyon, F-69622, Lyon, France,
IFSTTAR, Bron, Université Lyon1, Villeurbanne, France
IUT Lyon1, 17 rue de France 69627 Villeurbanne Cedex FRANCE
Email: michel.massenzio@univ-lyon1.fr, sylvie.ronel@univ-lyon1.fr

[2]Laboratoire INRETS Equipement de la Route (LIER-SA)
Lyon Saint Exupéry Aéroport, FRANCE
Email: clement.goubel@lier.fr

[3]SIMTECH
37, rue des acacias, 75017 Paris, FRANCE
Email: edmondo@simtech.fr

ABSTRACT

This paper presents an original methodology for the robust design and certification of Vehicle Restraint Systems (VRS). Considering a steel-wood VRS, where the not-well-known parameters are numerous and the evaluation and certification is based on very few experimental tests, the questions of trust is essential: what if the weather was rainy instead of sunny on the VRS performances?...

The proposed methodology is both based on the actual real tests and on a numerical model (validated by the experimental test regarding the modes of failure). Using numerical models give to opportunity to carry out parametric studies with an affordable cost. Hence the methodology takes advantages of interests of both numerical and experimental studies.

1 INTRODUCTION

Vehicle Restrain System (VRS) is a roadside safety equipment dedicated to avoid an errant vehicle to leave the road. In Europe, in order to be certified, the VRS have to pass two crash tests following the European Standard EN1317 [1,2]. One issue in VRS crash testing is the number of parameter which can vary and affect the interaction vehicle/VRS and the VRS performances; between others, the tolerances on the crash conditions (vehicle, impact point, speed…) and the characteristics of the VRS itself (e.g. mechanical properties of the materials). This point becomes more crucial as the VRS is made of wood and steel, as it is the trend where the safety barriers have to be discrete.
One can wonder if the very few number of experimental crash tests realized for the certification are sufficient? As it is economically not affordable to perform more crash tests, the paper present a strategy, taking advantages of virtual crash testing to be complementary to the real scale crash tests.

2 WHAT IS A GOOD VRS ?

2.1 Aim of a VRS – EN1317

Among the different types of VRS, this study is dedicated to hard shoulders devices. Hard shoulders devices aim to contain and to redirect the vehicle. In order to fulfil these objectives, most of VRS devices present a sequence of events called failure modes. The main mechanisms could be divided in three sub events:

- Yield of the rail under vehicle contact pressure and transfer of contact forces to the surrounded posts
- Bending of the post (formation of plastic hinge at the post base)
- Disconnection of post-rail link. The fusible link could be obtained by different ways: bolt failure or bolt pulled out.

European Norm EN1317 [1, 2] provide the guide lines for the full scale crash testing of a VRS and criteria for the evaluation of roadside safety features. Three main appraisal factors are investigated:

- Structural adequacy (i.e. dynamic deflexion (W) which is the maximum lateral dynamic displacement of the side facing the traffic of the VRS…)
- Occupant risk (i.e. the Acceleration Severity Index ASI, the Theoretical Head Impact Velocity THIV…)
- After collision trajectory (i.e. the car redirection must comply with the “CEN box”, not to intrude into adjacent traffic lanes…)

2.2 Main sources of incertitude

The failure modes leading to a good VRS show a sequential succession of event including nonlinear behaviour (plasticity, rupture). One must face two difficulties to handle the problem. First, the sequential aspect imply that a small error relative to one specific event of the sequence can lead to great discrepancies of the overall phenomena. Then, the material used for roadside hardware are not premium materials and for example only the lower value of the yield stress is defined (for S235 steel, the yield stress minimum value is 235 MPa, nether the less steel certificates analysis show frequently values higher than 330 MPa).

3 METHODOLOGY FOR A COMPLEMENTARY VIRTUAL TESTING

A detailed presentation of the methodology, experimental tests and numerical models are presented in [3]. A French steel-wood VRS has been modelled. The first step is to demonstrate the capacity of the model to reproduce a real test configuration (correlation step). The correlation step is based on the failure modes analysis (figure 1) and to the comparison between the experimental results (severity index, W and velocity) and a cloud of numerical simulations where the design variables in the parametric study are for instance steel and wood characteristics. In order to access the wood characteristics, a specific three point dynamic bending test is experimentally studied [4]. The lower cost of the experiment makes it possible to correlate the actual wood of the VRS and the LS-Dyna model. As a result of the first step, a validated numerical model of the VRS is available.

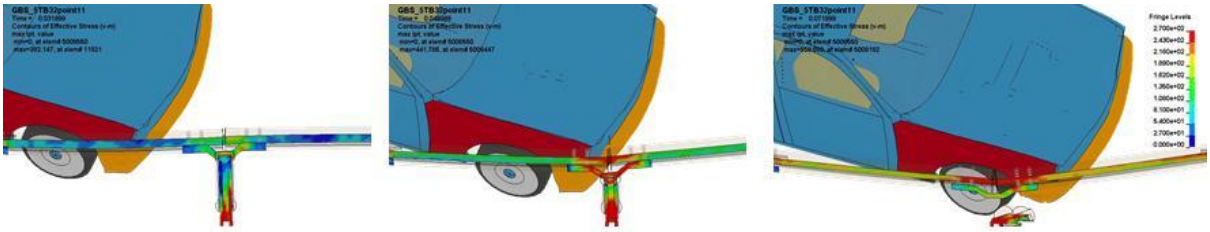

Figure 1. Some failure modes

The second step aims to evaluate the effect of wood mechanical properties (obtained by the specific experimental procedure) on the performances of the VRS device: severity and deflexion W. The figure 2 presents the cloud of results where the wood and the failure modes are varied. The deflexion is plotted versus the severity ASI. The cloud of results gives a good idea of the range of variation of the VRS performances (red box shows the tolerance of the experimental result). The three particular points in the circle shows for example a particular configuration where the wood beam does not break.

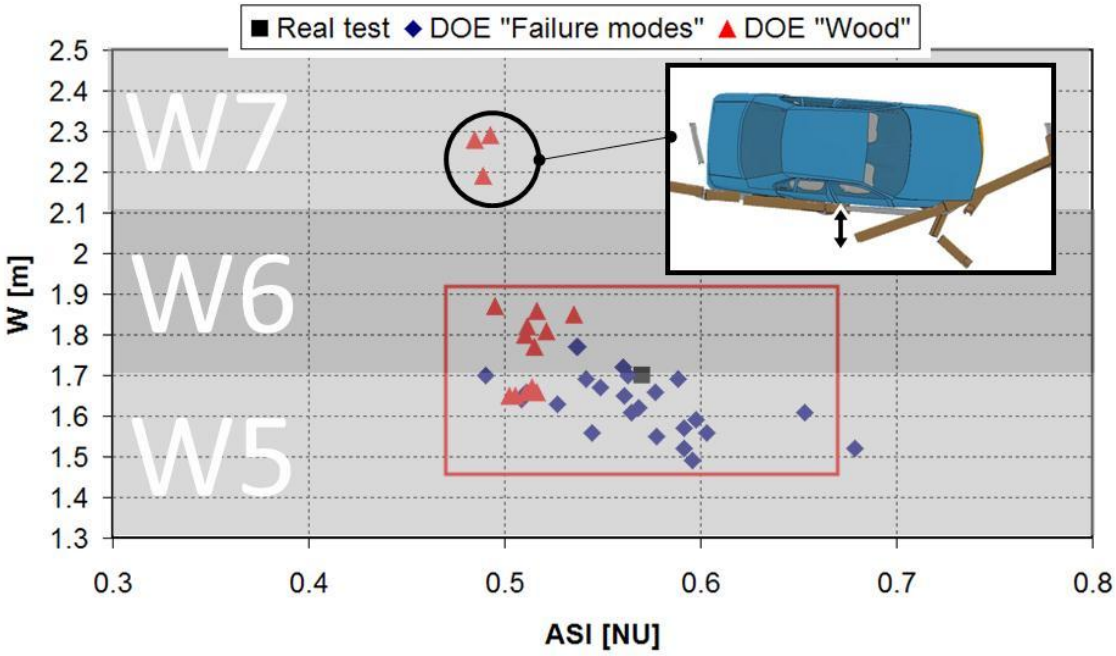

Figure 2. EN1317 results

4 CONCLUDING REMARKS

Some parameters of a VRS cannot be precisely defined because of the environment (moisture and temperature in the case of the wood, soil…) or because of the supply chain during industrial implantation of the VRS (steel or bolts quality…). One interest of the numerical model is to test the influence of parameters that can vary and cannot be controlled in order to assess their effect to the Vehicle Restraint System performances. This paper proposes a procedure to take advantages of both experimental study which is expensive and cannot be used for parametric studies, and numerical studies where parametric approach is affordable and observation of lots of data is possible. The figure 3 presents the synoptic of the proposed methodology. Based on a real crash test of the VRS device, a numerical model is evaluated and validated. Here some specific experimental tests can be necessary to feed the model and to obtain the range of the possible values (case of the wood). Then the device certification can be obtained from the real crash test and from the numerical model parametric results including the range of variation of the not-well-known data.

From a scientific point of view, the approach proposes a more robust certification of the VRS. From an industrial point of view, the approach can be useful in order to optimize the VRS regarding mean values of the VRS components, but on the other hand, the optimisation can also be established considering the variation of the VRS performances toward the not-well-known data (depending on industrial matter, environmental parameters or aging).

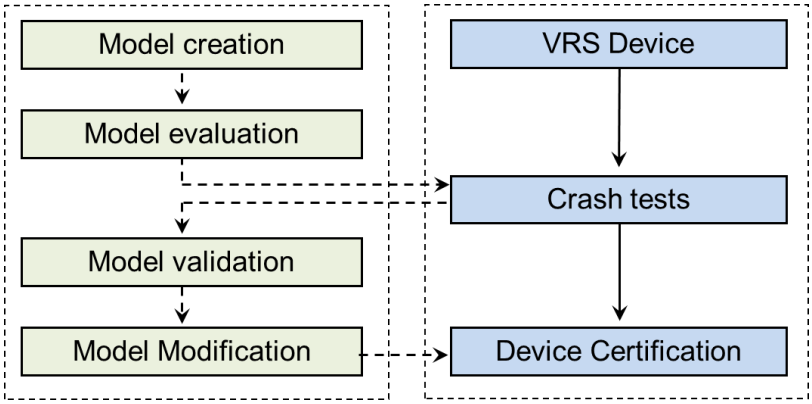

Figure 3. Synoptic of the proposed methodology

REFERENCES

[1] NF EN1317 Road restraint systems - part 1: Terminology and general criteria fortest methods – AFNOR , September 2010 ISSN 0335-3931

[2] NF EN1317 Road restraint systems - part 2: Performance classes, impact testacceptance criteria and test methods for safety barriers including vehicle parapets – AFNOR,September 2010, ISSN 335-3931

[3] C. Goubel, Vehicle restraint system crash test modeling using deterministic models and probabilistic approach – Application to steel-wood structures. *PhD Thesis*. UCB Lyon 1, 2012.

[4] C. Goubel, M. Massenzio, S. Ronel, Wood-steel structure for roadside safety barriers, *International Journal of Crashworthiness*, DOI:10.1080/13588265.2011.625678,1-11

FRICTION NOISE OF ROUGH SURFACES AND DISSIPATION OF VIBRATION

A. Le Bot[1] and V.H. Dang[1]

[1]Laboratory of tribology and dynamics of systems
Ecole centrale de Lyon, Ecully, FRANCE
Email: alain.le-bot@ec-lyon.fr, viet-hung.dang2@ec-lyon.fr

ABSTRACT

The sound produced by the friction of two objects with rough surfaces has a wide spectrum and generally a relatively low level. In this study, the dependence of the sound pressure level (SPL) with the contact area is investigated. It is found that for some solids, the acoustical power is proportional to the contact area while for some other solids, the sound is almost constant. These two regimes are interpreted in terms of energy balance. The thermodynamical approach highlights that these two regimes may be explained by introducing a dissipation law of vibration by the contact. This law states that the vibrational power dissipated by the contact is proportional to the contact area.

1 INTRODUCTION

Friction sound occurs in a wide variety of daily situations [1]. From insect sound to industrial mechanisms, friction noise is so common that we may recognize them generally without difficulty. Among them, the sound produced by the friction of two solids with rough surfaces is of particular interest.

When rubbing two rough surfaces, the sound produced has a wide spectrum and a relatively low level. The mechanism responsible of the sound production stems from the interface itself [2]. Surfaces are not flat but made of numerous asperities whose size is of order of micrometer. During the sliding, asperities of the top surface hit asperities of the antagonist surface and all these micro-impacts generate a vibration into the solids which, in turn, produces the sound.

The empirical laws of roughness noise have been investigated in several papers [3]. In particular, it has been found that the Sound Pressure Level is a log law of the sliding speed and the surface roughness.

This paper outlines the dependence of roughness noise with the contact area. It is observed that the sound is usually not proportional to the contact area but is related to it by a more complicated law.

2 OBSERVATION OF TWO REGIMES

Let us start by a simple observation. When rubbing sugar lumps on a table surface, a sound is produced which may be attributed to a roughness noise. The sugar lumps play the role of sound sources while the table in vibration plays the role of a resonator which radiates the sound. It can be checked with a sonometer or more simply by hearing the noise, that *the larger the number of lumps the stronger the sound*. Results of this experiment are shown in Figure 1, left. The noise level increases with a slope near 9 dB per decade.

But if the experiment is done on a drum membrane, the results are quite different. It may be observed that the sound pressure level remains almost constant as the number of sugar lumps varies (Figure 1, right).

Two regimes exist for roughness noise, a first regime where the constancy law applies and a second one where the additivity law applies [4].

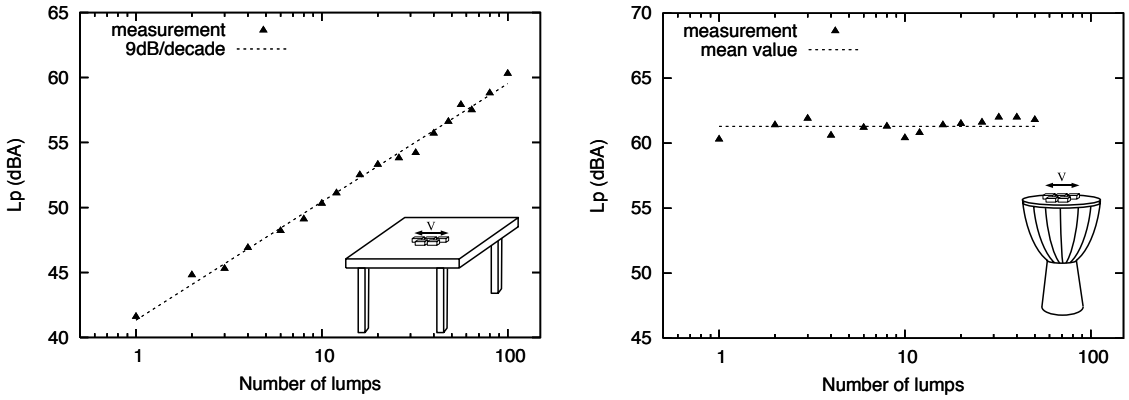

Figure 1: Evolution of SPL versus number of sugar lumps on a wood table (left) and on a drum membrane (right).

3 EXPERIMENT

In order to reproduce the above observation, the following experiment has been realized. A thin stainless steel is fixed at its corners on rigid supports. The surface of the plate is prepared by grinding in order to provide a Gaussian random roughness. On the plate, called the resonator, are pulled several identical solids, called the sliders. The slider surface is prepared in same condition as the plate. During the movement, a vibration is generated into the plate. The vibrational level is recorded by several accelerometers. The experiment consists in measuring the RMS-vibrational level versus the number of sliders. Results are shown in Figure 2.

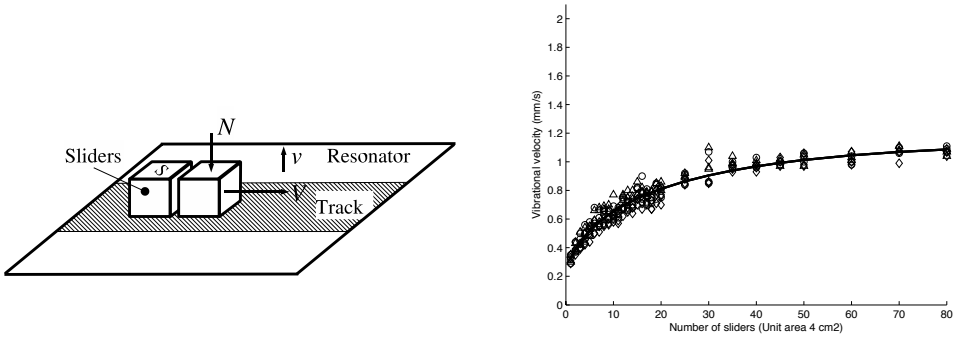

Figure 2: Left, principle of the experiment. Right, evolution of vibrational level versus number of sliders.

4 COMMENTS

The above experiment clearly shows that the slope of sound (vibrational level) versus contact area (number of sliders) is not constant. We observe for small area a strong slope (near 10dB/decade) which is associated to the linear regime of the wood table. But for large contact area, the slope decreases and becomes almost zero as in the case of a drum membrane. So, not only both regimes may be reproduced on the same system but also all intermediate regimes.

The following interpretation may be proposed [5].

The resonator is assimilated to a thermodynamical system which contains vibrational energy $E = WA$ where A is the plate area and W the energy density assumed to be uniform (diffuse field). The energy level results from an energy balance. The sliders are sources which supply energy to the resonator. The power being supplied is proportional to the contact area S (number of sliders),

$$P_{\text{inj}} = pS \tag{1}$$

The vibrational energy stored in the resonator is dissipated by two processes. The first process is the natural damping of the plate without contact. If the reverberation time is measured, then the damping loss factor $\eta\omega$ is inversely proportional to it. The dissipation law is,

$$P_{\text{diss}} = \eta\omega WA \tag{2}$$

But a second cause is responsible of dissipation, the contact itself. In practice for a reverberant structure, a contact for instance by bolts or rivets may generate more dissipation than natural damping. So, we introduce the following law,

$$P_{\text{fric}} = cWS \tag{3}$$

where c is an ad-hoc constant. The dissipation by friction is therefore assumed to be proportional to the contact area S.

By the energy balance $P_{\text{inj}} = P_{\text{diss}} + P_{\text{fric}}$, the energy density is readily obtained,

$$W = \frac{pS}{\eta\omega A + cS} \tag{4}$$

In the asymptotic case $cS << \eta\omega A$ (small contact area), the vibrational level is $W = pS/\eta\omega A$. It is found to be proportional to the contact area as in the wood table experiment. This is the regime where natural damping dominates. But in the limit case $cS >> \eta\omega A$, the energy density is constant $W = p/c$ as observed on a drum membrane. This is the regime where the damping induced by contact dominates.

5 CONCLUDING REMARKS

In conclusion, it has been shown that the sound pressure level is generally not proportional to the contact area. The saturation level is reached p/c for large contact area. These results may easily be interpreted if we adopt the ansazt that the dissipation of vibrational energy in a contact is proportional to the contact area.

ACKNOWLEDGMENTS

The authors acknowledge the Laboratoire d'excellence Celya and the Agence nationale de la recherche (ANR) for their financial support under the contract ANR-10-LABX-60.

REFERENCES

[1] Akay, A., "Acoustics of friction", *J. Acoust. Soc. Am.*, **111**, 1525-1548 (2002)

[2] H. Ben Abdelounis, H. Zahouani, A. Le Bot, J. Perret-Liaudet and M. Ben Tkaya, "Numerical simulation of friction noise," *Wear*, **271**, 621-624 (2011)

[3] Ben Abdelounis, H., Le Bot, A., Perret-Liaudet, J., Zahouani, H., "An experimental study on roughness noise of dry flat surfaces", *Wear*, **268**, 335-345 (2010)

[4] Le Bot, A., Bou Chakra, E., "Measurement of friction noise versus contact area of rough surfaces weakly loaded", *Tribol. Lett.*, **37**, 273-281 (2010)

[5] A. Le Bot, E. Bou Chakra and G. Michon, "Dissipation of vibration in rough contact", *Tribol. Lett.*, **41**, 47-53 (2011)

CHARACTERIZATION OF HYSTERETIC FRICTION OF VISCOELASTIC JOINTS

A. Hanen JRAD[1,2*], B. Jean Luc DION[1] , C. Franck RENAUD[1] , D. Imad TAWFIQ[1] and E. Mohamed HADDAR[2]

[1]Laboratoire d'Ingénierie des Systèmes Mécaniques et des Matériaux (LISMMA), Institut Supérieur de Mécanique de Paris, 3 rue Fernand Hainaut, 93407 Saint Ouen Cedex, Paris, France.
hanen.jrad@supmeca.fr, jean-luc.dion@supmeca.fr, franck.renaud@supmeca.fr, imad.tawfiq@supmeca.fr

[2]Unité Modélisation, Mécanique et Productique (U2MP), Ecole Nationale d'Ingénieurs de Sfax, BP N° 1173, Sfax, 3038, Tunisie.
mohamed.haddar@enis.rnu.tn

ABSTRACT

Viscoelastic components are a key element in designing desired dynamic behavior of mechanical systems. In this paper, a visco-tribological model was developed by coupling the rheological Generalized Maxwell model and Dahl friction model. Parameters of the proposed model are identified from Dynamic Mechanical Analysis (DMA) tests for different excitation frequencies. Comparison between measurements and simulations of hysteretic friction of the viscoelastic component has been carried on.

1 INTRODUCTION

In most of Multi-body simulations (MBS), the dynamic behavior of viscoelastic joints is usually overlooked or, at best, greatly simplified. Hence, to improve description and prediction, global models of mechanisms must represent joints between solids, not only to model the free relative degrees of freedom to take into account the kinematics involved but also stiffness and damping in the broad meaning. Several experimental studies have been carried out to characterize dynamic behavior of viscoelastic components depending on frequency (Oberst and Frankenfeld [1], Barbosa and Farage [2], Castello et al. [3] and Chevalier [4]). In this work, Dynamic Mechanical Analysis (DMA) is used to determine the dynamic characteristics of the viscoelastic component depending on the frequency. Furthermore, different models describing viscoelastic behavior have been developed (Gaul et al. [5], Park [6] Huynh et al. [7] and Koeller [8]). In this study, Generalized Maxwell Model is used to characterize dynamic behavior of viscoelastic joints. But, Energy losses are not only due to viscoelastic nature of joints but it is also strongly linked to the friction properties of joints. Numerous models of friction have been developed and presented in the literature namely Dahl model [9] which incorporates a state variable to model presliding displacement. Dahl model is used in this study to characterize friction of viscoelastic joints.

This paper focuses on both internal and interfaces damping of viscoelastic joints, a new visco-tribological model was developed by coupling the rheological linear Generalized Maxwell model and Dahl friction model. Comparison between measurements and simulations is performed and the validity of the proposed model is discussed.

2 EXPERIMENTAL CHARACTERIZATION

DMA tester is used to characterize the dynamic behavior of cylindrical rubber sample, see figure 1. Double shear tests are performed under different static preloads P= [150, 500, 1000] N and frequency range f= [2.5...70] Hz and at room temperature T=20°C . The mechanical solicitations are performed using hydraulic cylinder with a displacement sensor and a force sensor built into the base of the apparatus. Samples are placed between two rigid surfaces and devices measure the generated force F and the horizontal displacement x. The force and displacement signals after analog conditioning are returned on spectrum analyzer for digital processing.

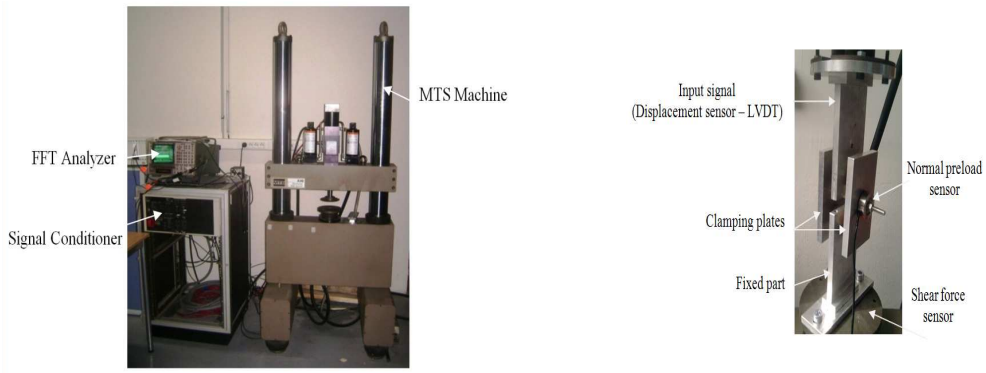

Figure 1. Test bench.

The dynamic stiffness is given by the ratio of the dynamic force and the horizontal displacement

$$K^* = \frac{F}{x} \tag{1}$$

Force-Displacement diagram is used here to characterize the dynamic behavior of the viscoelastic joint.

Area enclosed by the loading and unloading curves of hysteresis loops corresponds to the energy dissipated as heat during cycles. The more is the hysteresis in force-displacement curves, the greater is the energy dissipation and the higher is the damping ability.
The first cycles of the test show ellipsoid curves which correspond to the viscoelastic behavior. The non-linear behavior appears as a distortion of the pure elliptical form of the curves (Fig 2). These non-linearities are due to the frictional damping. For small displacements, friction is driven by micro-slip and partial slip, while for high displacement; the shape of the curve clearly shows macro slipping behavior. The quasi vertical part of the curve represents the system stiffness. The horizontal part of the curve is the significant behavior of the slip. Most parametric models Dahl [9], Canudas de Wit et al. [10], Al Majid and Dufour [11], Awrejcewicz [12] can be identified with this kind of curves.

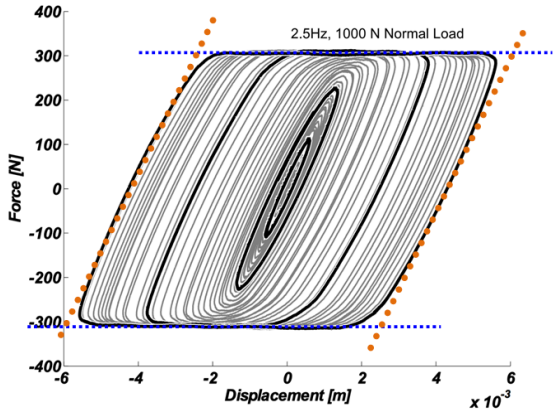

Figure 2. Force-Displacement relation for rubber component subjected to cyclic shear loading.

3 DESCRIPTION OF VISCO-TRIBOLOGICAL MODEL

The visco-tribological model was developed by coupling the rheological Generalized Maxwell model and Dahl friction model.

3.1 The Dahl model

The Dahl model [9] is a dynamic model of frictional behavior built with internal state variable of kinematic type. Dahl proposed to model friction by the following relation:

$$\begin{cases} \dfrac{dz}{dt} = v\left|1-\dfrac{F}{F_{\max}}sign(v)\right|^{\alpha} sign\left(1-\dfrac{F}{F_{\max}}sign(v)\right) \\ F(t)=\sigma z(t) \end{cases} \tag{2}$$

Where F is the frictional force, z is the internal displacement state variable, σ is homogeneous with stiffness, $F_{\max}$ the Coulomb force (maximum friction force reached) and $\alpha \in \mathrm{R}_*^+$ is a constant parameter, x is the relative displacement and $\dot{x}=v$ the relative velocity between two contact surfaces.

3.2 The Generalized Maxwell Model

Generalized Maxwell Model (GMM) allows an accurate description of the dynamic behavior of a viscoelastic joint. The linear GMM chosen is composed of a linear spring and N linear Maxwell cells [8] , see figure 3. The rheological formulation of the dynamic stiffness of GMM is

$$Z(\omega) = K_0 + \sum_{i=1}^{N} \frac{j\omega K_i C_i}{K_i + j\omega C_i} \tag{3}$$

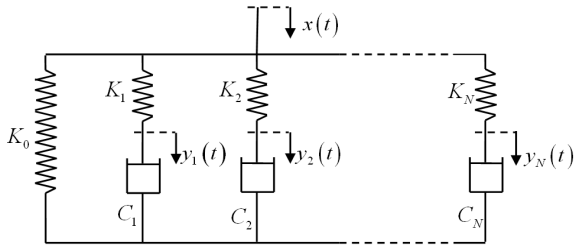

Figure 3.The proposed GMM.

K_0 is the stiffness taken at $\omega = 0$, ie. $t = +\infty$, K_i is the stiffness of the i^{th} spring and C_i is the damping of the ith dashpot.

3.3 *The visco-tribological model*

The visco-tribological model chosen is based on both of Dahl model and linear GMM model. These two models are combined by assuming that the force generated by the frictional spring of Dahl, $F(t) = \sigma z(t)$ is viscoelastic, that is to say that σ will be modeled by generalized Maxwell. During the imposed displacement $x(t)$, the frictional spring will stretch of $z(t)$. It is considered that $z(t) = x(t)$.

$$\begin{cases} \dot{z}(t) = \dot{x}(t)\left|1 - \dfrac{F(t)}{F_{\max}} sign\left(\dot{x}(t)\right)\right|^{\alpha} sign\left(1 - \dfrac{F(t)}{F_{\max}} sign\left(\dot{x}(t)\right)\right) \\ F(t) = K_0 z(t) + \sum_{i=1}^{N} K_i \left(z(t) - y_i(t)\right) \\ K_i \left(z(t) - y_i(t)\right) = C_i \dot{y}_i(t) \\ F_{\max} = \mu F_N \end{cases} \quad (4)$$

Where μ is the friction coefficient and F_N is the normal load.

4 VALIDATION RESULTS

Figure 4 shows comparison between measurement and simulation of the Force-Displacement curves. The proposed visco-tribological model describes the behavior of rubber specimen with satisfying accuracy.

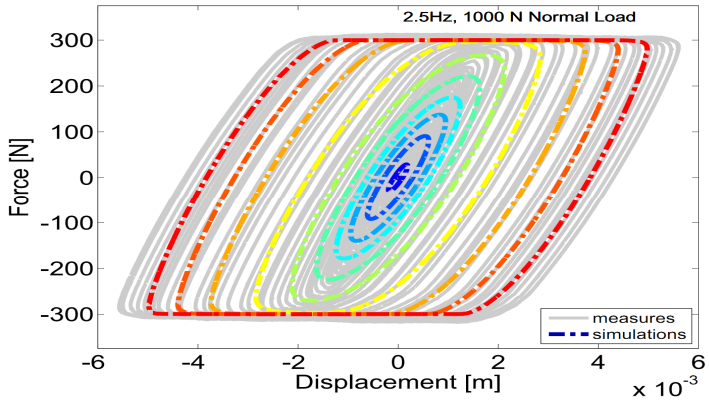

Figure 4. Measured and simulated Force-Displacement curves superposed one above the other.

The quality of fitting between simulations and measurements in figure 4 is similar for most of the carried out tests.

5 CONCLUSION

In a complex mechanism, the level of vibration strongly depends on its dissipation in the connected parts which present both friction and damping behavior.
The visco-tribological model proposed in this study is an internal state variable model which takes into account the viscoelastic dynamic behavior of the joint and can be employed on several scales and implemented in structural computations.

REFERENCES

[1] Oberst, H. and Frankenfeld, K., "Damping of the bending vibrations of thin laminated metal beams connected through adherent layer," Acustica 2, pp. 181–194, 1952.

[2] Barbosa, F. and Farage, M., "A finite element model for sandwich viscoelastic beams : Experimental and numerical assessment," Journal of Sound and Vibration, vol. 317, no. 1-2, pp. 91 – 111 , 2008.

[3] Castello, D., Rochinha, F., Roitman, N. and Magluta, C., "Constitutive parameter estimation of a viscoelastic model with internal variables," Mechanical Systems and Signal Processing, vol. 22, no. 8, pp. 1840 – 1857, 2008.

[4] Chevalier, Y., "Essais dynamiques sur composites. caractérisation aux basses fréquences.," tech. rep., Techniques de l'ingénieur, 2002.

[5] Gaul, L., Klein, P. and Kemple, S., "Damping description involving fractional operators,"Mechanical Systems and Signal Processing, vol. 5, no. 2, pp. 81 – 88, 1991.

[6] Park, S.W, "Analytical modeling of viscoelastic dampers for structural and vibration control," Int. J. of Solids and Struct., 38, pp. 8065 – 8092, 2001.

[7] Huynh, A., Argoul, P., Point, N. and Dion, J. L., " Rheological models using fractional derivatives for linear viscoelastic materials: Application to identification of the behavior of elastomers," 13th Symposium Noise, Shock & Vibration, Lyon, 2002.

[8] Koeller, R. C., "Applications of fractional calculus to the theory of viscoelasticity," Journal of Applied Mechanics, 51(2) :299–307, 1984.

[9] Dahl P. R., A solid friction model, The Aerospace Corporation, El-Secundo, TOR-158(3107-18), California, 1968.

[10] CanudasdeWit, C. H. Olsson, K. J. Åström, and P. Lischinsky, A new model for control systems with friction, IEEE Transactions on Automatic Control, AC-40, pp. 419-425, 1995.

[11] Al Majid A. et al. Harmonic response of a structure mounted on an isolator modelled with a hysteretic operator: experiments and prediction. Journal of Sound and Vibration, 277(1-2), 391-403, 2004.

[12] Awrejcewicz J., Lamarque C. H., Bifurcation and Chaos in Nonsmooth Mechanical Systems, World Scientific Publishing, Singapore, 2003.

COMPREHENSION OF FRICTION LAW INSTABILITY: APPLICATION TO WIPER BLADE SQUEAL NOISE

F. Dalzin[1], A. Le Bot[1], D. Mazuyer[1], J. Le Rouzic[1], J. Perret-Liaudet[1] and F. Bretagnol[2]

[1]LTDS-UMR 5513 CNRS-Ecole Centrale de Lyon
36 Avenue Guy de Collongue, 69134 Ecully Cedex, FRANCE
Email: fabien.dalzin@ec-lyon.fr, alain.lebot@ec-lyon.fr, denis.mazuyer@ec-lyon.fr, joel.perret-liaudet@ec-lyon.fr

[2]Valeo Systeme d'essuyage
1 Avenue Pierre et Marie Curie, 63500 Issoire, FRANCE
Email: frederic.bretagnol@valeo.com

ABSTRACT

This paper deals with the squeal noise of a wiper/windscreen contact. This contact consists of a single degree-of-freedom mass-spring-damper oscillator submitted to a velocity-dependent frictional force, which follows the Stribeck law. Using the first Lyapunov method, an instability criterion is defined. Starting from this knowledge, experiments were made to understand the origin of this instability on the tribometer LUG. This tribometer measures the friction coefficient, and allows to see the contact between the elastomer and the glass using a macroscope and optical interferometry.

1 INTRODUCTION

Whereas most of friction noise are characterised by its large frequency band response, squeal noise is characterised by a narrow frequency band around 1000 Hz. A lot of squeal noises exist: break squeal, wiper/windscreen contact, violin/bow contact, rail/road noise in curvature, shalkpiece of chalk / blackboard squeal...All of these examples concern mechanical instability, but have different origins. Studies were made to understand the apparition of instability, directly linked to the squeal noise phenomenon:

In the case of a elastomer/glass contact, A. Koenen $\&al.$ [1] analysed the major role of the Stribeck curve regarding the instability, and the importance of water and sliding velocity. Le Rouzic $\&al.$ [2] made experiments and built a model starting from their observation on the Stribeck curve.

The aim of this presentation is to understand the relationship between the instability and the evolution of elastomer/glass contact through the Stribeck curve.

2 INSTABILITY AND STRIBECK CURVE: OBSERVATION

2.1 Studied system

In this section, we study an elastomer/glass lubricated contact, for different sliding velocities. The elastomer sample is put on a rotating disk. Normal and tangential forces are measured, so the friction coefficient can be computed.

2.2 Stribeck curve

Squeal noise appears only for certain sliding velocities, and a certain quantity of water. Thus, Stribeck curve is a good tools to determinate the instability range.

Stribeck curve represents the evolution of the friction coefficient for a lubricated contact according to the Sommerfeld number S, depending of the sliding velocity v, as shown in figure 1.

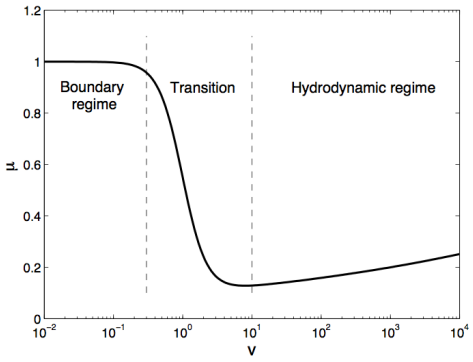

Figure 1. Example of Stribeck curve

There are three regimes in this curve:
- The boundary regime, corresponding to a high friction coefficient.
- The mixed/transition regime, corresponding to a decreasing friction coefficient.
- The elastohydrodynamic (EHD) regime, corresponding to a low friction coefficient.

2.3 Stribeck curve fitting

Bongaerts $\&al.$ [3] obtained an empirical equation fitting the Stribeck curve:

$$\mu(v) = \left[c * v^q + \frac{1}{1+(\frac{v\eta}{b})^p}(a * v^n - c * v^q)\right] \quad (1)$$

Thus, it is possible to construct an accurate Stribeck curve with only 15 points.
The coefficients a, b, c, n,p, and q could be directly "read" on the curve and have a physical meaning.

3 STABILITY ANALYSIS

3.1 Model

Le Rouzic $\&al.$ [2] constructed a model of the contact between the glass and the elastomer. This contact consists of a single degree-of-freedom mass-spring-damper oscillator submitted to a velocity-dependent frictional force, which follows the Stribeck law, see figure 2.

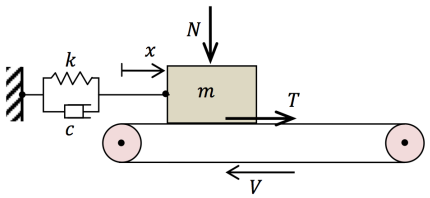

Figure 2. Friction-induced vibration of a mass spring oscillator.

The damping ratio ζ is defined as $\zeta = \frac{c}{2m\omega}$ and the natural frequency is $\omega^2 = \sqrt{\frac{k}{m}}$.

3.2 Stability analysis

Using the first method of Lyapunov, Le Rouzic $\&al.$ [2] shown the model leads to the criterion:

$$\begin{cases} \frac{d\mu}{dv} < \frac{-2\zeta k}{\omega N} : \text{UNSTABLE} \\ \frac{d\mu}{dv} > \frac{-2\zeta k}{\omega N} : \text{STABLE} \end{cases} \quad (2)$$

where v is the relative velocity between glass and elastomer: $v = V - \dot{x}$.
When $\frac{d\mu}{dv} < \frac{-2\zeta k}{\omega N}$, the equilibrium is unstable and leads to a periodical response (limit cycle).

3.3 Experimental verification

For different sliding velocity, the friction coefficient of an elastomer/glass lubricated contact is measured (figure3.a).
Figure 3.b shows the elastomer vibration measured with a vibrometer versus sliding velocity. The instability, i.e. an strong amplitude of the vibration, occurs only when the friction coefficient strongly decreases, in mixed regime.
So, the criterion is in adequacy to the observations on the Stribeck curve.

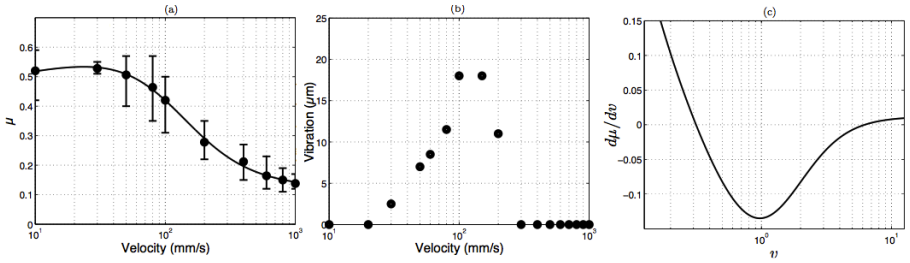

Figure 3: (a) Friction coefficient versus sliding velocity. (b), Vibration amplitude versus velocity. (c), Slope of the empirical fit translated by 2 ζ with $\zeta = 0.006$.

4 OBSERVATION OF THE CONTACT

Deleau $\&al.$ [4] observed the relation between the dynamic of the elastomer/glass contacts, and the Stribeck curve. Following his research, we analysed on the tribometer LUG the interferometry images we get, see figure 4. The tribometer LUG measures the friction coefficient, and allows to see the contact between the elastomer and the glass using a macroscope and optical interferometry.

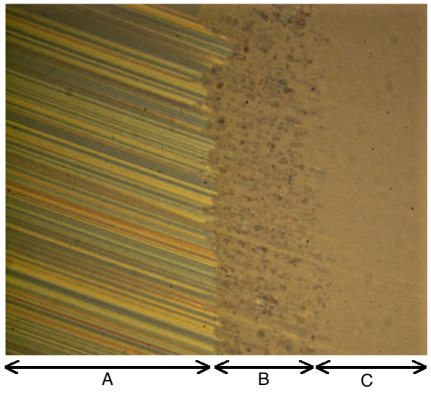

Figure 4. Contact between glass and elastomer.

On the left on the image (A), the different streaked colors correspond to different very thin water thickness.
On the center (B), the contact elastomer/glass can be seen. This contact is composed of a multitude of contact spots. As was mentioned previously, the different colors of these spots correspond to different water thin thickness.
On the right on the image (C), only water is present.

REFERENCES

[1] A. Koenen and A. Sanon. Tribological and vibroacoustic behaviour of a contact between rubber and glass (application to wiper blade). *Tribology International*, 40:1484–1491, 2007.

[2] J. Le Rouzic, J. Perret-Liaudet, A. Carbonelli, A. Le Bot, and D. Mazuyer. Some experimental and analytical results on self-excited vibration of a dynamic sliding system in the case of stribeck law for friction coefficient. In *International Design Engineering Technical Conferences & Computers and Information in Engineering Conference*, 2011.

[3] J.H.H. Bongaerts, K. Fourtouni, and J.R. Stokes. Soft-tribology lubrification in a compliant pdms-pdms contact. *Tribology International*, 40:1531–1542, 2007.

[4] F. Deleau, D. Mazuyer, and A. Koenen. Sliding friction at elastomer/glass contact: Influence of the wetting conditions and instability analysis. *Tribology International*, 42:149–159, 2009.

DIRECT NUMERICAL SIMULATION OF FRICTION NOISE

DANG Viet Hung[1] , LE BOT Alain[1*], Joel PERRET-LIAUDET and Julien SCHEIBERT [2]

[1]Laboratoire de Tribologie et Dynamique des Systèmes
Ecole Centrale de Lyon or address, 36 Avenue Guy de Collongue,69134 Ecully Cedex, FRANCE
Email: viet-hung.dang2@ec-lyon.fr, Alain.Le-Bot@ec-lyon.fr

ABSTRACT

The friction of two solids with rough surfaces produces a typical sound generally called roughness noise [1]. This study focuses on the numerical simulation of what happens into the contact during the sliding. The mechanical equations of vibrating solids in contact are first set. They are solved by a modal approach. The contact is modeled at the scale of surface asperities which requires a very fine discretization. The results show that this approach is several times faster than the classical finite element method. Furthermore, it reproduces the empirical laws observed experimentally and provides the statistical properties of local events which are not accessible by experiment.

1 INTRODUCTION

The sound produced by rubbing two rough surfaces under light contact pressure is called roughness noise [1]. Some examples of this noise are hand rubbing, stridulatory sound by insects or tyre/road contact noise [2]. The origin of this noise lies in the mechanical shocks between asperities of both surfaces [3]. The knowledge of what happens into the contact during the sliding is therefore the key for understanding the vibrational and acoustical behaviour of the system.

2 MODELLING

The simulation of is based on a 2D model which is made up of two nominally flat rough profiles in contact as shown in Figure 1. The top profile moves horizontally with a constant velocity V

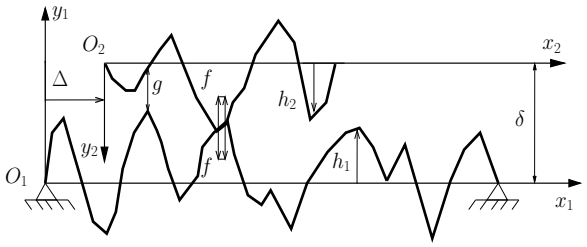

Figure 1. Sliding of two rough profiles. At time t, the horizontal offset is imposed $\Delta = Vt$

while the bottom profile is fixed at both ends. The initial vertical gap i.e. the separation between the two reference lines of the profiles is δ. During the movement asperities of the top profile can hit asperities of the bottom profile.

We make the following assumptions:

- The vertical deflection of the profiles follows the Euler-Bernoulli theory of beams (Small flexural vibration).

- The profiles are infinitely rigid in the horizontal direction and therefore the horizontal position of node is imposed (No longitudinal vibration).

- Profiles cannot penetrate each other (Signorini's condition).

- The persistence of contact is ensured by a vertical gravity force.

3 VALIDATION

The proposed modelling is implemented in the software Ra2D and validated by a comparison with the finite element software ABAQUS Explicit. A toy model formed by two simple rough surfaces rubbed against each other is used. The top profile consists of only one peak whereas the bottom profile consists of six peaks as illustrated in Figure 2a. In Figure 2b shows a good agreement between the displacement of the summit of top asperity obtained by RA2D (red) and ABAQUS (blue). Furthermore, the CPU time with RA2D is 30s which is faster around 10 times than those with ABAQUS (280s).

4 RESULTS

A realistic sliding contact problem between two multi-asperity profiles is presented. The system is made of two solids, a parallelepipedic solid moving on a simply supported Euler beam. The numerical simulation are performed with the following parameters: time step $\tau = 0.1\ \mu s$, duration of simulation $T = 1$ s, space step χ=5 μm, number of nodes of lower profile: 90000.

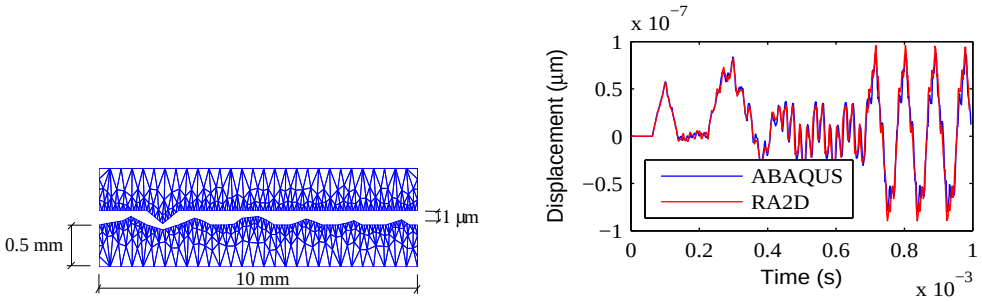

(a) (b)

Figure 2: Comparison between RA2D with ABAQUS.(a) Mesh in ABAQUS of the simple asperity problem. Displacement of the summit of top asperity obtained by RA2D (red) and ABAQUS (blue)

The shock between one node with the antagonist surface is determined mathematically from the time evolution of the contact force of this node. When the contact pressure is non-zero, the shock occurs. A shock may be caracterized by three properties the shock duration Δt, the maximal absolute value of contact force and the transferred energy ΔW.

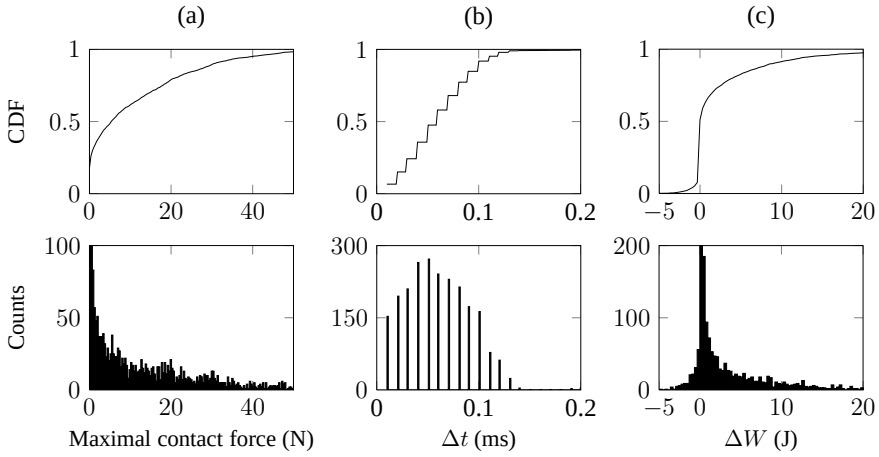

Figure 3: Cumulative distribution function (top) and histogram (bottom) of shock properties for Ra=5 μm, and V=70 cm/s. (a) Maximal contact force of shock, (b) Shock duration, (c) Transferred energy.

The macroscale vibration level Lv of the resonator can be obtained as the space and time average of the vibrational velocity of nodes in the simulation. The vibration level is found to be a linear increasing function of the logarithm of both the surface roughness and sliding speed in good agreement with experimental results from the literature.

Finally, the CPU time is 9930 s (2.8 hours) per simulation. This is to be compared with several days of CPU time using the finite element method.

5 CONCLUSION

The comparison with the finite element method allows to validate the proposal modelling and enhance its rapidity. The realistic problem allows the full consideration of the statistical properties of asperity-scale shocks. The shock durations are of order of 1e-4 s. The histogram of the transferred energy per shock is asymmetric. When the transferred energy is positive, shocks

act as the vibration and noise sources. On the contrary, the negative value of transferred energy dissipate the vibrational energy of the resonator.

REFERENCES

[1] A. Akay. Acoustics of friction. *Journal of the Acoustical Society of America*, 111(4):1525–1548, 2002.

[2] G. Dubois, J. Cesbron, H.P. Yin, and F. Anfosso-Lde. Numerical evaluation of tyre/road contact pressures using a multi-asperity approach. *International Journal of Mechanical Sciences*, 54(1):84 – 94, 2012.

[3] H. Ben Abdelounis, H. Zahouani, A. Le Bot, J. Perret-Liaudet, and M. Ben Tkaya. Numerical simulation of friction noise. *Wear*, 271(3-4):621 – 624, 2010.

VIBRATIONS OF A SELF-EXCITED TOWER UNDER TURBULENT WIND FLOW IN THE PRESENCE OF A HIGH FREQUENCY EXCITATION

I. Kirrou, L. Mokni and M. Belhaq

Laboratory of Mechanics
University Hassan II-Casablanca, Morocco
Email: ilhamkirrou@gmail.com, mbelhaq@yahoo.fr

ABSTRACT

This work investigates the effect of high frequency excitation (HFE) on tower oscillations under turbulent wind flow near the primary resonance. An averaging technique over the HFE is performed to derive an equation governing the slow dynamic. A perturbation technique is then used to obtain reduced autonomous slow flow equations governing the amplitude and the phase of the response. Analysis of quasi-periodic vibrations is carried out by performing multiple scales method on the slow flow. Results show that HFE may shift the frequency response and delay Hopf bifurcation. Also it is shown that this excitation can be used to eliminate quasi-periodic responses by frequency-locking phenomenon. For validation of the analytical results, comparisons with numerical simulations are given.

1 INTRODUCTION

Considerable efforts have been devoted to the control of linear and nonlinear vibrating structures in general and taller towers in particular. Many of these taller towers are more flexible and aerodynamically sensitive to the natural wind environment. There have been a number of reported failures of towers because of design, construction or maintenance problems and these failures were traced to the neglect of dynamic effects. Consequently, it is important to obtain more information on the dynamic response of tall towers subjected to time-varying wind forces in the natural environment. Wind induces aerodynamic forces in the tower structures. This is the case of structures subject to steady wind where the aerodynamic force introduces a damping term depending on the wind velocity [1].

In this work, attention will be focused on the effects of a high-frequency excitation (HFE) on the dynamic of a self-excited structure under turbulent wind. The structure consists of a tower considered as a linear elastic multistory shear-type frame, modelled through a corresponding homogeneous scheme of continuous shear cantilever and then discretized as one SDOF system via the Galerkin method. For details on the formulation, see [2]. The direct partition of motion (DPM) [3] technique is used to split up the fast and the slow dynamics. Then, the method of multiples scales (MSM) is applied under a specific resonance condition to derive the modulation equations, thereby the frequency-response curves. These curves are used to analyze the effect of the fast excitation on the Hopf bifurcation and on the frequency shift of the tower response. Quasi-periodic oscillations and frequency-locking phenomenon are also examined.

2 EQUATION OF MOTION AND SLOW DYNAMIC

Consider a SDOF model of a discrete non-dimensional, time periodic system, in the form [2]

$$\ddot{x} + x + (c_a(1-\bar{U}) - b_1 u(t))\dot{x} + b_2\dot{x}^2 + (\frac{b_{31}}{\bar{U}} + \frac{b_{32}}{\bar{U}^2}u(t))\dot{x}^3 = \eta_1\bar{U}u(t) + \eta_2\bar{U}^2 + Y\cos(\nu t) \tag{1}$$

where the dot denotes differentiation with respect to the non-dimensional time t. Equation (1) contains elastic, viscous and inertial linear terms, as well as quadratic and cubic components in the velocity, generated by the aerodynamic forces. Y and ν are the amplitude and the frequency of the fast excitation, respectively. The turbulent part is considered as periodic and constituted of its first two frequencies: $u(t) = u_1\sin(\Omega t) + u_2\sin(2\Omega t)$, where u_1 and u_2 are the amplitudes and Ω is the fundamental frequency. In this case, Eq. (1) contains a slow dynamic due to the external excitation and a rapid dynamic produced by the frequency ν. To investigate the effect of the rapid excitation on the slow dynamic of the tower, we use the method of DPM [3–5] which consists in introducing two different time scales, a fast time $T_0 = \nu t$ and a slow time $T_1 = t$, and splitting up $x(t)$ into a slow part $z(T_1)$ and a fast part $\phi(T_0, T_1)$ as

$$x(t) = z(T_1) + \mu\phi(T_0, T_1) \tag{2}$$

where z describes the slow main motions at time-scale of oscillations, $\mu\phi$ stands for an overlay of the fast motions and μ indicates that $\mu\phi$ is small compared to z. Substituting Eq. (2) into Eq. (1) gives the main equation governing the slow dynamic of the motion

$$\ddot{z}+(c_a(1-\bar{U})-b_1u(t)+H(\frac{b_{31}}{\bar{U}}+\frac{b_{32}}{\bar{U}^2}u(t)))\dot{z}+z+\phi+b_2\dot{z}^2+(\frac{b_{31}}{\bar{U}}+\frac{b_{32}}{\bar{U}^2}u(t))\dot{z}^3 = -G+\eta_1\bar{U}u(t)+\eta_2\bar{U}^2 \tag{3}$$

where $H = \frac{3Y^2}{2\nu^2}$ and $G = -\frac{b_2Y^2}{2\nu^2}$.

3 APPLICATIONS AND RESULTS

In this section, we analyze the frequency-response curve of the slow dynamic Eq. (3) by applying the MSM near the primary resonance and we examine the effect of various parameters on the tower response. The parameter values used for the present study are taken from [2].

3.1 Case of non-turbulent wind flow

The behavior of the system, in the absence of turbulence $(u_1 = u_2 = 0)$, for $\sigma = 0$, is described in Fig 1. The trivial solution exists everywhere and changes its stability at the bifurcation point. In this figure, we show the effect of the amplitude of the fast excitation on the frequency response of the system. It can be seen from this figure that increasing the amplitude of HFE, the amplitude of the tower response decreases and the Hopf bifurcation point shifts right.

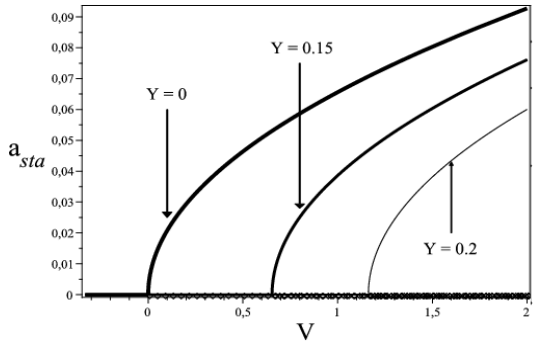

Figure 1: Equilibrium branches in the absence of turbulent wind, for $\nu = 8$. Solid line: stable; points: unstable.

3.2 Case of turbulent wind flow

In Fig. 2, we show the effect of the amplitude of the HFE on the frequency response when $(u_1 \neq 0, u_2 = 0)$. Figure 2a illustrates the amplitude of the tower response versus the velocity of the wind V, for $u_1 = 0.1$ and $\nu = 8$. These plots indicate that as the amplitude of the HFE increases, the amplitude of tower decreases and shifts right. If V is kept fixed and σ is varied, the amplitude of oscillations behave as shown in Fig. 2b, where different values of the amplitude Y are considered. It can be seen that as Y is increased the amplitude of the tower response decreases.

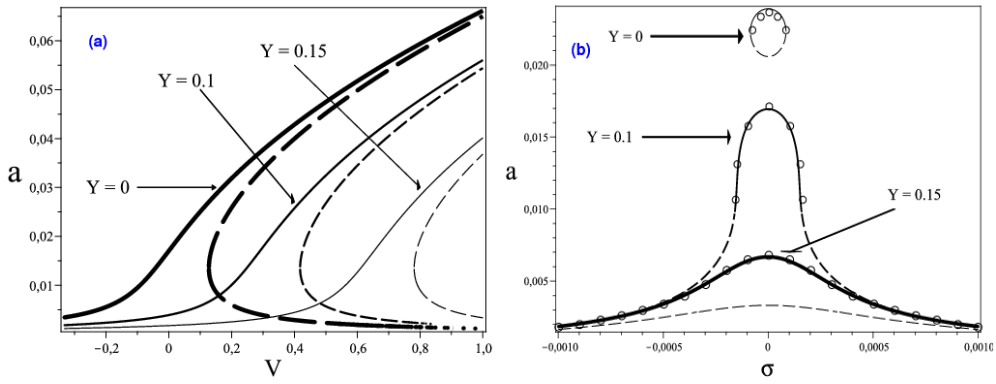

Figure 2: Amplitude response curve when $u_2 = 0$ and $\nu = 8$, (a): $\sigma = 0$, $u_1 = 0.1$, (b): $V = 0.117$, $u_1 = 0.033$, . Solid line: stable; dashed: unstable; circle: numerical simulation.

4 QUASI-PERIODIC MODULATION AND FREQUENCY-LOCKING

In Fig. 3, we show a global picture including the quasi-periodic modulation area and the amplitude frequency response for different values of the amplitude of HFE, for $\nu = 8$. These figures show that when we increase Y, the amplitude of the quasi-periodic modulations decreases and a synchronization phenomenon occurs near the resonance. The analytical approximation (solid line) of the synchronization area and the modulation amplitude is confirmed by the results obtained by numerical simulation (circles).

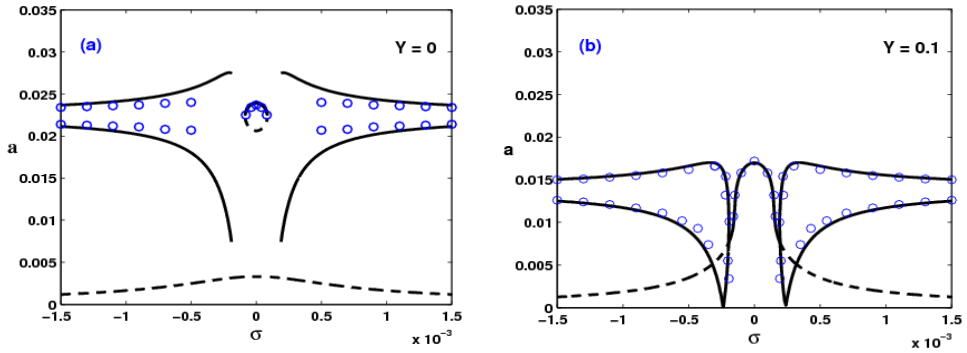

Figure 3: Amplitude versus σ when $V = 0.117$, $u_1 = 0.033$, $u_2 = 0$ and $\nu = 8$. Solid line: stable; dashed: unstable; circle: numerical simulation.

5 CONCLUSION

In this work, we have investigated the effect of a fast excitation on the response of a tall structure under turbulent wind flow near the primary resonance. The method of DPM and the MSM are used to derive a slow dynamic. Different cases of excitations are considered and analyzed in terms of equilibrium branches of amplitudes. When the wind is non-turbulent, results show that changing the amplitude of the fast excitation causes the Hopf bifurcations curve to shift right. When the turbulence produces external excitation only, fast frequency causes the amplitude response to decrease significantly and to shift right. It was also shown that increasing the amplitude of the fast excitation reduces the amplitude of the quasi-periodic response and produces a synchronization near the resonance.

REFERENCES

[1] R. Clark, A. Modern, Course in Aeroelasticity, fourth ed, Kluwer Academic Publishers, Dordrecht, The Netherlands, 2004.

[2] A. Luongo, D. Zulli, Parametric, external and self-excitation of a tower under turbulent wind flow, J. Sound Vib. 330, 3057-3069, 2011.

[3] I. I. Blekhman, Vibrational Mechanics, Nonlinear Dynamic Effects, General Approach, Applications. Singapore: World Scientific, 2000.

[4] M. Belhaq, A. Fahsi, Hysteresis suppression for primary and subharmonic 3:1 resonances using fast excitation. Nonlinear Dyn. 57, 275-287, 2009.

[5] F. Lakrad, M. Belhaq, Suppression of pull-in instability in MEMS using a high-frequency actuation. Commun Nonlinear Sci Numer Simulat. 15, 3640-3646, 2010.

Numerical simulation and experimental validation of gap supported tube subjected to fluid-elastic coupling forces for hybrid characterization tests

W.Benmalek[1&2], M.Collet[1], E.Foltete[1], M.Ouisse[1], M.Corus[2] and I.Negreanu[2]

[1]FEMTO-ST Institute, Applied Mechanics Department, 24 rue de l'épitaphe, 25000 Besançon, France
Email: wissam.benmalek@femto-st.fr, manuel.collet@univ-fcomte.fr
emmanuel.foltete@univ-fcomte.fr , morvan.ouisse@univ-fcomte.fr

[2] Electricité de France R&D, 1 Avenue du Général de Gaulle, 92141 Clamart Cedex, France
Email: mathieu.corus@edf.fr, ionut.negreanu@edf.fr

ABSTRACT

In steam generators, the primary loop tubes are subjected to fluid coupling forces and impacts. Understanding the behavior of these tubes is crucial when designing steam generators. In fact, it can afford an optimization of produced energy and a long average life of the structure.

Up to now, the effect of the coupling forces on structural behavior was identified on reduced scale structures. Thus, the aim of our research is to give a better understanding of stabilizing effects of shock and coupling with fluid elastic forces. In order to validate numerical investigations, since fluid elastic forces are difficult simulate and expensive to reproduce experimentally, the fluid coupling forces will be assumed to be represented using velocity dependant (fluid and structure) damping and stiffness matrices, and experimentally reproduced using active vibration control into hybrid experimental tests to simplify big structure characterization.

In this paper, a method for modeling the structure behavior in order to estimate the effects of the coupling between the fluid elastic forces and impacts is presented. This strategy implies lower costs and avoids difficulties associated to the case of fluid in the experiments. This model will be implemented in the active control loop in the next step of the study.

1 INTRODUCTION

Steam generators are heat exchangers used to convert water into steam from heat produced in a nuclear reactor core. They are used in pressurized water reactors between the primary and secondary coolant loops.

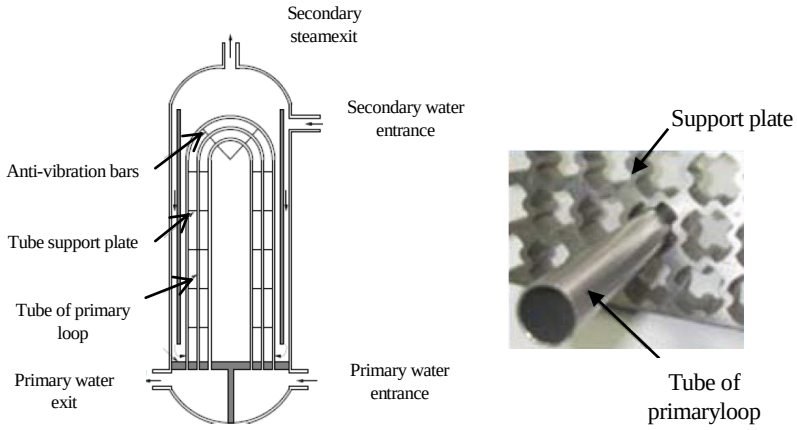

Figure 1. Steam generator

When the steam generator is working, the phase of water in the secondary loop changes partially form liquid to steam. This fluid, when rising up with high velocity and pressure, interacts with the tubes of the primary loop (inversed U shaped), thus the tube is subjected to flow excitation.
This excitation can be split into two kind of forces:Turbulence forces which are independent of the movement of the tube andthe so-called fluid-elastic coupling forces, depending on acceleration, velocity, displacement and fluid velocity [1], [2]. The total flow excitation can be finally expressed as:

$$F_t + F_f(\ddot{x}, \dot{x}, x, Vr) = F_t - M_f.\ddot{x} - C_f(Vr).\dot{x} - K_f(Vr).x \quad (1)$$

$$V_r = V/(f * D)$$

With
F_t : Fluid turbulence force
F_f : Fluid-elastic coupling force
V_r: Fluid reduced velocity
V: Fluid velocity
f : frequency of vibration
C_f: Fluid-elastic damping coupling matrix, depending on Vr
M_f: Fluid added mass Matrix
K_f: Fluid-elastic stiffness coupling matrix, depending on Vr
D : tube diameter

Under some specific conditions of steam pressure and velocity, $C_f$is enough negative to render the structure instable, this phenomenon is called fluid-elastic instability, which can damage the structure. However, the primary tubes as presented infigure 1,are supported by a plate which guide them and limit their amplitude of vibration. In fact, the impacts between tubes and the plate tend tostabilise the system. Thus, we can finally represent the whole problem as below:

$$M \cdot \ddot{x} + C \cdot \dot{x} + K \cdot x = F_t + F_f(\ddot{x}, \dot{x}, x, V_r) + F_c \quad (2)$$

With
F_c: Impact force
C: Structural damping matrix
M: Structural mass matrix
K: Structural stiffness matrix

Because these mechanisms are complex and difficult to realize into experimental set up,the mean aim of my study is to develop hybrid control loop for simulating this coupling effect into experimental characterization test bench.

2 SYSTEM DESCRIPTION

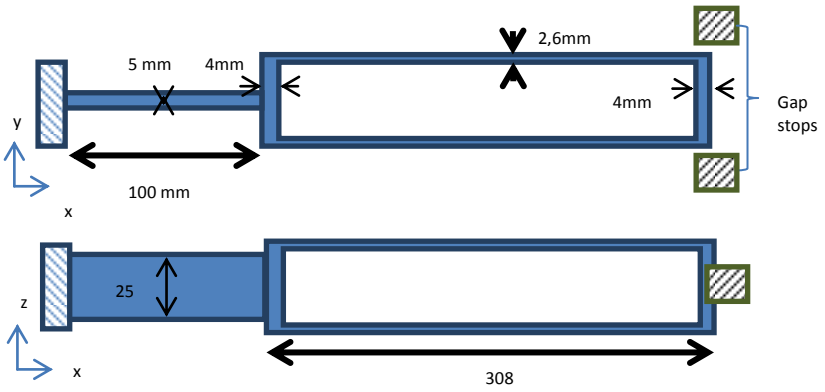

Figure 2. Gap supported tube

The studied structure (figure 2)is composed by a tube attached to a flat plate clamped in rigid block. On the free side, two gap stops are located to create punctual impacts depending on vibration amplitude.
A finite element shell model has been developed to generate mass matrix, damping matrix and stiffness matrix. This model was updated in order to match the numerical behavior with experimental one. Two criterions were used to compare the numerical and experimental model: modal analysis criterion (MAC) and frequency error criterion. The fig.3 summarizes the results for the 6 first modes.

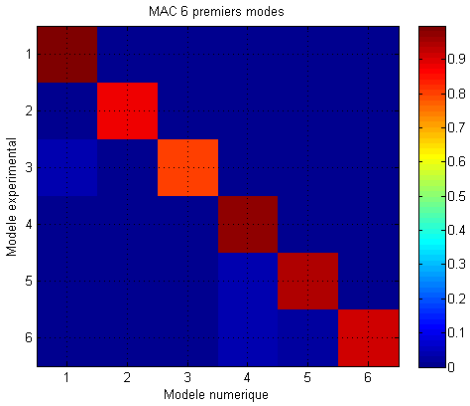

Modes	Numerical modal frequency	Experimental modal frequency	Error
1	23.1	23	~ 0%
2	103	100	3%
3	305	318	4%
4	426	407	4.6%
5	774	798	3%
6	1300	1404	8%
		Mean	3.7%

Figure 3. Modal updating

3 NUMERICAL SIMULATION

Tosimulate the temporal response of the tube, the fluid-elastic coupling forces are projected on the first mode which is predominant in the tube response and the effects of higher modes are almost negligible as explained in the CEA experiments[3]. Concerning the impact forces, they are computed in an explicit manner:

$$\begin{cases} F_c(t) = K_c.(x_c(t) - j) & if\ |x_c(t)| > j \\ F_c(t) = 0 & if\ |x_c(t)| \leq j \end{cases} \quad (3)$$

With

F_c: Impact force

j: Gap distance

x_c: Displacement of tube

K_c: Impact stiffness

The impact stiffness K_c has been identified experimentally by measuring impact duration. This method will be detailed in the presentation.

Figure 3 shows the time response of the free end when the tube is subjected to fluid-elastic and impact force. Newmark time integration method with mean acceleration combined with Newton-Raphson algorithm was used. Exceptionally the supported gap was located in the middle of the tube in order to compare numerical results with CEA experimental ones [3].

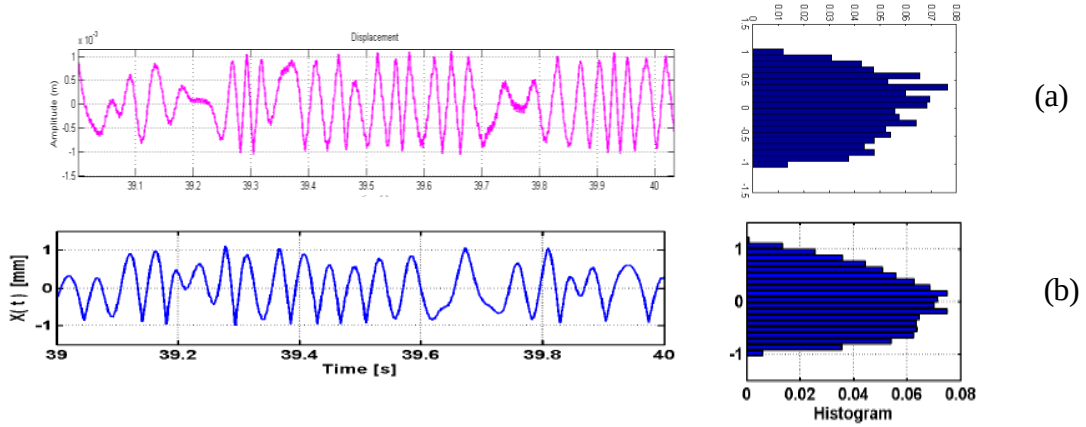

Figure 3. (a) Computed response at fluid velocity 2.5m/s with support gap 0.5mm
(b) Experimental response at fluid velocity 2.5m/s with support gap 0.5mm

As we can see in figure 3, the numerical estimation is close to the experimental one. Furthermore, the difference we notice between the computed and the experimental response is due to turbulence excitation which is a random force and also the uncertainty related to numerical model.

4 CONCLUSION

Actually a numerical model of the structure was gotten; this model was updated by experimental modal analysis. The Newmark integration method gave estimation about the response of the tube subjected to fluid excitation forces and impacts. The next step that we are working on is, to find a controller to reproduce experimentally the fluid effect on the real structure.

REFERENCES

[1] S. T. H. Tanaka, « Fluid elastic vibration of tube array in cross flow », *Journal of Sound and Vibration*, n° 1, p. 19‑37.

[2] H. J. Connors, « Fluidelastic vibration of tube arrays excited by cross-flow », *ASEMA*, p. 42‑46, 1970.

[3] P. Piteau, X. Delaune, J. Antunes, et L. Borsoi, « Vibro-Impact Experiments and Computations of a Gap-Supported Tube Subjected to Single-Phase Fluid-Elastic Coupling Forces », 2010, p. 395‑407.

Taking into account of surface defects in connections in the dynamics of structures assembled

N. PEYRET[1], G. CHEVALLIER[1],J.L. DION[1]and P. ARGOUL[2]

[1]LISMMA
SUPMECA, Saint Ouen, FRANCE
Email: nicolas.peyret@supmeca.fr

[2]Laboratoire NAVIER
(UMR 8205, CNRS, ENPC, IFSTTAR)
Ecole des PontsParisTech, Champs-sur-Marne, FRANCE

ABSTRACT

In structural dynamics, the problem of damping remains the biggest challenge. This paper deals with the energy losses caused by micro-slip in a nominaly planar interface of a structure. Taking into account friction in the joints during the analysis of dynamic systems remains a complex task. This paper proposes an analytical and experimental study of flexural vibrations of a clamped-clamped beam with innovative position of the interfaces.

First, the benchmark is described and the choice of the position of the interface is justified. The experimental bench, and the dynamic behaviour of this structure are presented. We propose to illustrate the mechanism of energy losses by micro-slip by making a comparison between the behaviour of a "monolithic" beam and a sectioned beam.

Secondly, a modelisation of the interface taking into account the surface defect is presented. The energy dissipated by friction in the interface is calculated during a loading cycle. This leads to a definition of the dissipated energy, thus, to a non linear loss factor.

Finally, we confront the loss factor calculated analytically and the measured one.

.

1 INTRODUCTION – PRESENTATION OF THE BENCHMARK

The present work starts from the idea of a previous paper, **Erreur ! Source du renvoi introuvable.**. Firstly the shape of the beam has been improved in order to obtain the greatest damping as possible by increasing the dimensions of the interfaces, see Peyret et al. 0. The final design of this new benchmark was presented in Dion et al. [3].The shape has been designed to avoid coupling between the normal stresses and the vibration motion even if the interfaces have been inaccurately located.

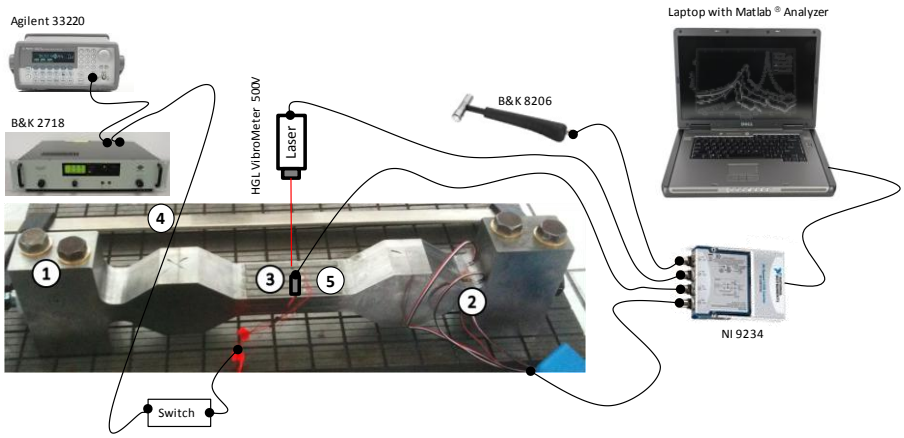

Figure 1. *View of the benchmark screwed on its Steel Surface Plate.Part 1 is a massive part designed to clamp the beam on the heavy Steel Surface Plate. Parts 2 are the strain gauges glued on both sides of the beam to measure the normal load. Part 3 are the piezoelectric patches glued on both sides of the beam to excite the first vibration mode. Part 4 is a quick clamp used to apply the normal load before the tests. Part 5 is the Bruel & Kjaer 4517 miniature accelerometer.*

Piezoelectric transducers have been glued in order to excite the first vibration mode; sensors allow to obtain the normal load in the interfaces and to measure the transverse motion.An original experimental procedure is proposed to stop-sine measurements. The authors justify that their excitation method is more efficient that Dirac (shock) or Heaviside (release of a static load) excitations. Signal processing tools are proposed to post-process the instantaneous damping and frequency of the first mode of the structure. Finally this work experimentally demonstrates the presence of micro-slip damping, by comparing the vibration behaviour of a monolithic part and a built-up structure with friction-joints.This comparison is the best way to determine the "added damping" [4].

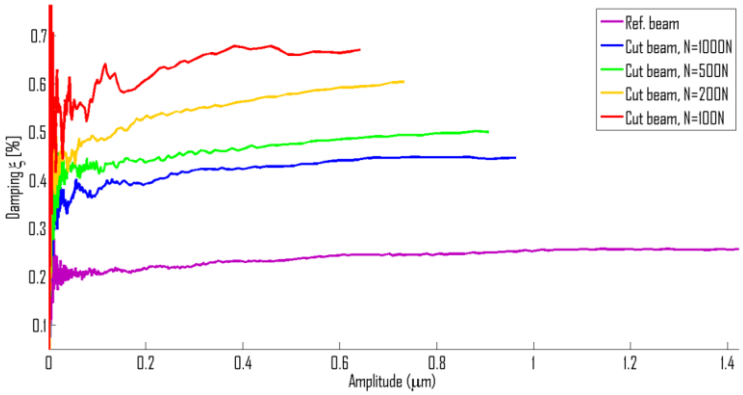

Figure 2. *.Evolutions of damping versus the normal load and versus the displacement magnitude. Both the monolithic (ref. beam) and the cut beam were tested. The latter was tested under four normal load levels in the range 100–1000 N*

2 MODELING OF THE INTERFACE : MULTIPLE SPHERICAL CONTACT

The modeling of the interface by a plane surface can not taking account the fact that there is energy losses for smallest oscillations (Figure 5), this is due to the surface defect.To take into account the geometrical defects with contacts on several sphere, the contact interface is modeled as follows: contact is made with two types of sphere (Figure 3):

- m spheres "G" ensuring the rigidity of the interface, they are the first to come into contact during the implementation of the normal load and can not slide completely (macro-slip) ;
- n spheres "P" potentially slide completely.

Interface load is defined by the normal approachδ_n of the two normal planes constituting the interface. Before loading, the differencebetween height of spheres is defined by h. The spheres are defined by their radius of curvature$\rho_G$etρ_P.

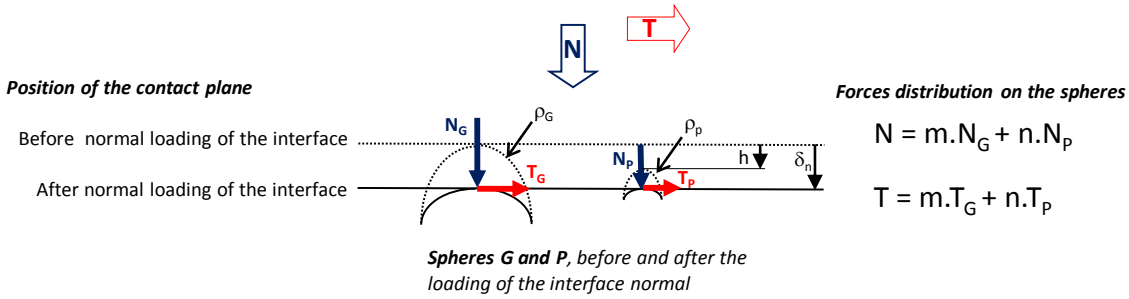

Figure 3. *Modeling of the interface.*

The distribution of forces on the interface is defined by: normal load N and tangential load T. The distribution of these forces on different spheres constituting the contact by N_i and T_i. The distribution of the normal load is a function of the normal approach δ_n and is defined by the Hertz theory[Hertz, 1882].

$$N = \frac{4}{3}E^{*}\left(m\,r_G^{\frac{1}{2}}d_n^{\frac{3}{2}} + n\,r_p^{\frac{1}{2}}\left(d_n - h\right)^{\frac{3}{2}}\right) \quad (1)$$

Once the normal load is applied, a tangential displacement δ is applied between both surfaces of the interface. The assumption is that this displacement is the same for each contact.

In function of the value of δ, two phases can be noticed:

- Spheres G and P did not slip totally: phase called "generalized partial slip" (GPS);
- Spheres G remain in partial slip and spheres P slip totally: phase called "pseudo-partial slip" (PPS).

The distribution of the tangentialload, is function of the normal approach δ_n and is defined by the Mindlin theory [5]:

For the phase of generalized partial slip

$$T = m\,mN_G\left(1-\left(1-\frac{16a_G}{3mN_G G^{*}}d^{\frac{3}{2}}\right)\right) + n\,mN_P\left(1-\left(1-\frac{16a_P}{3mN_P G^{*}}d^{\frac{3}{2}}\right)\right)$$

For the phase of pseudo- partial slip

$$T = m\,mN_G\left(1-\left(1-\frac{16a_G}{3mN_G G^{*}}d^{\frac{3}{2}}\right)\right) + n\,mN_P \quad (2)$$

3 LOSS FACTOR

The loading cycle of the contact and the energy losses are plotted on figure 4.
Taking into account the external force applied on the structure to obtain the dynamic behavior, it is possible to define the loss factor of the structure (see figure 5):

$$h = \frac{W_{diss}}{pW_{ext}} \quad (3)$$

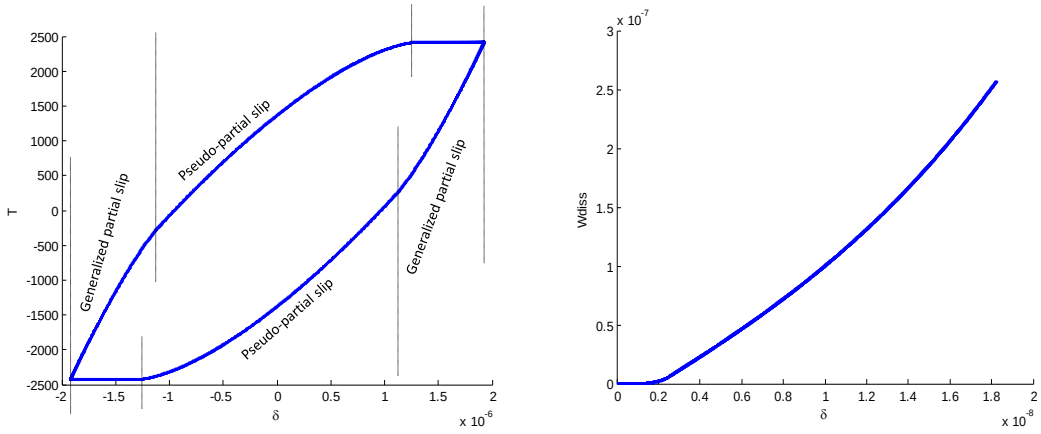

Figure 4. Tangential load Ti (N) (left), energy dissipated Wdiss (J) (right) vs diplacement δ (m)

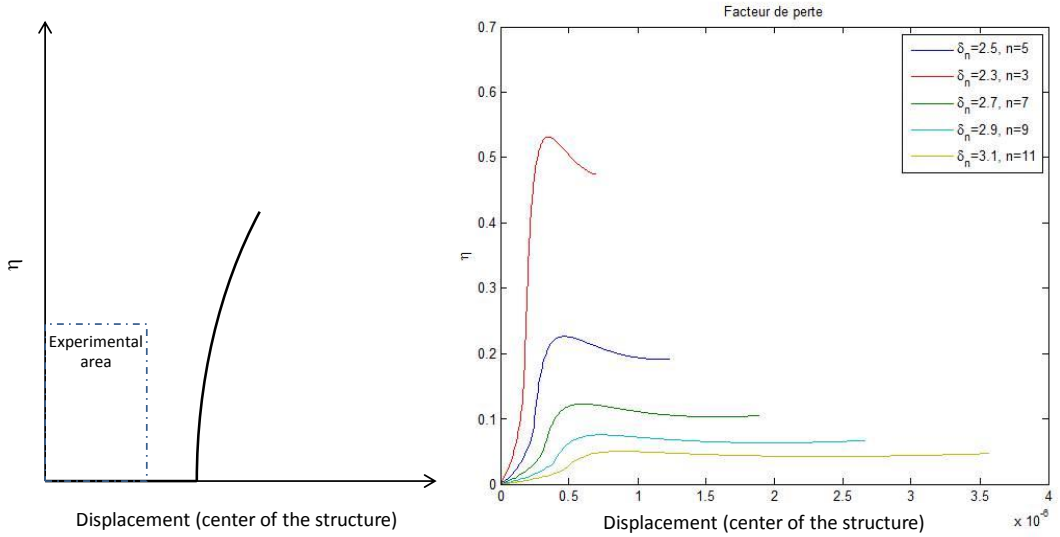

Figure 5. Loss factor η (%) vs υ (m) diplacement at the center of the structurefor plane surface (left) and multiple spherical contact surface (right).

4 CONCLUSION

Unlike a modelling taking into account the interface as a plan geometrically perfect [1], taking into account surface defects allows to model the presence of damping in the interfaces from the smaller amplitudes of oscillation of the structure. This modelling allows us to corroborate the loss factor found experimentally

REFERENCES

[1] N. Peyret, J.L. Dion, G.Chevallier, and P. Argoul.Micro slip Induced damping in planar contact under constant and uniform normal stress. *International Journal of Applied Mechanics*.2(2), 281-304, 2010.

[2] N. Peyret, J.L. Dion, G.Chevallier, and P. Argoul.P.Non linear dynamic behavior modelling of a planar friction interface in a structure assembly.*In Proc. IDETC ASME*, 2009

[3] J.L. Dion, G. Chevallier, and N. Peyret.Improvement of the measurement techniques for the damping induced by micro sliding.Mech. Syst. Signal Process.Article in press2012.

[4] D.J. Segalman. A Modal Approach to ModelingSpatially Distributed Vibration EnergyDissipation. *Sandia Report* , 2010.

[5] R.D. Mindlin. Compliance of elastic bodies in contact. *ASME J. Appl. Mech*, v. 16, p. 259-268, 1949.

THE WAVE BASED METHOD: CURRENT STATE OF THE ART

E. Deckers[1*], O. Atak[1], L. Coox [1], R. D'Amico[1], H. Devriendt[1], S. Jonckheere[1], K. Koo[1], B. Pluymers[1], D. Vandepitte[1] and W. Desmet[1]

[1]KU Leuven, Department of Mechanical Engineering
Celestijnenlaan 300B box2420, Heverlee, BELGIUM
Email: elke.deckers@mech.kuleuven.be, wim.desmet@mech.kuleuven.be

ABSTRACT

Most commonly, element based prediction techniques, such as the Finite Element Method and the Boundary Element Method are used to solve steady state dynamic problems. These procedures divide the problem domain or its boundary into a large number of small elements in which the dynamic fields are described using simple, most often polynomial, shape functions. When frequency increases and the wavelengths shorten, the mesh needs to be refined to obtain accurate solutions, due to interpolation and pollution errors. The sizes of the system matrices, and consequently the computational load, increase accordingly. From a certain frequency on, the models become computationally too demanding, such that the element based techniques are limited for solution at lower frequencies.

The Wave Based Method is also a deterministic numerical prediction technique to solve steady-state dynamic problems, developed to overcome some of these frequency limitations imposed by the use of small elements and simple interpolation functions. The method belongs to the family of indirect Trefftz approaches and uses a weighted sum of so-called wave functions, which are exact solutions of the governing partial differential equations, to approximate the dynamic field variables. Contrarily to element based techniques, the problem domain is subdivided into a small number of large, convex subdomains. By minimising the errors on boundary and interface conditions, a system of equations is obtained which can be solved for the unknown contribution factors of each wave function. As a result, the system of equations is smaller and a higher convergence rate and lower computational loads are obtained as compared to conventional prediction techniques. On the other hand, the method shows its full efficiency for moderately complex geometries. Various enhancements have been made to the method through the years, in order to extend the applicability of the Wave Based Method. This paper aims to give an overview of the current state of the art of the Wave Based Method, its modelling procedure, application areas and extensions to the method such as hybrid and multi-level approaches.

1 INTRODUCTION

The Wave Based Method (WBM) [1] belongs to the family of Trefftz approaches. It is designed for solving steady-state dynamic problems, governed by a (set of) Helmholtz equation(s) and can be applied to bounded as well as (semi-)unbounded problem domains. This paper gives an overview of the current state of the art of the WBM, summarising fifteen years of research. The first section describes which problem types can be solved with the WBM. Next, the four steps involved in the WB modelling procedure are discussed. Finally, the application areas of the WBM and hybrid and multi-level extensions are discussed.

2 GENERALISED HELMHOLTZ PROBLEM

Consider a general interior/exterior steady-state dynamic problem. It is assumed that the mathematical formulation of the physics inside the problem domain Ω gives rise to, or can be cast into N_H (modified) Helmholtz equations. The problem boundary $\Gamma = \partial\Omega$ consists of two parts in case the problem domain is unbounded: the finite part of the boundary, Γ_b, and the boundary at infinity, Γ_∞. The finite part of the boundary can be divided into non-overlapping parts: $\Gamma_b = \bigcup_i \Gamma_i$, on which different boundary conditions can be imposed. On each point of the boundary, N_H boundary conditions need to be defined to obtain a well-posed problem. At the boundary at infinity Γ_∞, non-reflecting boundary conditions are imposed.

3 THE WBM MODELLING PROCEDURE

The general modelling procedure of the WBM [1] to solve a generalised Helmholtz problem consists of four steps, which are detailed next.

3.1 Partitioning of the problem domain

When applied to bounded problems, the convexity of the considered domain is a sufficient condition for the WB approximations to converge towards the exact solution of the problem under study [1]. When the considered problem domain is non-convex, it is, in a first step, partitioned into a number of convex subdomains. When applied to unbounded problems, an initial partitioning of the unbounded domain into a bounded and an unbounded region by a truncation curve Γ_t precedes the partitioning into convex subdomains [2]. N_H continuity conditions are imposed for each subdomain on the interfaces between two adjacent subdomains.

3.2 Field variable expansion

The N_H steady-state dynamic field(s) are approximated in each subdomain by a solution expansion of wave functions which are exact solutions of the associated Helmholtz equation. In case a non-homogeneous Helmholtz equation is considered, a particular solution is added to the wave function set. In case of an unbounded subdomain, the wave functions are selected to additionally inherently fulfill the non-reflecting boundary condition at Γ_∞. The applied sets of wave functions within the WBM can be found in the theoretical sections of the papers cited in Section 4.

3.3 Construction of the system of equations

Within each subdomain, the proposed solution expansion always exactly satisfies the Helmholtz equation(s), irrespective of the values of the unknown contribution factors. The matrix system of

equations is constructed by minimising the errors on the boundaries and interfaces, by applying a weighted residual approach.

3.4 Solution and postprocessing

In a final step, the system matrix of equation is solved for the unknown wave function contribution factors. The backsubstitution of these values in the field variable expansions leads to an analytical expression of the approximation of the field variables in each of the subdomains. Derivative quantities can be easily obtained by applying differential operators to the wave function sets. Since also evanescent components are used in the wave function sets, also near field effects can be captured.

4 WBM STATE OF THE ART

The concept of the WBM was introduced by Desmet [1] and since then it has been the topic of continuous research. The method has been applied to interior [3] and exterior [4] acoustic problems, plate bending and plate membrane problems [5], assemblies of flat shells [6], coupled vibro-acoustic problems [7] and for poroelastic materials [8]. For each of the problems a comparison has been made to standard element-based prediction techniques. The WBM shows a better efficiency for problems of a low to moderate geometrical complexity

4.1 Multi-level WBM

In the case an unbounded problem geometry contains several scatterers, the WBM loses it attractiveness. The truncation Γ_t needs to enclose all scatterers and inside this truncation, the convexity requirement may lead to a very large number of subdomains. When, for instance, a number of circular scatterers are considered, it is even impossible to obtain convex subdomains. The same holds for a bounded subdomain with (a number of) inclusion(s). To overcome these difficulties, the concept of multi-level modelling was introduced considering each scatterer or inclusion in a separate level [9].

4.2 Hybrid WB methods

The second class of enhancements applies the combined use of two numerical methods to one problem under study. Each method is applied according to its own strengths. This way, a strong hybrid approach can be obtained, taking benefit of the best properties of two approaches. In these lines of thought, FE-WBM [10], BE-WBM and WBM-SEA [11] have been developed.

5 CONCLUSION

This paper discusses the state of the art of the WBM, summarising fifteen years of continuous research. The WB modelling procedure is presented and current application areas and extensions of the method are explained. The presentation will show the performance of the method with respect to element based prediction techniques for a number of applications.

ACKNOWLEDGMENTS

The institute for Promotion of Innovation by Science and Technology Flanders (Belgium) (IWT-Vlaanderen) is gratefully acknowledged for the support of the doctoral research of Laurens Coox, Hendrik Devriendt and Stijn Jonckheere. The authors also gratefully acknowledge

the European Commission for their support through the ITN Marie Curie project GA-290050 GRESIMO and the EID Marie Curie project GA-316422 eLiQuiD. The IWT Flanders within the ASTRA and the HEV-NVH project, the Fund for Scientic Research - Flanders (F.W.O.), Belgium and the Research Fund KU Leuven are also gratefully acknowledged.

REFERENCES

[1] W. Desmet. *A wave based prediction technique for coupled vibro-acoustic analysis*. KULeuven, division PMA, PhD. thesis 98D12, 1998.

[2] B. Pluymers, B. Van Hal, D. Vandepitte, and W. Desmet. Trefftz-based methods for time-harmonic acoustics. *Archives of Computational Methods in Engineering*, 14:343–381, 2007.

[3] B. Van Genechten, O. Atak, B. Bergen, E. Deckers, S. Jonckheere, J.S. Lee, A. Maressa, K. Vergote, B. Pluymers, D. Vandepitte, and W. Desmet. An efficient Wave Based Method for solving Helmholtz problems in three-dimensional bounded domains. *Engineering Analysis with Boundary Elements*, 36:63–75, 2012.

[4] B. Bergen, B. Van Genechten, D. Vandepitte, and W. Desmet. An efficient Trefftz-based method for three-dimensional Helmholtz problems in unbounded domains. *Computer Modeling in Engineering & Sciences*, 61(2):155–175, 2010.

[5] C. Vanmaele, D. Vandepitte, and W. Desmet. An efficient wave based prediction technique for dynamic plate bending problems with corner stress singularities. *Computer Methods in Applied Mechanics and Engineering*, 198:2227–2245, 2009.

[6] K. Vergote, C. Vanmaele, D. Vandepitte, and W. Desmet. An efficient wave based approach for the time-harmonic vibration analysis of 3D plate assemblies. *Accepted for publication in J. Sound Vib.*, 2013.

[7] B. Pluymers, W. Desmet, D. Vandepitte, and P. Sas. Application of an efficient wave-based prediction technique for the analysis of vibro-acoustic radiation problems. *J. Comput. Appl. Math.*, 168:353364, 2004.

[8] E. Deckers, N.-E. Hörlin, D. Vandepitte, and W. Desmet. A Wave Based Method for the efficient solution of the 2D poroelastic Biot equations. *Computer Methods in Applied Mechanics and Engineering*, 201-204:245–262, 2012.

[9] B. Van Genechten, B. Bergen, D. Vandepitte, and W. Desmet. A Trefftz-based numerical modelling framework for Helmholtz problems with complex multiple scatterer configurations. *Journal of Computational Physics*, 229(18):6623–6643, 2010.

[10] B. Van Genechten. *Trefftz-based mid-frequency analysis of geometrically complex vibro-acoustic problems - hybrid methodologies and multi-level modelling*. KULeuven, division PMA, PhD. thesis 2010D08, 2010.

[11] K. Vergote, B. Van Genechten, D. Vandepitte, and W. Desmet. On the analysis of vibro-acoustic systems in the mid-frequency range using a hybrid deterministic-statistical approach. *Computers & Structures*, 89:868–877, 2011.

NON RESONANT CONTRIBUTIONS IN MODAL ENERGY METHODS

N. Totaro[1], L. Maxit[1*]
[1]Laboratoire Vibrations Acoustique
25bis avenue Capelle, Villeurbanne Cedex, FRANCE
Email: nicolas.totaro@insa-lyon.fr, laurent.maxit@insa-lyon.fr

ABSTRACT

In many cases, the non resonant contributions of the vibro-acoustic systems is not negligible. In Statistical Energy Analysis (SEA), this contribution is often taken into account introducing indirect coupling between subsystems. In modal energy methods like Statistical modal Energy distribution Analysis (SmEdA), only resonant modes could be taken into account.
Recent developments of modal energy methods allow now to overcome the problem of non-resonant contribution. Two complementary approaches have been developed. The first one, in the framework of SmEdA, is based on the definition of indirect coupling between modes of two non-directly coupled subsystems. The second one considers modal energy exchanges at pure tone and defines a pure tone modal coupling loss factor between all modes of subsystems.
These two new approaches will be validated and compared in a cavity/structure/cavity test case.

1 INTRODUCTION

In modal energy methods like Statistical modal Energy distribution Analysis (SmEdA), the power balance is set on modes rather than subsystems like in SEA [1]. As in SEA, modal energy methods are based on the analysis of two coupled oscillators excited by random uncorrelated forces.

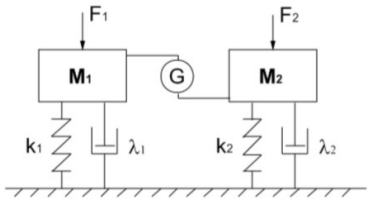

Figure 1 : Gyroscopic couplings between two oscillators

However, the subsystems are represented by their uncoupled modes and sets of oscillators (modes) are coupled through gyroscopic coupling. In SmEdA [2,3], the unkonwns are then the modal energies of each subsystems and modal coupling loss factors are defined.

2 INDIRECT COUPLING IN SMEDA APPROACH

Let's take the example of the three subsystems test case of a Cavity/Plate/Cavity. The basic idea of this approach is to represent the non resonant and non negligible contribution of one subsystems (that is to say the plate in the present example) by an indirect coupling between cavities.

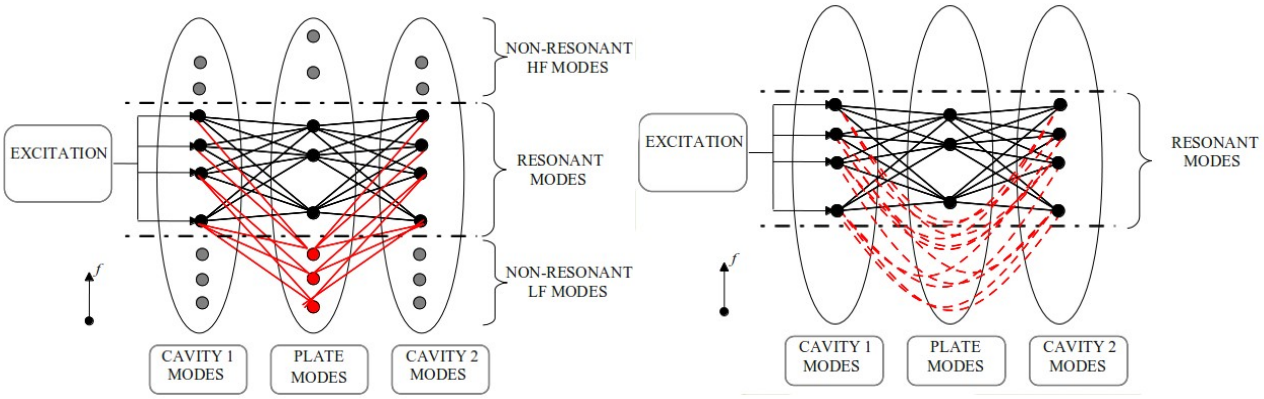

Figure 2 : (a) principle of SmEdA without non resonant modes (b) principle of SmEdA with indirect coupling to introduce non resonant modes of the plate.

Figure 2 presents the difference between SmEdA with or without non resonant contributions. In figure 2(a), a source excites modes of cavity 1 in a frequency band. With classical SmEdA, only couplings between resonant modes (that is to say in the frequency band of excitation) are taken into account. However, non resonant contribution of low frequency modes (in red) can't be neglected in some cases. To overcome this issue, indirect couplings between cavities 1 and 2 are introduced as presented in figure 2(b). As can be demonstrated using a condensation method and a dual modal formulation, the power exchanged from mode p of cavity 1 to mode r of cavity 2 due to non resonant modes of the plate writes

$$\Pi_{pr} = \beta_{pr}\left(E_p - E_r\right) \tag{1}$$

where E_p and E_r are respectively the energy of modes p and r and β_{pr} is the coupling loss factor between mode p of cavity 1 and mode r of cavity 2 due to non resonant modes of the plate which writes

$$\beta_{pr} = \left(\sum_{q \in Q_{nr}} W_{pq} W_{rq} \right)^2 \left\{ \frac{\left(\omega_p \eta_p + \omega_r \eta_r \right)}{\left[\left(\omega_p \right)^2 - \left(\omega_r \right)^2 \right]^2 + \left(\omega_p \eta_p + \omega_r \eta_r \right) \left[\omega_p \eta_p \left(\omega_r \right)^2 + \omega_r \eta_r \left(\omega_p \right)^2 \right]} \right\}. \quad (2)$$

W_{pq} and W_{rq} are the modal works between non resonant modes q of the plate and resonant modes p and r of cavities. ω_p and η_p are the natural angular frequency and the damping of mode p. Thus, taking into account this indirect coupling between cavities, the power balance of mode p of cavity 1 writes

$$\Pi_{inj}^{p} = \omega_p \eta_p E_p + \sum_{q \in \hat{Q}_r} \beta_{pq} \left(E_p - E_q \right) + \sum_{r \in \hat{R}} \beta_{pr} \left(E_p - E_r \right), \qquad \forall p \in \hat{P} \quad (3)$$

where the injected power is equal to the power dissipated by the mode plus the direct exchange between mode p and resonant modes of the plate plus the indirect exchange between mode p and modes of cavity 2 due to non resonant modes of the plate. Finally, modal energies of each subsystems can be computed solving a system of linear equations.

3 MODAL ENERGY ANALYSIS AT PURE TONE

Another way to solve this problem is to express the power balance between two modes p and q between two subsystems excited by random forces at pure tone. One can demonstrate that the injected power between modes at pure tone writes

$$\Pi_p^{\mathrm{inj}}(\omega) = \Pi_p^{\mathrm{diss}}(\omega) + \sum_q \alpha_{pq}(\omega) E_t^p(\omega) - \sum_q \alpha_{qp}(\omega) E_t^q(\omega). \quad (4)$$

where the power injected into mode p is equal to the power dissipated by mode p plus the net exchanged power between modes p and q. The coupling factor $\alpha_{pq}(\omega)$ depends on frequency and writes

$$\alpha_{pq}(\omega) = \frac{2\gamma_{pq}^2}{\left(1 + \frac{\omega_p^2}{\omega^2}\right)} \frac{\Delta_q^{\mathrm{visc}} \omega^2 \left((\omega_p^2 - \omega^2)^2 + \omega^2 (\Delta_p^{\mathrm{visc}})^2 \right) + \omega^4 \gamma_{pq}^2 \Delta_p^{\mathrm{visc}}}{\left((\omega_p^2 - \omega^2)^2 + \omega^2 (\Delta_p^{\mathrm{visc}})^2 \right) \left((\omega_q^2 - \omega^2)^2 + \omega^2 (\Delta_q^{\mathrm{visc}})^2 \right) - \omega^4 \gamma_{pq}^4}. \quad (5)$$

where ω is the angular frequency of the excitation, Δ_p^{visc} is the damping bandwith of the mode p and γ_{pq} is the gyroscopic coupling which can be related to modal works between modes as

$$\gamma_{pq} = \frac{1}{\sqrt{M_p M_q}} \int_{S_c} \Phi_p^{\mathrm{plate}}(Q) \Psi_q^{\mathrm{cav}}(Q) dQ. \quad (6)$$

where Φ_p^{plate} and Ψ_q^{cav} are respectively the displacement mode shape of modes of the plate and the pressure mode shape of modes of the cavity.Solving the system of linear equations as Eq. (4) at pure tone permits to take intrinsically into account non resonant contribution of modes (of each subsystem). No distinction of in-band or out-of-band modes is necessary and all the modes are necessary to solve the system.

4 CAVITY/STRUCTURE/CAVITY TEST CASE

The test case presented in figure 3 consists in a plate (Lx=0.9m, Ly=0.7m, ρ=7800kg/m^3, E=2e11Pa, ν=0.3, hp=1mm) in between two cavities filled of air (LzA=1m, LzB=1.2m, ρ0=1.2kg/m^3, c0=340m/s). A monopole is located in cavity A at point (0.1,0.1,0.1)

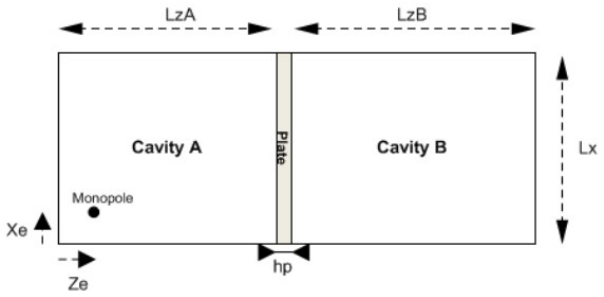

Figure 3 : Cavity/Plate/Cavity test case. A monopole is located in cavity A

The energy ratio between cavities in presented in figure 4 and a comparison between modal energy methods is done. As can be seen, without taking into account non resonant modes of the plate, SmEdA leads to an overestimation of the energy ratio. However, both presented approaches well compare with reference calculation. In figure 4, modal energy at pure tone is frequency averaged.

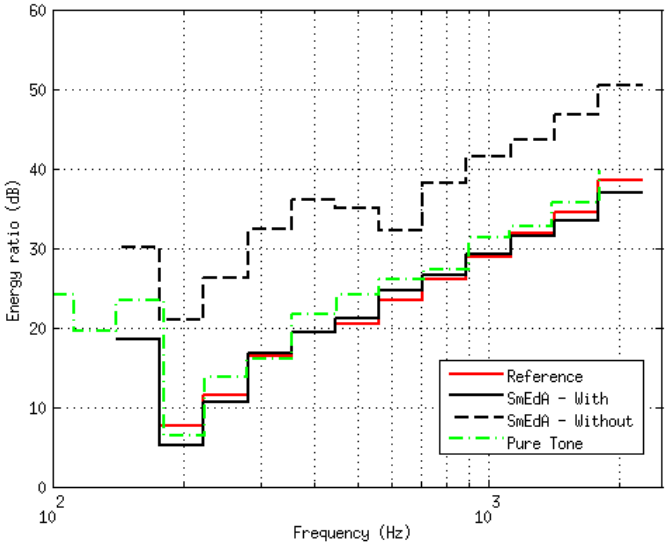

Figure 4 : Energy ratio between cavities. Comparison of modal energy approaches

5 CONCLUSION

Two modal energy methods has been validated and compared in the Cavity/plate/Cavity test case to take into account non resonant modes.

REFERENCES

[1] R.H. Lyon, R.G. Dejong, *Theory and application of statistical energy analysis,* Second ed. – Boston: Butterworth-Heinemann, 1995. 277p.

[2] L. Maxit, J.L. Guyader, Extension of SEA model to subsystem with non-uniform modal energy distribution, *Journal of Sound and Vibration,* 265, 337-358, (2003) .

[3] N. Totaro, C. Dodard, J.L. Guyader, SEA coupling loss factors of complex vibro-acoustic systems, *Journal of Vibration and Acoustics*, 131, (2009).

[4] L. Maxit, K. Ege, N. Totaro, J.L. Guyader, Extension of SmEdA to non-resonant transmission, ICA, Montréal, Canada (2013).

[5] N. Totaro, J.L. Guyader, MODal ENergy Analysis, RASD, Pise, Italie (2013).

DYNAMICS OF STOCHASTIC AND PERIODIC STRUCTURES IN MID-FREQUENCY RANGE

M. A. BEN SOUF[1,3] , O. BAREILLE[1] , M. ICHCHOU[1] , N. BOUHADDI[2] and M. HADDAR[3]

[1]LTDS
LTDS, École Centrale de Lyon, 36 Avenue Guy de Collongue, F-69134 Ecully Cedex, France
Email: {mohamed-amine.ben-souf,Olivier.Bareille,Mohamed.Ichchou}@ec-lyon.fr

[2] Mec'Appli
FEMTO-ST Institute UMR 6174, Applied Mechanics Laboratory, University of Franche-Comté, 24 Chemin de l'Epitaphe, 25000 Besanon, France
noureddine.bouhaddi@univ-fcomte.fr

[3]U2MP
École Nationale d'Ingénieurs de Sfax, Tunisie
Email: mohamed.haddar@enis.rnu.tn

ABSTRACT

Wave propagation in uncertain coupled structures is treated in this paper. The presented work is a hybridization of the Wave Finite Element Method (WFEM) with the Generalised Polynomial Chaos Expansion (GCE). The WFE is a spectral method dealing with wave propagation in periodic structure. This method proved its efficiency in different domains; structural vibration, non-destructive testing, etc. However, the WFE is limited to deterministic media. Knowing that uncertainties affect dynamic behavior in Mid- and High frequencies, the combination of WFE and GCE is used to predict the effect of uncertainties on the dynamic response of periodic media. The uses of the GCE is based on the iso-probabilistic transformations for usuel distributions to Gaussian one to use the Hermite-Chaos expansion.The presented approach is validated for two periodic waveguides connected through a junction with uncertain parameters. The obtained results are verified vs Monte Carlo simulations.

1 INTRODUCTION

Wave propagation in structures is of interest of many researchers in mechanical fields. There are many methods which allow the identification of wave characteristics such as Semi-Analytical Finite Element (SAFE) and Wave Finite Element method (WFE). The WFE is a spectral method dealing with wave propagation in structures with identical sub-systems (periodic waveguide)[1]. With a direct connection with the classical finite element method, the WFE can be simply developed. This study starts from the discretization of one sub-element, then a spectral eigenvalue problem is formulated regarding the periodicity of the structure. The WFE is then used for different problems; wave propagation [2], structural vibration, etc. If the structure contains some defects, the classical WFE is no longer applicable, so Mencik *et al.* developed a Diffusion Matrix Model (DMM) [2] which is based on the hybridization of the classical finite element method and the WFE to predict the reflection and transmission coefficients regarding these discontinuities. Knowing that uncertainties play a important role, this paper try to extend this formulation to non-deterministic structures. The use of the generalized chaos expansion allows the identification if uncertainty propagation in periodic media. This approach is based on the projection of stochastic parameters on the chaos base which allow, using non-intrusive approach, to quantify the statistics of outputs (kinematic and energetic parameters). The presented approach is then applied for two connected structures with uncertain inputs.

2 THE WAVE FINITE ELEMENT

This section deals with the dynamic behavior of a straight elastic dissipative structures, composed by N identical elements connected along the principal direction, say axis x, and whose left and right cross-sections are denoted as $\mathtt{L}$ and $\mathtt{R}$, respectively. The length of each subsystem is denoted as d. The formulation is based on the finite element model of a typical subsystem, and whose kinematic variables, displacements and forces, are written as $\mathbf{q}$ and forces $\mathbf{F}$ respectively. The dynamic equilibrium equation of on subsystem, at frequency $\omega/2\pi$, can be stated as follows:

$$\begin{pmatrix} \mathbf{D}_{\mathtt{LL}} & \mathbf{D}_{\mathtt{LR}} \\ \mathbf{D}_{\mathtt{RL}} & \mathbf{D}_{\mathtt{RR}} \end{pmatrix} \begin{pmatrix} \mathbf{q}_{\mathtt{L}} \\ \mathbf{q}_{\mathtt{R}} \end{pmatrix} = \begin{pmatrix} \mathbf{F}_{\mathtt{L}} \\ \mathbf{F}_{\mathtt{R}} \end{pmatrix} \tag{1}$$

where $(\mathtt{n}\times\mathtt{n})$ matrix $\mathbf{D}_{\mathtt{ij}} = \mathbf{K}_{\mathtt{ij}} - \omega^2\mathbf{M}_{\mathtt{ij}}$ $(\{\mathtt{i},\mathtt{j}\} \in \{\mathtt{L},\mathtt{R}\})$ stands for the $\mathtt{ij}$ component of the dynamic stiffness operator condensed on the left and right cross-sections, namely $\mathbf{D}$ [1]. Here, $\mathbf{K}$ and $\mathbf{M}$ stand for the stiffness and mass matrices, respectively. Based on the periodicity of the structure and the Bloch's theorem, the spectral eigenvalue problem can be expressed as:

$$\mathbf{S}\mathbf{\Phi}_{\mathtt{i}} = \mu_{\mathtt{i}}\mathbf{\Phi}_{\mathtt{i}}. \tag{2}$$

This problem was established using the state vector representation. The resolution of equation (2) allows the identification of waves characteristics; propagation constant (μ_i) and deformed shape ($\mathbf{\Phi}_i$).

3 GENERALIZED POLYNOMIAL CHAOS EXPANSION

The polynomial chaos expansion (PCE), based on homogeneous chaos theory, was established by Wiener to describe stochastic processes using gaussian random variables. Ghanem and Spanos [4] used this formulation to describe the uncertainty propagation in structures. A second ordre stochastic process with finite variance can be expressed as:

$$u = \sum_{i=0}^{\infty} u_i\Psi_i(\xi) \overset{Order\ p}{\longrightarrow} u \approx \sum_{i=0}^{p} u_i\Psi_i(\xi) \tag{3}$$

This formulation is used for Gaussian distributions. Xiu and Karniadakis [5] extended it to non-Gaussian uncertainties by using the iso-probabilistic transformations (see table 1) which allow the use of Chaos-Hermite formulation.

Type of distribution	Transformation
Uniform (a, b)	$a + (b - a)\,(0.5 + 0.5erf(\xi/sqrt2))$
Normal (μ, σ)	$\mu + \sigma\xi$
Lognormal (μ, σ)	$exp(\mu + \sigma\xi)$

Table 1: Transformation of usuel distributions to Gaussian one

4 NUMERICAL VALIDATION

Let's define a structure composed by two identical stochastic and multi-modal waveguides connected through a coupling element (see Figure 1) with two different origin of coordinates. The length of two stochastic waveguides is $L = 0.5\ (m)$, the coupling elements' length is $0.01(m)$. The mechanical properties of studied structures are (see table 2): Poisson's ratio $\nu = 0.3$, dimension of cross section area $5 \cdot 10^{-2}\ m \times 3 \cdot 10^{-2}\ m$.

Variables	Type of distribution	Mean	Standard deviation
Young's Modulus	Lognormal	$2 \cdot 10^{11} Pa$	2%
Density	Lognormal	7800 kg/m^3	3%
Damping	Uniform	0.01	10%
Force	Normal	1 N	2%
Stiffness of coupling element	Uniform	$2 \cdot 10^{10} Pa$	2%

Table 2: Characteristics of studied waveguides

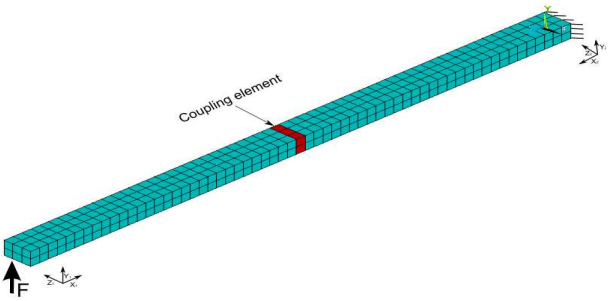

Figure 1: Two stochastic waveguides connected through a junction

The Figure 2 represents respectively the mean of reflection and transmission coefficients for different type of waves (1-2: flexural, 3; Torsional and 4; Longitudinal). The results of presented formulation (dashed line) are validated by Monte Carlo simulations.
The Figure 3 represents the mean of displacement calculed by spectral method and validated by MC simulations in $x_1 = 0.25$ m and $x_2 = 0.25$ m. The yellow area represents the envelope min-max of displacement regarding the stochastic input parameters.

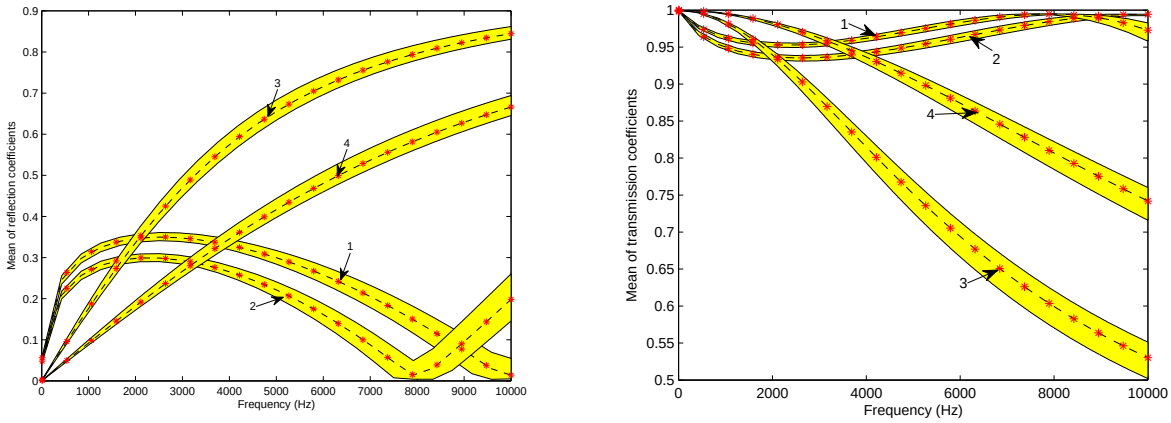

Figure 2: Mean of reflection (a) and transmission coefficients (b): (–) SWFE-Chaos, (*) Monte Carlo, yellow area: Interval min-max.

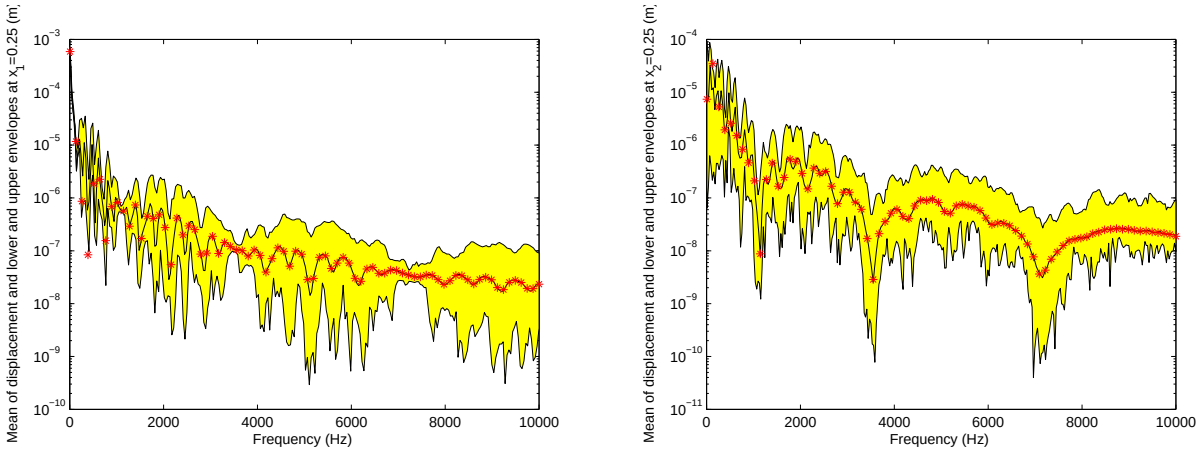

Figure 3: Mean of displacement at $x_1 = 0.25$ m (a)and $x_2 = 0.25$ m (b), (-) WFE-Chaos (4^{th} order expansion), (*) Monte Carlo.

REFERENCES

[1] W. X. Zhong and F. W. Williams. On the direct solution of wave propagation for repetitive structures. *Journal of Sound and Vibration*, 181:485–501, 1995.

[2] J. M. Mencik and M. N. Ichchou. Multi-mode propagation and diffusion in structures through finite elements. *European Journal of Mechanics - A/Solids*, 24(5):877–898, 2005.

[3] D. Duhamel, B.R. Mace, and M.J. Brennan. Finite element analysis of the vibrations of waveguides and periodic structures. *Journal of Sound and Vibration*, 294:205–220, 2006.

[4] R. Ghanem and P. Spanos. *Stochastic Finite Elements: A Spectral Approach*. Springer, New York, NY, 1991.

[5] D. Xiu and G. E. Karniadakis. Modeling uncertainty in steady state diffusion problems via generalized polynomial chaos. *Computer Methods in Applied Mechanics and Engineering*, 191:4927–4948, 2002.

SAMSARA FOR THIN STIFFENED SHELLS: FIRST MODELS

S. De Rosa and F. Franco

PASTA-Lab
Department of Industrial Engineering - Aerospace Branch
Universita' degli Studi di Napoli "Federico II", ITALY
sergio.derosa@unina.it, francesco.franco@unina.it

ABSTRACT

A general procedure for defining exact and distorted similitudes, to build prototype models able to reproduce given structural (and structural-acoustic) responses, is presented. This can be very useful for the engineering modeling and measurements purposes. This procedure is based on the Energy Distribution Approach which allows the exact derivation of input power and energy content in each subsystem. These fundamental parameters are expressed in terms of modal coordinates and allow the analysis versus the simulitudes ratios. The similitude laws are defined by imposing that the dynamic responses in the original and parent models are the same. The procedure has been already developed and applied for thin plates, assemblies of plates and interior noise inside a cylindrical thin shell with structural-acoustic coupling. In the present work, for the first time, it is applied to a stiffened circular cylinder in order to match more realistic configurations. Among all possible similitude parameters only some geometrical ones are used. The material properties are kept in order to not modify the material characteristics and the possibility to build an experimental prototype. The results of an exact and distorted similitude are compared with an analytical model. The proposed simple scheme leads to very promising results.

1 INTRODUCTION AND BACKGROUND

Previous experiences in terms of structural and structural-acoustic similitudes have been reported for simplified plates and thin shells, [1], [2]: here the goal is to present some advances for a thin stiffened cylinder. The complete procedure is named SAMSARA, *Similitude and Asymptotic Models for Structural-Acoustic Research and Application*.

A well-known general view of the problems of similitudes and analogies are in the text by Szucs, [3].

The similitude for linear systems can be built by using the Energy Distribution Approach (EDA), [4], a technique in which using the mode shapes and natural frequencies are the basis to obtain the distribution of energy in each subsystem; thus, the whole system can be thought as an assembly of NS subsystems in which NM modes are resonating at each excitation frequency. The energy influence coefficient matrix:

$$A_{rq}^{EIC}(\omega) = \frac{\sum_j \sum_k \Gamma_{jk}(\omega)\, \psi_{jk}^{(q)} \psi_{jk}^{(r)}}{\sum_j \eta_j \omega_j \Gamma_{jj}(\omega)\, \psi_{jj}^{(q)}} \quad \text{with} \quad \begin{matrix} r,q \in \{1,\dots NS\} \\ j,k \in \{1,\dots NM\} \end{matrix} \tag{1}$$

where the spatial coupling parameter for the generic rth subsystem is the following:

$$\psi_{jk}^{(r)} = \int_{\mathbf{x}\in r} \rho(\mathbf{x}) \phi_j(\mathbf{x}) \phi_k(\mathbf{x}) d\mathbf{x} \tag{2}$$

and the frequency dependent members are here recalled:

$$\Gamma_{jk}(\Omega) = \frac{1}{\Omega} \int_{\omega\in\Omega} \omega^2 Re\left[\frac{1}{\omega_j^2 - \omega^2 + iu\ \eta_j \omega_j^2} \frac{1}{\omega_k^2 - \omega^2 + iu\ \eta_k \omega_k^2} \right] d\omega \tag{3}$$

The term Ω represents a generic frequency interval in which the system response is analysed for a given excitation; ϕ_j is the jth global mode and ω_j the jth circular natural frequency; ρ is a density function; x is the running coordinate. The analysis of the cross terms is rather complicated and two further approximations can be used that allow separating the cross terms in large and small terms: $\Gamma_{jk}^{(large)}(\Omega)$ and $\Gamma_{jk}^{(small)}(\Omega)$, [4].

Assuming a given similitude ratio for the natural frequencies, $r_\omega = \frac{\bar{\omega}_j}{\omega_j}$, the similitudes for the frequency members are (the overbar denotes the items in similitude):

$$\bar{\Gamma}_{jj} = \frac{1}{r_\omega^2} \Gamma_{jj}; \quad \bar{\Gamma}_{jk}^{(large)} = \frac{1}{r_\omega^2} \Gamma_{jk}^{(large)} \quad ; \bar{\Gamma}_{jk}^{(small)} = \frac{1}{r_\omega^2} \Gamma_{jk}^{(small)} \tag{4}$$

2 THE SIMILITUDE FOR THIN STIFFENED SHELLS

The reference analytical model is well-known, [5], Fig. 1.

These are the main hypotheses introduced to build the similitude: (i) thin shells; (ii) the materials do not change in the parent models: any material variation can be interpreted as a modification in the distribution of the natural frequencies; (iii) the boundary conditions remain the same in the parent models; (iv) the damping values are such that the system response can be obtained using the undamped natural frequencies and the real mode shapes: more complicated models based on the complex mode shapes do not add further contributions to the present developments and results.The field of investigation is restricted to the analysis of the values of radius, R, thickness, h, lenght, L; the longitudinal and circumferential stiffeners are left unaltered in these simulations. Thus, these are the similitude parameters: $\alpha\alpha = \frac{\bar{L}}{L}$, $\beta\beta = \frac{\bar{R}}{R}$, $\gamma\gamma = \frac{\bar{h}}{h}$.

It is possible to show that there are two possibilities: (i) *replicas (exact similitude)*: $\alpha\alpha = \beta\beta = \gamma\gamma$; (ii) *avatars (distorted similitude)*: $\alpha\alpha \neq \beta\beta$; $\beta\beta \neq \gamma\gamma$; $\alpha\alpha \neq \gamma\gamma$.

3 RESPONSES

Two simple results are shown in Figures 2 and 3. In both, the distribution of natural frequencies is reported together with a forced response. This last is a radial component of the structural velocity as result of a mechanical point excitation. The knowledge of the r_ω allows defining the remodulation of the frequency axis, so that the original model and the avatar (or replica) can be directly compared, by remodulating the response axis too.

The replica, Fig. 2, perfectly replicates the original response even using a reduction of thickness, length and radius: $\alpha\alpha = \beta\beta = \gamma\gamma = 0.3$.

The avatar is a very good approximation too, Fig. 3, $\alpha\alpha = \beta\beta = 0.3; \gamma\gamma = 0.5$.

4 CONCLUDING REMARKS

Structural similitudes have been the aim of this short contribution. It has been shown that thanks to EDA and a knowledge of the natural frequencies distribution for any given choice of the similitude parameters it is possible to define parent models (replicas and avatars) of original ones. Replicas refer to complete similitude, while avatars refer to distorted one. Analytical investigations allow getting both for thin stiffened cylinders. Further work is clearly needed to fully define SAMSARA even introducing more complicated and realistic schemes, but the actual investigations are a good step forward a full validated procedure.

REFERENCES

[1] S. De Rosa, F. Franco and T. Polito. Structural similitude for the dynamic response of plates and assemblies of plates. Mechanical Systems and Signal Processing, 25(3), 969-980, 2011.

[2] S. De Rosa, F. Franco, T. Polito. SAMSARA for thin cylindrical shells. Proceed. of the NOVEM2012 Conference, Noise and Vibration: Emerging Methods, April 2012, Sorrento, Italy, ISBN:9788890648403, no.48

[3] E. Szucs. Similitude and Modelling. Elsevier Science Ltd, ISBN:0444997806, 1980.

[4] B. R. Mace. Statistical energy analysis, energy distribution models and system modes. Journal of Sound and Vibration, 264, 391-409, 2003.

[5] Martin M. Mikulas, Jr., and John A. McElman. On free vibrations of eccentrically stiffened cylindrical shells and flat plates. NASA TN D-3010, 1967

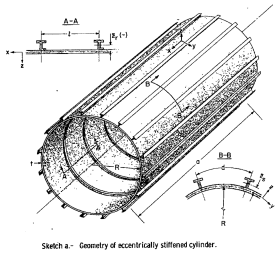

Figure 1. Model of the stiffened cylinder, from [5]

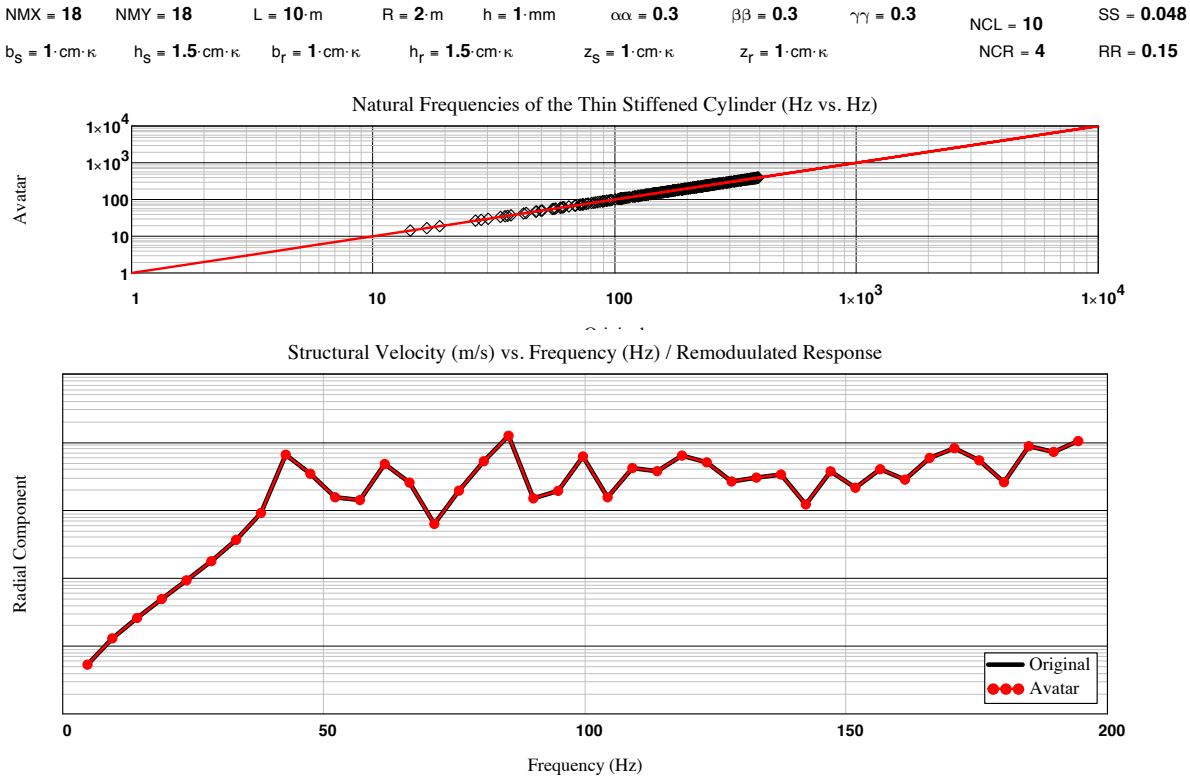

Figure 2. Exact similitude: replica natural frequencies and response

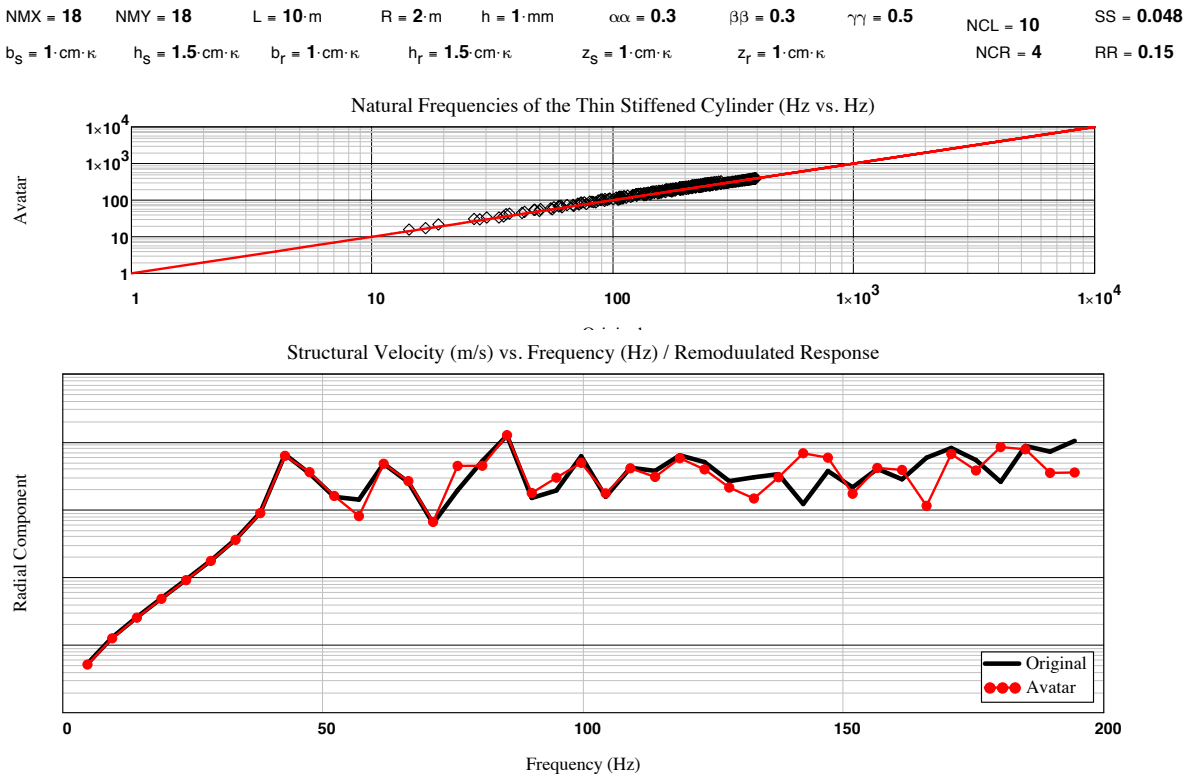

Figure 3. Distorted similitude: *avatar* natural frequencies and response

A new approach in reliability based design optimization of Tuned Mass Damper in seismic vibration control of structures with bounded uncertain parameters

E. MRABET[1], M. GUEDRI[2], S. GHANMI[1] and M. ICHCHOU[3]

[1]Nabeul Preparatory Engineering Institute
Carthage University, TUNISIA
Email: elyes.mrabet@yahoo.fr, samir.ghanmi@ipein.rnu.tn

[2]High Institute of Sciences and Techniques of Tunis
Tunis University, TUNISIA
Email: guedri.mohamed@isetn.rnu.tn

[3]LTDS UMR5513 Ecole Centrale de Lyon
36 Avenue Guy de Collongue, 69134 Ecully, FRANCE
Email: mohamed.ichchou@ec-lyon.fr

ABSTRACT

In this work a reliability based optimization of Tuned Mass Damper (TMD) parameters in seismic vibration control under uncertain system parameters is presented and two questions are asked. The former is, how can we transform a stochastic optimization problem of TMD into two deterministic problems when the structure parameters are uncertain but bounded? The second one is, can we adopt the monotonic assumption over the entire range of parameters box when the Rice's approximation is considered on the calculation of the probability of failure P_f. When the parameters of a structure are uncertain but bounded (UBB), it is natural to make use of theory of interval arithmetic. Indeed, a monotonicity-based extension interval is used to transform the initial stochastic problem into two deterministic sub-problems. This transformation is valid even with high levels of uncertainties and it can be used in structural optimization and in reliability based optimization. It has been demonstrated that the Rice's based approximation of P_f cannot be monotonic for any considered box. Therefore, a splitting box is performed to make possible the use of the proposed monotonicity-based extension method.
To validate this work, the stochastic counterpart method has been implemented and the results have proven that the proposed method is valid.

1 INTRODUCTION

When the structural parameters are uncertain but bounded, it is useful to transform an initial stochastic reliability based optimization problem, into two independents deterministic sub-problems. In [1], authors have proposed an interval extension based on a Taylor expansion of the objective function.

In this paper, a new approach using a monotonicity-based extension is presented. This approach is valid even when the objective function is not monotonic on its variables and even with high level of uncertainties. To highlight this new approach, a TMD system is considered.

2 STRUCTURAL MODEL AND THE STATE SPACE EQUATION

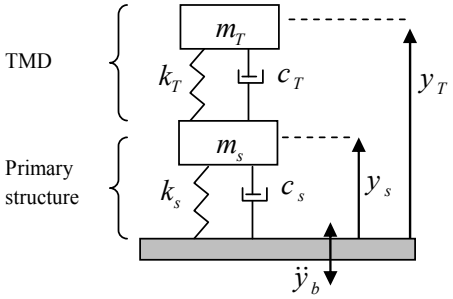

Figure 1 : The primary structure, TMD system

Figure 1 shows an idealized mechanical model of a TMD characterized by $\omega_T = \sqrt{k_T/m_T}$ and $\xi_T = c_T/2\sqrt{k_T m_T}$, attached with a single degree of freedom primary system characterized by $\omega_s = \sqrt{k_s/m_s}$ and $\xi_s = c_s/2\sqrt{k_s m_s}$. The system is excited by a base acceleration $\ddot{y}_b$ due to seismic motion which is modeled by the Kanai-Tajimi stationary stochastic process [1]. Considering the mass ratio $\mu = m_T/m_s$, the system equations written in the state space form is deduced from the characteristic system matrices:

$$A = \begin{pmatrix} 0 & 0 & 0 & 1 & 0 & 0 \\ 0 & 0 & 0 & 0 & 1 & 0 \\ 0 & 0 & 0 & 0 & 0 & 1 \\ -\omega_T^2 & \omega_T^2 & \omega_f^2 & -2\xi_T\omega_T & 2\xi_T\omega_T & 2\xi_f\omega_f \\ \mu\omega_T^2 & -(\mu\omega_T^2+\omega_s^2) & \omega_f^2 & 2\mu\xi_T\omega_T & -2(\xi_s\omega_s+\mu\xi_T\omega_T) & 2\xi_f\omega_f \\ 0 & 0 & -\omega_f^2 & 0 & 0 & -2\xi_f\omega_f \end{pmatrix}; B = 2\pi S_0 \begin{pmatrix} 0 & \cdots & 0 \\ \vdots & \ddots & \vdots \\ 0 & \cdots & 1 \end{pmatrix}$$

ξ_f, ω_f and y_f are the damping ratio, the natural frequency and the relative response (with respect to the ground) of the elastic filter [1]. The global space state vector is then $Y = \left(y_T, y_s, y_f, \dot{y}_T, \dot{y}_s, \dot{y}_f\right)^T$ and S_0 is the intensity of the stationary Gaussian zero mean white noise process applied at the bed rock. The stochastic response of the system is completely known by the space state covariance matrix R which is the solution of the Lyapunov equation $AR + RA^T + B = 0$. The root mean square displacement (rmsd) of the primary system can be obtained as: $\sigma_{y_s} = \sqrt{R(2,2)}$.

3 THE TMD OPTIMIZATION, MONOTONICITY-BASED EXTENSION

The optimal criterion proposed in this study for a mechanical system with a TMD is the minimization of the probability of failure $P_f(\mathbf{x})$ of the primary system defined as the exceedance of the displacement y_s to a given threshold value β in a given period $[0,T]$. The failure probability can be approximated by the classical Rice's formulation based on the Poisson assumption [1]:

$$P_f(\mathbf{x}) = 1 - \exp\left\{-\upsilon_\beta(\mathbf{x})T\right\} \;;\upsilon_\beta(\mathbf{x}) = \frac{1}{\pi\sigma_{y_s}(\mathbf{x})}\sigma_{\dot{y}_s}(\mathbf{x})\exp\left[-\frac{\beta^2}{2\sigma^2{}_{y_s}(\mathbf{x})}\right] \tag{1}$$

In the above expression $\mathbf{x} = (\omega_f, \xi_f, \omega_s, \xi_s, S_0)$ and the standard deviation $\sigma_{y_s}, \sigma_{\dot{y}_s}$ of the performance quantities y_s and $\dot{y}_s$ can be obtained from the covariance matrix R.Thus, the optimization problem consist to find $d = (\xi_T, \omega_T)$ that minimize $f = P_f(\mathbf{x})$.

It can be noted that if $\mathbf{x}$ is uncertain and described in probabilistic way, the above problem refers to a stochastic optimization problem and the stochastic counterpart method [2] can be used in this case.

When Structure parameters $\mathbf{x}$ are uncertain but bounded, it is natural to describe them using intervals. Let $X = (X_1,...,X_5)$ be the corresponding box then for every $x_i \in \mathbf{x}$ we have $X_i = [\underline{x}_i, \overline{x}_i] = [\mu_i - \Delta x_i, \mu_i + \Delta x_i]$; μ_i and Δx_i are the mean and the maximum deviation from the mean of X_i, respectively. Hence, the image of P_f will be an interval $P_f(X) = [\underline{P}_f, \overline{P}_f]$. Then the initial stochastic problem can be transformed into two independent deterministic optimization problems, Equation (2), involving the endpoints of $P_f(X)$:

$$\begin{array}{l} \textit{Find} \quad d = (\xi_T, \omega_T) \\ \textit{To minimize}: \; f = \underline{P}_f \end{array} \quad \text{and} \quad \begin{array}{l} \textit{Find} \quad d = (\xi_T, \omega_T) \\ \textit{To minimize}: \; f = \overline{P}_f \end{array} \tag{2}$$

According to [3], if $P_f(\mathbf{x})$ is monotonic of its variables $x_i \in \mathbf{x} = (x_1,...x_5)$, the evaluation of its image using the monotonicity-based extension gives the exact range of the function over the considered box X. $\underline{P}_f$ and $\overline{P}_f$ are functions of the endpoints of X and of the behaviour of $P_f(\mathbf{x})$.

4 MONOTONICITY OF $P_f(\mathbf{x})$, THE DETERMINISTIC PROBLEMS

To check the monotonicity of $P_f(\mathbf{x})$, an endpoints analysis [4] is performed. Let $\boldsymbol{\upsilon}_\beta = [\underline{\upsilon}, \overline{\upsilon}]$, $\boldsymbol{\sigma}_{\mathbf{y_s}} = [\underline{\sigma}_{y_s}, \overline{\sigma}_{y_s}]$ and $\boldsymbol{\sigma}_{\dot{\mathbf{y}}_\mathbf{s}} = [\underline{\sigma}_{\dot{y}_s}, \overline{\sigma}_{\dot{y}_s}]$ be the evaluations of $\upsilon_\beta, \sigma_{y_s}$ and $\sigma_{\dot{y}_s}$ over X using the natural interval extension [3]. Using Equation (1) and applying the interval arithmetic, we have: $\underline{\upsilon} = \frac{\underline{\sigma}_{\dot{y}_s}}{\pi\overline{\sigma}_{y_s}}\exp\left[-\frac{\beta^2}{2\underline{\sigma}^2{}_{y_s}}\right]$ and $\overline{\upsilon} = \frac{\overline{\sigma}_{\dot{y}_s}}{\pi\underline{\sigma}_{y_s}}\exp\left[-\frac{\beta^2}{2\overline{\sigma}^2{}_{y_s}}\right]$. According to Hansen [4], $P_f(\mathbf{x})$ cannot be monotonic $\forall\, x_i \in \mathbf{x} = (x_1,...x_n)$ and $\forall\, X_i \in X = (X_1,...X_n)$ because $\underline{\upsilon}$ is function of both $\overline{\sigma}_{y_s}$ and $\underline{\sigma}_{y_s}$. In spite of this fact, it is always possible to split X into tight sub-boxes on which the function will be considered as monotonic, thus it is possible to evaluate an approximation $\hat{P}_f(X) = [\underline{P}_f, \overline{P}_f]$ of $P_f(X)$ using the monotonicity-based extension.

Let S be the set of all possible endpoints combinations of X, problems of equation (2) can be written as:

$$\begin{array}{l} Find \quad d=(\xi_T,\omega_T) \\ To\ minimize:\ f=\min\limits_S\left(\hat{P}_f(S),d,t\right) \end{array} \quad \text{and} \quad \begin{array}{l} Find \quad d=(\xi_T,\omega_T) \\ To\ minimize:\ f=\max\limits_S\left(\hat{P}_f(S),d,t\right) \end{array} \tag{3}$$

5 NUMERICAL STUDY

For the numerical study, the considered system is represented on Figure 1. The nominal values are assumed: $\omega_f=9\pi$, $\xi_f=0.4$, $\omega_s=8.4\pi$, $\xi_s=0.03$, $S_0=0.03$, $\mu=0.02$, $T=20$ and $\beta=0.045$. For the stochastic counterpart method (dashed lines in Figure 2), the sample size is $N_{mc}=10^5$. Only one direction is split (ω_f) with a width of 0.03. According to Figure 2, it seems that the proposed transformation, of the initial stochastic problem, based on a monotonicity-based extension gives satisfactory result especially for the objective function P_f and the design parameter ω_T.

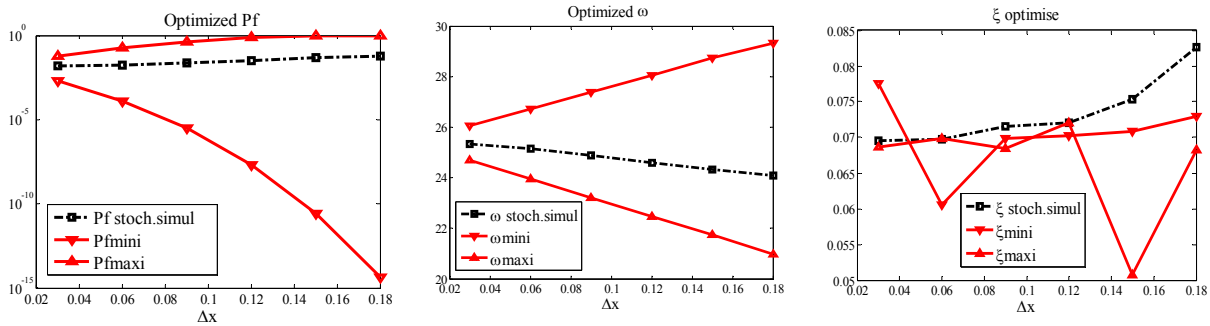

Figure 2: Reliability based design optimization results for the TMD

6 CONCLUDING REMARKS

We have shown that, in presence of uncertain but bounded parameters, it is always possible to transform an initial stochastic optimization problem into two deterministic problems using a monotonicity-based extension. In fact, even when the objective function is not monotonic, a box splitting can be performed and the function is then approximated as monotonic. Compared with the results of the stochastic counterpart method, the optimization results found in the numerical study have proved the efficiency of the proposed approach. Nevertheless, more efforts must be done for the choice of the splitting direction and the width of the sub-boxes.

REFERENCES

[1] S. Chakraborty, B. K. Roy ; Reliability based design optimum design of tuned mass damper in seismic vibration control of structures with bounded uncertain parameters; *Probabilistic Engineering Mechanics 26, 215-221,* 2011.

[2] Dirk P. Kroese, T. Taimre, Z. I. Botev : *Handbook of Monte Carlo Methods*; John Wiley & Sons, Inc., Hoboken, New Jersey, 2011.

[3] I. Araya, B. Neveu, G. Trombettoni : An Interval Extension Based on Occurrence Grouping; *Computing 94*, 2 (2012) 173-188, 2012.

[4] E. R. Hansen: Sharpness in interval computations; *Reliable computing 3:17-29*; Kluwer Academic Publishers, 1997.

DETECTION OF LOCALIZED DAMAGE IN RAILS BY USING ELASTIC WAVE PROPAGATION

S. Teidj[1], A. Khamlichi[1], A. Driouech[1*] and E. Jacquelin[2]

[1]Laboratory Communication systems
Abdelmalek Essaâdi University, Tetouan, MOROCCO
Sara.teidj@gmail.com, khamlichi7@yahoo.es, adriouach@hotmail.com

[2]Laboratory LMM
University of Lyon, Villeurbanne, FRANCE
eric.jacquelin@univ-lyon1.fr

ABSTRACT

In this work, detection of damage in rails is investigated. Elastic wave propagation technique is used. Rail modelling was performed by means of the finite element method. Interaction with the ground was considered through placing calibrated springs and dashpots. The methodology consisted in three steps. Giving some damage pattern scenario, the first step was performing calculation of the frequency response function between the excitation point where the excitation is imposed on the rail structure and the selected measurement points. Then, the discrete Toeplitz like matrix is constructed by using the inverse Fourier transform of this function. The second step consisted of calculation of the Mexican hat wavelet based spectra for the two signals associated to the undamaged and damaged states. Detectability of defects is finally discussed in the time-frequency diagram as function of the defect characteristics.

1 INTRODUCTION

With the increasing traffic and speed of trains experienced these last years, maintenance of rails has become of great importance. The main objective is to prevent catastrophic failures that can threaten passenger lives and cause huge material and economic losses. Derailments are frequent and the cost of rail failures can be very high [1]. Most of the time, these are caused by formation and propagation of cracks on the rails. Other defects can be associated to wear or result directly from rail manufacturing defects or even their improper use or handling [2].
The rail flaw detector was the first techniques used for rail inspection. The rail forms part of an electric circuit where a current is injected through contact brushes. In the presence of defects the currents are distorted and these are replicated in the magnetic field they induce. This can be detected by sensors placed on the inspection car. Since this method is sensitive to the contact conditions between the rail and the brushes, a contact-less method of inspection based on eddy currents was introduced [3]. This method uses a magnetic core to induce eddy currents in the rail, which losses can be correlated to a potential damage. It presents the advantage that bogies of a standard railway car at the standard speed of the line can be used, but has a crucial drawback because only damages on the surface or those which are enough close to it can be detected. This motivated the apparition of ultrasonic sensors which were used alone or integrated with the induction inspection technique. This way of rail monitoring constituted for a long time the common standard for rail inspection cars [1]. Ultrasonic techniques scan railhead through ultrasonic beams and detect the return of reflected or scattered energy using ultrasonic transducers. The amplitude of the reflections and their arrival times indicate the presence, the location and the severity of the damage. Ultrasonic testing has several drawbacks such as limited ultrasonic inspection car speed, for they are much slower than the line speed. This imposes to impede the railway traffic before carrying out the inspection operation. The operational speed can reach up to 100 km/h. But, if damage is detected the inspection is stopped to check the nature and the severity of the damage and this reduces further the effective inspection speed.
The ultrasonic inspection technique suffers also from the fact that small superficial cracks can shade more severe deep cracks by causing early reflection of waves [1]. In addition, false defect detection occurs frequently and in practice up to 75% of detections have been revealed to be false. This delays even more the inspection time and reduces the effective operational speed.
In the last decades new inspection methods have been developed such as those based on propagation of elastic guided waves through the rails [4].
The propagation based damage detection exploits the wave propagation phenomena by identifying the discrepancies, caused by damage, in the dynamic behaviour of the structure. In this analysis a first time history is stored when the structure is undamaged and serves as reference, the second time signal is acquired while performing health monitoring of the rails under servicing conditions. To detect damage, a coherence function is defined in the time-frequency space; the arrivals of the perturbation waves which are function of the frequency can be identified. By calculating the arrival time of the waves interacting with the defect surfaces, estimation of the damage location can be made [4].

2 DAMAGE DETECTION METHOD

Accuracy of ultrasonic techniques which are developed either in time or frequency domain was recognized to be poor [5]. They are in fact considerably affected by the presence of echo overlapping or by the inherent filtering phenomenon that trims the high frequencies. These limitations can largely be superseded by considering time-frequency representations. Accuracy of predictions can be increased dramatically while the attenuation phenomena is reduced the

monitoring of overlapping echoes is enhanced. Since the continuous wavelet transformation offers better time resolution at high frequency with superior robustness against noise [5], it is used in this work.

Wavelets enable to linearly decompose an arbitrary time signal by projecting it on functions that are simply constructed by means of dilations and translations of a mother wavelet. Among the mother wavelets, the Mexican hat wavelet has the propriety of providing magnitude and phase information that are very useful for visualisation of potential discontinuities.

Cracks and other structural changes generate, in the time-frequency domain obtained by the wavelet transform, vertical or stinted lines [6]. Because of similar behaviour occurs in the time-frequency diagram due to reflections produced by the boundaries of the structure, the analysis of time-frequency diagram should then consider the undamaged state of the structure to avoid misinterpretation. In this work, detection is based on the computed continuous wavelet transform of the difference between the damaged and undamaged time signals. As the variations in a time-frequency diagram can also be caused by noise, one can use the fact that these last induce randomly distributed peaks while defects are characterised by continuous changes of the spectra along a wide frequency range.

3 TRANSIENT RESPONSE MODEL OF RAILS

A finite element model was constructed for a standard rail system. Figure 1 shows the configuration for a rail mounted on stiffeners which are coupled to the ground through springs and dashpots that represent the ballast behaviour.

Figure 1. Rail system mounted on stiffeners through elastic spring and dashpots

The rails and the stiffeners are assumed to be made form homogeneous, isotropic and elastic materials. The considered impact excitation is assumed to result from a transient concentrated force $f(t)$, where t is time. Under the action of the applied force, the dynamic displacement response y is measured at a given point of the rail. The discrete output response $y(k)$ is related to the discrete input force $f(k)$ by a linear system: $Y = HF$, where H is the Toeplitz like transfer matrix connecting the force signal vector F to the measured signal vector Y. Construction of matrix H is performed through using finite element model modelling. Denoting i the measurement degree of freedom and j the degree of freedom giving the direction of the applied force, the frequency response function (FRF) is recovered as $X_{ij}(\omega) = \sum_{k=1}^{N_{modes}} \Phi_{ik}\Phi_{jk} / \left(\omega^2 - \omega_k^2 + 2i\beta_k\omega_k\omega\right)$, where Φ_{ik} is the kth mode normalized with respect to mass, ω_k the angular frequency, β_k the damping coefficient, ω the angular frequency and N_{modes} the total number of retained modes. The time response function can then be obtained using the inverse fast Fourier transform of the FRF X_{ij}.

4 RESULTS AND DISCUSSION

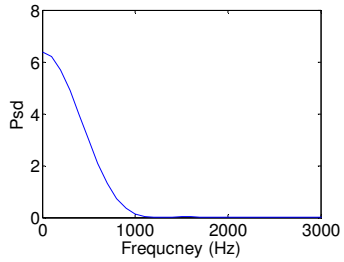

Figure 2: Power spectral density of the input excitation force

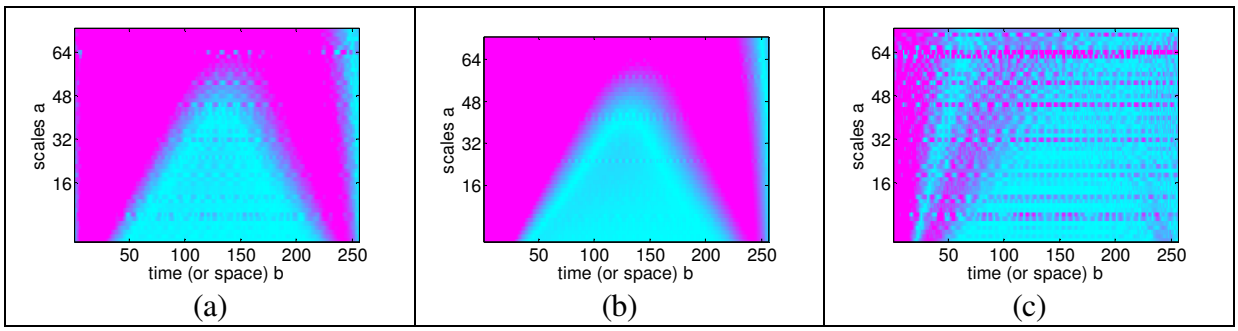

Figure 3: Absolute values of the wavelet transform coefficients as calculated for the differences between time-signals associated to undamaged and damaged rails; (a) localized damage of level 5% of Young modulus, (b) localized damage of level 25% of Young modulus, (c) Variation between the damages at 5% and 25%

Considering the force signal which spectrum is depicted in figure 2, the time-frequency diagram of the difference between the reference signal and the damaged signal was computed. Figure 3 shows the obtained results. Detection of defect is quite possible for both 5% and 25% levels of the defect. One can notice from comparison between cases (a) and (b) cases that, increasing the defect level, provides a more apparent diagram. Figure 3c shows that when the defect location is fixed, typical patterns revealing amplitude variation of the defect are observed.

REFERENCES

[1] D.F. Cannon, K.O. Edel, S.L. Grassie, K. Sawley. Rail defects: an overview. *Fatigue and Fracture of Engineering Materials and Structures* 26, 865-887, 2003.

[2] U. Zerbst, R. Lundén, K.O. Edel, R.A. Smith. Introduction to the damage tolerance behaviour of railway rails – a review. *Engineering Fracture Mechanics* 76:2563-2601, 2009.

[3] R. Clark. Rail flaw detection: overview and need for future developments. *NDT&E International* 37, 111-118, 2004.

[4] J.J Marais, K.C. Mistry. Rail integrity management by means of ultrasonic testing. *Fatigue and Fracture of Engineering Materials and Structures* 26, 931-938, 2003.

[5] J.L. Rose, M.J. Avioli, P. Mudge, R. Sanderson. Guided wave inspection potential of defects in rail. *NDT&E International* 37, 153-161, 2004.

[6] A. Kareem, T. Kijewski. Time-frequency analysis of wind effects on structures. *Journal of Wind Engineering and Industrial Aerodynamics* 90, 1435-1452, 2002

METHODOLOGY USING A HEAT REGULATED IMPEDANCE TUBE FOR THE TEMPERATURE DEPENDENT SOUND ABSORPTION PROPERTY OF MATERIALS

N. Merlette[1*], C. Gautrelet[2] and E. Pagnacco[2]

[1]TANGENT'DELTA
50 rue Ettore Bugatti, Saint Etienne du Rouvray, FRANCE
Email: nicolas.merlette@tgdelta.com

[2]Laboratoire LOFIMS
INSA de Rouen, Avenue de l'Université, Saint Etienne du Rouvray, FRANCE
Email: emmanuel.pagnacco@insa-rouen.fr

ABSTRACT

Knowledge of the absorption property of materials is required to achieve an efficient and robust acoustic design in the context of building, transport or industry applications. Up to now, whereas the mechanical properties of polymer foams are measured in function of the temperature, their acoustic properties are typically characterized in ambient temperature conditions of a laboratory. In this work, an experimental set up is presented to evaluate the temperature dependence of the absorption property of materials. According to the acoustic standards, a heat regulated impedance tube has been developed with a dedicated methodology. The aim of this paper is to explain it and discuss possible construction solutions. As a demonstration, the normal incidence sound absorption coefficient of a polyurethane foam is carried out ranging from +10°C up to +50°C. Results show a shift of the absorption peak by the effect of the temperature.

1 INTRODUCTION

The design of acoustic solutions based on sound absorbing materials requires the characterization of their acoustic properties. The sound absorption coefficient evaluates the efficiency of a material in absorbing the sound waves. Various experimental methods [1-3] with two to four microphones have been developed to measure this property in function of the frequency.

It is well known that polymers have frequency dependent mechanical properties (Young's modulus and loss factor), but also temperature dependent. Transitions within the microstructure explain these dependences. Whereas mechanical characterizations of polymers are typically performed in function of the temperature using dynamic mechanical analyzers, acoustic characterizations do not. Up to now, the sound absorption coefficients of polymer foams are measured in ambient conditions of a laboratory and the standard [4] recommends that the temperature be held constant during the test to within 1°C.

The aim of the paper is to propose an experimental method to evaluate the temperature dependence of the sound absorption property of materials. The first part describes the proposed methodology and the heat regulated impedance tube which has been developed. The construction choices are discussed. The second part presents an application to a polyurethane foam. The temperature dependence of the normal incidence sound absorption coefficient is observed. Finally, a conclusion and perspectives are given.

2 PRINCIPLE OF THE EXPERIMENT

2.1 Objective of the method

The aim of the test method is to measure the normal incidence sound absorption coefficient of porous materials in function of the temperature. The proposal is to extend the use of the impedance tube from ambient temperature to heat regulated conditions. The standardized two-microphone method [4] allows one to determine the normal incidence sound absorption coefficient α from the pressure transfer function between the two microphones. In this configuration, the sound absorbing sample is backed on the rigid termination of the tube at the opposite end of the sound source as shown in Figure 1.

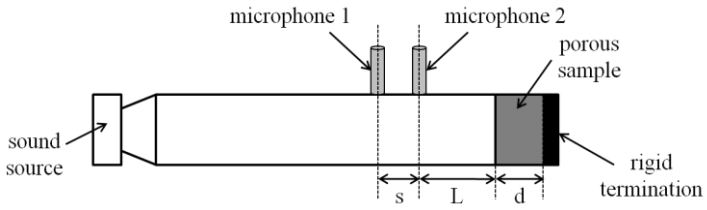

Figure 1. Normal incidence impedance tube with two microphones.

Considering temperature dependent acoustic properties, the normal incidence sound absorption coefficient α is given by

$$\alpha = 1 - \left|R\right|^2. \tag{1}$$

where R is the complex reflection coefficient which is function of the temperature T of the test. From the pressure transfer function H_{12} measured between microphones 1 and 2 at the temperature T, the expression of the complex reflection coefficient is

$$R = \frac{H_{12} - e^{-jks}}{e^{jks} - H_{12}} e^{2jk(L+s)}. \quad (2)$$

where s is the distance between the two microphones and L the distance between microphone 2 and the front surface of the test sample. Here, k represents the real wave number in the air cavity of the tube, assuming no dissipation. Considering the cavity is homogeneous at the temperature T, the wave number is given by

$$k = \frac{\omega}{c} = \frac{\omega}{20.047\sqrt{273.15 + T}}. \quad (3)$$

with ω the angular frequency, c the speed of sound in air changing with temperature T in °C.

2.2 Choices for the experimental setup

2.2.1 Tube, microphones and sound source

The tube (its dimensions and material), the microphones and loudspeaker are chosen according to their acoustic specifications but also to their temperature stability and operating range. Diaphragms made of titanium alloy should be more stable than diaphragms made of polymer.

2.2.2 Heat regulation

The objective of the heat regulation system is to move the temperature of the tube and the porous sample from the ambient temperature to a higher or lower temperature T. It must maintain this temperature constant during the acoustic measurement. It is decided to use a thermoelectric cooler which has the advantage to heat or cool by inversing the current. A heat chamber is realized around the tube. As shown in Figure 2 and Figure 3, the microphones and the diaphragm of the loudspeaker are included in the chamber in order to avoid temperature gradient between the acoustic apparatus. The temperature of the tube is controlled by two sensors.

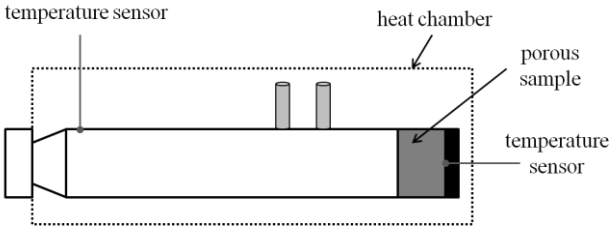

Figure 2. Scheme of the heat regulation system.

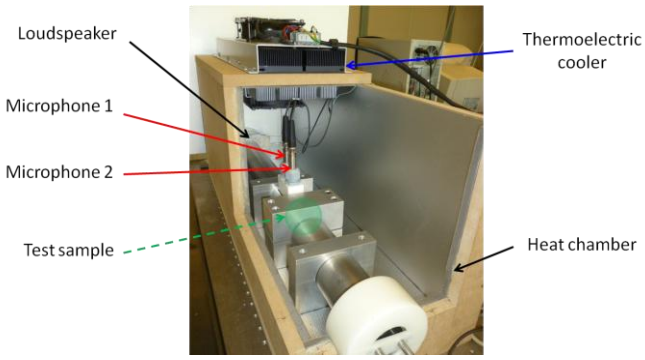

Figure 3. Heat regulated impedance tube setup.

3 APPLICATION TO A POLYURETHANE FOAM

A sample of polyurethane foam has been tested using the proposed apparatus. The procedure consists of the measurement of the pressure transfer at five target temperatures (+10, +20, +30, +40 and +50°C). For each target temperature, a stabilization stage of 10 minutes is performed and a mismatch correction [4] of the measurements is done by interchanging the microphones positions. The evaluated normal incidence sound absorption coefficients are presented in Figure 4.

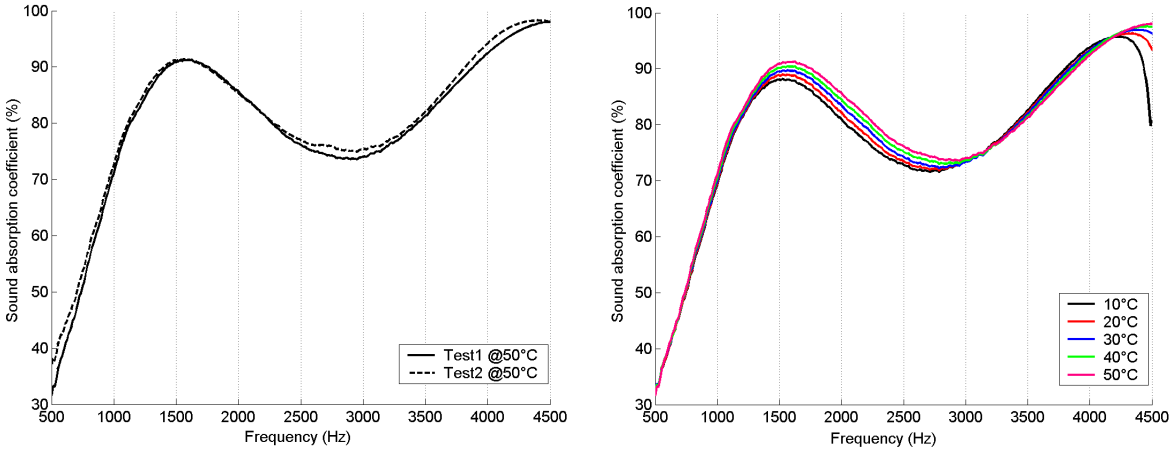

Figure 4. Left: sound absorption coefficient for a repeatability test at +50°C. Right: sound absorption coefficient for five test temperatures.

As shown on the left, measurements are repeatable with the foam sample. On the right, it is observed a shift of the sound absorption coefficient by the effect of the temperature. The higher the temperature, the higher the peak value of the sound absorption coefficient is (at 1500 Hz).

4 CONCLUSION

An experimental setup and a methodology are presented to measure the temperature dependence of the sound absorption coefficient of acoustic materials. Based on the acoustic standards, a heat regulated impedance tube has been realized. It is used to test a polyurethane foam. The sound absorption coefficient is shifted by the effect of the temperature between +10°C and +50°C.

More details about the methodology and the experimental setup will be given in the full paper of the conference, as well as applications and results.

REFERENCES

[1] A.F. Seybert, D.F. Ross. Experimental Determination of Acoustic Properties Using a Two-Microphone Random-Excitation Technique. *J. Acoust. Soc. Am.* 61(5):1362-1370, 1977.

[2] O. Doutres, Y. Salissou, N. Attala, R. Panneton. Evaluation of the acoustic and the non-acoustic properties of sound absorbing materials using a three-microphone impedance tube. *Applied Acoustics*. 71(2010):506-509, 2010.

[3] J. Kunio, T. Yoo, K. Hou, J. Enok. A Comparison of Two and Four Microphone Standing Wave Tube Procedures for Estimating the Normal Incidence Absorption Coefficient. Inter-noise 2009, Ottawa, 2009.

[4] ASTM E1050-10.Standard Test Method for Impedance and Absorption of Acoustical Materials Using a Tube, Two Microphones and a Digital Frequency Analysis System. 2010.

ACOUSTICS OF RIGID POROUS MEDIA WITH DAMPED HELMHOLTZ RESONATORS

C. Boutin[1]

[1]LGCB- CeLya- UMR CNRS 5513
University of Lyon - ENTPE, France
Email: claude.boutin@entpe.fr

ABSTRACT

This paper deals with the acoustics of gas saturated rigid porous media with inner resonators. The aim is first to identify microstructures of heterogeneous porous media in which inner resonance phenomena may occur, and second, to provide the modeling of acoustic waves in this situation. The conditions for observing inner resonance are detailed and used to design a periodic medium consisting in damped Helmholtz resonators embedded in a porous matrix. The macroscopic description of this system is established through the homogenization method. It is shown that the response of resonators brought a negative contribution to the effective stiffness of the gas. Then, the atypical features of acoustic wave propagation are determined and the occurrence of a broad band gap along with strongly dispersed waves is discussed according to the characteristics of the porous matrix and of the damped resonators.

1 INTRODUCTION

This paper studies the propagation of acoustic waves in gas saturated rigid porous media with embedded resonators periodically distributed. We focus on situations where the frequency of long waves (compared to the period size) coincides with the resonance of the damped resonators. The idea is to enforces a "partial" non equilibrium state at the local scale. Indeed, several examples e.g. [1], [5], [4], [3], [2], prove that media presenting such a local state are driven at the macroscopic scale by non conventional mechanics. Such materials are of prime interest for their unconventional properties. In this work we identify microstructures of heterogeneous porous media in which inner resonance phenomena may occur, and we provide the modelling of acoustic waves in this situation.

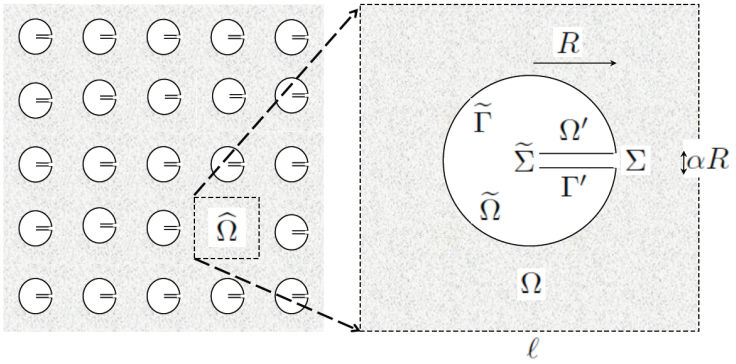

Figure 1. Porous matrix with inner resonators

2 MODELLING

The analysis leads to design a periodic medium consisting in damped Helmholtz resonators embedded in a porous matrix (Figure 1). The macroscopic description of this system is established through homogenization method. It is shown that the dynamic response of resonators brought a negative contribution in the effective stiffness of the gas at frequency higher than the resonance. The system - in the isotropic case - is governed by the following equations (V, P gas velocity and pressure ; μ, γ, P^e gas viscosity, adiabatic coefficient and equilibrium pressure ; ϕ_m, $K_m(\omega)$, $\Pi_m(\omega)$, porosity, dynamic permeability, and thermal permeability of the matrix, c volume concentration of resonators, ω_0 resonator eigen frequency, $\tau'(\omega)$ tortuosity of the duct of the resonator, A real geometrical coefficient) :

$$\begin{aligned} \mathrm{div}_x(V) \quad + \quad & i\omega \frac{P}{\gamma P^e} \left(\phi_m (1-c)\gamma (1-\Pi_m(\omega)) + \frac{c}{1-(\omega/\omega_0)^2 \tau'(\omega)} \right) = 0 \\ V \quad = \quad & -\frac{K_m(\omega)}{\mu} A.\nabla_x P \end{aligned}$$

From this description, the atypical features of acoustic wave propagation are determined : the occurrence of a broad band gap and of strongly dispersed waves is evidenced and related to the characteristics of the porous matrix and of the damped resonators. Figure 2 highlights that the effective properties departs very significantly from the usual poro-acoustic behavior, [6].

3 CONCLUSION

The homogenized model is quasi-analytic and its effective parameters are fully determined from the knowledge of the geometry and of the properties of the material constituting the period.

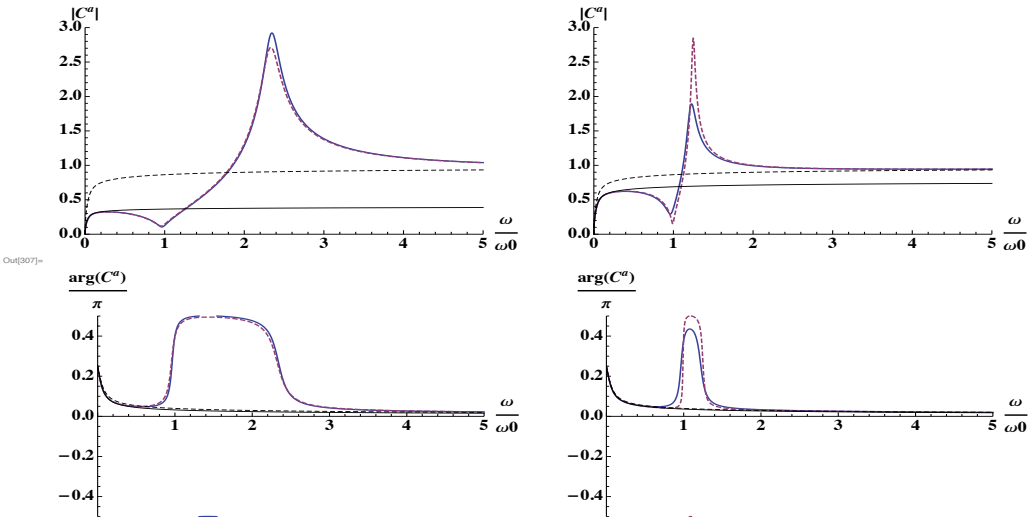

Figure 2: Effect of resonators on dimensionless acoustic celerity. Modulus (Top), and Phase (Bottom) for a concentration of resonator of 0.3 and matrix porosity of 0.1 (right) and 0.8 (left)

Therefore the model can be used to project unconventional acoustic media. Inner resonant porous media could be of interest for practical applications, that may concern the design of new systems, either for damping or for fast/low velocity purpose, at different spatial and/or frequency scales. Finally, it would be of interest to realise such materials and to perform tests in order appreciate experimentally their actual properties.

REFERENCES

[1] J.-L. Auriault and G. Bonnet : "Dynamique des composites élastiques périodiques", *Arch. Mech.* **37**(4-5), 269–284, (1985)

[2] J.-L. Auriault and C. Boutin "Long wavelength inner-resonance cut-off frequencies in elastic composite materials" *Int. Journal of Solid and Structures*. **49**: 3269-3281(2012)

[3] C. Chesnais, C. Boutin, S. Hans, "Effects of the local resonance on the wave propagation in periodic frame structures" *J. Acoust. Soc. Am.* (132), 4 ; 2873-2886, (2012)

[4] X. Olny and C. Boutin : "Acoustic wave propagation in double porosity media ", *J. Acoust. Soc. Am.* **113** (6), 73-89. (2003)

[5] Vasseur J.O., Deymier P.A., Prantziskonis G. and Hong G.: "Evidence of absolute acoustic band gaps in two-dimensional periodic composite", *J. Phys.: Condens. Mater* **10**, 6051-6064.(1998)

[6] C. Boutin : "Acoustic of rigid porous media with inner resonators ", submitted to *J. Acoust. Soc. Am.*

ACOUSTIC IMPEDANCE OF MICROPERFORATED HONEYCOMB PANELS

Margaux Regniez[1 2], François Gautier[2], Charles Pézerat[2] and Adrien Pelat[2]

[1]Centre National des Études Spatiales
18 avenue Edouard Belin, Toulouse, FRANCE
Email: margaux.regniez.etu@univ-lemans.fr

[2]Laboratoire d'Acoustique de l'Université du Maine
avenue Olivier Messiaen, Le Mans, FRANCE
Email: francois.gautier@univ-lemans.fr, charles.pezerat@univ-lemans.fr,
adrien.pelat@univ-lemans.fr

ABSTRACT

Composite materials as sandwich honeycomb panels are more and more used in industrial sectors as automotive, aeronautics or in the spatial domain, because it has the advantage to lighten the systems. The micro-perforations are quite used for acoustical absorption, and avoid adding mass. Thus, micro-perforated honeycomb panels seem to be a good agreement in terms of acoustical solution and lightening competition. The aim of this paper is to propose an acoustical impedance model based on the Maa's model and on electro-acoustical equivalence. This model is validated by measurements using an impedance tube and results are shown for two kinds of honeycomb sandwich panels.

1 INTRODUCTION

The aim of the work is to set an acoustic impedance model to describe the sound absorption behaviour of two kinds of honeycomb sandwich panels. The first panel is simply micro-perforated and the second one presents two kinds of holes population: it is naturally perforated because of its manufacturing process and it has additional micro-perforations. Both of the panels have coupled honeycomb cells, described by the presence of microperforations on cells' walls, which are taken into account in the model. The study is done for a linear and harmonic regime. The pressure is considered to carry as a plane wave. The model is based on Maa's works and uses electro-acoustical equivalences. The second part of the paper presents an experimental validation and some results for both panels.

2 ACOUSTICAL IMPEDANCE MODEL

The propagation of sound in microperforations is based on the acoustic propagation inside thin tubes. [1] Using Crandall's researches and experimental works, Maa [2] [3] set an expression for the impedance of a microperforation (see Equation 1) and then, the impedance of a microperforated panel, coupled or not with a cavity. Quickly, it has been shown that the resistive (relative to viscous and thermal effects) and the reactive (relative to the mass of air inside the perforation) parts of the microperforation impedance needed corrections because of additional viscous and radiation effects. [4] [5]

$$Z_{perf} = \frac{32\nu\rho_0 t}{d^2}\left[\sqrt{1+\frac{x^2}{32}}+\sqrt{2}x\frac{d}{8t}\right]+j\omega\rho_0 t\left[1+\frac{1}{\sqrt{3^2+\frac{x^2}{2}}}+\frac{8}{3\pi}\frac{d}{t}\right] \quad (1)$$

, where $x = \sqrt{\frac{\rho_0\omega}{\mu}}\frac{d}{2}$ is an adimensional perforation constant defined by Maa [3], ν is the kinematic viscosity $[m^2 \cdot s^{-1}]$, ρ_0 is the density of the fluid $[kg \cdot m^{-3}]$, t is the thickness of the skin in m and d the perforation's diameter, ω is the pulsation in $rad \cdot s^{-1}$, and μ is the dynamic viscosity of the fluid $[N \cdot s \cdot m^{-2}]$.

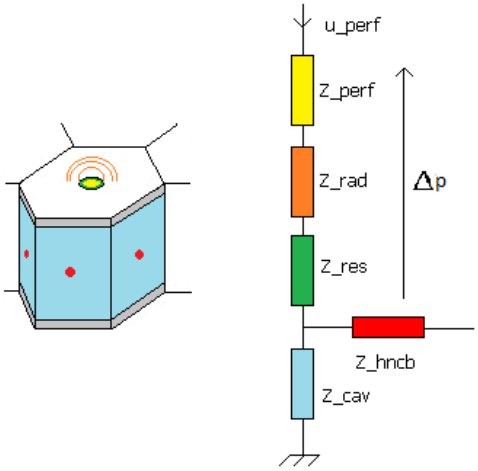

Figure 1: *On the left*: One elementary honeycomb cell. *On the right*: The equivalent electro-acoustical diagram of an elementary honeycomb cell.

Several works on microperforation [2] [3] [6] use an electrical representation which is based

on electro-acoustical equivalences. In order to take into account each element of an elementary honeycomb cell (see Figure 1), the model set chooses this representation too. If an infinite honeycomb sandwich panel is considered with a microperforation in each cell, the impedance Z_{hncb} of microperforations on honeycomb walls can be neglected thanks to a symmetrical effect. A typical result of the impedance calculation for a microperforated honeycomb is ploted on the Figure 2 and uses the Equation 1 divided by the perforation ratio $\sigma = 78,5(\frac{d}{b})^2$ with b the distance between two perforations.

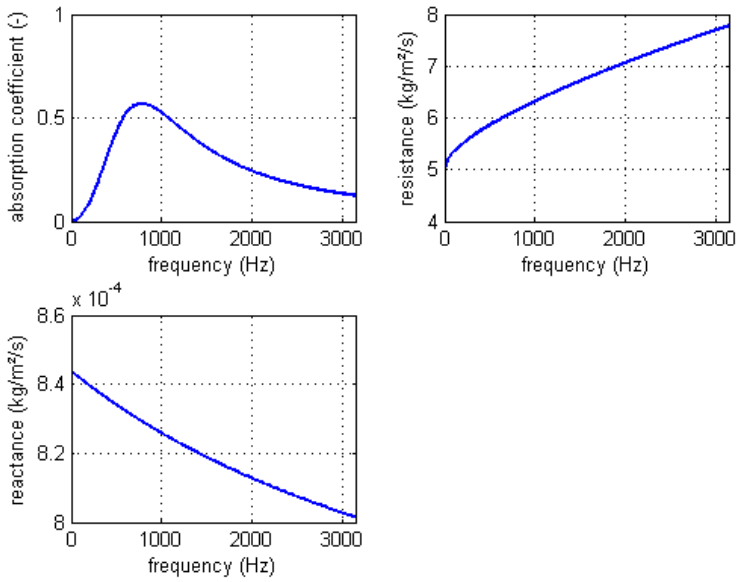

Figure 2: *At the top-left corner*: Absorption coefficient of a microperforated honeycomb sandwich panel. *At the top-right corner*: Resistive part of the acoustical impedance. *At the low-left corner*: Reactive part of the acoustical impedance.

3 ACOUSTIC IMPEDANCE MEASUREMENT

The acoustic impedance for plane wave incidence of both of the microperforated honeycomb sandwich panels can be measured using an impedance tube (see References [7] and [8]). On the Figure 3 are plotted experimental results for the empty tube and four different honeycomb sandwich samples.

On the left-top corner of the Figure 3, the non-microperforated honeycomb sandwich sample is perfectly reflective and the naturally micro-perforated one presents a non negligible absorption. On the low-left corner, if another type of micro-perforation is added to the naturally microperforated sample, its absorption performance is reduce for frequencies lower than 450 Hertz. On the right-top corner of the Figure 3, the absorption measurement has the same shape as the model, but the peak's frequency and the curve's amplitude are different.

4 CONCLUSION

In this paper is presented an impedance model for honeycomb sandwich panels which present a microperforation at each honeycomb cell, inspired by the works of Maa and using an electric equivalence to acoustics. Two kinds of composite panels are studied: one microperforated and the other doubly microperforated. It has be observed that low frequency absorption performances have been reduced because of the additional microperforations.

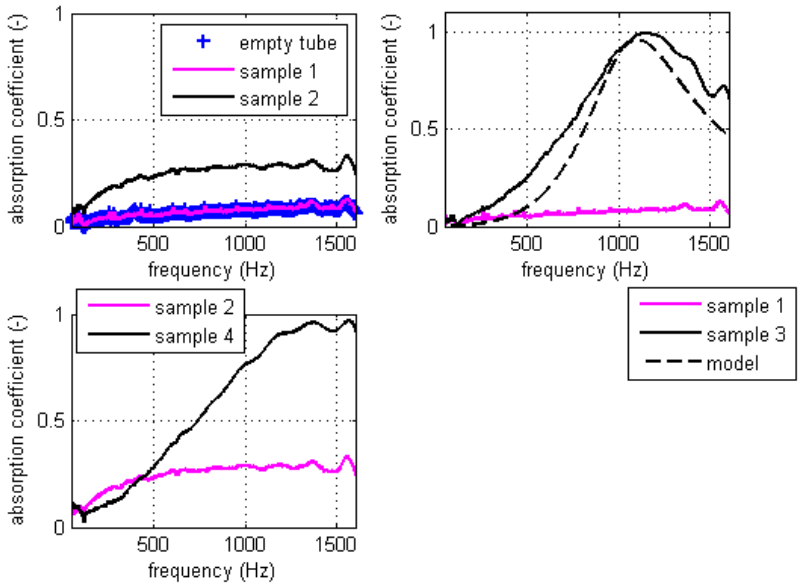

Figure 3: Absorption coefficients of several honeycomb sandwich samples placed in the impedance tube. *Sample 1*: non-microperforated. *Sample 2*: naturally microperforated. *Sample 3*: microperforated. *Sample 4*: doubly microperforated.

5 ACKNOWLEDGEMENTS

This work is supported by the french national center of spatial studies (CNES) and the french company Thales Alenia Space.

REFERENCES

[1] Crandall I. B. *Theory of vibrating systems and sound*. New York: Van Nostran, 1926.

[2] D-Y. Maa. Theory and design of microperforated panel sound-absorbing constructions. *Scientia Sinica*, XVIII(1), 1975.

[3] D-Y. Maa. Microperforated-panel wideband absorbers. *Noise Control Engineering Journal*, 29(3), 1987.

[4] G. B. Thurston and C. E. Martin Jr. Periodic fluid flow through circular orifices. *Journal of the Acoustical Society of America*, 1953.

[5] U. Ingard. On the theory and design of acoustic resonators. *Journal of the Acoustical Society of America*, 1953.

[6] T. Dupont. *Transparence et absorption acoustiques des structures micro-perforées*. PhD thesis, Institut National des Sciences Appliquées de Lyon, 2002.

[7] J. Y. Chung and D. A. Blaser. Transfer function method of measuring in-duct acoustic properties. part i: Theory. *Journal of the Acoustical Society of America*, 68:907–913, 1980.

[8] J. Y. Chung and D. A. Blaser. Transfer function method of measuring in-duct acoustic properties. part ii: Experiment. *Journal of the Acoustical Society of America*, 68:914–921, 1980.

AN ANALYTIC STUDY OF THE NOISE REDUCTION OF AN INFINITE MULTI-LAYERED CYLINDER

J. MAGNIEZ[1,*], M. A. HAMDI[1] and J. D. CHAZOT[1]

[1]Laboratory Roberval of Mechanics, Acoustics and Materials (UMR 7337)
University of Technology of Compiègne (UTC), Compiègne, FRANCE
Email: julien.magniez@utc.fr, mohamed-ali.hamdi@utc.fr, jean-daniel.chazot@utc.fr

ABSTRACT

An exact analytical method has been developed to calculate the Noise Reduction (NR) factor of an infinite multi-layered cylinder excited by an incident acoustic plane wave. This analytical formulation has been developed and numerical results have been validated by comparison to numerical results published on recent papers. A parametric study has been conducted to study the influence of various parameters such as the angle of incidence, the thickness and the mechanical properties of each material layer. In this paper only a brief review of the model is presented and illustrated with a result obtained for a cylinder composed by three layers of materials: two sheets separated by a polymer core inducing vibration damping. The idea of this work is to enhance the noise reduction at the low and medium frequencies by introducing a polymer core layer having optimized mechanical properties to achieve maximum damping around the ring frequency of the cylinder.

1 INTRODUCTION

Multi-layered shells are increasingly used in aeronautics and aerospace industries. They are found in a wide range of applications such as helicopters, space launch vehicles or aircrafts. Generally designed to reduce the mass of the structures, these shells must also take into account the problem of inner noise transmission. Indeed, whether it is for the passengers' comfort or the payload protection, a noise protection is still necessary in such structures. Consequently, the prediction of the sound transmission through multi-layered shell structures must be carefully examined.

In order to understand the main phenomena of sound transmission through multi-layered cylinders, many analytical studies have been led. Two kinds of analytical models can be distinguished. First, a 3-dimensional elastic model can be used for isotropic cylinders [1]. This model is not simplified and is accurate over all the frequencies. Then, for anisotropic cylinders, only a shell model is available [2]. It is based on a simplified displacement field which does not take into account the deformation through the thickness of the layer. Consequently, this model is only available for thin layers and can show some limitations in high frequencies.

The aim of this paper is to study the sound transmission through a sandwich cylinder with a damping core by using an exact 3-dimensional elastic model. The modal transfer matrices method is used to describe the response of the cylinder, and the Noise Reduction (NR) factor is obtained after solving the vibro-acoustic problem. The model is then validated by comparison to numerical results published by other authors. The results presented illustrate the influence of some acoustic and structural parameters on the sound transmission.

2 DESCRIPTION OF THE PROBLEM

The problem studied here is an infinite multi-layered cylinder, excited by an external oblique plane wave, as shown in Figure 1a. The cylinder is surrounded by an external fluid Ω_1 of characteristics $\{\rho_1, c_1\}$ and an internal fluid Ω_2 of characteristics $\{\rho_2, c_2\}$. The terms ρ_i and c_i are respectively the density and the speed of sound in the medium i. In the present paper the interior cavity of the cylinder is considered as reverberant, i.e. divergent waves are taken into account.

The cylinder is composed by three layers (see Figure 1b): two rigid sheets coupled with a soft polymer core.

3 ANALYTICAL MODEL

To treat this problem, the acoustic equations in the exterior and interior domain, and the equations governing the motion of the cylinder are solved with specific coupling and boundary conditions. The main equations are presented hereafter.

3.1 Acoustic pressure in fluid medium

The solutions of the Helmholtz equation for the external and internal pressure are developed on the cylindrical harmonics. Consequently, the external pressure p_1 and the internal pressure p_2 are expressed as follow:

$$p_1 = p^I + p^R = p_0 \sum_{n=0}^{\infty} \varepsilon_n i^n J_n\left(k_{1r} r\right) \cos\left(n\theta\right) e^{ik_{1z} z - i\omega t} + \sum_{n=0}^{\infty} A_n H_n^1\left(k_{1r} r\right) \cos\left(n\theta\right) e^{ik_{1z} z - i\omega t}, \tag{1}$$

$$p_2 = p^T = \sum_{n=0}^{\infty} B_n J_n\left(k_{2r} r\right) \cos\left(n\theta\right) e^{ik_{2z} z - i\omega t}, \tag{2}$$

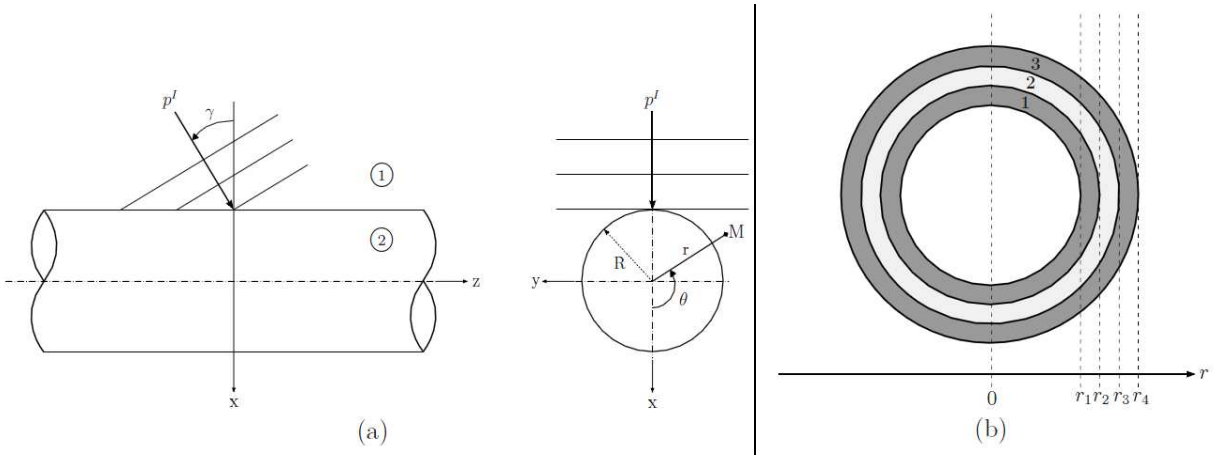

Figure 1. Infinite cylinder excited by an external plane wave. Notations: (a) General problem; (b) Material layers.

where p^I, p^R and p^T are the incident pressure, the reflected pressure and the transmitted pressure, of amplitude p_0, A_n and B_n respectively. Moreover, the subscript n denotes the circumferential modes of the cylinder, J_n and H_n^1 are the Bessel function and the Hankel function of first kind, respectively, k_{ir} and k_{iz} are the radial and axial wavenumbers in the medium i, and ε_n is the Neumann factor.

3.2 Cylinder vibrations

The solid displacements in the cylinder can be written in a similar form by solving the following equation of motion in cylindrical coordinates (see reference [1]):

$$\rho\omega^2\vec{U} + div\bar{\bar{\sigma}} = 0, \tag{3}$$

where ρ is the density of the layer, $\vec{U}$ is the displacement field and $\bar{\bar{\sigma}}$ is the stress tensor. The results are then expressed with a modal transfer matrix where displacements and stresses of the inner surface are connected to the displacements and stresses of the outer surface.

3.3 Coupling conditions

In our problem, the material layers are bounded together. Consequently, the coupling conditions between the layers are written with the continuity of the displacements and the stresses. Two coupling conditions with the fluid domains are also necessary. The first one is the condition of normal displacements continuity,

$$\left.\frac{\partial p_{1,2}}{\partial r}\right|_{r=r_4,r_1} = -\rho_{1,2}\left.\frac{\partial^2 U_r}{\partial t^2}\right|_{r=r_4,r_1}, \tag{4}$$

where U_r is the radial component of the displacement field. The second one is the normal stress continuity, given by

$$\sigma_{rr} = -p_{1,2},\ \sigma_{r\theta} = 0,\ \sigma_{rz} = 0 \quad \text{at } r = r_4, r_1. \tag{5}$$

4 RESULTS

The model is now used to calculate the noise reduction of the cylinder. The Figure 2 shows the result for a cylinder having a mean radius of 2.16 m composed by two aluminium sheets (E = 69 Gpa, ρ = 2768 kg/m^3 and ν = 0.3) having a thickness of 1mm, and a polymer core (E = 0.01 Gpa, ρ = 1000 kg/m^3 and ν = 0.49) having a thickness of 5 mm and a structural damping of 0.3. The incidence of the plane wave with respect to the normal is 45°. The classical stiffness and mass behaviours are still observed below and above the ring frequency at 300 Hz, while the internal cavity resonances are visible by the various dips in the curve.

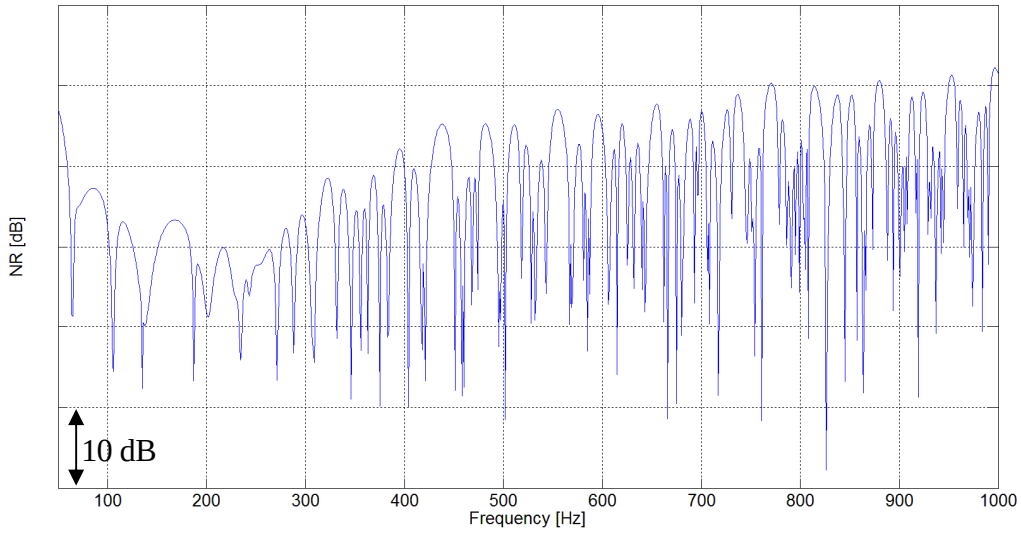

Figure 2. Noise reduction for an infinite cylinder excited by an external plane wave.

The present model is aimed to optimize the structural parameters, in particular those of the viscoelastic core layer, in order to increase the noise reduction in low and medium frequencies, where the isolation is low (below 400 Hz on Figure 2). In the following this model will therefore be used to realize a parametric study and an acoustical optimisation. More results will be presented in further works.

5 CONCLUSION

This paper deals with the analytical model of sound transmission through a multi-layered infinite cylinder. The model presented here uses the 3-dimensional theory of elasticity, without simplification over all the frequencies. The model will be used in further works to optimize the structural parameters in order to increase the noise reduction of a sandwich cylinder composed of two sheets coupled with a polymer core.

REFERENCES

[1] J. S. Sastry and M. L. Munjal. Response of a multi-layered infinite cylinder to two-dimensional pressure excitation by means of transfer matrices. *Journal of Sound and Vibration*. 209(1):123-142, 1998.

[2] S. Ghinet, N. Atalla, and H. Osman. Diffuse field transmission into infinite sandwich composite and laminate composite cylinders. *Journal of Sound and Vibration*. 289(4-5):745-778, 2006.

The transmission loss of sandwich-composite panels with attached noise control materials

H. Osman[1], N. Atalla[2]

[1]United Launch Alliance, Englewood, CO, USA 80112
Email: haisam.a.osman@ulalaunch.com

[2]Department of Mechanical Engineering, Université de Sherbrooke, Sherbrooke (QC), Canada J1K 2R1

ABSTRACT

This paper discusses the modeling of the transmission loss of sandwich composite panels with attached sound packages, using both analytical and numerical methods. First, the physics governing the vibroacoustic response of such panels is recalled. Next, two wave based models are presented and compared to a hybrid model based on the numerical or the experimental identification of the dispersion curve of the panel. The modeling of the effect of an added sound package is next presented. Finally, Experimental tests are presented to assess the performance of the presented models and demonstrate their range of applicability and usefulness.

DESIGN OF AN ACOUSTIC ANECHOIC ROOM FOR AN APPLICATION OF TEACHING AID

Y. Remram[1], H. Khelladi[1], M. Attari[1], S. Boukhenous[1]

[1]Laboratory of instrumentation
University of Science and technology Houari Boumediene, Faculty of electronics and computers, BP32 El-Alia, 16111 Bab-Ezzouar, Algiers, ALGERIA
Email: yremram@gmail.com,hassinakhelladi@yahoo.fr, attari.mo@gmail.com, sboukhenous@gmail.com

ABSTRACT

Many acoustic experiments should ideally be performed out of doors in order to overcome the problems of reflexions. However, it is essential that the environmental noise which is connected with the experiment should be low in intensity and meteorological conditions should be suitable. In addition the sound transmission by any of the paths is strongly affected by temperature gradients and the reflections coming from the earth's surface.

In practice these conditions are seldom met and it becomes necessary in many cases to carry out the experiments under conditions which have been specially designed to simulate stable open air conditions, that is, the interiors of anechoic room. In this paper we describe a room which has been constructed by Electronic staff with the aid of some final year students at the Faculty of Electronics and Computer of the University of Science and Technology Houari Boumediene of Algiers. Some acoustic characteristics of the room like the time reverberation, background noise and transmission loss measurement are exposed.

1 INTRODUCTION

Sound waves travel from source to receiver outdoors trough an atmosphere that is in constant motion. Turbulence, temperature and wind gradients, viscous and molecular absorption and reflection from the earth's surface all affect the amplitude and create fluctuations in the sound receiver, whereas in an anechoic room, all boundaries are highly absorbent creating free field region in stable air conditions. Beside the great absorption inside the room, the transmission loss of at least 40 dB should be achieved in order to obtain very low background level of the noise in the room. An anechoic room is an ideal environment for many standard tests such as the measurement of microphone and loudspeaker frequency responses [1]. Ananthapadmanabhant et all reported that absorption of acoustical materials can be precisely measured in anechoic chamber [2]. In this context and it was essential to have some sort of acoustic dead room in which students could carry out their experiments with the hope of obtaining reproducible results with reasonable accuracy.
In order that the room can be useful for acoustical measurements, every surface should be covered by absorbing materials so that the reverberation time at 500Hz approaches 0.1 s and the transmission loss (at normal incidence) of 30 to 35 dB at 500Hz. Before any contribution from us to make the room anechoic, the room had an enclosure walls already constructed from a double brick wall of 230 mm thick filled with dry sand which represent a good insulation from the external room, since the greater the mass, the larger the insulation is obtained between two partition [3].

2 DESCRPTION OF THE ANECHOIC ROOM

A sketch of the dead room is given figure 1 together with its location in laboratory. The internal dimensions of the chamber are 4.3m length, 2.90m width and 2.10m height. The inner walls and ceiling of the chamber were first covered from absorptive panel made from 4cm thick polystyrene panel fixed to the wall by metal screw. More than 480 egg plates were fixed to the polystyrene panels by pins leaving some holes for lighting and electrical outlet. Finally a thick rock-wool was easily fixed inside the egg plate holes overcoming the use of glue which make the surface harder that can increase the sound wave reflexions. Regarding the ground, a 4 cm thick carpet was laid on the floor to eliminate reflections coming from the ground.

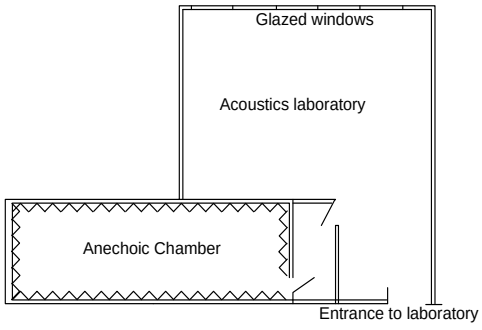

Fig.1 Location of the anechoic room in the acoustic laboratory

The basic room construction was completed and the interior view of the chamber under construction is shown in figure 2 and the finalized chamber is illustrated in figure 3 showing the final year students working on it.

Figure 2. Image of the anechoic room under construction.

Fig 3. Interior view of the room showing students finalising it.

3 TEST AND CHARACTERIZATION THE ANECHOIC ROOM

Once the room was finalized, characterization was fulfilled by measuring the background noise at different time of the day, the reverberation time and transmission loss. These are the essential characteristics which can show the behavior of the chamber before any acoustic experiments.

3.1 The background noise measurement

The background noise level measurements shown in figure 4 were made during an afternoon when a class of students was working in the laboratory outside the chamber.

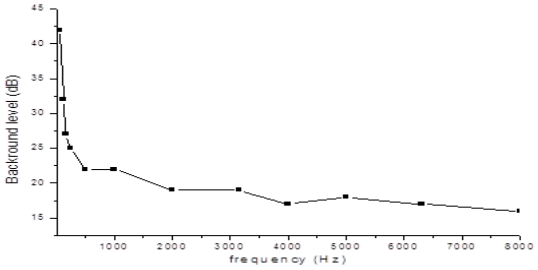

Figure 4. Background noise level in the room as a function of frequency.

3.2 The transmission loss measurements

The transmission loss measurements of figure 5 were carried out between the chamber and the laboratory trough double leaf partitions.

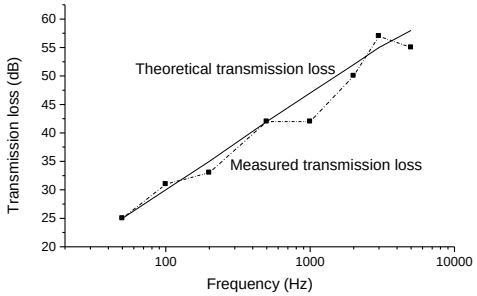

Figure 5.Transmission loss through room walls for normal incidence.

The source of noise was loudspeaker excited by pink noise generator at a level of approximately 100dB in the source room. The results of the transmission loss show a gap between approximately 7 and 2dB from 200Hz band and up, however the results obtained for the majority of the bands approach substantially the theoretical results.

3.3 The reverberation Time measurement

The study of reverberation of the chamber is one of the best parameter for the characterisation of the room. The sound source used to excite the chamber must have enough energy throughout the spectrum to assure decays sufficiently above the background noise to give required accuracy. In this context a short impulse source of 104 dB sound pressure level at 1 meter distance was used. The reverberation time measurements showed in figure 6 gives a fair agreement with theoretical reverberation time being measured. However, it should be pointed out that the measured points of reverberation time in figure 6 are essentially those values of the response time of the measuring equipment. This is certainly the reason why the measured values (dotted line) tend to flatten off above 2000Hz.

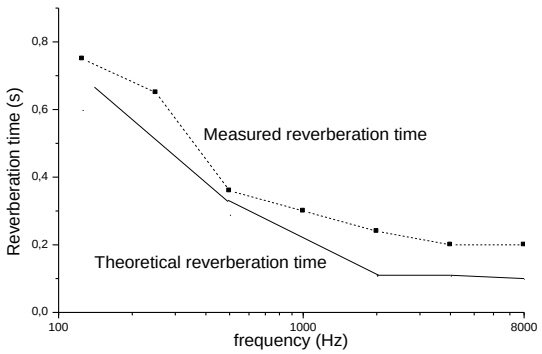

Figure 6. Reverberation time as a function of frequency

4 CONCLUSION

An inexpensive anechoic chamber having reasonable dead-room qualities has been constructed for comparatively small sum. It does not display the acoustic properties of commercial anechoic room, but the room described above will be fully adequate and will become an essential teaching aid in the faculty and as well for research purposes. In this preliminary work it has been shown that the chamber can accomplish many acoustic experiments whether in teaching or research domains.

5 REFERENCES

[1] V.E. Leishman, S. Rolling, M.H. Smith. An experimental evaluation of regular polyhedron loudspeakers as omnidirectional sources of sound. *J. AcoustSoc Am*, 120(3): 1411-1422, 2006.

[2] T. Ananthapadmanabhant, K.Krishnamurrthy, V. Radhakrishnan, S. Swarnamani.Design of an anechoic chamber to study acoustic characteristic of contacting surfaces .*Journal of the Institution of Engineers*. *India.* 63(5): 189-195, 1983.

[3] L.E. Kinsler, A. Frey, A.B. Coppens, J.V. Sanders. *Fundamentals of acoustics*, fourth edition, John Willey and Sons, Inc, (2000).

ON THE MODELING OF ADHESIVE CONTACT AND STICTION FAILURE IN MICRO-SWITCHES

L. Wu[1,2], L. Noels[1] and J.-C. Golinval[1*]

[1] Aerospace and Mechanical Engineering Department
University of Liege, BELGIUM
Email: L.Wu@ulg.ac.be, L.Noels@ulg.ac.be, JC.Golinval@ulg.ac.be

[2] School of Aeronautics
Northwestern Polytechnical University, Xi'an, CHINA

ABSTRACT

Undesirable stiction, which results from contact between surfaces, is a major failure mode in micro-switches. Indeed the adhesive forces can become so important that the two surfaces remain permanently glued, limiting the life-time of the MEMS. This is especially true when contact happens between surfaces where elasto-plastic asperities deform permanently until the surfaces reach plastic accommodation, increasing the surface forces. To predict this behavior, a micro adhesive-contact model is developed, which accounts for the surfaces topography evolutions during elasto-plastic contacts. This model can be used at a higher scale to study the MEMS behavior, and thus its life-time. For illustration purpose, an electrostatic-structural analysis is performed on a micro-switch.

1. INTRODUCTION

Stiction is one of the most common failure mechanisms in micro-electromechanical systems (MEMS) and remains a major issue for micro-switches [1]. Stiction happens when two components entering into contact permanently adhere to each-other because the restoring forces are smaller than the surface forces (capillary, van der Waals (VDW) or electrostatic). This can happen either during the fabrication process at etching (release stiction) or during normal use (in-use stiction). The risk of in-use stiction increases when plasticity is involved during the contact phase, as the contact surface of asperities increases.

2. MICRO-MODEL FOR ELASTO-PLASTIC ADHESIVE-CONTACT

2.1. Single Asperity Elasto-Plastic Contact

Let an asperity of tip radius R, Young modulus E, and yield stress S_Y, interacts with a rigid plane at an interference distance δ, positive in case of contact and negative otherwise, as illustrated in Figure 1.a and 1.b, defined as the distance between the original profile of the asperity tip and the plane. When the plane starts interacting with the asperity during loading, the critical yield interference δ_{CP} is defined as the interference at which the asperity starts yielding.

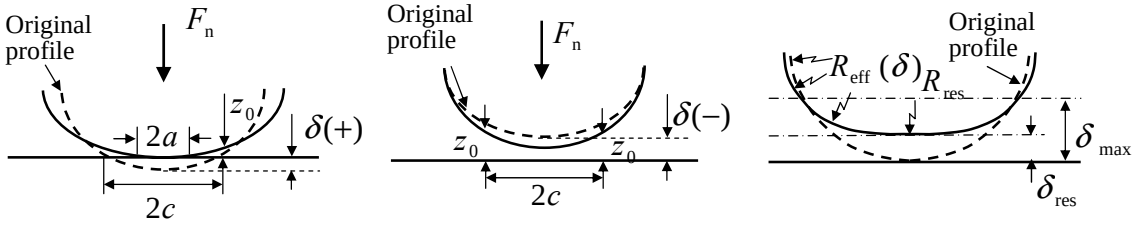

a. Positive interference b. Negative interference c. Effective profile

Figure 1. Definition of single asperity interference [2]

The adhesive contact theory taking into account the elasto-plastic behavior happening during contact (Figure 1.c) has been developed in details in reference [2]. This theory results in different adhesive-contact forces during loading $F_n^L(\delta)$ and unloading $F_n^U(\delta)$. The elastic-plastic adhesive contact of a micro sphere is considered here for Ruthenium (Ru) [3] for which material properties and initial asperity tip radius are reported in Figure 2. This figure compares the predicted adhesive-contact forces to the FE results for the loading and unloading adhesive-contact forces at three maximum interferences δ_{max} successively equal to 17, 34 and 51 nm. It is seen that an excellent agreement is obtained for the three loading conditions.

2.2. Rough Surfaces Interaction

Greenwood and Williamson ‘asperity-based model’ [4] is applied to simulate the rough surface/plane interaction. A rough surface is described by a collection of spherical asperities with identical end radii R, whose height h have a statistical distribution

$$\varphi(h) = \frac{1}{\sigma_s \sqrt{2\pi}} \exp\left(\frac{-h^2}{2\sigma_s^2}\right) \tag{1}$$

where σ_s is the standard deviations in asperity heights. Note that the contact of two rough surfaces can be represented by the contact between an equivalent rough surface and a smooth plane [5]. The interaction between two rough surfaces is also characterized by the distance d between the two rough surface mean planes of asperity heights, and by N the surface density of asperities. All these values can be identified from the study of the surfaces topography, and, in particular, depend on the surface RMS roughness R_q.

Properties of Ru films		
Initial asperity tip radius	R [μm]	4
Young modulus	E [GPa]	410
Poisson coefficient	ν [-]	0.3
Yield stress	S_Y [GPa]	3.42
Standard deviation in asperity height	σ_s [nm]	7.78
Surface RMS roughness	R_q [nm]	7.81
Surface density of asperities	N [μm^{-2}]	10

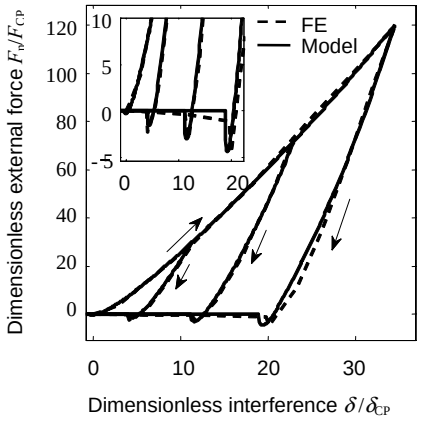

Figure 2. Comparison of the single asperity model with finite element results for Ru

The surface loading and unloading forces, respectively F_{nT}^{L} and F_{nT}^{U} can now be evaluated by integrating on the surface the effect of each asperity, for which the interference reads $\delta = h - d$ as described previously. It bears emphasize that as asperities enter into plasticity for different surface distances, the effective profile is different for each asperity. Details on the procedure of integration are provided in [2].

3. CYCLIC LOADING OF A MICRO-SWITCH

D_0 [μm]	2
t_d [μm]	0.15
ε_0 [pF/m]	8.854
$\varepsilon_d/\varepsilon_0$ [-]	7.6
t_s [nm]	180

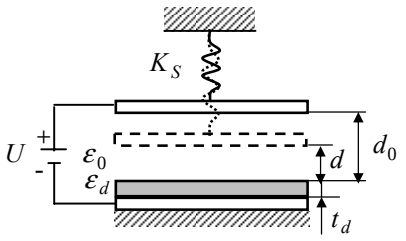

Figure 3. Geometry and properties of the micro-switch

A one-dimensional model of micro-switch is considered (Figure 3). In this model, a voltage difference U is applied between a movable electrode and a substrate electrode covered by a dielectric layer (SiN) of thickness t_d and permittivity ε_d. The movable electrode is attached to a spring of stiffness K_S per unit area, and is initially at a distance d_0 from the substrate. The switch

is supposed to work in vacuum (permittivity ε_0) so that any damping effect due to a squeeze film is neglected. Contact is assumed to occur between two Ru surfaces, for which typical topography values are reported in Figure 2. Ru films of thickness t_s are deposited on the movable electrode, and also on a part of the substrate. From these data, the pull-in voltage and the impact energy can be computed in terms of the stiffness K_S. This computation has been performed in [2], and in this application we consider an impact energy of E_I=0.5 J/m^2.

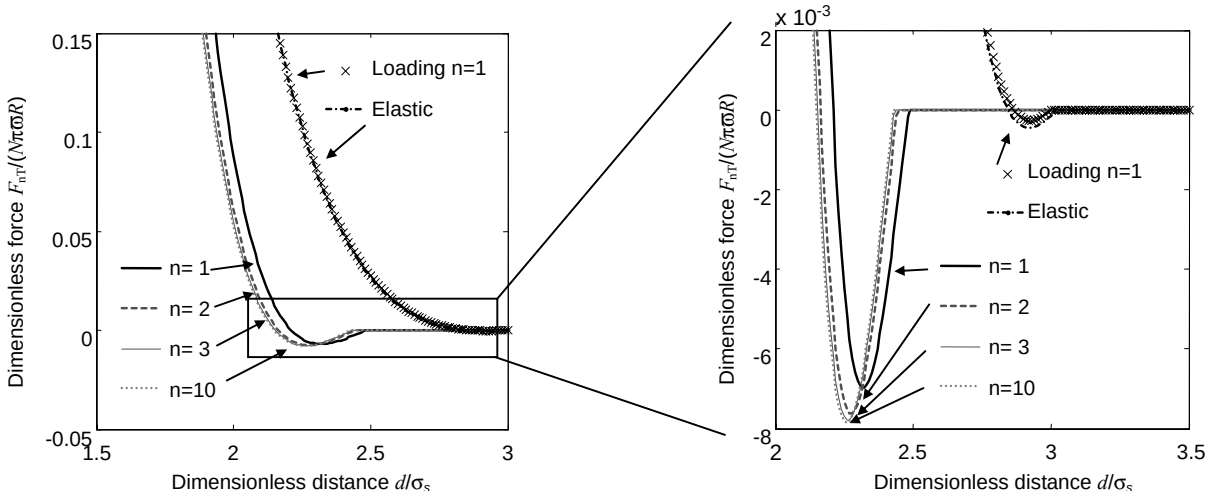

Figure 4. Cyclic loading of the 1D micro-switch

The loading/unloading cycles (accounting for asperities profiles modifications at each cycle) were calculated in [2]. The loading and unloading curves after 1, 2, 3 and 10 cycles are reported in Figure 4 as well as the pure elastic solution. It is observed that the unloading curves change after repeated interactions until accommodation is reached. It appears that the elastic solution underestimates the pull-out force which can be better predicted by the proposed approach, thus opening the way to stiction-free design.

REFERENCES

[1] Van Spengen W., Puers R., and DeWolf I. On the physics of stiction and its impact on the reliability of microstructures. Journal of Adhesion Science and Technology, 17(4):563–582, 2003.
[2] Wu L, Golinval J.-C, Noels L. A Micro Model for Elasto-Plastic Adhesive-Contact in Micro-Switches: Application to cyclic loading. Tribology International, 2013, Vol. 57, 137-146.
[3] Du Y., Chen L., McGruer N., Adams G. and Etsion I. A finite element model of loading and unloading of an asperity contact with adhesion and plasticity. Journal of Colloid and Interface Science, 312(2):522 – 528, 2007.
[4] Greenwood J. and Williamson J. Contact of nominally flat surfaces. Proceedings of the Royal Society of London A, 295(1442):300–319, 1966.
[5] Greenwood J. and J. Tripp J. The contact of two nominally flat rough surfaces. Proceedings of the Institution of Mechanical Engineers 1847-1996, 185(1970):625–633, 1971.

SENSITIVITY ANALYSIS AND OPTIMIZATION OF SHEET STEEL THICKNESS FOR VIBROACOUSTIC BEHAVIOR OF ENCLOSURES

T. Fourmaux[1*] , M. Ouisse[1] , S. Cogan[1] and E. Sadoulet-Reboul[1]

[1]FEMTO-ST Mec'Appli
University of Franche-Comte, Besancon, FRANCE
Email: titouan.fourmaux@femto-st.fr, morvan.ouisse@univ-fcomte.fr,
scott.cogan@univ-fcomte.fr, emeline.sadoulet-reboul@univ-fcomte.fr

ABSTRACT

In automotive applications, one of the keys to ensure weight reduction is the optimization of the sheet steel thickness. This paper presents a non-exhaustive list of sensitivity analysis methods (local, global and energy-based) allowing to determine which thicknesses could be reduced. The first results of an adaptive optimization procedure allowing reduction of the thicknesses under design constraints are also illustrated for the modal behaviour of an academic structure representing a simplified cab coupled with an acoustic cavity.
Keywords : sensitivity analysis, adaptive optimization procedure, sheet steel thickness.

1 INTRODUCTION

The design of novel cars and cabs for urban and peri-urban areas should take into account environmental constraints. Indeed one of the keys in the project is to reduce the weight of the cabs in order to reduce the energy consumption. Thus it is important to locate the different zones where the thickness of the sheet steel thickness could be reduced without deteriorating the dynamic and acoustic behaviours.

There are many sensitivity analysis methods allowing to know which sheet steel thicknesses could be reduced. Some of them are presented in the first part of this paper, divided into three classes : local, global and energy based. Each of them has different advantages and drawbacks. A benchmarking has been done in order to choose the one that can be used in the context of the optimization procedure of interest.

In a first step, an optimization procedure has been developed for modal behaviour. The procedure is adaptive and can iteratively reduce or increase the sheet steel thicknesses according to the constraints design in order to obtain a robust final design for the cab.

2 SENSITIVITY ANALYSIS METHODS

In order to describe the different sensitivity analysis methods, the test-case used is a finite element model of the aircraft used in the GARTEUR project (Group for Aeronautical Research and Technology in Europe) [1]. The sensitivities of the Young's modulus and mass density of each material are evaluated with respect to the eigenfrequencies and the value of the paired MAC (Modal Assurance Criterion) for the first five modes.

2.1 Finite difference sensitivity analysis

The most commonly employed technique to evaluate the sensitivity of parameters is the finite difference approach, which consists in evaluating the gradient of the responses of the system with respect to each parameter individually. The sensitivity indicator is given by [2]:

$$\phi_i = \frac{\frac{Y(X_1,...,X_i+\Delta X_i,...,X_n)-Y(X_1,...,X_i,...,X_n)}{Y(X_1,...,X_i,...,X_n)}}{\frac{\Delta X_i}{X_i}} \tag{1}$$

where Y is the response of the system, X_i the parameter i and ΔX_i the small variation of X_i.

This method is relative inexpensive but results can change according to the value of ΔX_i and it strongly depends on the nominal model which may be not validated. Figure 1 shows the results of the method for two different values for ΔX_i.

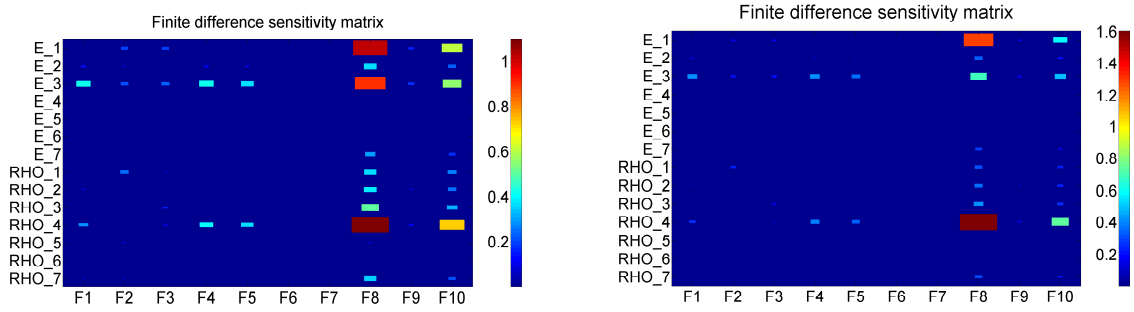

(a) $\Delta X_i = 0.1\%$ (b) $\Delta X_i = 10\%$

Figure 1. Results of the finite difference method with different values for ΔX_i

2.2 Global sensitivity analysis methods

Global sensitivity analysis methods take into account the probability density function of the parameters and explore all the design space. For example, the method of Morris [3] allows the computation of the sensitivity of parameters by calculating several times the elementary effect of each parameter. The sensitivity indicators are the mean (μ) and the standard deviation (σ) of the elementary effect. The mean gives information about the overall influence and the standard deviation indicates if the parameters have a coupling effect with other(s) parameter(s) or a non-linear effect. The results of the method are observed for each response in the (μ,σ) plane.

Other global sensitivity analysis methods have been tested on the structure such as the correlation coefficient allowing to know if it exists a linear relation between a parameter and a response, a principal component analysis which transforms the physical variables space into a purely mathematical space in which a singular value decomposition is performed. In order to compare different kinds of sensitivity analysis methods, we also performed a FAST [4] analysis which is based on the variance analysis. This method is efficient but time-consuming.

2.3 Energy-based methods

Two different energy indicators have been applied on the model to evaluate the sensitivity of the parameters. These indicators are interesting because one can calculate at low cost some spatial information related to sensitivities of responses due to changes in the structure. The first indicator is the strain energy which could be evaluated after a modal analysis as presented in [5], while the other one is an indicator developed in [6], based on a non-parametric sensitivity analysis [7] in which the mass and stiffness matrices are disturbed by a random matrix whose mean value is the identity.

3 OPTIMIZATION PROCEDURE

An optimization procedure is developed based on the strain energy normalized by the volume of the zone. The following indicator is used to rank the sheet metal zones:

$$I = \frac{1}{2} y_k^T K^i y_k \frac{V_i}{V_{tot}} \tag{2}$$

where y_k is the k^{th} eigenvector, K^i and V_i are the stiffness matrix and the volume of elements with the i^{th} thickness and V_{tot} the total volume of the structure. The flowchart of the optimization procedure is given in Figure 2 and can be summarized as follows:

1. Prepare the model features, the zones with imposed constant thickness, the parameters of the procedure such as the number of modes, make a first modal analysis to set the two different thresholds allowing to know which thicknesses could be modified.
2. Evaluate the indicator for each set.
3. Sets are selected for which the thickness has to be reduced.
4. Sets are selected for which the thickness has been too much reduced, so thickness is increased.
5. The model is updated according to step 3 and 4.
6. A modal analysis is performed with the new thicknesses.

7. The convergence is checked. If achieved the procedure will stop otherwise go to step 2.

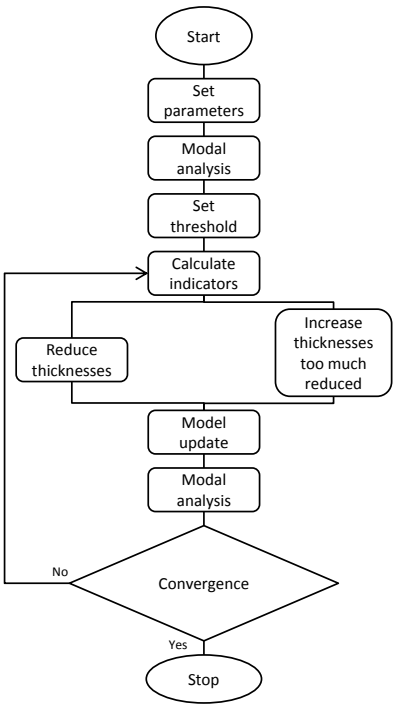

Figure 2. Flowchart of the adaptive optimization procedure.

Preliminary results with a simplified model of the cab show a weight reduction of 3% but with design constraints and threshold that have been set to an arbitrary value in order to test the procedure.

REFERENCES

[1] E. Balmes and J. Wright. Garteur group on ground vibration testing. results from the test of a single structure by 12 laboratories in europe. *OFFICE NATIONAL D ETUDES ET DE RECHERCHES AEROSPATIALES ONERA-PUBLICATIONS-TP*, 1997.

[2] DM Hamby. A review of techniques for parameter sensitivity analysis of environmental models. *Environmental Monitoring and Assessment*, 32(2):135–154, 1994.

[3] M.D. Morris. Factorial sampling plans for preliminary computational experiments. *Technometrics*, pages 161–174, 1991.

[4] A. Saltelli, S. Tarantola, and K.P.S. Chan. A quantitative model-independent method for global sensitivity analysis of model output. *Technometrics*, pages 39–56, 1999.

[5] Q.I. Bhatti, M. Ouisse, and S. Cogan. An adaptive optimization procedure for spot-welded structures. *Computers & Structures*, 89:1697–1711, 2011.

[6] M. Ouisse and S. Cogan. Robust design of spot welds in automotive structures: a decision-making methodology. *Mechanical Systems and Signal Processing*, 24(4):1172–1190, 2010.

[7] C. Soize. Random matrix theory and non-parametric model of random uncertainties in vibration analysis. *Journal of Sound and Vibration*, 263(4):893–916, 2003.

Optimum shape design of incompressible hyperelastic structures with analytical sensitivity analysis

JARRAYA Abdessalem, DAMMAK Fakhreddine, DHIAB Abderrazek

Research Unit of Mechanical, Modelisation and Manufacturing Unit, (U2MP), National school of engineers of Sfax, B.P.1173. 3038 Sfax Tunisia, Tel.: +216 20290035, Fax: +216 74666535
Email: abdessalem.jarraya@enis.rnu.tn , fakhreddine.dammak@enis.rnu.tn, abderrazek.dhiab@enis.rnu.tn
http://www.u2mp.org/membre.php

ABSTRACT

This paper is concerned a structural shape optimization of incompressible hyperelastic structures. An analytical sensitivity is developed for this rubber like materials. The whole shape optimization process is carried out by coupling a closed geometric shape in R2 with boundaries defined by B-splines curves, exact sensitivity analysis and mathematical programming method (S.Q.P: Sequential Quadratic Programming). Design variables are the control point's coordinates; objective is to minimize Von-Mises stress, constrained to the total material volume of the structure remains constant. In order to validate the exact Jacobian method, the sensitivity calculation is performed: numerically by an efficient finite difference scheme and by the exact Jacobian method. The feasibility of the proposed method is carried for a numerical example using elastic and hyperelastic optimization.

1 INTRODUCTION

The optimal design of structures is usually performed by using finite element method. Usually these are viewed as a shape optimization for minimum weight or fully stressed designs, or the determination of design parameters, like thickness, for given shape. To obtain a meaningful shape optimal design of hyperelastic solid, it is necessary to accurately describe the material properties, thoroughly understand the nonlinear structural analysis procedure, and to correctly formulate the structural design optimization problem. Many works have been published in the field of design sensitivity analysis (DSA) and shape optimization of hyperelastic structural materials. Design sensitivity analysis (DSA) method for structural components with hyperelastic material are developed by Choi et al. [1]. They employed the Mooney-Rivlin energy density function to describe the material property. Pajot and Maute [2] introduced the analytical sensitivity expressions for an element independent co-rotational formulation of a geometrically nonlinear finite element method. Tanaka and Noguchi [3] developed a shape optimization procedure for a flexible structure, which shows strong nonlinearity. Kai et al. [4] proposed a method for detection and elimination of errors in semi-analytical design sensitivities for any kind of finite element formulation.
The objective of this work is to develop an effective implementation of the shape optimization of isotropic incompressible hyperelastic structures. The isotropic hperelasticity can be described in term of either principal stretches or invariants. In contrast to author works on shape optimisation of hyperelastic structures, in this paper, we extend results reported in the work of Abid et al. (5] for linear elastic systems to incompressible plane stress hyperelastic structures. The incompressible hyperelasticity in principal stretches is based on the work of Gruttmann and Taylor [6]. However, the incompressible hyperelasticity in invariants is based on the formulation discussed in the work of Dammak et al. [7].

2 OBJECTIVE FUNCTION

Generally, an optimization problem with limitations (restrictions of optimization) is written in the following form:

$$\begin{aligned} &Min\ f(v). \\ &v \in \boldsymbol{R} \end{aligned} \tag{1}$$

Under limitations.

$$\begin{aligned} &g(v)=0 \qquad i=1,.....,m'. \\ &g(v) \le 0 \qquad i = m'+1 ,..... ,m. \end{aligned} \tag{2}$$

The functions f and g are considered differentiable. The search for a solution of the problem can be done, generally, numerically.
The principal goal through the optimization process (from the mechanical design point of view) is to seek the optimal shape of the structure. This makes it possible to reduce the maximum values of Von Mises stress in the structure, while satisfying certain geometrical limitations. By taking into account all these concerns, we developed a criterion of optimization, which consists in a continuous and differentiable function. The objective function is based on the Von Mises criteria.

$$f(v,\boldsymbol{U}) = Min\frac{1}{2}\int \boldsymbol{S}\, dV. \tag{3}$$

where $\boldsymbol{S}$ is the Piola-Kirchoff stress tensor. $\boldsymbol{U}$ is the vector of displacement.
The limitation consists in conserving the volume before and after optimisation.

3 SENSITIVITY ANALYSIS

In this section, the discrete analytical method for sensitivities calculation of the objective function $f = f(v, \boldsymbol{U})$ is presented. It is strongly nonlinear according to the n state variables (displacement), which are depending on the n optimization variables.
In the following, it is assumed that f and $\boldsymbol{U}$ are two continuous and differentiable functions. The sensitivity calculation consists in deriving the discrete cost function and limitations with respect to the optimization variables.
The sensitivities analysis problem is to calculate the total derivative of f such as:

$$\frac{df}{dv_i} = \frac{\partial f}{\partial v_i} + \frac{\partial f}{\partial u_k} . \frac{\partial u_k}{\partial v_i} \qquad i=1,....,n \; ; \; k=1,....,n_{eq} \tag{4}$$

Where n is the number of the optimization variables and v is the coordinate of control points defined in the B-spline curve.

4 NUMERICAL SIMULATIONS

In order to show the performance of the presented model, an example with hyperelastic materials is studied. In all the simulations, the structure is modeled by finite elements and the objective is to reduce the Von Mises constraints with conservation of volume. P1, P2, P3 and P4 are the control points. We use the same method to define the controls points by B-spline curve of Abid et al. [5] and Jarraya et al. [8] in shape optimization.
The Mooney- Rivlin type material model is defined by:

$$W = D_{10}(I_1 - 3) + D_{01}(I_2 - 3) \tag{5}$$

where D_{10} , D_{01} are the material constants $D_{10} = 0.0156\ MPa$, $D_{01} = 0.00967 MPa$
The structure geometry is shown in figure 1. Figures 2 present Von Mises stress distribution after optimization with the exact Jacobian method. The percentages of reduction for exact Jacobian are presented in table 1. This method permits a reduction of CPU times by 52.98 % and 61.53 % respectively for elastic and hyperelastic optimization.

5 CONCLUSIONS

The shape design sensitivity analysis is performed by an analytical computation of the exact Jacobien where the tangent stiffness matrix at the final equilibrium configuration of the discrete original design is used.
It has been shown that with analytical sensitivity the CPU is reduced compared to the finite difference method. We remark also that the formulation and numerical implementation discussed in this paper can be easily extended for the shape optimization of thin incompressible orthotropic hyperelastic three-dimensional thin shells and membranes shells.

6 REFERENCES

[1] Choi K.K. , Duan W.Design sensitivity analysis and shape optimization of structural components with hyperelastic material. Comput. Methods Appl. Mech. Engrg. 187, 219–243, 2000.

[2] Pajot J. M. , Maute K. Analytical sensitivity of geometrically structures based on the co-rotational finite element method. F. E. in Analy. and Desig. **42**, 900-913, 2006.

[3] Tanaka M., Noguchi H. Structural shape optimization of hyperelastic material by discrete force method. Theoretical and Applied Mechanics Japan. **53** 83-91, 2004.

[4] Kai-Uwe Bletzinger, mattias Firl and Fernass Daoud. Approximation of derivatives in semi-analytical structural optimization. Computer and structure. **86**, 1404-1416, 2008.

[5] Abid S., Jarraya A., Dammak F., Haddar M. Design sensitivity and shape optimization of geometrical non linear structure. Mécanique et industries, **9**, 17-23, 2008.

[6] Gruttmann F., Taylor R. L. Theory and Finite Element Formulation of Rubberlike Membrane Shells Using Principal Stretches. Internat. J. Numer. Methods. Engrg. **35**, 1111-1126, 1992.

[7] Dammak F., Regaieg A., Kallel Kammoun I. and Dhiab A. Modélisation de la loi de comportement hyperélastique transversalement isotrope des élastomères. Eur J. Comput Mech, **16** : 103-126, 2007.

[8] Jarraya A. Kallel K.I. and Dammak F. Optimisation de forme des structures hyperélastiques incompressibles et anisotropes. Mécanique et industries, **12**, 293-300, 2011.

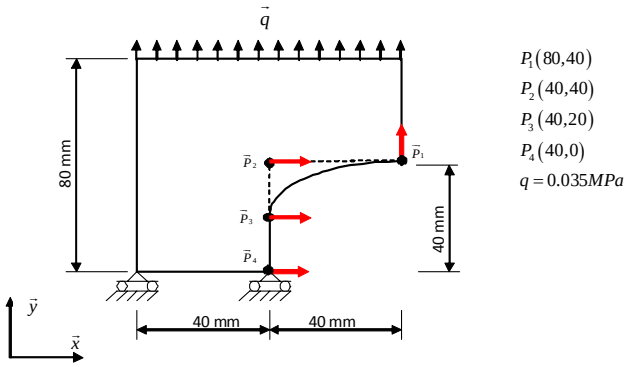

Figure. 1. Initial geometry and control points.

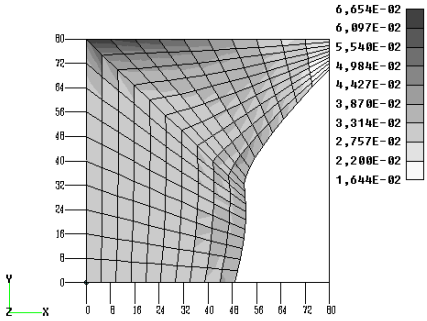

Figure. 2. Von Mises stress after optimization with exact Jacobian method.

	Elastic Optimization			Hyperelastic optimization		
	FD	**Exact Jacobian**	**% of reduction**	**FD**	**Exact Jacobian**	**% of reduction**
CPU time (s)	5.55	2.61	52.98 %	45.1	17.35	61.53%
Number of iterations	7	7	-	6	4	-

Table 1: CPU time and number of iterations for elastic and hyperelastic optimization.

ROBUST MODEL CALIBRATION OF A WIND TURBINE POWER TRAIN WITH LOAD UNCERTAINTIES

D. Pereiro[1] , S. Cogan[2] , E. Sadoulet-Reboul[2] and F. Martinez[1]

[1]IK4-Ikerlan
Pº J.M. de Arizmendiarrieta 2, 20500 Arrasate-Mondragón, Guipuzkoa, Spain
Email: dpereiro@ikerlan.es, Felix.martinez@ikerlan.es

[2]Department of Applied Mechanics
University of Franche-Comté, 24 rue de l'Epitaphe, 25000 Besançon, France
Email: scott.cogan@univ-fcomte.fr, emeline.sadoulet-reboul@univ-fcomte.fr

ABSTRACT

The goal of this work is to explore a model calibration strategy for an industrial problem consisting in a MW class geared wind turbine power train subjected to uncertain loads. Lack of knowledge is commonplace in this kind of engineering system and a realistic model calibration cannot be performed without taking into account this type of uncertainty. The question at stake in this study is how to perform a more robust model of a dynamic system given that the excitations are poorly known. The uncertainty in the latter will be represented with an info-gap model. This methodology is illustrated on a Megawat class wind turbine power train torsional model.

1 INTRODUCTION

Validating structural dynamic numerical models is a common engineering task. Confidence in simulation results is critical for product development and risk management, and the preferred framework to quantify this confidence is model verification and validation (V&V) [1]. The confrontation between numerical simulations and experimental observations often indicates that the model is unsatisfactory. Four different paradigms have been developed over the years to improve fidelity to data based on model calibration strategies, namely: Reference basis methods [2], Local deterministic methods [3],Local stochastic methods [4] and Local robust methods [5].

The first three paradigms have been studied extensively on both academic and industrial examples. As different as these approaches are, they share the same fundamental hypothesis, namely that the best solution to the calibration problem is the one that minimizes the defined test-analysis metric. While this assumption is commonplace, it fails to recognize that most real world problems are plagued by various sources of lack of knowledge due to poorly understood physics.

The present work is based on the concepts presented in [5] (the fourth paradigm) and serves to illustrate the relevance of robust parameter calibration under load uncertainties. The focus in this paper will be on the tradeoff between fidelity to data and robustness to uncertainty and the strategy is applied on a simple but realistic wind turbine power train model which is calibrated with respect to a simulated transient response. Wind turbine power trains are a good example to illustrate both the problem faced and the approach. This type of device is suitable to illustrate the approach because in the authors opinion the robust parameter calibration strategy presented here can be a step forward on the process of assessing models prediction credibility

2 ROBUST PARAMETER CALIBRATION

A numerical model can be denoted by:

$$y = \mathcal{M}(q) \tag{1}$$

The model $\mathcal{M}$ defines a relationship between y, the response feature of interest and q, model input parameters or decision variables. The impact of lack of knowledge on model responses will be studied using info-gap models of uncertainty [6]. The uncertain variable is denoted by u, and the info gap model of uncertainty is defined as $U(u_0;\alpha)$, hence:

$$y = \mathcal{M}(q;u),\ u \in U(u_0;\alpha) \tag{2}$$

where the parameter α is known as the horizon of uncertainty, while u_0 is the nominal value of the uncertain variable. The objective here is to study the robustness of the model fidelity to experimental data given uncertainty loads. The discrepancy between reference and simulation data can be assessed with a metric $D(q;u)$ defined as the norm of the difference between the test data y^{Test} with the results obtained from the model y:

$$D(q;u) = \left\| y^{Test} - y \right\|_2 \tag{3}$$

where y^{Test} ; y will be assumed here to be real vectors. Furthermore, let D_c denote the greatest level of discrepancy that can be tolerated:

$$D(q;u) \leq D_c \tag{4}$$

The robustness of the discrepancy with respect to uncertainty can now be formally defined as:

$$\hat{\alpha} = \underset{\alpha \geq 0}{Argmax} \underset{U(u;\alpha)}{max} \{D(q;u)/D(q;u) \leq D_c\} \tag{5}$$

The robustness function assesses the immunity of the discrepancy to uncertainty in u. Large $\hat{\alpha}$ means that discrepancy is relatively insensitive to variations in the uncertain quantities u, while small $\hat{\alpha}$ means that small variations in the uncertain quantities lead to large discrepancy.

Robust parameter calibration searches for a model design q which maximizes the robustness of the discrepancy for a given horizon of uncertainty:

$$\hat{\alpha}(D_c, q) = max(\alpha : \left\{ (\underset{u \in U(\alpha)}{max} D(q;u)) \leq D_c \right\}) \tag{6}$$

According to equation 6 the robust calibrated parameter can be defined as:

$$\hat{q}(D_c) = \underset{q}{argmax} (\hat{\alpha}(D_c, q)) \tag{7}$$

3 APPLICATION

The robust calibration strategy is applied to a MW class wind turbine power train model. This case study focuses on a wind gust as it is defined for certification purposes [7], the wind gust shape is translated as a torque input. A simulated Gearbox housing deflection is used to formulate the discrepancy function.

For this application, a discrete model is adopted consisting in a one degree of freedom per body rotational model. The gearbox support stiffness is modeled as a non linear spring. Such a model is widely used to represent this kind of rotating devices [8]. The dynamic system to solve can thus be written as:

$$[I] \cdot \left\{ \ddot{\theta} \right\} + [C] \cdot \left\{ \dot{\theta} \right\} + [K] \cdot \{\theta\} = \{T\} \tag{8}$$

The mathematical model is implemented in the Dymola software. The performance criteria is defined as the fractional error between the maximum displacement values during the wind gust (Figure 1b) for both reference and simulated responses in the gearbox housing θ_{HOU}.

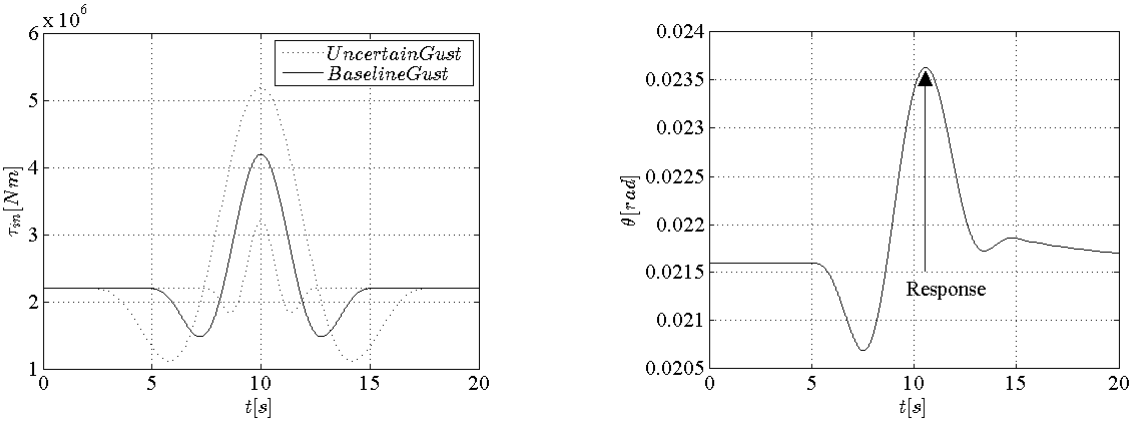

(a) Envelope bound uncertainty model

(b) Response feature of interest

Figure 1

The mexican hat wind gust type shape is set to be uncertain (Figure 1a). To model the uncertainty an envelope info-gap model [6] is used. The performance requirement is defined as the fractional error of the system response maximum difference between nominal and maximum gearbox housing displacement amplitude during the wind gust. This fractional error is not greater than a specified critical discrepancy D_c. Before the robustness curve is calculated a deterministic parameter calibration is conducted. The error for each point is calculated using the performance criteria defined. A robustness analysis is conducted for both the baseline model (before calibration) and the deterministic calibrated model. The robustness curves are calculated and compared. A robust parameter calibration strategy is conducted for the power train model (equation 8) and the uncertain wind gust. The calibrated robustness curves are obtained and commented.

4 CONCLUSION

Model calibration is an important phase in the overall model validation process and serves to improve fidelity to data. Model calibration methods generally seek to optimize fidelity. Meanwhile, the presence of lack of knowledge in the modeled physics renders fidelity-based approaches suspect given that the purported calibrated performance can no longer be guaranteed. A new robust calibration paradigm was proposed in [5] and forms the basis of ideas explored in this study which focused on the tradeoff between fidelity to data and robustness to uncertainty. It was shown that the best deterministic model does not necessarily provide the most robust predictions under lack of knowledge.

REFERENCES

[1] ASME. Guide for verification and validation in computational solid mechanics. Technical Report 10, American Society of Mechanical Engineers, New York, 2006.

[2] A. Berman and E.J. NAGY. Improvement of a large analytical model using test data. *AIAA Journal*, 21:1168–1173, 1983.

[3] G. Kerschen, K. Worden, A.F. Vakakis, and J. Golinval. Past, present and future of nonlinear system identification in structural dynamics. *Mechanical systems and signal processing*, 20:505–592, 2006.

[4] A. Calvi G.I. Schuëller B. Goller, M. Broggi. A stochastic model updating technique for complex aerospace structures. *Finite Elements in Analysis and Design*, 47(7):739–752, 2011.

[5] Y. Ben-Haim and F. Hemez. Robustness, fidelity and predictions looseness of models. *Physical Transactions of the Royal Society A*, 468:227–244, 2011.

[6] Yakov Ben-Haim. *Info-Gap decision theory: Decisions under severe uncertainty*. Academic Pres, London, 2006.

[7] Iec 61400-1 wind turbines - part 1 design requirements.

[8] A. Kahraman. Planetary gear train dynamics. *Journal of Mechanical design*, 116:713–720, 1994.

ROBUST DESIGN OF SPACECRAFT STRUCTURES UNDER LACK OF KNOWLEDGE

F. Maugan[1], S. Cogan[2], E. Foltête[3] and F. Buffe[4]

[1, 2 and 3]Institut FEMTO-ST, Département Mécanique appliquée, Université de Franche-Comté, 24 rue de l'Epitaphe 25000 Besançon France
Email: fabien.maugan@femto-st.fr, scott.cogan@univ-fcomte.fr, emmanuel.foltete@femto-st.fr

[4]Centre National d'Etudes Spatiales, 18 Avenue Edouard Belin
31470 Toulouse cedex France
Email: fabrice.buffe@cnes.fr

ABSTRACT

In robust design, lacks of knowledge are rarely taken into account explicitly, but this is the case in the RRDO-IG. This paper summarises the ongoing developments and perspectives for the use of the RRDO-IG methodology in a spatial industrial context, where non-linearities have to be treated. After shortly describing the RRDO-IG methodology and the actual encountered problems, we will construct an improvement strategy based on a state of the art in metamodelisation and failure probability computation.

1 INTRODUCTION

Methods for the robust design of mechanical systems have for objective to reduce the variability in system performance with respect to uncertainties in the material and geometrical properties of a mechanical structure as well as in the environmental loads. Two types of uncertainty are encountered in practice, namely random and epistemic uncertainties. Beside random ones, epistemic uncertainties are due to a lack of accurate knowledge concerning the physical laws governing the behaviour of a component or interface and can generally be reduced with more detailed modelling or experimental investigations. Epistemic uncertainties are difficult to characterize and as such are rarely taken into account explicitly in reliability analysis.

2 RRDO-IG METHOD

The RRDO-IG [1] approach is an extension of the RBDO one. It permits to design robustly a structure in regard with the lack of knowledge.

2.1 Formulation

A RRDO-IG optimization problem can be posed as follow:

$$\begin{cases} \min\limits_{\boldsymbol{d}\in R^{n_d}} f(\boldsymbol{d}) \\ with \\ \boldsymbol{m} \in U\left(\alpha, \boldsymbol{m}^{(0)}\right), \\ \alpha = \alpha_i, \\ \boldsymbol{d}_{min} \leq \boldsymbol{d} \leq \boldsymbol{d}_{max} \\ P_f(\boldsymbol{q}) \leq P_c. \end{cases} \quad (1)$$

Where:

- f is one or more cost function to optimize,
- $\boldsymbol{d}$ is the design parameters vector,
- $\boldsymbol{m}$ is the unknown parameters vector,
- $\boldsymbol{m}^{(0)}$ is the nominal value of $\boldsymbol{m}$,
- $\boldsymbol{q}$ is the concatenation of $\boldsymbol{d}$ and $\boldsymbol{m}$,
- $P_f(\boldsymbol{q})$ is the failure probability,
- P_c is the critical threshold failure probability,
- α is the horizon of uncertainty.

The first condition contains the lack of knowledge modelisation, here an info-gap method [4].
We can notice that, if $\alpha = 0$ (i.e. if no lack of knowledge) the problem becomes a simple RBDO one.

2.2 Results and perspectives

Previous works permitted to validate the RRDO-IG methodology [1], but various problems have appeared:

- Two different metamodels with comparable accuracy can give different robustness curves.
- Implemented failure probability computation method (i.e. FORM) does not always converge.

3 PROPOSED APPROACH

3.1 Improve the limit state approximation

3.1.1 Current problems

Metamodels currently used can only treat smooth functions because of their certain stiffness [1-2-7]. Indeed, in each case, the method consists in approximating the limit state globally on the entire design domain with continuous functions.
Even if it is possible to soft a metamodel increasing his functions degree, it is necessary to sample more and more the design domain to avoid bad generalization, although this action increases significantly the computation time.

3.1.2 Propositions

To avoid these problems, various methods of adaptive metamodelisation are proposed in the literature. The main idea is here to lead the sampling in accordance with the complexity of the explored area whereas currently, the sampling is done blindly before the metamodelisation.
This kind of method would permit to significantly reduce the sampling number.
As an instance, we will test an adaptive kriging method proposed by V. Dubourg [7] and an adaptive stochastic collocation method proposed by N. Agarwal [6] which can absorb non-linearities and discontinuities.

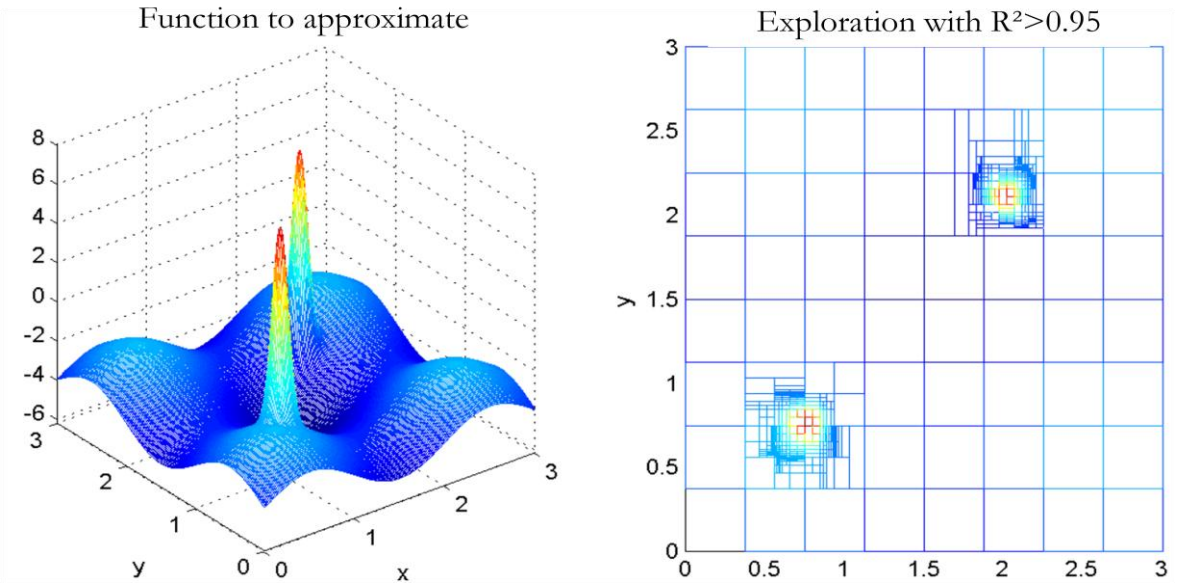

Figure 1. Design space exploration with a based
N. Agarwal's method. The refinement occurs only in highly non-linear areas.

3.1.3 Expectations

The aim of the proposed study is to determine the usage domain for each kind of metamodel regarding the type of limit state to approximate.
To attest the metamodels efficiency, generic comparison criteria will be used as R^2, ERAM, MERA [1] criteria and the number of sampling.

3.2 Compute accurately the failure probability

Previews studies show that the use of FORM method leads to important errors in the failure probability estimation in case of non-linear limit state. We propose here to test a priori more efficient methods.

3.2.1 Replace FORM by SORM

The SORM method is the extension of the FORM one to the second degree. It means that we can expect amelioration in the failure probability estimation, but it requires computing the curvatures in each dimension at the design point. On top of this, a priori, this method only permits to estimate exactly limit state until the degree two. Above, an error still occurs.

3.2.2 Test exact methods

To avoid FORM and SORM disadvantages, it would be interesting to also test exact methods like RGMR [5] which permits to exploit to the maximum the geometry of the standard space.
This kind of methods does not require finding the design point and can be optimized if quadrature points are cleverly chosen.

4 CONCLUSION

Exploring Adaptive metamodelisation methods and complex failure probability computation methods, we will try to develop the RRDO-IG methodology for an industrial use. The aim is to finally treat optimization problems with complex limit state due to non-linearities which are legion in the spatial field [3].

5 REFERENCES

[1] E. Pillet. *Conception Robuste d'une Structure Spatiale en Présence de Méconnaissances de modèle*. Besançon, 2012.

[2] N. Roussouly. *Approche probabiliste pour la justification par analyse des structures spatiales*. Thesis, Toulouse, 2011.

[3] A. Hot. *Validation expérimentale de structures localement non-linéaires dans un context spatial*. Thesis, Besançon, 2011.

[4] Y. Ben-Haim. *Info-gap decision theory, second edition*. Academic Press, Oxford, 2006.

[5] M. Lemaire, A. Chateauneuf, and J.C. Mitteau. *Fiabilité des structures, couplage mécano-fiabiliste statique*. Lavoisier, Paris, 2005.

[6] N. Agarwal, N.R. Aluru. A domain adaptive stochastic collocation approach for analysis of mems under incertainties. *Journal of Computational Physics*. 228(2009):7662-7688, 2009.

[7] V. Dubourg. *Méta-modèle adaptatif pour l'analyse de fiabilité et l'optimisation sous contrainte fiabiliste*. Thesis, Clermont-Ferrand, 2011.

REAL-TIME AND IN-SERVICE ESTIMATION OF THE DEGREE OF DAMAGE OF AUTOMOTIVE TRANSMISSION PARTS WITH THE AID OF A TORQUE MEASURE

S. Foulard[1,2*], S. Rinderknecht[2], M. Ichchou[1] and J. Perret-Liaudet[1]

[1]Laboratoire de Tribologie et Dynamique des Systèmes
Ecole Centrale de Lyon - Université de Lyon, Ecully, FRANCE
Email: mohamed.ichchou@ec-lyon.fr, joel.perret-liaudet@ec-lyon.fr

[2]Institut für Mechatronische Systeme
Technische Universität Darmstadt, Darmstadt, GERMANY
Email: foulard@ims.tu-darmstadt.de, rinderknecht@ims.tu-darmstadt.de

ABSTRACT

Light weight designs and designs appropriated to the loads are topics that are becoming even more important in the automotive industry. Concerning the development of transmissions, the standard is to design the mechanical parts in accordance with worst use cases, only representing a small part of the real drivers. Additionally, the corresponding average load profiles are not always truly known and thus considered with safety factors. This signifies an over-design for a big part of the customers and contradicts the development targets. To tackle this issue, a method able to monitor the loads in a transmission in real-time and in-service is proposed. The purpose is to continuously calculate the damage level of critical parts and to generate load limitation instructions in case of imminent failure. Such a system would allow developing transmissions for less exigent use cases while managing the worst ones with the method itself. A crucial aspect is to guarantee the accuracy and the conservatism of the method for all the potential real damage cases while staying at the same time as little conservative as possible. Final aim is to implement such a system in series-production vehicles, what implies severe requirements in terms of memory and computing capacities.

1 INTRODUCTION

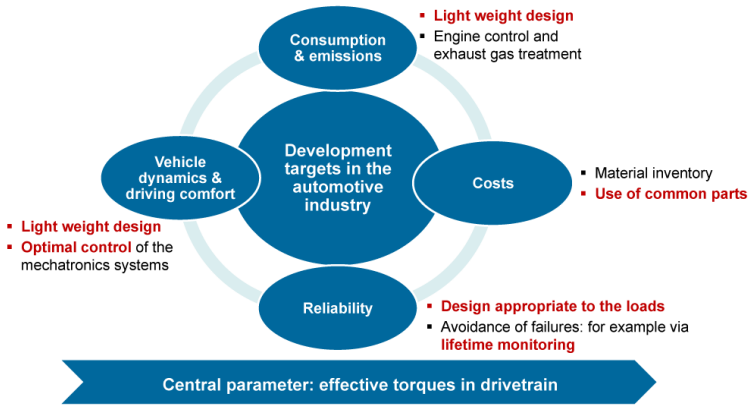

Figure 1. Development targets in the automotive industry

The in-service reliability of the mechanical parts is a central aspect in the automotive industry (Figure 1). Concerning the transmissions and especially the aspects ”avoidance of components failures” and ”improvement of the correlation between design and effective loads occurring during the operation of the vehicle”, a real-time and online method able to monitor the loads in a transmission and to calculate the remaining service life of critical transmission parts is proposed here [1].

Indeed components as transmissions are nowadays conceived to last as long as the life-time of the vehicle and to endure the worst use cases, which represent typically extreme driving situations. Actually only a small part of the drivers would generate such load cases (e.g. 2-3% of the drivers or less depending on car segments). So it means that transmissions are usually over-designed for a big part of the drivers. If an electronic system was able to monitor the actual level of damage of different transmission components, this would bring essential advantages in this regard.

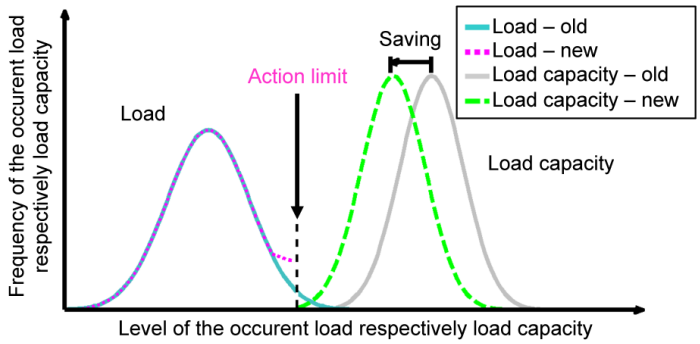

Figure 2. Possible saving by reduction of the strain through load limitation

For example, with regard to the above-mentioned design process, it can be concluded that, for a given application case, it would be more purposeful to develop a transmission in a more demand-oriented way, only for a specified driver category. Thus, the transmission would be conceived for a pre-determined class of drivers, which does not overload it and operates it under normal conditions, what would cover almost all of the users' load profiles. For the remaining e.g. 2-3%, the monitoring system will be able to give a real-time feedback on the

level of damage and, if necessary, to generate load limitation recommendations (e.g. a limitation of the engine torque). Thus, with this monitoring system, the critical operating conditions would be avoided, which could exceed the admissible damage level or the load capacity (Figure 2). However such a monitoring system should not be seen as an intrusive system, but rather as a potential input for an engine or transmission control unit for a better management of the powertrain.

Naturally, such a system may not function without the knowledge of the effective torques acting in the powertrain, which represent the main loads and stresses within a drivetrain. An accurate torque measurement, especially in case of rotating parts and during dynamic operations, is still problematic today. Additionally, torque sensors are rather expensive and require additional package space [2]. Thus, reliable, compact and cheap torque sensors or devices or methods in conjunction with specific torque identification methods are still needed and are a cornestone of the whole monitoring method. However, this aspect will not be discussed in more detail in this paper.

2 DEVELOPED SOLUTION

Generally, the industry - original equipment manufacturers or suppliers - does not want to take any risks in terms of safety and robustness and the use of reverse design methods predicated on norms and experience and deducing the geometry from the requirements is commonly spread [3–5]. Consequently the design is always very conservative and the values of the safety factors are not always truly known.

The philosophy here is based on an applicative approach: the commonly spread industry design processes are considered as a reference and the developed method can be defined as basic and simple while being able to generate accuracy and precision. The method handles the uncertainties due to real load profiles that affect the behavior of the damage accumulation methods (e.g. aleatory loads, high-low/low-high effects, variations of amplitudes and mean values, etc.) [6]. Thus the method ensures the in time identification of possible failures and stays at any time on the safe side. Even though additional scientific investigations are conducted in order to make the method as little conservative as possible.

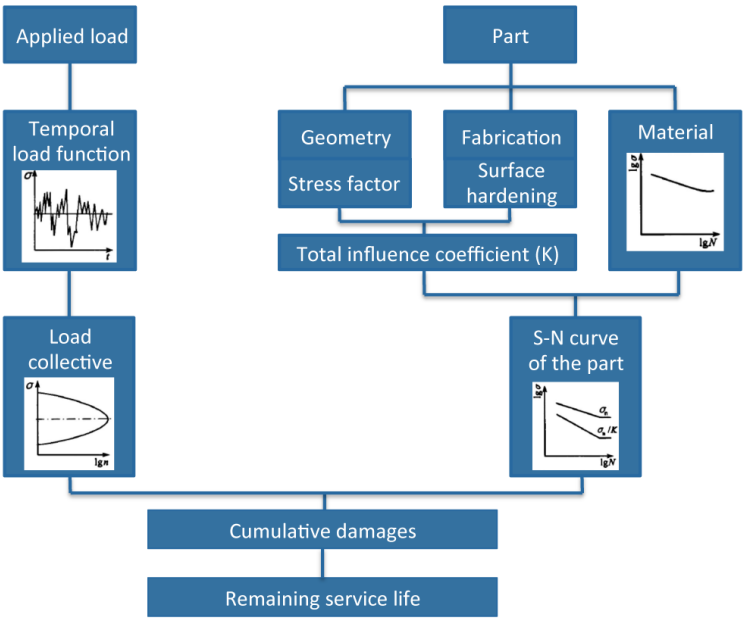

Figure 3. Lifetime prediction procedure based on a damage calculation

A global scheme of such a load or rather life-time monitoring method is represented in Figure 3. As shown in this scheme, the procedure can be dissociated into more or less three independent aspects. The right side concerns all the material and reference data in order to generate, for example, the necessary S-N curves of the different geometric parts to be monitored. This can be described as an offline process based on norms and experiments. The left side consists on the core of the system, the sensing and the counting of the applied loads. This allows generating a representation of the load profiles, which are then used as an input for the calculation of the remaining service life of the different mechanical parts, accordingly to the chosen method of damage accumulation. The latter represents the third aspect, at the bottom of the scheme. As already mentioned, the determination of the loads is supposed to be achieved with the aid of a torque measure, which is then converted into loads depending on transfer functions for the different elements and damage use cases.

3 CONCLUSION

In the general context of automotive transmissions, the whole approach is predicated on the will to develop a system that could be implemented in series-production cars. That is why the adopted strategy is to consider a concrete use-case for the development with the aim to transfer the system software on a real Transmission or Engine Control Unit (TCU/ECU). A first version of the method based on linear cumulative damage calculations has already been implemented and validated on an autonomous and plug-and-play micro-controller [7]. This hardware simulates the capacities of a TCU/ECU and is able to communicate with the vehicle bus. It is used as a prototype system in order to investigate the feasibility of the method and to further tests under real conditions. To limit the difficulty and especially the consideration of too many parameters, a restricted number of mechanical parts and damage possibilities are considered at the moment. Namely, only the flank pitting and the foot fracture of pinion teeth are examined. In the future, the shaft fractures due to torsional loadings should be integrated too.

REFERENCES

[1] T. Müller. Entwicklung, Implementierung und Verifizierung einer Methode zum Lebensdauermonitoring eines DKG. Master-Thesis, Technische Universität Darmstadt, 2011.

[2] Y. Zhang. Stand der Technik sowie funktionaler und wirtschaftlicher Vergleich von Drehmomentsensierungsmethoden. Research Seminar, Technische Universität Darmstadt, 2012.

[3] B. Hänel, E. Haibach, T. Seeger, G. Wirthgen, and H. Zenner. *Rechnerischer Festigkeitsnachweis für Maschinenbauteile*. VDMA Verlag, Frankfurt am Main, 2003.

[4] Deutsches Institut für Normung. *DIN743 - Tragfähigkeitsberechnung von Wellen und Achsen*. Beuth Verlag, Berlin, 2009.

[5] Deutsches Institut für Normung. *DIN3990 - Tragfähigkeitsberechnung von Stirnrädern*. Beuth Verlag, Berlin, 2009.

[6] E. Haibach. *Betriebsfestigkeit - Verfahren und Daten zur Bauteilberechnung*. VDI-Verlag, Düsseldorf, 1989.

[7] G. Gruber. Implementierung eines DKG-Lebensdauermonitoringmodells auf einer Arduino Hardware. Bachelor-Thesis, Technische Universität Darmstadt, 2012.

THEORY AND APPLICATIONS OF THE MACROSCOPIC QUANTIZATION EFFECT IN NONLINEARLY-COUPLED VIBRATING SYSTEMS

Danil B. Doubochinski and Jonathan Tennenbaum*

Quantix - Société de Recherche et Développement en Technique Vibratoire
86, Rue de Wattignies, 75012 Paris, France
Email: doubochinski.danil@gmail.com, j.tennenbaum@freenet.de

ABSTRACT

Among the most fruitful areas for research and application of vibrational processes today is a special type of nonlinear interaction between oscillating systems, known as argumental coupling, and the emergence of discrete, "quantized" dynamic regimes in systems of argumentally-coupled oscillators, known as the Macroscopic Quantization Effect (MQE). Many years' work in this area has led to the development of new technologies having potentially enormous economic benefits. These technologies include a highly-efficient nonlinear vibrational process for atomizing liquids into submicron-sized droplets, which opens the way toward drastically reducing energy requirements for evaporative cooling and refrigeration, as well as desalination of sea water. Closely related is a new method for producing highly-stable emulsions, with application to the production of synthetic fuels. The present paper summarizes essential features of argumental interactions and the theory and experimental demonstration of the Macroscopic Quantization Effect, and describes the basic principle behind the new atomization technology.

1 INTRODUCTION

Phenomena involving nonlinear interactions between oscillating systems have been studied for a long time, but their far-reaching implications for science and technology are only gradually being realized. Among the most promising areas for research and application is a special type of nonlinear interaction between oscillating systems, known as *argumental coupling*, and the emergence of discrete, "quantized" dynamic regimes in systems of argumentally-coupled oscillators – the so-called *Macroscopic Quantization Effect (MQE*) – having no equivalent in the classical theory of oscillations. Recent work in this area has led to new technologies having potentially enormous economic impacts, one of which we shall describe here.

2 THE MACROSCOPIC QUANTIZATION EFFECT (MQE)

Argumental interactions and the MQE were first discovered by Danil and Yakov Doubochinski in 1968, and were the subject of extensive experimental and mathematical investigations [1-5]. The classical example is the so-called argumental pendulum (see Figure 1): A low-friction pendulum with a natural frequency ω in range 0,5 - 1Hz and a small permanent magnet affixed to its end, interacts with the magnetic field of a solenoid located under the pendulum's equilibrium position and fed by alternating current of frequency ν between 30 and 1000 Hz. When released from any position, the pendulum's motion evolves into a stable, very nearly periodic oscillation, whose amplitude belongs to a *discrete set of values*. In each of these "quantized" regimes the pendulum oscillates with a frequency near its own undisturbed frequency, compensating its frictional losses by energy drawn from its interaction with the alternating field of the solenoid.

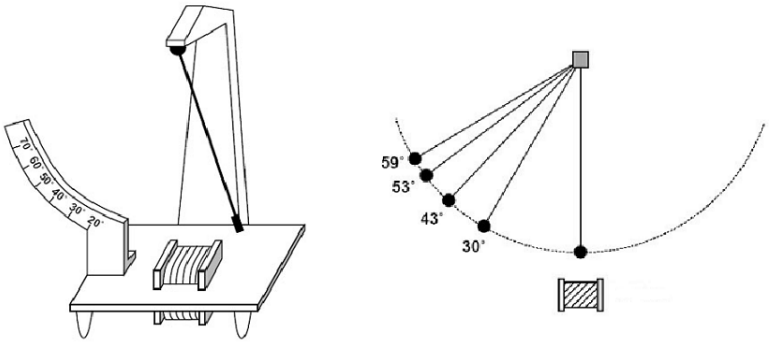

Figure 1. The argumental pendulum and its stable amplitudes (for ω = 0.5 Hz, ν = 50 Hz)

A precondition for this "quantization" phenomenon is the strong *spatial inhomogeneity* of the external field, permitting the pendulum to regulate its exchange of energy with the field by small advances and delays in the moment it enters the narrow "interaction zone", relative to the phase of the solenoid current. The term, "argument interaction", originally referring to the presence of the pendulum angle in the function defining the external force, came to be applied to a whole class of coupled oscillators whose energy exchanges are regulated by phase-frequency-amplitude fluctuations, while each participating oscillator operates at very nearly its own proper frequency.

We now briefly indicate the origin of the "quantized" spectrum of stable regimes in the argumental pendulum and similar systems. Represent the family of free motions of the pendulum (or similar mechanical oscillator) by a generalized coordinate function $X = X(A, \omega, \phi, t)$, such

that for each fixed value of the triple (A, ω, ϕ), X is a periodic function in t with frequency ω, amplitude A, and phase factor ϕ. In the simplest relevant cases, the interaction with an external field of frequency ν (ν >> ω) can be described by the differential equation

$$X'' + 2\beta X' + g(X) = f(X)\cos(\nu t) \tag{1}$$

where f(X) expresses the spatial dependency of the interaction with the field. For any *fixed* values of A, ω, ϕ, the function f(X) is a periodic function of t with frequency ω, so that the right side of equation (1) can be expanded in a complex Fourier series:

$$\begin{aligned} f(X)\cos(\nu t) &= (\Sigma\, c_n(A, \omega, \phi)\, e^{in\omega t})\cos(\nu t) = \tfrac{1}{2}\Sigma\, c_n(A, \omega, \phi)\, e^{in\omega}\,[e^{i\nu t} + e^{-i\nu t}] \\ &= \tfrac{1}{2}\Sigma\, c_n(A, \omega, \phi)\, e^{i(n\omega + \nu)t} + \tfrac{1}{2}\Sigma\, c_n(A, \omega, \phi)\, e^{i(n\omega - \nu)t}. \end{aligned} \tag{2}$$

From this we can see that in the special case when $\nu = N\omega$ for some whole number N, the Fourier series for the right-hand side of equation (1) will contain the term

$$[\, c_{1-N}(A, \omega, \phi) + c_{N+1}(A, \omega, \phi)\,]\, e^{i\omega t} \tag{3}$$

whose frequency coincides with that of the oscillator itself. This opens the possibility for a *special sort of resonant energy transfer from the high-frequency field to the low-frequency oscillator*. On account of the pendulum's amplitude-frequency dependence (anisochronicity), the condition $\nu = N\omega$ translates into a discrete set of amplitudes at which this energy transfer can occur.

To go beyond these qualitative remarks it is necessary to take into account the time-dependency of the values of A, ω and ϕ, which fluctuate slowly around certain average values, and which provide the regulatory element permitting stable, quasi-stationary oscillatory regimes to be maintained. Analysis leads to a complicated set of equations involving the coefficient functions. Applying the method of Krylov-Bogoliubov-Mitropolski, we can demonstrate the existence of quasi-stationary regimes corresponding to a discrete series of average values of (A, ω, ϕ), and account for the other main characteristics of argumentally-coupled systems. For details of the theory of argumental oscillations and the MQE we refer the reader to the technical literature [1-5]. The present authors emphasize the ability of argumental couplings to generate entire hierarchies of stable dynamic regimes, each of which can be regarded as a distinct physical object in its own right [6].

Theoretical and experimental studies have shown that a single high-frequency source can feed not just one, but a large number of different argumental oscillators at the same time, each operating near its own proper frequency and each in any one of a "quantized" array of modes. This is a special case of a more general principle called "*multiresonance"*: the simultaneous coupling of ensembles of oscillating systems, in a self-organizing and self-regulating manner, across an orders-or-magnitude-wide range of frequencies. This property of argumental couplings provides an enormous scope for technological applications [7], of which we shall now briefly describe one example.

3 THE ATOMIZING REACTOR

In a patented "atomizing reactor" [7,8] a pulsating flow of water is injected into a chamber at right angles to a flow of air arriving from a compressor through a second tube, and pulsated with much higher-frequency components. In current prototypes the air pulses are shaped as delta functions,

and hydrodynamic processes are used to prepare the water in a heterogeneous vibrational state prior to its injection. At the point of intersection with the pulsed air flow, the water stream breaks up into a cloud of droplets of different sizes, each vibrating with its own frequency. Multiresonant argumental interactions with the acoustical field cause droplets to pick up energy and explode into smaller droplets, in turn adding new high-frequency components to the acoustical field. The result is a cascade-like process producing an outlet mist of droplets with diameters less than 1 micron. The atomizing reactor is many times more energy-efficient than conventional atomization methods producing comparable droplet sizes. The performance and operating parameters of prototype devices have been measured and certified by Bureau VERITAS in France as well as the French industrial laboratory LAMI / ENPC-LCPC. Of particular interest is the extremely powerful cooling effect achieved by the atomizing reactor, which is the combined result of the nearly instantaneous evaporation of the submicron droplets upon exit from the reactor, together with the surprising fact – revealed by laboratory measurements –, that the atomization process itself consumes a significant portion of the thermal energy of the air and water entering the system. Projections by the AREVA Technical Center indicate that evaporative cooling systems based on the atomizing reactor, when fully optimized, could achieve Coefficients of Performance (COPs) *10 times higher than systems utilizing the closed Carnot cycle*, for the same inlet and outlet temperatures [8].

REFERENCES

[1.] D.B. Doubochinski, Ya.B. Duboshinsky at al., Oscillations with controlled interaction time. Sov. Phys. Doklady 17, 541(1972).

[2.] D.B. Doubochinski, Ya.B. Duboshinsky and D.I. Penner, Argumental oscillations. Sov. Phys. Izv. 7, 54 (1975).

[3.] D.B. Doubochinski, Ya.B. Duboshinski, A.S. Magarchak, V.Chabanski, Discrete modes of a system subject to an inhomogeneous high-frequency force. Sov. Phys.-Tech. Phys. 24, 642 (1979).

[4.] D.B. Doubochinski, Ya.B. Duboshinsky, Wave excitation of an oscillator having a discrete series of stable amplitudes. Sov. Phys. Doklady 27, 564 (1982).

[5.] D.B. Doubochinski, Ya.B. Duboshinsky, Amorçage argumentaire d'oscillations entretenues avec une série discrète d'amplitudes stables. E.D.F. Bulletin de la Direction des Etudes et Recherches, série C mathématique, informatique, n° 3, (1991).

[6.] D.B. Doubochinski, J. Tennenbaum, On the General Nature of Physical Objects and their Interactions, as Suggested by the Properties of Argumentally-Coupled Oscillating Systems. (2008), [http://arxiv.org/ftp/arxiv/papers/0808/0808.1205.pdf].

[7.] D.B. Doubochinski, Method and vibrating device for conditioning, air-conditioning, cooling and decontaminating, disinfecting and sterilization physical media, Europe n° 1216061, USA n° 7,531,131 B2 and Australia n° 780382, World Intellectual Property Organization: WO 01/41817 A2, June 2001.

[8.] D.B Doubochinski, J. Tennenbaum, Factor-of-Ten Reduction in Energy Requirements for Cooling. International Conference on Frontiers of Mechanical Engineering, Materials and Energy (ICFMEME 2012) Beijing, (2012).

NON-LINEAR DYNAMIC BEHAVIOR OF A WIND TURBINE SYSTEM WITH TORQUE LIMITER

A. Kamel Abboudi, B. Lassâad Walha*, C. Yassine Driss, D. Mohamed Maatar, E. Mohamed Haddar

Research Unit of Mechanical Dynamic System
Mechanical Engineering Department, National School of Engineers of Sfax
BP 1173-3038 Sfax, Tunisia
Tel.: +216 74 274 088; fax: +216 74 275 595
* walhalassaad@yahoo.fr

ABSTRACT

In this paper, we studied the nonlinear dynamic behavior of a wind turbine system including a torque limiter. The system is excited by the aerodynamic excitation. We developed a lamped mass dynamic model with 28 DOFs. The main source of vibration and noise is due to the wind force, which is never constant. Furthermore, there are other sources of vibration inside the machine due to the flexibility of the components of the geared system. We use the Runge Kutta numerical algorithm to solve the equations of motion. As a result, the obtained spectra have allowed us to identify the main sources of vibration in the wind turbine.
Keywords. *Wind turbine, dynamic behavior, two-stage helical gear, torque limiter, friction.*

1. INTRODUCTION AND DESCRIPTION OF THE SYSTEM DESIGN

The majority of the works in the field of the dynamics of horizontal-axis wind turbines are interested in the study of the main mechanisms such as power conversion system, gearbox and drive shafts. These studies treat the simple linear problems without taking into account the security mechanisms such as brakes and torque limiter. In addition, the majority of research has studied a perfect gearbox system [1, 2, 3]. In this study, we propose an analytical model of the dynamic behavior of the wind turbine system (three-bladed rotor / torque limiter / gearbox). We propose a new approach to calculate aerodynamic torque and thrust force taking into account the variation of Reynolds number which has a greater influence on energy performance parameters and aerodynamic forces acting on a three-bladed. Then, we presented a theoretical formulation and an assessment of the stability of the power conversion system subjected to variable loading.

The dynamic model of a speed multiplier and torque limiter used in wind turbines is shown in Figure 1. The rotor is usually consists of three blades mounted on a hub, which is linked to a

torque limiter through a transmission shaft. In the torque limiter, one shaft is typically driven by a rotor and the other shaft drives gearbox system. This device separates the two shafts when torque exceeds a critical value. The gearbox consists of two-stage helical gear which can drive a power generator. There are four blocks (j = 1:4) shown in Figure 1:

- first block (j = 1) :{ aerodynamic turbine, low speed shaft (drive side), limiter disc}
- second block (j = 2) :{ wheel of pressure plates, low speed shaft, helical gear (12)}
- third block (j = 3): {helical gear (12), intermediate shaft, helical gear (22)}
- fourth block (j = 4): { helical gear (31), high speed shaft, wheel (32)}

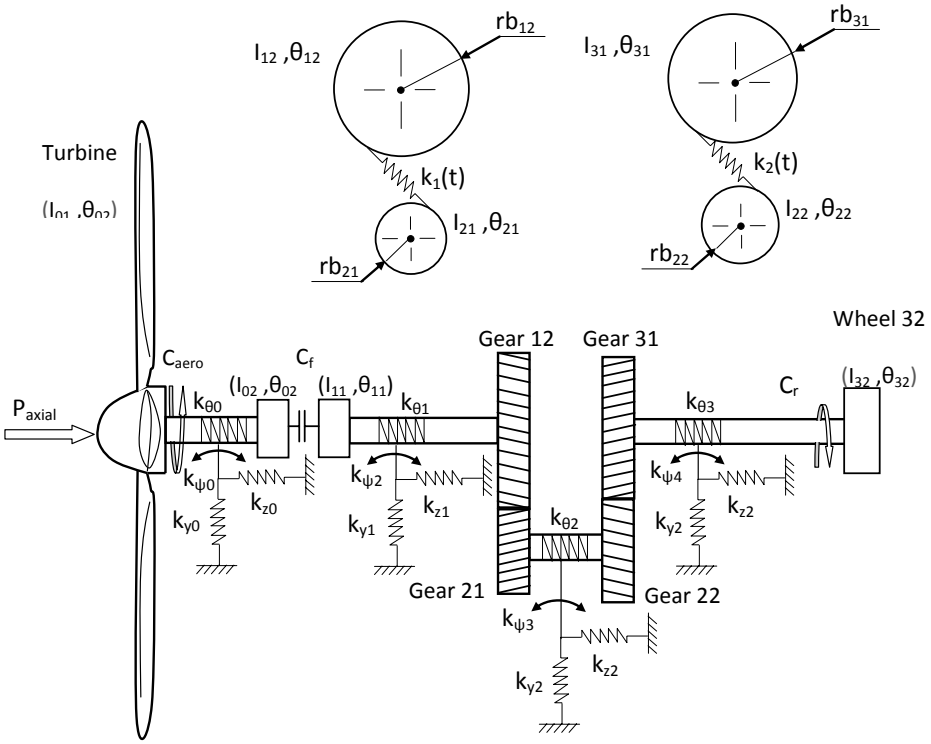

Figure 1. *Dynamic models of the wind turbine system*

The dynamic model has 28 degrees of freedom. Each block "j" is mounted on a flexible bearing. Linear stiffness of bearing sets is denoted by (k_{xj}, k_{zj} and k_{yj}) and the bending stiffness is denoted by $k_{\varphi j}$ and $k_{\psi j}$. The linear motion bearings (z_j) are identified along the axes of rotation and (x_j , y_j) in the plane perpendicular to this axes. The four intermediate shafts have a less mass, lower inertial and torsional rigidity ($k_{\theta j}$). The shaft lengths are considered to be of the same order of magnitude as the tooth width.

The friction torque is written as: [5]

$$C_f = \left[\left(\mu_s - \mu_k\right) \exp\left(-\left(\frac{\Delta\dot{\theta}}{V_{str}} \right)^{\delta_s} \right) + \mu_k \right] n_s \, r_m \, F_p \, \mathrm{sgn}(\Delta\dot{\theta}) \qquad (1)$$

Where $\Delta\dot{\theta}$ is the relative velocity, μ_s is the static friction coefficient, μ_k is the kinetic friction coefficient. The coupling between the frictional disks is provided by a pressing force F_p. The elements that create the pressing force are the bolt and washers Bellevilles. r_m is the average radius of the contact surface.

3. AERODYNAMIC PART

The rotor disc acts as a drag device slowing the wind speed from far upstream of the rotor to its proximity. The wind speed at the plane of rotor is equal to the wind speed from far upstream. In addition, we introduced a relative component of the wind speed in the direction of the chord in the aerodynamic approach. The calculation of unsteady aerodynamic forces is applied on a deformable rotor blade. These blades are deformed in the direction of the air flow, inclined at an angle of "β_c" (Figure 2).

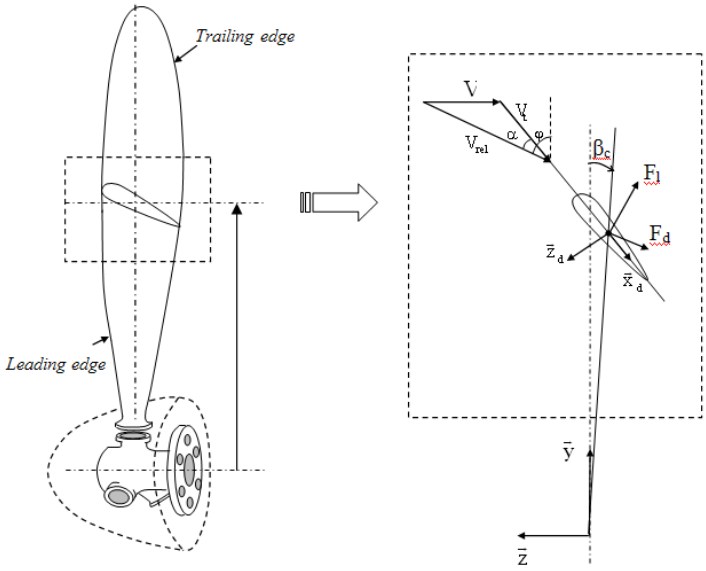

Figure 2. *Aerodynamic forces applied on a flexible blade.*

The aerodynamic forces are written in the following matrix form:

$$\begin{Bmatrix} F_x \\ F_z \end{Bmatrix} = \begin{bmatrix} -P\cos\beta_d + Q\sin\beta_d\cos\beta_c & P\cos\beta_d + Q\sin\beta_d\cos\beta_c \\ -P\sin\beta_d - Q\cos\beta_d\cos\beta_c & P\sin\beta_d - Q\cos\beta_d\cos\beta_c \end{bmatrix} \begin{Bmatrix} F_L \\ F_d \end{Bmatrix} \quad (2)$$

Where, P is the normal force (thrust) applied to the rotor. Q is the overall torque exerted on the rotor. β_d is the twist angle (variations in the geometric pitch of the blades, looking from the tip towards the root section). F_L , F_d represent the lift force and the drag force respectively. The wind velocity is a random stationary normal process [8]. In this section, we considered a wind speed sample for a short duration (V_{min}=11.5 m/s ;V_{max}=14 m/s ;V_{moy}=12.75 m/s) to calculate numerically the dynamic responses of the wind turbine system.

Figures 3 and 4 show the variation of the axial thrust force and the torque over time. The wind speed and the aerodynamic forces (Figure. 4) have the same shape, but they have different size.

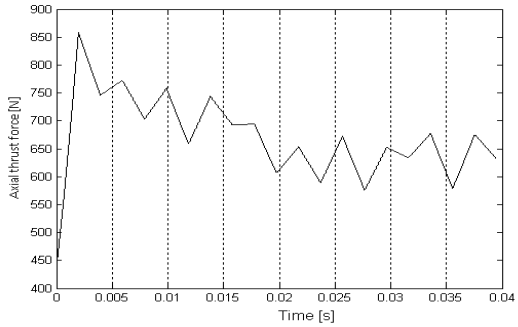

Figure 3. *Axial force fluctuation*

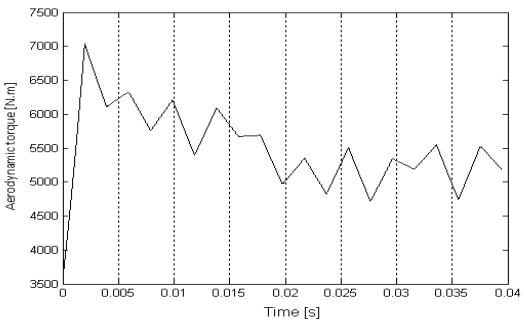

Figure 4. *Aerodynamic torque fluctuation*

4. NUMERICAL SIMULATIONS OF THE NONLINEAR DYNAMIC RESPONSE OF THE SYSTEM

The aerodynamic torque applied to the three-bladed rotor, and subsequently on the rest of components inside the nacelle. We proposed a sample of highly intense wind speed which progressively decreases over time. The wind generates a torque signal similar to its speed. The torque is limited at the start of functioning by the relative sliding between the friction surfaces of the limiter. From Figure 5, the two time signals are periodic, deflection periods corresponds to two periods meshing T_{e1} and T_{e2}. Figure 6 shows the evolution of the relative velocity between the friction surfaces of the torque limiter over time. We note that there is a fast slip followed by a continuous collage between the friction surfaces for a pressing force of 25 kN. When this force decreases the phases of stick-slip (slip-stick) appear.

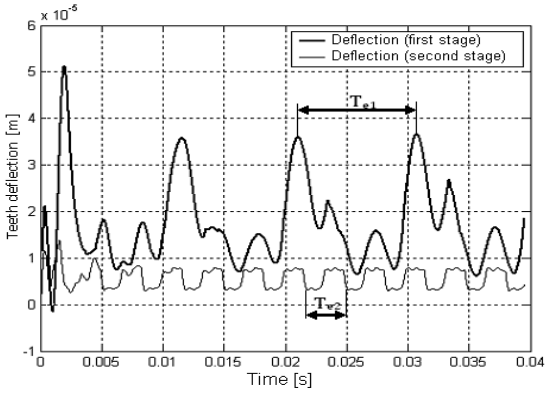

Figure 5. *Teeth Deflection*

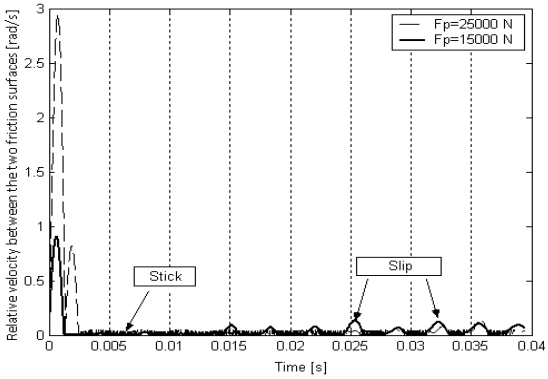

Figure 6. *Relative velocity between surfaces*

6. CONCLUSION

The nonlinear dynamic behavior of the studied system is modeled based on a mechanical safety component like the torque limiter. The latter allows the machine to protect against over-wind torques generated by the intense winds. In addition, it allows decoupling the two shafts between the three-bladed rotor and the speed multiplier when the torque exceeds a critical value. The non-stationary aerodynamic forces are calculated by the method developed in which it was considered important aspects such as the variation of the Reynolds number and the wind component along the chord line of the flexible blade. We have developed a mass-spring model with concentrated parameters with 28 degrees of freedom. The resolution of equations is done by the Runge kutta order 5. The numerical results presented in both time and frequency domains show the importance of the proposed security system.

REFERENCES

[1] Tempel J. V. D. and Molenaar D. P., Wind Turbine Structural Dynamics –A review of the Principles for Modern Power Generation, Onshore and Offshore, Wind Engineering Vol.26, N° 4, 211—220, 2002

[2] Gabriele M., Hansen A. D. and Hartkopf T., Variable speed wind turbines – Modeling, Control and Impact on Power Systems , European Wind Energy Conference and Exhibition, Brussels (BE), 100—104, 2008

[3] Abbas F. A. R. and Abdulsada M. A., Simulation of Wind-Turbine Speed Control by MATLAB,International Journal of Computer and Electrical Engineering, Vol. 2, N° 5, 915-918, 2010

[4] Det Norske V. , Guidelines for design of wind turbine, Copenhagen and Wind Energy Department, Risø National Laboratory , 1er edition, Danemark, 2002

[5] Linck V., Modélisation numérique temporelle d'un contact frottant, Mise en evidence d'instabilités locales de contact- Conséquences tribologiques, Thèse de doctorat, INSA de Lyon, 2005

[6] Abboudi K., Walha L., Driss Y., Maatar M.and Haddar M., Dynamic behavior of the two stage spur gear system with fixed speed turbine excitation, Mechanism and Machine Theory (46), 1888–1900, 2011

[7] Walha L., Driss Y., Fakhfakh T. and Haddar M. (2009), Effect of manufacturing defects on the dynamic behaviour for an helical two-stage gear system, Mécanique & Industrie (10), 365—376, 2009

[8] Abboudi K., Walha L., Driss Y., Maatar M., Haddar M., Effects of aerodynamic excitations on the dynamic behavior of helical gear system, Multidiscipline Modelling in Materials and Structures (MMMS),Vol. 8 Iss:2, pp. 178-196, 2012

EFFECT OF HIGH-FREQUENCY AC ELECTROMAGNETIC ACTUATION ON THE DYNAMIC OF AN EXCITED CANTILEVER BEAM

A. Bichri, J. Mahfoud, M. Belhaq

Laboratory of Mechanics, University Hassan II-Casablanca, Casablanca, Morocco
INSA-Lyon, LaMCoS UMR5259, Lyon, France
Email: amine.bichri@gmail.com, jarir.mahfoud@insa-lyon.fr, mbelhaq@yahoo.fr

ABSTRACT

The effects of the intensity of an electromagnetic actuation (EMA) on the dynamic behavior of a harmonically excited cantilever beam is analyzed in this paper. Analytical treatment based on perturbation analysis is performed on a simplified one degree of freedom equation modelling the first bending mode of the cantilever beam. The results show that under a certain specific condition relating the intensity of the fast AC to the displacement, the alternating current of the EMA has a significant influence on the nonlinear behavior of the system.

1 INTRODUCTION

EMAs are considered as simple means of excitation which can be exploited positively in industrial applications where attracting forces are needed. However, electromagnetic forces produce in general complicated behavior due to the nonlinearities generated by the force. The effect of DC EMAs on the dynamic of a periodically excited cantilever beam was investigated analytically, numerically and experimentally [1], near primary resonance. It was shown that EMAs with DC actuation produces a softening behavior in the system and a shift of the resonance curve towards lower frequencies. It was also concluded in [1] that an increase of the DC actuation increases the softening characteristic of the system.

The present paper investigates the influence of the AC intensity of an EMA, with high-frequency actuation, on the frequency response of an excited cantilever beam near primary resonance. Attention is focused on the case of a single mode approximation and where the frequency of the alternative electromagnetic force is larger than the frequency of the external excitation.

We perform analytical treatment on a one degree of freedom system modeling the first bending mode of the cantilever beam consisting in a nonlinear oscillator subjected to an external periodic excitation. The analytical approach based on a perturbation analysis leads to the amplitude-frequency response equation allowing the analysis of the influence of the AC EMA force on the frequency response. Specifically, we show the influence of the AC amplitude on the response of the system.

2 EQUATION OF MOTION AND SLOW DYNAMIC

The equation of motion that describes the dynamic behavior of a cantilever beam in a single mode approximation and subjected to a harmonic external excitation and to electromagnetic forces, F_{em}, can be written as [1]

$$m\ddot{\delta} + \alpha\dot{\delta} + k\delta = F\cos\omega t + F_{em} \tag{1}$$

where the EMAs are supplied by a constant current generating a static force F_{DC} and a high frequency actuation generating a fast alternative force F_{AC} such that

$$F_{em} = F_{AC} + F_{DC} \tag{2}$$

where

$$F_{AC} = \frac{C_1 i_1^2}{(\lambda-\delta)^2} - \frac{C_1 I_2^2}{(\lambda+\delta)^2}$$

and

$$F_{DC} = \frac{C_0 I_0^2}{(\lambda-\delta)^2}$$

Here λ, C_0 and C_1 depend on the geometrical characteristics of the actuators, δ is the colocolized displacement and F, ω are, respectively, the amplitude and the frequency of the external excitation. The current i_1 is given by $i_1 = I_1 cos\kappa t$ where I_1 and κ are, respectively, the amplitude of the modulated current and the corresponding frequency.
Assume that the currents I_1 and I_2 satisfy the relation

$$I_2 = \frac{I_1(\lambda+\delta)}{\sqrt{2}(\lambda-\delta)} \tag{3}$$

relating the intensity of the alternative current I_2 to the displacement. This assumption has to be satisfied in order to introduce some important effects on nonlinear behaviors in the system. Under this condition, the total electromagnetic force F_{em} reads

$$F_{em} = \frac{C_0 I_0^2}{(\lambda - \delta)^2} + \frac{C_1 I_1^2}{2(\lambda - \delta)^2} cos2\kappa t \tag{4}$$

Substituting Eq. (4) into Eq. (1), we obtain the dimensionless equation of motion

$$z^{''} + cz^{'} + z = fcos\nu t + \frac{a_0}{(1-z)^2} + \frac{a_1}{(1-z)^2} cos\Omega\tau \tag{5}$$

where $z = \frac{\delta}{\lambda}$, $c = \frac{\alpha}{m\omega_0}$, $\omega_0 = \sqrt{\frac{k}{m}}$, $\nu = \frac{\omega}{\omega_0}$, $\Omega = \frac{2\kappa}{\omega_0}$, $f = \frac{F}{\lambda m w_0^2}$, $a_0 = \frac{C_0 I_0^2}{\lambda^3 m\omega_0^2}$, $a_1 = \frac{C_1 I_1^2}{2\lambda^3 m\omega_0^2}$ and $\tau = \omega_0 t$.
Using Taylor series expansion of the nonlinear terms in the r.h.s. of Eq. (5) keeping only terms up to order three in z, the equation of motion takes the form

$$z^{''} + cz^{'} + z(1 - 2a_0) - 3a_0 z^2 - 4a_0 z^3 - a_0 = f\cos\nu\tau + a_1(1 + 2z + 3z^2 + 4z^3)\cos\Omega\tau \tag{6}$$

Applying the method of direct partition of motion [1, 2, 4], the equation of the slow dynamic, $x(t)$, is given by

$$x^{''} + cx^{'} + \Omega_0^2 x + \beta x^2 - \gamma x^3 + G = f\cos\nu\tau \tag{7}$$

where $\Omega_0^2 = 1 - 2a_0 + \frac{5a_1^2}{\Omega^2}$, $\beta = \frac{15a_1}{\Omega^2} - 3a_0$, $G = \frac{a_1}{\Omega^2} - a_0$ and $\gamma = 4a_0 - \frac{25a_1^2}{\Omega^2}$.
Performing the method of multiple scales [3] near primary resonance, we obtain the modulation equations of amplitude and phase

$$\begin{cases} \dfrac{dr}{d\tau} = Ar + H_1\sin\theta + H_2\cos\theta \\ \\ r\dfrac{d\theta}{d\tau} = Br + Cr^3 + H_1\cos\theta - H_2\sin\theta \end{cases} \tag{8}$$

where $A = \frac{-c}{2}$, $H_1 = (\frac{f\sigma}{8\nu^3} - \frac{f}{2\nu})$, $H_2 = \frac{fc}{8\nu^2}$, $B = \frac{\sigma}{2\nu} - \frac{c^2}{8\nu} - \frac{\sigma^2}{8\nu^3}$ and $C = -\frac{3\gamma}{8\nu} + \frac{5\beta^2}{12\nu^3}$.
Eliminating the phase θ from (8), we obtain the amplitude-frequency response equation

$$C^2 r^6 + 2BCr^4 + (A^2 + B^2)r^2 - (H_1^2 + H_2^2) = 0 \tag{9}$$

Figure 1a shows the frequency-response curves, as given by Eq. (9), for given values of the intensity I_0 and the frequency Ω and for different values of the intensity of the alternating current I_1. This figure indicates that for a critical value of the AC, $I_{1c} = 1.5A$, the system has a linear behavior. For values of $I_1 < I_{1c}$ the frequency response curve bends toward lower frequencies showing a softening behavior in the system, while for values of $I_1 > I_{1c}$ the resonance curve bends toward higher frequencies causing a hardening behavior.

Figure 1b shows the same frequency-response curves but in the absence of the DC ($I_0 = 0$). It can be seen that in the absence of the DC, the increasing of the intensity of the AC hardens the system.

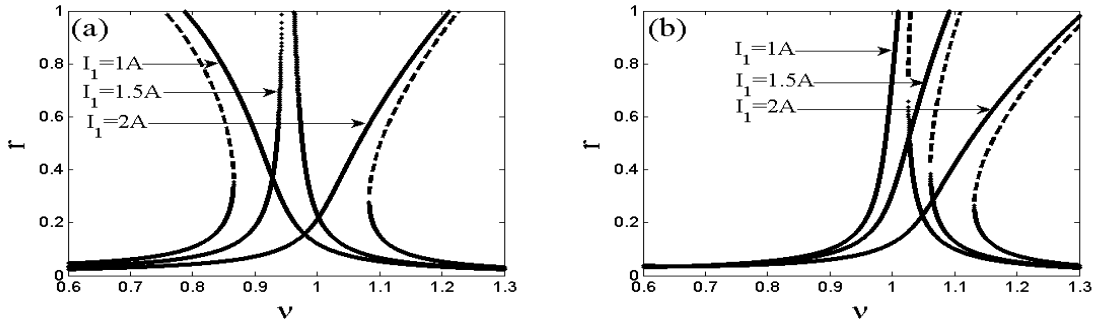

Figure 1: Amplitude-frequency response near the primary resonance for $\Omega = 5$, $c = 0.005$, $f = 0.02$, $m = 1Kg$, $K = 6.67 \times 10^3 N/m$, $C_1 = C_0 = 4.27 \times 10^{-27} Nm^2A^{-2}$, $\lambda = 1.1mm$; (a) $I_0 = 0.4A$, (b) $I_0 = 0A$.

3 CONCLUSION

We have studied the effect of the intensity of a high frequency AC of an EMA on the dynamic of an excited cantilever beam modeled by its first bending mode and presented by a single degree of freedom oscillator. Attention was focused on the dynamic near primary resonance and the approach was performed using perturbation analysis to approximate the frequency response curve. The results shown that depending on the amplitude of the alternative current of the EMA, the frequency response of the first bending mode to the cantilever beam can be shifted towards lower or higher values of frequencies producing softening or hardening behavior in the system. This result indicates that it is possible to control the amplitude of the response near the resonance by tuning the intensity of the AC.

Further investigations are in progress focusing on analyzing the influence of the high frequency on the response of the system.

REFERENCES

[1] M. Belhaq, A. Bichri, J. Der Hogapian, J. Mahfoud, "Effect of electromagnetic actuations on the dynamics of a harmonically excited cantilever beam", International Journal of Non-Linear Mechanics 46, 828-838, 2011.

[2] I.I. Blekhman. "Vibrational Mechanics - Nonlinear Dynamic Effects, General Approach, Application". Singapore: World Scientific, 2000.

[4] J.J. Thomsen , "Vibrations and Stability: Advanced Theory, Analysis, and Tools", Springer-Verlag, Berlin-Heidelberg, 2003.

[3] A.H. Nayfeh, D.T. Mook. "Nonlinear Oscillations". Wiley: New York, 1979.

INTERNAL RESONANCES IN NONLINEAR NANOCANTILEVER ARRAYS UNDER ELECTROSTATIC ACTUATION

S. Souayeh[1, 2] and N. Kacem[1*]

[1]FEMTO-ST Institute - UMR CNRS 6174
24, chemin de l'Épitaphe, F-25000 Besançon, France
Email: najib.kacem@femto-st.fr

[2]National School of Engineers of Sfax
BP, W3038 Sfax, Tunisia
Email: saoussen.saoussen@gmail.com

ABSTRACT

The nonlinear dynamics of nanoelectromechanical cantilever arrays is investigated using a comprehensive analytical multiphysics model that takes into account geometric and electrostatic nonlinearities. In particular, the internal resonances between the different cantilevers are analyzed using a multi-modal Galerkin discretization coupled with a perturbation technique. Such systems offer a perfect mechanical synchronization, interesting nonlinear behaviors and exchange of energy between their different components which makes them potential candidates for multi-mass sensing applications.

1 INTRODUCTION

Despite the fact that internal resonances (IR) have interesting dynamic properties, many designers strive to avoid it in their models. In recent years, this phenomenon is more and more used due to its property of suppressing oscillations in cantilever [1] or also enhancing the coupling effect in dynamical systems [2]. Sethna [3] was one of the first researchers who investigated the phenomenon of IR. He studied the influence of quadratic nonlineriarities in a system which exhibits two-to-one (2:1) internal resonances with subharmonic parametric resonance. He showed that the steady-state motions are more interesting when the system possesses external and internal resonances. Moreover, several studies were performed regarding resonant response of system under harmonic excitation forces [4, 5]. Nayfeh and Mook [6] have given a complete treatment of this subject. A common result from these researches is that the IR ratio depends on the type of coupling of the system. Recently, Gutchemidt and Gottilieb [7] modeled a continuum initial-boundary-value problem of a doubly-clamped microbeam array excited at several DC biases and periodic AC voltages. They showed that, for DC near systems first pull-in instability, three-to-one internal and combinational resonances were identified.

Motivated by the previously cited researches, and aware about the important influence of the internal resonances (IR) in nonlinear systems such as NEMS, this work is conducted to investigate the IR that can occur in a device composed by one or several coupled nanocantilevers under an electrostatic actuation. In this context, two types of configurations are considered: the first one, used by Kacem *et al* [8], is a single nanocantilever actuated by an electrosatic force while the second configuration consists of an array containing N coupled nanocantilevers actuated by a single electrode. The two systems are represented in Figure 1.

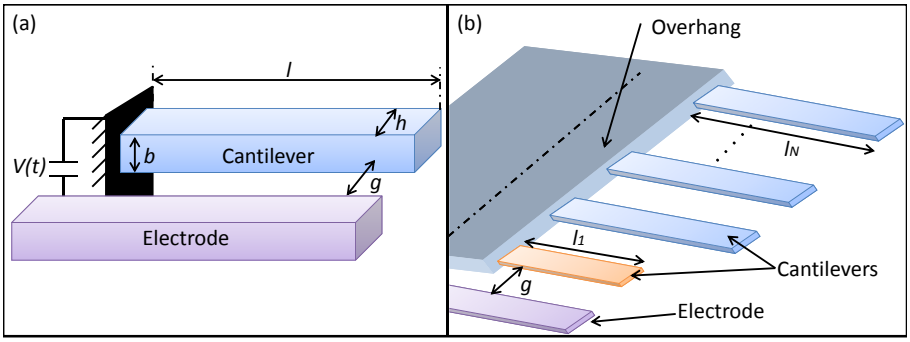

Figure 1: (a) A single nanocantilever electrostatically actuated. (b) An array of N nanocantilever beams. Only the first cantilever is excited by the electrode and $l_{i+1} = r_{i+1} * l_1$ with $r_{i+1} > 1$ and $i \in \mathbb{N}^*$.

2 MODEL

As a first step, a single nanocantilever (Figure 1 (a)) is considered. In order to identify the internal resonance conditions, a multi-modal Galerkin method is used to calculate the natural frequencies of the three lowest bending modes. Figure 2 (a) shows the variation of these frequencies with respect to the DC voltage. After a meticulous investigation of the possible IR and despite the fact that there are many possibilities of internal resonances, two major issues are noticed: the study of such systems gives a very complex set of amplitude and phase equations and above all, it is arduous to obtain in experiments such relations between the different modes.

In order to avoid these complexities, another approach is considered. It is inspired from [9] and consists of an array of N nanocatilevers depicted in Figure 1 (b). The dynamics of the considered system is modeled using a set of coupled nonlinear partial differential equations.

A reduced-order model is generated by modal decomposition transforming the equations of motion into a finite degree- of-freedom system. Then, the method of multiple scales is used as a direct attack of the resulting equations while assuming the dominance of the first bending mode for each cantilever. This permits deriving the phase and amplitude modulation equations.

For instance, we consider the case of two coupled cantilevers. The variation of the natural frequency of the first bending mode of each beam with respect to the DC voltage is presented in Figure 2 (b). The internal resonances 2:1 and 3:1 between the two cantilevers are possible for particular values of V_{dc} given by the intersection points of the corresponding curves. Figures 3 and 4 display simulated frequency-response curves of the considered device for 3:1 IR and two sets of design parameters. Remarkably, the model enables the capture of the transition from softening to hardening behavior for the second cantilever.

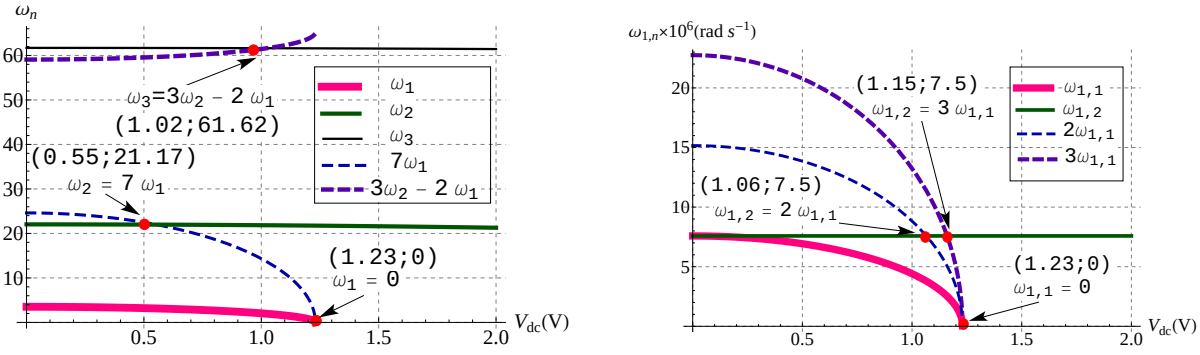

Figure 2: (a) Variation of the dimensionless natural frequencies of the first three bending modes for a single nanocantilever with respect to the driving voltage V_{dc}. 7:1 and a combinational $(\omega_3 = 3\omega - 2\omega_1)$ IR are identified. (b) Variation of the natural frequencies of a two-beam system with respect to the driving voltage V_{dc}. 2:1 and 3:1 IR are identified.

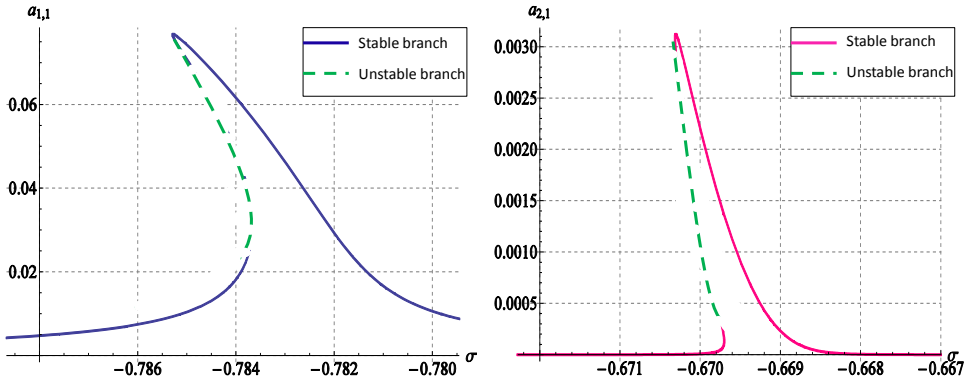

Figure 3: Variation of the modal amplitude $a_{1,i}$ of each cantilever with respect to the detuning parameter σ in the case of 3:1 IR, for $V_{ac} = 1\,mV$, $r_2 = 2$, $l_1 = 9\,\mu$m, $h = 100\,nm$ and $b = g = 200\,nm$. The quality factor is $Q = 5000$ and the coupling parameter is $d = 3$.

3 CONCLUSION

A simple electrostatic actuation of a nano-beam can provoke progressively the oscillation of several coupled nonlinear cantilevers due to internal resonances. This effect can be beneficial for multi-mass detection by providing a perfect control of the synchronization via the mechanical coupling between the cantilevers.

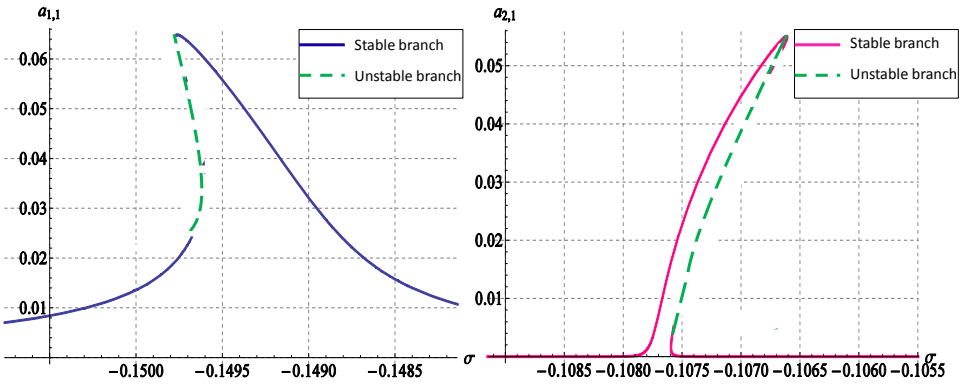

Figure 4: Variation of the modal amplitude $a_{1,i}$ of each cantilever with respect to the detuning parameter σ in the case of 3:1 IR, for $V_{ac} = 10\,mV$, $r_2 = 4.5$, $l_1 = 3\,\mu$m, $b = 200\,nm$, $h = 110\,nm$ and $g = 120\,nm$. The quality factor is $Q = 10000$ and the coupling parameter is $d = 0.5$.

REFERENCES

[1] K. L. Tuer, M. F. Golnaraghi, and D. Wang. Development of a generalised active vibration suppression strategy for a cantilever beam using internal resonance. *Nonlinear Dynamics*, 5(1):131–151, 1994.

[2] A. Q. Siddiqui and M. F. Golnaraghi. Vibration suppression in flexible gyroscopic system using modal coupling strategies. *Mathematical Problems in Engineering*, 2(2):107–129, 1996.

[3] P. R. Sethna. Vibrations of dynamical systems with quadratic nonlinearities. *Journal of Applied Mechanics*, 32(1):576–582, 1965.

[4] B. Balachandran and A. H. Nayfeh. Observations of modal interactions in resonantly forced beam-mass structures. *Nonlinear Dynamics*, 2(2):77–117, 1991.

[5] V. Kumar, J. K. Miller, and J. F. Rhoads. Nonlinear parametric amplification and attenuation in a base-excited cantilever beam. *Journal of Sound and Vibration*, 330(22):54015409, 2011.

[6] A. H. Nayfeh and D. T. Mook. *Nonlinear Oscillations*. Wiley, New York, 1979.

[7] S. Gutschmidt and O. Gottlieb. Bifurcations and loss of orbital stability in nonlinear viscoelastic beam arrays subject to parametric actuation. *Journal of Sound and Vibration*, 329(1):3835–3855, 2010.

[8] N. Kacem, J. Arcamone, F. Perez-Murano, and S. Hentz. Dynamic range enhancement of nonlinear nanomechanical resonant cantilevers for highly sensitive nems gas/mass sensor applications. *Journal of Micromechanics and Microengineering*, 20(4):9, 2010.

[9] S. Gutschmidt and O. Gottlieb. Nonlinear internal resonances of a microbeam array near the pull-in point. EUROMECH Conference ENOC, 2008.

Transverses linear vibration of cantilever beam carrying two lumped masses. Analogy between discrete models.

Ahmed EDDANGUIR[1], Rhali BENAMAR[2]
[1,2] University Mohammed V – Agdal,
LERSIM, Ecole Mohammadia d'Ingénieurs, Rabat, Maroc.
Email: eahmed66@hotmail.com, rbenamar@emi.ac.ma

ABSTRACT

The purpose of the present paper is to make the analogy between a physically discrete model for non-constrained linear transverse vibrations and cantilever beams carrying two lumped masses. The discrete model is N-degree of freedom system made of N masses placed at the end of solid bars connected with spiral springs. Calculations are made based on the classical vibration model involving the mass matrix $[m_{ij}]$ *and the linear rigidity matrix* $[k_{ij}]$*. The boundary conditions at the free ends are taken into account using that no flexural rigidity is present at the bar located at the free end, and for the boundary condition at the clumped end are taking into using a spiral spring with height rigidity. The numerical results show a good convergence of the first and second linear frequencies obtained by the discrete model and those obtained via the Dunkerley second formula.*

1 INTRODUCTION

A cantilever is a beam clumped on only one end and generally used in much construction, principally in cantilever bridges balconies. The cantilever beam can also be used in fixed-wing airplane. The objective of this work is to make the analogy between the cantilever beam carrying two lumped masses and the discrete model, leading to the expressions for the equivalent spiral and axial stiffness, in terms of the continuous beam geometrical and mechanical characteristics. Some numerical results are given and compared to those obtained via the Dunkerley second formula.

2 GENERAL THEORIES

2.1 Presentation of the discrete system for transverse vibration

The discrete system shown in Figure 1 is a multi-degree-of-freedom system (*N*-dof) made of *N* masses and *N+2* spiral springs, with C_l being the linear rigidities r^{th} of the *r* spiral spring. The springs are attached by identical bars of length l, which are supposed to be massless, not infinitely rigid, and made of an elastic material which may be slightly deformed. The momentum M_r in the r^{th} spiral spring is given by: $M_r = -C_r^l \theta$ [1].

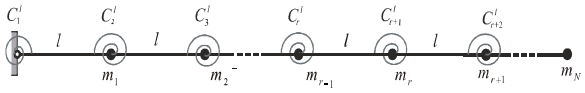

Figure 1: The multi degree of freedom discrete system

The linear potential energy stored in the *N+2* spiral springs, subjected to the rotations shown in Figure 1, can be written as:

$$V_l = \frac{1}{2}\sum_{i=1}^{N} C_i^l(\theta_i - \theta_{i-1})^2 = \frac{1}{2l^2}\left[\sum_{i=1}^{N} C_i^l\left(y_i - 2y_{i-1} + y_{i-2}\right)^2\right] \tag{1}$$

2.2 Presentation of the continuous model for transverse vibration of beams:

Consider transverse vibrations of the cantilever beam shown in Figure 2 and having the following characteristics; *E*, Young's modulus; *L*, length of beam; *S*, area of the cross section; *I*, second moment of area of cross section; $y(x,t)$, transverse displacement $y(x,t) = y(x)\sin\omega t$.

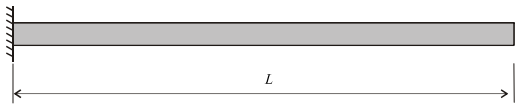

Figure 2: The clamped-free uniform beam

The linear potential energy due to the bending of a continuous beam is given by:

$$V_l = \frac{1}{2}\int_0^L EI\left(\frac{d^2y}{dx^2}\right)^2 dx = \frac{1}{2l}\sum_{i=1}^{N} E_i I(y_{i+1} - 2y_i + y_{i-1})^2 \tag{2}$$

By identification between equation (1) and equation (2), we get:

$$C_i = \frac{EI}{l} = \frac{N}{L}EI \quad \forall i,\ 2 \le i \le N+1 \tag{3}$$

2.3 Calculation of the coefficients k_{ij} of the stiffness matrix:

In order to express the linear rigidity matrix k_{ij} in terms of the beam characteristics, we recall the following expressions established in ref [2] and equation (3).

$$k_{r,r} = \frac{1}{l^2}(C_r^l + 4C_{r+1}^l + C_{r+2}^l) = \frac{I}{l^3}(E_r + 4E_{r+1} + E_{r+2}) \quad r = 1,..,N$$
$$k_{r,r+1} = -\frac{2}{l^2}(C_{r+1}^l + C_{r+2}^l) = -\frac{2I}{l^3}(E_{r+1} + E_{r+2}) \qquad r = 1,...,N-1 \tag{4}$$
$$k_{r,r+2} = \frac{C_{r+2}^l}{l^2} = \frac{E_{r+2}I}{l^3} \qquad r = 1,...,N-2$$

2.4 General terms of the rigidity matrix [K_{ij}] and the mass matrix [M_{ij}] for the uniform cantilever beam

Consider the clumped-free uniform beam shown in Figure 2, subdivided into *N* elements and the correspondent discrete system will be as follows:
The mass matrix and the rigidity matrix of this clumped-free beam are given by:

$$\left[M_{ij}\right] = \frac{\rho SL}{N}\left[m_{ij}\right] \quad ; \quad \left[K_{ij}\right] = \frac{N^3 EI}{L^3}\left[k_{ij}\right] \tag{5}$$

To obtain the linear stiffness matrix of the clumped-free beams we should have:
$C_1=3C_i$ *and* $C_{N+2}=0$, $m_i = m$ *for* $(1 \le i \le N-1)$ and $m_N = 0,5m$ with: $m = \rho SL/N$
The eigen value problem describing the linear system is given by:

$$\left[K_{ij}\right]\{X\} = \omega_n^2\left[M_{ij}\right]\{X\} \tag{6}$$

with:

$$\left[K_{ij}\right] = \frac{N^3 EI}{L^3}\begin{bmatrix} 8 & -4 & 1 & 0 & \cdots & \cdots & 0 \\ -4 & 6 & -4 & 1 & 0 & & \vdots \\ 1 & -4 & 6 & -4 & \ddots & \ddots & \vdots \\ 0 & 1 & \ddots & \ddots & \ddots & 1 & 0 \\ \vdots & \ddots & \ddots & -4 & 6 & -4 & 1 \\ \vdots & & \ddots & 1 & -4 & 5 & -2 \\ 0 & \cdots & \cdots & 0 & 1 & -2 & 1 \end{bmatrix} \qquad \left[M_{ij}\right] = \frac{\rho SL}{N}\begin{bmatrix} 1 & 0 & & \cdots & 0 \\ 0 & 1 & \ddots & & \vdots \\ & \ddots & \ddots & \ddots & \\ \vdots & & \ddots & 1 & 0 \\ 0 & & \cdots & 0 & 0{,}5 \end{bmatrix} \quad 1 \le i, j \le N \tag{7}$$

2.5 General terms of the mass matrix [M_{ij}] for the uniform cantilever beam carrying two lumped masses

Consider now a cantilever beam carrying two lumped masses M_1 and M_2 figure 3-a. In order to apply the second Dankerley formula [3] for modelling an aeroplane wing figure 3-b, as a two degrees of freedom lumped mass system, (*EI* = constant).

(a) (b)

Figure 3: cantilever beam carrying two lumped masses M_1 and M_2 (a) and the corresponding airplane wing (b)

The expression of Dunkerley second formula gives the first and second frequencies of vibration of the system figure 3-a as follows:

$\omega_{1r}^2 = \dfrac{1}{\delta_{11}M_1 + \delta_{11}M_2}$ for the first mode, and $\omega_{1r}^2 = \dfrac{\delta_{11}M_1 + \delta_{22}M_2}{\delta_{11}M_1\delta_{22}M_2 - \delta_{12}^2 M_1 M_2}$ for the second mode

with: $\delta_{11} = \dfrac{a^3}{3EI}$ $\delta_{22} = \dfrac{(L-b)^3}{3EI}$ and $\delta_{12} = \dfrac{a^2}{2EI}(L - b - a/3)$

The first and the second linear frequencies of the cantilever without lumped masses are given by:

$\omega_{01}^2 = \frac{1{,}87510^4}{L^3}\frac{EI}{M_T}$ for the first mode and $\omega_{02}^2 = \frac{4{,}69409^4}{L^3}\frac{EI}{M_T}$ for the second mode

The square of the first and second frequencies of vibration for the given real system can be calculated using the expression:

$\omega_1^2 = \frac{\omega_{01}^2\omega_{1r}^2}{\omega_{01}^2+\omega_{1r}^2}$ for the first mode and $\omega_2^2 = \frac{\omega_{02}^2\omega_{2r}^2}{\omega_{02}^2+\omega_{2r}^2}$ for the second mode

3 APPLICATION:

The characteristic of the cantilever beam is carrying two lumped masses (figure 3-a) are given in the table 1:

L (m)	a=b=L/3	S (m^2)	I (m^4)	ρ (kg/m^3)	E (N/m^2)	M_T (kg)
5	5/3	0,25	1/192	2700	7.10^{10}	3375

Table 1: characteristic of the cantilever beam made of aluminium

To obtain the linear stiffness matrix of the clumped-free beams carrying two lumped masses we should change the matrix element i.e. $m_{pp} = m(1+N\alpha_1)$ with $(p = N/3\ ;\ \alpha_1 = M_1/M_T)$ and $m_{qq} = m(1+N\alpha_2)$ $(q = 2N/3;\ \alpha_2 = M_2/M_T)$. The comparison between the linear frequencies of the first and the second mode calculated with our model and the expressions of Dunkerley second formula shows a good convergence (Table 2).

α_1	α_2	First linear mode			Second linear mode		
		$\omega(numerical)$	$\omega(Dunkerley)$	$Error(\%)$	$\omega(numerical)$	$\omega(Dunkerley)$	$Error(\%)$
0	0	103,9153	103,3611	0,5333	650,6312	647,7531	0,4423
0,1	0,2	92.9125	92.1012	0.8731	583,7035	611,1403	4,7004
0,2	0,1	97.2550	96.2750	1.0076	564,1289	588,9171	4,3940

Table 2: comparison between the numerical and Dunkerley formulas frequencies

4 CONCLUDING REMARKS

A physical model for discrete linear transverse vibrations of beams has been applied with the objective to present a cantilever beam carrying two masses. The model proposed in reference [1,2] has been valued using the analogy between the discrete system and its equivalent continuous model. The results obtained for the frequency of the linear discrete system compare well with those based on Dunkerley formulas frequencies theory [3]. Moreover, the model proposed in this work may be representative of the bending vibration of a cantilever beam with many concentred masses and different types of discontinuities. This will be developed later.

REFERENCES

[1] A. Eddanguir, Contribution à une théorie d'analyse modale non linéaire : Application aux vibrations transversales libres et forcées à non linéarités localisées des systèmes discrets à deux et à plusieurs degrés de liberté. Thèse de doctorat, Ecole Mohammadia d'Ingénieurs (Juillet 2012)

[2] A. Eddanguir, Z. Beidouri, and R. Benamar, Geometrically nonlinear transverse steady-state periodic forced vibration of multi-degree-of-freedom (N-dof) systems with a distributed nonlinearity, *Ain Shams Engineering Journal Elsevier,* september 2012.

[3] A. Igora Karnovsky and I. Olga Lebed *Book* Formulas for Structural Dynamics: Tables, Graphs and Solutions, 2004 McGraw-Hill Companies.

Authors Index